Universitat Jaume I

Departamento de Química Inorgánica y Orgánica

Instituted of advances materials

THE IMPORTANCE OF LIGAND DESIGN FOR THE DEVELOPMENT OF SUPRAMOLECULAR CATALYSTS AND ION RECEPTORS

Doctoral Thesis
Sheila Ruiz Botella
PhD. Supervisors: Prof. Eduardo Peris
Castellón de la Plana , Abril 2017

Prof. Dr Eduardo V. Peris Fajarnés, Catedràtic de l'àrea de Química Inorgànica pertanyent al Departament de Química Inorgànica i Orgànica de la Universitat Jaume I.

Certifica: Que la tesi Doctoral amb títol "The importance of ligand design for the development of supramolecular catalysts and ion receptors" ha sigut desenvolupada sota la seua direcció, en l'àrea de Química Inorgànica del Departament de Química Inorgànica i Orgànica de la Universitat Jaume I, per Sheila Ruiz Botella.

Castelló de la Plana, a

Sign. Prof. Eduardo V. Peris Fajarnés

Acknowledgements/ Agradecimientos

Antes de empezar con los agradecimientos, me gustaría hacer una pequeña reflexión acerca de todos los significados etimológicos de la palabra GRACIAS, una de las palabras más mágicas del diccionario. La palabra gracias proviene del latín, *gratia*, la cual deriva de *gratus* (agradable, agradecido). Me gustaría destacar que *gratia,* en su origen latín, significaba únicamente la honra, la alegría compartida o alabanza que sin más se tributa a otro, y que posteriormente paso a significar el favor y reconomiento de un favor. Quiero resaltar todos estos significados porque a veces el uso excesivo de las palabras hace que pierdan su trasfondo y la importancia real que tienen. De esta forma, quisiera dar las gracias a mi director de tesis, Eduardo Peris, principalmente por darme la oportunidad de formar parte de su grupo de investigación, por toda la confianza que ha depositado en mí, por todos los conocimientos que me ha transmitido y por esas discusiones científicas en su despacho, que hacían que realmente aprendiera y creciera profesionalmente. A su vez, haciendo uso de la definición inicial de la palabra *gratia* (honra o alabanza), gracias simplemente porque su pasión y dedicación por la química es insuperable.

Me gustaría dar las gracias a Macarena, por estar siempre ahí para resolverme cualquier duda, ayudarme con el Olex, corregirme documentos,…y cientos de cosas más, independientemente del montón de trabajo que tuviera por hacer. Por un motivo similar quería dar las gracias a Goyo, por su apoyo y ayuda cuando lo he necesitado. A Jose por ser tan agradable conmigo, por esa paciencia que te caracteriza y también por la ayuda ofrecida. A Susana, por todas las correcciones y la ayuda prestada durante estos meses tan duros de trabajo. A todos los ya nombrados y al resto de miembros que forman parte o han formado parte del grupo, os quiero dar las gracias por ser mi segunda familia durante estos años, por todos los momentos vividos y por todas las risas compartidas: Sara, Sergio, Candela, Arturo, Elena+, Carmen, Hugo, Víctor, David, Daniel y a la recién llegada Chiara. Entre ellos me gustaría destacar a Víctor, porque hemos compartido muchas horas juntos en el lab y hemos aprendido mil cosas el uno del otro. Ha sido un placer haber trabajado contigo. Como no, dar las gracias a esas personas que vienen por un tiempo al grupo y de las que tantas cosas aprendemos: Jo, Ian, Marco, George y Tobias.

Thanks to the Professor Dmitri Gusev for the computational studies and for your corrections. Mil gracias también al Dr. Cristian Barrera por ayudarme a introducirme en el campo de la química *host-guest*, por los cientos de masas medidos en el Q-TOF y por sus ánimos en los momentos de bajón. Y como no, gracias al Profesor Gregori Ujaque y Dr. Pietro Vidossich por los cálculos teóricos tan espectaculares que habéis realizado en mis últimos trabajos.

A todos los miembros de los servicios centrales, en especial a Gabriel Peris, por ayudarme con mis queridos cristales, y a José Miguel Pedra, por los cientos de masas medidos.

Thanks to Prof. Paul De Beer for giving me the opportunity to join his group and of course thanks to the rest of the members from the Beer group for all your help.

Por último quería dar las gracias a todos mis amig@s (PBL y Siempre juntas) y a mi familia, por vuestra compañía y apoyo incondicional durante todos estos años. Y muy especialmente quería dar las gracias a mi novio Fran, a mi hermana Sara y a mis queridos padres Mari y Alfonso, por ser el motor de mi vida, por darme tanto amor y porque simplemente todo os lo debo a vosotros. MIL GRACIAS!!

Nomenclature

The nomenclature employed to name the compounds described in this work is:

Imidazolium or benzimidazolium salts and organic molecules, which are precursors of the metallic complexes or the organic receptors: letters of the alphabet (**A**-**K**)

Metallic complexes and organic receptors: numbers and when the compound is a salt, the nomenclature employed is the corresponding number followed by its counterion.

List of abbreviations

QOMCAT	the group of organometallic chemistry at the Universitat Jaume I
NHC	N-heterocyclic carbene
rt	room temperature
EA	Elemental Analysis
ESI-TOF-MS	Electrospray Ionization Time-of flight mass spectrometry
HRMS	High resolution Mass Spectrometry
SEM	Scanning Electron Microscopy
TEM	Transmission Electron Microscopy
EDS	Energy-Dispersive X-ray Spectroscopic analysis
ICP-MS	Inductively Coupled Plasma optical Emission-Mass Spectrometry
UV/Vis	Ultraviolet/Visible
IR spectroscopy	Infrared spectroscopy
NMR	Nuclear Magnetic Resonance
GC	Gas Cromatography
DFT	Density Functional Theory
Cat.	Catalyst
COD	Cyclooctadiene

Cp*	1,2,3,4,5-pentamethylcyclopentadienyl
E	potential
CV	Cyclic Voltammetry
DPV	Differential Pulse Voltammetry
TBTA	Tris[(1-benzyl-1*H*-1,2,3-triazol-4-yl)methyl]amine
DIPEA	N,N-Diisopropylethylamine
DMF	Dimethylformamide
DMSO	Dimethylsulfoxide
iPrOH	2-propanol
M	Metal
L	Ligand
Me	Methyl
Pyr	pyrene
Pyrid	pyridine
Fc	ferrocene
Ph	phenyl
Δ	increase
J	coupling constant
d	doublet
s	singlet
m	multiplet
ppm	parts per million
t	triplet
δ	chemical shift

GO	Graphene Oxide
rGO	reduced Graphene Oxide
h	hour
Kobs	observed constant
TEP	Tolman Electronic Parameter

Thesis Description

The present thesis is divided in two different parts. Part 1 is titled the importance of ligand design for the development of supramolecular catalysts. This part includes three different chapters: introduction chapter 1, chapter 2 and chapter 3. Chapter 1 shows a brief overview of the most interesting items related to supramolecular catalysis. In chapter 2 is described the synthesis and characterization of three different *p*-xylylbis-benzimidazolylidene iridium and rhodium complexes. Chapter 3 reports the synthesis, characterization and catalytic studies of different palladium, iridium and rhodium complexes, which are formed by N-heterocyclic ligands featuring different topologies, and some of them decorated with pyrene functionalities. The importance and influence of these ligands in the conformational and catalytic behaviour of the metal complexes is studied in detail, providing evidences of the effects produces due to non-covalent interactions such as π-π interactions.

Part 2 is titled the importance of ligand design for the development of ion receptors. This part includes three chapters: introduction chapter 4, chapter 5 and chapter 6. Chapter 4 is a brief introduction of the most relevant aspects related to supramolecular host-guest chemistry. The approaches described in chapter 5 consist of two different strategies for the preparation of imidazole resorcinarene based cavitands for the recognition of anions or cations. Chapter 6 reports the synthesis of tris-azolium and tris-iodoazolium tripodal receptors for the recognition of anions. In both chapters (5 and 6) are studied the binding capabilities of the receptors towards several ions, showing the importance of the development in ligand design to improve the properties of the receptors.

Part 1: The importance of ligand design for the development of supramolecular catalysts

Chapter 1.
Introduction. Part 1

1.1 Introduction

This chapter is meant to provide a general introduction to the first part of this Ph.D. Thesis, which refers to Chapters 2 and 3. A brief overview of the most relevant aspects related to organometallic supramolecular catalysis is given. Apart from that, more specific information will be given in Chapters 2 and 3.

1.2 Supramolecular catalysis: merging supramolecular chemistry with homogeneous catalysis

The term "*supramolecular catalysis*" was introduced in 2008[1] by Van Leeuwen, and since then, a large number of articles related to this topic have been published.[2] Supramolecular catalysis refers to an application of supramolecular chemistry to the field of homogeneous catalysis. Supramolecular catalysis is inspired in enzymatic catalysis, because it is based on the use of non-covalent interactions to accelerate rates of reactions, and to achieve high selectivities.

Non-covalent interactions are difficult to predict, so the "*a priori*" chances to correctly predict a catalyst-substrate combination are low. For this reason, many of the supramolecular effects in catalysis are recognized "*post-factum*". The challenge is to determine the nature and the strength of the supramolecular interactions between the catalyst and the substrates, and to relate them with the specific changes (preferably beneficial) produced in the catalytic outcome.[3]

The control of the process in terms of reactivity and selectivity depends on the mutual interactions established between the partners along the whole catalytic cycle. Raynal and co-workers recently proposed a very useful classification of interactions that have to be considered in supramolecular catalysis.[2c] These interactions are basically of three types: (i) interactions between ligands, (ii) interactions between a ligand and an additive, and (iii) interactions between a ligand and a substrate. These types of interactions are depicted in Scheme 1.1.

Ligand-ligand interactions may occur by the non-covalent binding of ligands from two molecules of catalyst (*inter* ligand-ligand interaction). A dimer will be formed whose reactivity –or catalytic activity- is different compared to the activity shown by the mother monomer. The ligand-ligand interaction may also occur between ligands from the same catalyst, and this is known as *intra* ligand-ligand interaction.

Ligand-additive interactions may happen when an additive is added to the vessel of the catalytic reaction, and a non-covalent interaction between the additive and one of the ligands of the catalyst is produced. This produces a change in the steric and/or electronic properties of the ligand, and thus a modification of the activity of the catalyst is produced.

Finally, a substrate-ligand interaction involves the non-covalent binding of a substrate and a ligand. This interaction may place the substrate in a privileged position, favouring its interaction with the metal centre.

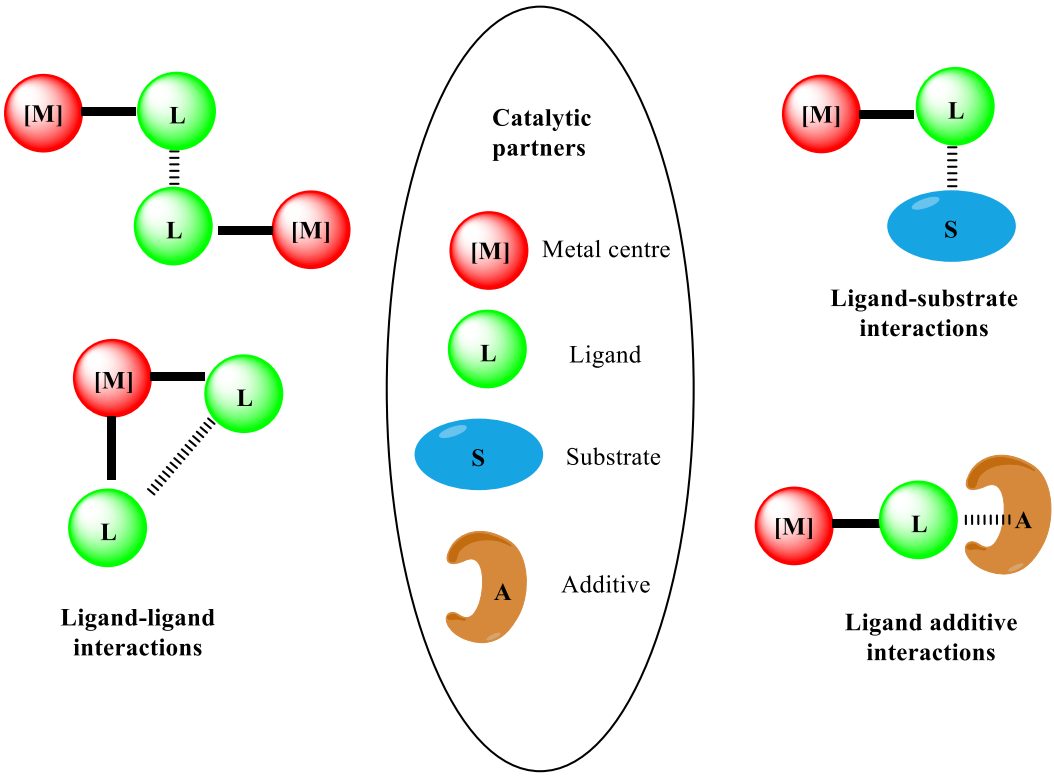

Scheme 1.1. Supramolecular interactions in catalysis

Most of the studies regarding the use of supramolecular interactions in catalysis refer to the control of the reaction paths for mediating a high selectivity.[4]

An excellent example of the role of π-π interactions on the selectivity of a catalytic reaction was described by van Leeuwen and co-workers in 2010.[4f] The ligand shown in Scheme 1.2 was found to improve the selectivity in the rhodium-catalyzed hydroformylation reaction of olefins. An interesting trend between the *ee* values, obtained for the branched aldehyde products, and the value of the σ-Hammet constant of the respective *p*-substituted styrene substrates was found. The selectivity was attributed to a π-π interaction occurring between the P-aromatic rings of the phosphole moiety and

the phenyl group of the styrene substrates, which plays an important role in the stabilization of the reaction intermediate and undergoes in an improvement of the selectivity.[4f]

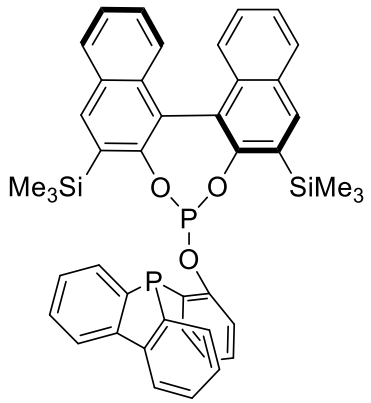

Scheme 1.2. Structures of phenol-phosphine compound

The use of $(DHQD)_2PYDZ$ (dihydroquinine 1,4-pyridazinediyl diether) and other related bis-cinchona alkaloid ligands, allowed achieving higher rates and enantioselectivities[5] in the OsO_4-catalized asymmetric *cis*-hidroxylation of olefins. There was a long-lasting debate about the mechanistic reasons governing the enantioselectivity of this reaction. Finally, several studies supported that the formation of a binding pocket[5a,6] is essential to accommodate hydrophobic substrates (styrenes,[6b] 2-vinylnaphtalene,[6b] allylic[6a] and homoallylic[7] alcohol derivatives) by non-covalent interactions, such as π-π interactions between the substrates and the methoxyquinoline rings of the bis-cinchona ligand. Scheme 1.3 shows the transition state that leads to the observed enantiomer for the hydroxylation of styrene.

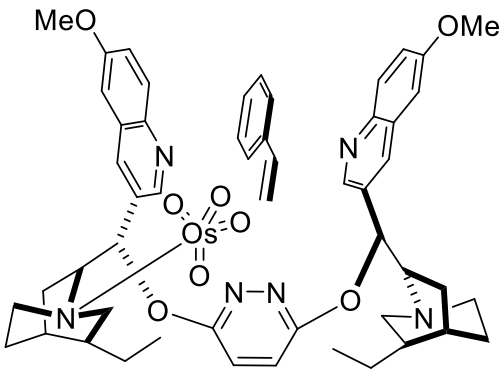

Scheme 1.3. Representation of the complex of styrene, OsO_4 and $(DHQD)_2PYDZ$ ligand, which leads to the observed enantiomer for the hydroxylation of styrene

Despite the large number of examples regarding the influence of supramolecular interactions in the improvement of selectivities in homogeneous catalysis, few examples have been focused on the catalytic consequences related with the modification of the activity or kinetic parameters due to reasons related to supramolecular interactions.[8] In fact, most of the examples regarding this type of studies were developed by the QOMCAT group during the last five years, as will be described in the next sections.

Clear evidences of the influence of π-staking and catalysis were reported by Grela and co-workers back in 2008.[9] Their results demonstrated that interactions between aromatic fluorinated solvent molecules and the aromatic ligands of second generation Ru-Grubbs catalysts can significantly influence the activity of the olefin methatesis reactions (Scheme 1.4).[8b] Computational studies indicated that these interactions contribute to the stabilization of the ruthenium active species.[8b] In fact, several authors had previously proposed that π-π staking interactions should play an important role in the Ru-catalyzed methatesis reactions.[10]

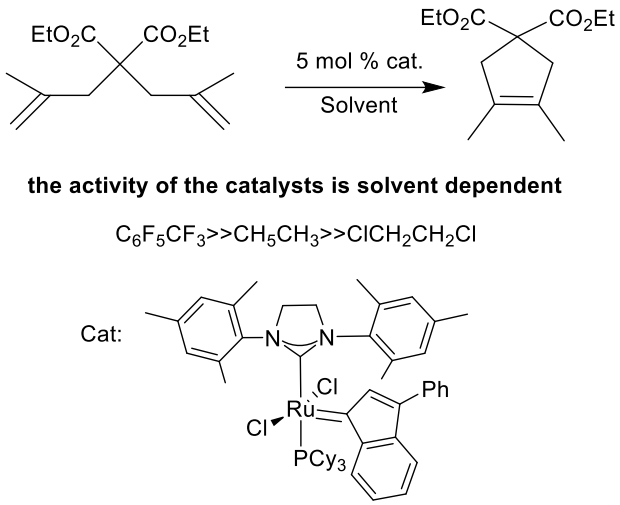

Scheme 1.4. Influence of the fluorinated aromatic solvents in the activity of the Ru-Grubbs catalyst in the olefin metathesis

Π-stacking interactions may be boosted if the ligand is functionalized with rigid polyaromatic functionalities. An interesting example of this approach was developed by Peinador, Quintela and co-workers, who described a Pt(II) diazapyrenium-based metallacycle, which they used as a reusable catalyst for the S_NAr reaction between halodinitrobenzenes and sodium azide.[8a] The authors observed that the addition of pyrene to the reaction mixture resulted in the formation of an inclusion complex

between pyrene and the metallacycle, which had a regulatory effect over the system, resulting in allosteric-like inhibition of the S_NAr reaction (Scheme 1.5).

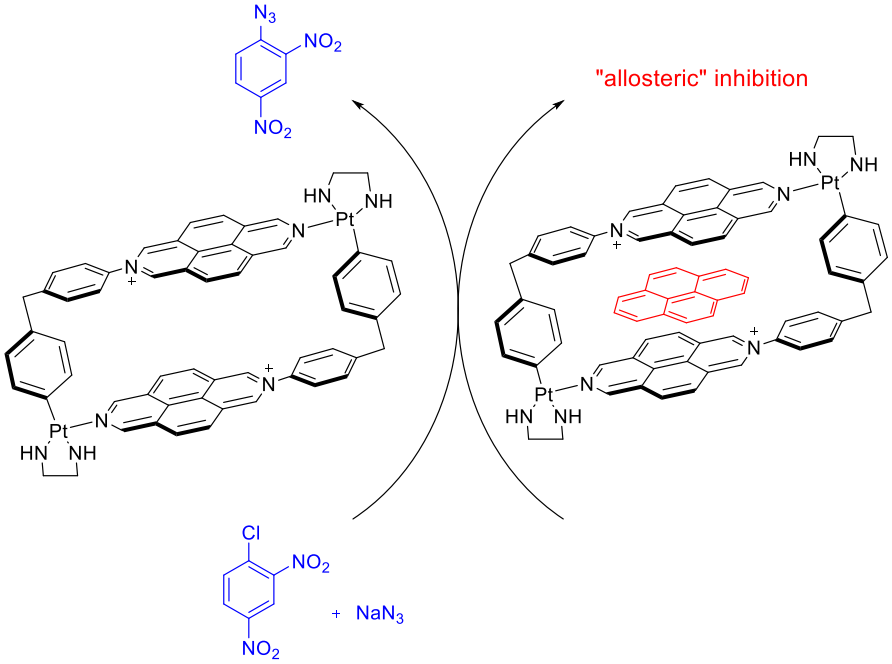

Scheme 1.5. Representation of the S_NAr reaction carry out by the Pt(II) diazapyrenium-based metallacycle and the "allosteric" inhibition under the presence of pyrene additive

Related to all this, in the next section is provided a summary of the most relevant results developed by the group of organometallic chemistry at the Universitat Jaume I (QOMCAT), regarding the catalytic consequences of using NHC ligands decorated with rigid polyaromatic fragments in homogenous catalysis.

1.3 Catalysts with π-conjugated extended ligands and π-staking interactions

1.3.1 The ligand-substrate interaction

During the last few years, the QOMCAT group focused the attention on the preparation of a number of ditopic and tritopic N-heterocyclic carbenes (NHCs) connected by π-extended polyaromatic rings (Scheme 1.6). This was initially made pursuing two objectives: (1) to find neat examples of catalytic cooperativity between the metals comprising the multimetallic catalyst, and (2) to prepare heterometallic catalysts for the design of tandem reactions by the combination of mechanistically distinct reactions.[11]

Initially, it was believed that the extended polyaromatic systems should facilitate the electronic communication between metals, but the fact is that the electronic

communications was negligible in most of the cases.[8c,8e,12] The ligands under study were the ones depicted in Scheme 1.6. Except for the benzobisimidazolylidene ligand (**B**) described by Bielawski and co-workers in 2005,[13] the rest of the ligands were prepared by the QOMCAT group or in collaborative works.[8c,8g,12b,14]

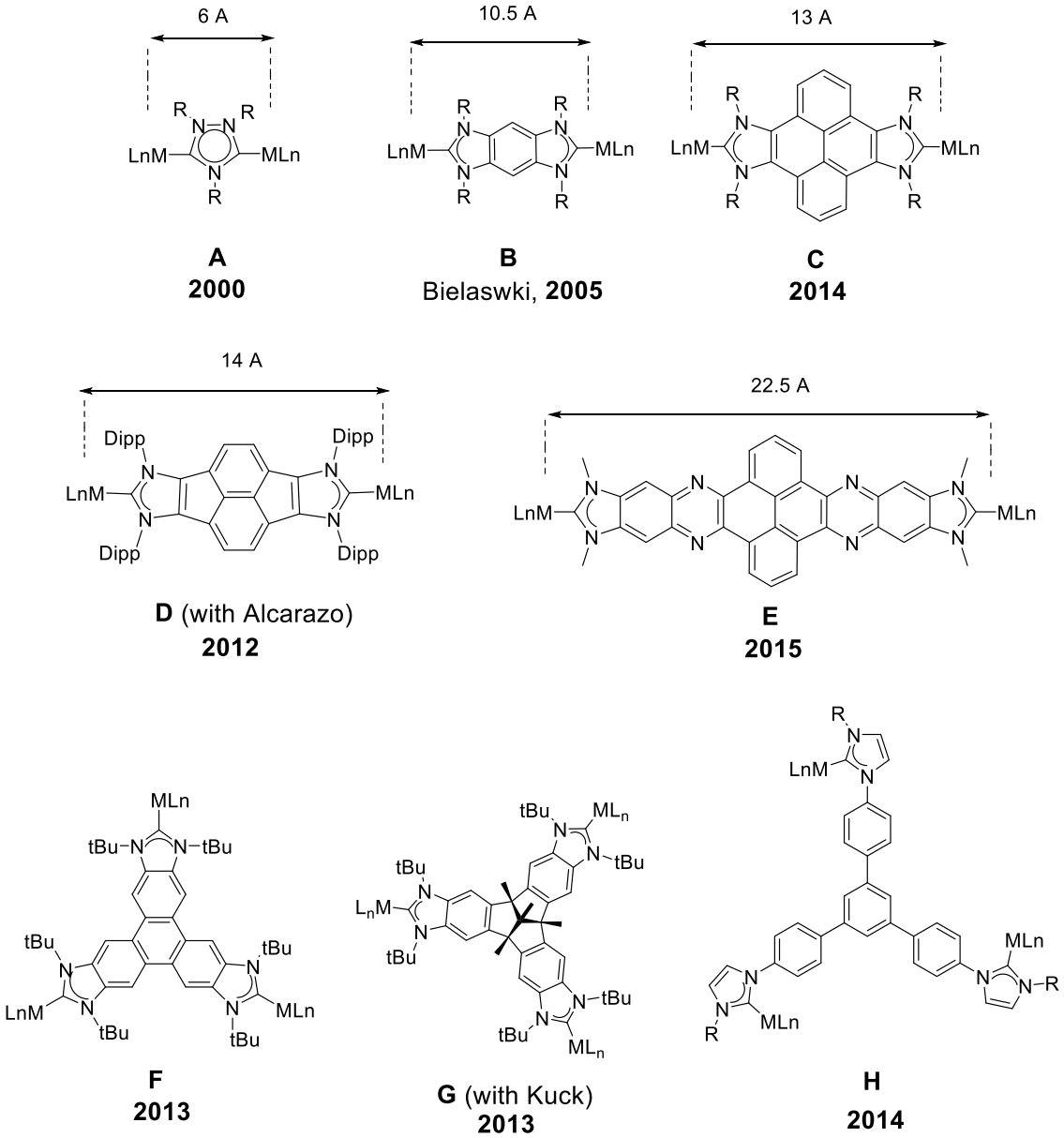

Scheme 1.6. Some representative poly-NHC ligands with extended aromatic fragments

A common feature of all the ligands depicted in Scheme 1.6 is that their related metal complexes often display better catalytic performances than their monometallic analogues. It was initially hypothesized that these benefits could be attributed to supramolecular effects, mostly due to π-π-interactions between the ligand of the catalyst and the substrates used. Detailed studies were carried out in order to confirm this idea.

The first evidences of the influence of π-stacking interactions between aromatic substrates and a polyaromatic-based NHC ligand were observed for the triphenylene-tris-imidazolylidene-based palladium and gold catalysts **5** and **6** shown in Scheme 1.4.[8g] These trimetallic complexes may be regarded as the exact combination of three molecules of the related monometallic benzimidazolylidene complexes (**7** and **8,** Scheme 1.7). For this reason, the studies of their catalytic performances constituted an excellent opportunity to compare the activity of the trimetallic complexes with their closest related monometallic analogues. The studies were carried out by comparing the catalytic efficiency of the catalysts in three different reactions (the palladium-catalysed π-arylation of propiophenone with aryl bromides, the Suzuki-Miyaura coupling between aryl bromides and aryl boronic acids and the gold-catalysed hydroamination of phenylacetylene).

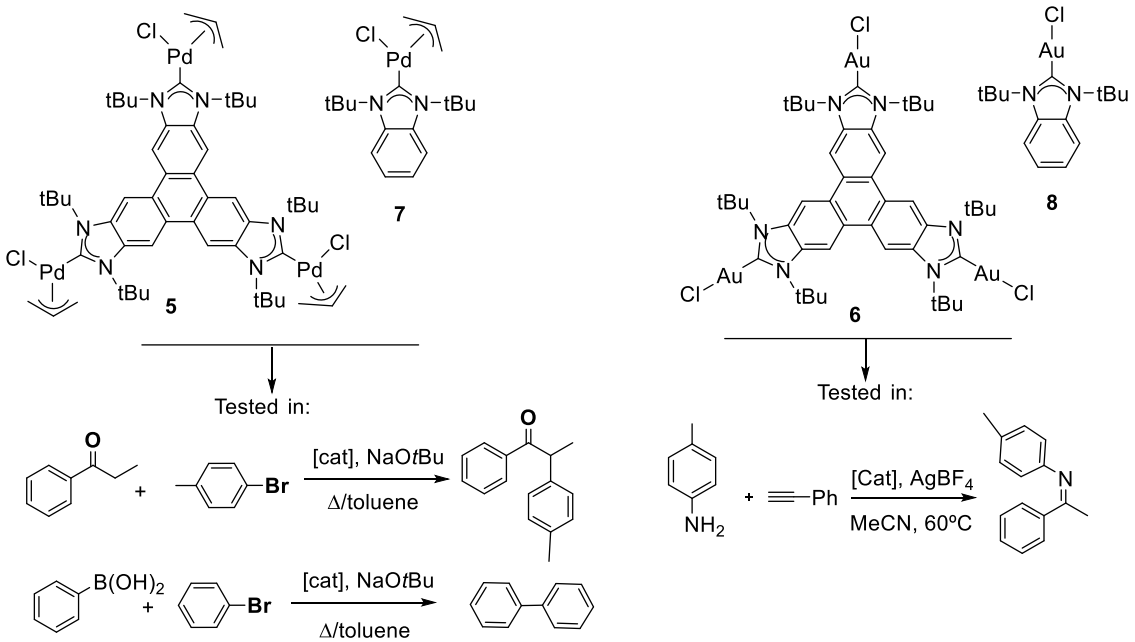

Scheme 1.7. Triphenylene-based NHC complexes of palladium and gold, the related monometallic analogues and catalytic reaction tested

The results demonstrated that the catalytic activity of **5** and **6** was higher than the activity of the monometallic analogue complexes. The higher activity shown by these two complexes was hypothesized to be consequence of the π-stacking interaction between the triphenylene core of the catalysts and the aromatic substrates, which should have an effect on the catalytic performance of the catalysts. One of the main supports of this hypothesis was the fact that the addition of catalytic amounts of π-stacking

additives, such as pyrene or hexafluorobenzene, produced the partial inhibition of the activity of **5** and **6**.

1.3.2 Influence of the ligand-additive interaction in the electronic properties of ligands with extended polyaromatic fragments

The preparation of a series of mono-NHC ligands decorated with polyaromatic functionalities was useful to study the influence of the π-stacking additives on the electronic properties of the NHC ligands.

The electrochemical studies of a series of [NiClCp(NHC)] complexes (NHC = imidazolylidene, benzimidazolylidene and pyrene-imidazolylidene **9-11**, respectively) were carried out. The Cyclic Voltammetric (CV) titration of the complexes with a π-stacking additive, such as pyrene, yielded interesting information (Scheme 1.8).[8f] While the imidazolylidene and benzimidazolylidene nickel complexes were relatively insensitive to the addition of pyrene (maximum positive shift of the half-wave potential observed, $\Delta E_{1/2}$ = 20-30 mV), the addition of pyrene to the pyrene-imidazolylidene complex of nickel (**11**) produced a maximum positive shift of the potential of 75 mV. This result demonstrated that the complex with the pyrene-imidazolylidene ligand was the one to show the most pronounced effect upon addition of pyrene, thus strongly suggesting that the π-stacking between pyrene added and the pyrene core of the ligand is taking place.[8f]

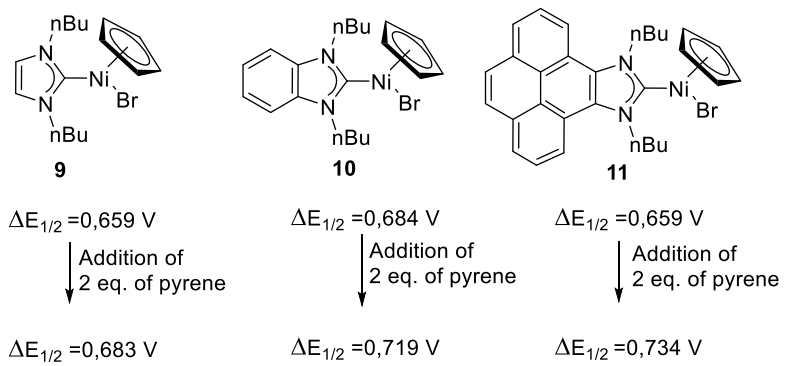

Scheme 1.8. Effect of the addition of pyrene on the redox potential of three NHC complexes of nickel (II)

The analysis of the IR spectra of a series of [IrCl(NHC)$(CO)_2$] complexes allowed to experimentally quantify the variation of the C-O stretching upon the addition of pyrene or hexafluorobenzene (Scheme 1.9).[8d] The variations were negligible for the imidazolylidene and benzimidazolylidene complexes (**12** and **13**, respectively). However, the rest of the compounds with extended polyaromatic fragments revealed

significant variations of the C-O stretching frequencies, thus indicating that the interaction between the extended polyaromatic ligand and the π-stacking additive had important implications in the modification of the electronic character of the NHC ligand. In all cases, the addition of hexafluorobenzene produced a decrease of the C-O frequency, while the addition of pyrene produced the opposite effect.

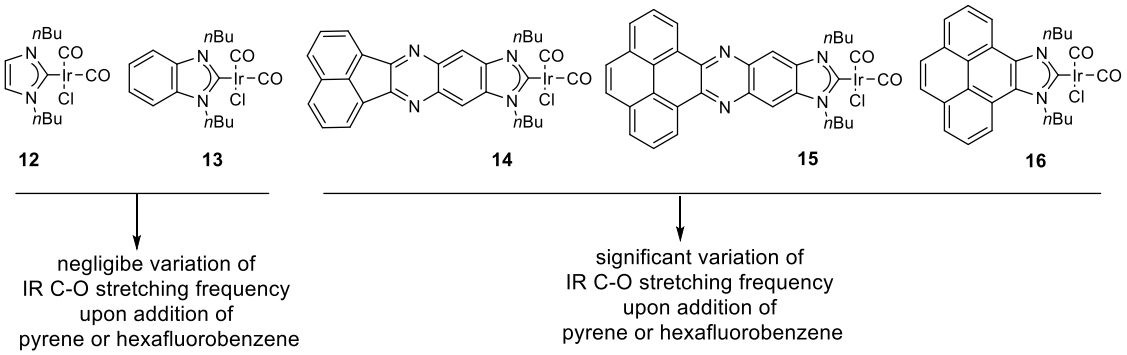

Scheme 1.9. Qualitative variation of the IR C-O stretching frequencies of a series of $[IrCl(NHC)(CO)_2]$ upon addition of pyrene or hexafluorobenzene

These results demonstrated, the electronic character of the ligand should be post-modified by adding the suitable π-stacking additive.[8d]

1.4 Objectives

During the last few years, the main focus of the QOMCAT group was the development of new NHC-based ligands with extended polyaromatic systems for the preparation of novel homogenous catalysts with magnified supramolecular properties. This should facilitate the study of the nature and strength of non-covalent interactions in catalysis. In continuation with this general objective, the work described in Chapters 2 and 3 was developed in order to achieve the following goals:

- To find new forms of coordination complexity, by preparing fluxional cyclophane azolium salts, for the generation of fluxional isolated bis-NHC cyclophane ligands and their related rhodium and iridium metal complexes. Study and analysis of their geometries
- Preparation of NHC-based metal complexes with extended polyaromatic fragments for the rational evaluation of the intimate effects produced by π-staking interactions in catalysis.
- Kinetic studies in order to distinguish between all the possible types of supramolecular interactions produced along the catalytic reaction.

1.5 References

(1) *Supramolecular Chemistry*; Leeuwen, P. W. N. M. V., Ed.; Wiley-VCH, Weinheim: Germany, **2008**.

(2) a) Hermann, K., Ruan, Y., Hardin, A. M., Hadad, C. M., Badjic, J. D. *Chem. Soc. Rev.* **2015**, *44*, 500-514; b) Brown, C. J., Toste, F. D., Bergman, R. G., Raymond, K. N. *Chem. Rev.* **2015**, *115*, 3012-3035; c) Raynal, M., Ballester, P., Vidal-Ferran, A., van Leeuwen, P. *Chem. Soc. Rev.* **2014**, *43*, 1660-1733; d) Leenders, S., Gramage-Doria, R., de Bruin, B., Reek, J. N. H. *Chem. Soc. Rev.* **2015**, *44*, 433-448; e) Koblenz, T. S., Wassenaar, J., Reek, J. N. H. *Chem. Soc. Rev.* **2008**, *37*, 247-262; f) Raynal, M., Ballester, P., Vidal-Ferran, A., van Leeuwen, P. W. N. M. *Chem. Soc. Rev.* **2014**, *43*, 1734-1787.

(3) Peris, E. *Chem. Commun.* **2016**, *52*, 5777-5787.

(4) a) Knowles, R. R., Jacobsen, E. N. *Proc. Natl. Acad. Sci. U. S. A.* **2010**, *107*, 20678-20685; b) Brak, K., Jacobsen, E. N. *Angew. Chem. Int. Ed.* **2013**, *52*, 534-561; c) Corey, E. J., Loh, T. P. *J. Am. Chem. Soc.* **1991**, *113*, 8966-8967; d) Corey, E. J., Loh, T. P., Roper, T. D., Azimioara, M. D., Noe, M. C. *J. Am. Chem. Soc.* **1992**, *114*, 8290-8292; e) Hayashi, Y., Rohde, J. J., Corey, E. J. *J. Am. Chem. Soc.* **1996**, *118*, 5502-5503; f) Doro, F., Reek, J. N. H., van Leeuwen, P. *Organometallics* **2010**, *29*, 4440-4447; g) Goudriaan, P. E., Kuil, M., Jiang, X. B., van Leeuwen, P., Reek, J. N. H. *Dalton Trans.* **2009**, 1801-1805.

(5) a) Corey, E. J., Noe, M. C. *J. Am. Chem. Soc.* **1996**, *118*, 11038-11053; b) Nelson, D. W., Gypser, A., Ho, P. T., Kolb, H. C., Kondo, T., Kwong, H. L., McGrath, D. V., Rubin, A. E., Norrby, P. O., Gable, K. P., Sharpless, K. B. *J. Am. Chem. Soc.* **1997**, *119*, 1840-1858; c) DelMonte, A. J., Haller, J., Houk, K. N., Sharpless, K. B., Singleton, D. A., Strassner, T., Thomas, A. A. *J. Am. Chem. Soc.* **1997**, *119*, 9907-9908.

(6) a) Corey, E. J., Guzmanperez, A., Noe, M. C. *J. Am. Chem. Soc.* **1994**, *116*, 12109-12110; b) Kolb, H. C., Andersson, P. G., Sharpless, K. B. *J. Am. Chem. Soc.* **1994**, *116*, 1278-1291; c) Corey, E. J., Noe, M. C., Sarshar, S. *Tetrahedron Lett.* **1994**, *35*, 2861-2864.

(7) Corey, E. J., Guzmanperez, A., Noe, M. C. *Tetrahedron Lett.* **1995**, *36*, 3481-3484.

(8) a) López-Vidal, E. M., Fernández-Mato, A., García, M. D., Pérez-Lorenzo, M., Peinador, C., Quintela, J. M. *J. Org. Chem.* **2014**, *79*, 1265-1270; b) Samojlowicz,

C., Bieniek, M., Pazio, A., Makal, A., Wozniak, K., Poater, A., Cavallo, L., Wojcik, J., Zdanowski, K., Grela, K. *Chem. Eur. J.* **2011**, *17*, 12981-12993; c) Valdés, H., Poyatos, M., Peris, E. *Organometallics* **2015**, *34*, 1725-1729; d) Valdés, H., Poyatos, M., Peris, E. *Inorg. Chem.* **2015**, *54*, 3654-3659; e) Gonell, S., Poyatos, M., Peris, E. *Chem. Eur. J.* **2014**, *20*, 9716-9724; f) Valdés, H., Poyatos, M., Ujaque, G., Peris, E. *Chem. Eur. J.* **2015**, *21*, 1578-1588; g) Gonell, S., Poyatos, M., Peris, E. *Angew. Chem. Int. Ed.* **2013**, *52*, 7009-7013.

(9) Bieniek, M., Michrowska, A., Usanov, D. L., Grela, K. *Chem. Eur. J.* **2008**, *14*, 806-818.

(10) a) Ledoux, N., Allaert, B., Pattyn, S., Mierde, H. V., Vercaemst, C., Verpoort, F. *Chem. Eur. J.* **2006**, *12*, 4654-4661; b) Fürstner, A., Thiel, O. R., Ackermann, L., Schanz, H.-J., Nolan, S. P. *J. Org. Chem.* **2000**, *65*, 2204-2207.

(11) Mata, J. A., Hahn, F. E., Peris, E. *Chem. Sci.* **2014**, *5*, 1723.

(12) a) Mas-Marza, E., Mata, J. A., Peris, E. *Angew. Chem. Int. Ed.* **2007**, *46*, 3729-3731; b) Prades, A., Peris, E., Alcarazo, M. *Organometallics* **2012**, *31*, 4623-4626.

(13) a) Boydston, A. J., Williams, K. A., Bielawski, C. W. *J. Am. Chem. Soc.* **2005**, *127*, 12496-12497; b) Boydston, A. J., Bielawski, C. W. *Dalton Trans.* **2006**, 4073-4077; c) Boydston, A. J., Rice, J. D., Sanderson, M. D., Dykhno, O. L., Bielawski, C. W. *Organometallics* **2006**, *25*, 6087-6098; d) Khramov, D. M., Boydston, A. J., Bielawski, C. W. *Angew. Chem. Int. Ed.* **2006**, *45*, 6186-6189.

(14) a) Segarra, C., Linke, J., Mas-Marza, E., Kuck, D., Peris, E. *Chem. Commun.* **2013**, *49*, 10572-10574; b) Mejuto, C., Guisado-Barrios, G., Peris, E. *Organometallics* **2014**, *33*, 3205-3211.

Chapter 2.
Coordination Singularities of a bis(*p*-xylyl)bis(benzimidazolylidene) ligand and the bis-iridium and –rhodium –Related complexes

2.1 Introduction

During the last few years, N-heterocyclic carbene (NHC) complexes have been massively used in the design of homogeneous catalysts due to several reasons, such as:

- NHC-based metal complexes are often very robust compounds due to strong M-C bond.
- NHC ligands are very versatile from the coordination point of view, in the sense that they can provide a wide variety of topologies, and they can be incorporated into many different metal fragments.
- NHC precursors (often azolium salts), are ready accessible, therefore the library of easy-accessible NHC ligands is almost limitless.

Attracted by their topology and fluxional behaviour, we fixed our attention onto cyclophanes since their singular topological properties did not seem to have been explored in the field of homogeneous catalysis. The name of *cyclophane* was coined for compounds in which two benzene rings are held in a face to face orientation by methylene bridges in *para* positions.[1] The most recent recommendation of the IUPAC defines cyclophanes as compounds having (i) *mancude* (maximum number of *non*cumulative double bonds)-ring systems, or assemblies of mancude-ring systems, and (ii) atoms and/or saturated or unsaturated chains as alternate components of a large ring. Pellegrin et al, was the pioneer in the history of cyclophane chemistry with the preparation of [2,2]metacyclophane.[2] Later on, Cram and Steinberg developed new cyclophanes and proposed the class name paracyclophanes.[1b,3]

Associated with their great flexibility, bis-azolium-based cyclophanes[4] are known for showing intriguing conformational behaviour. In fact, their chemistry is based on the challenges related to their synthesis, fluxional behaviour and potential applications in anion recognition. As NHC precursors, cyclophane- based bis-azolium salts have been used in the preparation of a huge variety of complexes, which normally display a chelate coordination with a *syn* (boat) disposition of the azole rings,[5] although several examples are known in which this type of ligands is bridging two metal units (Scheme 2.1 **A** and **B**).[4d,5c,6]

Cyclophane- based bis-azolium salts linked by xylyl groups are a very interesting class of cyclophanes, and their fluxional behaviour has been studied in detail.[4e,4f,7] Among them, those with *ortho*- and *meta*- xylyl disubstituted patterns have been used in the

preparation of several NHC-based metal complexes.[4a,4d,5b,8] However, to the best of our knowledge, there were no examples in the literature of a cyclophane bis-NHC metal complex containing the *para*-xylyl bridge.

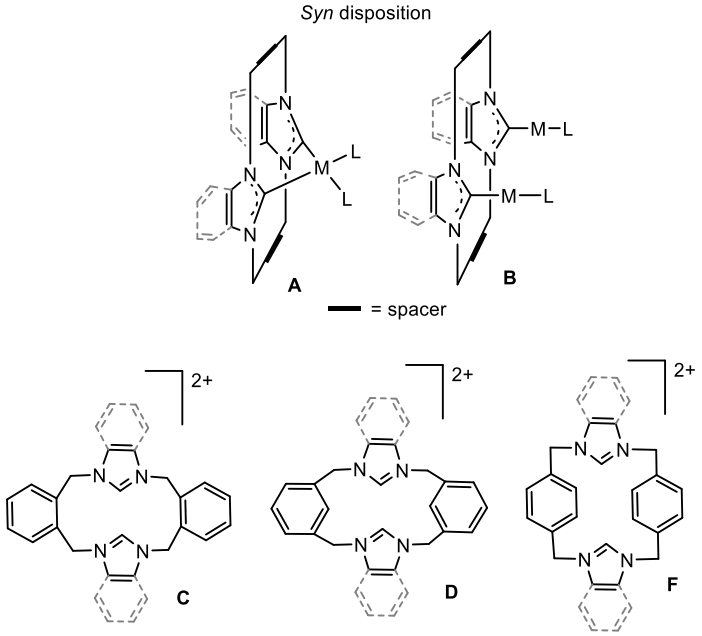

Scheme 2.1. Cyclophane-based-bis NHC complexes (above) and bis-azoliums (below)

Attracted by the complexity of the fluxional behaviour of these NHC-based cyclophanes, we decided to explore the coordination abilities of the *p*-xylyl-bis-benzimidazolium salt with different iridium and rhodium metal precursors, and study the structural features of the resulting NHC-metal products. Herein, the following sections will be devoted to the synthesis, characterization and properties of several metal complexes containing this fluxional cyclophane ligand.

2.2 Results and discussion

2.2.1 Synthesis and characterization of 1,1´,3,3´-bis(α,α´,-p-xylyl)bis(benzimidazolium) dichloride salt (A).

For the preparation of 1,1´,3,3´-bis(α,α´,-*p*-xylyl)bis(benzimidazolium) dichloride salt (**A**), we reproduced the synthesis reported by Cabildo and co-workers (Scheme 2.2).[4e] A mixture of benzimidazole, α,α´-dichloro-*p*-xylene and KOH in acetonitrile was stirred during 12 h under reflux (Scheme 2.2). The reaction was allowed to cool down to room temperature. Finally, the entitled compound **A** was obtained pure by recrystallization in ethanol (60% yield).

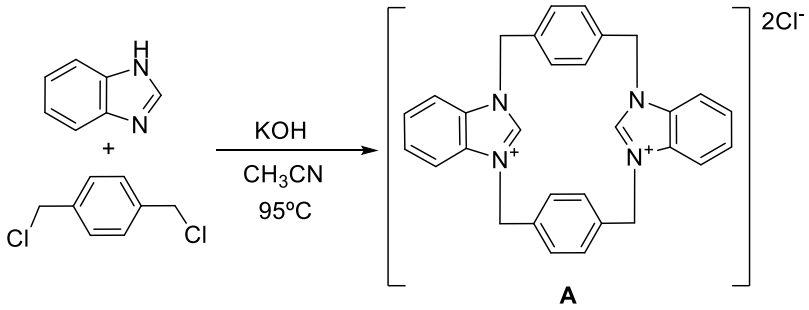

Scheme 2.2. 1,1´,3,3´-bis(α,α´,-*p*-xylyl)bis(benzimidazolium) dichloride (**A**)

In order to get some insight about the structural features of **A**, suitable crystals for X-ray diffraction of **A** were obtained by slow evaporation of a solution of the bis-imidazolium salt in methanol.

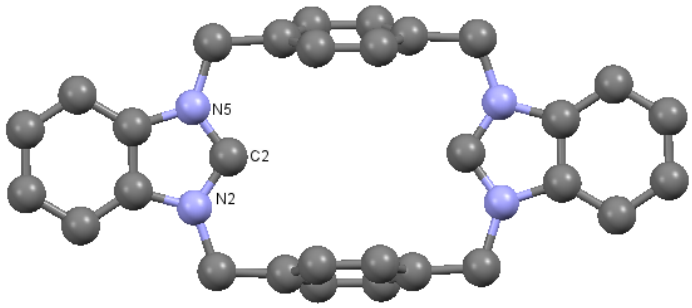

Figure 2.1. Molecular structure of **A** is shown. Solvent (CH_2Cl_2), counter ion ($2Cl^-$) and hydrogen atoms have been omitted for clarity. Ellipsoids are at 50% of probability. Selected bond distances (Å) and angles (°): C(2)-N(2) 1.328(3), C(2)-N(5) 1.335(3), N(2)- C(2)- N(5) 110.29(19)

Figure 2.1 shows the molecular structure of **A** and a list of the selected distances and angles. The two benzimidazolium fragments are connected by two *p*-xylyl linkers. The two phenyl rings from the xylyl groups deviate from coplanarity in 21.71°. The two benzimidazoliums are coplanar, and are facing one to each other by their C2-H functionalities. An interesting feature about this structure, is that the distance between the two C2 carbons is 5.2 Å, therefore exceeding the sum of two potential M-$C_{carbene}$ distances, which should typically range between 3.8-4.3 Å.[9] This observation indicates that the bis-NHC ligand resulting from the deprotonation of this bis-azolium salt, should be unable to coordinate the two NHC fragments to a single metal, and therefore, the bis-NHC is expected to solely be able to coordinate in the bridging form to two metal fragments.

2.2.2 Synthesis and characterization of metal complexes

2.2.2.1 *Synthesis and characterization of complex **1***

Compound **1** was obtained through a transmetallation reaction as depicted in Scheme 2.3. First, the corresponding bis-NHC-silver derivative is prepared by reacting **A** with 1 equivalent of Ag_2O at room temperature during 9 h in CH_2Cl_2, followed by the addition of the iridium metal precursor $[IrCp^*Cl_2]_2$ and stirring was maintained at room temperature overnight. The resulting mixture was filtered over celite and the solvent was removed under reduce pressure. Precipitation from CH_2Cl_2/diethyl ether gave **1** as a yellow solid, which was recrystallized in methanol (50% yield).

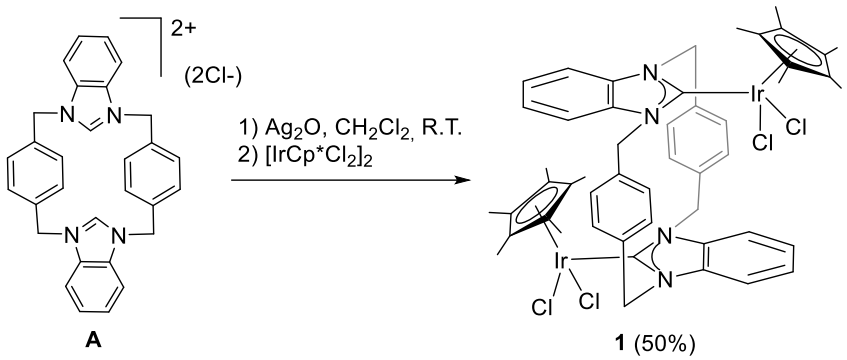

Scheme 2.3. Synthesis of complex **1**

The dimetallic nature of the complex was confirmed by high resolution mass spectrometry (HRMS), showing two main peaks at m/z 1192.3075 and 583.1482, assigned to $[M\text{-}Cl]^+$ and $[M\text{-}2Cl]^{2+}$, respectively. The conformation of the complex was elucidated by NMR spectroscopy and by X-ray diffraction, and it will be discussed in more details in the next few paragraphs.

Once the dimetallic nature of **1** was confirmed, we analyzed the different conformations that may arise from the coordination of the bis-benzimidazolylidene ligand in **1**. There are two possible configurations *syn* (boat) or *anti* (chair) that will arise depending on the orientation of the benzimidazolylidene fragments (see Scheme 2.4). In addition, three possible atropisomers for each *syn* or *anti* forms may be obtained depending whether the relative orientation of the metals is *in* or *out*. The *in* and *out* labels, are referred to the orientation of the Cp* ring relative to the two parallel planes formed by the benzimidazolylidenes (*in*, Cp* is between the planes; *out*, Cp* is outside the planes). Taking into account all these possibilities, a total of six different atropisomers may be

formed, (displayed in Scheme 2.4). From a perusal of the different conformations, can be predicted that the *syn* conformation of the ligand should afford a highly encumbered situation arising from the close proximity of the two bulky metal fragments, and therefore we considered this conformation highly unlikely.

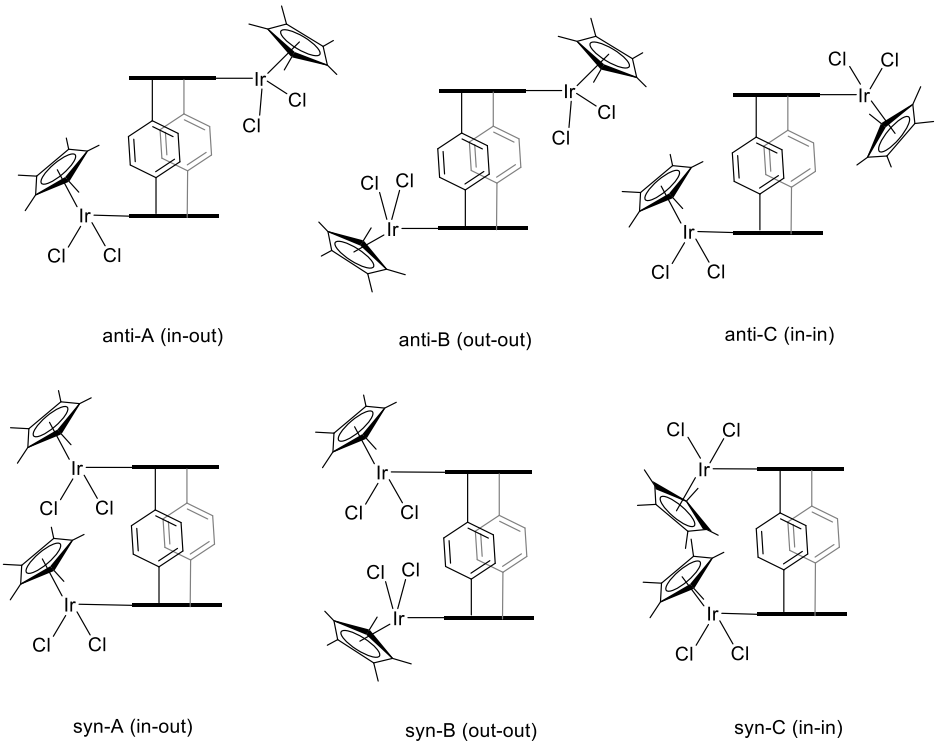

Scheme 2.4. Six possible isomers resulting from the *anti* and *syn* conformation of the ligand

*^{1}H NMR spectrum of **1***

Figure 2.2 shows the ^{1}H NMR spectrum of **1**. This spectrum suggests that the two metal centres are surrounded by different coordination environments. This conclusion arises, for example, from the presence of two different sets of signals corresponding to the protons of the methyl groups (**d**) of the Cp* rings at 1.38 and 0.76 ppm, which indicates that the two Cp* ligands (and therefore the two metal fragments) are in different chemical environments. The inequivalence of the two metal fragments is also consistent with the number of signals due to the CH_2 protons, which appear as four different doublets at 6.84 ($^3J_{H\text{-}H}$=14.2 Hz), 5.86 ($^3J_{H\text{-}H}$=16.8 Hz), 5.60 ($^3J_{H\text{-}H}$=16.8 Hz) and 4.90 ($^3J_{H\text{-}H}$=14.1 Hz) ppm (**c**). The signals assigned to the aromatic protons of the xylyl groups are two doublets ($^3J_{H\text{-}H}$=8.7 Hz) at 7.38 and 6.48 ppm (**b**). The resonances due to the aromatic benzimidazole protons (**a**) appear as four multiplets at 7.53, 7.23, 6.98 and 7.38 ppm.

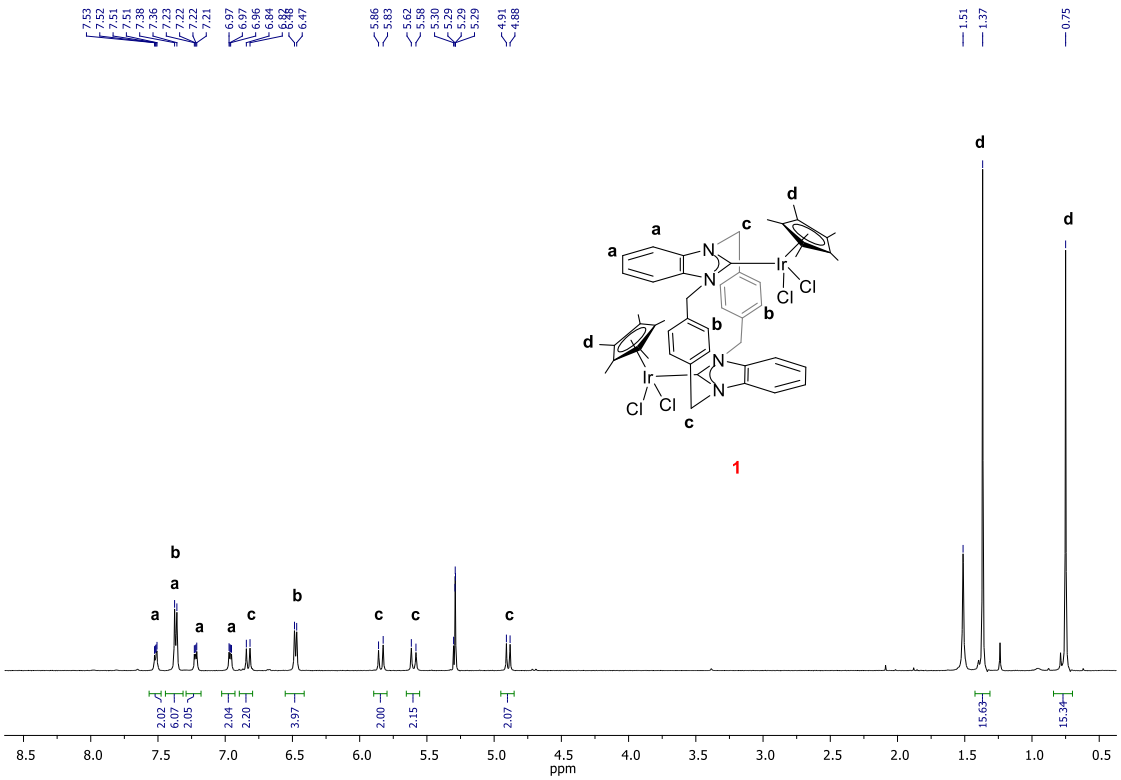

Figure 2.2. ^{1}H NMR spectrum of **1** in CD_2Cl_2.

*^{13}C {^{1}H} NMR spectrum of **1***

The ^{13}C {^{1}H} NMR spectrum of **1** is shown in Figure 2.3. Again, the number of signals is consistent with the two metals in a different environment. The most direct evidence is the appearance of two different peaks at low field, 179.4 and 167.2 ppm respectively, which corresponds to two carbene carbons (**1**). The signal at 138.1 ppm (**2**) was assigned to the quaternary xylyl carbon atoms. The peaks at 136.7 and 136.5 ppm (**3**) were attributed to the quaternary benzimidazole carbons. The chemical shift of the *C*H xylyl carbon atoms is 129.0 and 126.2 ppm (**4**) respectively. The benzimidazole *C*H carbons show their resonances at 124.3, 123.0, 111.4 and 110.7 ppm (**5**). The quaternary carbon atoms of the two Cp* rings resonance appear at 90.7 and 89.1 ppm (**6**). The signals due to the aliphatic *C*H$_2$ carbons appear at 50.9 and 49.0 ppm (**7**). Finally, the resonance due to the methyl carbons of the Cp* ring appears at 8.2 ppm (**8**).

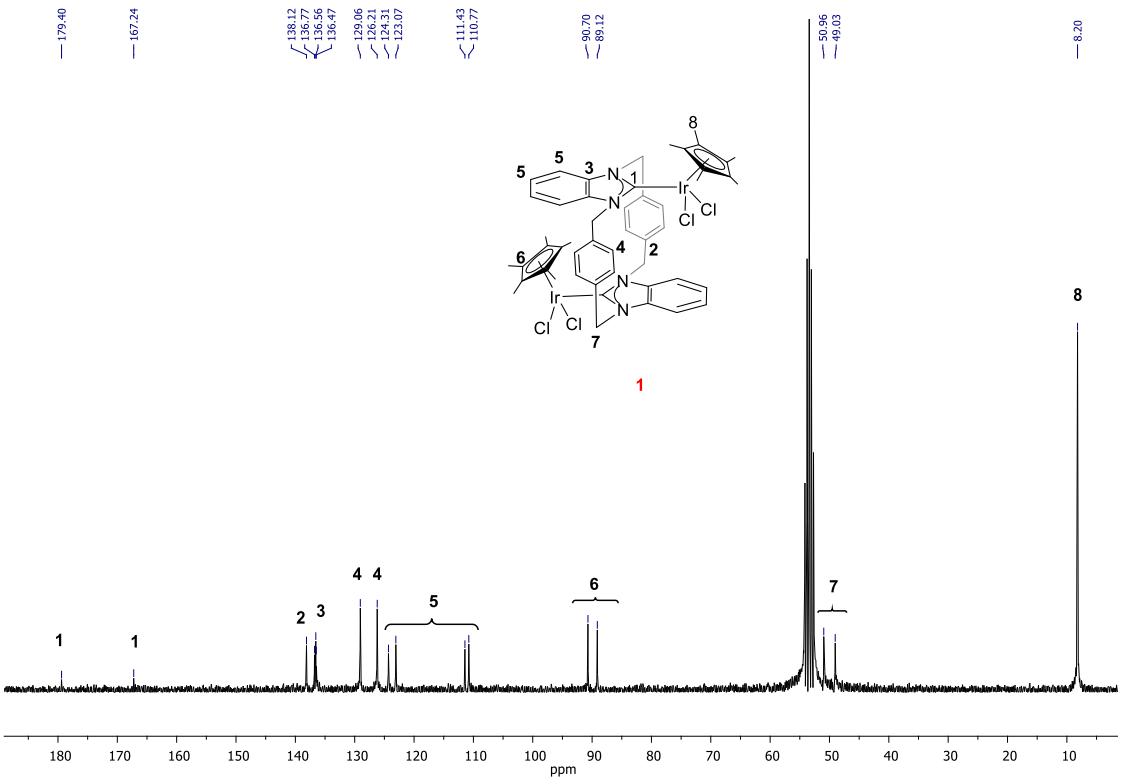

Figure 2.3. ^{13}C $\{^{1}H\}$ NMR spectrum of **1** in

*Molecular Structure of **1***

Crystals of **1** suitable for X-ray diffraction analysis were obtained by slow diffusion of methanol into a concentrated solution of **1** in dichloromethane. Figure 2.4 shows the molecular structure and the most representative bond distances and angles of the complex.

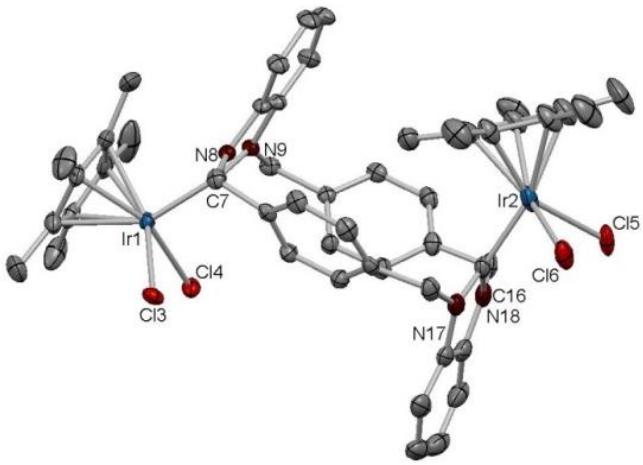

Figure 2.4. Molecular structure of compound **1**. Hydrogen atoms and solvent (MeOH, H_2O and CH_2Cl_2) have been omitted for clarity. Ellipsoids are at 50% of probability. Selected bond distances (Å) and angles (°): Ir(1)-C(7) 2.037(6), Ir(1)-Cl(3) 2.4569(16), Ir(1)-Cl(4) 2.4334(15), Ir(1)-Cp*$_{centroid}$ 1.812, Ir(2)-C(16)

2.047(8), Ir(2)-Cl(15) 2.471(2), Ir(2)-Cl(16) 2.461(2), Ir(2)-Cp*$_{centroid}$ 1.822, C(7)-Ir(1)-Cl(3) 98.42(18), C(7)-Ir(1)-Cl(4) 97.68(16), Cl(3)-Ir(1)-Cl(4) 86.41(6), Cl(6)-Ir(2)-Cl(5) 87.29(8), C(16)-Ir(2)- Cl(16) 86.7(2), C(16)-Ir(2)- Cl(15) 86.7(2)

As previously observed by ^{1}H and ^{13}C NMR, the molecular structure of complex **1** confirms that the two iridium centers are in different geometric environment. The structure consists of a bis(α,α´,-*p*-xylyl)bis(benzimidazolylidene) ligand bridging two Ir(III) fragments. The coordination sphere about each iridium center is completed by one Cp* and two chloride ligands. The relative conformation of the two benzimidazolylidenes is *anti*, and the two metal fragments are in an "*in-out*" disposition, according to the conformation depicted in Scheme 2.4. As described earlier, the *in* and *out* tags, refer to the orientation of the Cp* ring relative to the two parallel planes formed by the benzimidazolylidenes (*in*, Cp* is between the planes; *out*, Cp* is outside the planes). The molecule contains a mirror plane, which is bisecting the two benzimidazolylidene fragments. The two benzimidazolylidenes deviate from coplanarity by 13.78º. The two metal centers are out of the plane defined by the benzimidazolylidenes in 0.668 and 1.008 Å, for the *in* (Ir2) and *out* (Ir1) metals, respectively. The Ir-$C_{carbene}$ distances are 2.047 and 2.037 Å (*in* and *out*, respectively). The two xylyl groups are quasi-perpendicular as reflected by the angle of 85.75º between the two planes of these arene groups.

*DFT-Energy minimized structures of **1***

We thought that the reasons governing the formation of the *in-out* atropisomer may need some further studies, since it may seem to be the least intuitive species to be formed, from all the *anti* conformers depicted in Scheme 2.5. In order to understand the reasons to the formation of this atropisomer, DFT calculations were performed in collaboration with Prof. Dmitri Gussev from the Wilfrid Laurier University. The analysis revealed three energy-minimized structures, which are coincident with the three possible isomers (Figure 2.5). In agreement with the experimental findings, the most stable conformation is *in-out* atropisomer. The *in-in* and *out-out* isomers are higher in 4.1 and 3.5 kcal/mol, respectively. The *in-out* structure is likely to be stabilized by non-covalent interactions, probably arising from H-bonding interactions between the chloride ligands of the *in*-metal fragment with the closest protons from the methylene linker. This assumption is supported by the close Cl-C (methylene) distances of 3.29

and 3.34 Å shown in the X-Ray molecular structure of **1**, which indicates Cl-H distances of 2.64 and 2.72 Å, respectively. Furthermore, there is another possible non-covalent interaction that can stabilize this conformation which is a C-H···arene π-interaction between the C-H bonds from the (*in*) Cp* ligand in the '*in'* metal fragment and the xylyl groups of the bis-NHC ligand.

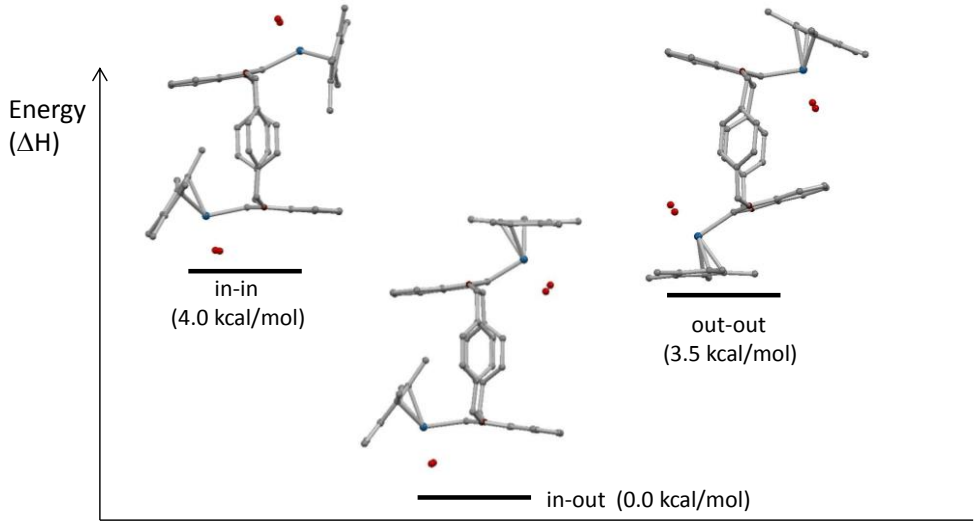

Figure 2.5. Optimized structures of the three possible atropisomers of complex **1**. Calculations made with the M06L-DFT method

In order to discard that the differences in stabilities may arise from the steric repulsions derived from the presence of the bulky Cp* ligand, the energies of the isomers with reduced Cp ligands were also calculated. Unexpectedly, under this new situation, the *in-out* isomer becomes more stable than the *out-out* isomer in 13.7 kcal/mol, therefore is stabilized by additional 11.1 kcal/mol compared with the Cp* analogue. This finding is strongly suggestive that non-covalent interactions are playing a decisive role in the stabilization of the complexes formed with this ligand.

2.2.2.2 *Synthesis and characterization of complex **2***

In order to obtain a rhodium derivative of complex **1**, we tried to coordinate **A** to $[RhCl(COD)]_2$, by following the synthetic methodology used for the preparation of **1**. However, the desired rhodium complex could not be prepared via transmetallation reaction from the pre-formed silver-NHC species. Instead, the coordination of the cyclophane-bis-NHC ligand to Rh was achieved by reacting the bis-azolium **A** with $[RhCl(COD)]_2$ in THF, in the presence of NaO*t*Bu at low temperature (-78ºC) and allowing the mixture to stir at room temperature for 12 h. In this case, the base

deprotonates the bis-azolium salt generating the corresponding free bis-NHC, which directly reacts with the rhodium dimer. Pure complex **2** was obtained in 48% as a yellow solid by precipitation from CH_2Cl_2/diethyl ether (Scheme 2.5).

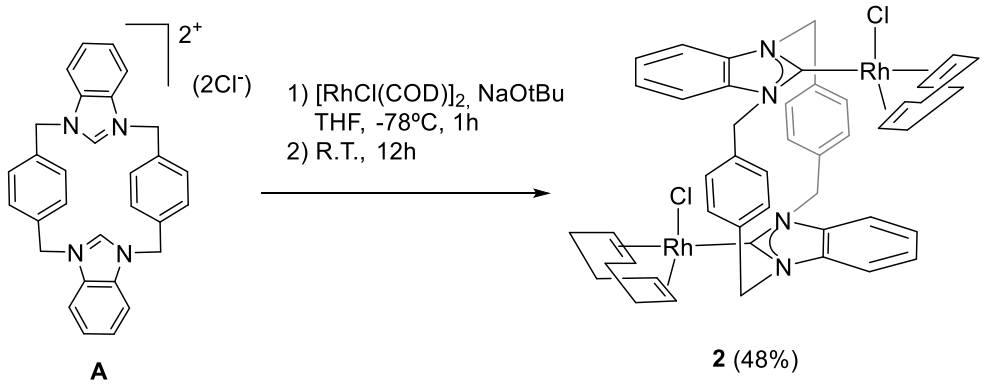

Scheme 2.5. Synthesis of complex **2**

The dimetallic nature of the complex was confirmed by HRMS, which showed a main peak at m/z 897.1667 assigned to $[M\text{-}Cl]^+$.

*^{1}H NMR spectrum of **2***

Figure 2.6 shows the ^{1}H NMR spectrum of **2**. As in the case of the previous iridium complex **1**, the spectrum is suggestive of a structure in which the two metal centres are surrounded by different coordination environments. The signals corresponding to the aromatic benzimidazole protons appear as four multiplets at 7.41, 7.32, 7.05 and 6.88 ppm (**a**). The signals due to the aromatic protons of the xylyl groups are displayed as three multiplets 7.71, 6.53 and 5.25 ppm (**b**). The resonances attributed to the aliphatic protons of the C*H*$_2$ appear as four doubles at 6.53 ($^3J_{H\text{-}H}$=13.4 Hz), 6.11 ($^3J_{H\text{-}H}$=16.2 Hz), 5.63 ($^3J_{H\text{-}H}$=16.3 Hz) and 5.11 ($^3J_{H\text{-}H}$=13.6 Hz) ppm (**c**). The signals due to the C*H* resonances of the cyclooctadiene ligand appear as a two signals at 5.26 and 4.79 ppm (**d**). The remaining signals due to the C*H*$_2$ protons of the cyclooctadiene ligand appear between 3.00 and 1.00 ppm (**e**).

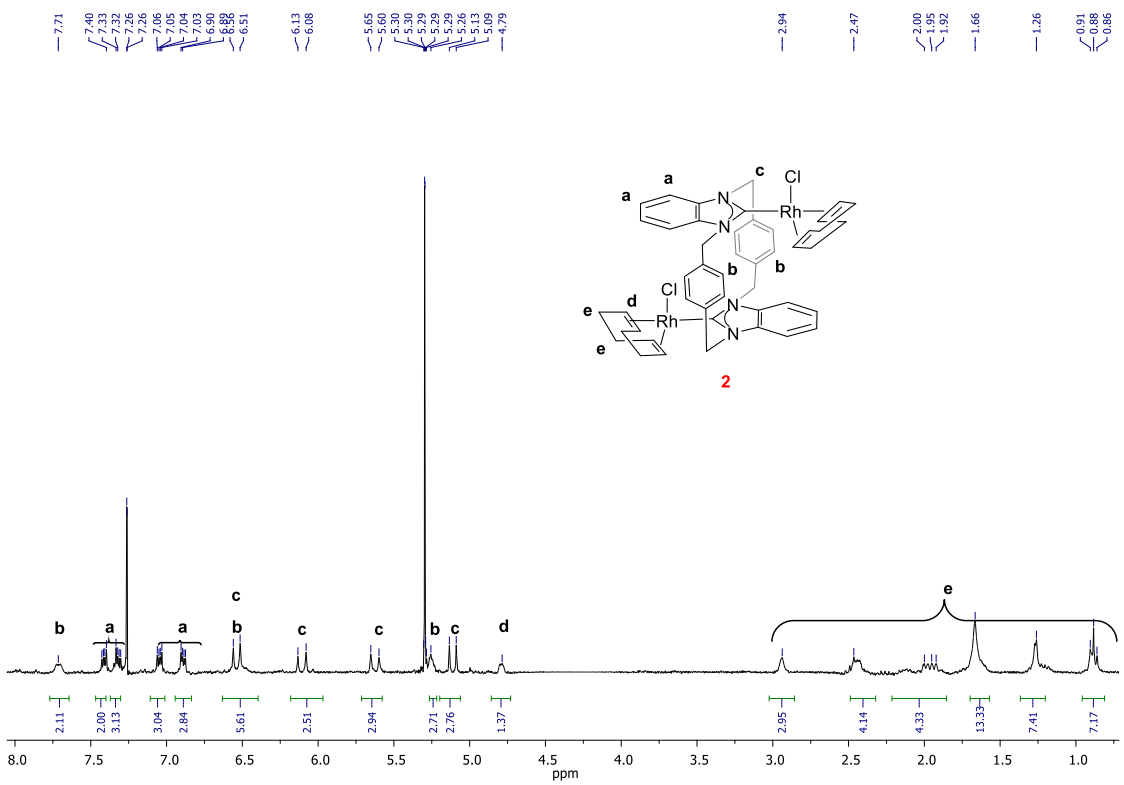

Figure 2.6. ^{1}H NMR spectrum of **2** in $CDCl_3$

*$^{13}C\{^{1}H\}$ NMR spectrum of **2***

Figure 2.7 shows the ^{13}C $\{^{1}H\}$ NMR spectrum of **2**. As expected, the pattern suggests that the two metal centers are in different environments. The two doublets at 201.6 and 199.0 ppm ($^{1}J_{Rh\text{-}C}$=75.6 and 88.2 Hz, respectively) correspond to two different metallated carbene carbons (**1**). The resonances corresponding to the quaternary and *C*H carbons of the benzimidazole appear at 136.4, 134.4 125.8, 123.4, 122.0, 110.3 and 109.9 ppm (**2** and **3**). The resonances from the quaternary and *C*H carbons atoms of the xylyl groups appear at 139.8, 135.1, 130.0 ppm (**4** and **5**). The signals attributed to the carbons of the methylene linkers appear at 51.9 and 50.7 ppm (**7**). The rest of the resonances correspond to the *C*H and CH_2 carbons of the cyclooctadiene ligand (**6** and **8**)

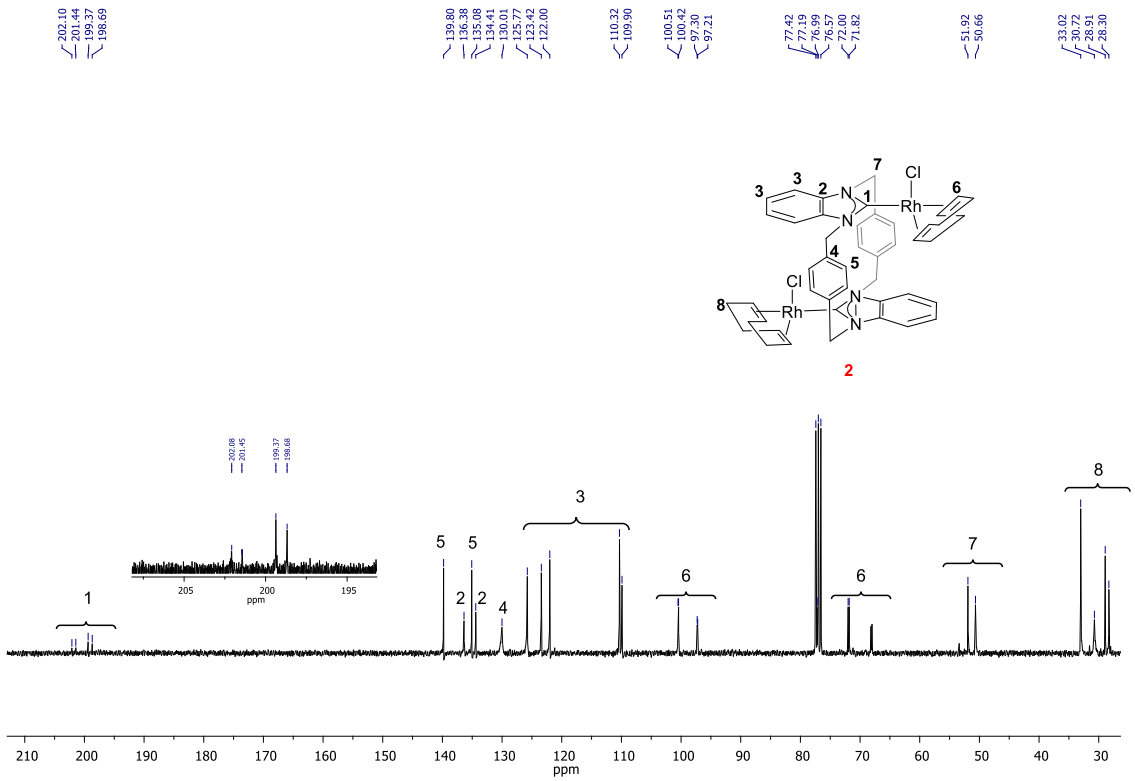

Figure 2.7. $^{13}C\{^{1}H\}$ NMR spectrum of **2** in CD_2Cl_2

*Molecular Structure of **2***

Crystals of **2** suitable for X-ray diffraction were obtained by slow diffusion of hexane into a concentrated solution of **2** in dichloromethane. Figure 2.8 shows the molecular structure and the most representative bond distances and angles of this complex.

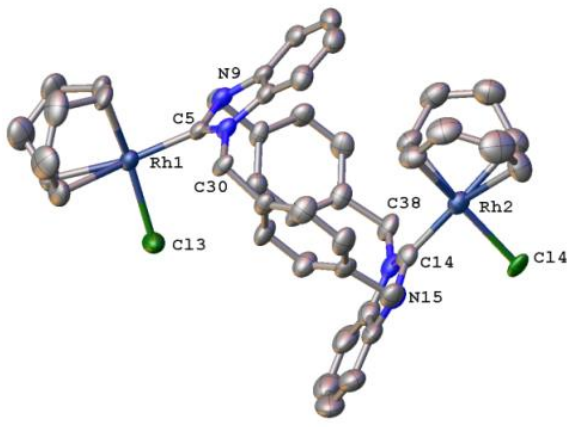

Figure 2.8. Molecular structure of compound **2**. Hydrogen atoms and solvent (Et_2O) have been omitted for clarity. Ellipsoids are at 50% of probability. Selected bond distances (Å) and angles (°): Rh(1)-Cl(3) 2.379(2), Rh(1)-C(5) 2.037(7), Rh(2)-Cl(4) 2.3973(18), Rh(2)-C(14) 2.039(9), C(5)-Rh(1)-Cl(3) 87.7(3), C(14)-Rh(2)-Cl(4) 83.6(2)

The structure shows that the bis(α,α′,-*p*-xylyl)-bis(benzimidazolylidene) ligand is bridging two $Rh^{I}Cl(COD)$ fragments, which are disposed in a relative *anti* disposition. This results in a different coordination environment for each rhodium centre. One of the chlorides bound to rhodium (Cl3) is pointing to the inner part of the ligand, while the other chloride (Cl4) is pointing out of the bis-NHC ligand, thus resulting in a relative *in–out* configuration. As observed in **1**, the molecule has a twofold symmetry, as a consequence of the presence of mirror plane bisecting the two xylyl rings. The Rh-$C_{carbene}$ distances are 2.037 and 2.039 Å (*in* and *out*, respectively). The two metal centers are out of the plane defined by the benzimidazolylidenes in 0.664 and 0.671Å, for the *in* (Rh2) and *out* (Rh1) fragments, respectively. The distance between the two rhodium atoms is 8.87 Å, slightly shorter than the distance between the two iridium atoms in **1** (9.46 Å), therefore reflecting some degree of flexibility in the coordination of the ligand. The molecular structure shows that the olefinic C-H bonds at the (*in*) COD ligand, are close to the xylyl groups of the bis-NHC ligand, thus suggesting that there may be some C-H···arene stabilizing interaction, as previously suggested for **1**.

2.2.2.3 *Synthesis and characterization of complex **3***

The substitution of the COD ligand in [M(L)(COD)Cl] (M = Rh, Ir; L = ligand), is often performed by bubbling CO into CH_2Cl_2 solutions of the complex. However, this procedure failed for the case of the replacement of the COD ligands of the dimetallic COD-containing complex **2**. Our group recently reported the preparation of $[RhCl(NHC)(CO)_2]$ complexes by direct reaction between the NHC ligand and $[RhCl(CO)_2]_2$,[10] which may serve as a useful alternative to the more widely used replacement of the COD ligand by CO bubbling. The coordination of the bis-benzimidazolium dichloride salt **A** to $[RhCl(CO)_2]_2$, was performed by transmetallation of the previously obtained silver-carbene in CH_2Cl_2. The resulting yellow product was obtained after precipitation from a CH_2Cl_2/diethyl ether mixture (yield, 44%).

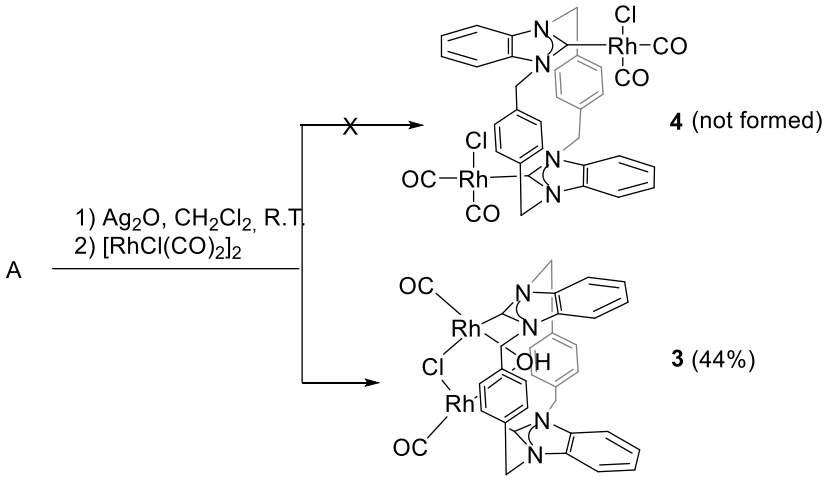

Scheme 2.6. Synthesis of metal complex **3** in CH_2Cl_2

The analysis of the NMR and IR spectra of the resulting complex suggested that, rather than obtaining the expected complex **4**, the complex obtained should be assigned to compound **3**, as depicted in Scheme 2.6. The NMR spectra of the carbonylated complex resulting from the reaction revealed a higher degree of symmetry when compared to **1** and **2**. A complete description of **3** is included in the following sections. It is worth mentioning some spectroscopic features of the complex that corroborate the proposed structural assignment. For example, the ^{13}C NMR spectrum displays two doublets at 194.4 ($^1J_{Rh\text{-}C}$= 74.34 Hz) and 189.54 ($^1J_{Rh\text{-}C}$= 60.48 Hz), which may be assigned to the metallated carbons from the carbonyls and carbene, respectively. The IR spectrum of the complex shows a single band at 1941 cm^{-1}, assigned to the CO vibration.

*^1H NMR spectrum of **3***

The ^1H NMR spectrum of **3** (Figure 2.9) reveals a high degree of symmetry. The aromatic signals due to the xylyl proton appear as two multiplets 8.41 and 6.22 ppm (**a**) ($^4J_{HH}$= 2.0 Hz). The signals due to the aromatic benzimidazole protons appear as two signals at 7.52 and 7.32 ppm (**b** and **c**). The signals assigned to the CH_2 protons of the cyclophane bridges appear as two doublets ($^3J_{H\text{-}H}$= 14.4 Hz) at 5.60 and 5.51 ppm (**d**).

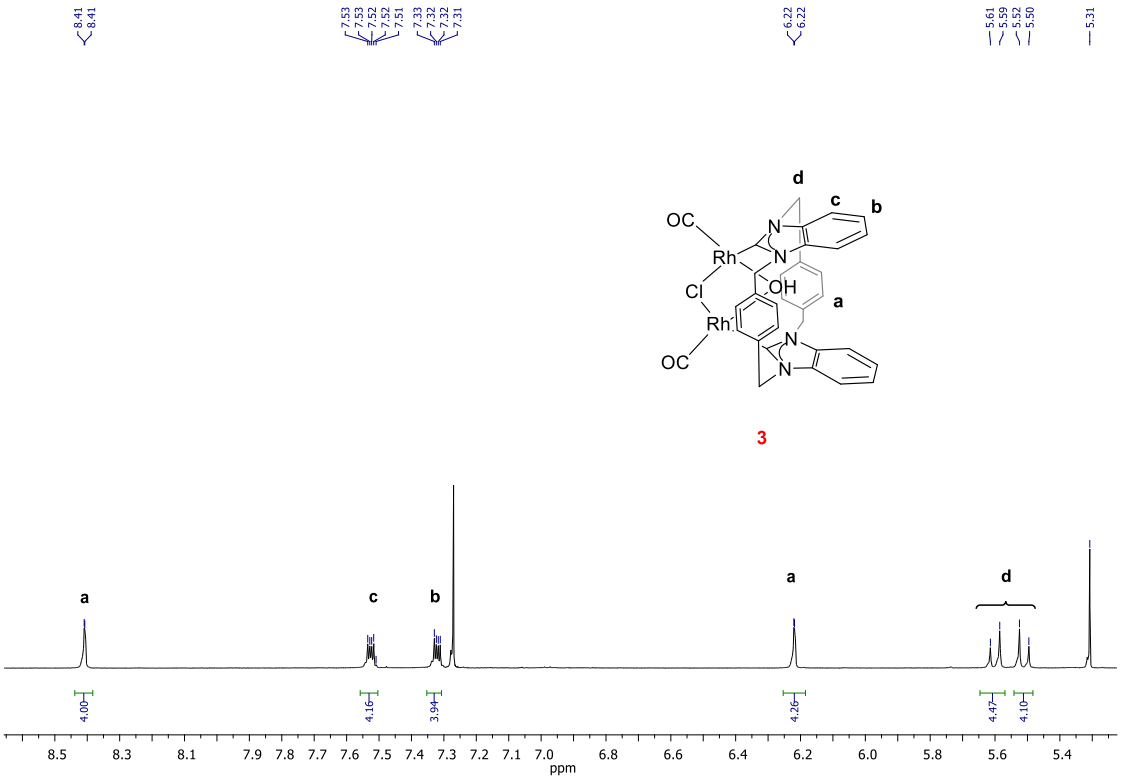

Figure 2.9. ^{1}H NMR spectrum of **3** in $CDCl_3$

Interestingly, the determination of the $^{3}J_{H\text{-}H}$ couplings between the protons of the xylyl groups of the bis-NHC ligand provided us one of the most useful hints for the determination of the conformation of the molecule. The $^{3}J_{H\text{-}H}$ coupling for the *syn* conformation and the *anti* conformation must be different as a consequence of the different symmetry operations relating the aromatic protons of the bridging xylyl group.[4e] In the *syn* conformation these protons are related by a mirror plane, therefore making that the two mutually *ortho* protons are equivalent. In the *anti* conformation these protons are related by a C_2 axis (Scheme 2.7), therefore the mutually *ortho* protons present different chemical shift. This simple picture implies that in the *anti* disposition of the benzimidazolylidenes the coupling between the protons of the xylyl group is a $^{3}J_{ortho}$ coupling (typically 8 Hz), while in the *syn* disposition is a $^{4}J_{meta}$ coupling (typically 2 Hz).[4e] The bimetallic rhodium complex **3** has a *syn* conformation since shows a coupling constant of 2 Hz was observed for the resonances of aromatic protons.

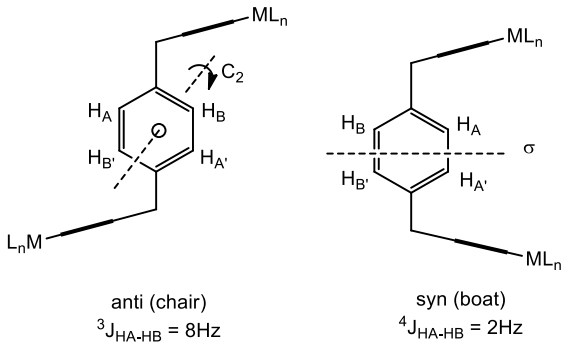

Scheme 2.7. ^{1}H-H NMR couplings for *anti* and *syn para*-cyclophanes

*^{13}C {^1H} NMR spectrum of **3***

The ^{13}C {^{1}H} NMR spectrum of **3** is shown in Figure 2.10. The pattern of the spectrum is suggestive of a highly symmetry structure. The signal due to the carbonyl carbons (**1**) appears as a doublet at 194.4 ($^1J_{Rh-CO}$= 74.34 Hz). The signal due to metallated carbene carbons (**2**) appears as a doublet at 190.1ppm ($^1J_{Rh-c}$= 60.48 Hz). The signal due to the *C*H$_2$ groups from the xylys of the cyclophane ligand appears at 51.7 ppm (**8**). All other signals are displayed and assigned in Figure 2.10.

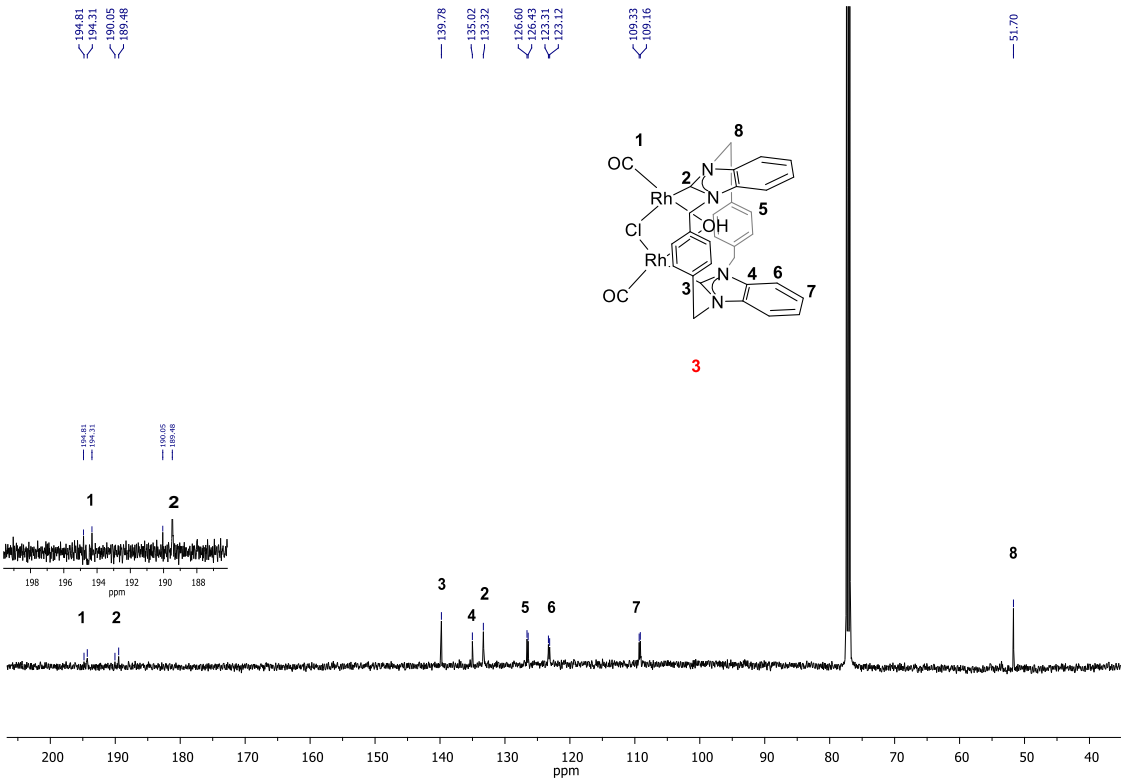

Figure 2.10. ^{13}C{^{1}H} NMR spectrum of **3** in $CDCl_3$

*Molecular Structure of **3***

Single Crystals of **3** were grown by slow diffusion of methanol into a concentrated solution of **3** in dichloromethane. The molecular structure of **3** was determined by X-ray diffraction. Figure 2.11 shows the molecular structure and the selected distances and angles of the complex.

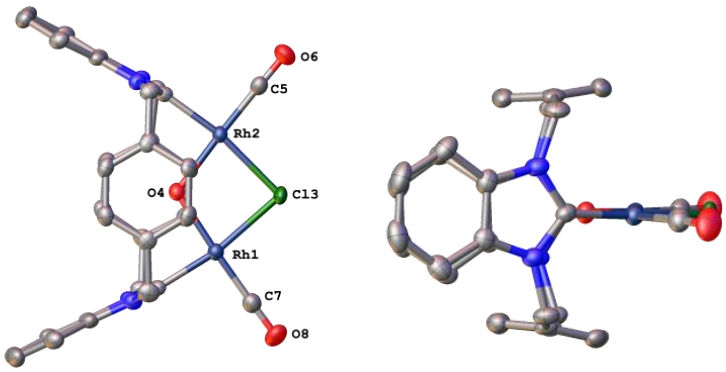

Figure 2.11. Molecular structure of compound **3**. Hydrogen atoms and solvent (CH_2Cl_2) have been omitted for clarity. Ellipsoids are at 50% of probability. Selected bond distances (Å) and angles (º): Rh(1)-Cl(3) 2.4518(10), Rh(1)-O(4) = 2.050(3), Rh(1)-C(27) = 1.965(4), Rh(1)-C(7) 1.791(4), Rh(2)-Cl(3) = 2.4516(9), Rh(2)-O(4) 2.053(3), Rh(2)-C(9) 1.960(4), Rh(2)-C(5) 1.785(4), O(4)-Rh(2)-Cl(3) 81.58(9), C(9)-Rh(2)-Cl(3) 170.51(11), C(9)-Rh(2)-O(4) 89.01(13), C(5)-Rh(2)-Cl(3) 96.63(12), C(5)-Rh(2)-O(4) 177.62(16), C(5)-Rh(2)-C(9 92.81(16), O(4)-Rh(1)-Cl(3) 81.63(9), C(27)-Rh(1)-O(4) 88.72(14), C(27)-Rh(1)-Cl(3) 170.29(10), C(7)-Rh(1)-O(4) 177.25(15), C(7)-Rh(1)-Cl(3) 96.22(13), C(7)-Rh(1)-C(27) 93.46(17), Rh(2)-Cl(3)-Rh(1) 86.64(3), Rh(1)-O(4)-Rh(2) 110.15(15)

The structure confirms our assignment arising from the analysis of the NMR spectra. The molecule consists of two rhodium fragments bridged by the *para*-cyclophane-bis-imidazolylidene ligand in a *syn* configuration, resulting in a pseudo-C_{2v} symmetrical molecule. The two rhodium atoms are bridged by a chloride and a hydroxyl ligand. The coordination sphere about each metal is completed by the presence of a terminal carbonyl ligand, which is *trans* to the bridging hydroxyl group. The planes formed by the two benzimidazolylidenes are at a relative angle of 54.7º, and the average Rh-$C_{carbene}$ distance is 1.962 Å.

Complex **3** is an interesting and rare example in which a bis-Rh(I) complex bridged by a chloride and a OH ligand simultaneously. The presence of the hydroxyl group may be justified as a transfer of the OH group from AgOH formed during the preparation of the silver complex intermediate.

2.3 Conclusions

In this chapter we described a series of iridium and rhodium complexes using a bis(*p*-xylyl)bis(benzimidazolium) dichloride salt **A**. The X-ray diffraction of **A** suggested that due to the distance between the two C2 carbons, which exceed the sum of two potential M-$C_{carbene}$, dimetallic complexes rather than monometallic ones should be formed.

In all previously reported examples of cyclophane-based bis-NHCs metal complexes, the coordination of the ligand tends to be chelating,[5] unless gold or silver metal fragments are used. They benefit from the low steric hindrance provided by their linear coordination arrangements.[4d,6,11] Herein, in this case, the dimetallic complexes always display a *syn* conformation of the cyclophane-based bis-NHC.

In this chapter, it has been shown that depending on the metal fragment coordinated to the bis-NHC ligand, the complexes adopt an *anti* or a *syn* conformation.

The *anti* conformation provides the more sterically favoured situation, because it allows the bulky metal fragments to remain at longer distance. This situation is exemplified in complexes **1** and **2**. The *syn* conformation was observed only in the case of complex **3**, for which a chloride and hydroxyl are present, thus forcing the two metals to be on the same face of the ligand. DFT studies on the bis-iridium complex **1** demonstrated that the atropoisomer *in-out* was the most stable one, probably due to non-covalent interactions, which are dominant over other steric reasons.

In summary, the new chemistry described for the bis(*p*-xylyl)bis(benzimidazolylidene) ligand allowed us to disclose its rich structural versatility, which may be useful for the preparation of new complexes with novel topologies that should depend on the metal and coligands that are used.

2.4 References

(1) a) Cram, D. J., Steinberg, H. *J. Am. Chem. Soc.* **1951**, *73*, 5691-5704; b) Cram, D. J., Cram, J. M. *Acc. Chem. Res.* **1971**, *4*, 204-&.

(2) Pellegrin, M. M. *Chim. Pays-Bas* **1899**, *18*, 457-465.

(3) Cram, D. J. S., H. *J. Am. Chem. Soc.* **1951**, *73*, 5691-5704.

(4) a) Baker, M. V., Brown, D. H., Haque, R. A., Skelton, B. W., White, A. H. *Dalton Trans.* **2010**, *39*, 70-72; b) Lappert, M. F., Alvarez, S., Aullon, G., Fandos, R., Otero, A., Rodriguez, A., Rojas, S., Terreros, P. *Eur. J. Inorg. Chem.* **2009**, 1851-1860; c) Baker, M. V., Brown, D. H., Haque, R. A., Simpson, P. V., Skelton, B. W., White, A. H., Williams, C. C. *Organometallics* **2009**, *28*, 3793-3803; d) Baker, M. V., Brown, D. H., Haque, R. A., Skelton, B. W., White, A. H. *Dalton Trans.* **2004**, 3756-3764; e) Cabildo, P., Sanz, D., Claramunt, R. M., Bourne, S. A., Alkorta, I., Elguero, J. *Tetrahedron* **1999**, *55*, 2327-2340; f) Shi, Z., Thummel, R. P. *J. Org. Chem.* **1995**, *60*, 5935-5945; g) Garrison, J. C., Simons, R. S., Kofron, W. G., Tessier, C. A., Youngs, W. J. *Chem. Commun.* **2001**, 1780-1781.

(5) a) Shi, Z. Q., Thummel, R. P. *Tetrahedron Lett.* **1995**, *36*, 2741-2744; b) Baker, M. V., Skelton, B. W., White, A. H., Williams, C. C. *Organometallics* **2002**, *21*, 2674-2678; c) Baker, M. V., Brown, D. H., Heath, C. H., Skelton, B. W., White, A. H., Williams, C. C. *J. Org. Chem.* **2008**, *73*, 9340-9352; d) Baker, M. V., Skelton, B. W., White, A. H., Williams, C. C. *J. Chem. Soc.-Dalton Trans.* **2001**, 111-120; e) Baker, M. V., Brown, D. H., Hesler, V. J., Skelton, B. W., White, A. H. *Organometallics* **2007**, *26*, 250-252.

(6) a) Garrison, J. C., Simons, R. S., Talley, J. M., Wesdemiotis, C., Tessier, C. A., Youngs, W. J. *Organometallics* **2001**, *20*, 1276-1278; b) Barnard, P. J., Baker, M. V., Berners-Price, S. J., Skelton, B. W., White, A. H. *Dalton Trans.* **2004**, 1038-1047; c) Melaiye, A., Sun, Z. H., Hindi, K., Milsted, A., Ely, D., Reneker, D. H., Tessier, C. A., Youngs, W. J. *J. Am. Chem. Soc.* **2005**, *127*, 2285-2291; d) Barnard, P. J., Wedlock, L. E., Baker, M. V., Berners-Price, S. J., Joyce, D. A., Skelton, B. W., Steer, J. H. *Angew. Chem. Int. Ed.* **2006**, *45*, 5966-5970.

(7) Baker, M. V., Bosnich, M. J., Brown, D. H., Byrne, L. T., Hesler, V. J., Skelton, B. W., White, A. H., Williams, C. C. *J. Org. Chem.* **2004**, *69*, 7640-7652.

(8) a) Baker, M. V., Brayshaw, S. K., Skelton, B. W., White, A. H., Williams, C. C. *J. Organomet. Chem.* **2005**, *690*, 2312-2322; b) Chapman, M. R., Shafi, Y. M., Kapur, N., Nguyen, B. N., Willans, C. E. *Chem. Commun.* **2015**, *51*, 1282-1284.

(9) Herrmann, W. A. *Angew Chem, Int Ed.* **2002**, *41*, 1291-1309.

(10) Gonell, S., Alabau, R. G., Poyatos, M., Peris, E. *Chem. Commun.* **2013**, *49*, 7126-7128.

(11) a) Brinke, C. S. T., Pape, T., Hahn, F. E. *Dalton Trans.* **2013**, *42*, 7330-7337; b) Hahn, F. E., Radloff, C., Pape, T., Hepp, A. *Chem. Eur. J.* **2008**, *14*, 10900-10904.

Chapter 3.
Study of the influence of the presence of pyrene tags in the catalytic activity of palladium and iridium complexes

3.1 Introduction

The Organometallic Chemistry and Catalysis Group at the Universitat Jaume I (QOMCAT), has been recently interested in developing polyaromatic NHC-based multimetallic systems for the study of their catalytic properties.[1] In a certain number of cases, a clear enhancement of the catalytic activities was observed for those catalysts introducing polyaromatic functionalities.[2] As we already mentioned in the general introduction in Chapter 1, this improvement was hypothesized to be due to π-stacking interactions between the aromatic substrates and the polyaromatic ligands. This hypothesis was supported by the fact that the addition of π-stacking additives, such as pyrene or hexafluorobenzene, produced the partial inhibition of the activity, when the catalysts contained ligands with rigid polyaromatic fragments.[2b,3]

In order to shed some more light on to this research, we decided to prepare a family of bis-NHC ligands featuring different topologies, and decorated with pyrene functionalities. The aim of the work is to study how these small topological variations may influence the catalytic behavior of the resulting metal (palladium and iridium) complexes. The framework consists of a bis-NHC bound by a phenylene (n = 1) or a biphenylene (n = 2) linker (Scheme 3.1). The N-substituents at the NHCs are methyl or pyrene-methylene groups. These variations may allow to determine what is the influence of the metal-to-metal distance in the reactivity and catalytic behavior of the complexes (by changing the spacers- phenylene or biphenylene). It should also allow to evaluate how presence of the π-stacking functionality (pyrene) influences the activity, compared to the situation in which a methyl group is present. The related mono-NHC was also prepared, in order to evaluate the influence of the presence of two metals compared to the situation in which only one metal is present. We thought that these ligands should provide an excellent basis for comparison and constitute a good set for establishing all control experiments required. The ligands were coordinated to palladium and iridium. In the case of the palladium complexes, the catalysts were tested in the acylation of aryl halides with hydrocinnamaldehyde, and in the Suzuki-Miyaura coupling between aryl halides and boronic acids. In the case of the iridium complexes, the catalysts were tested in typical borrowing-hydrogen catalyzed processes, such as the reduction of ketones by transfer hydrogenation, and the β-alkylation of secondary alcohols with primary alcohols.

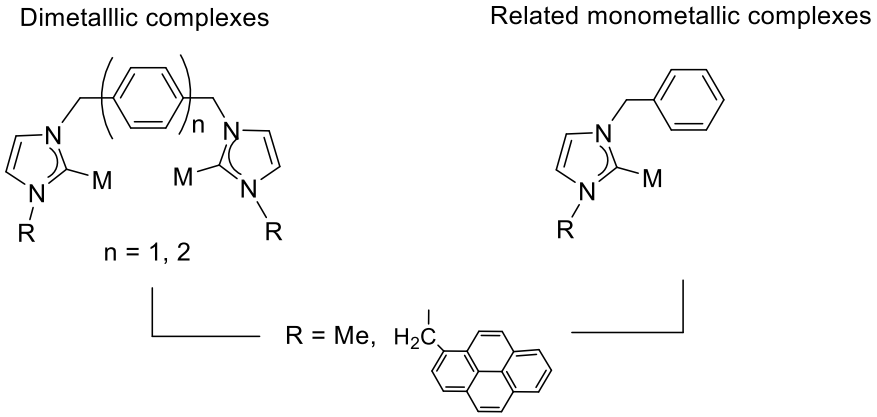

Scheme 3.1. Ligands employed in this Chapter

3.2 Results and discussion

3.2.1 Synthesis and characterization of imidazolium salts

The N-Me substituted bis-imidazolium salt **B** (Scheme 3.2a), was obtained according to the known literature procedure.[4] The preparation of the pyrene-functionalized bis-azoliums **C** and **D** (Scheme 3.2b), was performed by reacting 1,4-bis(1H-imidazol-1-yl)benzene, or 4,4'-bis(1H-imidazol-1-yl)biphenyl with 1-bromomethylpyrene in refluxing THF. The final suspensions were cooled to room temperature, and the precipitation of the compounds was produced by addition of diethyl ether. The resulting white precipitates were collected by filtration, and washed with diethyl ether. The bis-azoliums **C** and **D** were obtained in 82 and 94% yields, respectively. These new salts were characterized by NMR spectroscopy, ESI-MS and Elemental Analysis.

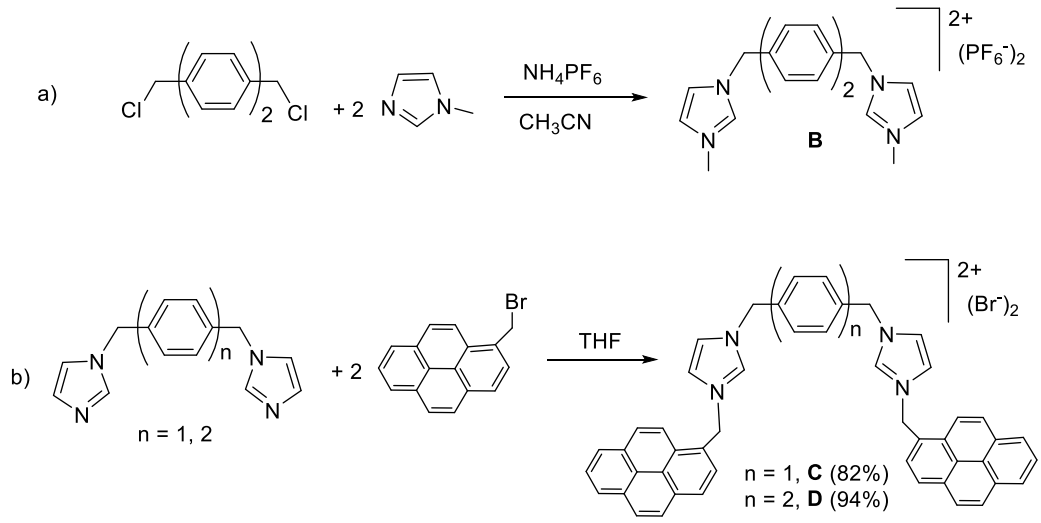

Scheme 3.2. Synthesis of bis-azolium salts **B**, **C** and **D**

*a) Characterization of **C***

*^{1}H NMR spectrum of **C***

Figure 3.1 shows the ^{1}H NMR spectrum of **C**. The number of signals displayed is in agreement with the twofold symmetry of the compound. The signal due to the acidic protons from the NC*H*N is displayed at 9.38 ppm (**a**). The signals assigned to the protons of the pyrene fragment are displayed between 8.45 - 8.13 ppm. The signals due to the C*H* protons of the imidazole appear at 7.88 and 7.80 ppm (**b** and **c**). The signal due to the protons of the phenylene bridge appears at 7.39 ppm (**d**). The signals due to the protons of the two types of methylene linkers are displayed at 6.22 and 5.37 ppm (**f** and **e**).

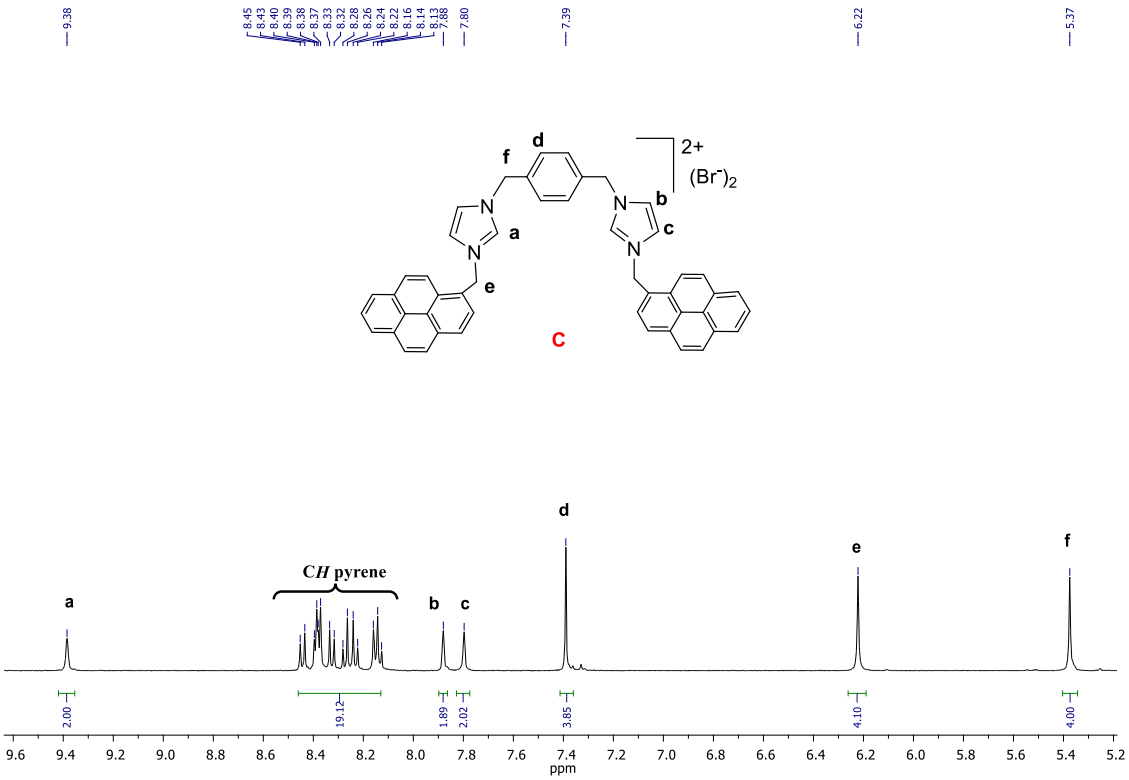

Figure 3.1. ^{1}H NMR spectrum of **C** in DMSO-d^{6}

*^{13}C {^{1}H} NMR spectrum of **C***

Figure 3.2 shows the ^{13}C {^{1}H} NMR spectrum of **C**. Again, the number of signals is in agreement with the twofold symmetry of the compound. The signal produced by the N*C*HN carbon appears at 136.9 ppm (**1**). The signals attributed to the pyrene functionalities and the aromatic carbons from the phenylene bridge are displayed between 135.9-123.8 ppm. The signals attributed to the *C*H carbon of the imidazole appear at 123.3 and 122.8 ppm (**5** and **6**). The signals due to the *C*H$_2$-bridge carbons are displayed at 52.0 and 50.7 ppm (**7** and 8).

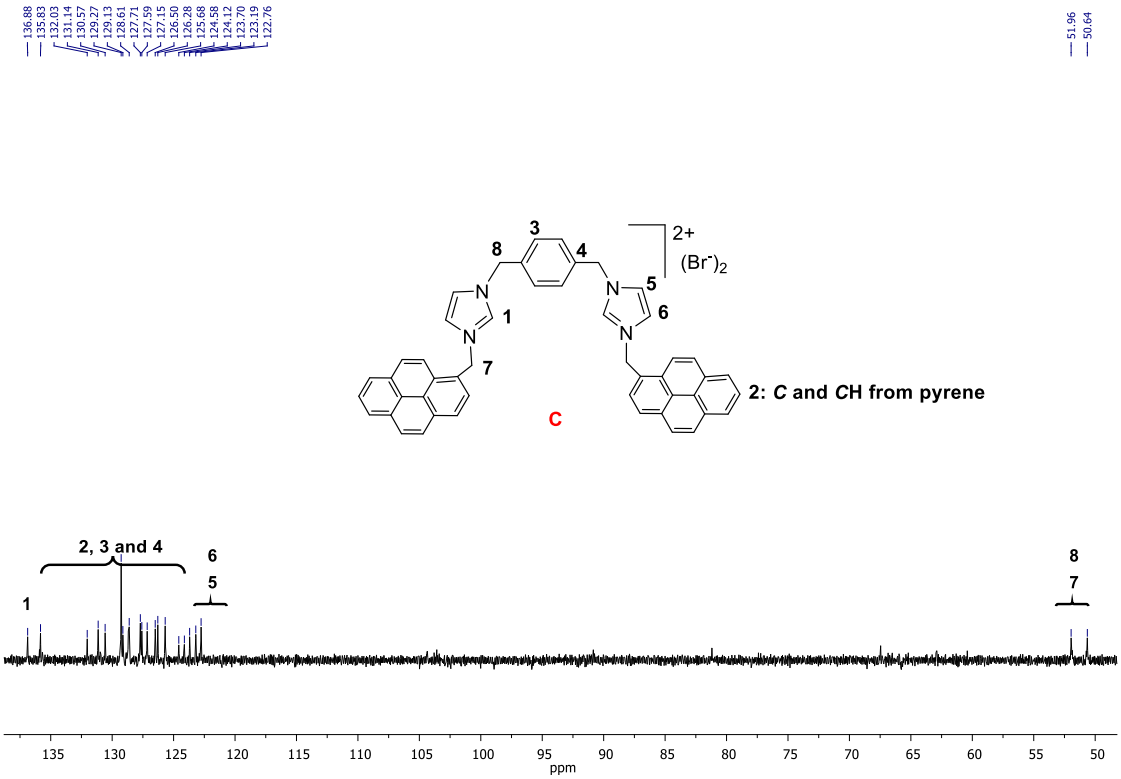

Figure 3.2. ^{13}C {^{1}H} NMR spectrum of **C** in DMSO-d^6

Optimized structures of bis-azolium salt **C**

The bis-azolium salts **C** and **D** were designed aiming that the pyrene may non-covalently interact with aromatic substrates. The topology of the salts themselves may also be influenced by their intramolecular π-stacking abilities. In collaboration with Prof. Dmitri Gusev from the Wilfrid Laurier University, a DFT analysis of the pyrene-containing bis-azolium salt **C** was performed, in order to evaluate if an intramolecular interaction conformation ('π-locked') through the pyrene functionalities could be possible.

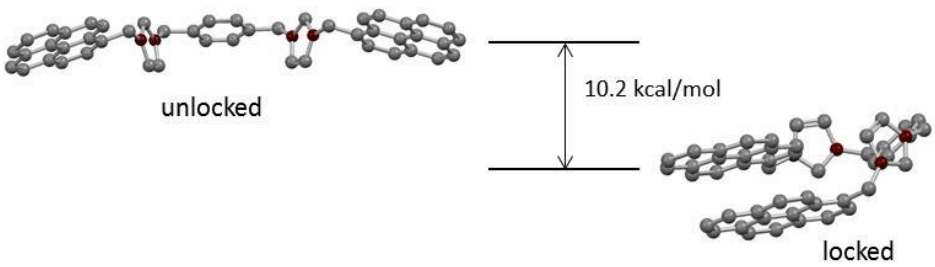

Figure 3.3. Optimized structures of the π-unlocked and π-locked structures of the bis-azolium salt **C**. Calculations made with the M06L-DFT method

The DFT calculated structures for the two possible conformations of **C** (Figure 3.3) reveal that the π-stacked geometry is favored in 10.2 kcal/mol, compared to the situation in which the π-stacking interaction does not occur. Although this energy may be related to the energy of the π-stacking interaction of the salt in the gas phase, we believe that this type of conformation may also be possible for the related metallated complexes with the resulting bis-NHC ligand, and therefore its influence in the catalytic activity of these complexes should not be underestimated.

*b) Characterization of compound **D***

*^{1}H NMR spectrum of **D***

Figure 3.4 shows the ^{1}H NMR spectrum of **D**. The number of signals displayed is in agreement with the twofold symmetry of the compound. The signal due to the acidic protons of the NC*H*N appears at 9.45 ppm (**a**). The signals assigned to the protons of the pyrene functionality are displayed between 8.48 - 8.13 ppm. The signals due to the C*H* protons of imidazole appear at 7.92 and 7.88 ppm (**b** and **c**). The signals due to the protons of the biphenylene bridge labelled as **d** and **e** appear as two doublets at 7.67 and 7.47 ppm. The signals produced by the CH_2–bridge protons are displayed at 6.26 and 5.44 ppm (**f** and **g**).

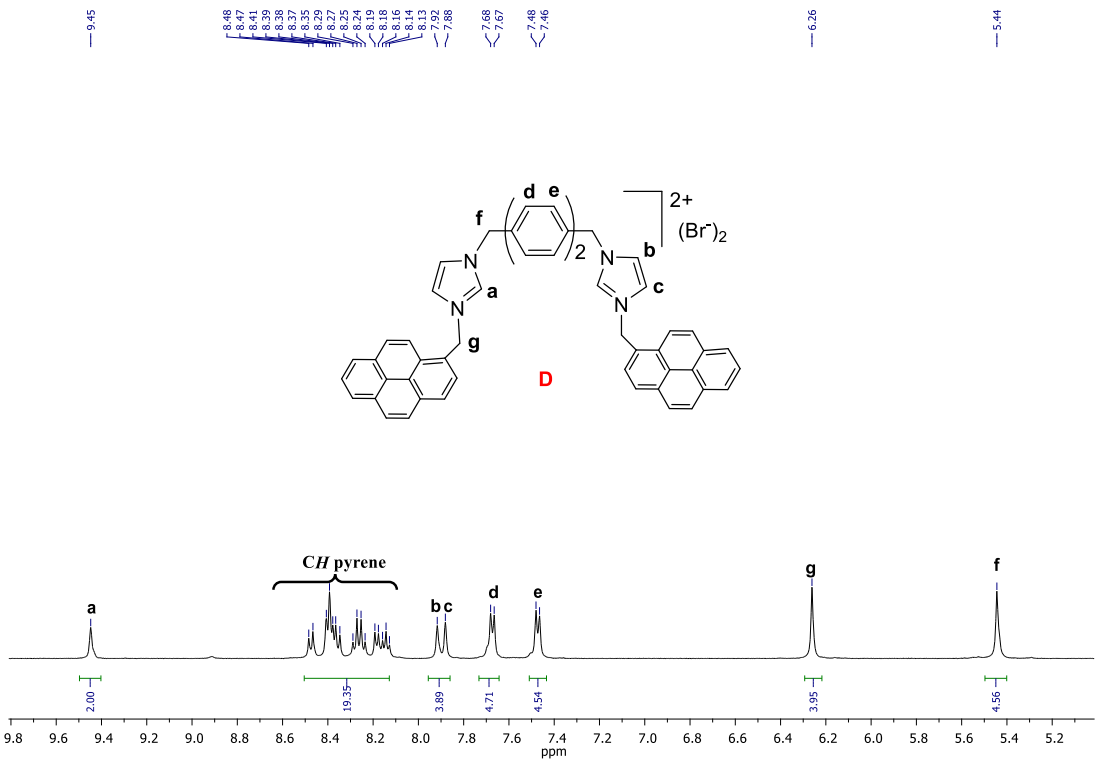

Figure 3.4. ^{1}H NMR spectrum of **D** in DMSO-d^6

*^{13}C {^{1}H} NMR spectrum of **D***

Figure 3.5 shows the ^{13}C {^{1}H} NMR spectrum of **C**. Again, the number of signals is in agreement with the twofold symmetry of the compound. The signal corresponding to the N*C*HN carbon appears 140.1 at ppm (**1**). The signals attributed to the pyrene fragments and the aromatic carbons of biphenylene bridges are displayed in the 136.8–123.7 region. The signals attributed to the *C*H carbons of the imidazole appear at 123.2 and 122.7 ppm (**6** and **7**). The signals due to the *C*H_2-bridge carbons appear at 52.0 and 50.6 ppm (**8** and **9**).

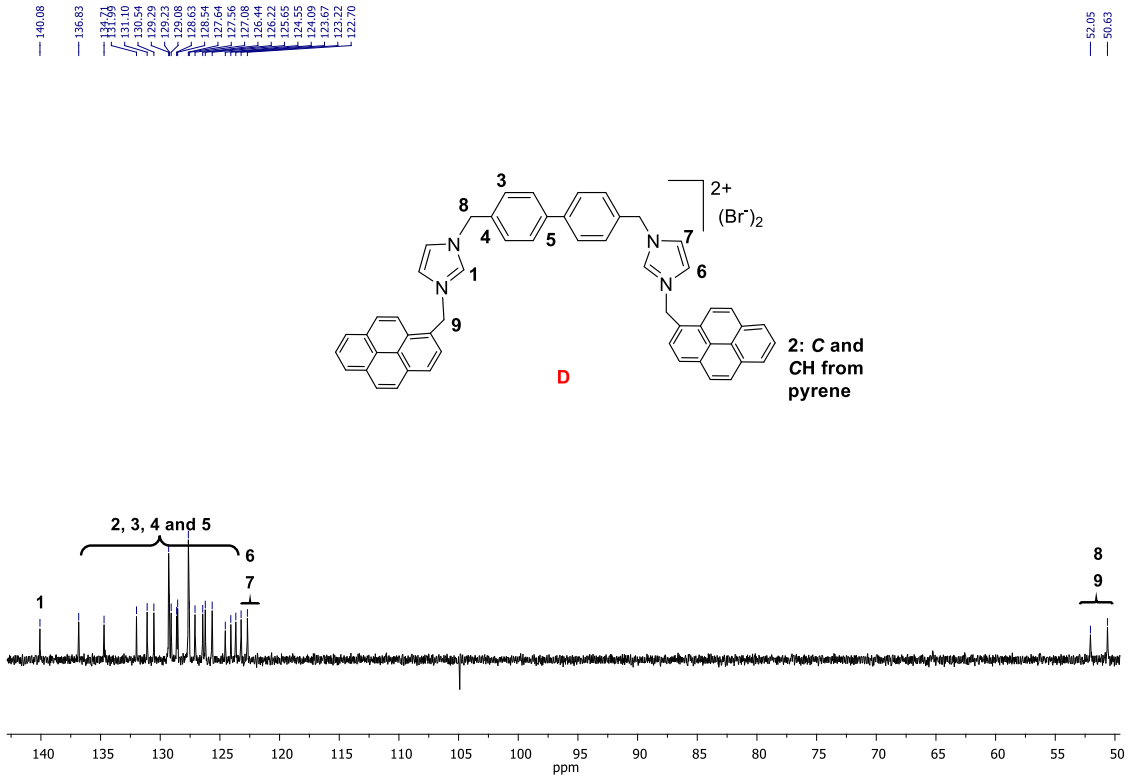

Figure 3.5. ^{13}C {^{1}H} NMR spectrum of **D** in DMSO-d^6

3.2.2 Synthesis and characterization of complexes

A series of Pd(II) and Ir(I) complexes were prepared from the imidazolium and bis-imidazolium salts described in this chapter. Different metalation strategies were used depending on the metal precursors utilized. All metal complexes were characterized by NMR spectroscopy, ESI-MS and Elemental Analysis.

3.2.2.1 Synthesis and characterization of Palladium complexes

The preparation of the dipalladium complexes **5-7** was performed by reacting the bis-azolium salts **B-D** with palladium dichloride in 3-chloropyridine in the presence of K_2CO_3 at 100 ºC (Scheme 3.3). Addition of KBr to the reaction was needed, in order to

facilitate the preparation of the bromide-containing palladium complexes and avoid mixtures of halides in the final products. The resulting products were purified by column chromatography, affording the pure compounds in yields ranging 30-50%.

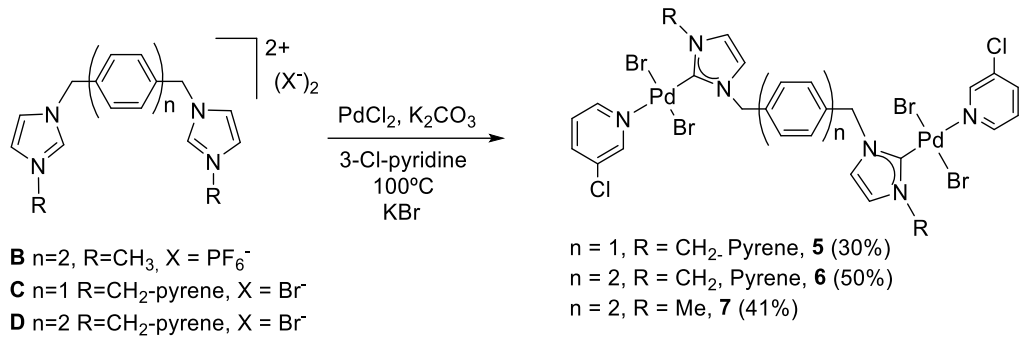

Scheme 3.3. Preparation of metal complexes **5-7**

The monometallic complexes **8** and **9** were prepared by following a similar methodology. Their detailed characterization may be found in the experimental section, Chapter 7.

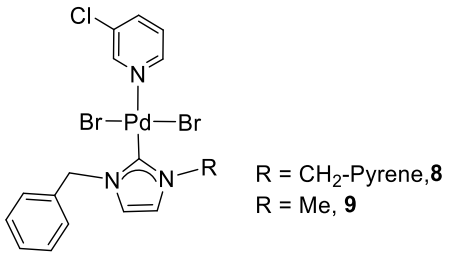

Scheme 3.4. Complexes **8** and **9**

*a) Characterization of complex **5***

As will be described, the pattern of the NMR spectra of complex **5** is strongly suggestive of a situation in which the two metal centres are geometrically equivalent.

*^{1}H NMR spectrum of **5***

Figure 3.6 shows the ^{1}H NMR spectrum of complex **5**. The NMR spectrum of this complex indicates that the two metal centres are in a geometrically equivalent environment. This observation is exemplified by the observance of only two signals due to the protons of the backbone of the imidazolylidenes (**b** and **c**), at 6.35 and 6.64 ppm. The protons due to the Cl-pyridines exhibit their resonances as one singlet, two doublets and one triplet at 9.10, 8.96, 7.63 and 7.22 ppm, respectively (**h**, **i**, **j**, **k**). The resonances ascribed to the protons of the pyrene fragment appear as a doublet at 8.53 ppm, and then as several multiplets between 8.24-8.00 ppm. The resonance due to protons of the

phenylene linker appears at 7.58 ppm (**d**).The signals due to the methylene protons are displayed at 5.82 and 6.45 ppm (**f** and **e**, respectively).

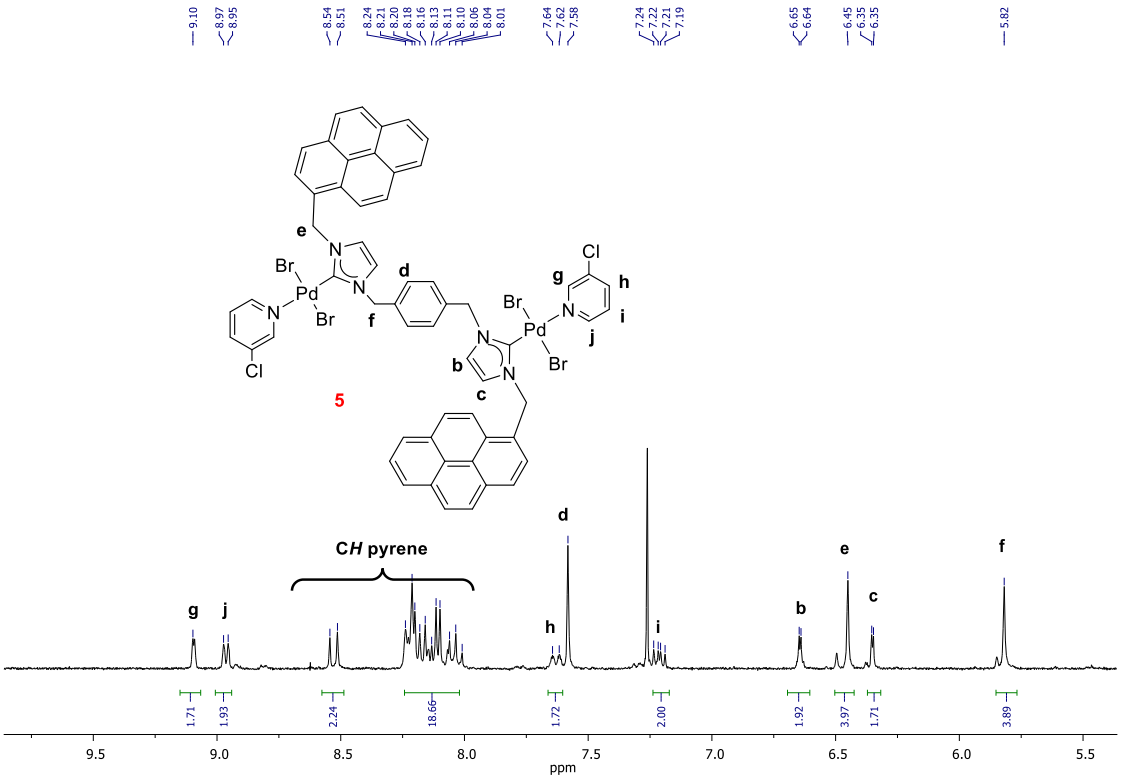

Figure 3.6. ^{1}H NMR spectrum of **5** in $CDCl_3$

*^{13}C {^{1}H} NMR spectrum of **5***

Figure 3.7 shows the ^{13}C {^{1}H} NMR spectrum of **5**. Again, the number of signals is in agreement with the two metal centres in a geometrically equivalent environment. Probably, the most significant signal is the one due to the metallated carbon, which appears at 147.5 ppm (**1**). The signals due to the carbons of the *C*H groups of the imidazole are observed at 124.7 and 121.9 ppm (**5** and **6**). The resonances of the carbons of the methylene groups appear at 55.1 and 53.9 ppm (**7** and **8**). All other signals observed in the spectrum are due to the aromatic carbons from the Cl-pyridine, pyrene and phenyl fragments.

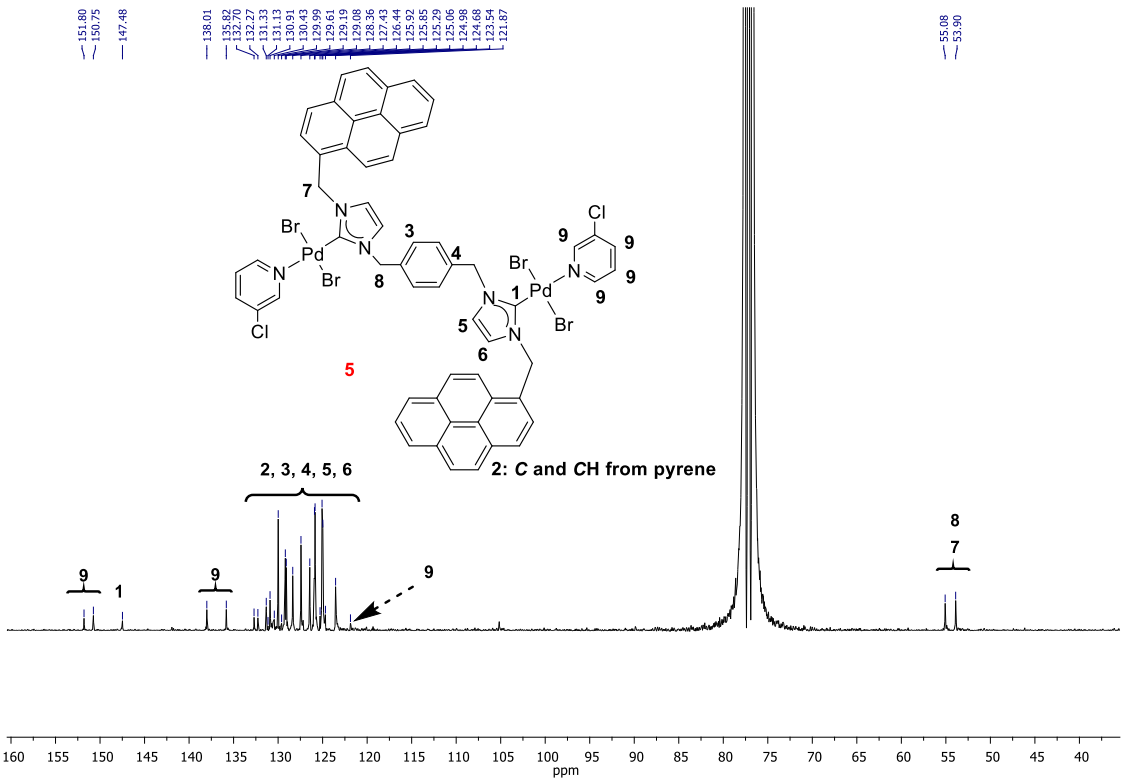

Figure 3.7. ^{13}C {^{1}H} NMR spectrum of **5** in $CDCl_3$

*b) Characterization of complex **6***

As will be described, the pattern of the NMR spectra of complex **6** is suggestive of the presence of two species in equilibrium, probably rotamers arising from the different relative orientation of the metal fragments along the axis formed by the biphenylene linker. Unfortunately, we do not have clear evidences for providing a definitive explanation of the origin of the NMR patterns shown, although the Elemental Analysis and mass spectra, suggest that the species in solution must be isomers.

*^{1}H NMR spectrum of **6***

Figure 3.8 shows the ^{1}H NMR spectrum of **6**. The spectrum was recorded in $CDCl_3$, in which the broadening of the signals evidences a fluxional behaviour of the complex. The pattern of the spectrum suggests the presence of two different isomers in equilibrium. This conclusion can be derived from the number of signals of the spectrum. For example, the protons of the methylene linkers (**f** and **g**) induce the appearance of four different signals of unequal intensity, at 6.52, 6.50, 5.90 and 5.87 ppm. In fact, these are the only signals that clearly indicate the presence of two species. The hydrogen atoms at the Cl-pyridines (**h**, **i**, **j**, **k**) exhibit their resonances at 9.15, 9.03, 7.77 and 7.32 ppm. The aromatic signal due to the byphenylene linker appears at 7.60

ppm (**e** and **d**). The signals attributed to the C*H* protons of the imidazoles appear as two very broad signals at 6.60 and 6.38 ppm (**b** and **c**). The rest of the signals correspond to the protons of the pyrene tags.

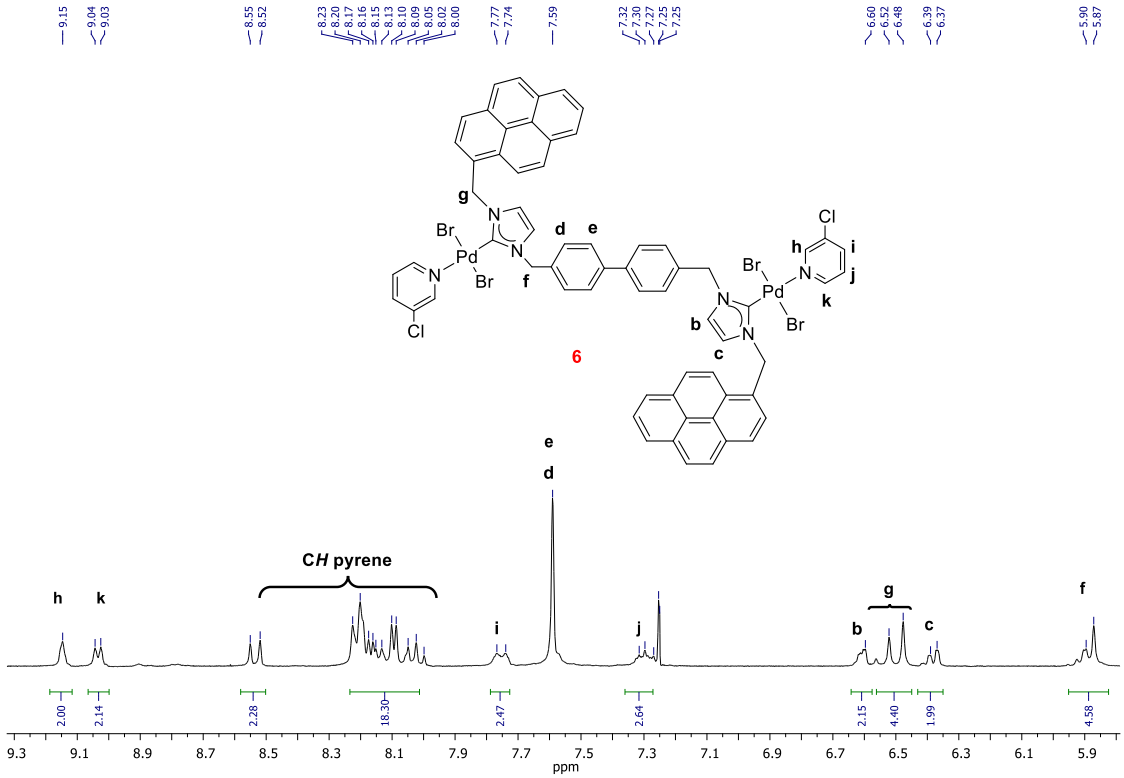

Figure 3.8. ^{1}H NMR spectrum of **6** in $CDCl_3$

*^{13}C {^{1}H} NMR spectrum of **6***

Figure 3.9 shows the ^{13}C {^{1}H} NMR spectrum of **6**. In accordance with the ^{1}H NMR spectrum, the number of signals suggests the presence of two rotamers in equilibrium. For instance, the signals ascribed to the metallated carbene carbons appear as two singlets at 147.7 and 147.1 ppm (**1**); and the resonances of the carbons of the methylene groups appear as four signals of different intensity at 54.82, 54.7, 56.6 and 53.3 ppm (**8, 8'** and **9, 9'**). All other signals are due to the pyrene, phenyl, *C*H carbons from the imidazole and pyridine groups.

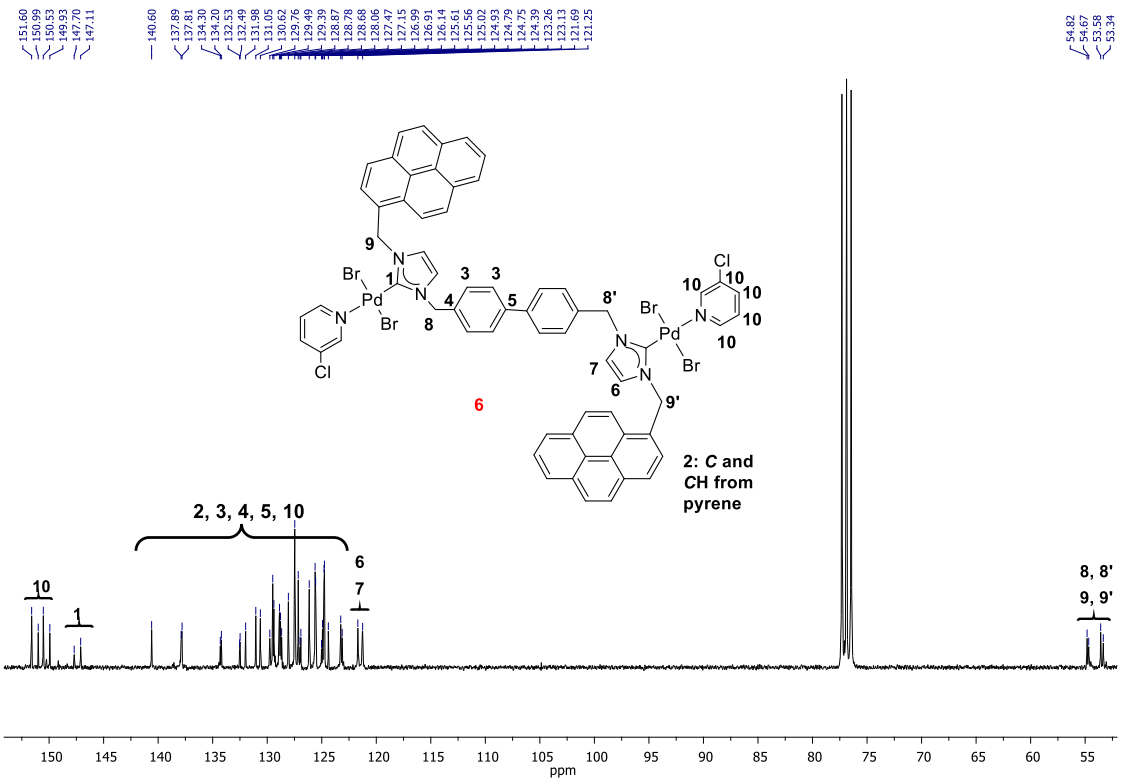

Figure 3.9. ^{13}C $\{^{1}H\}$ NMR spectrum of **6** in $CDCl_3$

Molecular Structure of ***6***

Single crystals of **6** were grown by slow diffusion of hexane into a concentrated solution of the complex in dichloromethane. The molecular structure of **6** was determined by X-ray diffraction. Figure 3.10 shows the structure of the complex. The molecule consists of two palladium centres bound by a biphenylene-bridged bis-imidazolylidene ligand. Despite the observation of the two different species by the solution NMR spectra, only one of them is observed by X-ray diffraction. The two palladium centres are symmetry-related, and therefore their coordination environments are identical. Each palladium atom completes its coordination sphere with two bromides in a relative *trans* conformation, and a 3-chloropyridine. The relative orientation of the two palladium fragments with respect to the bis-NHC ligand is *anti*, with each palladium centre located on one side of the plane defined by the biphenylene bridge. This conformation leads to a metal-to-metal through-space separation of 14.18 Å. The Pd-C (carbene) distance is 1.963(7) Å. The crystal packing of the molecule reveals the π-π-stacking interaction between the pyrene groups of adjacent molecules (Figure 3.11)

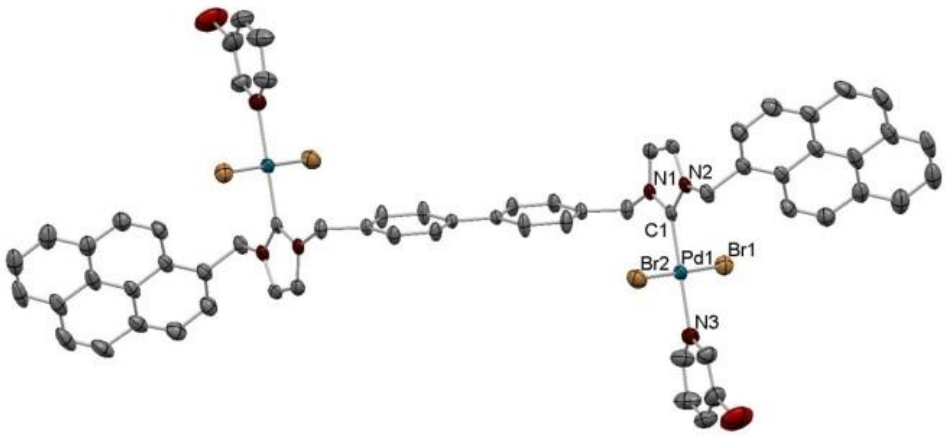

Figure 3.10. Molecular structure of compound **6**. Hydrogen atoms and solvent (3 molecules of $CHCl_3$) have been omitted for clarity. Ellipsoids are at 50% of probability. Selected bond distances (Å) and angles (°): Pd(1)-C(1) 1.963(7), Pd(1)-Br(1) 2.4027(12), Pd(1)-Br(2) 2.4010(12), Pd(1)-N(3) 2.101(7), C(1)-Pd(1)-N(3) 179.3(3), C(1)-Pd(1)-Br(1) 88.7(2), C(1)-Pd(1)-Br(2) 90.5(2), N(3)-Pd(1)-Br(1) 90.6(2), N(3)-Pd(1)-Br(2) 90.1(2), Br(2)-Pd(1)-Br(1) 179.12(4)

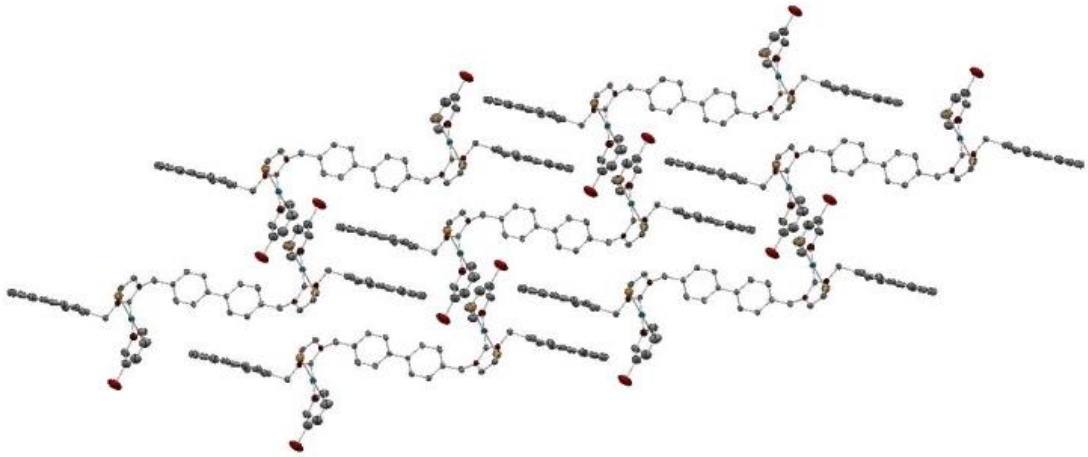

Figure 3.11. One section of the crystal packing of complex **6**, showing the π-stacking between the pyrene groups. Hydrogen atoms and solvent are omitted for clarity

c) Characterization of complex 7

The pattern of the NMR spectra of **7** indicates that the two metal centres are in a geometrically equivalent environment.

^{1}H NMR spectrum of 7

Figure 3.12 shows the ^{1}H NMR spectrum of **7**. The hydrogen atoms corresponding to the Cl-pyridines exhibit their resonances as one singlet, two doublets and one doublet of doublets 9.09, 8.99, 7.76 and 7.30 ppm (**h**, **k**, **i** and **j**). The signal due to the protons of the biphenylene linker appears as an AB system centred at 7.59 ppm (**d** and **e**). The

signals attributed to the C*H* proton of the imidazole are displayed at 6.92 and 6.76 ppm (**b** and **c**). The rest of the signals correspond to the protons of the CH_2 and CH_3 linkers next to the biphenylene bridge (**f** and **g**)

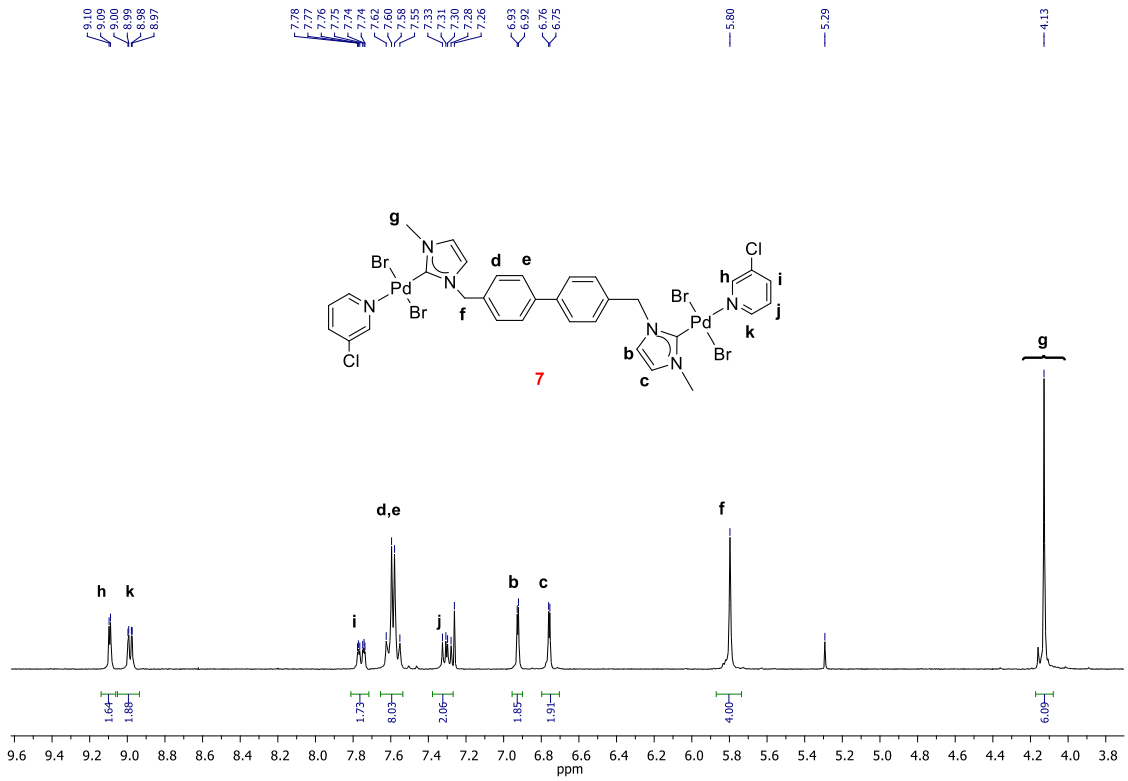

Figure 3.12. ^{1}H NMR spectrum of **7** in $CDCl_3$

$^{13}C\{^{1}H\}$ NMR spectrum of 7

Figure 3.13 shows the $^{13}C\{^{1}H\}$ NMR spectrum of **7**. The number of signals are consistent with the two metal centres in geometrically equivalent environment. For instance, the signal due to the metallated carbon appears at 147.6 ppm (**1**). The signals due to the *C*H carbons of the imidazole appear at 123.9 and 121.6 ppm (**6** and **7**). The resonances due to the *C*H_2 and *C*H_3 carbon atoms appear at 54.8 and 38.7 ppm respectively (**8** and **2**, respectively). All other signals are due to the phenyl and pyridine groups.

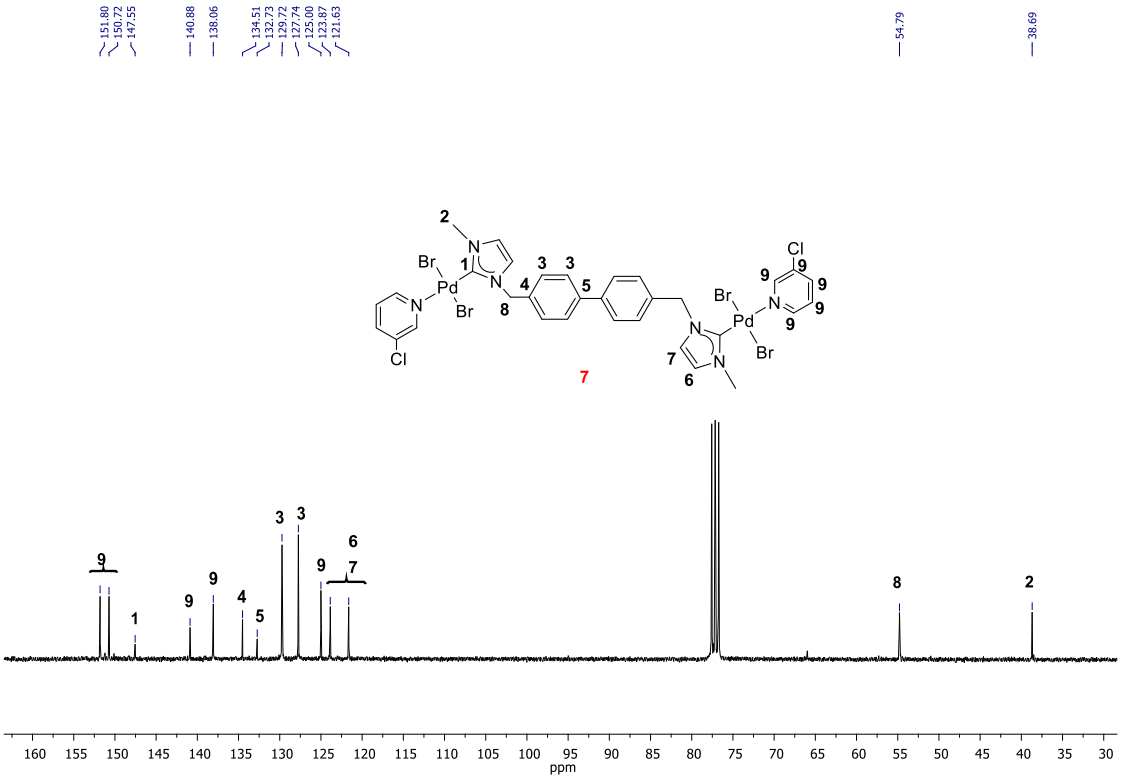

Figure 3.13. ^{13}C {^{1}H} NMR spectrum of **7** in $CDCl_3$

3.2.2.2 Synthesis and characterization of Iridium complexes

The bis-azolium salts **C** and **D** were coordinated to iridium by the method depicted in Scheme 3.5. The reactions of either of the azolium salts with $[IrCl(COD)]_2$ (COD = 1,5-cyclooctadiene) were carried out on in a mixture of THF/DMF at 75 ºC, in the presence of K_2CO_3 and KBr. The resulting suspensions were cooled to room temperature and the solvent was removed under vacuum. The crude products were purified by column chromatography. Complexes **10** and **11** were obtained in 65 and 67 % yields, respectively.

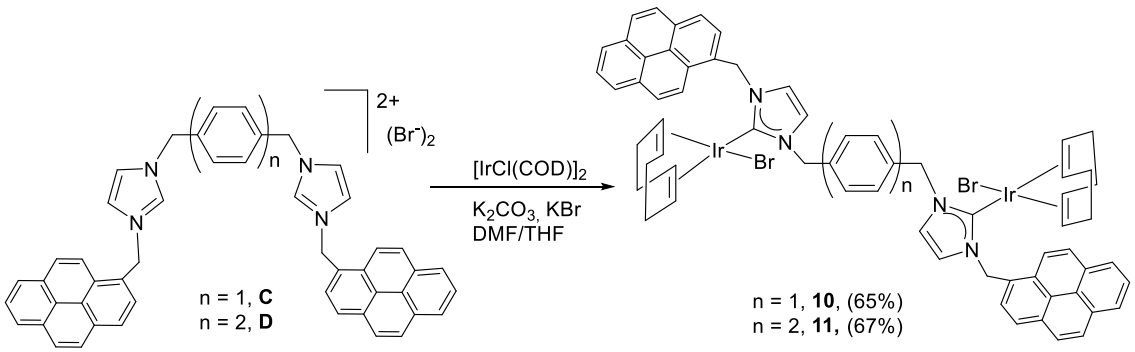

Scheme 3.5. Preparation of compounds **10** and **11**

The monometallic complexes **12** and **13** were prepared by using the same methodology. Complex **14**, which is the Rh analogue of **12**, was also obtained in a similar method, but using $[RhCl(COD)]_2$ as the metal source (Scheme 3.6). These monometallic complexes were synthesized for comparative purposes, so that their reactivity and catalytic activity could be compared with their dimetallic analogues. All the details regarding characterization of complexes **12**, **13** and **14** may be found in the experimental section.

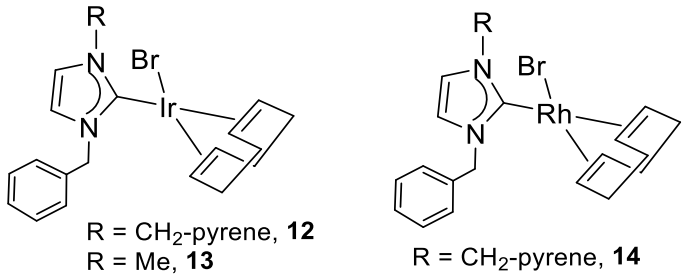

Scheme 3.6. Complexes**12**, **13** and **14**

*a) Characterization of complex **10***

The pattern of the NMR spectra of complex **10** indicates that the two metal centres are in a geometrically equivalent environment. However, for reasons that we were unable to fully explain, the signals due to the protons and carbons of the methylene linkers of the ligand appeared to be unequivalent. As will be described in the following sections, this effect is only observable for the complexes bearing the pyrene functionalities; therefore, it may be attributable to conformational changes of the complex in solution.

*^{1}H NMR spectrum of **10***

Figure 3.14 shows the ^{1}H NMR spectrum of **10**. Both metals centres seem to be in a geometrically equivalent environment, in accordance with the appearance of one sharp signal due to the aromatic protons from the bridging phenylene ring at 7.43 ppm (**d**). This symmetric environment is also supported by the number of resonances due to the cyclooctadiene protons (**g** and **h**), and the number of resonances ascribed to the protons of the pyrene fragment, which are displayed as a doublet and several multiplets at 8.48 and between 8.23-8.00 ppm. In the case of the signals due to the protons at the backbone of the imidazolylidene, four signals are observed (6.46, 6.43 ppm for **c** and **c'**, and two overlapping signals centred at 6.57 ppm for **b** and **b'**). The protons at the four methylene groups appear as inequivalent, as shown by the presence of eight doublets (**e1**, **e2**, **e'1**, **e'2**, **f1**, **f2**, **f'1** and **f'2**; note that each methylene group has two diasterotopic protons, and this makes all protons from the four CH_2 groups be

inequivalent). These two latter observations indicate some type of a conformational orientation of the complex that makes these protons to become non-equivalent.

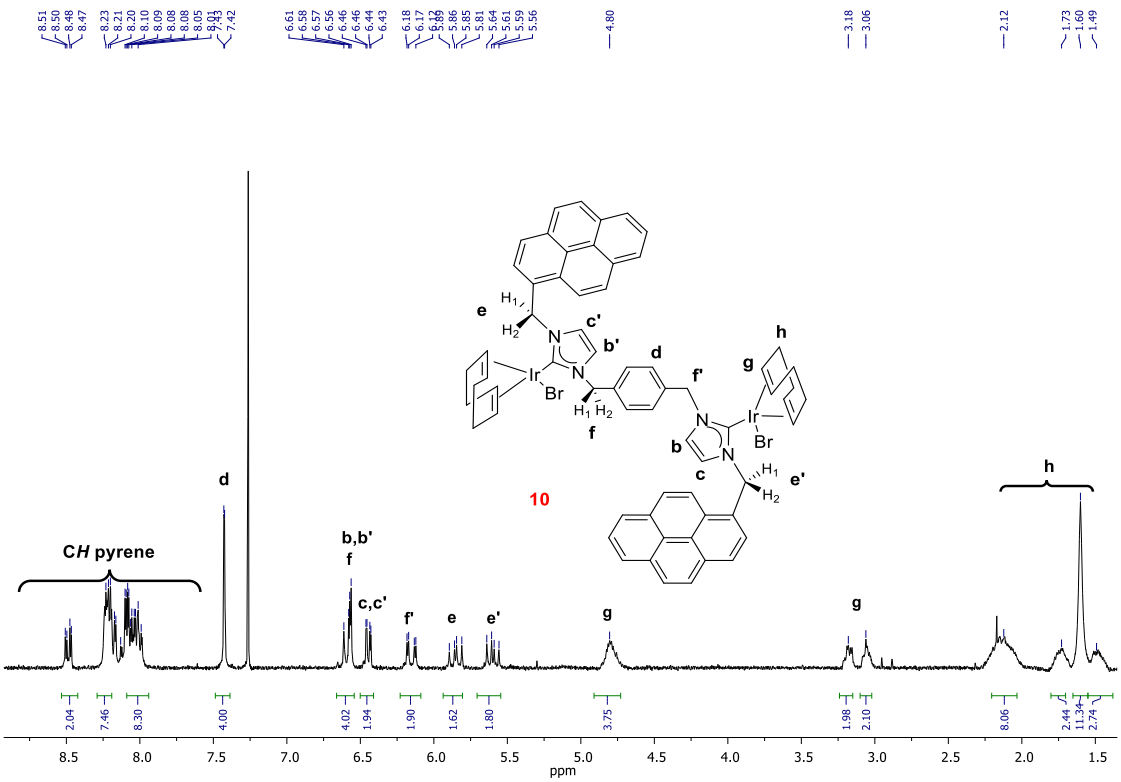

Figure 3.14. ^{1}H NMR spectrum of **10** in $CDCl_3$

*^{13}C {^{1}H} NMR spectrum of **10***

Figure 3.15 shows the ^{13}C {^{1}H} NMR spectrum of **10**. The fact that both metal centres are found in a geometrically equivalent environment is exemplified by the presence of one signal due to the carbene carbons at 180.8 ppm (**1**). In accordance with this, the signals due to the *C*H carbons of the imidazole groups appear as two resonances at 120.6 and 120.0 ppm (**5** and **6**). The rest of the signals correspond to the *C*H and *C*H_2 carbons of the cyclooctadiene ligand (**9** and **10**) also are in accordance with the symmetry of the complex. The signals due to the carbons of the pyrene and phenyl groups appear between 136.3 -123.0 ppm (**2**, **3** and **4**). The carbons due to the methylene groups display their resonances as four distinctive signals, at 54.0, 52.92, 52.60 and 52.2 ppm (**7** and **8**), therefore indicating some kind of asymmetry, which is fundamentally observed by these four carbon atoms.

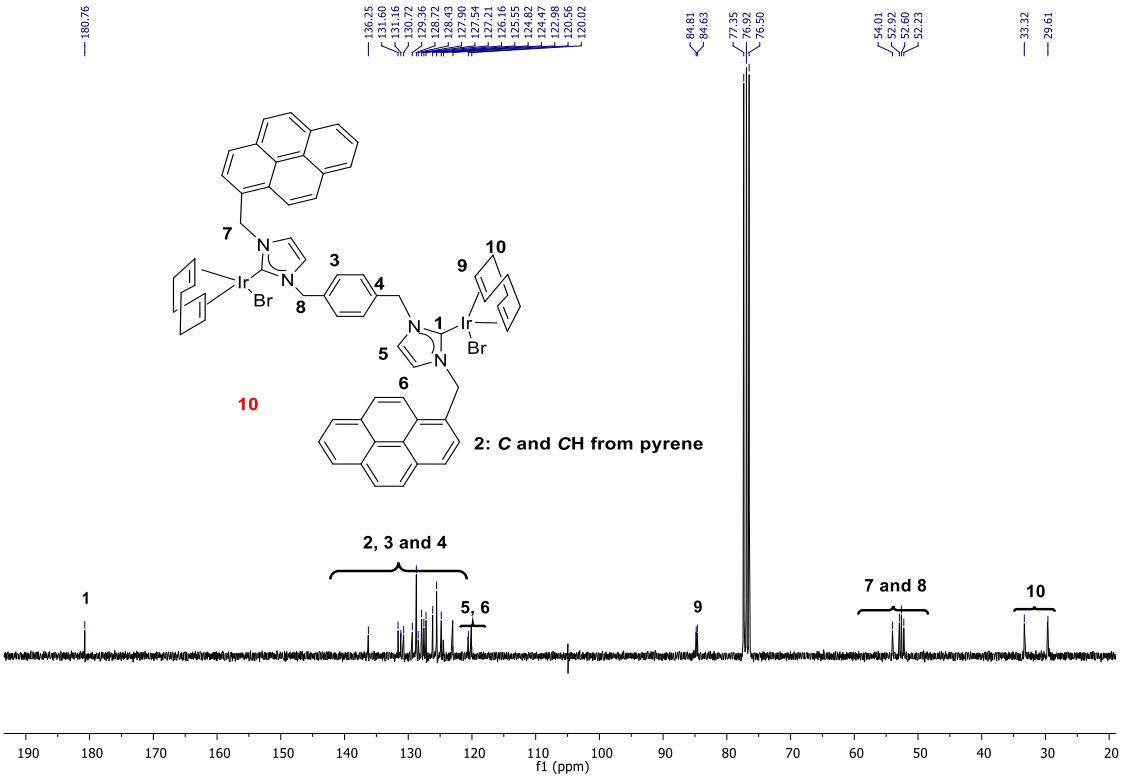

Figure 3.15. ^{13}C {^{1}H} NMR spectrum of **10** in $CDCl_3$

*b) Characterization of complex **11***

The pattern of the NMR spectra of complex **11** is suggestive of a situation in which the two metal centres are in an equivalent geometrical environment.

*^{1}H NMR spectrum of **11***

Figure 3.16 shows the ^{1}H NMR spectrum of **11**. The number of signals observed is in agreement with the twofold symmetry of the compound. This observation is exemplified by the presence of two doublets for the two phenylene ring protons at 7.58 and 7.47 ppm (**d** and **e**), and the two signals due to the protons of the backbone of the imidazolylidenes at 6.62 and 6.46 ppm (**b** and **c**). The resonances corresponding to the protons of the pyrene groups are displayed as a doublet at 8.50 ppm, and as several doublets and multiplets between 8.29-8.00 ppm. The signals due to the protons of the CH_2 groups appear as doublets at 6.60, 6.17, 5.87 and 5.67 ppm (**f**, **f'**, **g** and **g'**) (note that these protons are diastereotopic due to the asymmetry introduced by the cyclooctadiene ligands, which make the metal fragment lack of a mirror plane). The rest of the signals correspond to the CH_2 and CH protons of the cyclooctadiene ligand (**h** and **i**).

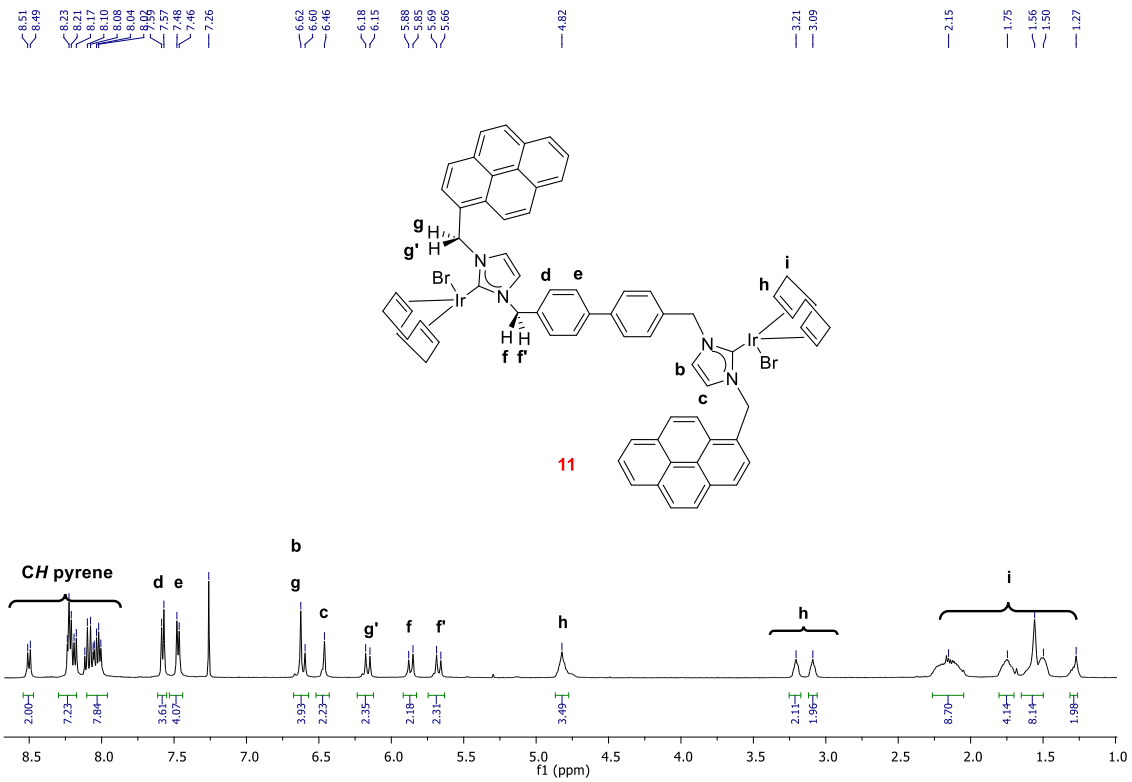

Figure 3.16. ^{1}H NMR spectrum of **11** in $CDCl_3$

*^{13}C {^{1}H} NMR spectrum of **11***

Figure 3.17 shows the ^{13}C {^{1}H} NMR spectrum of **11**. The twofold symmetry is exemplified by a single resonance due to the equivalent carbene carbons at 180.9 ppm (**1**). The signals corresponding to the *C*H and *C*H$_2$ carbon of the cyclooctadiene ligand appear at 84.7, 33.4 and 29.7 ppm (**10** and **11**). A set of signals from 140.4 to 123.1 ppm correspond to the pyrene and biphenyl carbon resonances (**2**, **3**, **4** and **5**). The signals assigned to the *C*H imidazole carbons appear at 120.6 and 120.2 ppm (**6** and **7**). As was observed for complex **10**, the *C*H$_2$ carbon resonances appear at 54.1, 53.0 52.6 and 52.3 ppm (**8** and **9**), therefore indicating some kind of a conformational asymmetry, which is fundamentally observed by these four carbon atoms.

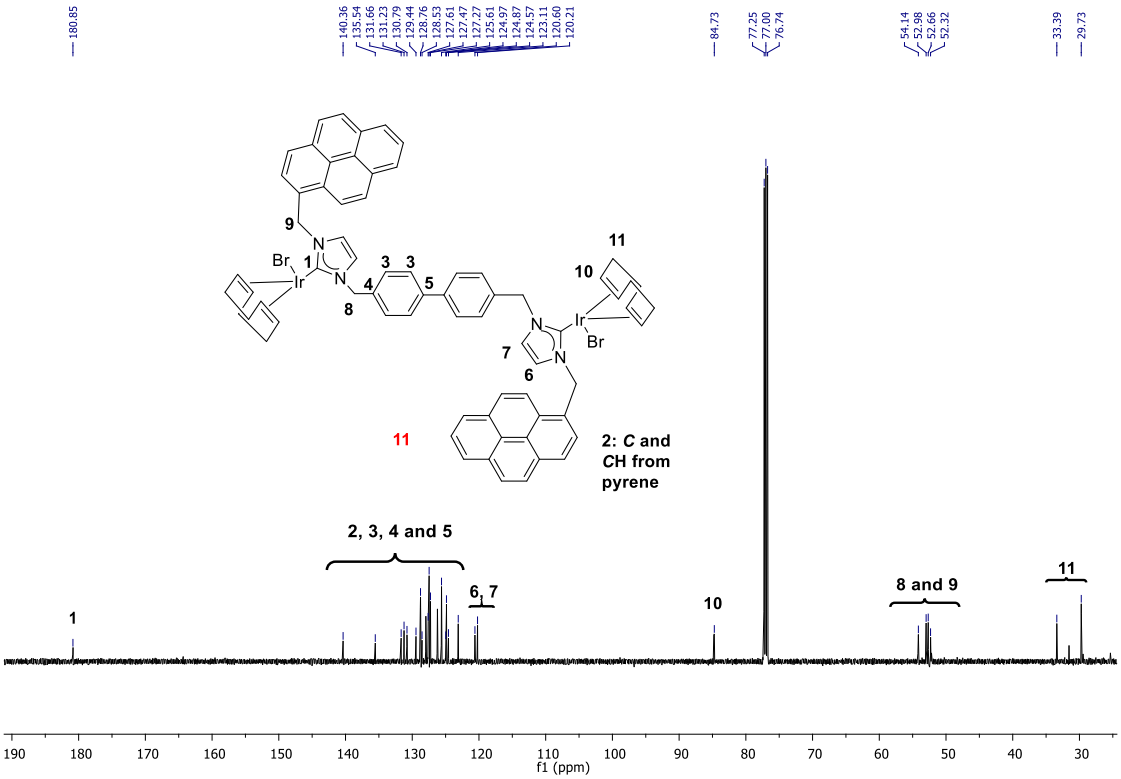

Figure 3.17. ^{13}C {^{1}H} NMR spectrum of **11** in $CDCl_3$

3.2.3 Catalytic studies

3.2.3.1 Catalytic properties of the palladium complexes

The catalytic activity of the palladium complexes **5-9** was tested in the acylation of aryl halides with hydrocinnamaldehyde and in the Suzuki-Miyaura cross-coupling between aryl halides and arylboronic acids.

a) Acylation of aryl halides with hydrocinnamaldehyde

Alkyl-aryl ketones are intermediates in the pharmaceutical, fragance, dye and agrochemical industries.[5] These compounds have been usually prepared by traditional Friedel-Crafts acylation, which involves handling hazardous reagents.

The palladium catalyzed acylation of aryl halides with aldehydes offers another interesting approach to alkyl-aryl ketones. The reaction was first reported by Xiao and co-workers who reported an efficient alternative route due to the possibility of achieving high yields in one-pot reaction.[6] The reaction consists of the coupling between an aryl halide and an aldehyde (hydrocinnamaldehyde) in the presence of a pyrrolidine, to afford the corresponding aryl-alkyl ketone. It was suggest that the acylation takes place via a Heck-type pathway.[6b] A possible catalytic cycle is depicted in Scheme 3.7. Pyrrolidine plays two roles in the reaction: one is to form an enamine in

a catalytic fashion, and the other is to act as a base for neutralizing the resulting HX acid. The *in situ* formation of the enamine from the aldehyde is the key step of the catalytic cycle.

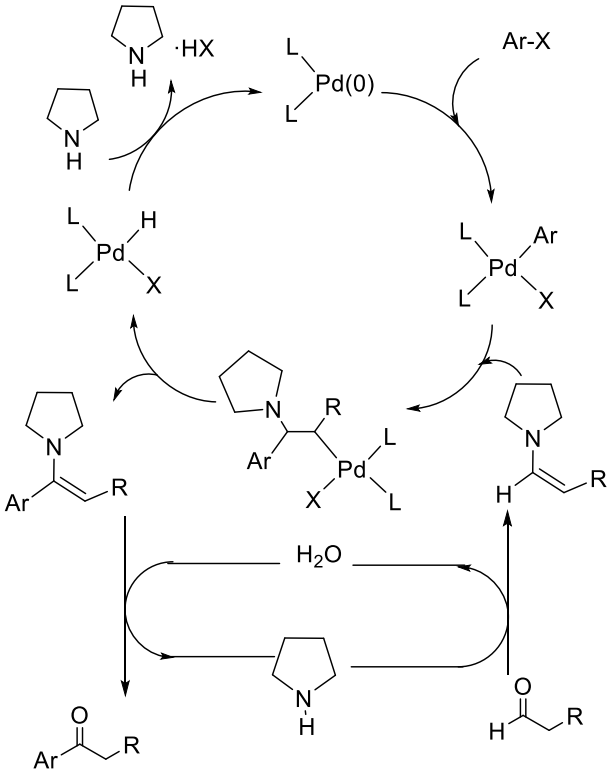

Scheme 3.7. Proposed acylation mechanism by Xiao

Although this process is a very useful reaction, there are just a few reported examples of the acylation of aryl halides with aldehydes, most of them referring to intramolecular processes, and very few referring to intermolecular processes.[2a,6-7]

We carried out the reactions between a benzyl halide and hydrocinnamaldehyde in DMF at 115ºC, in the presence of pyrrolidine, using a catalyst loading of 1 or 2 mol % referred to the concentration of palladium (this means that in the case of the dimetallic complexes **5-7**, the molar concentrations used were 0.5 or 1 mol%). We used the same reaction conditions as used in previous works carried out in our research group for the acylation of aryl halides with hydrocinnamaldehyde.[2a] The results that we obtained are summarized in table 3.1.

Table 3.1: Acylation of arylhalides with hydrocinnamaldehyde.[a]

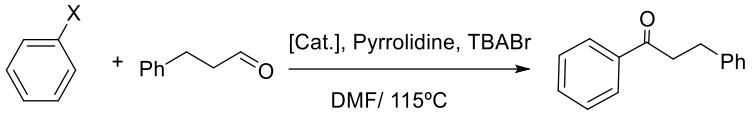

Entry	Catalyst	Pd (%)	X	Yield (%)[b]
1	6	2	I	67
2	5	2	I	62
3	7	2	I	60
4	8	2	I	54
5	9	2	I	32
6	6	1	I	61
7	6	2	Br	65
8	5	2	Br	49
9	7	2	Br	51
10	8	2	Br	30
11	9	2	Br	26
12	6	1	Br	61
13	6	2	Cl	13
14[b]	6	2	Br	66

[a]Molecular sieves (1g), tetrabutyl-ammoniumbromide (16 mg, 0.05 mmol), [Pd] (1 or 2 mol%), arylhalide (0.5 mmol), hydrocinnamaldehyde (0.6 mmol), pyrrolidine (1 mmol), and DMF (2 mL) were added to a 50 mL high-pressure Schlenk tube. The mixture was stirred and heated at 115 ºC for 16 h. Yields calculated by GC and using anisole as internal standard. [b]Reaction carried out in the presence of a drop of mercury.

The comparative study of the activities shown by complexes **5-9**, indicates that the pyrene-containing catalyst **6** is the most active one under the reaction condition used. This catalyst shows better activity than its monometallic analogue **8** (compare entries 1 and 4; 7 and 10). Complex **6** is also slightly more active than the two other dimetallic complexes **5** and **7**. It may be important to recall that the dimetallic catalyst **5** only differs from **6** in the linker between the imidazolylidene ligands, (xylyl in **5**, and biphenyl in **6**). Catalyst **7** contains a N-Me group, instead of pyrene. The results shown in Table 3.1 indicate that some structural features regarding the conformation of the di-NHC ligand influence the activity of the complexes in the reaction.

By comparing the activity of the monometallic complexes **8** and **9** (compare entries 4 and 5), it becomes evident that the presence of the pyrene tag improves the activity of the complex in the reaction (the activity of **8** is significantly higher than the activity

shown by **9**). We also performed a mercury drop experiment in order to discard that the reaction could be heterogeneously catalysed.[8] As can be seen from comparing the results shown in the table (compare entries 7 and 14), the yields obtained do not vary upon addition of the drop of mercury, and therefore we believe that the heterogeneity of the process is very unlikely.

b) Suzuki-Miyaura coupling between aryl halides and aryl boronic acids

The same palladium complexes were tested in the Suzuki-Miyaura coupling between aryl halides and aryl boronic acids. This reaction consists of the coupling between an arylboronic acid and an arylhalide, as depicted in Scheme 3.8.

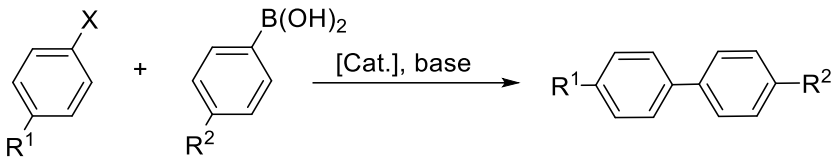

Scheme 3.8. Suzuki-Miyaura coupling reaction

The reactions were carried out in toluene at 80 ºC, in the presence of Cs_2CO_3. For all the reactions the catalyst loading was 2 mol%, based on the concentration of metal (1 mol % referred to the concentration of the dimetallic complexes **5-7**). The conditions were similar to those previously used in our group[2a] for the Suzuki-Miyaura coupling reaction. However, in order to favor the solubility of the substrates and catalysts, toluene was used instead of dioxane. The results are summarized in table 3.2.

Table 3.2: Suzuki–Miyaura coupling between aryl halides and aryl boronic acids.[a]

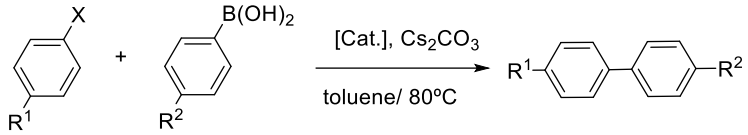

Entry	Catalyst	X	R^1	R^2	Yield (%)[b]
1	6	Br	H	Me	88
2	5	Br	H	Me	85
3	7	Br	H	Me	84
4	8	Br	H	Me	71
5	9	Br	H	Me	68
6	6	Br	H	H	69
7	5	Br	H	H	60
8	7	Br	H	H	62
9	8	Br	H	H	60
10	9	Br	H	H	55
11	6	Br	H	OMe	70
12	6	Br	COMe	Me	90
13	6	Br	OMe	Me	85
14	6	Br	OMe	H	78
15	5	Br	OMe	H	42
16	7	Br	OMe	H	44
17	8	Br	OMe	H	40
18	9	Br	OMe	H	35
19	6	Br	COMe	OMe	90
20	6	Br	Me	H	60
21[b]	6	Br	Me	H	60
22[c]	6	Cl	H	Me	20
23[d]	6	Cl	H	Me	30
24[d]	6	Cl	OMe	Me	69

[a]Reactions were carried out with aryl halide (0.5 mmol), aryl boronic acid (0.5 mmol), Cs_2CO_3 (1 mmol), and [Pd] (2 mol%) in toluene (2 mL) at 80 ºC for 2 h. [b]Yields obtained by GC analysis using anisole as internal reference. [b]Reaction carried out in the presence of a drop of mercury. [c]Reaction carried out at 120 ºC. [d]Reaction carried out at 120 ºC, 4 hours.

Under the reaction conditions used, complex **6** affords high activities in the coupling of a wide set of aryl bromides (yields range from 80 to 90 %). Again, **6** shows slightly better activities than the related dipalladium complexes **5** and **7**, so the linker and the pyrene tag seem to have some influence in the catalytic activity. Complex **6** is also moderately active in the coupling of aryl chlorides (see entries 22-24), although harsher

reaction conditions were needed. In order to discard that the process is heterogeneously catalysed, we also performed an experiment using the mercury drop test, which did not show any measurable differences compared to the experiment carried out in the absence of the drop of mercury (compare entries 20 and 21).

In general, the activities of these catalysts follow the same trend as the one observed for the acylation of aryl halides, in the sense that: i) all complexes having a pyrene tag display better activities than those with a methyl group; ii) the dimetallic complexes show better activities than the related monometallic analogues, and iii) the dimetallic complex with the longer metal-to-metal distance (**6**) is more active than the related one with the shorter distance (**5**).

If we assume that the stereoelectronic properties of the ligands present in **5-9** are similar due to their structural similarities around the metal centre, then the differences in the catalytic activities shown by their related palladium complexes should be ascribed to specific geometrical features, or to ligand-substrate π-interactions not related with the steric crowdening or electron donating character given by the ligands.

In order to test if π-staking interactions have an influence on the activity of the catalysts, we decided to perform the reactions under the same conditions used in table 3.2, but adding a catalytic amount of pyrene (10 mol % with respect to the initial amount of substrate). For the same reason, some other reactions were performed in the presence of anthracene. The idea of adding these rigid polyaromatic compounds is to determine if they have an influence on the activity of the catalysts. Previous studies developed in our laboratory demonstrated that the addition of π-stacking additives may have a strong influence on the catalytic outcome of catalysts bearing rigid polyaromatic fragments in their structure.[2b] In most of the cases an inhibition of the activity was observed, presumably as a consequence of the π-stacking interactions between the π-stacking additives and the polyaromatic tags in the structure of the catalyst, this probably producing an electronic or steric influence on the properties of the metal complex. The results obtained are shown in Table 3.3.

Table 3.3. Suzuki–Miyaura coupling between phenyl bromide and two aryl boronic acids, in the presence and absence of additives.[a]

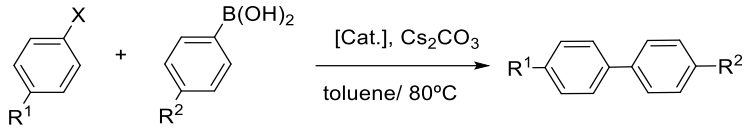

Entry	Cat.	X	R^1	R^2	Additive (mol%)	Yield (%)[b]
1	6	Br	H	Me	0	88
2	6	Br	H	Me	10 (pyrene)	80
3	6	Br	H	Me	10 (anthracene)	80
4	5	Br	H	Me	0	85
5	5	Br	H	Me	10 (pyrene)	57
6	5	Br	H	Me	10 (anthracene)	55
7	7	Br	H	Me	0	84
8	7	Br	H	Me	10 (pyrene)	85
9	8	Br	H	Me	0	71
10	8	Br	H	Me	10 (pyrene)	59
11	9	Br	H	Me	0	68
12	9	Br	H	Me	10 (pyrene)	68
13	6	Br	H	H	0	69
14	6	Br	H	H	10 (pyrene)	53
15	6	Br	H	H	10 (anthracene)	60
16	5	Br	H	H	0	60
17	5	Br	H	H	10 (pyrene)	30
18	7	Br	H	H	0	62
19	7	Br	H	H	10 (pyrene)	60
20	8	Br	H	H	0	60
21	8	Br	H	H	10 (pyrene)	50
22	9	Br	H	H	0	55
23	9	Br	H	H	10 (pyrene)	55

[a]Reactions carried out with phenyl bromide (0.5 mmol), aryl boronic acid (0.5 mmol), Cs_2CO_3 (1 mmol), and [Pd] (2 mol%) in toluene (2 mL) at 80 ºC for 2 h. Yields obtained by GC analysis using anisole as internal reference.

For all reactions catalyzed by the pyrene-containing palladium complexes (**5**, **6**, and **8**), the addition of a catalytic amount pyrene or anthracene produced a partial inhibition of the catalytic activity. On the contrary, the activity of both complexes with the N-methyl groups (**7** and **9**) remained unchanged upon addition of pyrene.

As previously observed for some other examples described in the Peris' laboratory,[2b] we interpreted these results as a consequence of π-staking interactions between the π-

stacking additive and the pyrene tags contained in the catalysts. In order to verify this hypothesis, we monitored the reaction progress of the coupling between the bromo benzene and 4-tolylboronic acid, using catalysts **6** and **7**, under the same reaction conditions shown in Table 3.3. We also monitored the reaction by using **6** in the presence of pyrene. Figure 3.18 shows the three reaction profiles. By comparing all three profiles, it becomes clear that the catalytic activity of **6** is higher than that shown by **7** all along the reaction course, thus indicating that the higher yields afforded by **6** are due to kinetic (higher catalytic activity) rather than thermodynamic (i.e. stability of the catalyst) reasons. The reaction reaches an 80% yield of the product after 20 minutes when catalyst **6** is used, while 1 hour is needed to reach the same yield when **7** is used. This result discards that the difference in activity between **6** and **7** may be ascribed to the different stabilities of the two catalysts. On the other hand, the addition of pyrene reduces the activity of **6**. This result is more obvious during the first 30 minutes of the reaction, for which the product yields are maintained significantly lower, suggesting that the inhibiting character of pyrene is kinetic in nature.

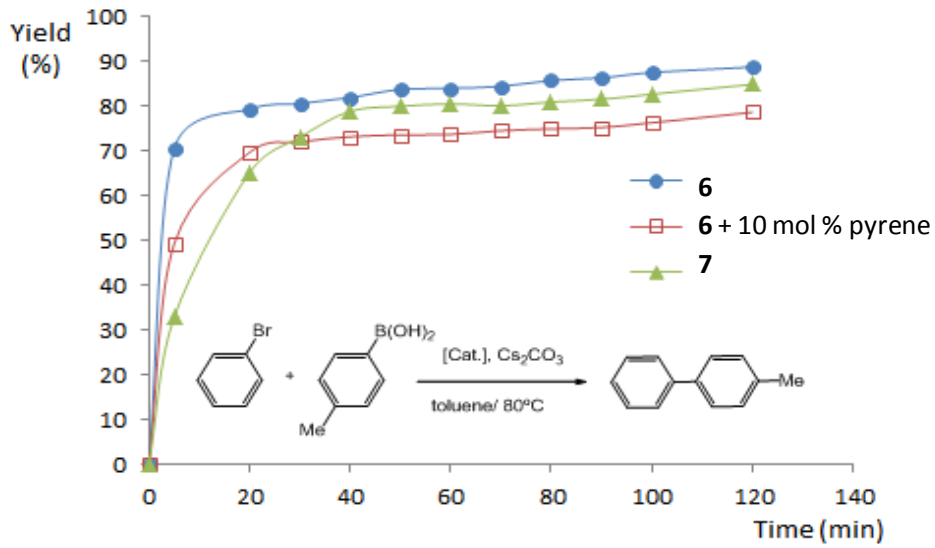

Figure 3.18. Time-course reaction profiles for the reaction of bromo benzene and 4-tolylboronic acid. Reaction conditions: phenyl bromide (0.5 mmol), 4-tolylboronic acid (0.5 mmol), Cs_2CO_3 (1 mmol), and [Pd] (2 mol%) in toluene (2 mL) at 80 ºC

The interaction between the pyrene-containing monometallic complex **8** with pyrene was also studied by ^{1}H NMR spectroscopy, by titrating a solution of **8** [10mM] with increasing amounts of pyrene. The spectra showed that only the resonances due to the protons from the aromatic tag in **8** were upfield shifted upon addition of increasing

amounts of pyrene (Figure 3.19). This result is strongly suggesting that a π–π stacking interaction is taking place between the pyrene tag and the pyrene additive.

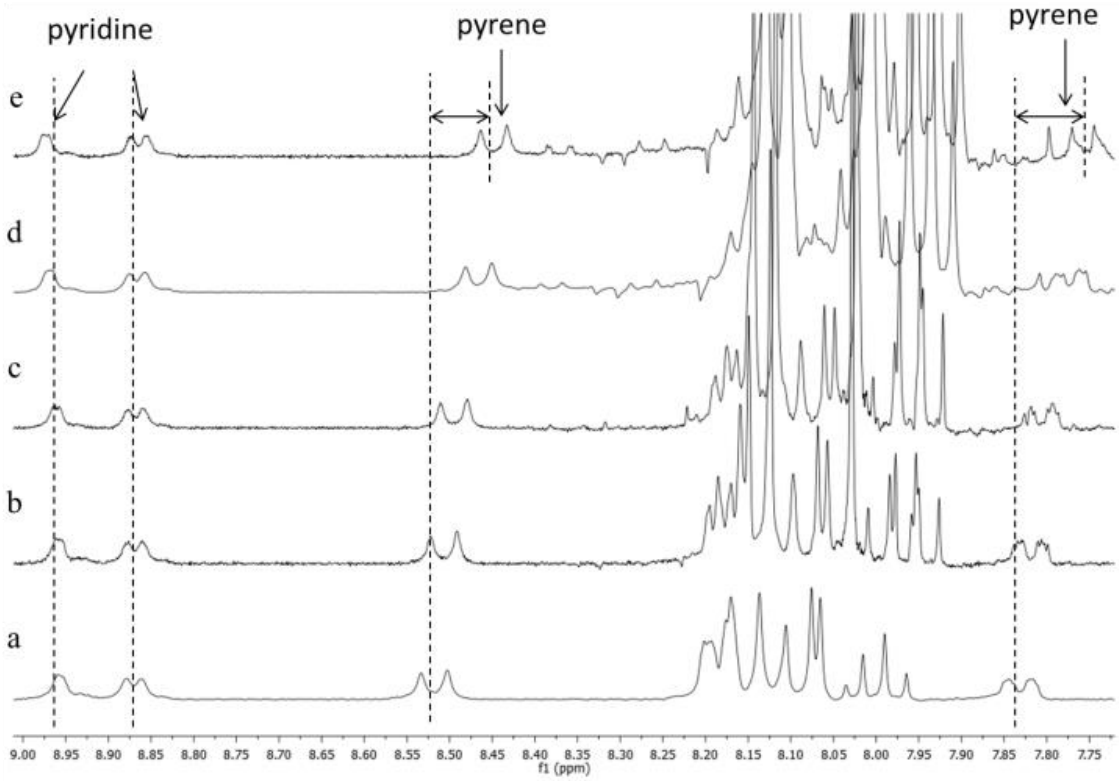

Figure 3.19. ^{1}H NMR spectra (300 MHz, $CDCl_3/CD_3OD$, 298K) of a) complex **8**; b) **8** + 1 equiv. of pyrene; c) **8** + 2 equiv. of pyrene; d) **8** + 5 equiv. of pyrene, e) **8** + 7 equiv. of pyrene

3.2.3.2 Catalytic properties of the iridium complexes

The catalytic activity of the iridium complexes **10-14** was tested in the reduction of ketones by transfer hydrogenation, and in the β-alkylation of secondary alcohols with primary alcohols, two processes for which rhodium and iridium have proved to be very effective catalysts.[9]

The aim of the study was to shed some light onto the effect of adding an additive (pyrene) in the catalytic activities, when substrates or catalysts with different features (aromatic or non-aromatic functionalities) were used.

a) Reduction of ketones by transfer hydrogenation

A transfer hydrogenation is the addition of hydrogen to an unsaturated molecule (typically olefins, imines, ketones or aldehydes) from a source other than hydrogen gas. The process circumvents the inconvenience of using gaseous H_2. For example, an alcohol (typically iPrOH) can be used as hydrogen source for the reduction of a ketone to a secondary alcohol (Scheme 3.9).[10]

From a mechanistic point of view, two general reaction path ways are widely accepted for the transfer hydrogenation,[10a] when a secondary alcohol is used as the hydrogen source (Scheme 3.8). The mechanism may either involve a dihydride (a) or a monohydride (b and c) intermediate. In the latter case two possible variants are also possible: the inner-sphere (b, without ligand assistance), or the outer-sphere (c, with participation of the ligand, typically a NH bond) process.

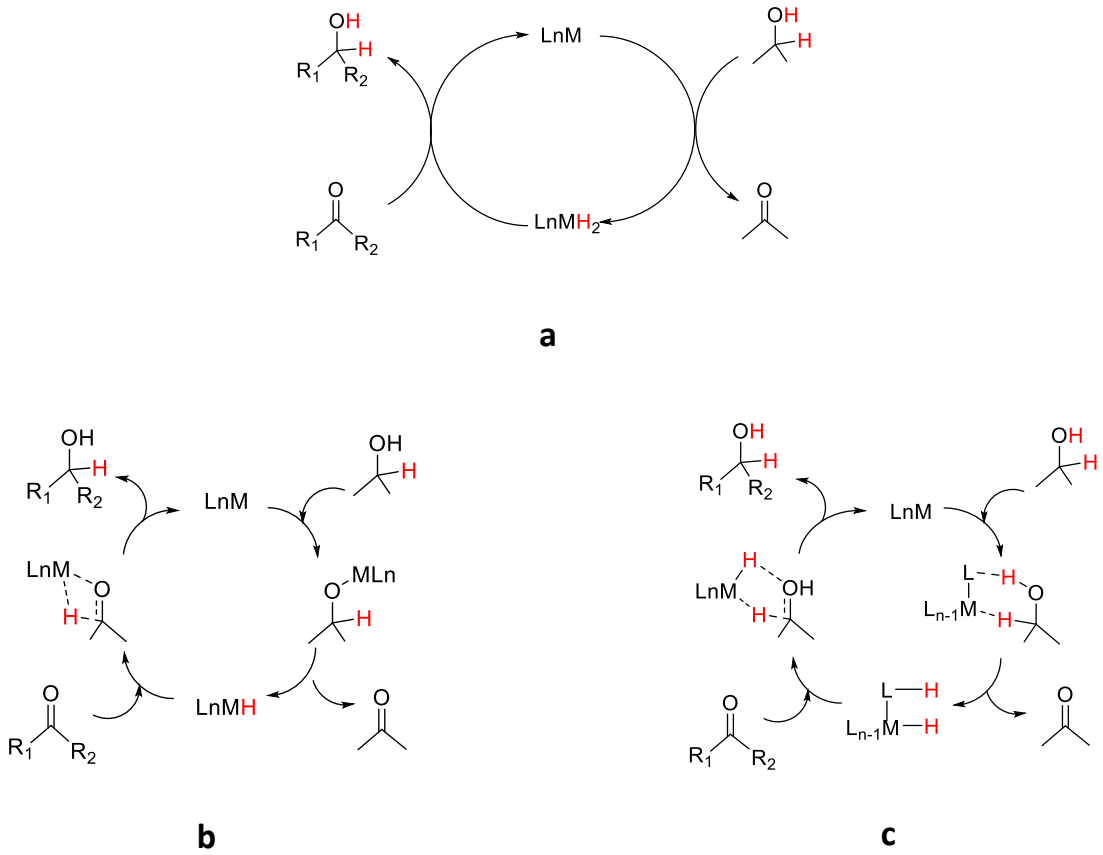

Scheme 3.9. Mechanisms for transfer hydrogenation (a) dihydride route; (b) monohydride inner sphere mechanism; (c) monohydride outer sphere mechanism

We decided to study the reduction of two model ketones, namely acetophenone and cyclohexanone. These two ketones represent good examples of an aromatic and an aliphatic substrate. We expected that, if π-stacking interactions are at play in the mechanism under study, this should have a clearer effect on the aromatic substrate, rather than on the aliphatic one.

The reactions were carried out by using a 0.5 mol % load of catalyst (based on the concentration of metal), in refluxing *i*PrOH (82 ºC), in the presence of KOH (10 mol%)

during one hour.[9g] The results are given in Table 3.4. Under these reaction conditions, the background activity of the base was found to be negligible (< 1%).

Table 3.4. Catalysts **10-14** in the reduction of acetophenone and cyclohexanone by transfer hydrogenation in *i*PrOH.[a]

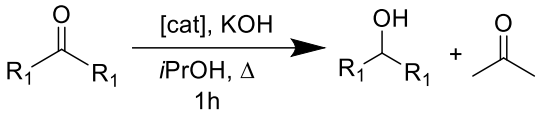

Entry	Cat.	Ketone	Pyrene (mol)	Yield
1	10	cyclohexanone	-	91 (±1)
2	11	cyclohexanone	-	86 (±1)
3	12	cyclohexanone	-	91 (±1)
4	13	cyclohexanone	-	80 (±1)
5	14	cyclohexanone	-	16 (±1)
6	10	cyclohexanone	0.05	89 (±1)
7	11	cyclohexanone	0.05	87 (±1)
8	12	cyclohexanone	0.05	89 (±1)
9	13	cyclohexanone	0.05	81 (±1)
10	10	acetophenone	-	94 (±1)
11	11	acetophenone	-	94 (±1)
12	12	acetophenone	-	30(±1)
13	13	acetophenone	-	79 (±1)
14	10	acetophenone	0.05	21 (±1)
15	11	acetophenone	0.05	75 (±1)
16	12	acetophenone	0.05	16 (±1)
17	13	acetophenone	0.05	81 (±1)

[a]Reaction conditions: ketone (0.5 mmol), isopropanol (2 mL), KOH (0.05 mol) and [Ir] (0.5 mol%) at 82 ºC. Time: 1h. Yields determined by GC, averaging a minimum of two runs, using anisole as internal standard.

One of the first evidences that can be extracted from the results shown in Table 3.4, is that all iridium complexes **10-13** are significantly more active than the rhodium complex **14** (compare entries 1-4 with entry 5). This made us discard complex **14** for further catalytic studies. All iridium complexes are very active in the reduction of cyclohexanone. For the reduction of acetophenone, the dimetallic complexes, **10** and **11**, are slightly more active than the monometallic complexes **12** and **13**. Interestingly, the addition of pyrene has significant different effects depending on the catalyst and the nature of the ketone used. For the reduction of cyclohexanone, the addition of pyrene did not produce any modification in the activity of all four catalysts, compared to the

reactions in which pyrene was not added (compare 1-4 entries with 6-9). For the reduction of acetophenone, the addition of a 10 mol% of pyrene produced a significant inhibition of the activity of catalysts bearing the pyrene tag (compare 10, 11 and 12 entries with 14, 15 and 16), while the activity of the complex lacking of the pyrene functionality, **13**, remained unchanged (compare entries 13 and 17). These data are graphically represented in Figure 3.20, where this effect is probably better illustrated. These results are in accordance with our previous results that indicate that the activity of catalysts bearing rigid polyaromatic ligands is influenced by the π-stacking with aromatic substrates,[2b] but in this case the effect becomes more evident, since we were able to directly compare the effects produced over one aliphatic and one aromatic substrate. These results clearly indicate that only when both, an aromatic substrate and a catalyst with polyaromatic tags are used, a supramolecular effect is observed in the catalytic outcome, hence supporting the idea that π-stacking interactions are responsible for the alteration of the activity of the catalyst.

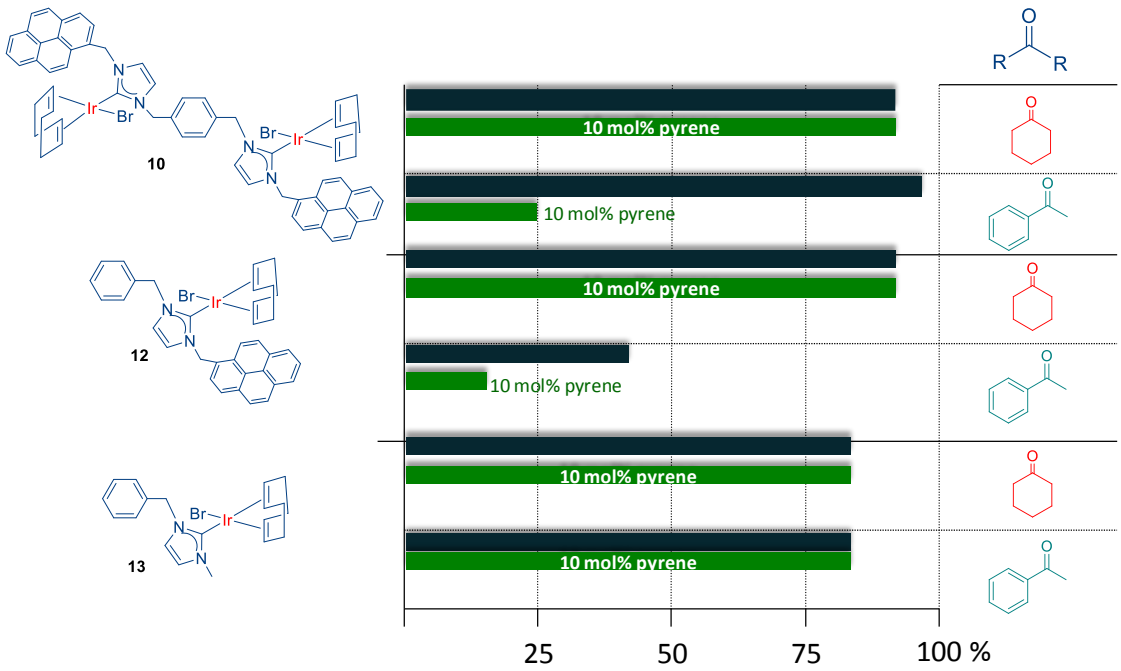

Figure 3.20. Effect of adding pyrene in different transfer hydrogenation of ketones using catalysts **10**, **12** and **13**. Reaction conditions as in Table 3.4

b) β-alkylation of secondary alcohols with primary alcohols

The *β*-alkylation of secondary alcohols with primary alcohols is a typical Borrowing Hydrogen (BH) process, also named as hydrogen auto transfer. This methodology combines the advantages of transfer hydrogenation with additional transformations,

which can be regarded as a type of domino reaction.[11] The term borrowing refers to the transfer from the hydrogen to the catalyst and further devolution to the unsaturated intermediate.

The *β*-alkylation of secondary alcohols with primary alcohols is a typical example of BH process. This reaction has been deeply studied by the group of Fujita[12] and by Peris' group.[9g,13] Mechanistically, such reactions are believed to involve first the oxidation of both alcohols, followed by an aldol condensation to yield an *α,β*-unsaturated ketone. In this process the catalyst withdraws "H_2" from the substrates; and in the final step of the reaction the catalyst returns this "H_2" to the unsaturated ketone to generate the final product, which is the alkylated alcohol. A byproduct ketone may be generated. (Scheme 3.10).

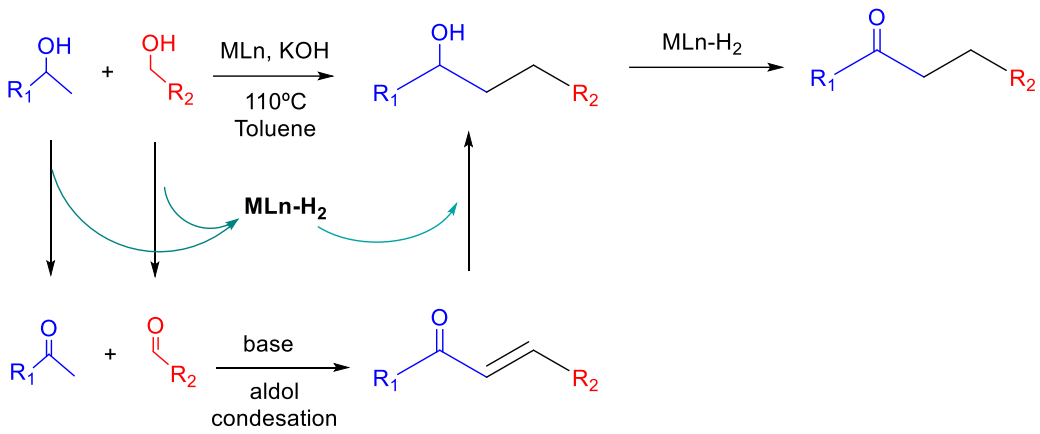

Scheme 3.10. Three-step transformation in the β-alkylation of a secondary alcohol with another alcohol

By studying this reaction our aim is to evaluate the catalytic properties of our complexes and to determine whether π-stacking interactions between the substrates and the catalyst may influence the activities of the complexes. For the study, we decided to couple 1-phenylethanol with a series of benzyl alcohols (benzyl alcohol, 3-chlorobenzyl alcohol and 4-chlorobenzyl alcohol) and *n*-butanol (*n*BuOH), aiming to cover a set of aromatic and aliphatic substrates. The reactions were carried out using a catalyst loading of 0.5 mol % (based on the concentration of Ir) in 0.5 mL of toluene, using an equimolecular amount of both alcohols (1 mmol) and KOH (1 mmol), at 100 ºC during 8 h.[13] The results are summarized in Table 3.5.

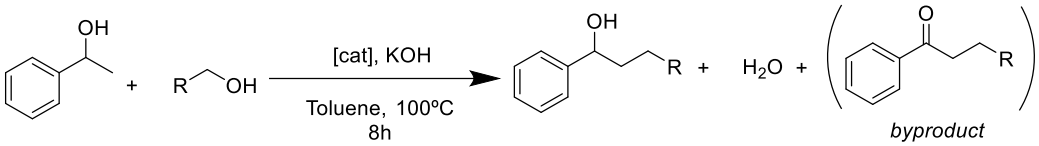

Table 3.5. Catalysts **10-13** used in the β-alkylation of 1-phenylethanol with primary alcohols.[a]

Entry	Cat.	R	Conv.	Yield (alcohol)
1	10	Ph	99 (±1)	99 (±1)
2[a]	10	Ph	99 (±1)	99 (±1)
3	11	Ph	51 (±1)	50 (±1)
4	12	Ph	50 (±1)	50 (±1)
5	13	Ph	43 (±1)	41 (±1)
6	10	3-Cl(C_6H_5)	92 (±1)	92 (±1)
7	11	3-Cl(C_6H_5)	40 (±1)	40 (±1)
8	12	3-Cl(C_6H_5)	43 (±1)	43 (±1)
9	13	3-Cl(C_6H_5)	53 (±1)	52 (±1)
10	10	4-Cl(C_6H_5)	90 (±1)	90 (±1)
11	11	4-Cl(C_6H_5)	49 (±1)	47 (±1)
12	12	4-Cl(C_6H_5)	32 (±1)	30 (±1)
13	13	4-Cl(C_6H_5)	31 (±1)	31 (±1)
14	10	*n*Pr	50 (±1)	47 (±1)
15	11	*n*Pr	40 (±1)	38 (±1)
16	12	*n*Pr	43 (±1)	40 (±1)
17[b]	13	*n*Pr	45 (±1)	40 (±1)

[a]Reaction conditions: 1-phenylethanol (1 mmol), primary alcohol (1 mmol), KOH (1 mmol) and [Ir] (0.5 mol%) in 0.5 mL of toluene at 100 ºC. Yields determined by GC, averaging a minimum of two runs, using anisole as internal standard. [b]Reaction carried out in the presence of a drop of Hg

From the results shown in Table 3.5, it can be observed that all catalysts **10-13** are very selective in the production of the final alcohols. Only in some cases, traces of the α,β-unsaturated ketone byproduct are detected (the small differences between conversions and yields are due to the formation of the ketone byproduct). Complex **10**, with the phenylene linker, is the most active catalyst in all the reactions tested. This catalyst afforded quasi-quantitative conversions for the coupling of aromatic alcohols. In order to discard that the process is heterogeneously catalysed, we performed an experiment using the mercury drop test, which did not show any significant differences compared to the experiment in the absence of the mercury drop (compare entries 1 and 2).

In order to shed some light on to the reaction mechanism, especially with regard to the interaction of the catalysts with the alcohols in the initial steps of the processes, some kinetic studies were performed.

i) Time-dependent reaction profile studies (reaction order with respect the substrate)

The time-dependent reaction profile of the *β*-alkylation of 1-phenylethanol with benzyl alcohol using catalyst **10** at different concentrations (0.01-5mol %) is shown in Figure 3.21. All reaction profiles are indicative of a *zeroth* order rate in the substrate. This result, which resembles enzymatic catalysis, is suggestive of a situation in which the catalyst is saturated by the substrate, and reflects that only a portion of the substrate is in a position where it is able to react. Our interpretation of this result is that this situation may arise from the non-covalent interaction between the aromatic substrate and the pyrene-tag of the catalyst (Scheme 3.12), which locates the substrate in a privileged position where it can be activated by the metal fragment.

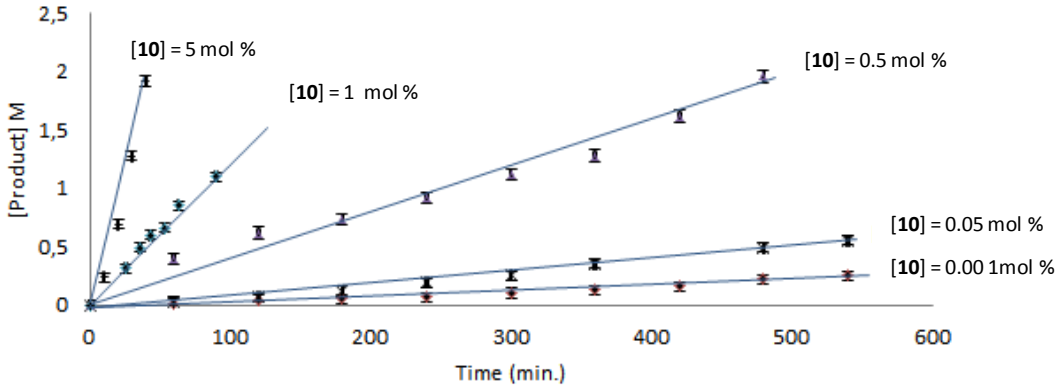

Figure 3.21. Time-dependent reaction profile for the reaction between 1-phenylethanol and benzyl alcohol using catalyst **10**. Reaction conditions: 1-phenylethanol (1 mmol), benzyl alcohol (1 mmol), KOH (1 mmol) in 0.5 mL of toluene at 100 ºC. Yields determined by GC, using anisole as internal standard. Product: 1-phenyl hexanol. The concentration of the catalyst (**10**) is shown for each plot. Straight lines drawn to guide the eye

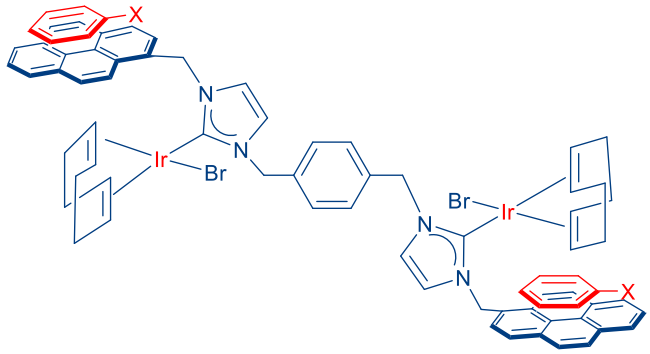

Scheme 3.12. Representation of the non-covalent interaction between the pyrene tags from catalyst **10** and an aromatic substrate

In order to further support this hypothesis we carried out two experiments. We first monitored the time-dependent reaction profile of the coupling of 1-phenylethanol and benzyl alcohol using the monometallic catalyst **13**. As can be observed from the profile shown in Figure 3.22, this profile suggests a second order rate with respect to the concentration of the substrates. The second order rate is consistent with the two substrates reacting in a 1:1 stoichiometry. Catalyst **13** does not have pyrene functionality and therefore it is not expected to form any sort of non-covalent interaction with the aromatic substrates.

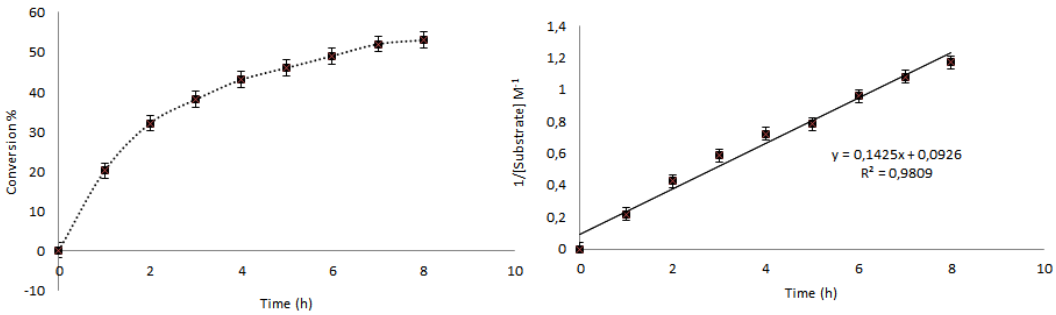

Figure 3.22. The plot on the left represents the time dependent reaction profile for the reaction between 1-phenylethanol and benzyl alcohol. Reaction conditions: 0.05 mmol of catalyst **13**, 1-phenylethanol (1 mmol), benzyl alcohol (1 mmol), KOH (1mmol) in 0.5 mL of toluene at 100 ºC. The plot on the right represents 1/[1-phenylethanol] *vs* time

Then, the coupling of 1-phenylethanol with *n*-butanol using catalyst **10** was studied**.** Again, the reaction profile is consistent with a second order reaction rate with respect to the substrates (Figure 3.23). In this case a catalyst with a pyrene functionality is used, but the primary alcohol is aliphatic, and therefore, the π–π-stacking interaction with the catalyst is not taking place.

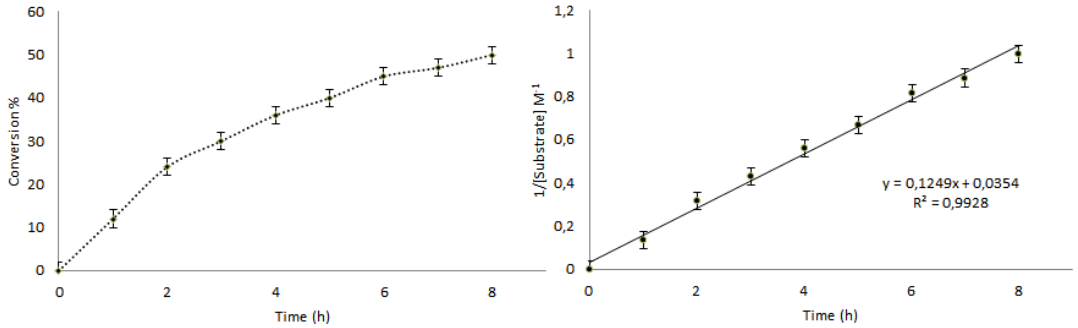

Figure 3.23. The plot on the left represents the time dependent reaction profile for the reaction between 1-phenyletanol and *n*butanol. Reaction conditions: 0.05 mmol of catalyst **10**, 1-phenylethanol (1 mmol), *n*-butanol (1mmol), KOH (1 mmol) in 0.5 mL of toluene at 100 ºC. The plot on the right represents the 1/[1-phenylethanol] *vs* time

The results reflected in this section indicate that when the reaction is carried out with a catalyst containing a polyaromatic fragment, and the substrates are aromatic, the supramolecular interaction between the substrate and the catalyst is clearly influencing the kinetics of the reaction.

ii) Reaction order with respect the catalyst

The determination of the rate orders with respect to the concentration of the catalysts also revealed very interesting information regarding the supramolecular interactions influencing the catalytic behavior of all three catalysts.

In order to determine the rate orders with respect to the concentration of catalysts **10**, **12** and **13**, the observed kinetic constants of the processes were obtained for concentrations of the catalysts ranging from 0.01-5 mol %. These results are given in Table 3.5.

Table 3.5. Observed kinetic constant of the processes for catalyst **10, 12** and **13** obtain for concentration from 0.01-5 mol %

	Cat. 10		**Cat. 12**		**Cat. 13**	
mol % Iridium	**Slope= k_{obs} (min^{-1})**	**[Ir] (M)**	**Slope= k_{obs} (min^{-1})**	**[catalyst] (M)**	**Slope= k_{obs} (min^{-1})**	**[catalyst] (M)**
5	0,0292	0,0597	0,0036	0,0625	0,0241	0,0597
1	0,0074	0,0119	0,0014	0,0125	0,0042	0,0119
0,5	0,0028	0,0060	0,0010	0,0063	0,0024	0,0060
0,05	0,0006	0,0006	0,0002	0,0005	0,0003	0,0006
0,01	0,0003	0,0001			0,0000	0,0001

The representation of log(k_{obs}) against log[**cat**], allowed to determine the rate orders with respect to the concentration of each of the catalysts under study, for the coupling of 1-phenyl ethanol with benzyl alcohol.

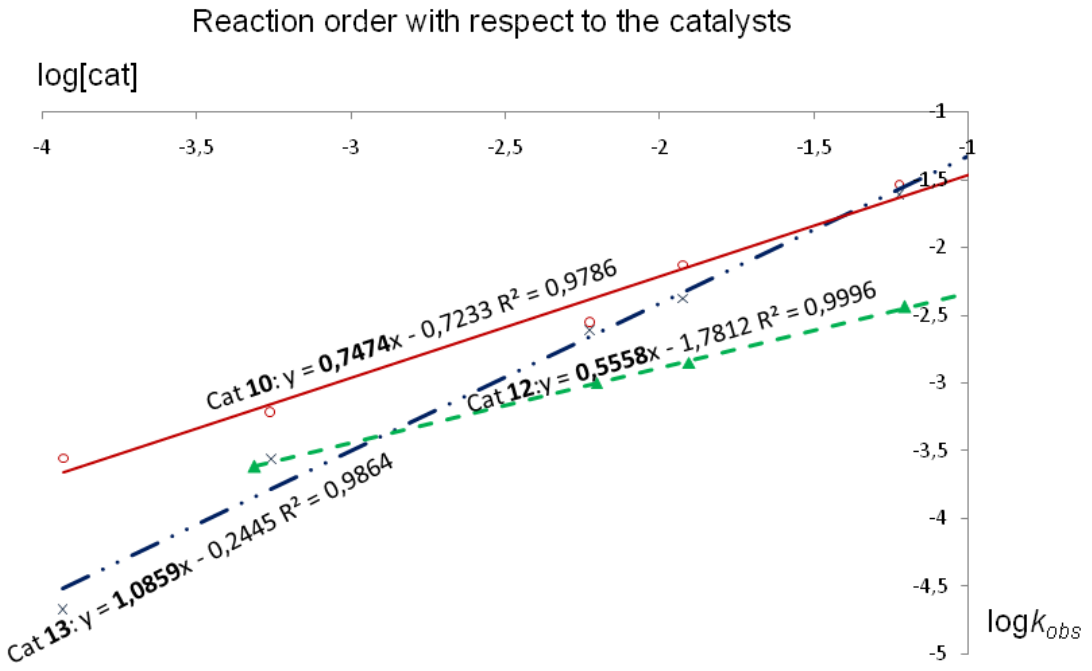

Figure 3.24. Determination of the reaction order with respect the catalyst concentration. Plot of log(k_{obs}) against log[**cat**]. The values of the slopes with errors are: 1.08±0.07 (**13**), 0.555±0.008 (**12**) and 0.75±0.06 (**10**).

The slopes of the corresponding straight lines directly provided us the rate orders with respect to the concentration of the catalysts. From the results shown in Figure 3.24 it was clearly observed that the use of the catalyst without the pyrene functionality (**13**), derived into a first order dependence on the concentration of the catalyst. This result clearly indicates that the active specie is monometallic.

The reactions carried out with the pyrene-containing catalysts (**10** and **12**) followed a fractional reaction order (<1) with respect to the concentration of the catalysts. In particular, the reaction order with respect to the dimetallic complex **10** was 0.75, while the order with respect to the monometallic complex **12** was 0.55. The half-order dependence is strongly suggestive of monomer-dimer equilibrium,[14] with the monomer being the active catalytic species. This may be explained by considering that the concentration of the monomeric species may be expressed as $[monomer] =$

$\left(\frac{[dimer]}{Ka}\right)^{1/2}$, where K_a is the self-association constant. In our case, the self-association may arise from the π- π-stacking of the pyrene functionalities present in complex **12**, which should form non-active non-covalently attached dimers (Scheme 3.13).

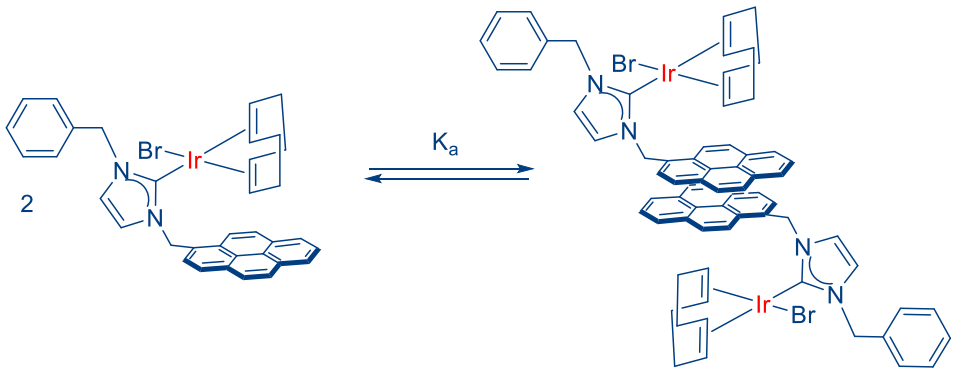

Scheme 3.13. Self-association of compound **12**

In the case of the dimetallic complex **10**, for which the reaction rate order in the catalyst is 0.75, the same self-association should be taking place, although in this case the dimetallic nature of the complex may give rise to aggregates in which the activity of the two metals may be retained, therefore leading to an order of reaction between 0.5 and 1.

This experiment strongly supports that the pyrene functionality has an important contribution to the reaction mechanism, most likely due to the formation of aggregates with inhibited activity in the cases of **10** and **12**. The inhibition of the activity of **10** and **12** produced upon self-association through the pyrene-tags (ligand–ligand interaction), supports the idea that the interaction between pyrene and the substrate has an important role in the overall catalytic reaction.

3.2.4 Immobilization of catalysts with pyrene tags onto graphene derivatives

The non-covalent immobilization between a catalyst and a support constitute an interesting alternative to the more widely used covalent immobilization because it avoids the functionalization of both, the catalyst and the surface, which may turn into the modification of the inherent properties of the catalyst. However, because non-covalent interactions are weaker than covalent ones, some other problems may arise, such as leaching.[15] In connection with the results described in the previous sections, we became interested in evaluating whether we could use the π-stacking abilities of pyrene-containing metal complexes for their non-covalent immobilization onto graphene

derivatives. Some other studies were performed, some of them in our group, regarding the immobilization of pyrene-containing metal complexes onto graphitized surfaces[16] demonstrating interesting recyclability properties.[17]

Taking all this into account, the aim of this part of the work was to immobilize the iridium pyrene-containing complexes (**10** and **12**) onto reduced graphene oxide (rGO) and study the recyclability capabilities of the resulting materials in the *β*-alkylation of secondary alcohols with primary alcohols. We decided to use catalysts **10** and **12**, because the comparison of their activities should provide us interesting information about, (a) the influence of the mono- or dimetallic nature of the catalyst (complex **10** may be regarded as exactly the combination of two molecules of **12**), and (b) about the influence of the presence of one or two pyrene tags for the immobilization onto the solid surface. The immobilization of the catalysts described in this work may be of especial interest, because we are unaware of any heterogeneized catalysts used for the *β*-alkylation of alcohols with efficient recyclability properties.

*3.2.4.1 Synthesis and characterization of hybrid rGO-**10** and rGO-**12***

Complexes **10** and **12** were supported onto reduced graphene oxide (rGO) by mixing the molecular complexes and the rGO material in dichloromethane. The resulting suspension was sonicated for 30 minutes and stirred at room temperature for 12 h until the solution became colorless. The resulting dark solids (**10**-rGO and **12**-rGO) were filtered and washed thoroughly with dichloromethane, affording the resulting product as a black solid.

The first evidence of the formation of the complex anchored to the rGO surface is the disappearance of the color of the solution. The ^{1}H NMR spectroscopy analyses of the filtrate residues also revealed the absence of the complex in the solution. The exact iridium content on **10**-rGO and **12**-rGO was determined by digestion of the samples in hot HCl/HNO_3 followed by ICP-MS analysis. The results obtained accounted for a 2.8 wt% of **12**-rGO, and 6.8 of **10**-rGO.

The presence of the metal complexes on the surface of the solid is also confirmed by UV/Vis measurements (experimental section 7.7, Chapter 7). The spectra of the hybrid materials consist of the overlap of the molecular complexes (**10** or **12**) with rGO, as seen by the pyrene UV/Vis characteristic signals.

10-rGO and **12**-rGO were also characterized by Scanning Electron Microscopy (SEM), which revealed that morphology of the solids consisted of randomly aggregated thin sheets. HRTEM was used to characterize the microstructure and qualitative composition of the hybrids. The elemental mapping by Energy-Dispersive X-ray Spectroscopic analysis (EDS) performed by means of HRTEM of rGO-**10** and rGO-**12**, confirmed the homogeneous distribution of iridium in the two hybrid materials (Figure 3.25 shows the STEM and HRTEM images obtained for rGO-**12**).

All the characterization details, including the SEM and HRTEM images and UV/Vis spectra of rGO-**10** and rGO-**12** are given in experimental section 7.8, Chapter 7.

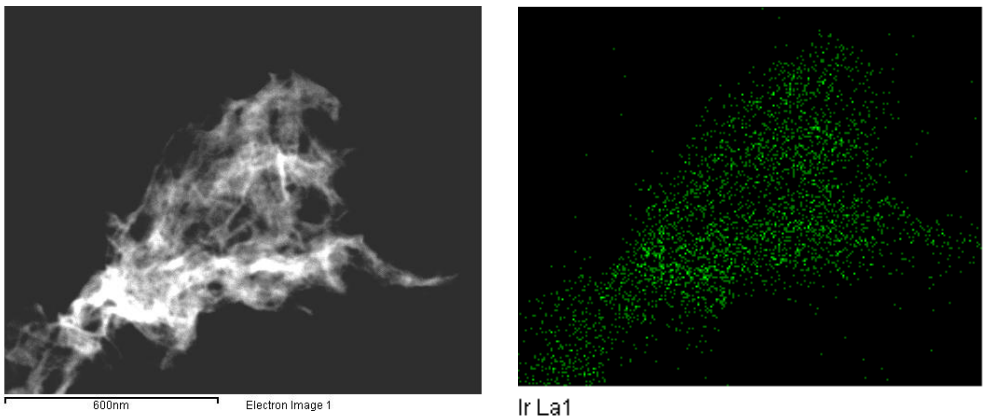

Figure 3.25. STEM image of rGO-**12**, and EDS elemental mapping (HRTEM) images showing the homogeneous distribution of iridium.

3.2.4.2 Catalytic Studies

For the study of the recyclability properties of rGO-**10** and rGO-**12**, we monitored the reaction between 1-phenylethanol with benzyl alcohol. The reaction conditions used for each individual run was carried out using a catalyst loading of 0.5 mol% (based on the amount of Iridium, as determined by the ICP-MS analysis) in toluene (1.5 mL) at 100 ºC, using 1 mmol of each of the alcohols and 1 mmol of KOH. After completion of each run (8 h), the solid was filtered, washed with CH_2Cl_2, dried and re-used in the following run. An interesting feature of the results shown in Figure 3.26 is that the activity shown in the first run is significantly lower than the activity shown for the rest of the cycles. This situation is common for rGO-**10** and for rGO-**12**, and may be explained as a consequence of the activation of both catalysts, which is produced during the first reaction run. As can be seen from the results shown in the graphic, catalyst rGO-**10** could be recycled for up to 12 runs without detectable loss of activity. In the case of

rGO-**12**, the results revealed a gradual decrease in the activity, until the complete deactivation of the catalyst, which was produced after 7 runs.

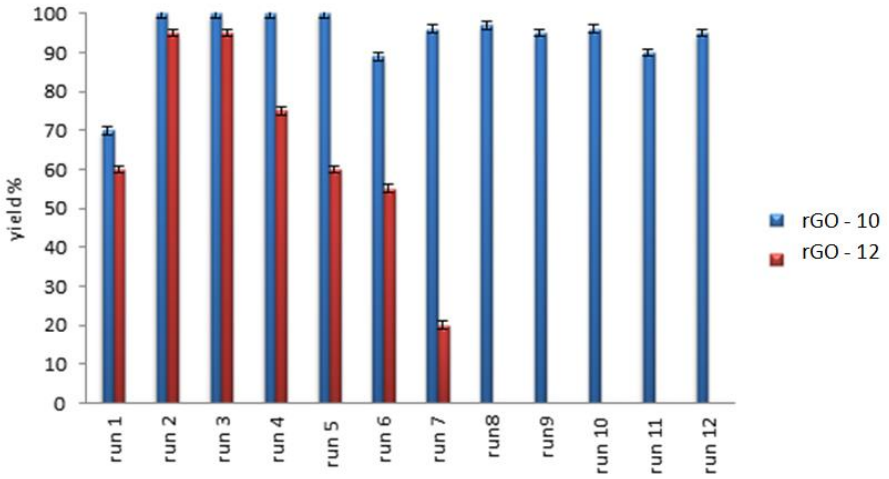

Figure 3.26. Recycling experiments of the *β*-alkylation of 1-phenylethanol with benzyl alcohol. Reaction conditions: 1-phenylethanol (1 mmol), benzyl alcohol (1 mmol), KOH (1 mmol) and catalyst **12**-rGO or **10**-rGO (0.5 mol% based on Ir) in 1.5 mL of toluene at 100 ºC. Yields determined by GC, using anisole as internal standard

Our results indicate that having two pyrene tags helps to avoid the leaching, compared to the situation in which only one pyrene functionality is present in the catalyst. For related pyrene-containing non-covalently immobilized catalysts, it has been published that the desorption is temperature dependent,[17a,17b] and that leaching is significantly reduced when the metal complex is decorated with more than one pyrene tag.[16b] In order to quantify the level of leaching in our two heterogeneized catalysts, ICP-MS analyses were performed after the recycling experiments. The results revealed a 1.5 wt % of rGO-**12** (after all seven runs) and a 6.3 wt % content of rGO-**10** (after all twelve runs). This result indicated that catalyst leaching is very important for the case of the material containing the complex with only one pyrene functionality (rGO-**12**), while being negligible for the material with the complex with two pyrene groups (rGO-**10**).

The time dependent reaction profiles of the first three cycles using rGO-**10** were also performed, in order to get a more detailed insight about its recycling properties. Figure 3.27 shows these three profiles. During the first eight hours, the reaction rate in the first run proceeds slowly, and a then speed up and equals the rate of runs 2 and 3. This result is suggestive of catalyst activation during the first hours of the reaction. The fact that the kinetics of run 2 and 3 are superimposable, is a clear indication that the deactivation

of the catalyst is undetectable between subsequent runs. Also interesting to point out is that the profiles of runs 2 and 3 are indicative of a *zeroth* order reaction rate with respect to the concentration of the substrates. We interpreted this result as a consequence of the saturation of the surface of the solid with the substrate,[16c,16d,18] therefore suggesting that there is some non-covalent interaction between the substrate and the support.

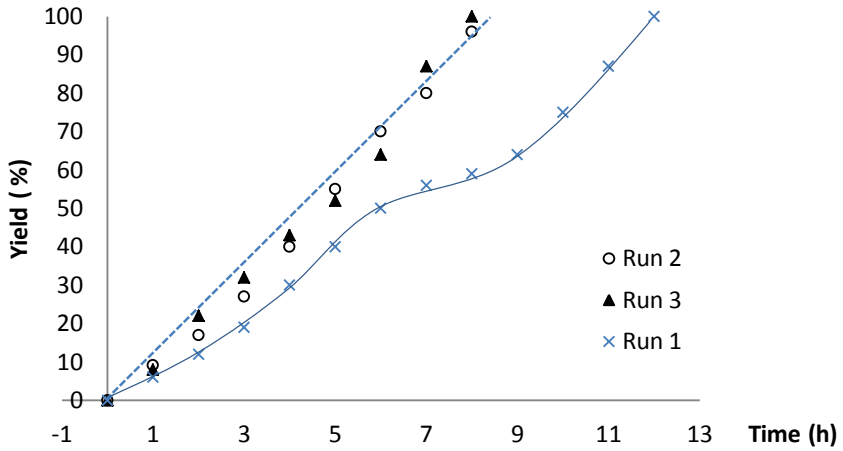

Figure 3.27. Reaction profiles for three successive cycles of the *β*-alkylation of 1-phenylethanol with benzyl alcohol. Reaction conditions are the same as those shown in Figure 3.26. Lines drawn to guide the eye

3.3 Conclusions

This chapter illustrates the different properties exhibited by homogenous catalysts with pyrene functionalities compared with the analogous systems lacking these polyaromatic moieties. The differences arise from the ability of pyrene groups to afford non-covalent interactions with aromatic molecules, which can either be substrates in homogenous catalysed reaction or the same catalysts to afford self-assembled systems. In addition, this sort of interactions may also be effective for the preparation of heterogeneized catalysts. By performing a detail study, we have reached to the following conclusions:

1. The addition of an external polyaromatic additive, such as pyrene or anthracene, to the catalytic reaction produces a decrease of the catalytic activity only for those reactions where both, aromatic substrates and pyrene-tagged catalysts, were used. The analogous reactions with a non aromatic catalyst or a non aromatic substrate are completely unaffected.
2. The catalytic reactions with a pyrene-tagged catalyst and an aromatic substrate shows a *zeroth* order reaction rate with respect the substrate as a consequence of the saturation of the catalyst with the aromatic substrate.

This situation, which strongly resembles enzymatic catalysis, arises from the π-staking bonding between the substrate and the ligand (ligand-substrate interaction).

3. Kinetic studies shows that the reaction rates with respect the catalyst concentration for pyrene–tagged catalyst follow a fractional reaction order <1. These results suggest self-association of the pyrene-tagged catalysts and that the monomer are the active species in the catalysis. In contrast, the use of similar catalyst without the pyrene functionality derives into a first-order dependence on the concentration of the catalyst. These results show how the presence of a pyrene substituent in a catalyst strongly modifies the catalyst reactivity.
4. The presence of the pyrene functionality in some of the iridium complexes was useful for the immobilization of them onto rGO surfaces, creating an hybrid that can be used in catalysis several times. The number of pyrene tags attached to the catalyst determines the efficiency of the immobilization and the leaching phenomena.

In summary, this work provides relevant information about the implication of π-π interactions, between ligand-substrate, ligand-additive or ligand-ligand, in catalysis. The main goal is to improve the basis of organometallic-based supramolecular catalysis by given results that may inspire future researchers in the design of improved catalysts.

3.4 References

(1) Mata, J. A., Hahn, F. E., Peris, E. *Chem. Sci.* **2014**, *5*, 1723-1732.

(2) a) Guisado-Barrios, G., Hiller, J., Peris, E. *Chem. Eur. J.* **2013**, *19*, 10405-10411; b) Gonell, S., Poyatos, M., Peris, E. *Angew. Chem. Int. Ed.* **2013**, *52*, 7009-7013.

(3) a) Valdés, H., Poyatos, M., Peris, E. *Organometallics* **2015**, *34*, 1725-1729; b) Valdés, H., Poyatos, M., Peris, E. *Inorg. Chem.* **2015**, *54*, 3654-3659.

(4) Vlahakis, J. Z., Mitu, S., Roman, G., Rodriguez, E. P., Crandall, I. E., Szarek, W. A. *Bioorg. Med. Chem.* **2011**, *19*, 6525-6542.

(5) *Industrial Aromatic Chemistry*; Franck, H. G. S., J. W, Ed.; Springer-Verlag, **1988**.

(6) a) Ruan, J. W., Saidi, O., Iggo, J. A., Xiao, J. L. *J. Am. Chem. Soc.* **2008**, *130*, 10510-10511; b) Colbon, P., Ruan, J. W., Purdie, M., Xiao, J. L. *Org. Lett.* **2010**, *12*, 3670-3673.

(7) Zanardi, A., Mata, J. A., Peris, E. *Organometallics* **2009**, *28*, 1480-1483.

(8) Crabtree, R. H. *Chem. Rev.* **2012**, *112*, 1536-1554.

(9) a) Hamid, M., Slatford, P. A., Williams, J. M. J. *Adv. Synth. Catal.* **2007**, *349*, 1555-1575; b) Edwards, M. G., Jazzar, R. F. R., Paine, B. M., Shermer, D. J., Whittlesey, M. K., Williams, J. M. J., Edney, D. D. *Chem. Commun.* **2004**, 90-91; c) Guillena, G., Ramon, D. J., Yus, M. *Angew. Chem. Int. Ed.* **2007**, *46*, 2358-2364; d) Black, P. J., Cami-Kobeci, G., Edwards, M. G., Slatford, P. A., Whittlesey, M. K., Williams, J. M. J. *Org. Bio. Chem.* **2006**, *4*, 116-125; e) Saidi, O., Williams, J. M. J. In *Iridium Catalysis*; Andersson, P. G., Ed., **2011**; Vol. 34; pp 77-106; f) Suzuki, T. *Chem. Rev.* **2011**, *111*, 1825-1845; g) Pontes da Costa, A., Viciano, M., Sanaú, M., Merino, S., Tejeda, J., Peris, E., Royo, B. *Organometallics* **2008**, *27*, 1305-1309; h) Hegg, E. L., Mortimore, S. H., Cheung, C. L., Huyett, J. E., Powell, D. R., Burstyn, J. N. *Inorg. Chem.* **1999**, *38*, 2961-2968; i) Fujita, K., Asai, C., Yamaguchi, T., Hanasaka, F., Yamaguchi, R. *Org. Lett.* **2005**, *7*, 4017-4019.

(10) a) Foubelo, F., Yus, M. *Chem. Rec.* **2015**, *15*, 907-924; b) Zassinovich, G. *Chem. Rev.* **1991**, *92*, 1051-1069.

(11) a) Tietze, L. F., Modi, A. *Med. Res. Rev.* **2000**, *20*, 304-322; b) Pellissier, H. *Tetrahedron* **2006**, *62*, 1619-1665.

(12) Fujita, K., Yamamoto, K., Yamaguchi, R. *Org. Lett.* **2002**, *4*, 2691-2694.

(13) Segarra, C., Mas-Marza, E., Mata, J. A., Peris, E. *Adv. Synth. Catal.* **2011**, *353*, 2078-2084.

(14) a) Srivastava, R. S., Nicholas, K. M. *Organometallics* **2005**, *24*, 1563-1568; b) Hegg, E. L., Mortimore, S. H., Cheung, C. L., Huyett, J. E., Powell, D. R., Burstyn, J. N. *Inorg. Chem.* **1999**, *38*, 2961-2968.

(15) a) Fraile, J. M., Garcia, J. I., Mayoral, J. A. *Chem. Rev.* **2009**, *109*, 360-417; b) Cole-Hamilton, D. J. *Science* **2003**, *299*, 1702-1706.

(16) a) Le Goff, A., Reuillard, B., Cosnier, S. *Langmuir* **2013**, *29*, 8736-8742; b) Mann, J. A., Rodriguez-Lopez, J., Abruna, H. D., Dichtel, W. R. *J. Am. Chem. Soc.* **2011**, *133*, 17614-17617; c) Sabater, S., Mata, J. A., Peris, E. *Acs Catalysis* **2014**, *4*, 2038-2047; d) Sabater, S., Mata, J. A., Peris, E. *Organometallics* **2015**, *34*, 1186-1190.

(17) a) Keller, M., Colliere, V., Reiser, O., Caminade, A.-M., Majoral, J.-P., Ouali, A. *Angew. Chem. Int. Ed. Engl.* **2013**, *52*, 3626-3629; b) Wittmann, S., Schaetz, A., Grass, R. N., Stark, W. J., Reiser, O. *Angew. Chem. Int. Ed. Engl.* **2010**, *49*, 1867-1870; c) Kang, P., Zhang, S. H., Meyer, T. J., Brookhart, M. *Angew. Chem. Int. Ed.* **2014**, *126*, 8853-8857; d) Xing, L., Xie, J.-H., Chen, Y.-S., Wang, L.-X., Zhou, Q.-L. *Adv. Synth. Catal.* **2008**, *350*, 1013-1016.

(18) a) Kung, H. H., Pellet, R. J., Burwell, R. L. *J. Am. Chem. Soc.* **1976**, *98*, 5603-5611; b) Lee, T. R., Whitesides, G. M. *Acc. Chem. Res.* **1992**, *25*, 266-272; c) Zaera, F. *Progress in Surface Science* **2001**, *69*, 1-98; d) Pomogailo, A. D. *Catalysis by Polymer-Immobilized Metal Complexes*; Gordon and Breach Science Publishers: Amsterdam, **1998**.

Part 2: The importance of ligand design for the development of ion receptors

Chapter 4.
Introduction. Part 2

4.1 Introduction

This chapter is meant to provide a general introduction to the second part of this Ph.D. Thesis, which refers to the chapters dealing with the preparation of supramolecular architectures for the recognition of ions (Chapters 5 and 6). A brief overview of the most relevant aspects related to supramolecular chemistry is given below. Apart from that, more specific information regarding resorcinarene based cavitands (examples of imidazolium and redox switchable sensors), tripod receptors and halogen bonding will be given in the next chapters.

4.2 Non-covalent interactions

Non-covalent interactions include a variety of weak, reversible, inter- or intramolecular attractive forces. Generally, their energies range about 0.5 – 5 kcal/mol in solution and up to 40 kcal/mol in the gas phase. These values are much lower than those of covalent bonds (80 or 100 kcal/mol, for typical C–C or C–H bonds, respectively),[1] although they often play important roles in chemical reactivity and are responsible for all aspects governing host-guest supramolecular chemistry. Some key types of non-covalent interactions are depicted in Scheme 4.1.

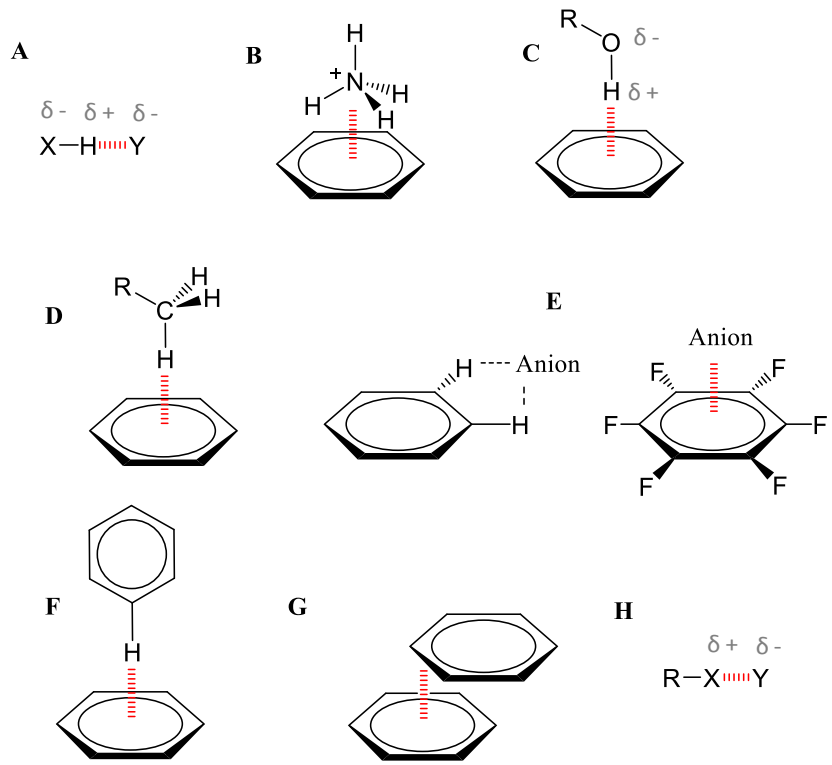

Scheme 4.1. Simple schematic illustrations of selected noncovalent interactions, which are important in biological and synthetic, supramolecular systems. (A) hydrogen bonding; (B) cation–π interaction; (C)

polar–π interaction; (D) CH–π interaction; (E) anion-π interaction (F) aromatic CH–π, or *T*-shaped stacking interaction; (G) π–π stacking interaction; (H) Halogen bonding.

a) Hydrogen Bonding

The term 'hydrogen bond' was introduced by Linus Pauling in 1931,[2] and numerous experimental and theoretical studies in organic systems have broadened the scope of hydrogen bonding partners and further developed the hydrogen bond concept.[3] A hydrogen bond is the attractive force between the hydrogen attached to an electronegative atom of one molecule and an electronegative atom of a different molecule. It can also be regarded as one archetypical three-centre four-electron (3c-4e) interaction.[4] Not only the electronegative elements X of the first period, but also those from periods II-IV and their conjugate XH acids are now well known to engage in hydrogen bonding. The binding energy goes from very strong (gas phase enthalpies of around 40kcal/mol, for example F···HF) to weak (gas phase enthalpies of 2-4 kcal, for instance HOH···OH_2). Nature makes extensive use of hydrogen bonding to stabilize and direct the formation of complex biological architectures. One of the most well-known examples of this is the hydrogen bonding between nucleotide base pairs in (A-T and G-C) provides both the strong attractive forces that hold strands of DNA together, as well as the genetic information required for cellular function (Scheme 4.2).

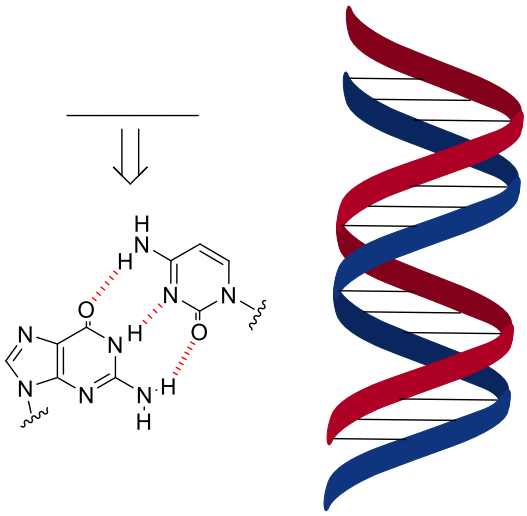

Scheme 4.2. G-C base pair hydrogen bonding interactions and a representative segment of a DNA helix

In coordination chemistry, intermolecular hydrogen bonding of proton donors to transition metal d electrons, M···HX are known since 1990.[5] Several systems with M···HX interactions in common solvents were studied by IR spectroscopy by the groups of Kazarian[6] and Poliakoff.[7] As an especial type of H-bonding, the unusual MH···HX

bonding was first described by Crabtree in 1994, as an attractive *intra*molecular interaction (Scheme 4.3a).[8] Very soon thereafter, an *inter*molecular H···H bond in the solid state was reported by Crabtree,[9] who also coined the term 'dihydrogen bonding (Scheme 4.3b).

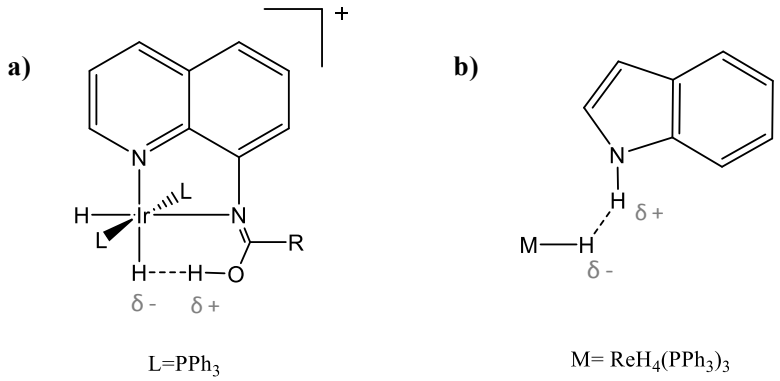

Scheme 4.3. a) Iridium complex with an intramolecular interaction. b) Intermolecular interaction of a rhenium complex

b) Cation–π Interactions

The cation–π interaction is a predominantly electrostatic nonbonding attraction resulting from the favorable association of a cation and the quadrupole of an aromatic π system (Scheme 4.4).[10] Apart from the electrostatic contribution, the polarizability of the arene under the presence of the cation is another important factor that plays a relevant role in this interaction. The binding is often quite strong, with gas phase energies of up to ~40 kcal/mol [often stronger than the analogous (H_2O ··cation) interaction] and aqueous phase binding energies as high as 5 kcal/mol. Dougherty and coworkers recently demonstrated that cation–π interactions are quite ubiquitous in biology, with an estimated one cation–π interaction for every 77 amino acids in a protein.[11]

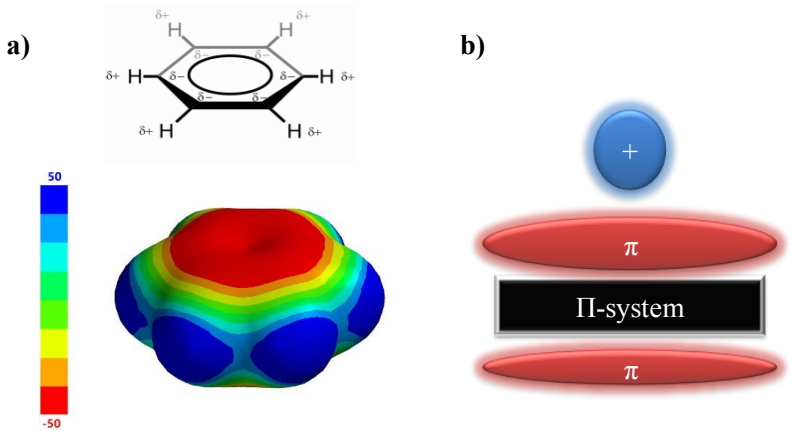

Scheme 4.4. a) The benzene quadrupole. (Top) structure of benzene showing the partial positive (δ+) charges that lie near the hydrogen atoms and partial negative charges (δ-) that lie near the carbon atoms

and above the ring; (bottom) electrostatic potential map of benzene, blue is positive and red is negative. b) Polarizability of the arene under the presence of a cation

c) XH–π Interactions

The quadrupole of aromatic π systems may also interact favorably with polarized X–H bonds, analogously to a hydrogen-bonded donor-acceptor pair, and this is often termed a polar–π interaction. Polar OH–π and NH–π interactions are commonly observed in proteins[12] and their calculated gas-phase interaction energies range from 2 – 5 kcal/mol. Related to these polar-π interactions, but classified different, are the CH-π interactions. The smaller electronegativity difference between C and H compared to O and H, makes the C–H bond less polar than the O–H bond, therefore, for the CH–π interactions the electrostatic contribution to the overall attractive energy is much lower than for polar–π interactions. CH–π interactions are dominated by electron delocalization effects and their stabilization energy typically range from 0.5 – 2.5 kcal/mol.[13] This sort of interaction is commonly observed in the solid-state crystal packing of organic molecules.[14]

d) Anion–π Interactions

Anion−π interactions are defined as attractive interactions between negatively charged species and electron-deficient aromatic rings. The electrostatic forces and ion-induced polarization have been demonstrated to be the main energetic contributors to the anion–π interaction.[15] There are two general types of anion−π interaction motifs depending on the benzene quadrupole (Scheme 4.5a): i) a weak σ-interaction describing a special contact mode where an anion is located over the periphery of an aromatic ring (Scheme 4.5b1); and ii) a typical anion−π interaction indicating the attraction of an anion species to the centroid of an aromatic ring (Scheme 4.5b2).[15-16]

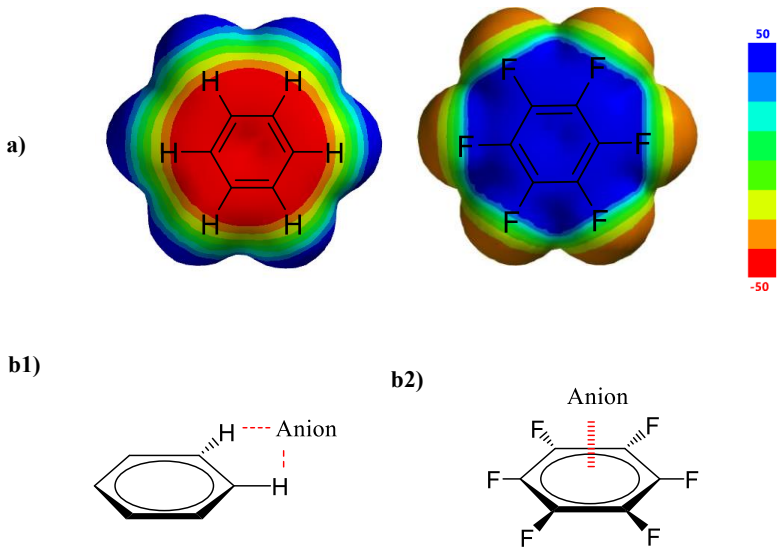

Scheme 4.5. (a) Molecular electrostatic potential (MEP) of benzene and hexafluorobenzene; MEP surfaces computed at the M06/6-311++G** level of theory. (b) two general types of anion−π interaction.

e) π–π Interactions

π-π interactions are associated with the interaction between the π-orbitals of a molecular system.[17] For a simple example, a benzene ring, with its fully conjugated π cloud, will interact in two major ways (and one minor way) with a neighbouring benzene ring through a π-π interaction (see Scheme 4.6). The two major ways that benzene stacks are *T*-shaped geometry (with enthalpy of ~2 kcal/mol) and displaced (with an enthalpy of ~2.3 kcal/mol). Displaced π–π interactions play an important role in DNA structure, where π–π stacking can occur between the aromatic groups of adjacent oligonucleotides, and also with small molecule intercalators.[18] The sandwich configuration is not very stable compared to the previous ones, due to the high electrostatic repulsion of the electrons in the π orbital. However, it may be more much stable when there is a reversed polarity of one of the π-systems .[17-18] Scheme 4.6 shows a summary of all the typical π–π aromatic interactions.

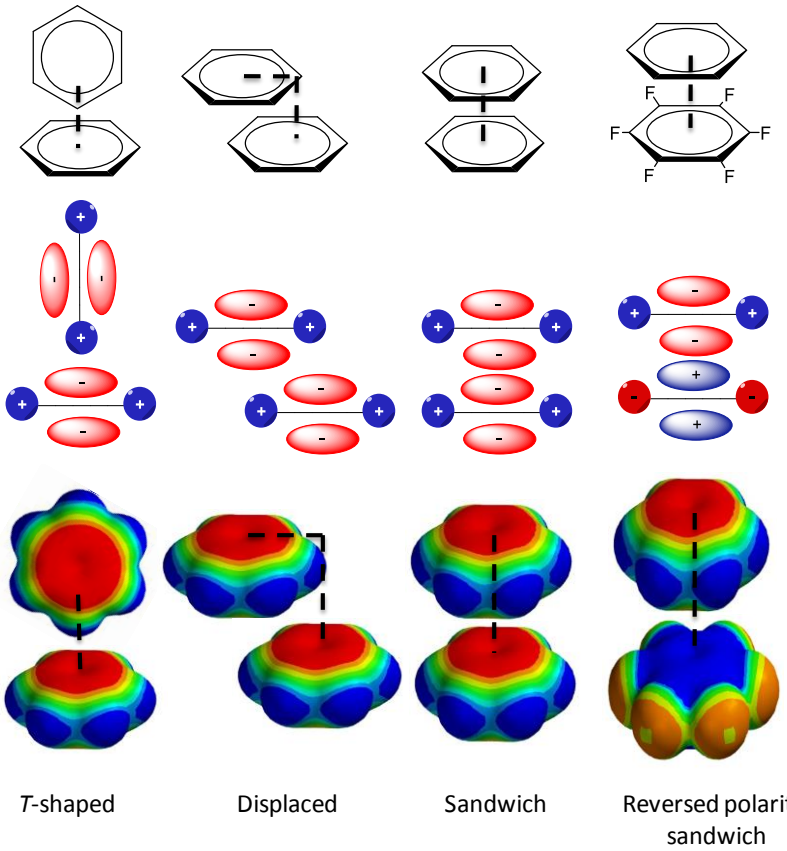

Scheme 4.6. Geometries, quadrupole moments and MEP (blue is positive and red is negative) of typical π–π aromatic interactions

f) Halogen bonding

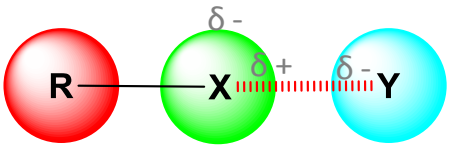

Scheme 4.7. Halogen bonding interaction

A typical halogen bonding interaction is denoted as R-X···Y, where X is the electrophilic XB acceptor (Lewis acid) and Y the XB donor (Lewis base). Consequently, halogen bonding (XB) refers to the attractive non-covalent interaction arising between the electron-deficient *σ*-hole of a polarized halogen atom, such as bromine or iodine and an electron-rich Lewis base. The XB stabilization energy typically ranges from 10 – 200 kcal/mol. The strength of the interaction increases in the order Cl<Br<I.[19] This sort of interaction has been commonly studied in crystal engineering.[20]

4.3 Supramolecular Host-guest chemistry

Despite the importance of non-covalent interactions in chemistry and biology, the chemistry community did not take advantage of non covalent interaction until recently.[21] Supramolecular chemistry is inspired in the chemistry around living systems in order to seek how to use all types of weak interactions for controlling structural and reactive factors. Therefore, supramolecular chemistry is all about interactions between molecules: how they can recognize each other, assemble and function on molecular scale.[21]

The host-guest chemistry is a field of the supramolecular chemistry based on the study of the selective interactions between host and guest molecules. In general, the host species is a larger molecule than the guest molecule, and has a large cavity volume. Some typical examples of hosts are ciclodextrins, curcubiturils or calixarenes. Typically, the guest molecule is smaller than the host. The guest needs to have a complementary shape with the host, which helps improve their affinity/selectivity between them. When host and guest molecules interact by non-covalent interactions a *"host-guest complex"* system is produced.[22]

The pioneering works by Cram,[23] Lehn[24] and Pedersen[25] examined the inclusion chemistry of simple molecular hosts, such as crown ethers, cryptands, cavitands and carcerands (Scheme 4.8). In 1987, these researchers were awarded with the Nobel price of chemistry "*for their development and use of molecules with structure-specific interactions of high selectivity*".

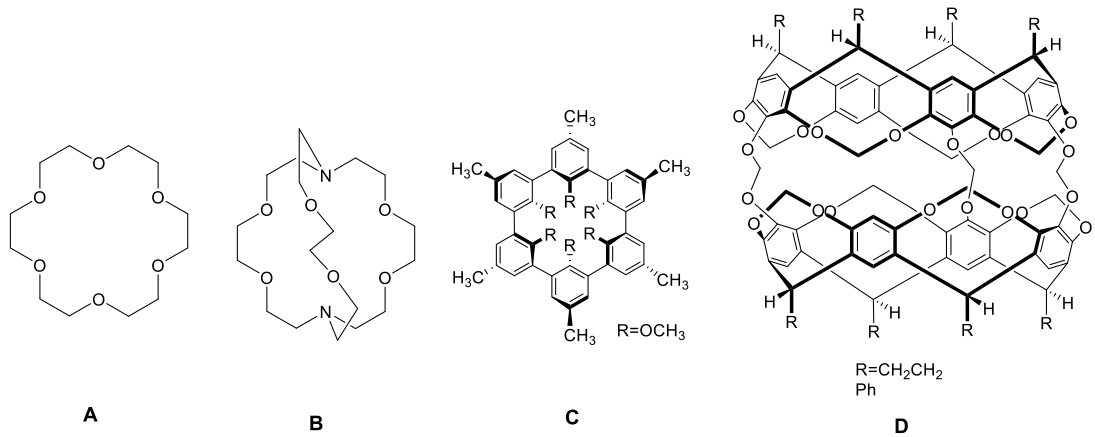

Scheme 4.8. Early supramolecular host molecules. Crowns (A) and cryptands (B) form host-guest complexes with cations such as K^+ or NH^{4+}; cavitands (C) and carcerands (D) can encapsulate small organic molecules such as benzene, chloroform, or acetonitrile

Host molecules may bind different guests making use of non-covalent interactions, which mediate their chemical reactivity. For example, Cram and coworkers demonstrated that the highly reactive, antiaromatic cyclobutadiene is stable at room temperature when bound to the interior of a carcerand host (Scheme 4.9).[26]

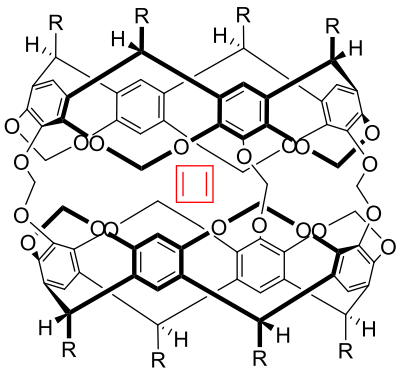

Scheme 4.9. Cram's carcerand encapsulates and stabilizes a highly reactive cyclobutadiene

More recently, supramolecular chemists have started using non-covalent interactions to build large and complex host structures through directed self-assembly. Many researchers have used hydrogen bonding interactions to produce the self-assembly of supramolecular hosts. The hexameric calix[4]arene-based capsules is one of the most representative examples,[27] where hydrogen bond interactions are established between the 60 OH ···O from the 6 resorcinarene subunits and 8 water molecules (Scheme 4.10)

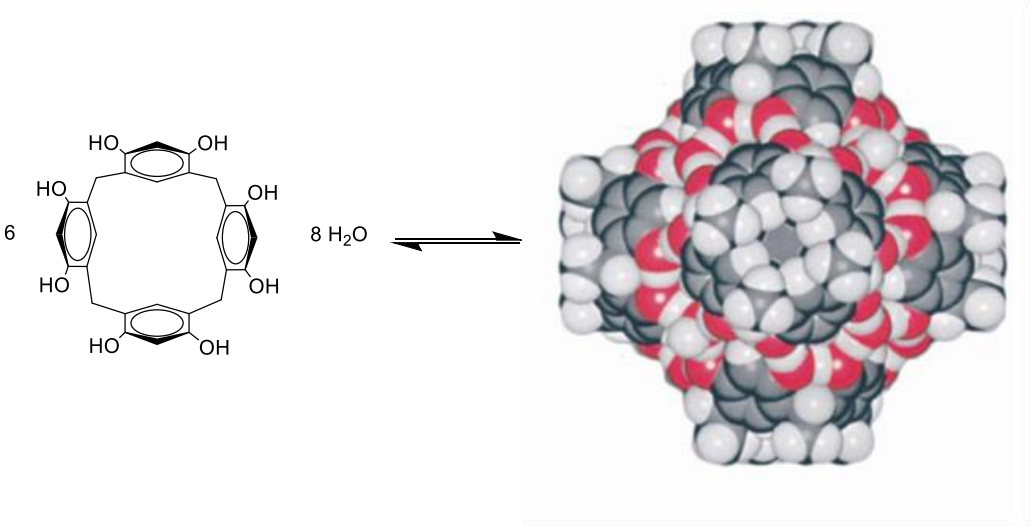

Scheme 4.10. The hexameric spheroid assembles from 6 resorcinarene units and 8 water molecules, to give a hollow capsule with a volume of ~1400 Å. Adapted from reference 27

Other interesting example illustrating how supramolecular hosts may mediate in guest reactivity was provided by the group of Rebek, who described a cavitand molecules in

which a simple SN_2 reaction takes place inside the host molecule.[28] The conformation of the cavitand is bowl-shaped, which is formed thanks to a network of hydrogen bonding interactions around the rim of the capsule, thus forming a molecule with a hydrophobic pocket. Quinuclidine is the guest, which is bound to the inside of the pocket. When an alkyl bromide is added to a solution of the host-guest complex, the encapsulated quinuclidine is alkylated to form the quinuclidinium salt. Surprisingly, the encapsulated quinuclidine reacts ~1000 times faster than quinuclidine in bulk solution, despite the amine nitrogen of the former being sterically less accessible due to the surrounding host cavitand. This rate acceleration is attributed to the stabilization of the positive charge on the quiniuclidine NCH_2 groups in the transition state for SN_2 substitution, by favorable cation–π interactions between the guest and the host aromatic walls (Scheme 4.11).

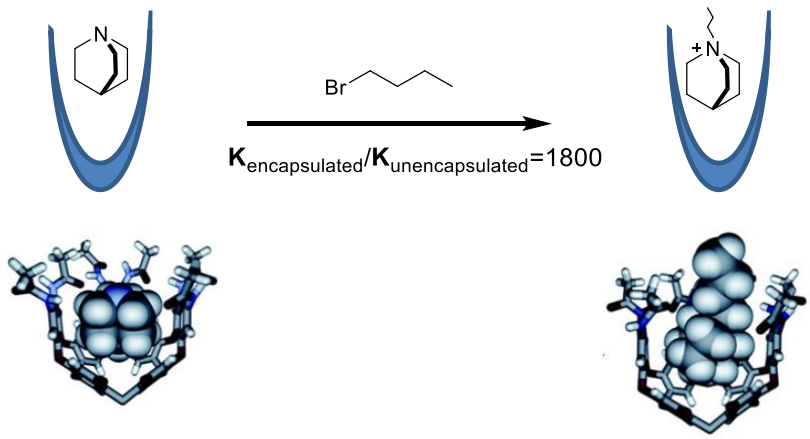

Scheme 4.11. A deep-cavity cavitand host, whose bowl shape is enforced by hydrogen bonding interactions along the rim of the cavitand, accelerates the alkylation of quinuclidine, relative to the alkylation in bulk solution. Favorable cation–π interactions between host and guest at the transition state are thought to be responsible for the rate acceleration. Adapted from reference 28

Another application of supramolecular host-guest chemistry is found for anion or cation recognition.[29] Recognition of anions is an area of intense study due to the enormous impact of anions upon our lives. In our own bodies for instance, the carrier of our genetic information is anionic, as well as in the majority of enzyme substrates and cofactors (for example ATP). In the case of halides, chloride is found extensively in extracellular fluid, with its misregulation being linked to diseases such as cystic fibrosis.[30] Iodide is required for the biosynthesis of hormones by the thyroid gland, [31] while fluoride is considered essential for healthy bone and teeth growth, which has led

to the (sometimes controversial) artificial fluoridation of water supplies.[32] In the case of other anions, it is well-known that bicarbonate is vital to maintain the body pH levels, whereas cyanide is highly toxic. In contrast, certain anions have a negative effect on the environment around us. For example, nitrate and sulphate are the responsible components in the production of acid rain. [33]

Cations are also important for similar reasons. Calcium ions, Ca^{2+}, are the most abundant cations in the body, making up about 1.5% of total body weight. About 99% is found in bones and teeth, largely in combination. They combine with phosphate ions to form calcium phosphate, which increases the rigidity and hardness of bones and the enamel in teeth. Magnesium ions, Mg^{2+}, are important because of their role in the normal functioning of muscle and nerve tissue, bone formation and as a component of many coenzymes. One interesting example is the binding of neurotransmitter acetylcholine and nicotine to the acetylcholine receptor in the human brain and muscles, by cation–π interaction involving a tryptophan residue in the hydrophobic binding pocket (Scheme 4.12).[34]

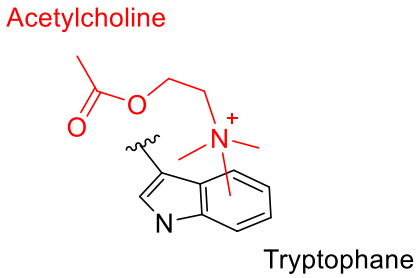

Scheme 4.12. Schematic of the critical cation–π interaction between the TrpB residue in the binding pocket and acetylcholine

Inspired on the acetylcholine recognition, Rebek and co-workers developed a deep pocket receptor cavitand, which is able to recognize acetylcholine and choline in water with high thermodynamic and kinetic stability (Scheme 4.13). The recognition was possible through anion pair binding, which was demonstrated because the selectivity towards *L*-carnitine was established by the positioning of a negative charge in the upper rim of the deep pocket.[35]

All these examples are illustrative of the considerable motivation for investigating the binding and sensing of anionic species, which justify the increasing interest towards anion or cation receptor design. [36]

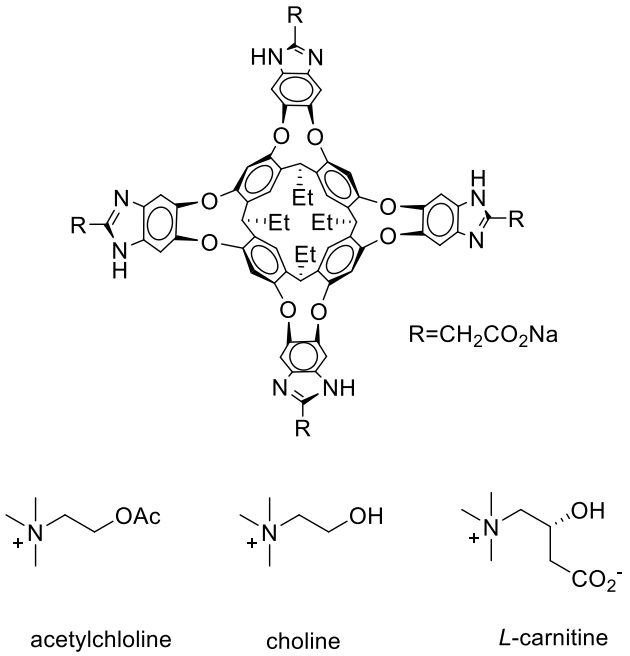

Scheme 4.13. The receptor described by Rebek and co-workers and the structures of the guests that form kinetically stable compounds in water

Another example of anion or cation sensors are based on tripod receptors, which afford multiple interaction sites toward given analytes. A huge number of compounds with tripodal topology have been prepared during years.[37] One of the most interesting examples is the first redox-active class of anion receptor based on the cobaltocenium moiety (Scheme 4.14), which was reported by Beer and Keefe in 1989.[38] Cyclic voltammetric experiments demonstrated that this receptor could electrochemically sense anions. The complexed anionic guest effectively stabilizes the positively charged cobalt centre making it more difficult to reduce. Complexation of chloride ions by the receptor induced a cathodic shift of 30 mV.

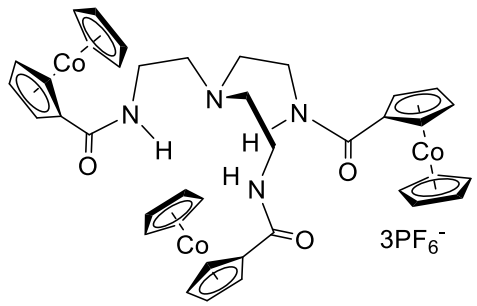

Scheme 4.14. Cobaltocenium tripod receptor

Tripodal azacrown ether calix[4]arenes, **A** and **B** (Scheme 4.15), are able to bind transition metal ions such as Co^{2+} , Ni^{2+} and Cu^{2+} in a 1:1 fashion.[39] These receptors

may be potentially used as switchable receptors for metal ions. The binding ability of the receptor can be switched by varying the pH of the solution.

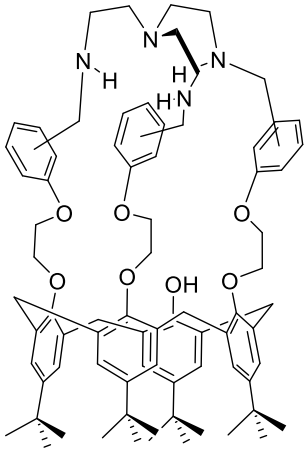

A = ortho
B = para

Scheme 4.15. Tripodalazacrown ether calix[4]arenes

In short, supramolecular host-guest chemistry is an enormous and unlimited field, which is still growing due to its importance and impact on science, providing knowledge for developing novel container host molecules for different purposes (drug delivery, sensing, molecular encapsulation, catalysis,…)

4.4 Objectives

Azolium ligand design and the preparation of novel homogenous catalyst have been among the main interests of the Organometallic Chemistry group at the UJI during the past years. This experience may now be applied for the design of host molecules with novel sensing abilities. Thus, the following specific objectives will be pursued:

- Design and functionalization of the benzimidazole-resorcinarene based cavitands with redox centers for the preparation of redox-switchable cation receptors.
- Synthesis of new resorcinarene-based receptors with imidazolium and triazolium moieties for anion recognition.
- Comparison of the halogen bonding and hydrogen bonding binding abilities on a series of tripod-based azolium molecules.

4.5 References

(1) *Chemical Bonds and Bond Energy*; Sanderson, R. T., Ed.: New York, **1976**.

(2) Pauling, L. *J. Am. Chem. Soc.* **1931**, *53*, 3225-3237.

(3) a) Bernstein, J., Davis, R. E., Shimoni, L., Chang, N. L. *Angew. Chem. Int. Ed.* **1995**, *34*, 1555-1573; b) Etter, M. C. *Acc. Chem. Res.* **1990**, *23*, 120-126; c) Koch, U., Popelier, P. L. A. *J. Phys. Chem.* **1995**, *99*, 9747-9754; d) Pauling, L., Corey, R. B., Branson, H. R. *Proc. Natl. Acad. Sci. U. S. A.* **1951**, *37*, 205-211; e) Steiner, T. *Angew. Chem. Int. Ed.* **2002**, *41*, 48-76; f) Abraham, M. H. *Chem. Soc. Rev.* **1993**, *22*, 73-83; g) Baker, E. N., Hubbard, R. E. *Prog. Biophys. Mol. Biol.* **1984**, *44*, 97-179; h) Desiraju, G. R. *Acc. Chem. Res.* **1996**, *29*, 441-449; i) McDonald, I. K., Thornton, J. M. *J. Mol. Biol.* **1994**, *238*, 777-793.

(4) *An Introduction to Hydrogen Bonding*; Jeffrey, G. A., Ed.; Oxford University Press: Oxford, **1997**.

(5) Simoes, J. A. M., Beauchamp, J. L. *Chem. Rev.* **1990**, *90*, 629-688.

(6) Kazarian, S. G., Hamley, P. A., Poliakoff, M. *J. Am. Chem. Soc.* **1993**, *115*, 9069-9079.

(7) Poliakoff, M., Howdle, S. M., Kazarian, S. G. *Angew. Chem. Int. Ed.* **1995**, *34*, 1275-1295.

(8) a) Lee, J. C., Peris, E., Rheingold, A. L., Crabtree, R. H. *J. Am. Chem. Soc.* **1994**, *116*, 11014-11019; b) Peris, E., Lee, J. C., Crabtree, R. H. *Chem. Commun.* **1994**, 2573-2573.

(9) a) Peris, E., Wessel, J., Patel, B. P., Crabtree, R. H. *Chem. Commun.* **1995**, 2175-2176; b) Wessel, J., Lee, J. C., Peris, E., Yap, G. P. A., Fortin, J. B., Ricci, J. S., Sini, G., Albinati, A., Koetzle, T. F., Eisenstein, O., Rheingold, A. L., Crabtree, R. H. *Angew. Chem. Int. Ed.* **1995**, *34*, 2507-2509.

(10) Ma, J. C., Dougherty, D. A. *Chem. Rev.* **1997**, *97*, 1303-1324.

(11) a) Gallivan, J. P., Dougherty, D. A. *Proc. Natl. Acad. Sci. U. S. A.* **1999**, *96*, 9459-9464; b) Gallivan, J. P., Dougherty, D. A. *Org. Lett.* **1999**, *1*, 103-105; c) Gallivan, J. P., Dougherty, D. A. *Abstr. Pap. Am. Chem. Soc.* **1999**, *217*, U87-U87.

(12) a) Bertolotti, A., Zhang, Y. H., Hendershot, L. M., Harding, H. P., Ron, D. *Nat. Cell Biol.* **2000**, *2*, 326-332; b) Uetz, P., Giot, L., Cagney, G., Mansfield, T. A., Judson, R. S., Knight, J. R., Lockshon, D., Narayan, V., Srinivasan, M., Pochart,

P., Qureshi-Emili, A., Li, Y., Godwin, B., Conover, D., Kalbfleisch, T., Vijayadamodar, G., Yang, M. J., Johnston, M., Fields, S., Rothberg, J. M. *Nature* **2000**, *403*, 623-627.

(13) Nishio, M., Umezawa, Y., Hirota, M., Takeuchi, Y. *Tetrahedron* **1995**, *51*, 8665-8701.

(14) a) Tsuzuki, S. *Annu. Rep. Prog. Chem., Sect. C: Phys. Chem.,* **2012**, *108*, 69-95; b) Nishio, M., Umezawa, Y., Suezawa, H., Tsuboyama, S. In *The Importance of Pi-Interactions in Crystal Engineering*; John Wiley & Sons, Ltd, **2012**; pp 1-39.

(15) Frontera, A., Gamez, P., Mascal, M., Mooibroek, T. J., Reedijk, J. *Angew. Chem. Int. Ed.* **2011**, *50*, 9564-9583.

(16) a) Hay, B. P., Bryantsev, V. S. *Chem. Commun.* **2008**, 2417-2428; b) Berryman, O. B., Bryantsev, V. S., Stay, D. P., Johnson, D. W., Hay, B. P. *J. Am. Chem. Soc.* **2007**, *129*, 48-58; c) Wang, D.-X., Wang, M.-X. *J. Am. Chem. Soc.* **2013**, *135*, 892-897.

(17) *Modern Physical Organic Chemistry*; Anslyn, E. D., A. Dennis, Ed.;
Sausalito, CA, **2004**.

(18) Matthews, R. P., Welton, T., Hunt, P. A. *Phys. Chem. Chem. Phys.* **2014**, *16*, 3238-3253.

(19) a) Wang, G., Chen, Z., Xu, Z., Wang, J., Yang, Y., Cai, T., Shi, J., Zhu, W. *J. Phys. Chem. B* **2016**, *120*, 610-620; b) Brown, A., Beer, P. D. *Chem. Commun.* **2016**, *52*, 8645-8658.

(20) a) Nguyen, S. T., Rheingold, A. L., Tschumper, G. S., Watkins, D. L. *Cryst. Growth Des.* **2016**, *16*, 6648-6653; b) Ramakrishnan, R., Mallia, A. R., Sethy, M., Hariharan, M. *Cryst. Growth Des.* **2016**, *16*, 6327-6336; c) Surmann, S. A., Mezei, G. *Acta Cryst. E* **2016**, *72*, 1517-+; d) Bent, H. A. *Chem. Rev.* **1968**, *68*, 587-&; e) Murrayrust, P., Motherwell, W. D. S. *J. Am. Chem. Soc.* **1979**, *101*, 4374-4376.

(21) Huang, F., Anslyn, E. V. *Chem. Rev.* **2015**, *115*, 6999-7000.

(22) Yang, H., Yuan, B., Zhang, X., Scherman, O. A. *Acc. Chem. Res.* **2014**, *47*, 2106-2115.

(23) Cram, D. J. *Nobel lecture* **1987**.

(24) Lehn, J. M. *Nobel lecture* **1987**.

(25) Pedersen, C. J. *Nobel lecture* **1987**.

(26) Cram, D. J., Tanner, M. E., Thomas, R. *Angew Chem, Int Ed.* **1991**, *30*, 1024-1027.

(27) MacGillivray, L. R., Atwood, J. L. *Nature* **1997**, *389*, 469-472.

(28) Purse, B. W., Gissot, A., Rebek, J. *J. Am. Chem. Soc.* **2005**, *127*, 11222-11223.

(29) a) Alfonso, M., Tarraga, A., Molina, P. *Inorg. Chem.* **2013**, *52*, 7487-7496; b) Mahadevi, A. S., Sastry, G. N. *Chem. Rev.* **2013**, *113*, 2100-2138; c) Flink, S., van Veggel, F., Reinhoudt, D. N. *J. Phys. Chem. B* **1999**, *103*, 6515-6520; d) Miura, Y., Kimura, S., Kobayashi, S., Imanishi, Y., Umemura, J. *Biopolymers* **2000**, *55*, 391-398.

(30) Rowe, S. M., Miller, S., Sorscher, E. J. *N. Engl. J. Med.* **2005**, *352*, 1992-2001.

(31) Delange, F. *Thyroid* **1994**, *4*, 107-128.

(32) Cametti, M., Rissanen, K. *Chem. Commun.* **2009**, 2809-2829.

(33) Chang, S. G., Littlejohn, D., Hu, K. Y. *Science* **1987**, *237*, 756-758.

(34) Fraenkel, Y., Gershoni, J. M., Navon, G. *FEBS Lett.* **1991**, *291*, 225-228.

(35) Hof, F., Trembleau, L., Ullrich, E. C., Rebek, J. *Angew. Chem. Int. Ed.* **2003**, *42*, 3150-3153.

(36) a) Chawla, H. M., Kar, J. R., Siddiqui, W. A., Kumar, N., Black, D. S. *Tetrahedron Lett.* **2014**, *55*, 4517-4520; b) Kim, B., Kim, T. H. *J. Anal. Methods Chem.* **2015**; c) Lochman, L., Svec, J., Roh, J., Novakova, V. *Dyes Pigm.* **2015**, *121*, 178-187; d) Zhao, W. X., Wang, C. Z., Zhang, Y. Q., Xue, S. F., Tao, Z., Zhu, Q. J. *Supramol. Chem.* **2015**, *27*, 661-668; e) Bozkurt, S., Turkmen, M. B., Soykan, C. *J. Inclusion Phenom. Macrocyclic Chem.* **2016**, *84*, 35-41; f) Flood, A. H. *Beilstein J. Org. Chem.* **2016**, *12*, 611-627; g) Langton, M. J., Serpell, C. J., Beer, P. D. *Angew. Chem. Int. Ed.* **2016**, *55*, 1974-1987; h) Xu, Y. X., Chen, H. H., Guan, R. F., Cao, D. X., Wu, Q. Q., Yu, X. Y. *Fibers and Polymers* **2016**, *17*, 181-185; i) Zhai, X. T., Yu, H. J., Wang, L., Deng, Z., Abdin, Z. U., Chen, Y. S. *J Zhejiang Univ Sci A* **2016**, *17*, 144-154.

(37) a) Azizoglu, S. S., Kaplan, S., Ozturk, G., Turgut, Y., Togrul, M. *Arkivoc* **2016**, 44-58; b) Bao, S., Gong, W. T., Chen, W. D., Ye, J. W., Lin, Y., Ning, G. L. *J. Inclusion Phenom. Macrocyclic Chem.* **2011**, *70*, 115-119; c) Bhardwaj, V. K., Sharma, S., Singh, N., Hundal, M. S., Hundal, G. *Supramol. Chem.* **2011**, *23*, 790-800; d) Lopez, T., Currie, R. A., Alvarado, R. J., Kavallieratos, K. *Abstr. Pap. Am. Chem. Soc.* **2006**, *231*; e) Lopez, T., Kavallieratos, K. *Abstr. Pap. Am.*

Chem. Soc. **2007**, *233*, 284-284; f) Wei, L. H., He, Y. B., Wu, J. L., Qin, H. J., Xu, K. X., Meng, L. Z. *Chin. J. Chem.* **2005**, *23*, 608-612; g) Yu, F., Li, B. *Inorg. Chem. Commun.* **2012**, *22*, 37-39.

(38) Beer, P. D., Keefe, A. D. *J. Organomet. Chem.* **1989**, *375*, C40-C42.

(39) Tuntulani, T., Thavornyutikarn, P., Poompradub, S., Jaiboon, N., Ruangpornvisuti, V., Chaichit, N., Asfari, Z., Vicens, J. *Tetrahedron* **2002**, *58*, 10277-10285.

Chapter 5.
Imidazole and imidazolium-based resorcinarene cavitands for the recognition of cations and anions

5.1 Introduction

5.1.1 Resorcinarene-based cavitands

The first definition of '*cavitand*' was given by Cram 35 years ago.[1] Cavitands are molecular containers with large cavities that are able to accommodate simple molecules or ions. Cavitands have also been defined as open-ended host molecules with vase-shaped cavities, in which complementary species can be detained.[2] Examples of cavitands include cyclodextrins,[3] calixarenes,[4] pillararenes[5] and cucurbiturils.[6] This chapter will focus its attention on the development of calixarene-based cavitands. Calixarenes are macrocycles, or cyclic oligomers formed by hydroxyalkylation of phenols with aldehydes.[1] One of the most widely used types of calixarenes is the family of resorcin[4]arenes.[7] Resorcin[4]arenes may adopt a rigidified closed (*vase*) conformation that can be used for trapping small molecules and ions,[8] or an expanded (*kite*) conformation, depending on various parameters such as pH, solvent, temperature, functionalization, etc. (Scheme 5.1).[7]

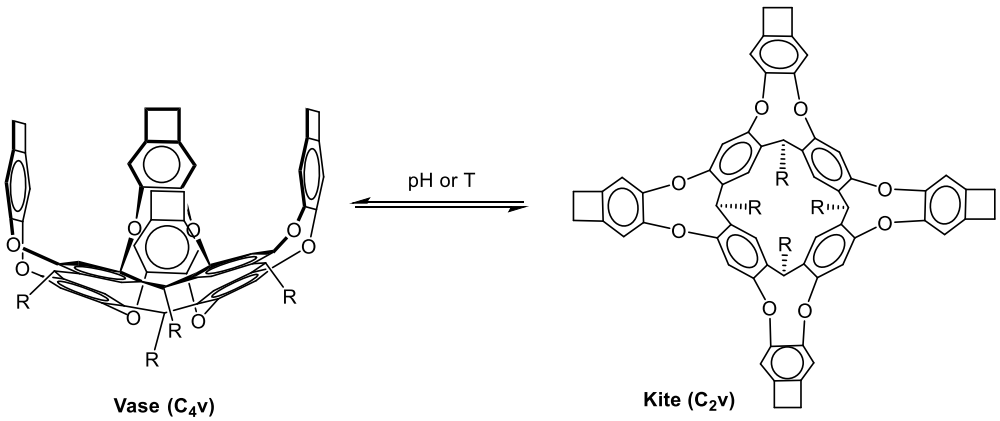

Scheme 5.1. Main conformations of a resorcin[4]arene cavitand

The conformational properties of these cavitands may be deduced from ^{1}H NMR spectroscopy. The methyne protons, which are located directly below the wall, are sensitive to the conformation of the molecule, suffering important shift changes, and thus offering a clear diagnostic of the conformation of the molecule. For the *vase* conformation, the chemical shift of the methyne proton is usually observed between 5.6 and 6.5 ppm. For the *kite* conformation, the methyne proton chemical shift is observed at about 4 ppm.[7-8]

Tetra-benzimidazole-resorcinarenes are known to be effective receptors for hosting and selectively recognizing small molecules.[8c,9] Based on these promising features, the approaches that we describe in this chapter consist of two different strategies for the preparation of imidazole-based resorcinarenes for the recognition of anions and cations. On the one hand, we prepared a tetra-ferrocenyl-imidazole-based resorcinarene (**15**) for the recognition of cations. On the other hand, we prepared two new tetra-benzimidazolium resorcinarenes (**16I$_4$** and **17I$_4$**) for the recognition of anions. The reasons that justify these two approaches are discussed below. These two types of systems can be obtained from an octamino-resorcinarene, as depicted in Scheme 5.2.

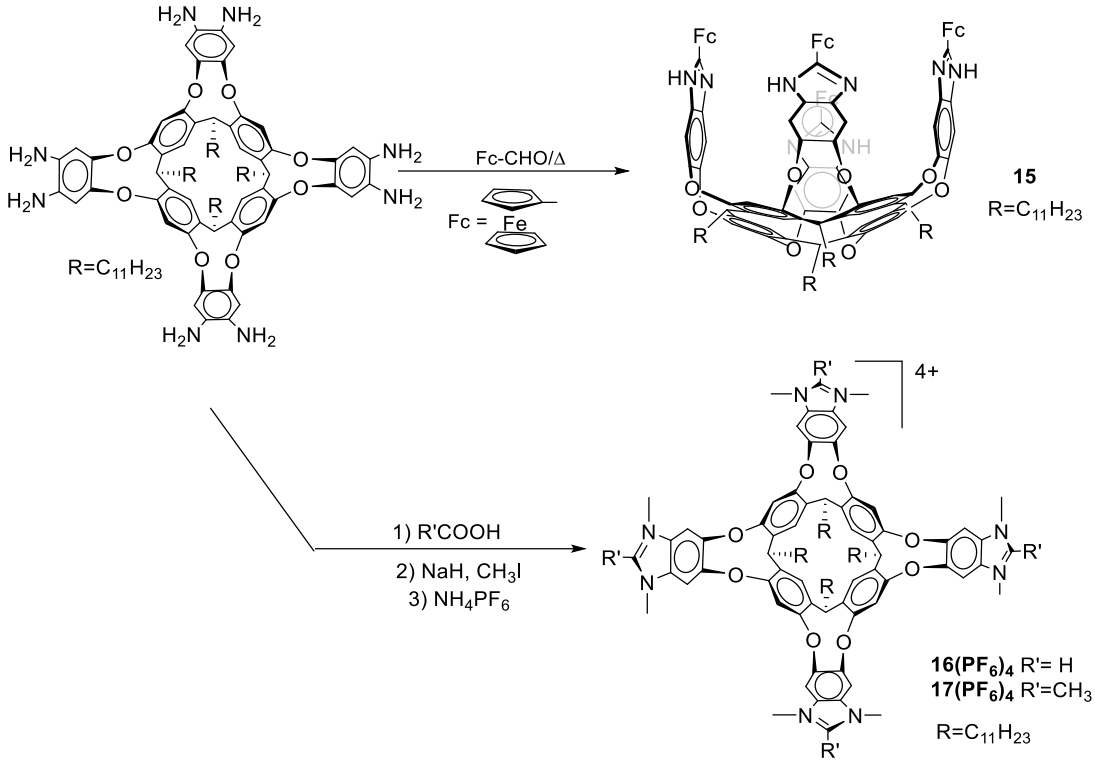

Scheme 5.2. Imidazole-based resorcinarenes for the recognition of anions and cations

Originally, we have been interesting in the design of new azolium salts for the synthesis of N-heterocyclic carbene-based organometallic complexes. Therefore, we fixed our attention in salt **16^{4+}**, which may be used as NHC ligand precursor for the preparation of novel and fascinating organometallic compounds. By using this salt, a new tetra-benzimidazolylidene resorcinarene-based rhodium cavitand (**18**) was prepared (Scheme 5.3). The synthetic procedure and characterization of complex **18** are also described in this chapter.

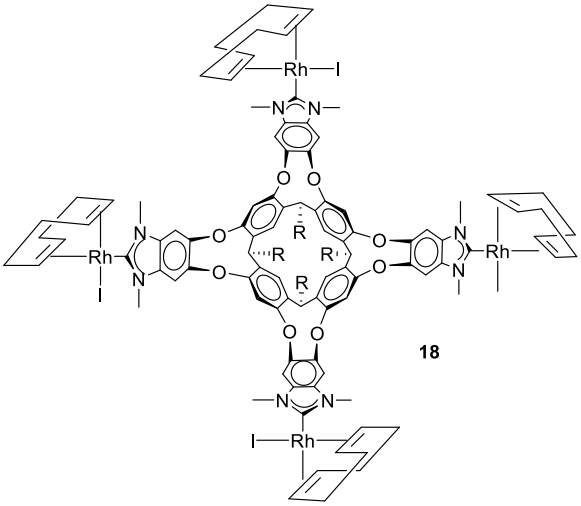

Scheme 5.3. Tetra-benzimidazolylidene resorcinarene-based rhodium cavitand

5.1.2 Redox-switchable resorcinarene cavitands. The introduction of ferrocene as redox-active centre

The functionalization of the upper rim of the resorcin[4]arene cavitand with metal fragments offers the possibility to form unique supramolecular architectures with tunable shapes and sizes. These new materials may be used for the preparation of improved systems for catalytic purposes, or for the construction of stimuli-responsive metallosupramolecular architectures, which may be useful to trap or release therapeutic guest molecules.

Redox-switchable metal-based cavitands have been scarcely studied. Ferrocene may be used as an effective electroactive marker of the complexation of cavitands, because it retains its reversible one-electron redox character, with the possibility of showing substantial redox changes depending on the microenvironment and, in particular, on the presence of guest molecules.[10] Since Beer and co-workers described the first ferrocene-amide receptors for binding and sensing anions,[11] several authors have provided different strategies for introducing ferrocene to the lower and upper rims of calixarenes and resorcinarenes,[12] and most of these sensors were used for the recognition of anions, due to the ability of the oxidized form of ferrocene, ferrocenium, to electrostatically interact with anions. All in all, we found that while most of the works regarding the description of new ferrocene-containing macromolecules were focused on providing effective preparative methodologies, and on the description of the electrochemical properties of the resulting materials, the enormous potential derived from the redox-

switchable conformational changes, which can be used to tune the trapping ability of the cavitand, remains fundamentally unexplored. Because tetra-benzimidazole-resorcinarene cavitands are known to be effective receptors for hosting and selectively recognizing small molecules,[8c,9] we thought that marrying these molecules with ferrocenes, may result in unique systems with redox-switchable trapping properties. In this part of the work, we describe the preparation of a ferrocenyl-substituted tetra-benzimidazole (Scheme 5.2, **15**), which forms kinetically stable (in the NMR timescale) inclusion complexes with a series of ammonium salts. The thermodynamic affinity for a series of ammonium-based molecules is assessed by NMR spectroscopy, as well as by Mass Spectrometry and Cyclic Voltammetry.

5.1.3 Tetra-azolium-resorcinarene cavitands for the recognition of anions

Given the importance of anion recognition from the environmental and biological points of view,[13] the design of anion selective receptors continues to attract great interest in the supramolecular chemistry community.[14]

Among the various types of receptors, imidazolium-based supramolecules have been extensively investigated[13d,15] since the pioneering works by Sato,[16] Alcalde[17] and Kim.[18] It is now well accepted that anion recognition is dominated by a combination of electrostatic interactions and hydrogen bonding [$(C\text{-}H)^{+}\cdots A$]. Although there is a huge variety of anion receptors, in the form of tweezers, dipodal, tripodal or other open forms,[18-19] little attention has been given to the preparation of imidazolium-based macrocycles with closed conformations.[8d,17,20] The preparation of receptors combining positively charged imidazoliums with a cavity may enhance the binding affinity and selectivity toward anions, depending on the adaptability of the cavity to the steric and electronic requirements of the guest. The idea of combining imidazolium salts with cavities was first proposed by Yoon and co-workers one decade ago,[8d] by preparing a calixarene-based cavitand with four imidazolium rings as anion receptor (Scheme 5.4).

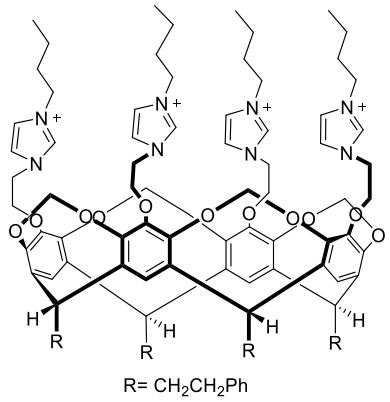

Scheme 5.4. Calixarene-based cavitand with four imidazolium rings described by Yoon and co-workers

Since then, only few examples have been reported, most likely due to the difficult synthetic procedures involved in their preparation.[8d,20b-d]

Based on these precedents, in the second part of this chapter we will describe the preparation of two tetra-benzimidazolium-based cavitands, which we used for the recognition of anions (Scheme 5.2, **16(PF$_6$)$_4$** and **17(PF$_6$)$_4$**). These new molecules contain the four benzimidazolium fragments directly embedded into the rigid structure of the cavitand, thus providing an organized macromolecule for the encapsulation of negatively charged guests.

5.2 Results and discussion

5.2.1 Preparation of a tetra-(imidazolyl-ferrocenyl)-resorcinarene as redox-switchable host for cations

5.2.1.1 *Synthesis and characterization of tetra-(imidazolyl-ferrocenyl)-resorcinarene **15***

The tetra-(imidazolyl-ferrocenyl)-resorcinarene compound **15**, was obtained by the tetra-annulation of the related octaamino-based cavitand **E**[21] with ferrocene-carboxaldehyde (Scheme 5.5). The compound was isolated in high yield (65%) as an air-stable red solid. Compound **15** was characterized by NMR spectroscopy, ESI Mass Spectrometry and Elemental Analysis. The molecule adopts a vase conformation, as indicated by the representative ^{1}H NMR signal due to the proton at the resorcinarene-methyne group (triplet at 5.1 >δ > 6.3 ppm, depending on the solvent used).

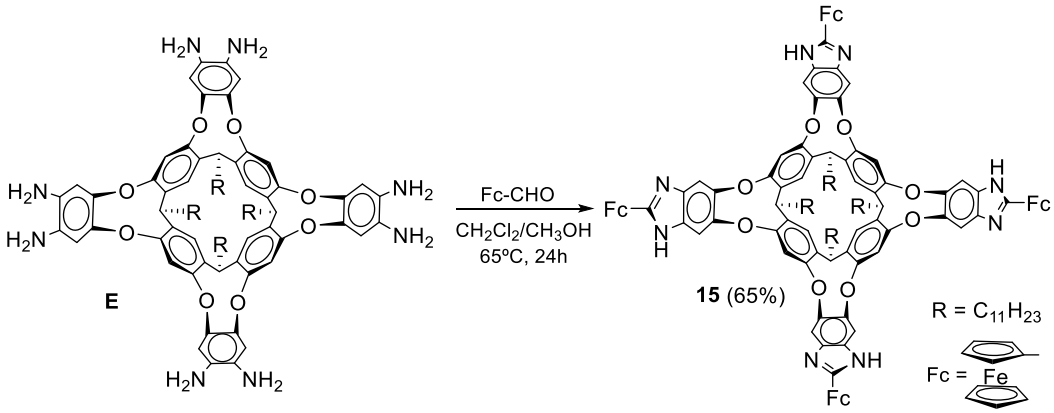

Scheme 5.5. Synthesis of Cavitand **15**

*^{13}C {^{1}H} NMR spectrum of **15***

Figure 5.1 shows the ^{13}C {^{1}H} NMR spectrum of **15**. It shows one signal due to the N*C*N carbon at 181.6 ppm (**1**). The signals due to the aromatic *C*H and quaternary carbons from the benzimidazoles and the phenyl groups appear at 156.7, 149.7, 135.7 and 117.6 ppm (**2**, **3**, **4** and **5**). The resonance due to the *C*H methyne carbons appears at 33.8 ppm (**6**). The signals assigned to the *C*H and the quaternary carbons of ferrocenium are observed at 69.7 and 67.7 ppm (**8** and **7**). The rest of the signals correspond to the carbons of the $C_{11}H_{23}$ fragments, which are conveniently assigned in the spectrum.

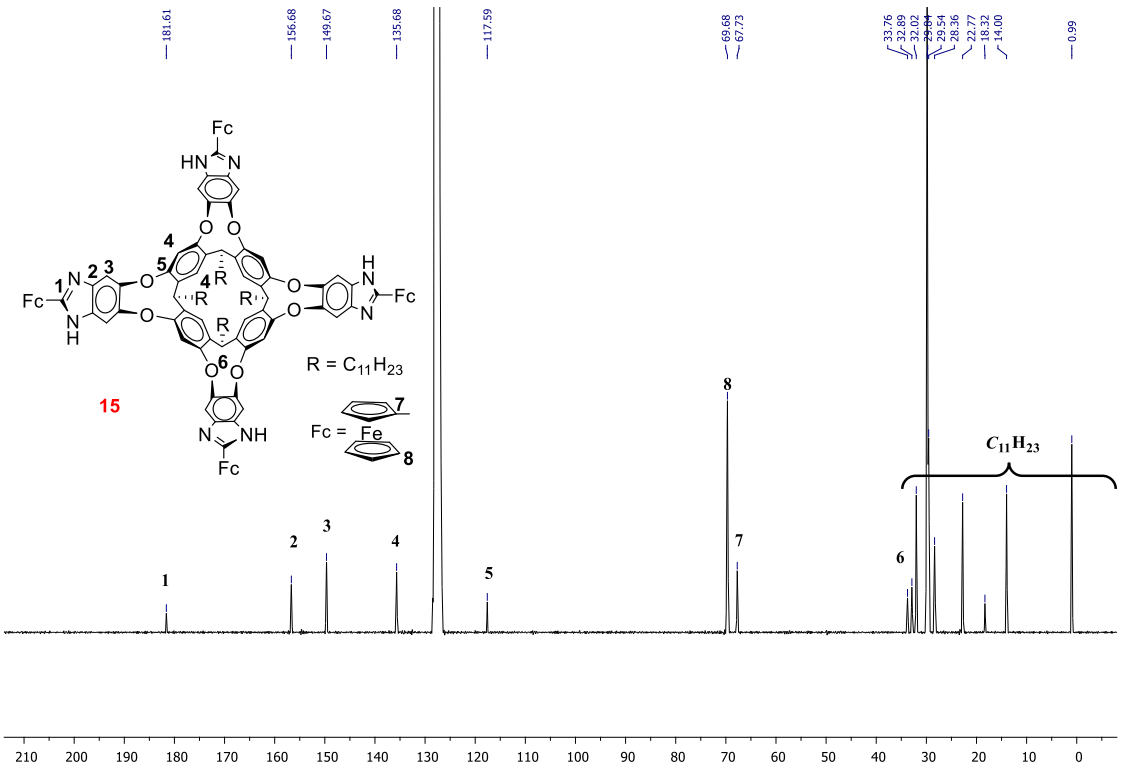

Figure 5.1. ^{13}C {^{1}H} NMR spectrum of **15** in benzene-d^6

*Cyclic Voltammetry of **15***

Figure 5.2 shows the cyclic voltammetry diagram obtained for compound **15**. The electrochemical analysis revealed a single reversible redox event ($E_{1/2}$ = 0.65 V). This process is associated with the simultaneous oxidation of the four ferrocenyl fragments, thus indicating that these units are electronically uncoupled.

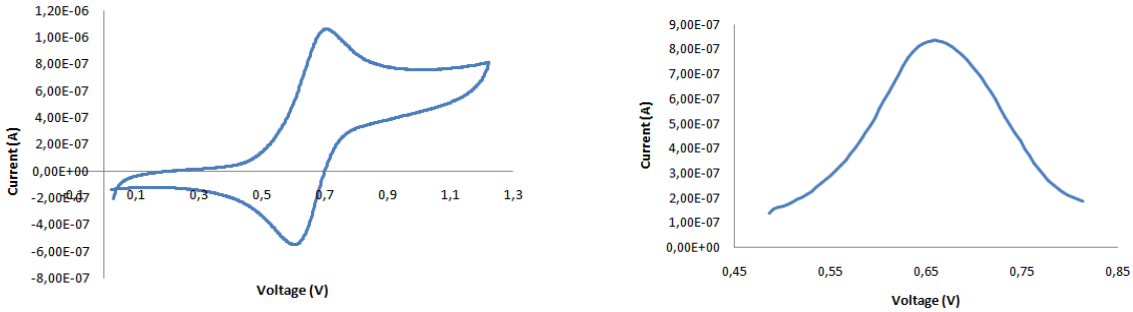

Figure 5.2. Cyclic voltammetry diagram and the relevant section of the Differential Pulse Voltammetry (DPV) obtained for 0.2 mM of compound **15** in CH_2Cl_2, in the presence of 0.1 M NBu_4PF_6. The scan potential was initiated from E_{ocp} to positive direction. Scan rate 0.1 V s^{-1}. Platinum electrode was used.

*Optimized structures of **15'** and **[15']$(Cl)_4$***

The *vase*-type conformation of the molecule was also supported by DFT (PBE-D3) calculations, which were carried out by Prof. Gregori Ujaque and Dr. Pietro Vidossich from the Universitat Autónoma de Barcelona. DFT calculations show that the energy-minimized structure of the ferrocene-containing molecule adopts a closed structure with C_4-symmetry (Figure 5.3a. for simplification of the calculation R = Me was used, and the molecule was labelled as **15'**). Interestingly, the four ferrocenyl moieties are partially closing the upper rim of the molecule, therefore forming a top-closed molecular container, rather than an open-ended cavity. The energy difference between the open and closed conformations (*vase* and *kite* shapes, respectively) for **15'** in solution is 27.5 kcal/mol, favouring the closed (*vase*) structure. In order to determine if the oxidation of the four ferrocenyl fragments would introduce a significant conformational change in the resulting tetracationic molecule, the structure of [**15**]$(Cl)_4$ was also optimized. The oxidized form opens the cavity by the upper rim separating the arms and the ferrocenium moieties from the gate of the cavity, but the *vase* conformation of the cavitand is still maintained. The four chloride ions are alternatively located between the metallic fragments, thus minimizing the electrostatic repulsions of ferrocenium fragments (Figure 5.3b). The optimization of $\mathbf{15}^{4+}$ (without the four

chlorides) shows a more expanded conformation (Figure 7.115c in chapter 7, experimental section), with the four arms of the cavitand leaving a wide open structure. Hence, oxidation of the iron centre results in a marked change between open and closed conformations.

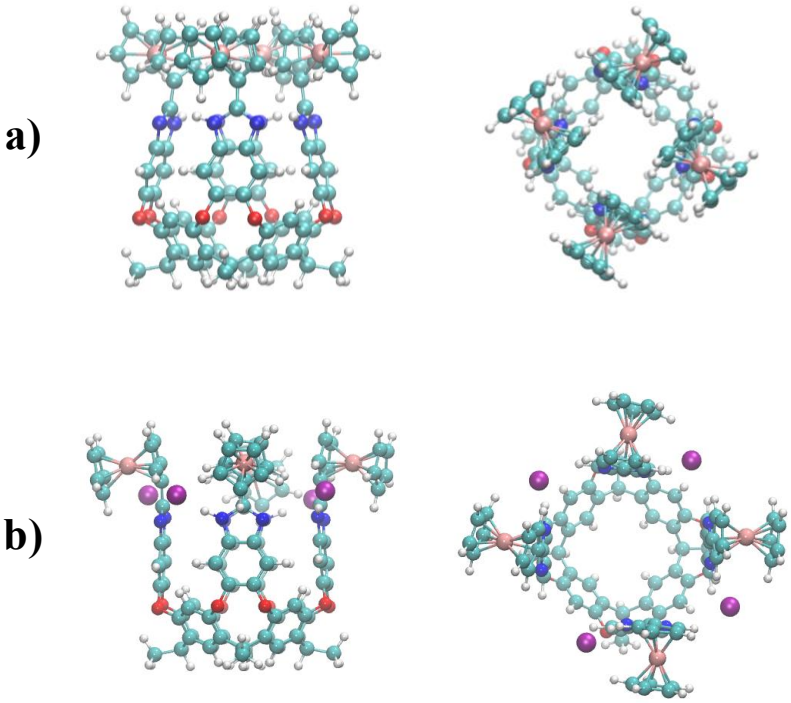

Figure 5.3. Two perspectives of the energy-minimized geometry at DFT(PBE-D3) of a) **15'** (R = Me), and b) [**15'**](Cl)$_4$

5.2.1.2 *Recognition of cations by ^{1}H NMR studies*

Neutral imidazole-based resorcinarenes have been used for the encapsulation of small cations.[22] From our computational analysis of the neutral and tetracationic forms, we thought that **15** may be used as a redox-switchable receptor of cations, because the neutral form should be able to encapsulate small positively charged molecules, while the tetracationic oxidized form should release cations due to electrostatic repulsion. In order to prove this, we first tested the binding affinity of **15** with several tetralkylammonium salts and also with *L*-carnitine. We performed our tests in different solvents. For the experiments carried out in $CDCl_3$ and CD_2Cl_2, the encapsulation was evidenced by the characteristic upfield chemical shifts of the alkyl groups of the guest molecules, but signals from both the cavitand **15** and the guests were typically broad, likely due to a fast equilibrium between the complexed and the free host and guest

molecules. Under these circumstances, we decided to avoid the use of $CDCl_3$ and CD_2Cl_2 for the NMR studies, and used other solvents (benzene-d^6 or toluene-d^8) for which the signals due to the encapsulated molecules provided sharper diagnostic signals. The ^{1}H NMR spectra of equimolar mixtures of **15** with guest ions **a**$^+$-**e**$^+$ and **f** (Scheme 5.6) in benzene-d^6 showed the formation of kinetically stable host-guest complexes on the ^{1}H NMR timescale.

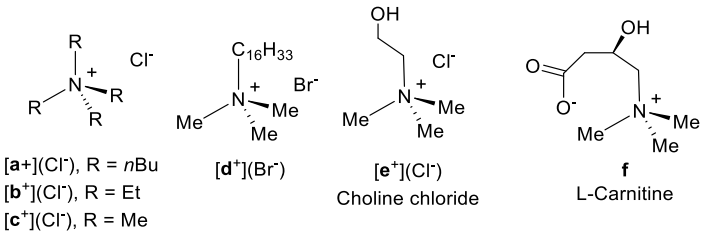

Scheme 5.6. Structures of ammonium guests **a**$^+$-**e**$^+$ and **f**

The comparison of the ^{1}H NMR spectra of **15** with equimolecular amounts of the guests revealed important information. Tetramethylammoniun chloride revealed a single resonance at -1.2 ppm, which is diagnostic of encapsulation. The association constant was estimated as 260 M^{-1} by integration of the signals due to free and complexed **15** (see below for details regarding the calculation of the constants). ^{1}H diffusion-ordered NMR spectroscopy (DOSY) revealed that the signals of the cavitand and that of the encapsulated NMe_4^+ at -1.2 ppm diffused at the same rate (D = 3.1 x 10^{-10} m^2/seg, see Figure 7.23 in the experimental section).[23] Figure 5.5 shows the representative regions of a series of ^{1}H NMR spectra of **15** with increasing amounts of NMe_4Cl.

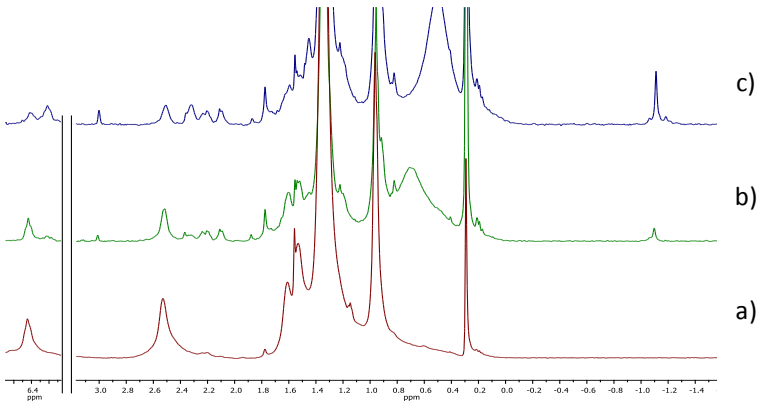

Figure 5.4. Representative regions of the ^{1}H NMR spectra in benzene-d^6 of a series of samples containing cavitand **15** with increasing amounts of NMe_4Cl. Concentration of **15**: 3.5 mM. Concentration of NMe_4Cl, a) 0 mM, b) 3.5 mM and c) 7 mM. The signal at 6.44 ppm corresponds to the proton at the resorcinarene-methyne group of the uncomplexed cavitand. The signal at 6.31 ppm corresponds to the

resorcinarene-methyne group of the host:guest complex. The signal at -1.2 ppm is assigned to the protons of the methyl group of the encapsulated NMe_4^+

Tetrabutylammonium $\mathbf{a}^+$ did not show any detectable evidences of binding. Tetraethylammonium $\mathbf{b}^+$, hexadecyltrimethylammonium $\mathbf{d}^+$ and choline $\mathbf{e}^+$, formed host-guest complexes with **15**, as observed by the appearance of resonances at -2.0, -1.61 and -1.06 ppm, respectively. Under the same experimental conditions, *L*-carnitine did not show any signals that could be assigned to the formation of a host-guest complex, but the addition of tetrabutylammonium chloride to the equimolecular mixture of $\mathbf{a}^+$ and **f**, resulted in the appearance of a sharp signal at -0.87 ppm, ascribed to the protons of the methyl groups of **f**. This result is relevant because it indicates that the presence of the salt is crucial for assisting the binding affinity between the tetraalkylammoniums and **15**, most likely due to the formation of ion-pairs within the cavity where either ion-π or electrostatic interactions are needed to stabilize the host-guest interactions. The formation of ion-pairs has precedents in closely related cavitands decorated with benzyl benzimidazoles.[22b]

Since there is a slow-exchange within the NMR timescale, it is possible to calculate the host-guest association constant by integrating the ^{1}H NMR signals due to the free cavitand and those due to the host-guest complex, and using equations (1) and (2) shown below. For these equations, $[H]_0$ and $[G]_0$ are the initial concentrations of host and guest, respectively, and C stands for the host-guest complex.

$$H + G \rightleftharpoons C$$

$$Ka = \frac{[C]}{([H]_0 - [C])([G]_0 - [C])} \quad \textbf{(1)}$$

The integrals of the signals due to the host and the complex (I_h and I_c) are used to obtain the molar fraction of the complex.

$$X_c = \frac{I_c}{I_h + I_c} \quad \textbf{(2)}$$

Then,

$$Ka = \frac{\frac{X_c}{[H]_0}}{(1-X_c)(r-X_c)} \quad (3)$$

where $[C]=Xc[H]_o$ and $r=[G]_o/[H]_o$

Table 5.1 shows the association constants for the encapsulation of $\mathbf{b}^+$-$\mathbf{e}^+$ and **f** in benzene-d^6 and toluene-d^8. The comparison of these association constants of **15** with equimolecular amounts of the $\mathbf{b}^+$-$\mathbf{e}^+$ and **f**, revealed that there is a clear size cutoff for the binding affinities. This is in agreement with the fact that there was no evidence of $\mathbf{a}^+$ encapsulation.

Table 5.1. Association constants for tetraalkylammonium salts with **15**. Determined by ^{1}H NMR spectroscopy at 298 K

Entry	Guest	Solvent	K_a (M^{-1})
1	NMe_4Cl, [$\mathbf{c}^+$](Cl^-)	benzene-d^6	260
2	NEt_4Cl, [$\mathbf{b}^+$](Cl^-)	benzene-d^6	60
3	$N(C_{16}H_{33})Me_3Cl$, [$\mathbf{d}^+$](Br^-)	benzene-d^6	500
4	Choline chloride, [$\mathbf{e}^+$](Cl^-)	benzene-d^6	70
5	Carnitine[a], **f**	benzene-d^6	110[a]
6	NMe_4Cl, [$\mathbf{c}^+$](Cl^-)	Toluene-d^8	350
7	NEt_4Cl, [$\mathbf{b}^+$](Cl^-)	Toluene-d^8	130
8	Choline chloride, [$\mathbf{e}^+$](Cl^-)	Toluene-d^8	30
9	Carnitine[a], **f**	Toluene-d^8	70

[a]In the presence of an excess of NBu_4Cl

5.2.1.3 *Recognition of cations by ESI Mass Spectrometry*

The encapsulation abilities of **15** were also investigated by ESI Mass Spectrometric techniques. ESI-MS-based methods have been previously used to study binding events between alkylammonium salts and resorcinarenes.[24]

In the present study, the ESI mass spectra of equimolar mixtures ($5\cdot10^{-4}$ M) of **15** and the ammonium guests were investigated in $CHCl_3$:CH_3OH (1:1). Illustrative ESI mass

spectra for the tetramethylammonium guest are shown in Figure 5.5. Prominent peaks formulated as [**15** + **c**]$^+$ and [**15** + **c** + 2Cl]$^-$ in the positive and negative scan modes, respectively, are clearly distinguished, thus confirming the 1:1 stoichiometry of the host-guest complex.

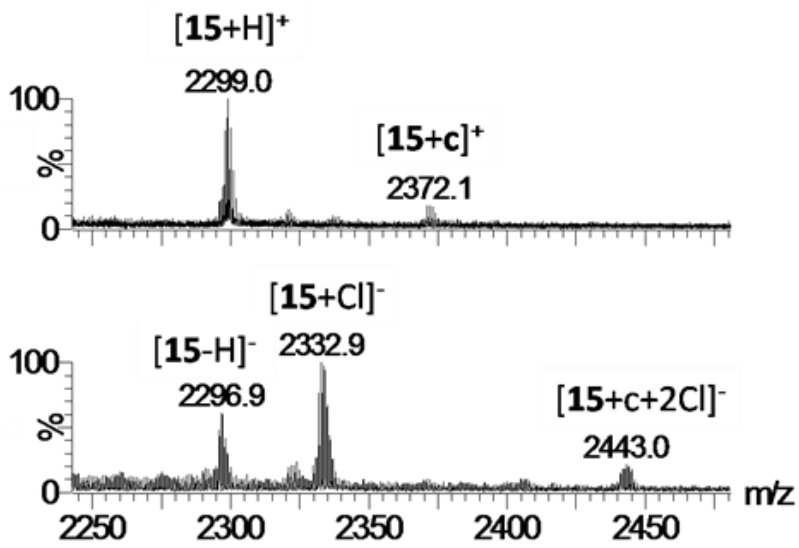

Figure 5.5. ESI-MS spectra of an equimolar mixture of **15** and **c**$^+$. In the positive (top) and negative (bottom) scan modes

For the experiments carried out with the rest of the ammonium salts, we observed the formation of the supramolecular complexes between host **15** and all guests, except for the case of **a**$^+$ (NBu_4^+), for which we did not detect any peak. For *L*-carnitine, **f**, the 1:1 adduct [**15** + **f** + Cl]$^-$ was observed, whereas for the rest of the cationic guests **b**$^+$-**e**$^+$, the formation of adducts with 1:1 stoichiometry of general formula [**15** + guest + 2Cl]$^-$ was manifested.

Furthermore, a competitive experiment was also carried out. The experiment was based on the mixture of **15** with a solution of equimolar **a**$^+$-**e**$^+$ and **f** guests, which were added in a five-fold excess with respect to the host. The relation between the intensity of the mass peaks is a qualitative measure of the binding affinities, and compares well with the association constants shown in Table 5.1.

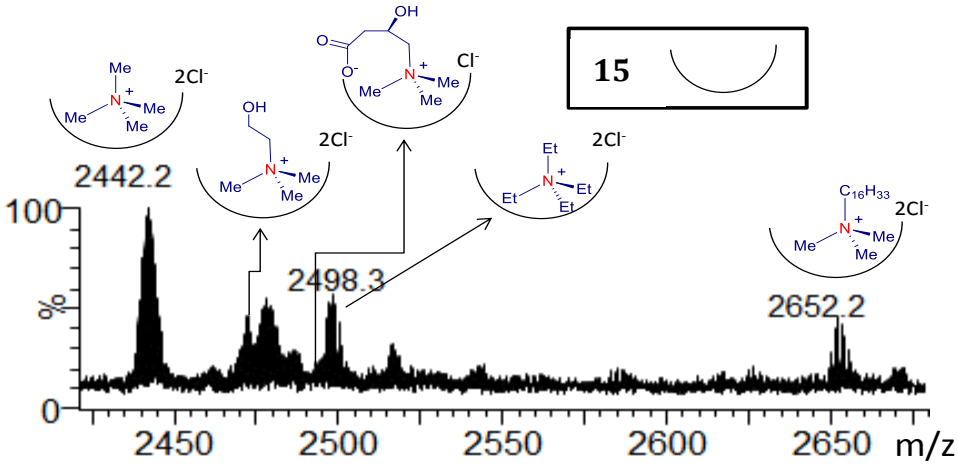

Figure 5.6. Selected region of the ESI-MS spectrum (negative scan mode) of a mixture of **15** and a five-fold excess of the halides of $\mathbf{a}^+$-$\mathbf{e}^+$ and **f**. Non-assigned peaks correspond to uncomplexed forms of **15**, such as [**15** + 5H + 4Cl]$^-$ and [**15** + 6H + 5Cl]$^-$

To get more information about the strength of the encapsulation, a gas-phase study using soft ionization tandem mass spectrometric techniques was performed. This study provides very rich information about the reactivity of the encapsulated guests and also about structural factors.[25] In some previous studies, this technique has been applied to the cucurbi[n]turil family, to investigate reactions inside the container.[26]

By Collision Induced Dissociation (CID) experiments, we explored the gas-phase dissociation properties of the supramolecular adducts formed between **15** and $\mathbf{a}^+$-$\mathbf{e}^+$ and **f**. For the supramolecular ions with guests $\mathbf{b}^+$-$\mathbf{e}^+$, namely, [**15** + guest + 2Cl]$^-$ (guest = $\mathbf{b}^+$-$\mathbf{e}^+$), the CID mass spectra were similar. As an illustrative example, the fragmentation channels for the encapsulation of $\mathbf{b}^+$ are depicted in Figure 5.7, together with the CID mass spectrum.

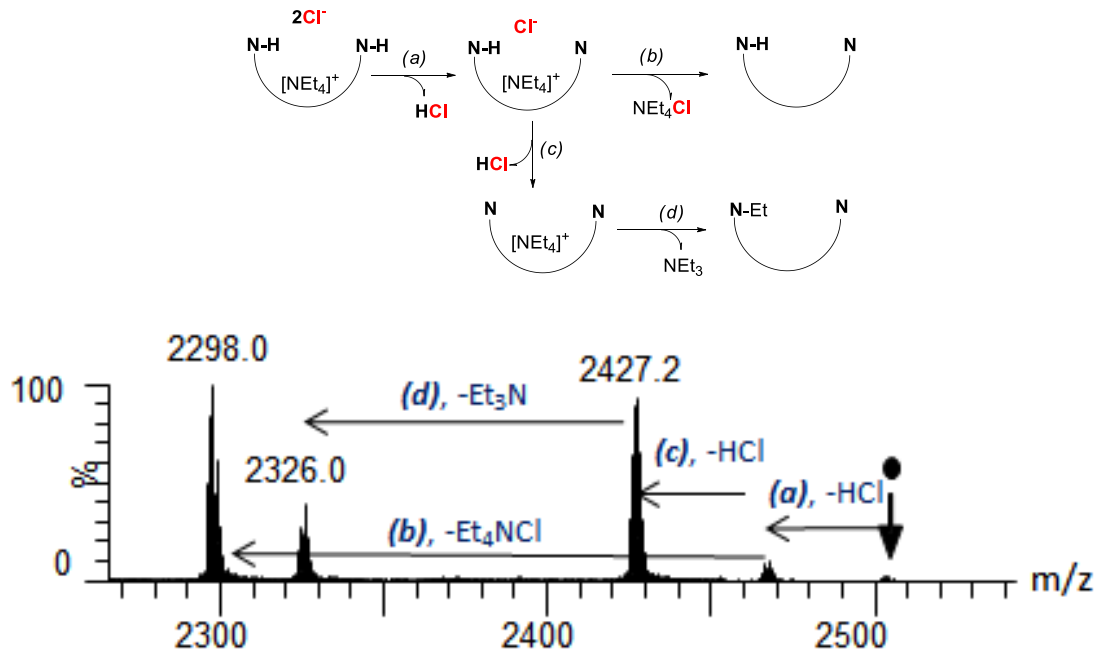

Figure 5.7. (Top) Schematic representation of the fragmentation channels *(a)-(d)* of the [**15** + **b** + 2Cl]$^-$ adduct. Two NH groups are schematically drawn in the precursor ion to depict the imidazoles involved in the fragmentation pathway. (Bottom) CID mass spectrum of [**15** + **b** +2Cl]$^-$

For [**15** + **b** + 2Cl]$^-$, a first fragmentation channel involves the liberation of HCl (*a*). Two competitive steps are then observed upon increasing the collision energy: the expulsion of the ion pair Et_4NCl *(b)*, which formally leads to [**15** - H]$^-$, and the loss of a second HCl molecule *(c)*. For channels *(a)* and *(c)*, the release of HCl, most likely involves the loss of the two NH protons at the imidazoles. The final fragmentation channel *(d)* corresponds to the liberation of Et_3N, which implies the cleavage of a N-C covalent bond of the Et_4N^+ group. It is important to highlight that fragmentation channel *(d)* is not observed until the two imidazole rings are deprotonated, and for that reason it may be assumed that the N-C bond breaking occurs concomitant with the ethylation of the imidazole, as is illustrated in Figure 5.7 top.

Cavitand **15** reported, herein, displays two important features; first, it enables strong guest encapsulation and, second, it provides reactive walls that trigger the coupling between host and guest entities.

5.2.1.4 *Ammonium salts recognition by Cyclic Voltammetry*

Voltammetric studies were carried out to evaluate the potential electrochemical sensing capabilities of the ferrocenyl-cavitand **15**. A square–scheme thermodynamic cycle (Scheme 5.7),[27] is the best way to represent the equilibrium between the neutral and the oxidized form of **15** and the corresponding guest (G).

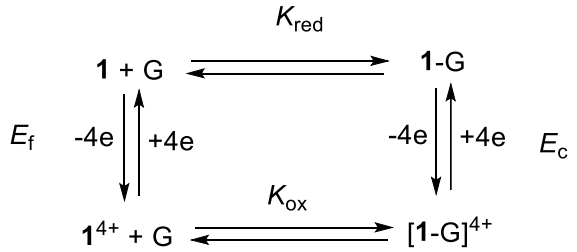

Scheme 5.7. Square scheme for the equilibrium between the neutral and oxidized forms of **15**, and G (guest)

K_{red} and K_{ox} represent the association constants related to **15** and $\mathbf{15}^{4+}$, respectively. E_f and E_c, represent the formal potentials of the free and complexed cavitand, which can be directly determined from the voltammetric responses.

The titration experiment of cavitand **15** with progressive addition of guest ($\mathbf{b}^{+}$-$\mathbf{e}^{+}$) produces a significant anionic perturbation of the ferrocenes' oxidation potential ($\Delta E \approx$ 90-180 mV). No shift was produced when NBu_4Cl was added (table 5.2), in a clear indication of the negligible affinity shown by this substrate, in accordance with the NMR and ESI experiments. These results provide relevant information. Firstly, the receptor only gives a response when the encapsulation is effective, and the anionic shifts should be due to cation encapsulation rather than a process implying the association of the counter-anions with the protons at the rim of the cavitand. The anionic shift of the oxidation potential may be explained as a consequence of the lower tendency of the ferrocene moieties to be oxidized in a cationic environment. In fact, the reverse effect (a cathodic shift) has been described when anions are encapsulated in other ferrocenyl-containing cavitands.[12n]

Secondly, the K_{red}/K_{ox} ratios (calculated using eq. 4) demonstrate that guests show high preference for the neutral host **15** over the oxidized host $\mathbf{15}^{+}$, or in other words, guests are bounded hardly to the reduced state (top-closed) of the cavitand and are released from the oxidized state (top-open). This preference may be understood more clearly by

comparing the ΔG_{red} - ΔG_{ox} values (ΔG_{red} and ΔG_{ox} refer to the free energies for the reactions of association of the ammonium salts with **15** and $\mathbf{15}^{4+}$, respectively; eq. 5). For tetraethylammonium chloride, this energy difference is significantly lower (8.6 kcal/mol), probably as a consequence of size factors, which produces that the differences between the encapsulation capabilities of the neutral and oxidized cavitand become less pronounced, both due to the lower affinity of **15** to complex with the larger salts like $\mathbf{b}^+$, and for the relative higher tendency of $\mathbf{b}^+$ to accommodate in the expanded oxidized form, $\mathbf{15}^{4+}$.

$$\frac{K_{red}}{K_{ox}} = e^{\frac{nF\Delta E_{1/2}}{RT}} \quad \textbf{(4)}$$

$$\Delta G_{red} - \Delta G_{ox} = RTlnK_{red} - RTlnK_{ox} \quad \textbf{(5)}$$

Table 5.2. Electrochemical cation recognition data and association constants for cavitand **15**

Entry	Guest	ΔE (mV)	K_{red}/K_{ox}	ΔG_{red}-ΔG_{ox} (kcal/mol)
1	NMe_4Cl, [**c**$^+$](Cl^-)	160	$8.2\cdot10^{10}$	-14.9
2	NEt_4Cl,[**b**$^+$](Cl^-)	93	$2.1\cdot10^{6}$	-8.6
3	$N(C_{16}H_{33})Me_3Cl$, [**d**$^+$](Cl^-)	182	$2.25\cdot10^{12}$	-16.8
4	Choline chloride, [**e**$^+$](Cl^-)	173	$4.5\cdot10^{11}$	-15.9
5	NBu_4Cl, [**a**$^+$](Cl^-)	20	--	--

The data potentials were collected by Differential Pulse Voltammetry and Cyclic Voltammetry using 0.2 mM of compound **15** in CH_2Cl_2 in the presence of 0.1 M NBu_4PF_6. Scan rate 0.1 V s^{-1}

As an illustrative example, Figure 5.8 shows the voltammograms of **15** in the presence of increasing amounts of $\mathbf{b}^+$, and the plot of the redox potential as function of the concentration of $\mathbf{b}^+$-$\mathbf{e}^+$.

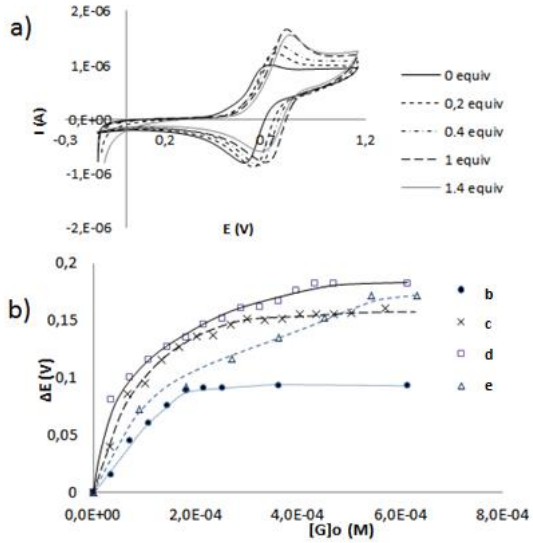

Figure 5.8. a) Cyclic voltammograms of **15**, with increasing amounts of NEt_4Cl [$\mathbf{b}^+$](Cl^-). b) Plots of the ΔE values of **15** upon the addition of incremental amounts of [$\mathbf{b}^+$](Cl^-), [$\mathbf{c}^+$](Cl^-), [$\mathbf{d}^+$](Br^-) and [$\mathbf{e}^+$](Cl^-). The data were collected by taking the potentials at the maximum current values from the differential pulse voltammetry (DPV), using 0.2 mM of compound **15** in CH_2Cl_2 in presence of 0.1 M NBu_4PF_6. The scan potential was initiated from E_{ocp} to positive direction. Scan rate 0.1 V s^{-1}

The stoichiometry of the host:guest complexes was also confirmed by using the Method of Continuous Variations (MCV, also known as Job plot).[28] For this purpose, we prepared a series of solutions of **15** and NMe_4Cl in varying proportions, so that a complete range of mole ratios were sampled, while maintaining the total concentration, [**15**] + [NMe_4Cl], constant for each solution (see Figure 5.9). This allowed us to determine that the maximum ΔE shift was achieved when the molar fraction is 0.5, and therefore the stoichiometry of the aggregates is 1:1, confirming the results obtained by Mass Spectrometry and NMR spectroscopy.

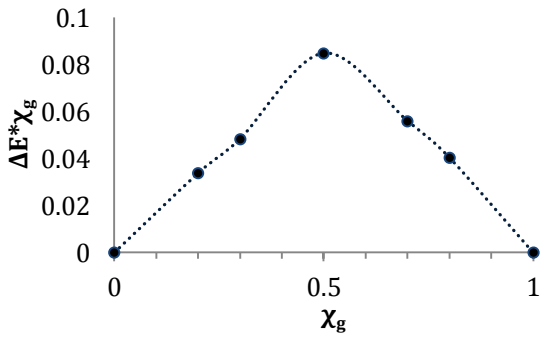

Figure 5.9. Job plot for the titration of **15** with NMe_4Cl in CH_2Cl_2. The sum of the concentration of **15** and NMe_4Cl was kept constant as [**15**] + [NMe_4Cl] = 1.7 mM. Cyclic Voltammetry data were collected in presence of 0.1 M NBu_4PF_6. χ_g is the guest molar fraction

5.2.2 Tetra-azolium-resorcinarene cavitands for the recognition of anions

5.2.2.1 *Synthesis and characterization of cavitand salts* ***16(PF$_6$)$_4$*** *and* ***17(PF$_6$)$_4$***

Tetra-benzimidazole cavitand **F** (Scheme 5.8) was synthesized according to the literature procedure.[8c] The methyl-substituted resorcinarene-based tetra-benzimidazole cavitand **G** was prepared by a condensation reaction between octaamino-based cavitand **E**[21] and acetic acid, which also acts as solvent. Cavitand salts **16I$_4$** and **17I$_4$** were prepared by reaction of **F** and **G** respectively, with NaOH in dimethylsulfoxide (DMSO). This was followed by methylation with CH_3I. The related hexafluorophosphate salts, **16(PF$_6$)$_4$** and **17(PF$_6$)$_4$**, were readily prepared by anion exchange with $[NH_4][PF_6]$ in CH_3OH. A summary of all these reactions and the yield obtained for each step are displayed in Scheme 5.8.

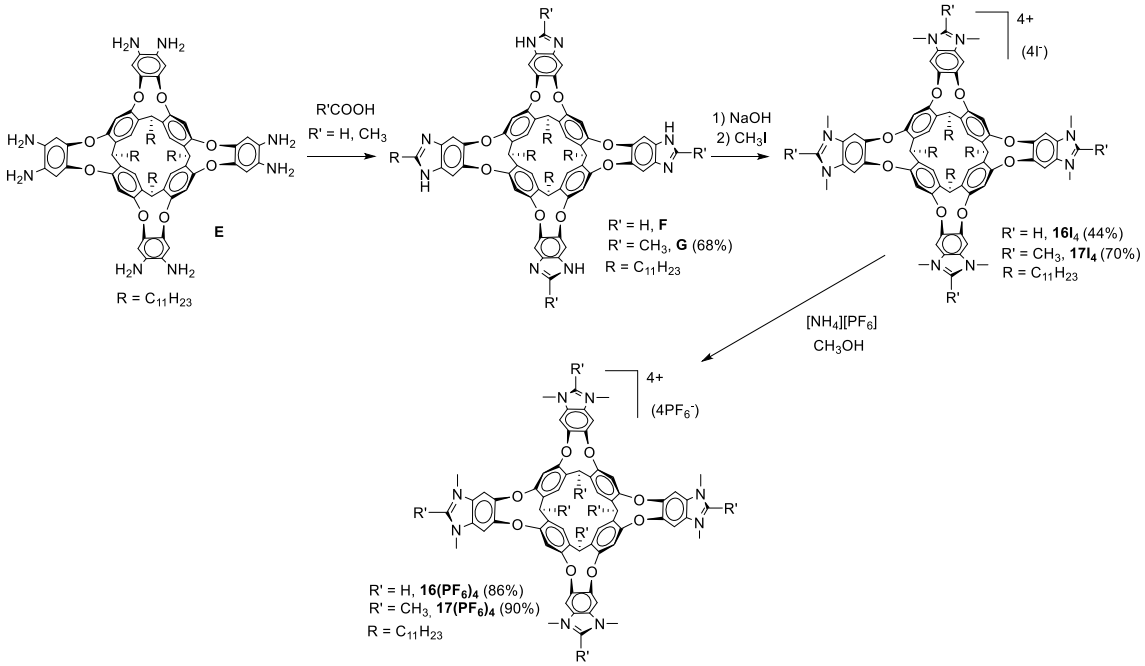

Scheme 5.8. Preparation of cavitands **16(PF$_6$)$_4$** and **17(PF$_6$)$_4$**

A full characterization of compounds **F**, **G** and **16I$_4$** and **17I$_4$** is provided in the experimental section (Chapter 7)

a) Characterization of compound ***16(PF$_6$)$_4$***

^{1}H NMR spectrum of compound **16(PF$_6$)$_4$**

Figure 5.10 shows the ^{1}H NMR spectrum of **16(PF$_6$)$_4$**. The number of signals is in accordance with the fourfold symmetry of the compound. This is exemplified by the appearance of only one signal corresponding to the more acidic proton (NC*H*N) at 9.57 ppm (**a**). The resonance attributed to the benzimidazole aromatic protons appears at 8.63 ppm (**b**). The signals at 7.99 and 7.80 ppm are assigned to the phenyl protons (**c** and **d**). The resonance corresponding to the four methyne protons appears as one triplet at 5.66 ppm (**e**), supporting that the molecule adopts a vase confomation. The signal at 3.91 ppm corresponds to the C*H*$_3$ proton resonances (**f**). The rest of the signals are attributed to the C$_{11}$*H*$_{23}$ chain.

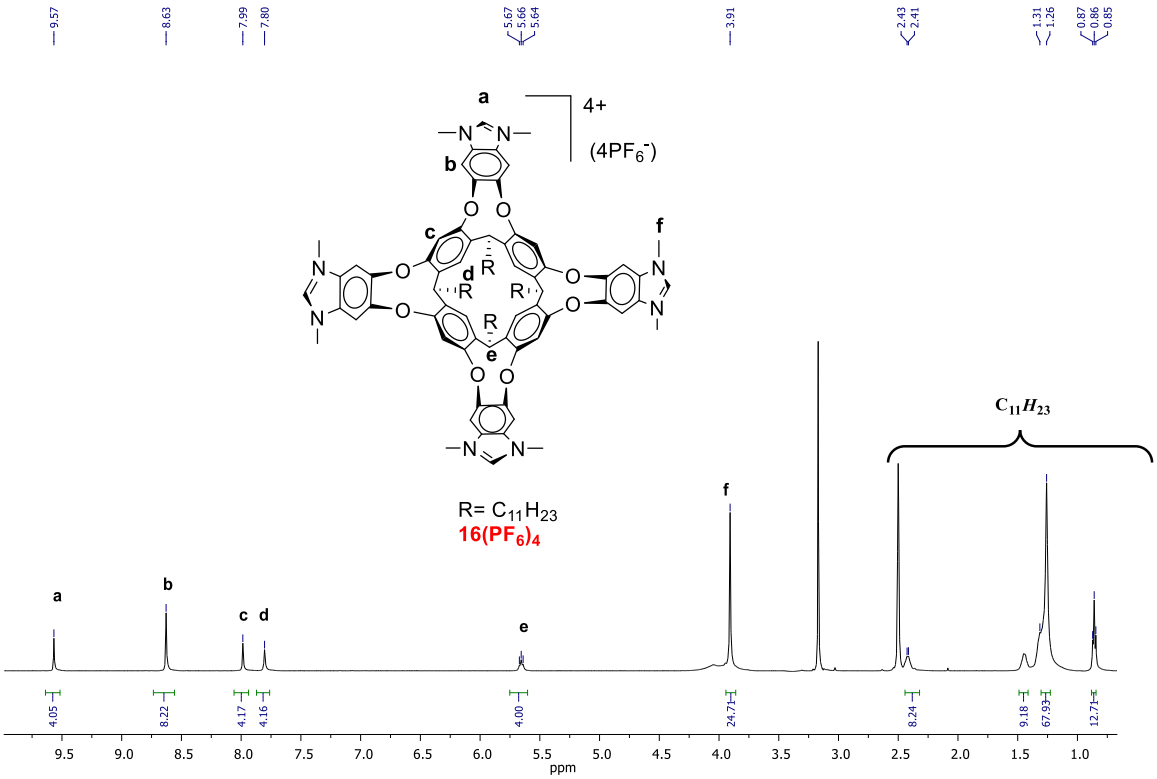

Figure 5.10. ^{1}H NMR spectrum of **16(PF$_6$)$_4$** in DMSO-*d*^{6}

^{13}C {^{1}H} NMR spectrum of compound **16(PF$_6$)$_4$**

Figure 5.11 shows the ^{13}C {^{1}H} NMR spectrum of **16(PF$_6$)$_4$**, which is also consistent with the fourfold symmetry of the compound. The signal corresponding to the N*C*N carbon appears at 154.8 ppm (**1**). The resonances due to the aromatic *C*H and quaternary carbon atoms of the benzimidazoles (**3, 4** and **5**) and the phenyl group (**6**, **7** and **8**) appear in the range between 109 and 152 ppm. The resonance corresponding to the *C*H$_3$ carbons at the rim of the molecule appears at 49.1 ppm (**2**). The resonance due to the *C*H methyne carbons appears at 34.0 ppm (**9**). The rest of the signals correspond to the carbons of the $C_{11}H_{23}$ chain.

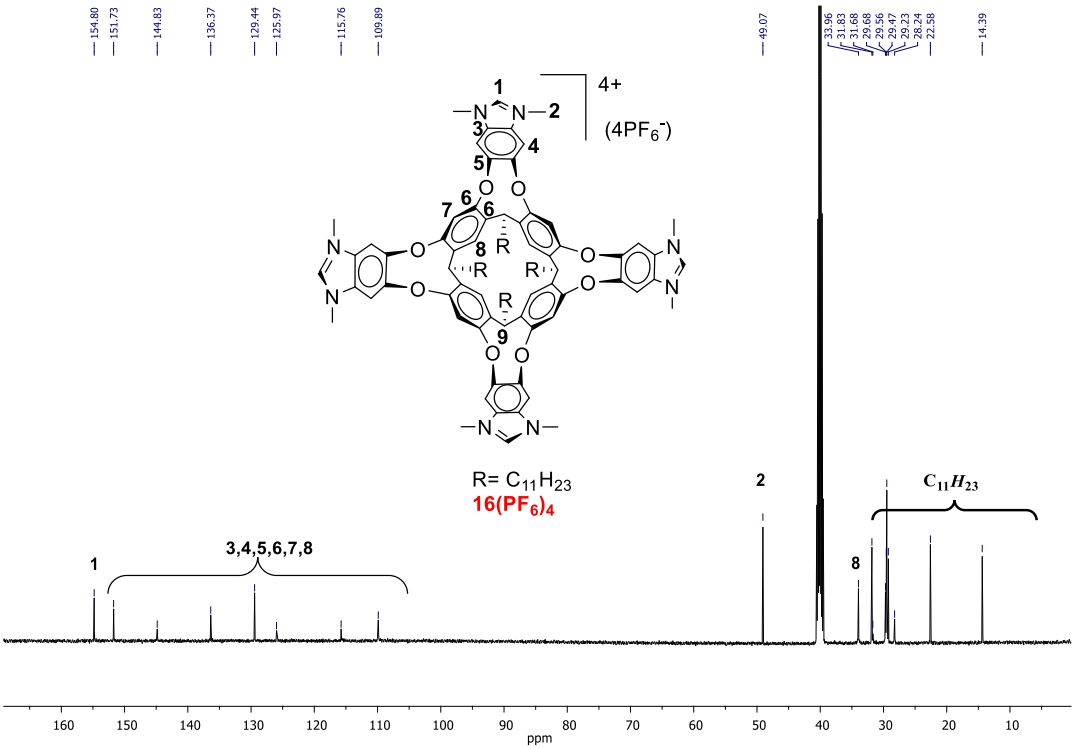

Figure 5.11. ^{13}C {^{1}H} NMR spectrum of **16(PF$_6$)$_4$** in DMSO-*d*^{6}

b) Characterization of compound ***17(PF$_6$)$_4$***

^{1}H NMR spectrum of compound **17(PF$_6$)$_4$**

Figure 5.12 shows the ^{1}H NMR spectrum of **17(PF$_6$)$_4$**. The number of signals is in accordance with the fourfold symmetry of the compound. This is exemplified by the presence of one signal attributed to the benzimidazole aromatic protons at 8.55 ppm (**a**). The signals at 7.95 and 7.80 ppm are assigned to the benzene protons (**b** and **c**). The resonance due to the four methyne protons appears as one triplet at 5.67 ppm (**d**). The signal at 3.84 ppm corresponds to the N-C*H*$_3$ proton resonances (**e**). The resonance attributed to the C*H*$_3$ in the upper rim appears as one singlet at 2.69 ppm (**f**). The rest of the signals are due to the C$_{11}$*H*$_{23}$ chain.

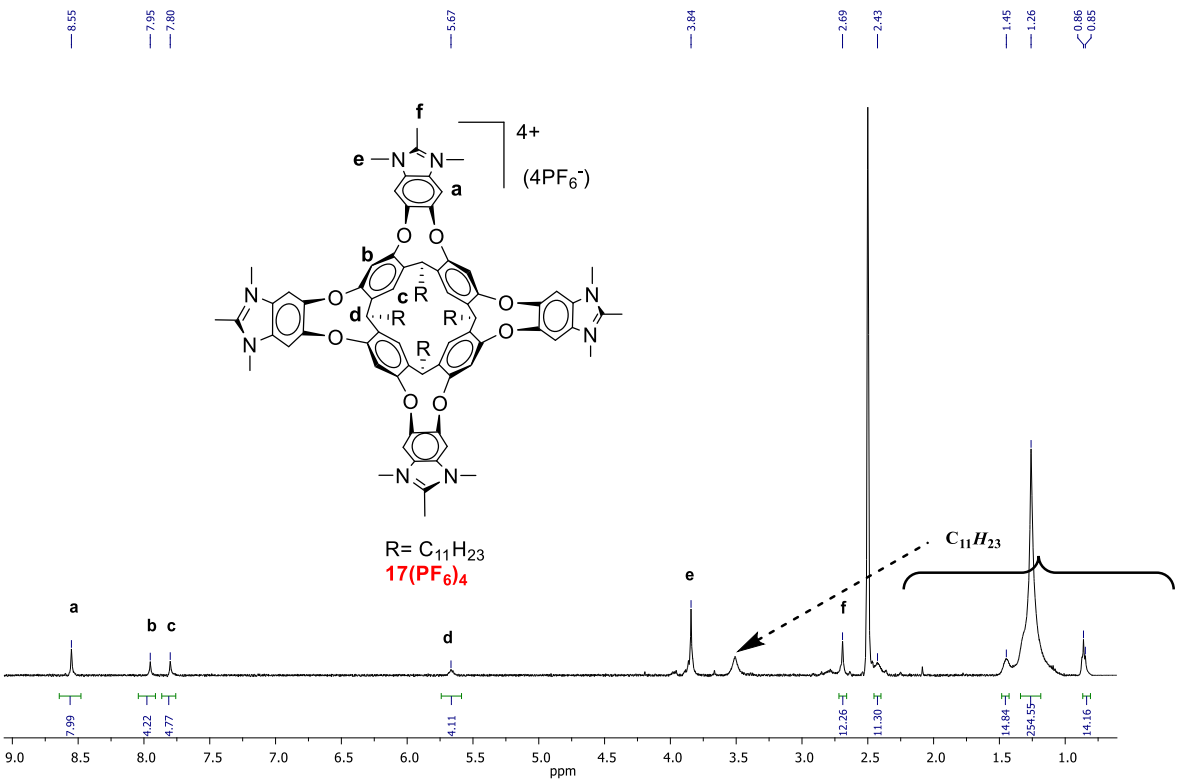

Figure 5.12. ^{1}H NMR spectrum of **17(PF$_6$)$_4$** in DMSO-*d*^{6}

^{13}C {^{1}H} NMR spectrum of compound **17(PF$_6$)$_4$**

Figure 5.13 shows the ^{13}C {^{1}H} NMR spectrum of **17(PF$_6$)$_4$**, which is also in agreement with the fourfold symmetry of the compound. The signal corresponding to the N*C*N carbon appears at 154.60 ppm (**1**). The resonances due to the aromatic *C*H and

quaternary carbon atoms of the benzimidazole functionality (**3, 4** and **5**) and the phenyl group (**6**, **7** and **8**) appear in the range between 154 and 108 ppm. The resonances attributed to the N-CH_3 (**2**) carbons and the CH_3 carbons from the rim (**10**) appear at 31.9 and 10.7 ppm, respectively. The resonance due to the *C*H methyne carbon (**9**) appears at 31.6 ppm. The rest of the signals correspond to the carbons of the $C_{11}H_{23}$ chain.

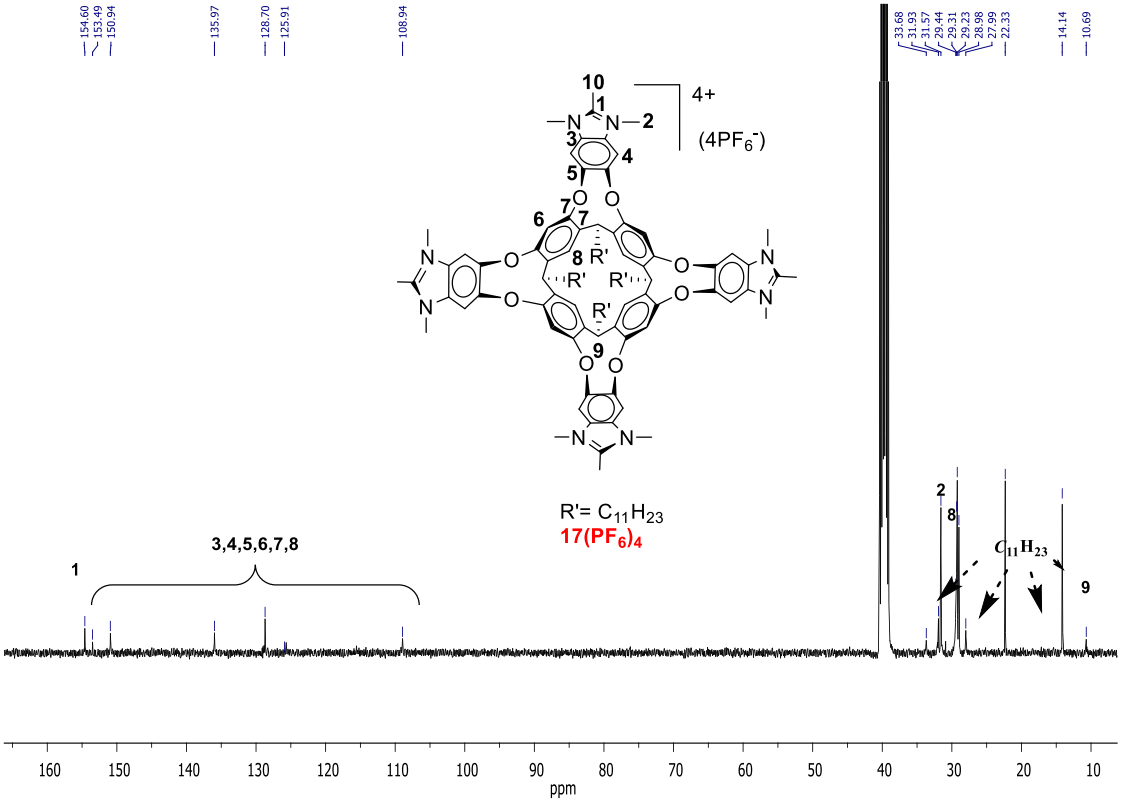

Figure 5.13. ^{13}C {^{1}H} NMR spectrum of **17(PF$_6$)$_4$** in DMSO-d^6

c) Optimized geometries of ***16***$^{4+}$ *and* ***17***$^{4+}$

The vase conformation of the cavitand salts is also supported by Molecular Dynamics (MD) simulations, which were also carried out by Prof. Gregori Ujaque and Dr. Pietro Vidossich from the Universitat Autonoma de Barcelona. The MD simulations were done in explicit DMSO (see chapter 7, section 7.11, for parameters development and simulation details; note that in order to simplify the calculations methyl groups were used instead of the full $C_{11}H_{23}$ chains). Reports on MD simulations of supramolecular systems are rare, especially those regarding resorcinarene-based cavitands.[29] The conformational dynamics of the cavitand may be described as an antisymmetric stretch,

in which the distances between adjacent arms are maintained, whereas the distances between opposing arms are anticorrelated (Figure 5.14a,b). Simulations show that the cavitands' cavities are occupied by DMSO molecules: one molecule is found at the bottom of the cavity, and one or two other molecules occupy the rim region (Figure 5.14c). The deeper DMSO molecule inside the cavitand exchanges with bulk solvent molecules on a slower timescale than the molecules at the rim (Figure 7.117 in the experimental section). In line with Rebek's rule,[30] the packing coefficient is around 50% for both cavitands.

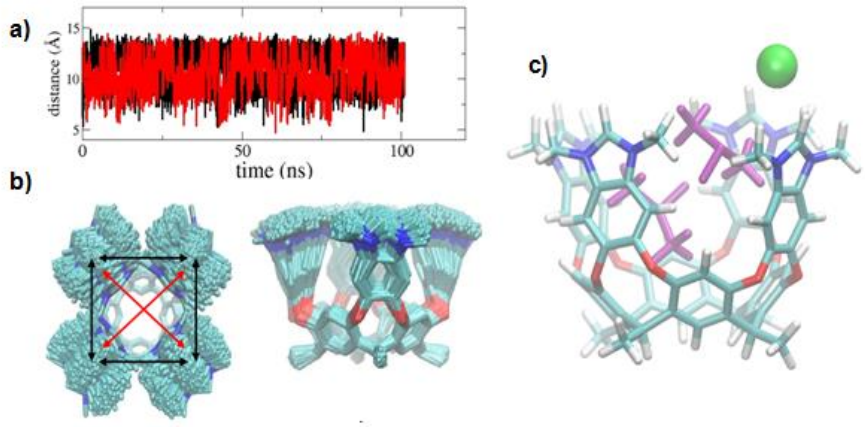

Figure 5.14. MD simulation of $\mathbf{16}^{4+}$. a) The variation in time of the distances between opposing arms of the cavitand; b) a set of 500 equally spaced conformations along the simulation were overlapped to show the movements of the arms (top and side views); c) representative snapshot showing two DMSO solvent molecules (purple sticks) occupying the cavity and an iodide (green sphere) interacting with an arm's tip at the rim

5.2.2.2 *Anion recognition and determination of the affinity constants*

We first studied the recognition scope of $\mathbf{16(PF_6)_4}$ with a variety of anions, which were added as tetrabutylammoium salts. The binding affinities were studied by ^{1}H NMR spectroscopic methods in DMSO. The anions chosen for this study (chloride, bromide, iodide, perchlorate, nitrate, cyanide, hexanoate, phenylsulfonate and *p*-tolylsulfonate) are of contrasting geometries and charge densities. Other anions such as fluoride and acetate were also tested, but in the course of the titrations, we observed the oxidation of the benzimidazoliums to benzimidazolidones (detected by mass spectrometry), as a consequence of the deprotonation of the azoliums by the basic anions and the subsequent oxidation of the resulting N-heterocyclic carbenes.

In general, addition of the anions caused downfield shifts in the imidazolium proton resonance, which is in agreement with previous works regarding the use of imidazoliums for anion recognition.[13d,15] However, in the case of the titrations with chloride and bromide, the signals due to the protons at the arms of the cavity also showed significant downfield shifts, indicating that the anion is not only interacting with the rim of the molecule, where the more acidic C-H bonds are located. This observation is particularly relevant for the case of the titrations with Cl^-, for which the shifts in the resonances of the phenylene protons (signal labelled as **b** in the spectra, Figure 5.15) are downfield shifted by 0.37 ppm, compared to the shifts in the resonances of the imidazolium protons, which are 0.25 ppm. All other inorganic anions such as nitrate, hexanoate, cyanide, perchlorate or iodide, only shifted the resonance of the more acidic imidazolium proton.

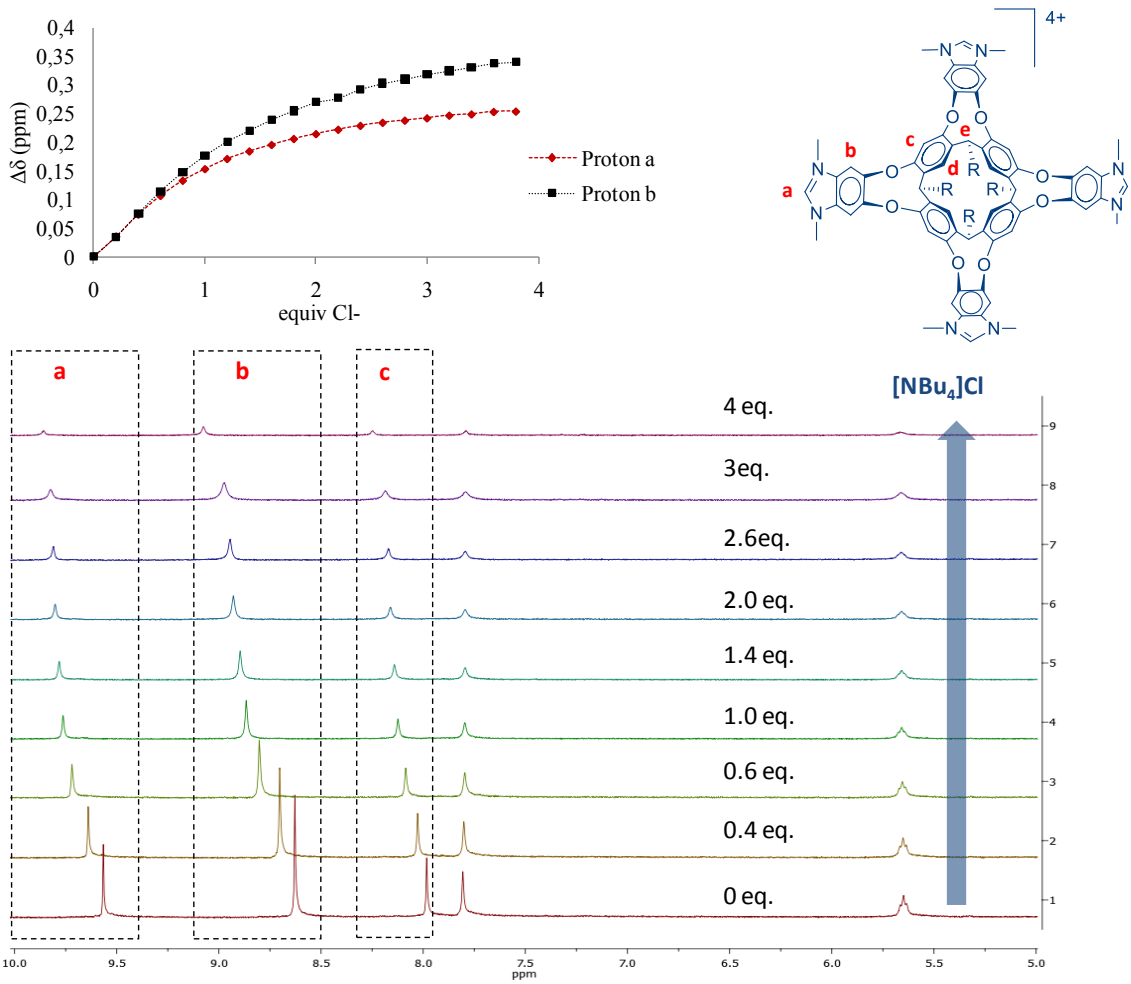

Figure 5.15. Truncated ^{1}H NMR (500 MHz) spectra of the titration of **16(PF$_6$)$_4$** with [NBu$_4$](Cl) in DMSO-d^6 and experimental data fitted binding isotherms

In contrast to the inorganic anions, addition of phenyl-sulfonate (BNZ-SO_3^-) or *p*-tolylsulfonate (PT-SO_3^-) results in the upfield shift of the signals of both the phenylene protons of the cavitand, and of the signals due to the aromatic protons of the anions (Figure 5.16). This result is strongly suggestive of a situation in which the anion is encapsulated inside the cavity of the tetra-benzimidazolium cavitand. The signals due to the protons of these two guests are broad, and despite being strongly upfield shifted with respect to the resonances of the free anions, their chemical shifts are dependent on the amount of the anion added, thus indicating a dynamic situation in which free and encapsulated guests are in fast exchange on the NMR timescale. Similar features were observed in the spectra of **17(PF$_6$)$_4$** treated with chloride, bromide, benzene- and toluene-sulfonates (experimental section).

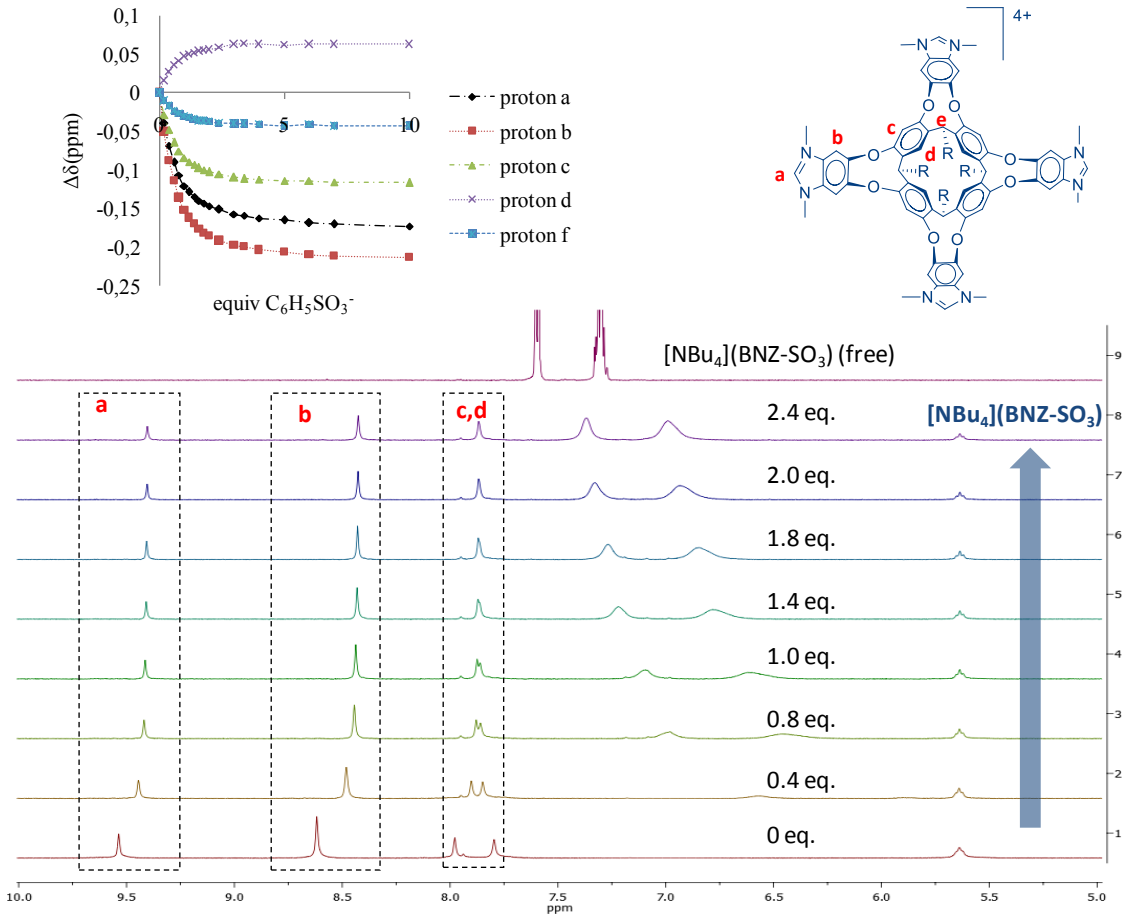

Figure 5.16. Truncated ^{1}H NMR (500 MHz) spectra of the titration of **16(PF$_6$)$_4$** with [NBu$_4$](BZN-SO_3) in DMSO-d^6 and experimental data fitted binding isotherms. The upper spectrum of spectra series, corresponds to free [NBu$_4$](BZN-SO_3)

The stoichiometry of the host:guest complexes was obtained by different means. The binding isotherms resulting from the ^{1}H NMR titrations (Figure 5.15 and 5.16) were best fitted to the formation of host-guest complexes in 1:1 stoichiometries. This stoichiometry was also supported by ESI Mass Spectrometry, because the m/z peaks due to the tricationic complexes formed by the association of $\mathbf{16^{4+}}$ with one equivalent of anion were the only ones revealed.

The association constants (K_{11}) for all the host-guest complexes formed were calculated by global nonlinear regression analysis, by considering all protons showing chemical shift variations (Table 5.3).

Table 5.3. Binding constants of $\mathbf{16(PF_6)_4}$ and $\mathbf{17(PF_6)_4}$ with [NBu_4]X (DMSO-d^6, 25ºC)[a]

		Host K_{11}, M^{-1}	
Entry	**Anion**	**$16(PF_6)_4$[a]**	**$17(PF_6)_4$[a]**
1	Cl^-	470 (3.3%)	6.9 (3%)
2	Br^-	215 (9.7%)	13.2 (2 %)
3	I^-	71 (4%)	≈ 0
4	ClO_4^-	370 (4%)	≈ 0
5	NO_3^-	100 (4%)	≈ 0
6	CN^-	93 (4%)	≈ 0
7	hexanoate	106 (5%)	≈ 0
8	*p*-tolylsulfonate	$>10^4$	$>10^4$
9	phenylsulfonate	8677 (8.6%)	3720 (49%)

[a]K_{11} values calculated by global nonlinear regression analysis.[31] Errors given in parenthesis

For $\mathbf{16^{4+}}$, K_{11} values follow the order $Cl^->Br^->I^-$, in agreement with the basicity trend of the anions. Inorganic anions and hexanoate, which mainly interact with the upper rim of the cavitand, showed association constants ranging between 100-500 M^{-1}. In contrast, larger association constants were obtained for PT-SO_3^- and BNZ-SO_3^-, indicating high degree of selectivity. The reason for this may be attributed to the higher affinity of these two organic bases by the solvophobic pocket of the cavitand, which produces a much more stable host-guest complex than those formed with the rest of the inorganic anions. However, the determination of an estimated K_{11} value for these aryl-substituted anions

was not accurate due to the well-accepted limitations in the determination of high affinity constants (> 10^4 M^{-1}) by ^{1}H NMR titrations.[31]

For receptor $\mathbf{17}^{4+}$, the upper rim of the molecule is functionalized with four methyl groups instead of the four protic hydrogens. Consequently, and comparing with receptor $\mathbf{16}^{4+}$, receptor $\mathbf{17}^{4+}$does not show hydrogen bonding abilities in this area, but the positive charges and the solvophobic pocket are maintained. The presence of the methyl groups in the upper rim of the molecules produces the inhibition of the affinity of the cavitand for the inorganic anions and also for hexanoate. Only chloride and bromide maintain small binding constants (6-13 M^{-1}) because these two anions also interact with the aromatic C-H protons located in the arms of the cavitand.

In order to shed some more light onto the anion-cavitand interaction, Prof. Gregori Ujaque and Dr. Pietro Vidossich carried out MD simulations of $\mathbf{16I_4}$, $\mathbf{16Cl_4}$ and $\mathbf{16(BNZ\text{-}SO_3)_4}$, and of $\mathbf{17I_4}$, $\mathbf{17Cl_4}$ and $\mathbf{17(BNZ\text{-}O_3)_4}$. A 100 ns simulation was performed for each system in DMSO, providing a picture of the preferred interaction modes between the cavitands and each anion, and a qualitative estimation of their relative strength. Figure 5.17a,b shows the most visited regions of chlorides and benzene sulphonate around the positively charged of cavitand $\mathbf{16}^{4+}$.

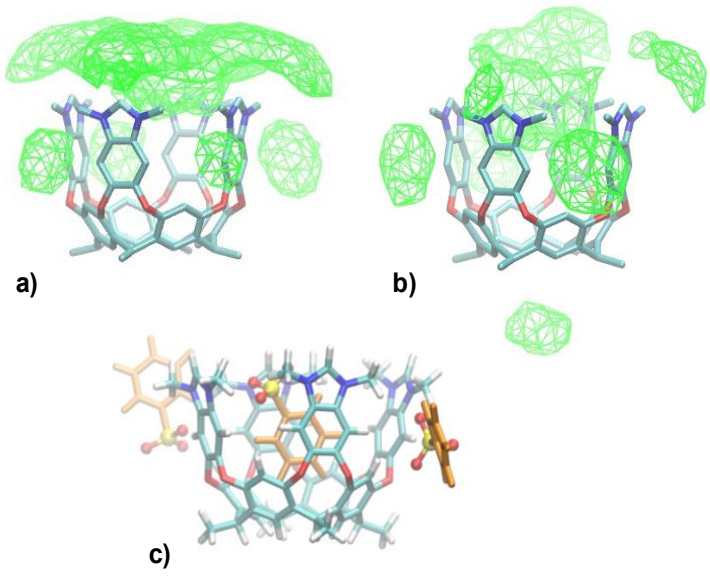

Figure 5.17. MD simulations of $\mathbf{16Cl_4}$ (a) and $\mathbf{16(BNZ\text{-}SO_3)_4}$ (b,c). In a) and b) the occupancy of anions around the cavitands: green isosurface at 1‰ probability. In c), snapshot of the cavitand showing the phenylsulfonate molecules in orange sticks, with oxygen atoms as red balls.

For halides, two favorable binding regions may be recognized, as it was expected in accordance with the ^{1}H NMR shifts, along the titrations. One is at the rim of the cavity, with the acidic C-H bonds of the azoliums and the other is on the side of the cavitand, with the anions simultaneously interacting with the benzene C-H bonds of adjacent benzimidazolium fragments and with the resorcinarene aromatic CH bonds, which are pointing toward the cationic side of the molecule. The participation of aryl C-H bonds in the recognition of anions is rather unusual,[32] although the earliest examples were reported in 2002.[33]

For the case of **16(BNZ-SO$_3$)$_4$** and **17(BNZ-SO$_3$)$_4$**, simulations show a different behaviour than for halides. In this case one anion persistently occupies the interior of the cavitand (Figure 5.16c), while all other three are about the rim. The strength of interactions of benzenesulfonate with the sites at cavitands **16^{4+}** and **17^{4+}** was estimated as: cavity interior > arms > rim.

All the results described along this section indicate that cavitands **16^{4+}**and **17^{4+}** display three and two different recognition sites, respectively. Their recognition sites operate depending on the nature of the anions used. In short, for **16^{4+}**:

- Large inorganic anions (iodide, perchlorate, cyanide, nitrate and hexanoate) and smaller-sized (chloride and bromide) are recognized at the rim of the molecule by hydrogen bonding interactions with the acidic protons of the benzimidazolium.
- Smaller-sized inorganic anions, such as chloride and bromide are also interacting with the adjacent arms of the molecule, by hydrogen-bonding interactions with the C-H bonds of the phenylene rings of the benzimidazolium, and with those from the rim of the resorcinarene.
- Anions with an aromatic functionality such as phenylsulfonate and *p*-tolylsulfonate are recognized by the encapsulation of the aromatic part of the anion inside the hydrophobic pocket of the host.

The ability to recognize large inorganic anions was suppressed for receptor **17^{4+}**, for which the protons of the upper rim of the cavity have been substituted by introducing methyl groups. Chloride and bromide are still recognized because they are able to

interact with the adjacent arms of the cavitand. Finally, $\mathbf{17}^{4+}$ maintains its ability to recognize anions with aromatic functionalities.

All these results provide valuable information and reflect the importance of ligand design for anion sensor development, by highlighting how slight changes in the functionalities can affect to the overall anion recognition capabilities of the receptors.

5.2.3 Synthesis of a new tetra rhodium benzimidazolium based-cavitand

5.2.3.1 *Synthesis of a tetra-NHC-rhodium cavitand complex **18***

As mentioned in the introduction of this chapter, the tetra-imidazolium salt $\mathbf{16I_4}$, constitutes a potential N-heterocyclic carbene precursor, which can be potentially coordinated to a wide variety of metal fragments. After many failed attempts of coordination, we managed to coordinate the ligand to RhCl(COD). In order to prepare the tetra-carbene rhodium complex, a mixture of $\mathbf{16I_4}$, 2 equivalents of $[RhCl(COD)]_2$ and K_2CO_3 was refluxed in acetone for 20 h. (Scheme 5.9). After purification by column chromatography, the resulting tetra-NHC-rhodium complex **18** was obtained in 30 % yield as an air-stable orange solid. The complex was characterized by means of NMR spectroscopy and ESI-MS, and gave satisfactory Elemental Analysis.

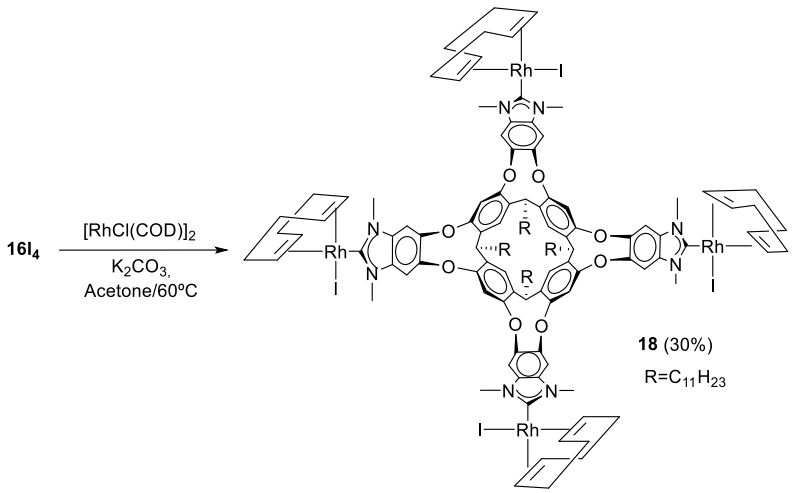

Scheme 5.9. Preparation of complex **18**

*^{1}H NMR spectrum of complex **18***

Figure 5.18 shows the ^{1}H NMR spectrum of **18**. This spectrum revealed broad signals, indicating a highly fluxional molecule behaviour (low temperature ^{1}H NMR experiments and the use of different solvents did not produce the sharpening of the signals, indicating that the fluxional behaviour involved conformers correlated by very low activation energies). The fluxional behaviour of the molecule may be due to the combined rotation of the metal fragment about the NHC-Rh bond, together with the inherent fluxionality shown by the resorcinarene-based tetra-NHC ligand (vase-kite conformation). In the spectrum, the aromatic resonances appears as broad signals from 7.5 to 6.5 ppm. The resonance due to the methyne protons appear at 5.9 ppm, indicating that the complex maintains the vase conformation. The resonance due to the CH_3 protons appears at 4.1 ppm, and the rest of the signals are attributed to the CH_2 and CH protons from the COD ligands and to the $C_{11}H_{23}$ chain.

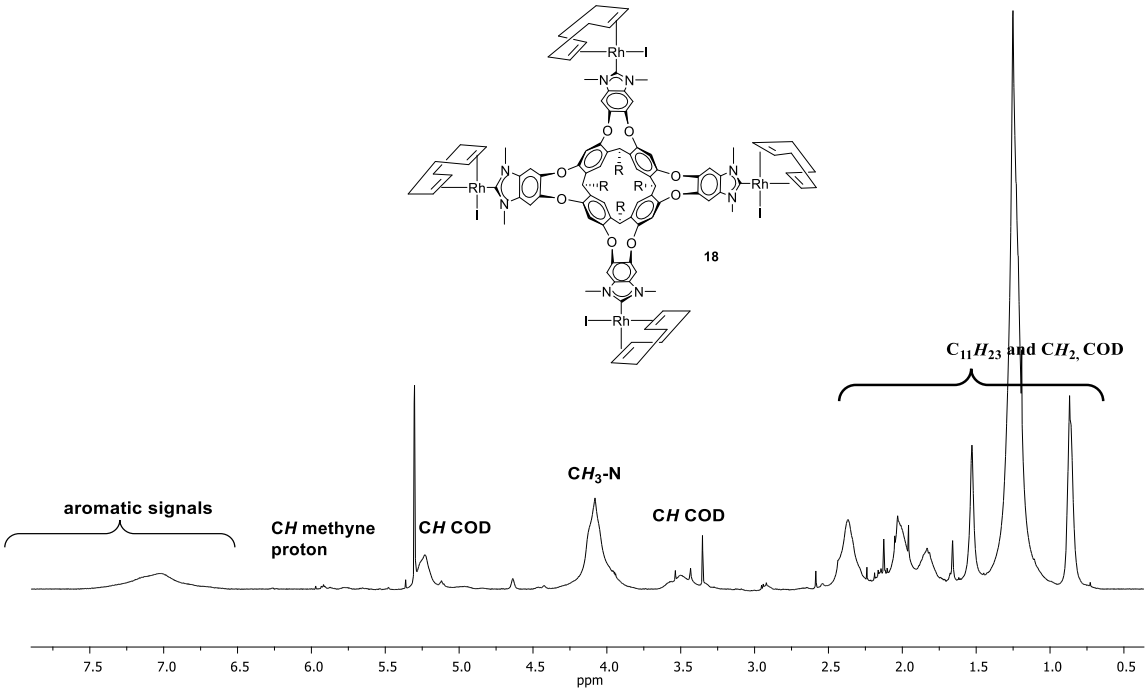

Figure 5.18. ^{1}H NMR spectrum of **17(PF$_6$)$_4$** in DMSO-d^6

*Electrospray spectrum of compound **18***

The ESI Mass Spectrum revealed two maximum peaks at m/z values of 2898.8 and 1386.0, assigned to $[M-I]^+$ and $[M-2I]^{2+}$, respectively.

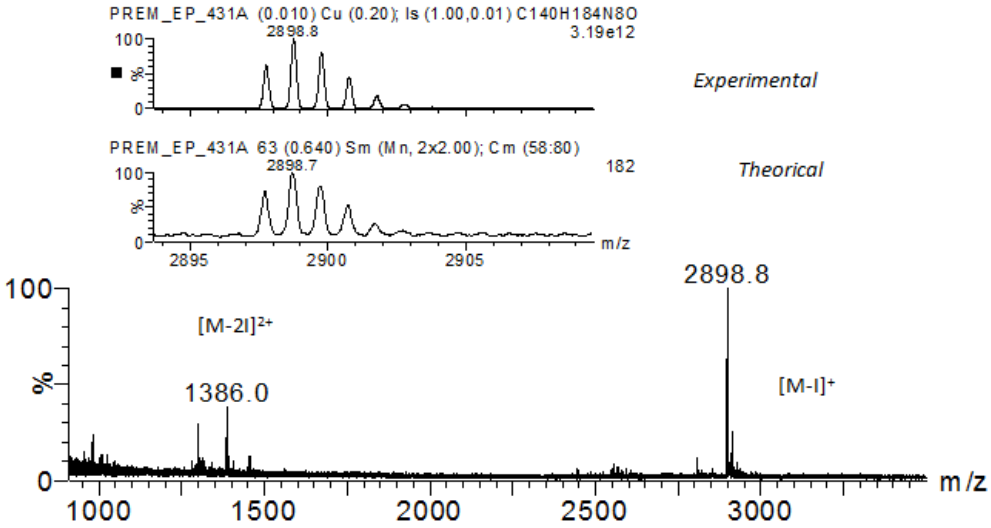

Figure 5.19. ESI-MS spectrum of **18**

*Optimized structure of **18***

Full QM methods were used in order to get more information about the structure of **18**. These studies were also developed by Prof.Gregori Ujaque and Dr. Pietro Vidossich. Several energy minima of the complex were obtained, ranging between 0.0 – 17.0 kcal/mol. Figure 5.20 shows the two structures with the lowest energies, both showing a distorted vase conformation of the cavitand. Despite their structural differences, their energies differ just in 0.04 kcal/mol. This suggests that the movement of the arms of the cavitand is relatively easy, in agreement with the high fluxionality observed experimentally. As mentioned in the previous sections of this chapter, this fluxionality was also observed for the cavitand without metal fragment (*vide supra*). Moreover, the rhodium fragments adopted also different relative conformations, as expected by the easy rotation about the NHC-Rh bond.

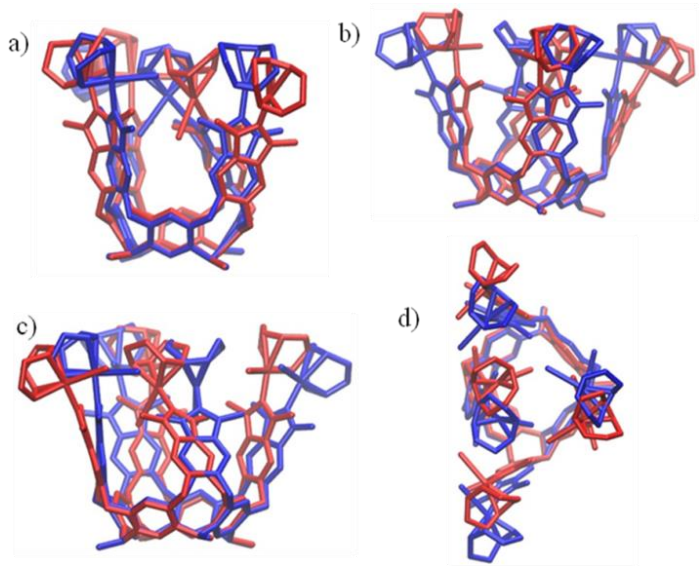

Figure 5.20. Superimposed optimized geometries for cavitand-Rh with an energy difference of 0.04 kcal/mol. (a), (b), and (c) side views, (d) top view

Despite the great coordination versatility and large topological diversity proven by poli-NHC ligands,[34] this is the first example of a cavitand-derived poly-NHC.

5.3 Conclusions

We prepared a series of novel tetra-benzimidazole resorcinare cavitands, which we used for different purposes:

1) A tetra-(imidazolyl-ferrocenyl)-resorcinarene cavitand **15** was prepared, and was proven to behave as a redox-switchable molecular gripper. DFT analysis displayed that there is a change in the disposition of the ferrocenyl groups from the neutral cavitand to its oxidized form. In the neutral form the ferrocenyl moieties are closing the upper rim of the molecule, while in the oxidised form the ferrocenyl moieties are pointing away from the cavity. Tetra-ferrocenyl cavitand was useful in the recognition of different ammonium salts. Studies by ^{1}H NMR spectroscopy, Cyclic Voltammetry and ESI mass spectrometry revealed the higher encapsulation capability of the neutral form of the cavitand compared to its oxidized form, indicating the clear redox-switchable trapping abilities of the host.
2) Two tetra-benzimidazolium-resorcinarene cavitands **16(PF$_6$)$_4$** and **17(PF$_6$)$_4$** were prepared. Their anion recognition capabilities were studied by proton NMR spectroscopy and Mass Spectrometry. Cavitand **16(PF$_6$)$_4$** showed three clear recognitions sites, at the rim, on the side arms and inside the cavity. The interaction at the rim is produced by H-bonding interaction with the acidic protons of the benzimidazolium with larger-sized and also smaller-size inorganic anions, such as iodide, perchlorate, cyanide, nitrate, hexanoate, chloride and bromide. The interaction between adjacent arms is the result of H-bonding interactions with C-H bonds of the phenylene rings of the benzimidazoliums and smaller size anions, such as chloride or bromide. Finally, anions with an aromatic functionality, such as benzenesulfonate and *p*-tolylsulfonate, are recognized inside the cavity due to solvophobic effects. For the methyl-substituted cavitand **17(PF$_6$)$_4$**, the presence of the methyl groups at the rim of the cavity suppressed the H-bonding affinity around this area, therefore the interaction at the rim with larger-sized inorganic anions is suppressed. Thus, this cavitand displayed two interaction sites (side arms and cavity).
3) A resorcinarene-based macromolecule bearing four rhodium benzimidazolylidenes was prepared from the tetra-benzimidazolium salt **16I$_4$**.

This molecule constitutes a new class of poly-NHC complex, with unprecedented structural features.

All these results demonstrate the huge and diverse capabilities of benzimidazole-resorcinarene cavitands. These results also show the importance of molecular design in order to develop new models that may be useful in different fields of supramolecular chemistry, among them molecular recognition, molecular grippers, molecular sensors, drug delivery, etc. There is a world of possibilities and we would like to improve our knowledge and our understanding of these fascinating molecules to obtain the best benefits from them.

5.4 References

(1) Moran, J. R., Karbach, S., Cram, D. J. *J. Am. Chem. Soc.* **1982**, *104*, 5826-5828.

(2) a) D. J. Cram, J. M. C., J. F. Stoddart, *Container Molecules and Their Guests*, The Royal Society of Chemistry, **1994**; b) Palmer, L. C., Rebek, J. *Org. Biomol. Chem.* **2004**, *2*, 3051-3059; c) Trembleau, L., Rebek, J. *Science* **2003**, *301*, 1219-1220; d) Rudkevich, D. M., Rebek, J. *Eur. J. Org. Chem.* **1999**, 1991-2005.

(3) a) Roy, A., Saha, S., Roy, M. N. *Fluid Phase Equilib.* **2016**, *425*, 252-258; b) Saz, J. M., Marina, M. L. *J. Chromatogr., A* **2016**, *1467*, 79-94; c) Sun, W., She, M. Y., Yang, Z., Zhu, Y. L., Ma, S. Y., Shi, Z., Li, J. L. *J. Incl. Phenom. Macrocycl. Chem.* **2016**, *86*, 45-54.

(4) a) Zhou, Y., Li, H., Yang, Y. W. *Chin. Chem. Lett.* **2015**, *26*, 825-828; b) Rebek, J. *Chem. Commun.* **2000**, 637-643.

(5) Ogoshi, T., Yamagishi, T. *Eur. J. Org. Chem.* **2013**, 2961-2975.

(6) a) Assaf, K. I., Nau, W. M. *Chem. Soc. Rev.* **2015**, *44*, 394-418; b) Chaban, V. V., Fileti, E. E., Malaspina, T. *Comp. Theor. Chem.* **2016**, *1083*, 7-11; c) Guo, D. S., Uzunova, V. D., Assaf, K. I., Lazar, A. I., Liu, Y., Nau, W. M. *Supramol. Chem.* **2016**, *28*, 384-395; d) Venkataramanan, N. S., Ambigapathy, S. *J. Inclusion Phenom. Macrocyclic Chem.* **2015**, *83*, 387-400; e) Zhang, M. M., Sigwalt, D., Isaacs, L. *Chem. Commun.* **2015**, *51*, 14620-14623.

(7) Azov, V. A., Beeby, A., Cacciarini, M., Cheetham, A. G., Diederich, F., Frei, M., Gimzewski, J. K., Gramlich, V., Hecht, B., Jaun, B., Latychevskaia, T., Lieb, A., Lill, Y., Marotti, F., Schlegel, A., Schlittler, R. R., Skinner, P. J., Seiler, P., Yamakoshi, Y. *Adv. Funct. Mater.* **2006**, *16*, 147-156.

(8) a) Hof, F., Craig, S. L., Nuckolls, C., Rebek, J. *Angew. Chem. Int. Ed.* **2002**, *41*, 1488-1508; b) Hooley, R. J., Biros, S. M., Rebek, J. *Chem. Commun.* **2006**, 509-510; c) Choi, H. J., Park, Y. S., Song, J., Youn, S. J., Kim, H. S., Kim, S. H., Koh, K., Paek, K. *J. Org. Chem.* **2005**, *70*, 5974-5981; d) Kim, S. K., Kang, B. G., Koh, H. S., Yoon, Y. J., Jung, S. J., Jeong, B., Lee, K. D., Yoon, J. *Org. Lett.* **2004**, *6*, 4655-4658.

(9) a) Adhikari, B. B., Fujii, A., Schramm, M. P. *Eur. J. Org. Chem.* **2014**, *2014*, 2972-2979; b) Far, A. R., Shivanyuk, A., Rebek, J. *J. Am. Chem. Soc.* **2002**, *124*, 2854-2855; c) Schramm, M. P., Hooley, R. J., Rebek, J., Jr. *J. Am. Chem. Soc.* **2007**, *129*, 9773-9779; d) Kobayashi, K., Yamanaka, M. *Chem. Soc. Rev.* **2015**, *44*, 449-466.

(10) Evtugyn, G. A., Stoikova, E. E., Shamagsumova, R. V. *Russ. Chem. Rev.* **2010**, *79*, 1071-1097.

(11) Beer, P. D., Keefe, A. D., Drew, M. G. B. *J. Organomet. Chem.* **1988**, *353*, C10-C12.

(12) a) Beer, P. D. *Adv. Inorg. Chem.* **1992**, *39*, 79-157; b) Beer, P. D., Keefe, A. D., Bohmer, V., Goldmann, H., Vogt, W., Lecocq, S., Perrin, M. *J. Organomet. Chem.* **1991**, *421*, 265-273; c) Beer, P. D., Hayes, E. J. *Coord. Chem. Rev.* **2003**, *240*, 167-189; d) Tomapatanaget, B., Tuntulani, T. *Tetrahedron Lett.* **2001**, *42*, 8105-8109; e) Dumazet, I., Beer, P. D. *Tetrahedron Lett.* **1999**, *40*, 785-788; f) Beer, P. D., Chen, Z., Drew, M. G. B., Gale, P. A. *J. Chem. Soc.-Chem. Commun.* **1995**, 1851-1852; g) Beer, P. D., Chen, Z., Goulden, A. J., Graydon, A., Stokes, S. E., Wear, T. *J. Chem. Soc.-Chem. Commun.* **1993**, 1834-1836; h) Beer, P. D., Tite, E. L., Ibbotson, A. *J. Chem. Soc.-Dalton Trans.* **1991**, 1691-1698; i) Tomapatanaget, B., Tuntulani, T., Chailapakul, O. *Org. Lett.* **2003**, *5*, 1539-1542; j) Bondy, C. R., Loeb, S. J. *Coord. Chem. Rev.* **2003**, *240*, 77-99; k) Valderrama, M. I. R., Garcia, R. A. V., Klimova, T., Klimova, E., Ortiz-Frade, L., Garcia, M. M. *Inorg. Chim. Acta* **2008**, *361*, 1597-1605; l) Han, J., Cai, Y. H., Liu, L., Yan, C. G., Li, Q. *Tetrahedron* **2007**, *63*, 2275-2282; m) Sharma, R., Margani, R., Mobin, S. M., Misra, R. *Rsc Advances* **2013**, *3*, 5785-5788; n) Evans, A. J., Matthews, S. E., Cowley, A. R., Beer, P. D. *Dalton Trans.* **2003**, 4644-4650.

(13) a) Martinez-Manez, R., Sancenon, F. *Chem. Rev.* **2003**, *103*, 4419-4476; b) Sessler, J. L., Gross, D. E., Cho, W. S., Lynch, V. M., Schmidtchen, F. P., Bates, G. W., Light, M. E., Gale, P. A. *J. Am. Chem. Soc.* **2006**, *128*, 12281-12288; c) Evans, N. H., Beer, P. D. *Angew Chem, Int Ed.* **2014**, *53*, 11716-11754; d) Gale, P. A., Garcia-Garrido, S. E., Garric, J. *Chem. Soc. Rev.* **2008**, *37*, 151-190.

(14) a) Gale, P. A., Busschaert, N., Haynes, C. J. E., Karagiannidis, L. E., Kirby, I. L. *Chem. Soc. Rev.* **2014**, *43*, 205-241; b) Busschaert, N., Caltagirone, C., Van Rossom, W., Gale, P. A. *Chem. Rev.* **2015**, *115*, 8038-8155.

(15) a) Cai, J., Sessler, J. L. *Chem. Soc. Rev.* **2014**, *43*, 6198-6213; b) Xu, Z., Kim, S. K., Yoon, J. *Chem. Soc. Rev.* **2010**, *39*, 1457-1466; c) Caltagirone, C., Gale, P. A. *Chem. Soc. Rev.* **2009**, *38*, 520-563; d) Yoon, J., Kim, S. K., Singh, N. J., Kim, K. S. *Chem. Soc. Rev.* **2006**, *35*, 355-360; e) *Anion Recognition in Supramolecular Chemistry*; Gale, P., Dehaen, W., Eds.; Springer: Heidelberg, **2010**.

(16) Sato, K., Arai, S., Yamagishi, T. *Tetrahedron Lett.* **1999**, *40*, 5219-5222.

(17) Alcalde, E., Alvarez-Rua, C., Garcia-Granda, S., Garcia-Rodriguez, E., Mesquida, N., Perez-Garcia, L. *Chem. Commun.* **1999**, 295-296.

(18) Ihm, H., Yun, S., Kim, H. G., Kim, J. K., Kim, K. S. *Org. Lett.* **2002**, *4*, 2897-2900.

(19) a) Alhashimy, N., Brougham, D. J., Howarth, J., Farrell, A., Quilty, B., Nolan, K. *Tetrahedron Lett.* **2007**, *48*, 125-128; b) Yun, S., Ihm, H., Kim, H. G., Lee, C. W., Indrajit, B., Oh, K. S., Gong, Y. J., Lee, J. W., Yoon, J., Lee, H. C., Kim, K. S. *J. Org. Chem.* **2003**, *68*, 2467-2470; c) Czirok, J. B., Bojtar, M., Hessz, D., Baranyai, P., Drahos, L., Kubinyi, M., Bitter, I. *Sens. Actuator B-Chem.* **2013**, *182*, 280-287; d) Luo, K., Jiang, H. Y., You, J. S., Xiang, Q. X., Guo, S. J., Lan, J. B., Xie, R. G. *Lett. Org. Chem.* **2006**, *3*, 363-367; e) Faggi, E., Porcar, R., Bolte, M., Luis, S. V., Garcia-Verdugo, E., Alfonso, I. *J. Org. Chem.* **2014**, *79*, 9141-9149; f) Gonzalez-Mendoza, L., Altava, B., Burguete, M. I., Escorihuela, J., Hernando, E., Luis, S. V., Quesada, R., Vicent, C. *Rsc Advances* **2015**, *5*, 34415-34423; g) Sabater, P., Zapata, F., Caballero, A., de la Visitacion, N., Alkorta, I., Elguero, J., Molina, P. *J. Org. Chem.* **2016**, *81*, 7448-7458; h) Cai, J. J., Sessler, J. L. *Chem. Soc. Rev.* **2014**, *43*, 6198-6213; i) Bhardwaj, V. K., Sharma, S., Singh, N., Hundal, M. S., Hundal, G. *Supramol. Chem.* **2011**, *23*, 790-800; j) Kuswandi, B., Nuriman, Verboom, W., Reinhoudt, D. N. *Sensors* **2006**, *6*, 978-1017.

(20) a) Chun, Y., Singh, N. J., Hwang, I. C., Lee, J. W., Yu, S. U., Kim, K. S. *Nat. Commun,* **2013**, *4*; b) Dinares, I., de Miguel, C. G., Font-Bardia, M., Solans, X.,

Alcalde, E. *Organometallics* **2007**, *26*, 5125-5128; c) Dinares, I., de Miguel, C. G., Mesquida, N., Alcalde, E. *J. Org. Chem.* **2009**, *74*, 482-485; d) Wong, W. W. H., Vickers, M. S., Cowley, A. R., Paul, R. L., Beer, P. D. *Org. Biomol. Chem.* **2005**, *3*, 4201-4208.

(21) a) Zhang, K.-D., Ajami, D., Rebek, J. *J. Am. Chem. Soc.* **2013**, *135*, 18064-18066; b) Hof, F., Trembleau, L., Ullrich, E. C., Rebek, J. *Angew. Chem. Int. Ed.* **2003**, *42*, 3150-3153; c) Purse, B. W., Gissot, A., Rebek, J. *J. Am. Chem. Soc.* **2005**, *127*, 11222-11223.

(22) a) Amrhein, P., Shivanyuk, A., Johnson, D. W., Rebek, J. *J. Am. Chem. Soc.* **2002**, *124*, 10349-10358; b) Kvasnica, M., Purse, B. W. *New J. Chem.* **2010**, *34*, 1097-1099; c) Ballester, P., Sarmentero, M. A. *Org. Lett.* **2006**, *8*, 3477-3480.

(23) a) Macchioni, A., Ciancaleoni, G., Zuccaccia, C., Zuccaccia, D. *Chem. Soc. Rev.* **2008**, *37*, 479-489; b) Cohen, Y., Avram, L., Frish, L. *Angew. Chem. Int. Ed.* **2005**, *44*, 520-554; c) Avram, L., Cohen, Y. *Chem. Soc. Rev.* **2015**, *44*, 586-602.

(24) a) Beyeh, N. K., Goeth, M., Kaufmann, L., Schalley, C. A., Rissanen, K. *Eur. J. Org. Chem.* **2014**, *2014*, 80-85; b) Beyeh, N. K., Weimann, D. P., Kaufmann, L., Schalley, C. A., Rissanen, K. *Chem. Eur. J.* **2012**, *18*, 5552-5557; c) Mansikkamaki, H., Schalley, C. A., Nissinen, M., Rissanen, K. *New J. Chem.* **2005**, *29*, 116-127.

(25) Qi, Z., Heinrich, T., Moorthy, S., Schalley, C. A. *Chem. Soc. Rev.* **2015**, *44*, 515-531.

(26) Lee, T.-C., Kalenius, E., Lazar, A. I., Assaf, K. I., Kuhnert, N., Grun, C. H., Janis, J., Scherman, O. A., Nau, W. M. *Nat. Chem.* **2013**, *5*, 376-382.

(27) a) Laviron, E., Roullier, L. *J. Electroanal. Chem.* **1985**, *186*, 1-15; b) Sobransingh, D., Dewal, M. B., Hiller, J., Smith, M. D., Shimizu, L. S. *New J. Chem.* **2008**, *32*, 24-27.

(28) a) Renny, J. S., Tomasevich, L. L., Tallmadge, E. H., Collum, D. B. *Angew. Chem. Int. Ed.* **2013**, *52*, 11998-12013; b) Fielding, L. *Tetrahedron* **2000**, *56*, 6151-6170; c) Gil, V. M. S., Oliveira, N. C. *J. Chem. Educ.* **1990**, *67*, 473-478; d) Job, P. *Ann. Chim. Fr.* **1928**, *9*, 113-203.

(29) Pochorovski, I., Knehans, T., Nettels, D., Mueller, A. M., Schweizer, W. B., Caflisch, A., Schuler, B., Diederich, F. *J. Am. Chem. Soc.* **2014**, *136*, 2441-2449.

(30) Mecozzi, S., Rebek, J. *Chem. Eur. J.* **1998**, *4*, 1016-1022.

(31) a) Thordarson, P. *Chem. Soc. Rev.* **2011**, *40*, 1305-1323; b) Lowe, A. J., Pfeffer, F. M., Thordarson, P. *Supramol. Chem.* **2012**, *24*, 585-594.

(32) Tresca, B. W., Zakharov, L. N., Carroll, C. N., Johnson, D. W., Haley, M. M. *Chem. Commun.* **2013**, *49*, 7240-7242.

(33) Abouderbala, L. O., Belcher, W. J., Boutelle, M. G., Cragg, P. J., Steed, J. W., Turner, D. R., Wallace, K. J. *Proc. Natl. Acad. Sci. U. S. A.* **2002**, *99*, 5001-5006.

(34) a) Poyatos, M., Mata, J. A., Peris, E. *Chem. Rev.* **2009**, *109*, 3677-3707; b) Mata, J. A., Poyatos, M., Peris, E. *Coord. Chem. Rev.* **2007**, *251*, 841-859.

Chapter 6.
Tripodal tris-azolium salts for anion recognition through halogen and hydrogen bonding

6.1 Introduction

During the last decades, the design of new anion receptors has attracted a considerable amount of research stimulated by the crucial roles that anions play in many chemical, biological, and environmental processes.[1] Hydrogen bonding interactions (HB), have dominated the field of anion coordination, recognition, and transport,[1d,2] but the application of halogen bonding (XB) for the recognition of anions is gaining acceptance as the intimate mechanism of this type of interaction is being understood.[2-3] XB is the attractive non-covalent interaction arising between the electron-deficient σ-hole of a polarized halogen atom (Scheme 6.1), such as bromine or iodine, and an electron-rich Lewis base. [4] The utilization of XB in solution is relatively underexploited, but some seminal applications in the areas of reactivity, catalysis, self-assembly, transport, and medicinal chemistry are currently illustrating the great potential of this type of interaction.[5]

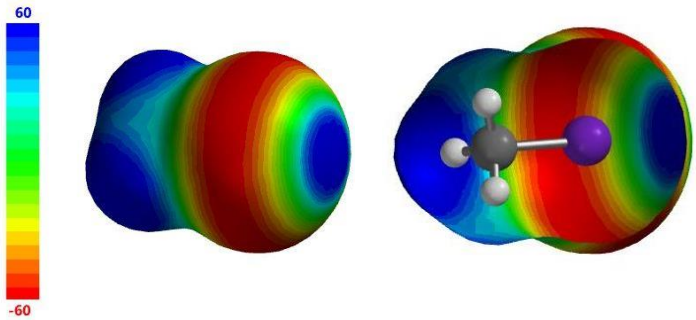

Scheme 6.1. Electron-deficient σ-hole of a polarized halogen atom (CH_3I)

A typical halogen bonded complex may be represented as ***R-X···Y*** where X is the electrophilic XB acceptor (Lewis acid) and Y the XB donor (Lewis base).[6] The description of this halogen bonding interaction requires mentioning the following features:

- The interatomic X···Y distance is shorter than the sum of the Van der Waals radii of the two interacting atoms, and this distance becomes shorter for stronger XB interactions.
- The R–XY angle is close to 180º.
- The interaction strength lies within the range 10–200 kJ/mol, which is broadly similar to the range spanned by hydrogen-bonding (HB) interactions.

One of the main differences between XB and HB interactions, is that XB has a more stringent preference for linearity than HB,[7] and that HB is solvent dependent and more hydrophobic in character.[8]

In the development of new anion receptors, it is worth mentioning to consider two important parameters: The choice of the receptor's functionalities and their relative topology, which must be designed to complement the size and shape of the guests.

Tripod-shaped molecules have been considered as excellent receptors to complement the size and shape of some anions, because it is possible to rationally tune their binding properties by modifying the three arms' functionalities.[9] Imidazoliums and triazoliums are also benefited from their relative simple synthesis, allowing the preparation of a library of topologies. In this chapter we report the synthesis of a new class of proto- and iodo-triazolium and imidazolium tripod receptors (**19(PF$_6$)$_3$-22(PF$_6$)$_3$** in Scheme 6.2), and their binding capabilities toward several anions. This work was developed in collaboration with Prof. Paul De Beer, from the University of Oxford.

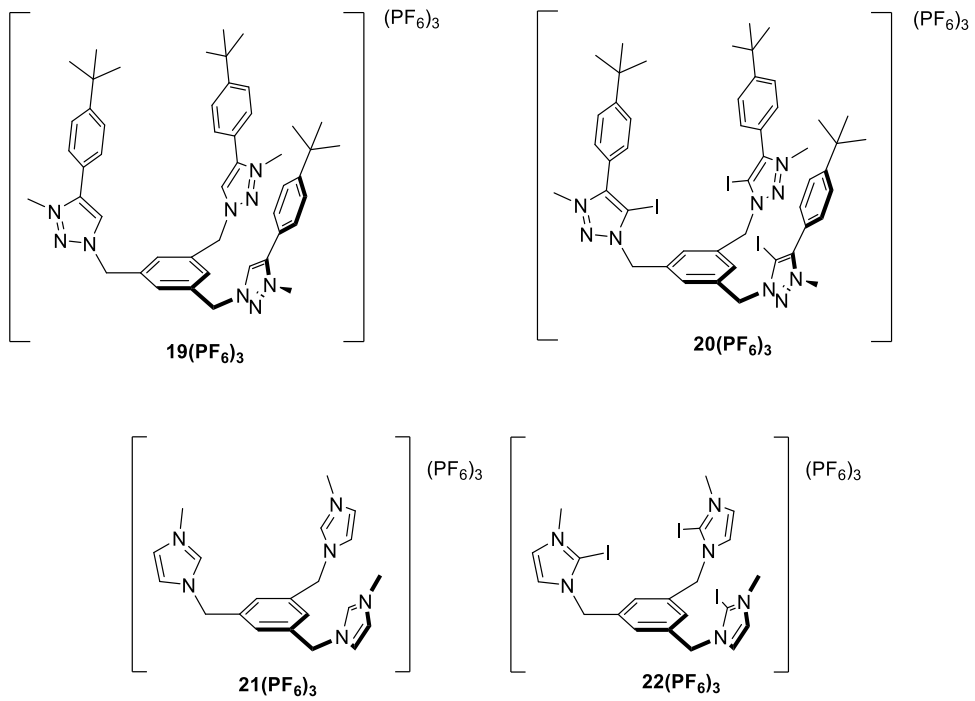

Scheme 6.2. From the left to right and top to bottom: proto-triazolium, iodo-triazolium, proto-imidazolium and iodo-imidazolium tripod receptors

With this study, we intended to provide information for the development of new anion receptors, and to evaluate if XB may provide any benefits in anion recognition compared to HB.

6.2 Results and discussion

6.2.1 Synthesis and characterization of tripod receptors

Proto- and iodo-triazolium receptors 19(PF$_6$)$_3$ and 20(PF$_6$)$_3$

The triazolium receptors **19(PF$_6$)$_3$** and **20(PF$_6$)$_3$** were prepared following the procedure depicted in Scheme 6.3. The reaction of 1,3,5-tris(azidemethyl)benzene[10] with the corresponding alkyne in the presence of [Cu(CH$_3$CN)$_4$](PF$_6$), tris(benzyltriazolylmethyl)amine (TBTA) and N,N-diisopropiletilamina (DIPEA, only in the case of the preparation of **H**), afforded **H** and **I** as white solids in 65 and 70% yields, respectively.

Compounds **H** and **I** were methylated using trimethyloxonium tetrafluoroborate in dry dichloromethane, affording **19(BF$_4$)$_3$** and **20(BF$_4$)$_3$**, respectively. After anion exchange with a saturated NH$_4$PF$_6$ aqueous solution, compounds **19(PF$_6$)$_3$** and **20(PF$_6$)$_3$** were obtained as white solids in 90 % and 82% yield, respectively.

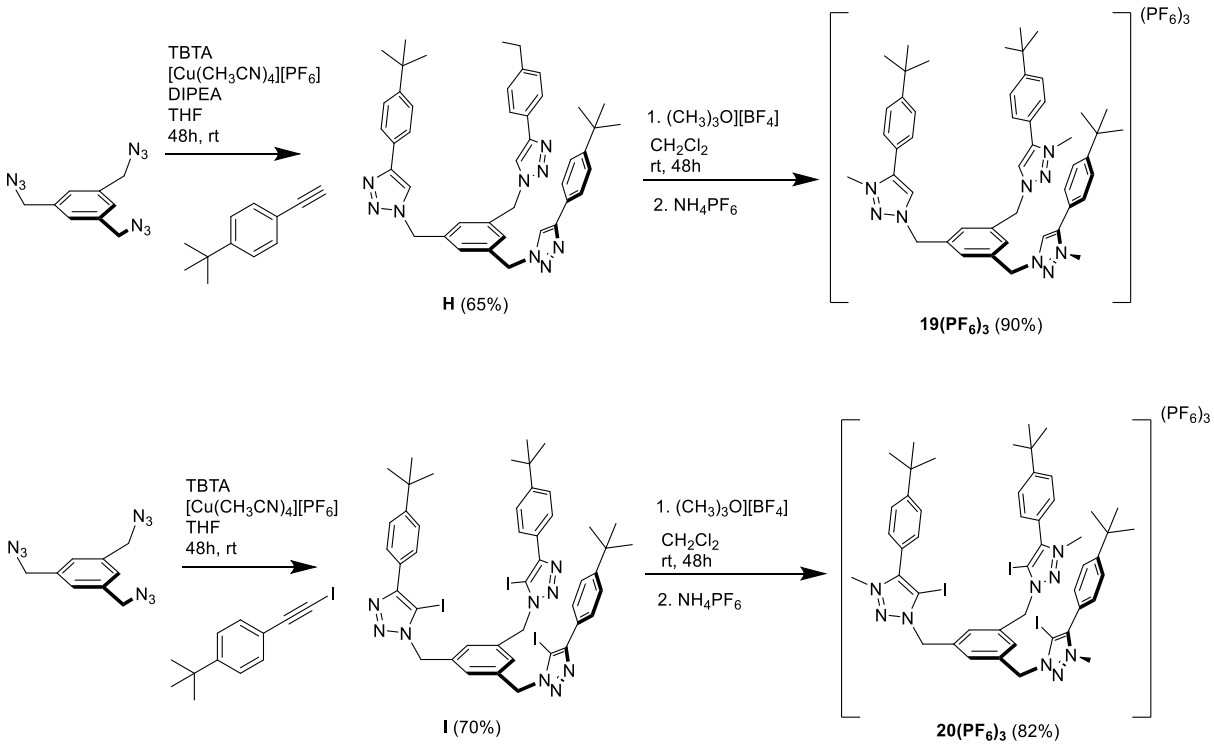

Scheme 6.3. Synthesis of proto- and iodo-triazolium tripod receptor **19(PF$_6$)$_3$** and **20(PF$_6$)$_3$**

Proto- and iodo-imidazolium receptors 21(PF$_6$)$_3$ and 22(PF$_6$)$_3$

The imidazolium receptors **21(PF$_6$)$_3$** and **22(PF$_6$)$_3$** were prepared following the procedure depicted in Scheme 6.4. The neutral imidazole compound **J** was synthesized according to the literature procedure.[11] The neutral iodo-imidazole **K** was synthesized following a similar methodology. Compounds **J** and **K** were methylated with trimethyloxonium tetrafluoroborate producing the precipitation of **21(BF$_4$)$_3$** and **22(BF$_4$)$_3$**. In order to obtain the hexafluorophosphate salts, anion exchange was performed by washing the compound several times with a saturated NH_4PF_6 aqueous solution. The tris-imidazolium salts **21(PF$_6$)$_3$** and **22(PF$_6$)$_3$** were obtained as white solids in 56 and 96% yield, respectively.

A different procedure for the preparation of the tris-imidazolium salt **21(PF$_6$)$_3$** was reported previously.[12]

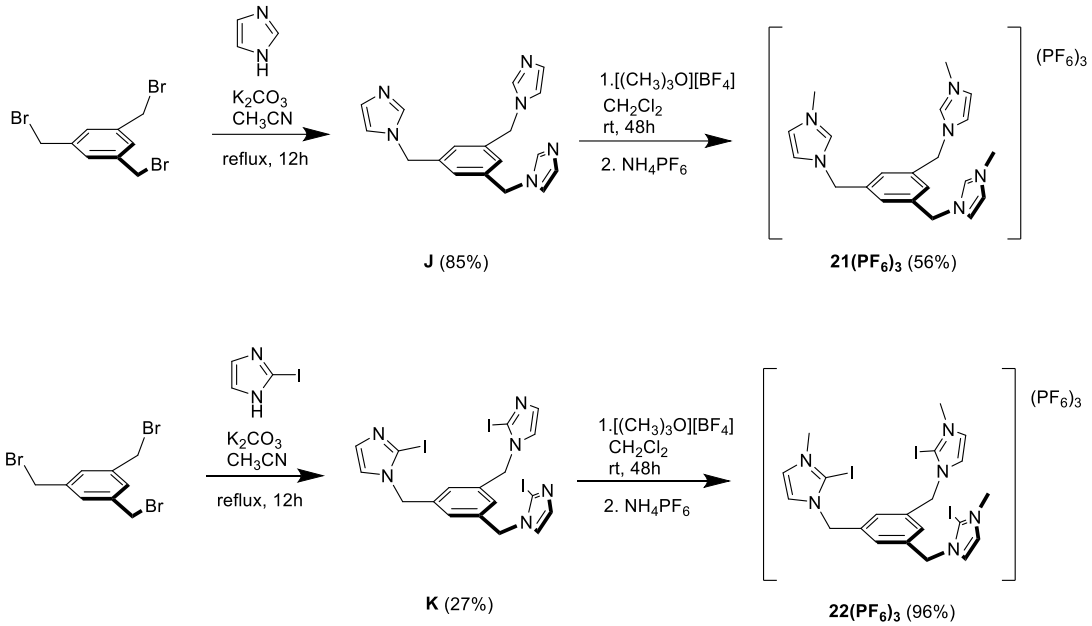

Scheme 6.4. Synthesis of proto and iodo-imidazolium tripod receptor salts **21(PF$_6$)$_3$** and **22(PF$_6$)$_3$**

All tripodal tris-azolium salts were characterized by NMR spectroscopy, Mass Spectrometry and Elemental Analysis. As an illustration of the characterization of these compounds, a detailed analysis of the ^{1}H NMR spectrum of **20(PF$_6$)$_3$** will be described in the following paragraphs. The full description of the NMR spectra of the rest of the tripodal triazolium and imidazolium salts may be found in the experimental chapter. As a general pattern for all different tripodal tris-azolium salts reported here, the NMR spectra are in agreement with the threefold symmetry of their structures.

*^{1}H NMR spectrum of **20(PF$_6$)$_3$***

Figure 6.1 shows the ^{1}H NMR spectrum of **20(PF$_6$)$_3$**. The signal at 7.79 ppm (**d**), corresponds to the C*H* protons of the benzene. The signals due to the C*H* aromatic protons of the *tert*-butylphenyl group appear as two doublets at 7.57 and 7.47 ppm (**a** and **b**). The resonance due to CH_2 linkers (**c**) appears as a singlet at 5.81 ppm. The signal attributed to the N-CH_3 protons appears as a singlet at 4.11 ppm (**e**). Finally, the singlet at 1.34 ppm corresponds to the CH_3 groups of the *tert*-butylphenyl group (**f**).

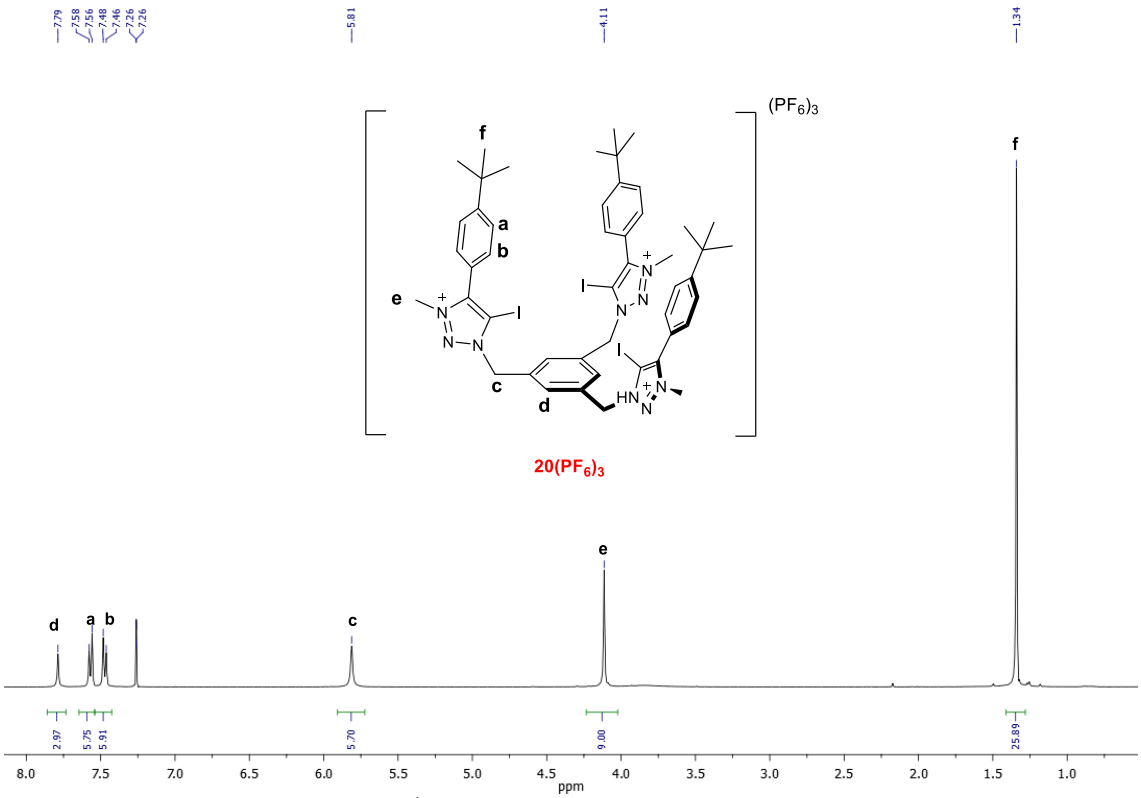

Figure 6.1. ^{1}H NMR spectrum of **20(PF$_6$)$_3$** in $CDCl_3$

6.2.2 Binding studies and calculation of the association constants

The anion recognition properties of the tripod receptors **19(PF$_6$)$_3$-22(PF$_6$)$_3$** were studied using ^{1}H NMR titration experiments, by monitoring the shift of the signals upon addition of anion aliquots (Cl^-, Br^-, I^- and $H_2PO_4^-$). The anion solutions were prepared by dissolving the corresponding tetrabutylammonium salts. For our studies, we used DMSO-*d*^{6}, because CD_3CN, $CDCl_3$, MeOD or D_2O, produced the precipitation of the resulting aggregate complexes. For each titration, two solutions were prepared: a host solution (2mM), and a titrating solution that contained the guest (100 mM). In a typical experiment, the host solution was poured into an NMR tube and aliquots of the solution of guest were added, until the host:guest concentration reached 1:10. The exact host and guest concentrations were recalculated at each point along the titration, by integrating the corresponding signals.

In general, the addition of the anions caused downfield shifts of the resonances, in agreement with previous works regarding the use of azoliums for anion recognition.[1d,13] We also observed that some signals suffered upfield shifts, suggesting that the interaction may occur in the inner part of the tripod receptor (Figure 6.2, signal labelled as **a**; Figure 6.3, signal labelled as **b**).

It is important to mention that for the proto-receptors (**19(PF$_6$)$_3$** and **21(PF$_6$)$_3$**) the most perturbed signals were those due to the acidic hydrogens of the azolium rings, which appear at higher chemical shifts. For instance, for the titrations with tetrabutylammonium chloride, the signals due to the acidic hydrogens of the azolium rings experienced maximum downfield shifts of $\Delta\delta \approx 0.42$ ppm and $\Delta\delta \approx 0.43$ ppm, for **19(PF$_6$)$_3$** and **21(PF$_6$)$_3$,** respectively. In all cases, the titrations produced the perturbation of several signals of the hosts, including the one due to the three equivalent protons of the central phenyl ring.

As an illustrative example, Figure 6.2 shows the selected region of the spectra of the titration of **20(PF$_6$)$_3$** with a solution of tetrabutyl ammonium bromide (TBABr). The series of spectra show that the signals due to of the aromatic C*H* of the benzene (**d**) are downfield shifted upon guest addition. There is also a slight shift of the resonances due to the C*H tert*-butyl phenyl functionality (**a,** upfield and **b**, downfield).

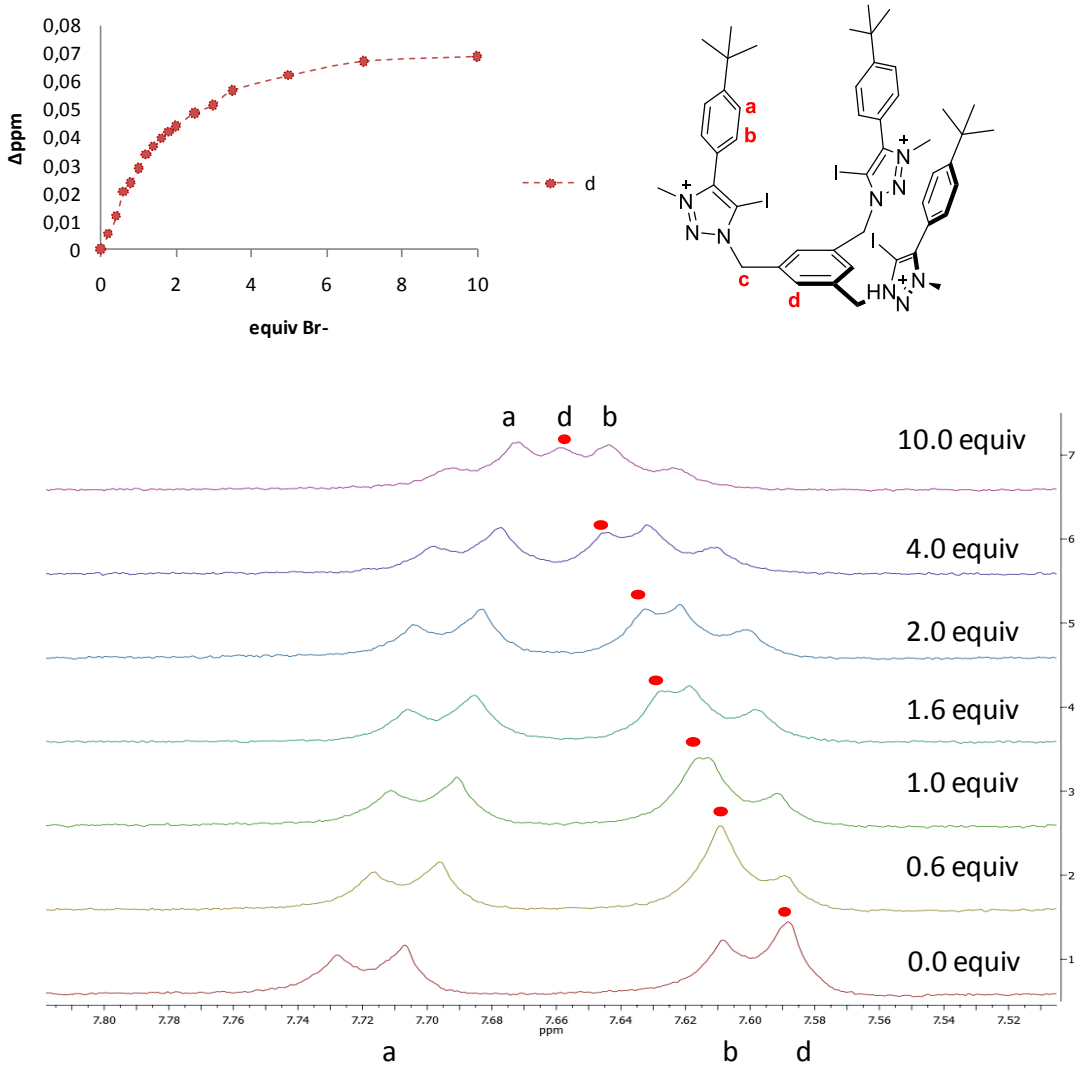

Figure 6.2. Experimental data fitted binding isotherms and truncated ^{1}H NMR spectra of **20(PF$_6$)$_3$** upon the addition of TBABr in DMSO-d^6. The plot represents the binding isotherm

Figure 6.3 shows the selected region of the spectra of the titration of **22(PF$_6$)$_3$** with TBACl. The series of spectra show that the signals due to the protons at the benzene ring (**d**) and one of the protons at the imidazolium (**a**) are downfield shifted upon guest addition, while the signal due to the remaining proton of the imidazolium is upfield shifted (**b**).

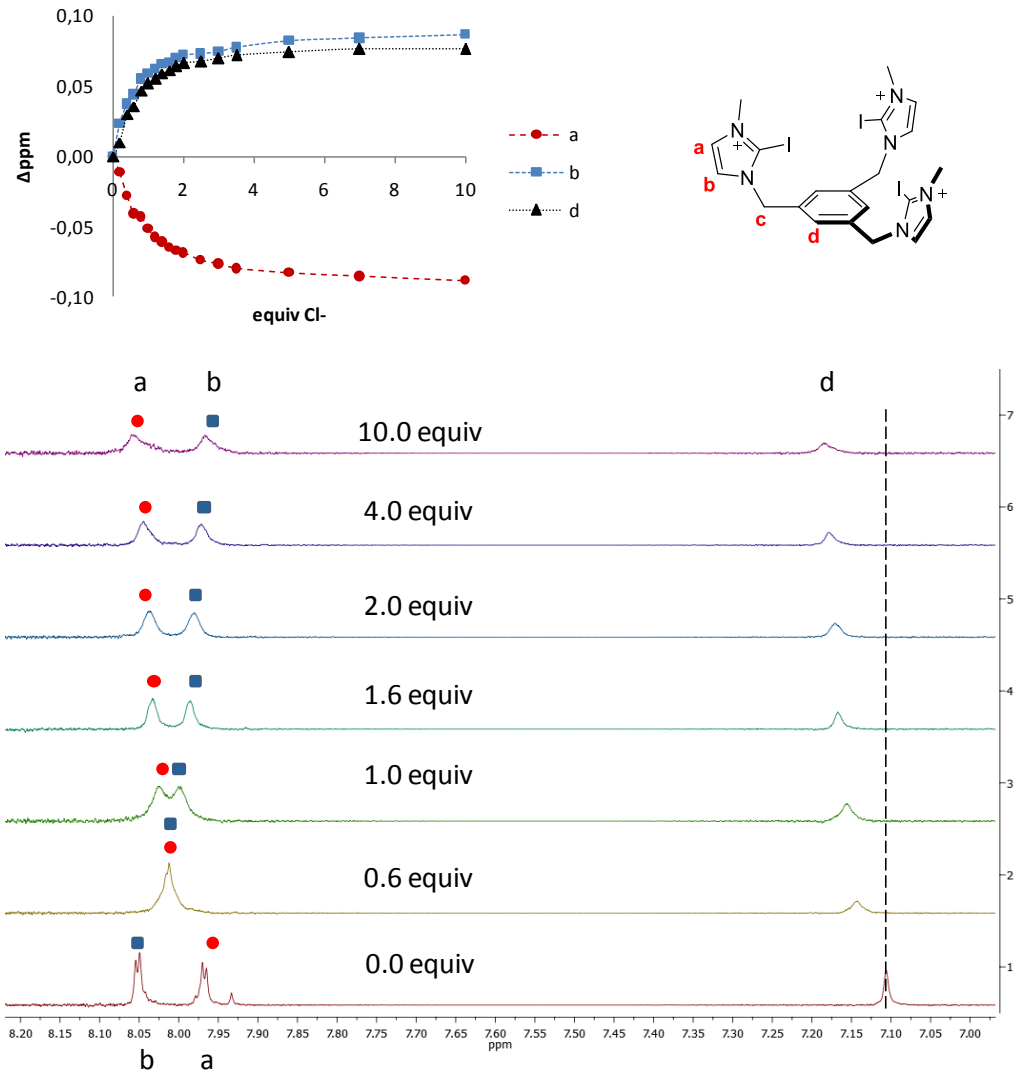

Figure 6.3. Experimental data fitted binding isotherms and truncated ^{1}H NMR spectra of **22(PF$_6$)$_3$** upon the addition of TBACl in DMSO-*d*^{6}. The plot represents the binding isotherms

Analysis of the ^{1}H NMR titrations allowed determining the stoichiometry of the host:guest complexes formed and their binding constants (K_a).[14] *Bindfit* analysis of the titration data obtained from monitoring the triazolium and imidazolium protons of the tripod receptors gave binding isotherms that indicate a host:guest 1:1 stoichiometry. This conclusion was supported by the fact that the fittings to a 1:1 stoichiometry gave the lowest residuals compared to other potential stoichiometries.[14a] The 1:1 association constants, K_{11}, were calculated by global nonlinear regression analysis by simultaneously including all protons showing significant chemical shift variations. [14a,15] The results of the association constants obtained for each receptor are summarized in Table 6.1. As can be seen in Table 6.1, K_{11} values for **19(PF$_6$)$_3$-22(PF$_6$)$_3$** follow the order Cl^-> Br^-> I^-, in agreement with the basicity trend of the anions (Figure 6.4).

Table 6.1. Association constants for the complexation of anion with receptors **19(PF$_6$)$_3$ -22(PF$_6$)$_3$**

		Host K_{11}, M^{-1}			
Entry	**anion**	**19 (PF$_6$)$_3$**	**20 (PF$_6$)$_3$**	**21 (PF$_6$)$_3$**	**22 (PF$_6$)$_3$**
1	Cl-	589.94±3%	829.84± 8%	1341±4%	2480±9%
2	Br-	377±6%	595 ± 2.7%	884±4%	1078±6%
3	I-	329± 4.7%	522 ± 6.3%	300±5%	551.04±9%
4	$H_2PO_4^-$	2543.16±7.4%	514±5% /378±4[a]	1950[b]	pp/311±2%[a]

Association constants (K_{11}) calculated by global nonlinear regression analysis for the complexation of the tris-azolium receptors in DMSO-*d*^{6} at 298 K. [a]Titration in DMSO-*d*^{6}:D_2O (9:1).[b] Data taken from reference[12]

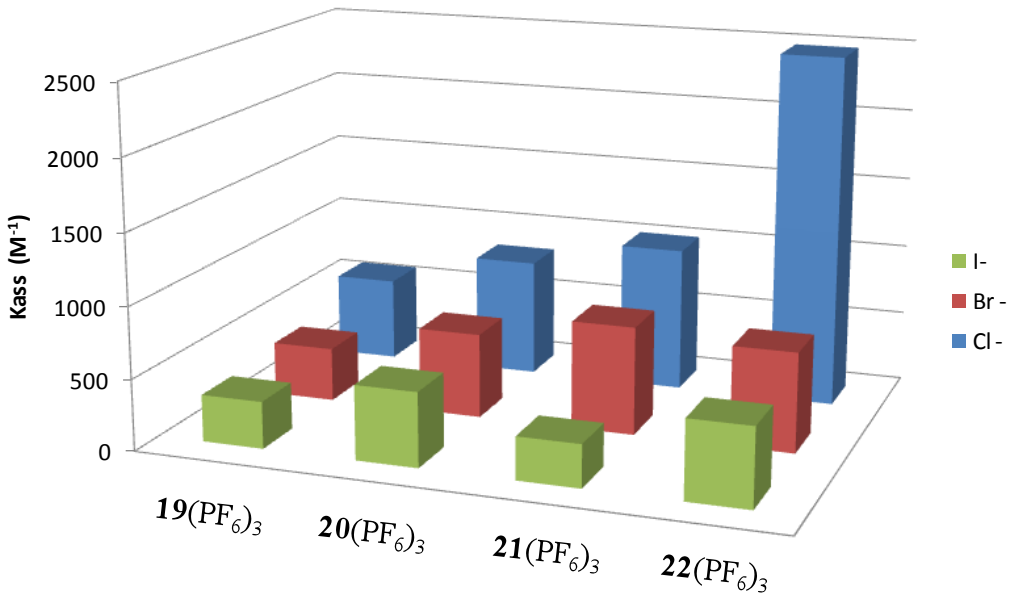

Figure 6.4. Association constant K_{11} for the complexation of receptors **19(PF$_6$)$_3$-22(PF$_6$)$_3$** with halides

For the recognition of halides, the association constants determined for the iodo-tripod receptors (XB) were found higher than those for the related proto-tripod (HB) receptors [compare binding constants of **20(PF$_6$)$_3$** and **22(PF$_6$)$_3$**, with those of **19(PF$_6$)$_3$** with **21(PF$_6$)$_3$**]. Also, imidazoliums were found to be better receptors than their related triazoliums [compare the binding constants of **21(PF$_6$)$_3$** with those of **19(PF$_6$)$_3$**, and the binding constants of **22(PF$_6$)$_3$** with those of **20(PF$_6$)$_3$**]. This makes the iodo-imidazolium tripod receptor **22(PF$_6$)$_3$** to show the highest affinity toward Cl^- versus Br^- and I^-, among all tripod receptors under study. As seen from the results shown in Table

6.1, this situation is inverse for the case of the recognition of the oxoanion $H_2PO_4^-$, for which receptor **19(PF$_6$)$_3$** shows the highest affinity.

We believe that this inversion of the affinity of the receptors when changing from halides to $H_2PO_4^-$, may be justified as a consequence of the need of directional attraction required for the formation of the halogen bonding interaction, which in the case of $H_2PO_4^-$, may be hindered by the tetragonal geometry of the oxoanion and the charge transfer and/or dispersion contributions of the C-I···A$^-$ XB interaction.[6]

*X-Ray Diffraction of **22(BF$_4$)$_3$***

Although titration studies were done with **22(PF$_6$)$_3$**, compound **22^{3+}** was isolated with PF_6^- and BF_4^- counter-anions. Single crystals of **22(BF$_4$)$_3$** were grown by slow diffusion of methanol into a concentrated chloroform solution of the compound to which one equivalent of tetrabutylammonium chloride (TBACl) was added. Figure 6.5 shows the molecular structure of the compound, where a clear interaction between the tris-azolium and the chloride ion is observed. Two iodo-imidazolium fragments are interacting with the chloride anion. The C-**I**···**Cl1** distances are 2.996 (I1) and 3.127 (I2) Å. The C-I-Cl1angles are 176.88 (I1) and 177.44º (I2), therefore very close to 180º, as expected for a halogen bonding interaction. By expanding the structure, it is possible to observe that Cl1 is also interacting with iodine atom of another molecule (I3 in Figure 6.6), therefore all three iodines of the tris-azolium are halogen-bonded to chloride, thus yielding an overall host:guest stoichiometry of 1:1.

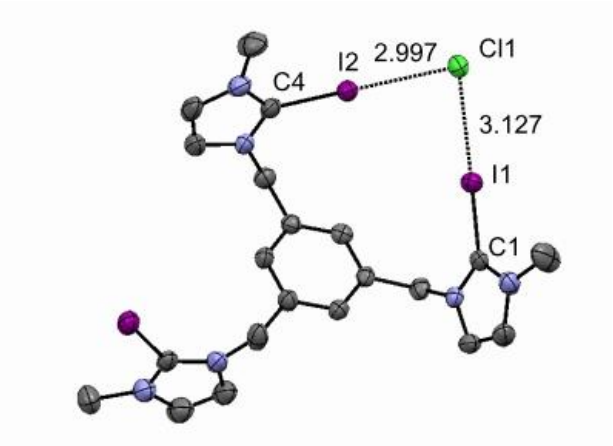

Figure 6.5. Molecular structure of **22^{3+}**. Solvent ($CHCl_3$), BF_4^- anions and hydrogen atoms have been omitted for clarity. Ellipsoids are at 50% of probability. Selected bond distances (Å) and angles (º): I(1)-Cl(1) 2.996(2), I(1)-Cl(1) 3.127(1); C(2)-I(1)-Cl(1) 176.88 and C(4)-I(2)-Cl(1)177.44º

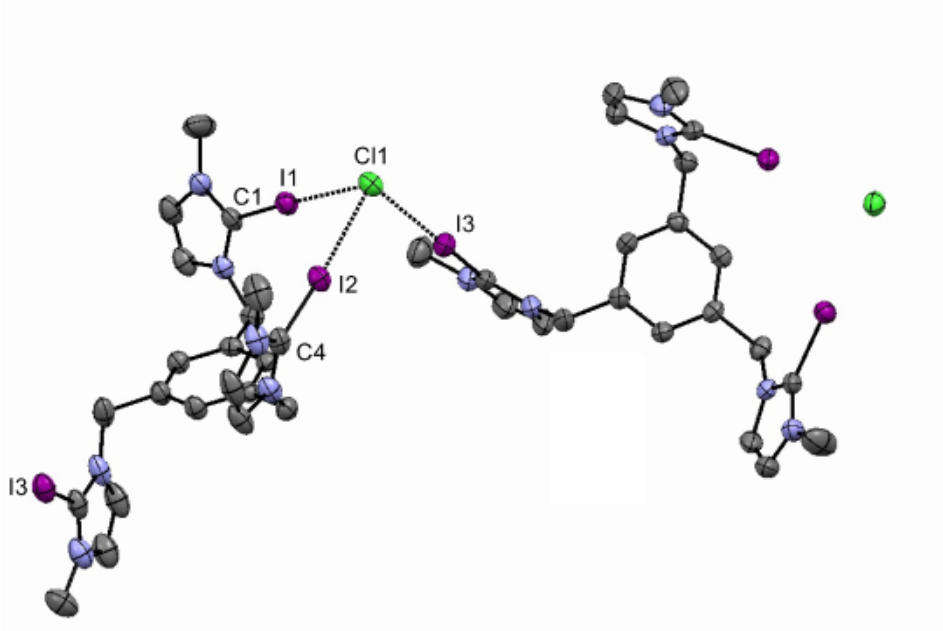

Figure 6.6. One section of the crystal packing of $\mathbf{22}^{3+}$ is shown. Solvent ($CHCl_3$), BF_4^- anions and hydrogen atoms have been omitted for clarity. The crystal packing is showing the halogen bonding interaction the iodo atoms from two molecules with the chloride

6.2.3 Computational studies

A computational molecular modelling study was carried out to characterize the conformational dynamics of receptors $\mathbf{21}^{3+}$ and $\mathbf{22}^{3+}$ and their interactions with the counter-anions. This study was performed by Dr. Gregori Ujaque and Pietro Vidossich from the Department of Chemistry of the Universitat Autònoma of Barcelona. Each arm of the receptor has two rotable bonds, giving rise to a high number of conformers. Moreover, several different interaction modes with the counterions may be also taken into account. Therefore, classical molecular dynamics (MD) simulations was used to efficiently explore the conformational space. Simulations were performed in explicit solvent and starting from different conformations of the receptor. Two counterions were considered, PF_6^- and Cl^-. About 100 ns simulations were collected for each system (see experimental chapter 7, section 7.11.2 for a description of the computational methods and an expanded account of the results obtained).

The simulation showed that the nature of the counterion has a remarkable impact on the receptor's conformational properties due to the strength of the interactions they establish. For both receptors, PF_6^- displayed unspecific and short-lived interactions with the receptor's arms, which experienced rapid interchange of orientation. However, chloride anions showed longer lived binding to the imidazolium and iodoimidazolium

rings. In the case of $\mathbf{21}^{3+}$, the simulation revealed the formation of a tri-coordinated species (Figure 6.7a), in which Cl^- is trapped within the interior of the tripod. This species appears to have a lifetime of the order of tens of ns (Fig. 6.7b, central part of the graph).

For $\mathbf{22}^{3+}$ a tri-coordinated species may actually form (Figure 6.7d), although this is not the preferred binding mode, which consists of the formation of halogen bonding interactions with two arms of the receptor. The simulations show that halogen bondings are highly stable interactions, so once formed, they are maintained for the rest of the simulation (Figure 6.7e). Binding of Cl^- to two arms was observed in simulations of models $\mathbf{22}(Cl)_3$ and $\mathbf{22}(Cl)(PF_6)_3$, thus suggesting that it is independent of the number of equivalents of chloride. A second anion binds to the third arm of the receptor as shown in Figure 6.7c, therefore affording a situation which is fully consistent with the X-Ray structure

DFT Calculations (B3LYP) (see Chapter 7, section 7.11.2) support the picture arising from the MD simulations of $\mathbf{22}^{3+}$. Representative structures from the MD simulations were optimized and used to compare the energetics of Cl^- binding to one, two and three arms of the receptor. Successive binding of the arm's receptor is favorable (Table 7.27, experimental section). However, when increasing from two to three arm's coordination the gain in stability is small, due to the cost of bringing together the positively charged arms. In fact, the energy difference between the open and closed conformations of $\mathbf{22}^{3+}$ is 9.9 kcal mol^{-1} in favor of the open structure (Figure 7.137, experimental section), which is similar to the binding energy of Cl^- to iodoimidazolium (-10.6 kcal mol^{-1}, Figure 7.138, experimental section). We also compared the energies of the receptor interacting with two Cl^- in different conformations (Figure 7.136, experimental section). In line with the above results and those from the MD study, binding of one Cl^- to two arms and another Cl^- to one arm (Figure 7.136b,c) is favored compared to the binding of one Cl^- to three arms and one Cl^- interacting unspecifically with the receptor (Figure 7.136a, experimental section), in a situation that clearly resembles our experimental solid state structure.

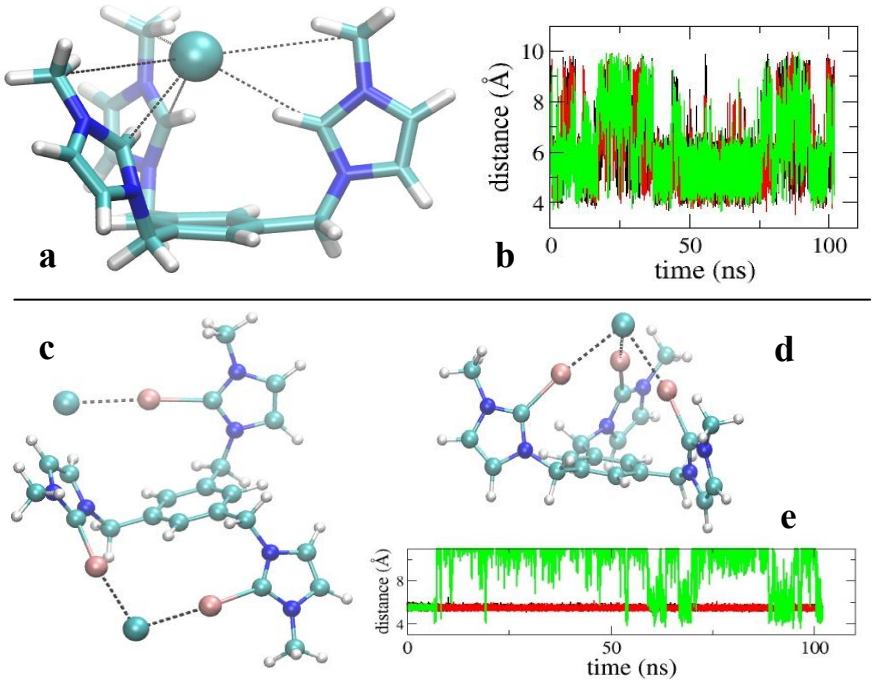

Figure 6.7 Molecular modeling studies of the recognition properties of the $\mathbf{21}^{3+}$ (top panel) and $\mathbf{22}^{3+}$ (bottom panel) receptors. In **b**, the time series of the distances between the NCN carbon of the imidazolium rings of $\mathbf{21}^{3+}$ are shown. In **c**, the distances between one chloride anion and the iodide of the iodoimidazolium rings of $\mathbf{22}^{3+}$ are shown

6.3 Conclusions

This chapter describes the synthesis, characterization and binding capabilities of four tripod receptors combining imidazoliums, triazoliums and their iodo substituted analogues. The analysis of their anion binding capabilities towards several anions (Cl^-, Br^-, I^- and $H_2PO_4^-$) was carried out by using NMR spectroscopy techniques. The binding association constants were obtained by the treatment of the data using the *Bindfit* programme. The results from the studies demonstrated that the XB receptors (**20(PF$_6$)$_3$** and **22(PF$_6$)$_3$** were superior halide complexants compared to the HB receptors. In contrast, the HB tripod receptors **19(PF$_6$)$_3$** and **21(PF$_6$)$_3$** show higher affinity by $H_2PO_4^-$ then the related iodoazoliums. This observation is very useful in order to custom design selective receptors for anions of different nature.

The study sheds important information for the design and development of novel receptors for anions, and specially stresses the importance of XB interactions versus the ubiquitous HB interactions for the recognition of halides.

6.4 References

(1) a) Martinez-Manez, R., Sancenon, F. *Chem. Rev. (Washington, DC, U. S.)* **2003**, *103*, 4419-4476; b) Sessler, J. L., Gross, D. E., Cho, W. S., Lynch, V. M., Schmidtchen, F. P., Bates, G. W., Light, M. E., Gale, P. A. *J. Am. Chem. Soc.* **2006**, *128*, 12281-12288; c) Evans, N. H., Beer, P. D. *Angew Chem, Int Ed.* **2014**, *53*, 11716-11754; d) Gale, P. A., Garcia-Garrido, S. E., Garric, J. *Chem. Soc. Rev.* **2008**, *37*, 151-190.

(2) Mullaney, B. R., Thompson, A. L., Beer, P. D. *Angew Chem, Int Ed.* **2014**, *53*, 11458-11462.

(3) a) Gilday, L. C., Beer, P. D. *Chem. Eur. J.* **2014**, *20*, 8379-8385; b) Cametti, M., Raatikainen, K., Metrangolo, P., Pilati, T., Terraneo, G., Resnati, G. *Org. Biomol. Chem.* **2012**, *10*, 1329-1333; c) Cavallo, G., Metrangolo, P., Pilati, T., Resnati, G., Sansotera, M., Terraneo, G. *Chem. Soc. Rev.* **2010**, *39*, 3772-3783; d) Priimagi, A., Cavallo, G., Metrangolo, P., Resnati, G. *Acc. Chem. Res.* **2013**, *46*, 2686-2695; e) Busschaert, N., Caltagirone, C., Van Rossom, W., Gale, P. A. *Chem. Rev.* **2015**, *115*, 8038-8155; f) Wang, H., Wang, W., Jin, W. J. *Chem. Rev.* **2016**, *116*, 5072-5104; g) Beale, T. M., Chudzinski, M. G., Sarwar, M. G., Taylor, M. S. *Chem. Soc. Rev.* **2013**, *42*, 1667-1680.

(4) Wang, G. M., Chen, Z. Q., Xu, Z. J., Wang, J. N., Yang, Y., Cai, T. T., Shi, J. Y., Zhu, W. L. *J. Phys. Chem. B* **2016**, *120*, 610-620.

(5) a) Langton, M. J., Robinson, S. W., Marques, I., Felix, V., Beer, P. D. *Nature Chem.* **2014**, *6*, 1039-1043; b) Gilday, L. C., Lang, T., Caballero, A., Costa, P. J., Felix, V., Beer, P. D. *Angew Chem, Int Ed.* **2013**, *52*, 4356-4360; c) Serpell, C. J., Kilah, N. L., Costa, P. J., Felix, V., Beer, P. D. *Angew Chem, Int Ed.* **2010**, *49*, 5322-5326; d) Jungbauer, S. H., Schindler, S., Kniep, F., Walter, S. M., Rout, L., Huber, S. M. *Synlett* **2013**, *24*, 2624-2628.

(6) Brown, A., Beer, P. D. *Chem. Commun.* **2016**, *52*, 8645-8658.

(7) Shields, Z. P., Murray, J. S., Politzer, P. *Int. J. Quantum Chem.* **2010**, *110*, 2823-2832.

(8) Robertson, C. C., Perutz, R. N., Brammer, L., Hunter, C. A. *Chem. Sci.* **2014**, *5*, 4179-4183.

(9) Kuswandi, B., Nuriman, Verboom, W., Reinhoudt, D. N. *Sensors* **2006**, *6*, 978-1017.

(10) Mancuso, L., Knobloch, T., Buchholz, J., Hartwig, J., Moller, L., Seidel, K., Collisi, W., Sasse, F., Kirschning, A. *Chem. Eur. J.* **2014**, *20*, 17541-17551.

(11) D'Anna, F., Gunaratne, H. Q. N., Lazzara, G., Noto, R., Rizzo, C., Seddon, K. R. *Org. Biomol. Chem.* **2013**, *11*, 5836-5846.

(12) Fahlbusch, T., Frank, M., Schatz, J., Schmaderer, H. *Eur. J. Org. Chem.* **2006**, 1899-1903.

(13) a) Cai, J., Sessler, J. L. *Chem. Soc. Rev.* **2014**, *43*, 6198-6213; b) Xu, Z., Kim, S. K., Yoon, J. *Chem. Soc. Rev.* **2010**, *39*, 1457-1466; c) Caltagirone, C., Gale, P. A. *Chem. Soc. Rev.* **2009**, *38*, 520-563; d) Yoon, J., Kim, S. K., Singh, N. J., Kim, K. S. *Chem. Soc. Rev.* **2006**, *35*, 355-360; e) *Anion Recognition in Supramolecular Chemistry*; Gale, P., Dehaen, W., Eds.; Springer: Heidelberg, **2010**.

(14) a) Thordarson, P. *Chem. Soc. Rev.* **2011**, *40*, 1305-1323; b) Hirose, K. *J. Incl. Phenom. Macrocycl. Chem.* **2001**, *39*, 193-209.

(15) Lowe, A. J., Pfeffer, F. M., Thordarson, P. *Supramol. Chem.* **2012**, *24*, 585-594.

Chapter 7.
Experimental Section

7.1 Analytical techniques

Nuclear Magnetic Resonance (NMR)

^{1}H and ^{13}C $\{^{1}H\}$ NMR spectra were recorded on the following spectrometers at 298 K:

- Varian Innova 300 MHz (^{1}H 300 MHz, ^{13}C $\{^{1}H\}$ 75 MHz)
- Varian Innova 500 MHz (^{1}H 500 MHz, ^{13}C $\{^{1}H\}$125 MHz)
- Bruker 400 MHz (^{1}H 400 MHz, ^{13}C $\{^{1}H\}$100 MHz)
- Bruker 500 MHz (^{1}H 500 MHz, ^{13}C $\{^{1}H\}$125 MHz)

Chemical shifts are given in ppm (δ), referred to the residual peak of the deuterated solvent ($CDCl_3$, CD_2Cl_2, CD_3CN, acetone-d^6, CD_3OD and DMSO-d^6) and reported downfield of $Si(CH_3)_4$.

Electrospray Mass Spectra (ESI-MS) and High Resolution Mass Spectroscopy (HRMS)

Electrospray Mass Spectra (ESI-MS) were recorded on a Micromass Quatro LC instrument; CH_3OH or CH_3CN were used as mobile phase and nitrogen was employed as the drying and nebulizing gas. High Resolution Mass Spectra (HRMS) were recorded on a Q-TOF I (quadrupole-hexapole-TOF) mass spectrometer with an orthogonal Z-spray-electrospray interface (Micromass, Manchester, UK). The drying gas as well as nebulizing gas was nitrogen at a flow of 400L/h and 80 L/h respectively. The temperature of the source block was set to 120ºC and the desolvation temperature to 150ºC. A capillary voltage of 3.5 KV was used in the positive scan mode and the coe voltage was set to 30V. Both positive and negative ESI mass spectra displayed very useful information about the stoichiometry of the supramolecular recognition on the basis of the m/z values and comparison between the observed and the theoretical isotopic pattern of the identifies species. The chemical composition of each peak was assigned by comparison of the isotope experimental and theoretical patterns, considering natural abundance for all elements, using the MassLynx 4.1 program.

For Collision Induced Dissociation (CID) experiments, the complete isotopic envelope of the species of interest was mass-selected with the first quadrupole (isolation width *ca.* 4 Da), interacted with argon in the T-wave collision cell while analyzing the ionic fragments with the TOF analyzer. The collision energy was systematically stepped in

the E_{lab}= 15-30 eV range. Validation of the proposed fragmentation scheme was provided by in-source generation of the desired intermediates and subsequent CID investigation. For this purpose, higher cone voltages (typically Uc = 90-100 V) were used.

Elemental Analysis

Elemental analyses were carried out on a TrueSpec Miro Series.

Gas Chromatography (GC)

GC analyses were obtained on a Shimadzu GC-2010 apparatus equipped with a FID and Teknokroma (TRB-5MS, 30 m x 0.25 mm x 0.25 μm) column was used.

Infrared Spectroscopy (FT-IR)

Infrared spectra (FT-IR) were performed on a Bruker EQUINOX 55 spectrometer with a spectral window of 4000-600 cm^{-1}. Liquid samples were placed between KBr windows.

Electrochemical measurements

Electrochemical studies were carried out by using an Autolab Potentiost at (Model PGSTAT101) using a three-electrode cell. The cell was equipped with platinum working and counter electrodes, as well as a silver wire reference electrode. In all experiments CH_2Cl_2 was used as solvent and $[NBu_4][PF_6]$ was used as the supporting electrolyte. All redox potentials were referenced to the Fc/Fc^+ couple as internal standard with $E_{1/2}(Fc/Fc^+)$ vs. SCE = -0.446 V.

UV-Vis spectroscopy

The UV/Vis spectra were recorded between 250 and 500 nm by a Cary 300 Bio UV−Vis Varian spectrophotometer.

High Resolution Transmission Microscopy (HRTEM)

High-Resolution Transmission Electron Microscopy images (HRTEM) and high-angle annular dark-field HAADF-STEM images of the samples were obtained using a Jem-2100 LaB6 (JEOL) transmission electron microscope coupled with an INCA Energy TEM 200 (Oxford) Energy-Dispersive X-ray spectrometer (EDX) operating at 200 kV. Samples were prepared by drying a droplet of methanolic dispersion on a carbon-coated copper grid.

Scanning Electron Microscopy (SEM)

Scanning electron micrographs were taken with a field emission gun scanning electron microscope (FEG-SEM) model JEOL 7001F, equipped with a spectrometer of energy dispersion of X-ray (EDS) from Oxford instruments.

Inductively Coupled Plasma optical Emission-Mass Spectrometry (ICP-MS)

The determination of the metal loading was done by ICP−MS Agilent 7500 CX. The digestion of the samples was carried out under reflux of a mixture of concentrated nitric and hydrochloric acids (3:1) for 12 h. The digestion of the samples after the recycling experiments were carried out after several washes with milli-Q water (10 × 10 mL).

7.2 Synthesis and Characterization

All the reactions were carried out by using standard Schlenk tube techniques under nitrogen atmosphere unless otherwise stated. Anhydrous solvents were dried using a solvent purification system (SPS M BRAUN) or purchased and degassed prior to use by purging with nitrogen and kept over molecular sieves. All other reagents were used as received from commercial suppliers. Column chromatography was performed on silica gel Merck 60, 62-200 mm unless otherwise stated, using the mixtures of solvents.

7.2.1 Synthesis and characterization of complexes of Chapter 2

Ligand **A**, 1,1´,3,3´-bis(α,α´,-*p*-xylyl)bis(benzimidazolium) dichloride, was prepared according to literature procedures.[1]

Synthesis of 1

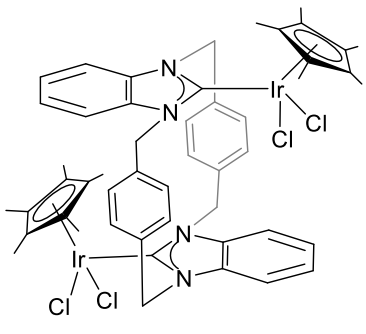

1

A mixture of **A** (100.0 mg, 0.19 mmol), silver oxide (I) (44.0 mg, 0.19 mmol) in CH_2Cl_2 (10 mL) was stirred at room temperature for 1 h in the absence of light. Then $[IrCp^*Cl_2]_2$ (133.3 mg, 0.19 mmol) was added and stirred at room temperature overnight. The final suspension was filtered over celite and the solvent was removed under reduce pressure. Precipitation from dichloromethane/diethyl ether gave **1** as a yellow solid, after being recrystallized in methanol. Yield: 50% (108.4 mg). ^{1}H NMR (300 MHz, CD_2Cl_2) δ 7.53 (m, 2H, C*H*$_{benzimidazole}$), 7.38 (m, 2H, C*H*$_{benzimidazole}$), 7.38 (d, 4H,

CH_{xylyl}), 7.23 (m, 2H, Ph), 6.97 (m, 2H, C$H_{benzimidazole}$), 6.84 (d, 4H, CH_2), 6.49 (d, $^3J_{HH}$= 8.3Hz, 2H, CH_{xylyl}), 5.89 (d, 2H, CH_2), 5.64 (d, 2H, CH_2), 4.91 (d, $^3J_{HH}$= 14.1Hz, 2H, CH_2), 1.38 (s, 15H, CH_3-Cp*), 0.76 (s,15H,CH_3-Cp*).^{13}C NMR (75 MHz, CD_2Cl_2) δ 179.4 ($C_{carbene}$-Ir), 167.2 ($C_{carbene}$-Ir), 138.1, 136.7, 136.4, 129.0, 126.2, 124.3, 123.0, 111.4 and 110.7 (aromatic *C* and *C*H from xylyl and benzimidazole), 90.7 ($C_5(CH_3)_5$), 89.1 ($C_5(CH_3)_5$), 50.9 (CH_2), 49.0 (CH_2), 8.2 ($C_5(CH_3)_5$). Anal. Calcd. for $C_{52}H_{58}N_4Cl_8Ir_2$ (1407.18): C, 44.38; H, 4.15; N, 3.98. Found: C, 44.20; H, 4.70 N, 3.73. Electrospray MS (Cone 20V) (m/z, fragment): 583.3 $[M - 2Cl]^{2+}$. HRMS ESI-TOF-MS (positive mode): $[M - 2Cl]^{2+}$ monoisotopic peak 583.1482, calc. 583.1483, ε_r: 0.17. Decomposition temperature: 220-222ºC.

Synthesis of 2

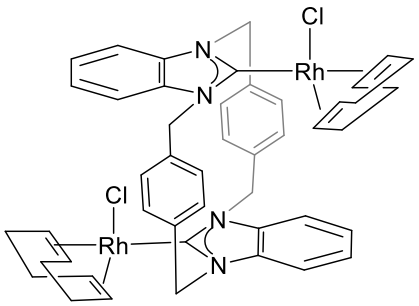

2

A mixture of $[RhCl(1,5\text{-}COD)]_2$ (48.0 mg, 0.098 mmol) and NaO*t*Bu (20.7 mg, 0.22 mmol) was stirred in THF (5 mL) for 30 min. at room temperature. The resulting dark orange solution was slowly added to a suspension of **A** (51.6 mg, 0.098 mmol) in THF (10 mL) at -78ºC. The mixture was allowed to warm to room temperature overnight. The yellow solution was filtered over celite and solvent was remove under reduce pressure. Recrystallization from dichloromethane/diethyl ether gave **2** as an orange solid. Yield: 48% (38.3 mg). ^{1}H NMR (300 MHz, $CDCl_3$) δ 7.71 (m, 2H, CH_{xylyl}), 7.41 (m, 2H, C$H_{benzimidazole}$), 7.32 (m, 2H, C$H_{benzimidazole}$), 7.05 (m, 2H, C$H_{benzimidazole}$), 6.88 (m, 2H, C$H_{benzimidazole}$), 6.53 (d, 2H, CH_2), 6.53 (d, 4H, CH_{xylyl}), 6.11(d, $^3J_{HH}$=16.2Hz, 2H, CH_2), 5.63(d, $^3J_{HH}$=16.3Hz, 2H, CH_2), 5.25 (m, 2H, CH_{xylyl}), 5.11(d, $^3J_{HH}$= 13.6Hz, 2H, CH_2), 4.79(m, 2H, COD), 3-1 (COD). ^{13}C NMR (125 MHz, CD_2Cl_2) δ 201 ($^1J_{Rh\text{-}C}$=75.6Hz, $C_{carbene}$-Rh), 199.0 ($^1J_{Rh\text{-}c}$=88.2Hz, $C_{carbene}$-Rh), 139.8, 136.4, 135.1, 134.4, 130.0, 125.8, 123.4, 122.0, 110.3, 109.9 (aromatic *C* and *C*H from xylyl and benzimidazole), 100.5, 97.3, 73.0, 69.0 (*C*H-COD), 51.9 and 50.7 (CH_2), 30.7, 30.0, 28.9 and 28.3 (CH_2-COD). Anal. Calcd for $C_{49}H_{51}N_4Cl_{11}Rh_2$ (1172.3783): C, 45.56; H, 3.90; N, 4.33. Found: C, 45.81; H, 4.10; N, 4.91. Electrospray MS (Cone 20V) (m/z, fragment): 897.2 $[M\text{-}Cl]^+$. HRMS ESI-TOF-MS (positive mode): $[M\text{-}Cl]^+$ monoisotopic peak 897.1667, calc.897.1678, ε_r: 0.12. Decomposition temperature: 193-195 ºC.

Synthesis of 3

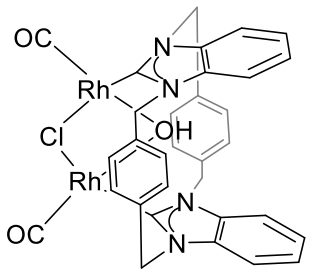

3

A mixture of **A** (100.0 mg, 0.19 mmol), silver oxide (I) (45.2 mg, 0.19 mmol) in CH_2Cl_2 (10 mL) was stirred at room temperature for 12 h. Reaction was carried out in darkness. Then $[RhCl(CO)_2]_2$ (63.8 mg, 0.19 mmol) was added and stirred at room temperature overnight. The final suspension was filtered over celite and solvent was removed under reduce pressure. Recrystallization from dichloromethane/hexane gave **3** as a yellow solid. Yield: 43.70% (64.3 mg).^{1}H NMR (500 MHz, $CDCl_3$) δ 8.41 (d, 4H, $^4J_{HH}$= 2.0Hz, CH_{xylyl}), 7.52 (m, 4H, C$H_{benzimidazole}$), 7.32 (m, 4H, C$H_{benzimidazole}$), 6.22 (4H, $^4J_{HH}$= 2.0Hz, CH_{xylyl}), 5.60 (d, $^3J_{HH}$= 14.4Hz, 4H, CH_2), 5.51 (d, $^3J_{HH}$= 14.5Hz, 4H, CH_2). ^{13}C NMR (75 MHz, $CDCl_3$) δ 195.2 ($^1J_{Rh-C}$= 137Hz, C_{CO}-Rh), 190.1 ($^1J_{Rh-C}$= 71.26Hz, $C_{Carbene}$-Rh), 139.7, 135.0, 133.3, 126.5, 123.3, 109.3, 109.2 (aromatic *C* and *C*H from xylyl and benzimidazole), 51.67 (CH_2). IR (CH_2Cl_2) = 1941 ($\nu_{C=O}$) cm^{-1}. Anal. Calcd. for $C_{33}H_{26}N_4Cl_4O_3Rh_2$ (874.2113): C, 45.33; H, 2.90; N, 6.40. Found: C, 45.30; H, 2.60; N, 5.95. Electrospray MS (Cone 20V) (m/z, fragment): 719.0 $[M-Cl]^+$, 691.0$[M-Cl-CO]^+$, 663.1 $[M-Cl-2CO]^+$. HRMS ESI-TOF-MS (positive mode): $[M-Cl]^+$ monoisotopic peak 719.0044, calc.719.0037, ε_r: 0.10. Decomposition temperature: 243-245 ºC.

7.2.2 Synthesis and characterization of compounds of Chapter 3

Synthesis of B

The N-Me substituted bis-imidazolium salt **B** was obtained according to the known literature procedure.[2]

Synthesis of C

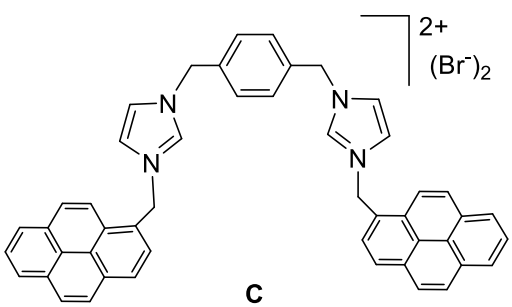

C

A mixture of 1,4-bis((1H-imidazol-1-yl)methyl)-xylyl (500.0 mg, 2 mmol) and 1-(bromomethyl)pyrene (1.5 g, 5 mmol) in THF (10 mL) was stirred at 75 ºC for 24 h. The final suspension was cooled to room temperature and diethyl ether (10 mL) was added. The resulting white precipitate was collected by filtration and washed with diethyl ether. High-vacuum drying gave **C** as a white solid. Yield: 82% (1.32 mg). ^{1}H

NMR (500 MHz, DMSO-d^6) δ 9.38 (s, 2H, NC*H*N), 8.44 (d, $^3J_{HH}$= 9.2 Hz, 2H, CH_{pyrene}), 8.38 (m, 6H, CH_{pyrene}), 8.33 (d,$^3J_{HH}$= 9.2 Hz, 2H, CH_{pyrene}), 8.25 (dd, $^3J_{HH}$= 20.5, 8.9 Hz, 4H, CH_{pyrene}), 8.14 (t, $^3J_{HH}$= 8.2 Hz, 4H, CH_{pyrene}), 7.88 (s, 2H, C$H_{imidazole}$), 7.80 (s, 2H, CH_{xylyl}), 7.39 (s, 4H, C$H_{imidazole}$), 6.22 (s, 4H, CH_2), 5.37 (s, 4H, CH_2). ^{13}C NMR (75 MHz, DMSO-d_6) δ 136.9 (N*C*HN), 135.9 (C_{xyly}), 132.1 (Pyr), 131.2 (Pyr), 130.6 (Pyr), 129.3 (*C*H$_{xylyl}$), 129.2 (Pyr), 128.8 (Pyr), 127.8 (Pyr), 127.6 (Pyr), 127.3 (Pyr), 126.6 (Pyr), 126.4 (Pyr), 125.8 (Pyr), 124.7 (Pyr), 124.2 (Pyr), 123.8 (Pyr), 123.3 (*C*H$_{imidazole}$), 122.8 (*C*H$_{imidazole}$), 52.0 (*C*H$_2$), 50.7 (*C*H$_2$). Anal. Calcd. for $C_{48}H_{36}N_4Br_2$ (828.6342): C, 69.60; H, 4.37; N, 6.80. Found: C, 70.13; H, 3.90; N, 6.24. Although these results are slightly outside the range viewed as establishing analytical purity, they are provided to illustrate the best values obtained. Electrospray MS (Cone 20V) (m/z, fragment): 748.2 [M-Br]$^+$. Decomposition temperature: 234-236 ºC.

Synthesis of D

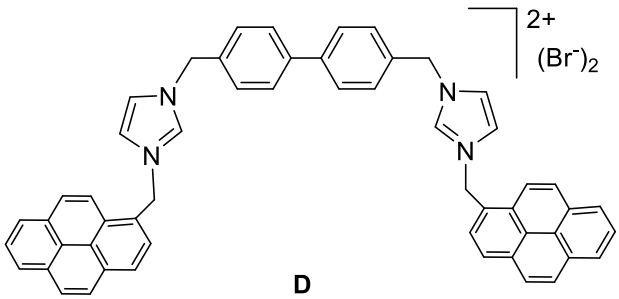

D

A mixture of 4,4'-bis((1H-imidazol-1-yl)methyl)-1,1'-biphenyl (209.1 mg, 0.66 mmol) and 1-(bromomethyl) pyrene (491.3 mg, 1.66 mmol) in THF (10 mL) was stirred at 75ºC for 24h. The final suspension was cooled to room temperature and diethyl ether (10 mL) was added. The resulting white precipitate was collected by filtration and washed with diethyl ether. High-vacuum drying gave **D** as a white solid. Yield: 94% (500.0 mg). ^{1}H NMR (500 MHz, DMSO-d^6) δ 9.44 (s, 2H, NC*H*N), 8.47 (d, $^3J_{HH}$= 9.2 Hz, 2H, CH_{pyrene}), 8.39 (m, 6H, CH_{pyrene}), 8.35 (d, $^3J_{HH}$= 9.2 Hz, 2H, CH_{pyrene}), 8.26 (dd, $^3J_{HH}$= 18.0, 8.9 Hz, 4H, CH_{pyrene}), 7.92 (s, 2H, C$H_{imidazole}$), 7.87 (s, 2H, C$H_{imidazole}$), 7.67 (d, $^3J_{HH}$= 7.9 Hz, 4H, CH_{biphe}), 7.47 (d, $^3J_{HH}$= 7.9 Hz, 4H, CH_{biph}), 6.26 (s, 4H, CH_2), 5.44 (s, 4H, CH_2). ^{13}C NMR (75 MHz, DMSO-d_6) δ 140.08 (N*C*HN), 136.7 ($C_{biphenil}$), 134.5 ($C_{biphenil}$), 131.8 (Pyr), 130.9 (Pyr), 130.4 (Pyr), 129.2 (*C*H$_{biphenil}$), 129.1(*C*H$_{biphenil}$), 128.9 (Pyr), 128.5 (Pyr), 128.4 (Pyr), 127.5 (Pyr), 127.4 (Pyr), 126.9 (Pyr), 126.3 (Pyr), 126.1 (Pyr), 125.5 (Pyr), 124.4 (Pyr), 123.9 (Pyr), 123.5 (Pyr), 123.1 (*C*H$_{imidazole}$), 122.5 (*C*H$_{imidazole}$), 51.9 (*C*H$_2$), 50.5 (*C*H$_2$). Anal.Calcd. for $C_{54}H_{40}N_2Br$ (904.7302): C, 71.68; H, 4.46; N, 6.20. Found: C, 71.84; H, 4.40; N, 6.22.

Electrospray MS (Cone 20V) (m/z, fragment): 372.3 $[M\text{-}2Br]^+$. Decomposition temperature: 255-258 ºC.

Synthesis of 5

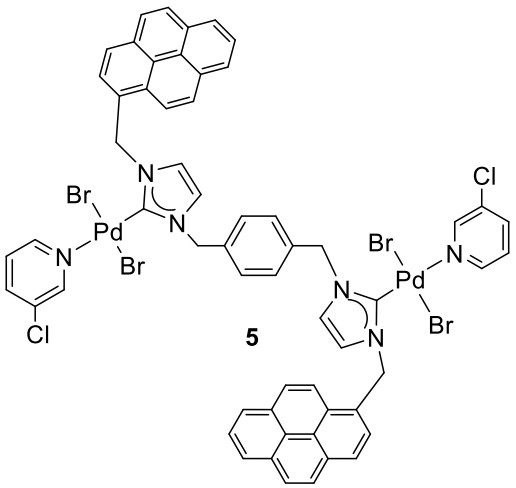

5

A mixture of **C** (80.0 mg, 0.1 mmol), palladium (II) chloride (34.3 mg, 0.19 mmol), K_2CO_3 (80.4 mg, 0.58 mmol) and KBr (60.0 mg) in 3-chloropyridine (2 mL) was stirred at 100 ºC for 6 h. The reaction was carried under N_2. The resulting suspension was cooled to room temperature and the solvent was removed under vacuum. The crude product was purified by column chromatography. The pure compound **5** was eluted with dichloromethane: acetone (8:2) and precipitated in a mixture of dichloromethane/ hexane to give a yellow solid. Yield 30% (45.1 mg). ^{1}H NMR (300 MHz, $CDCl_3$) δ 9.10 (s, 2H, CH_{pyrid}), 8.96 (d, $^3J_{HH}$=4.2 Hz, 2H, CH_{pyrid}), 8.53 (d, $^3J_{HH}$= 9.2 Hz, 2H, CH_{pyrene}), 8.24 – 8.00 (m, 16H, CH_{pyrene}), 7.63 (d, 2H, CH_{pyrid}), 7.58 (s, 4H, CH_{xylyl}), 7.22 (t, 2H, CH_{pyrid}), 6.64 (s, 2H, C$H_{imidazole}$), 6.45 (s, 4H, CH_2), 6.35 (s, 2H, C$H_{imidazole}$), 5.82 (s, 4H, CH_2).^{13}C NMR (75 MHz, $CDCl_3$) δ 151.8 (*C*H$_{pyrid}$), 150.8 (*C*H$_{pyrid}$), 147.5 ($C_{carbene}$-Pd), 138.0 (*C*H$_{pyrid}$), 135.8 (C_{pyrid}), 132.7 (C_{pyrene}), 132.3 (C_{pyrene}), 131.3 (C_{pyrene}), 130.92 (C_{pyrene}), 130.4 (*C*H$_{xylyl}$), 130.0 (*C*H$_{pyrene}$), 129.6 (*C*H$_{pyrene}$), 129.2 (*C*H$_{pyrene}$), 129.1 (*C*H$_{pyrene}$), 128.4 (*C*H$_{pyrene}$), 127.4 (C_{pyrene}), 127.2 (C_{pyrene}), 126.5 (*C*H$_{pyrene}$), 125.9 (*C*H$_{pyrene}$), 125.86 (*C*H$_{pyrene}$), 125.30 (*C*H$_{pyrene}$), 125.2 (C_{pyrene}), 125.08 (*C*H$_{pyrene}$), 125.0 (*C*H$_{pyrid}$), 124.7 (C_{xylyl}), 123.6 (*C*H$_{imidazole}$), 121.9 (*C*H$_{imidazole}$), 55.1 (*C*H$_2$), 53.9 (*C*H$_2$). Anal.Calcd for $C_{58}H_{42}N_6Br_4Cl_2Pd_2CHCl_3$ (1563.7492): C, 45.31; H, 2.90; N, 5.37. Found: C, 44.80; H, 3.19; N, 5.18. Electrospray MS (Cone 20V) (m/z, fragment): 1346.8 $[M\text{-}Br]^+$. Decomposition temperature: 236-238 ºC

$^{13}C\ \{^{1}H\}$ APT NMR spectrum of 7 in $CHCl_3$

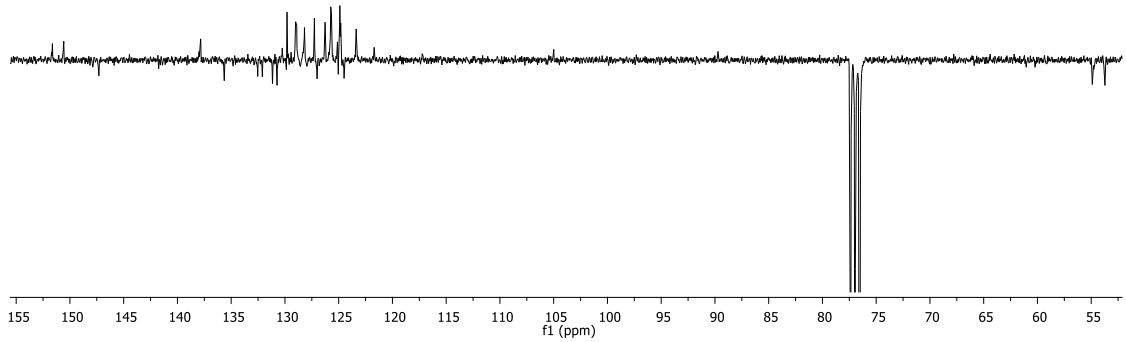

Figure 7.1. ^{13}C APT NMR spectrum of **5** in $CDCl_3$

Synthesis of 6

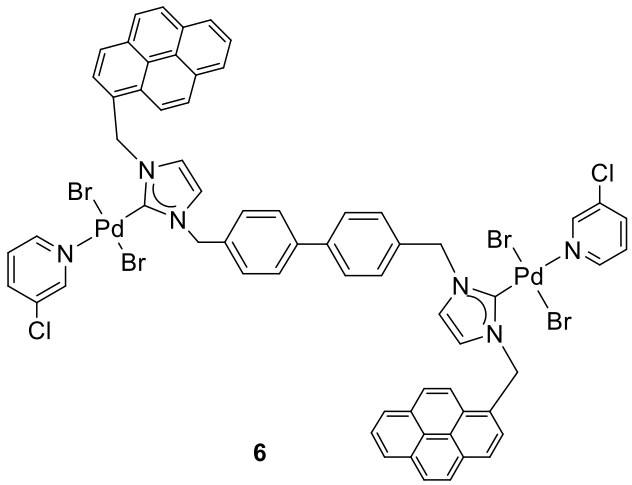

6

A mixture of **D** (80.0 mg, 0.089 mmol), palladium (II) chloride (35.5 mg, 0.2 mmol), K_2CO_3 (82.9 mg, 0.6 mmol) and KBr (60.0 mg) in 3-chloropyridine (2 mL) was stirred at 100 ºC for 12 h. The reaction was carried under N_2. The resulting suspension was cooled to room temperature and the solvent was removed under vacuum. The crude product was purified by column chromatography. The pure compound **6** was eluted with dichloromethane: ethyl acetate (1:1) and precipitated in a mixture of dichloromethane/ hexane to give a yellow solid. Yield: 50% (85 mg).^{1}H NMR (500 MHz, $CDCl_3$) δ 9.15 (s, 2H, CH_{pyrid}), 9.03 (m, 2H, CH_{pyrid}), 8.56 (d, $^{3}J_{HH}$= 9.2 Hz, 2H, CH_{pyrene}), 8.23 (t, $^{3}J_{HH}$=9.2 Hz, 8H, CH_{pyrene}), 8.20 – 8.14 (m, 2H, CH_{pyrene}), 8.14 – 8.08 (m, 4H, CH_{pyrene}), 8.05 (t, $^{3}J_{HH}$=7.6 Hz, 2H, CH_{pyrene}), 7.77 (m, 2H, CH_{pyrid}), 7.60 (s, 8H, C$H_{biphenilene}$), 7.32 (m, 2H, CH_{pyrid}), 6.60 (m, 2H , C$H_{imidazole}$), 6.52 (s, 2H, CH_2), 6.50 (s, 2H, CH_2), 6.38 (m, 2H, C$H_{imidazole}$), 5.90 (m, 2H, CH_2), 5.87 (s, 2H, CH_2). ^{13}C NMR (75 MHz, $CDCl_3$) δ 151.6 (*C*H$_{pyrid}$), 151.1 (*C*H$_{pyrid}$), 150.6 (*C*H$_{pyrid}$), 150.0 (*C*H$_{pyrid}$), 147.8 ($C_{carbene}$-Pd), 147.2 ($C_{carbene}$-Pd) , 140.7 (*C*H$_{pyrene}$), 138.0 (C_{pyrid}), 137.9 (C_{pyrid}), 134.4 (C_{pyrene}), 134.3

(C_{pyrene}), 132.6 ($C_{biphenyl}$), 132.0 ($C_{biphenyl}$), 131.1 (CH_{pyrene}), 130.7 (CH_{pyrid}), 129.8 (CH_{pyrid}), 129.6 (CH_{pyrene}), 129.5 (CH_{pyrene}), 129.0 (CH_{pyrene}), 128.9 (CH_{pyrene}), 128.8 (CH_{pyrene}), 128.1 (CH_{pyrene}), 127.6 (C_{pyrene}), 127.2 (CH_{pyrene}) , 127.1 ($CH_{biphenyl}$), 127.0 ($CH_{biphenyl}$), 126.2 (C_{pyrene}), 125.7 (C_{pyrene}), 125.1 (C_{pyrene}), 125.0 (C_{pyrene}), 124.9 (CH_{pyrid}), 124.8 (CH_{pyrid}), 124.5 (CH_{pyrene}), 123.3 ($CH_{biphenil}$), 123.2 ($CH_{biphenil}$), 121.7 ($CH_{imidazole}$), 121.3 ($CH_{imidazole}$), 54.8 (CH_2),54.7 (CH_2),56.6 (CH_2), 53.3 (CH_2). Anal. Calcd. for $C_{64}H_{48}N_6Cl_2Br_4Pd_2$ (1522.4834): C, 51.10; H, 3.22; N, 5.58. Found: C, 51.01; H, 2.82; N, 5.54. Decomposition temperature: 225-227ºC.

^{1}H-^{1}H COSY NMR spectrum of 6 in $CDCl_3$

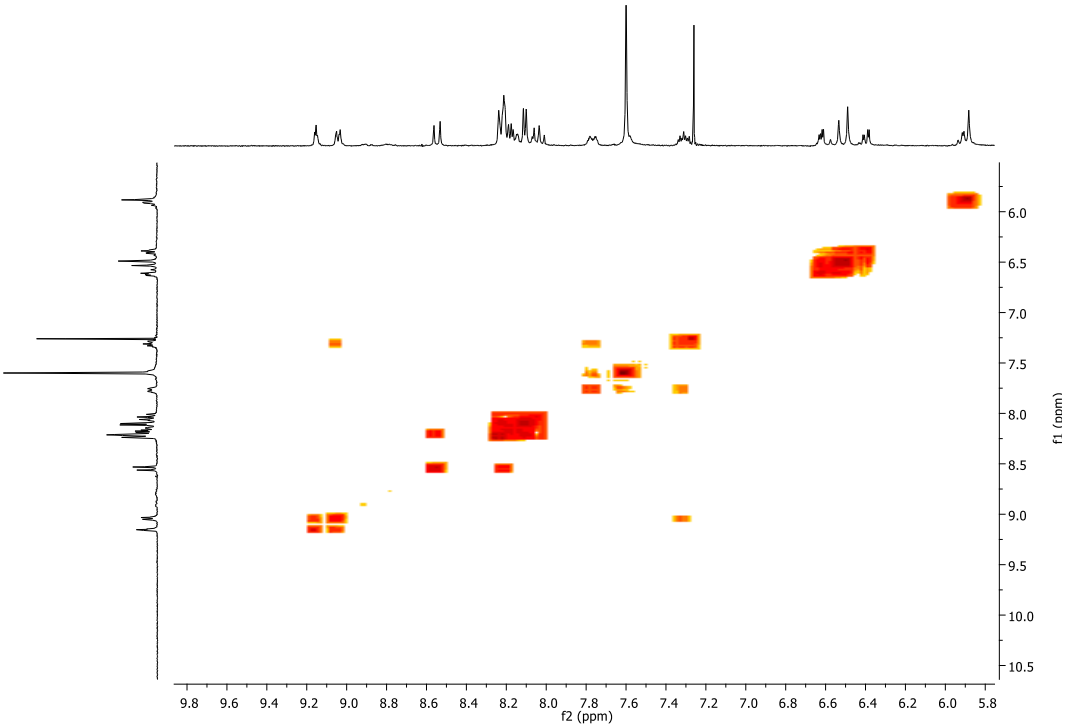

Figure 7.2. ^{1}H-^{1}H COSY NMR spectrum of **6** in $CDCl_3$

Synthesis of 7

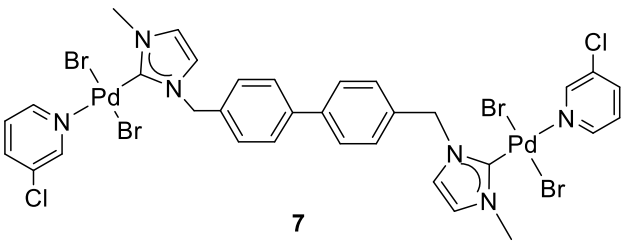

7

A mixture of **B** (80.0 mg, 0.19 mmol), palladium (II) chloride (70.6 mg, 0.39 mmol), K_2CO_3 (161.7 mg, 1.16 mmol) and KBr (100.0 mg) in 3-chloropyridine (2 mL) was stirred at 100 ºC for 8 h. The reaction was carried under N_2. The resulting suspension was cooled to room temperature and the solvent was removed under vacuum. The crude product was purified by column chromatography. The pure compound **7** was eluted with

dichloromethane: acetone (9:1) and precipitated in a mixture of dichloromethane/ hexane to give a yellow solid. Yield: 41% (85 mg). ^{1}H NMR (300 MHz, $CDCl_3$) δ 9.09 (d, $^{3}J_{HH}$ = 2.3 Hz, 2H, CH_{pyrid}), 8.99 (dd, $^{3}J_{HH}$= 5.5, 1.2 Hz, 2H, CH_{pyrid}), 7.81 – 7.68 (m, 2H, CH_{pyrid}), 7.59 (q, $^{3}J_{HH}$ = 8.5 Hz, 8H, C$H_{biphenilene}$), 7.30 (dd, $^{3}J_{HH}$= 5.5 Hz, 2H, CH_{pyrid}), 6.92 (d, $^{3}J_{HH}$ = 2.0 Hz, 2H, C*H*), 6.76 (d, $^{3}J_{HH}$ = 2.0 Hz, 2H, C*H*), 5.80 (s, 4H, CH_2), 4.14 (d, $^{3}J_{HH}$= 9.5 Hz, 6H, CH_3).^{13}C NMR (75 MHz, $CDCl_3$) δ 151.8 (*C*H$_{pyrid}$), 150.7 (*C*H$_{pyrid}$), 147.6 ($C_{carbene}$-Pd), 140.9 (C_{pyrid}), 138.1 (*C*H$_{pyrid}$), 134.5 ($C_{biphenil}$), 132.7 ($C_{biphenil}$), 129.7 (*C*H$_{biphenil}$), 127.7 (*C*H$_{biphenil}$), 125.0 (*C*H$_{pyrid}$), 123.9 (*C*H$_{imidazole}$), 121.6 (*C*H$_{imidazole}$), 54.8 (*C*H$_2$), 38.7 (*C*H$_3$). Anal.Calcd. for $C_{32}H_{30}N_6Br_4Cl_2Pd_2CHCl_3CHCl_3$ (1340.7381): C, 30.46; H, 2.41; N, 6.27. Found: C, 30.60; H, 2.81; N, 6.02. Electrospray MS (Cone 20V) (m/z, fragment): 907.8 [M-Br-C_5H_4NCl]$^{+}$. Melting point: 165-170 ºC

^{13}C {^{1}H} APT NMR spectrum of 7 in $CHCl_3$

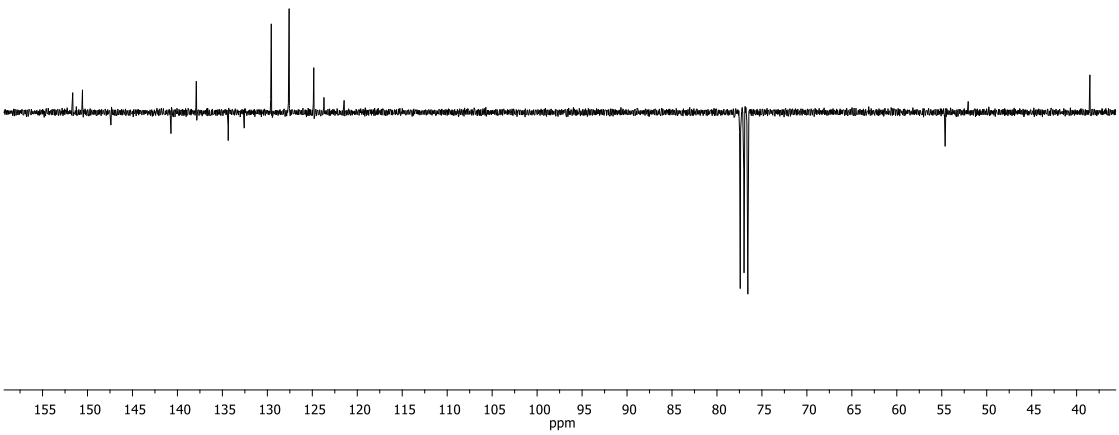

Figure 7.3. ^{13}C {^{1}H} APT NMR spectrum of **7** in $CDCl_3$

Synthesis of 8

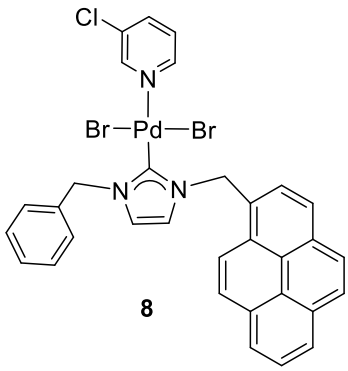

8

A mixture of 1-benzyl-3-(pyren-2-ylmethyl)-1H-imidazol-3-ium bromide (80.0 mg, 0.18 mmol), palladium (II) chloride (32.2 mg, 0.18 mmol), K_2CO_3 (75.2 mg, 0.54 mmol) and KBr (60.0 mg) in 3-chloropyridine (2 mL) was stirred at 100 ºC for 6 h. The reaction was carried under N_2. The resulting suspension was cooled to room temperature and the solvent was removed under vacuum. The crude product was purified by column chromatography. The pure compound **8** was eluted with dichloromethane: acetone (9:1) and precipitated in a mixture of dichloromethane/ hexane to give a yellow solid. Yield: 61% (83 mg). ^{1}H NMR (300 MHz, $CDCl_3$) δ 9.16 (d, $^3J_{HH}$=2.3 Hz, 1H, CH_{pyrid}), 9.09 (m, 1H, CH_{pyrid}), 8.54 (d, $^3J_{HH}$= 9.3 Hz, 1H, CH_{pyrene}), 8.23 -8.02 (m, 8H, CH_{pyrene}), 7.78 (s, 1H, CH_{pyrid}), 7.75 (d, $^3J_{HH}$= 1.3 Hz, 1H, CH_{pyrid}), 7.54 (d, $^3J_{HH}$= 6.5 Hz, 2H, CH_{Ph}), 7.44 – 7.28 (m, 4H, CH_{Ph} and CH_{pyrid}), 6.56 (d, $^3J_{HH}$= 2.0 Hz, 1H, C$H_{imidazole}$), 6.48 (s, 2H, CH_2), 6.36 (d, $^3J_{HH}$= 2.1 Hz, 1H, C$H_{imidazole}$), 5.85 (s, 2H, CH_2). ^{13}C NMR (75 MHz, $CDCl_3$) δ 151.9 (*C*H$_{pyrid}$), 150.8 (*C*H$_{pyrid}$), 147.3 (*C*$_{carbene}$-Pd), 138.1 *C*H$_{pyrid}$), 135.2 (*C*H$_{pyrid}$), 132.8 (*C*$_{pyrene}$), 132.3 (*C*$_{pyrene}$), 131.3 (*C*$_{pyrene}$), 130.9 (*C*$_{pyrene}$), 130.1 (*C*$_{pyrene}$), 129.3 (*C*H$_{pyrine}$), 129.2 (*C*H$_{phenylene}$), 129.1 (*C*H$_{pyrene}$), 129.1 (*C*H$_{pyrene}$), 128.7 (*C*H$_{pyrene}$), 128.4 (*C*H$_{pyrene}$), 127.4 (*C*H$_{pyrene}$), 127.2 (*C*$_{pyrene}$), 126.4 (*C*H$_{pyrene}$), 125.9 (*C*H$_{pyrene}$), 125.9 (*C*H$_{pyrid}$), 125.2 (*C*$_{pyrene}$), 125.1 (*C*H$_{phenylene}$), 125.0 (*C*H$_{pyrene}$), 124.7 (*C*$_{phenylene}$), 123.6 (*C*H$_{phenylene}$), 121.8 (*C*H$_{imidazole}$), 121.5(*C*H$_{imidazole}$), 55.5 (*C*H$_2$), 53.9 (*C*H$_2$). Anal. Calcd. for $C_{32}H_{24}N_3Br_2ClPd$ (752.2341): C, 51.10; H, 3.22; N, 5.58. Found: C, 51.93; H 2.60; N, 5.31. Although these results are slightly outside the range viewed as establishing analytical purity, they are provided to illustrate the best values obtained. Electrospray MS (Cone 20V) (m/z, fragment): 672.1 $[M\text{-}Br]^+$. Decomposition temperature: 153-155 ºC

^{1}H-^{1}H COSY NMR spectrum of 8 in $CDCl_3$

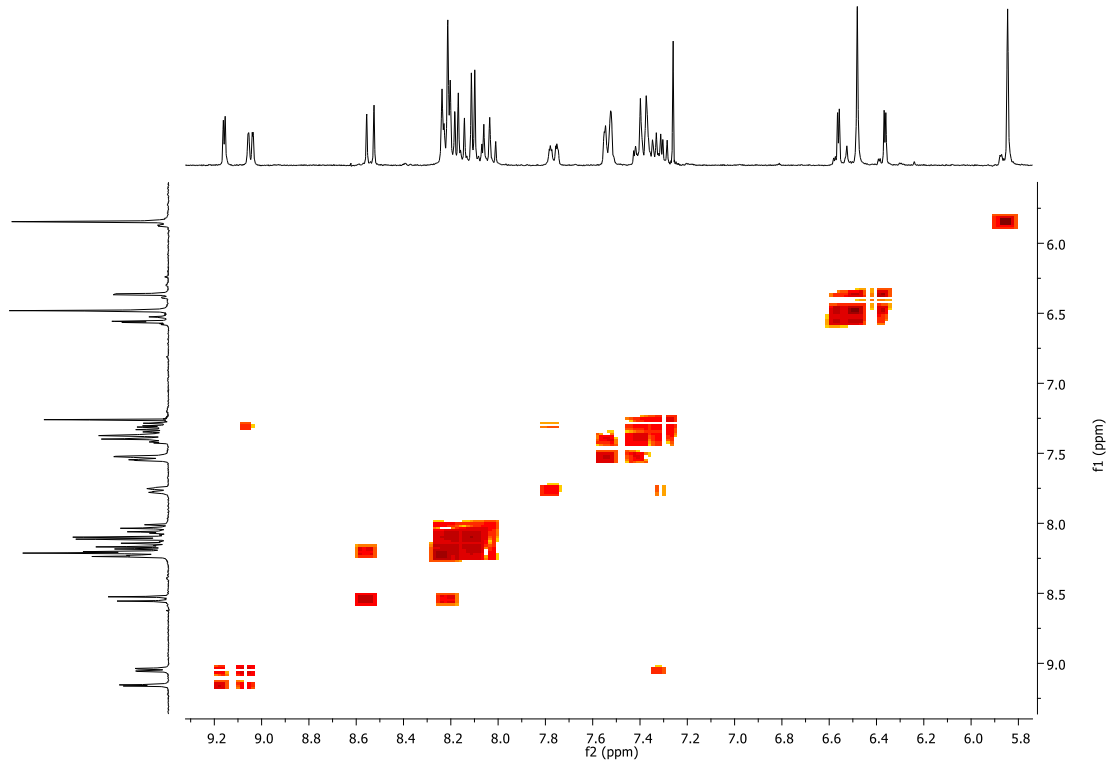

Figure 7.4. ^{1}H-^{1}H COSY NMR spectrum of **8** in $CDCl_3$

^{13}C {^{1}H} APT NMR spectrum of 8 in $CDCl_3$

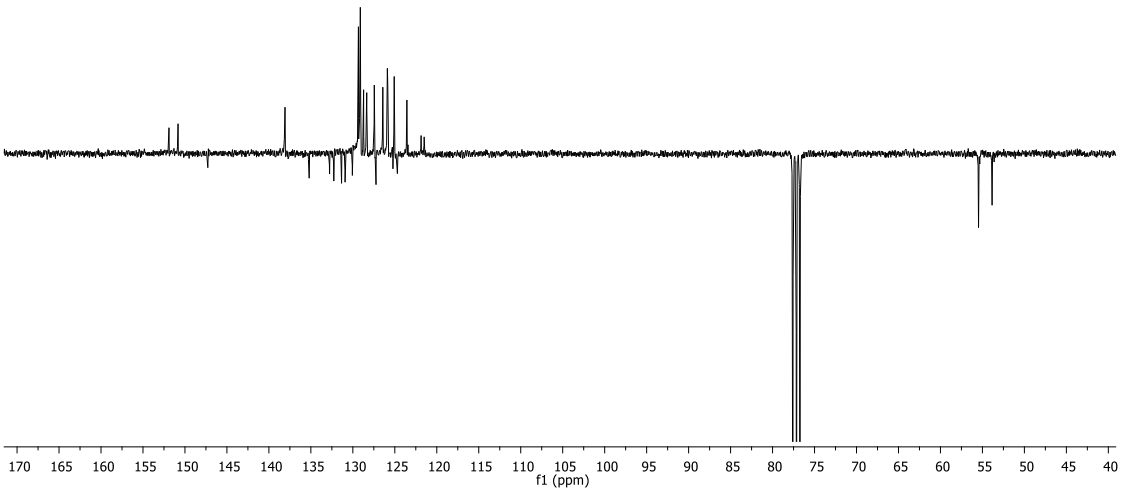

Figure 7.5. ^{13}C {^{1}H} APT NMR spectrum of **8** in $CDCl_3$

Synthesis of 9

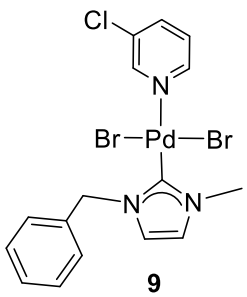

9

A mixture of 1-benzyl-3-methyl-1H-imidazol-3-ium bromide (80.0 mg, 0.31 mmol), Palladium (II) chloride (56.3 mg, 0.31 mmol), K_2CO_3 (129.5 mg, 0.93 mmol) and KBr (100.0 mg) in 3-chloropyridine (2 mL) was stirred at 100 ºC for 8 h. The reaction was carried under N_2. The resulting suspension was cooled to room temperature and the solvent was removed under vacuum. The compound **9** was washed with hexane and collected by filtration. Yield: 51% (85 mg). ^{1}H NMR (300 MHz, $CDCl_3$) δ 9.09 (d, $^3J_{HH}$= 2.2 Hz, 1H, CH_{pyrid}), 8.99 (d, $^3J_{HH}$= 5.4 Hz, 1H, CH_{pyrid}), 7.76 (d, $^3J_{HH}$= 8.2 Hz, 1H, CH_{pyrid}), 7.50 (d, $^3J_{HH}$ = 6.3 Hz, 2H, C$H_{phenylene}$), 7.38 (d, $^3J_{HH}$= 7.0 Hz, 3H, C$H_{phenylene}$), 7.34 – 7.29 (m, 1H, CH_{pyrid}), 6.90 (s, 1H, C$H_{imidazole}$), 6.70 (d, $^3J_{HH}$= 1.8 Hz, 1H, C$H_{imidazole}$), 5.76 (s, 2H, CH_2), 4.14 (d, $^3J_{HH}$ = 9.4 Hz, 3H, CH_3). ^{13}C NMR (75 MHz, $CDCl_3$) δ 151.6 (*C*H$_{pyrid}$), 150.6 (*C*H$_{pyrid}$), 147.6 ($C_{carbene}$-Pd), 137.9 (*C*H$_{pyrid}$), 135.0 (C_{pyrid}), 132.6 ($C_{phenylene}$), 129.1 (*C*H$_{phenylene}$), 128.9 (*C*H$_{phenylene}$), 128.5 (*C*H$_{phenylene}$), 124.8 (*C*H$_{pyrid}$), 123.6 (*C*H$_{imidazole}$), 121.4 (*C*H$_{imidazole}$), 55.0 (*C*H$_2$), 38.5 (*C*H$_3$). Anal. Calcd. for $C_{16}H_{16}N_3Br_2ClPd$ (551.9993): C, 34.81; H, 2.92; N, 7.61. Found: C, 34.7; H, 3.4; N, 7.1. Electrospray MS (Cone 20V) (m/z, fragment): 531.1 [M-Br-C_5H_4NCl]$^+$ Melting point: 145-150 ºC.

Synthesis of 10

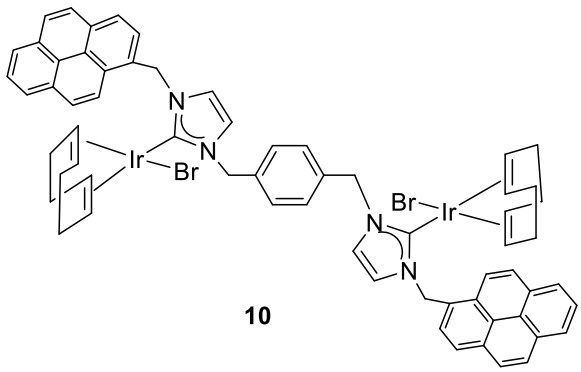

10

A mixture of **C** (80.0 mg, 0.10 mmol), $[IrCl(COD)]_2$ (64.5 mg, 0.10 mmol), K_2CO_3 (82.9 mg, 0.6 mmol) and KBr (70.0 mg) in THF/DMF (10:3 mL) was stirred at 75 ºC for 8 h. The reaction was carried under N_2. The resulting suspension was cooled to room temperature and the solvent was removed under vacuum. The crude product was purified by column chromatography. The pure compound **10** was eluted with dichloromethane: ethyl acetate (8:2) and precipitated in a mixture of dichloromethane/hexane to give a yellow solid. Yield: 65% (90.2 mg). ^{1}H NMR (300 MHz, $CDCl_3$) δ 8.48 (dd, $^3J_{HH}$= 9.3, 3.2 Hz, 2H, CH_{pyrene}), 8.23 – 7,98 (m, 8H, CH_{pyrene}), 8.09 – 7.98 (m, 8H, CH_{pyrene}), 7.43 (s, 4H, CH_{xylyl}), 6.58

(m, 4H, C$H_{imidazole}$ andCH_2), 6.44 (d, $^2J_{HH}$= 8.0 Hz, 2H, C$H_{imidazole}$), 6.14 (m, 2H, CH_2), 5.85 (dd, $^2J_{HH}$=14.6, 11.0 Hz, 2H, CH_2), 5.59 (dd, $^2J_{HH}$= 15.1, 9.5 Hz, 2H, CH_2), 4.80 (s, 4H, CH_{COD}), 3.18 (s, 2H, CH_{COD}), 3.06 (s, 2H, CH_{COD}), 2.12 (m, 8H, C$H_{2,COD}$), 1.72 (m, 8H, (C$H_{2,COD}$), 1.48 (m, 8H, (C$H_{2,COD}$). ^{13}C NMR (75 MHz, $CDCl_3$) δ 180.8 ($C_{carbene}$-Ir), 136.3 (Pyr), 131.6 (Pyr), 131.2 (Pyr), 130.7 (Pyr), 129.4 (Pyr), 128.7 (Pyr), 128.4 (Pyr), 127.9 (Pyr), 127.57 (Pyr), 127.23 (Pyr), 126.2 ($C_{Phenylene}$), 125.6 ($CH_{Phenylene}$), 124.8($CH_{imidazole}$), 124.5, (Pyr), 123.0 ($CH_{imidazole}$), 120.6(Pyr), 120.1 (Pyr), 84.8 (CH_{COD}), 84.6 (CH_{COD}), 54.0 (CH_2), 53.0 ($CH_{2,COD}$), 52.6 ($CH_{2,COD}$), 52.2 (CH_2), 33.3 ($CH_{2,COD}$), 29.7 ($CH_{2,COD}$). Anal. Calcd. for $C_{64}H_{58}N_4Br_2Ir_2 \cdot CHCl_3$ (1904.9247): C, 42.87; H, 3.28; N, 2.90. Found: C, 42.56; H, 2.75; N, 3.14. Electrospray MS (Cone 20V) (m/z, fragment): 1347 $[M\text{-}Br]^+$.

^{1}H-^{1}H COSY NMR spectrum of 10 in $CDCl_3$

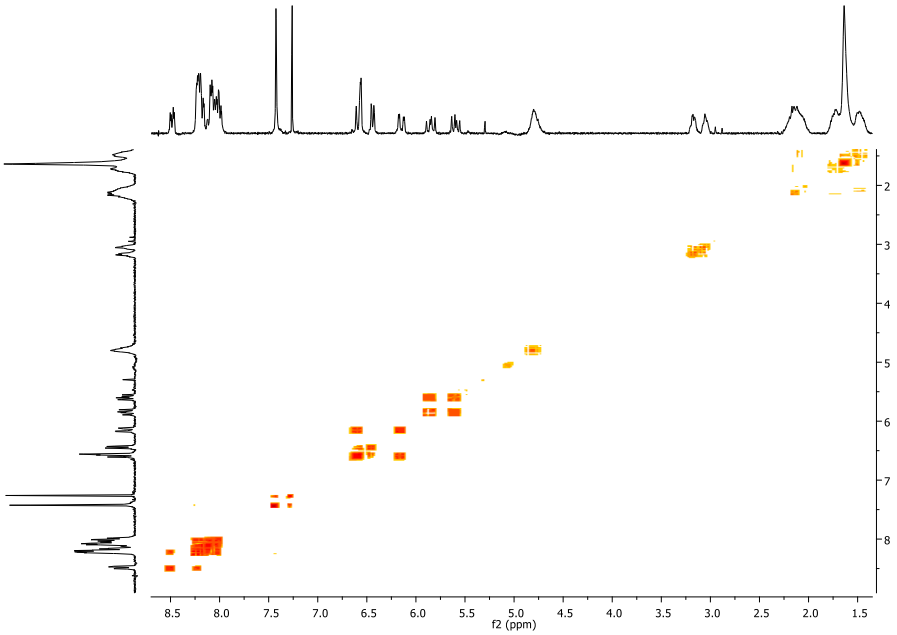

Figure 7.6. ^{1}H-^{1}H COSY NMR spectrum of **10** in $CDCl_3$

Synthesis of 11

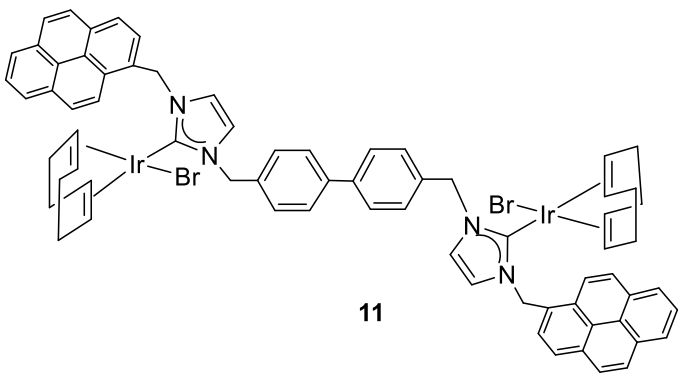

11

A mixture of **D** (80.0 mg, 0.09 mmol), $[IrCl(COD)]_2$ (67.2 mg, 0.09 mmol), K_2CO_3 (82.9 mg, 0.6 mmol) and KBr (70.0 mg) in THF/DMF (10:3 mL) was stirred at 75 ºC for 8 h. The reaction was carried under N_2. The resulting suspension was cooled

to room temperature and the solvent was removed under vacuum. The crude product was purified by column chromatography. The pure compound **11** was eluted with dichloromethane: ethyl acetate (8:2) and precipitated in a mixture of dichloromethane/hexane to give a yellow solid. Yield: 66% (87.1 mg). ^{1}H NMR (500 MHz, $CDCl_3$) δ 8.50 (d, $^{3}J_{HH}$=9.2 Hz, 2H, CH_{pyrene}), 8.23 – 8.02 (m, 16H, CH_{pyrene}), 7.58 (d, $^{3}J_{HH}$= 7.9 Hz, 4H C$H_{biphenylene}$), 7.47 (d, $^{3}J_{HH}$=7.9 Hz, 4H, C$H_{biphenylene}$), 6.69 – 6.54 (m, 4H, C$H_{imidazole}$ and CH_2), 6.46 (s, 2H, C$H_{imidazole}$), 6.17 (d, 2H, CH_2), 5.87 (d, 2H, CH_2), 5.67 (d, 2H, CH_2), 4.82 (m, 4H,CH_{COD}), 3.21 (m, 2H, CH_{COD}), 3.09 (m, 2H, CH_{COD}), 2.35 – 1.97 (m, 8H, C$H_{2,COD}$), 1.71 (m, 4H, C$H_{2,COD}$), 1.37 – 1.23 (m, 2H, C$H_{2,COD}$), 0.89 (m, 2H, C$H_{2,COD}$). ^{13}C NMR (75 MHz, $CDCl_3$) δ 180.8 ($C_{carbene}$-Ir), 136.3 (Pyr), 131.6 (Pyr), 131.2 (Pyr), 130.7 (Pyr), 129.4 (Pyr), 128.7 (Pyr), 128.4 (Pyr), 127.9 (Pyr), 127.57 (Pyr), 127.23 (Pyr), 126.2(Pyr), 125.6 (Pyr), 124.8(Pyr), 124.5 (C$H_{biphenilene}$), 123.0 ($C_{biphenilene}$), 120.6(C$H_{imidazole}$), 120.1 (C$H_{imidazole}$), 84.8 (CH_{COD}), 84.6 (CH_{COD}), 54.0 (CH_2), 53.0 (C$H_{2,COD}$), 52.6 (C$H_{2,COD}$), 52.2 (CH_2), 33.3 (C$H_{2,COD}$), 29.7 (C$H_{2,COD}$). Anal. Calcd. for $C_{70}H_{64}N_4Br_2Ir_2CHCl_3$ (1622.8877): C, 52.55; H, 3.91; N, 3.45. Found: C, 52.1; H, 3.5; N, 3.4. Electrospray MS (Cone 20V) (m/z, fragment): 1464.0 $[M\text{-}Br+MeCN]^+$.

Synthesis of 12

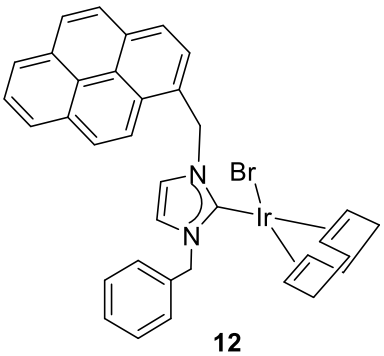

12

A mixture of 1-benzyl-3-(pyren-2-ylmethyl)-1H-imidazol-3-ium bromide (70.0 mg, 0.16 mmol), $[IrCl(COD)]_2$ (53.73 mg, 0.08 mmol), K_2CO_3 (67.0 mg, 0.48 mmol) and KBr (70.0 mg) in THF/DMF (7:2 mL) was stirred at 75 ºC for 8 h. The reaction was carried under N_2. The resulting suspension was cooled to room temperature and the solvent was removed under vacuum. The pure compound **12** was precipitated in a mixture of dichloromethane/ hexane to give a yellow solid. Yield: 54% (65.0 mg). ^{1}H NMR (300 MHz, $CDCl_3$) δ 8.50 (d, $^{3}J_{HH}$= 9.2 Hz, 1H, CH_{pyrene}), 8.31 – 8.18 (m, 4H, CH_{pyrene}), 8.08 (m, 4H, CH_{pyrene}), 7.58 – 7.32 (m, 5H, CH_{Ph}), 6.61 (d, $^{2}J_{HH}$ = 14.4 Hz, 2H, CH_2 and C$H_{imidazole}$), 6.46 (s, 1H, C$H_{imidazole}$), 6.16 (d,$^{2}J_{HH}$= 14.8 Hz , 1H, CH_2) 5.79 (d, $^{2}J_{HH}$= 15.0 Hz, 1H, CH_2), 5.68 (d, $^{2}J_{HH}$= 14.8 Hz, 1H, CH_2), 4.82 (s, 2H, CH_{COD}), 3.21 (s, 1H, CH_{COD}), 3.09 (s, 1H, CH_{COD}), 2.15 (m, 4H, C$H_{2,COD}$), 1.6 (m, 4H, C$H_{2,COD}$). ^{13}C NMR (126 MHz, $CDCl_3$) δ 180.9 ($C_{carbene}$-Ir), 136.4 (Pyr), 131.8 (Pyr), 131.3 (Pyr), 130.9 (Pyr), 129.6

(Pyr), 198.0 (Pyr), 128.9 (Pyr), 128.7 (Pyr), 128.4 (Pyr), 128.2 (Pyr), 128.1 (Pyr), 127.7 (Pyr), 127.4 (Pyr), 126.3 (Pyr), 125.7 (Pyr), 125.7 (Pyr), 125.1 (C_{Ph}), 125.0 (CH_{Ph}), 124.7 (CH_{Ph}), 123.2 (CH_{Ph}), 120.6 ($CH_{imidazole}$), 120.3 ($CH_{imidazole}$), 84.8 (CH_{COD}), 84.8 (CH_{COD}), 54.6 (CH_2), 53.0 (CH_2), 52.7 ($CH_{,COD}$), 52.4 ($CH_{,COD}$), 33.4 ($CH_{2,COD}$), 29.8 ($CH_{2,COD}$). Anal. Calcd. for $C_{35}H_{32}N_2BrIrH_2O$ (770.7783): C, 54.74; H, 4.44; N, 3.50. Found: C, 54.53; H, 4.44; N, 3.63. Electrospray MS (Cone 20V) (m/z, fragment): 671.2$[M\text{-}Br]^+$.

Synthesis of 13

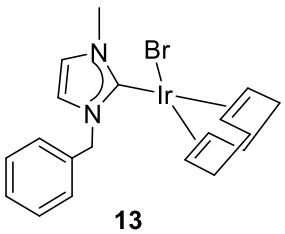

13

A mixture of 1-benzyl-3-methyl-1H-imidazol-3-ium bromide (93.5 mg, 0.39 mmol), $[IrCl(COD)]_2$ (133.5 mg, 0.2 mmol), K_2CO_3 (165.9 mg, 0.48 mmol) and KBr (80.0 mg) in THF/DMF (7:2 mL) was stirred at 75 ºC for 8 h. The reaction was carried under N_2. The resulting suspension was cooled to room temperature and the solvent was removed under vacuum. The pure compound **13** was precipitated in a mixture of dichloromethane/ hexane to give a yellow solid. Yield: 46% (100.0 mg). ^{1}H NMR (300 MHz, $CDCl_3$) δ 7.39 – 7.28 (m, 4H. CH_{Ph}), 6.80 (m, 1H, C$H_{imidazole}$), 6.66 (m, 1H, C$H_{imidazole}$), 5.75 (d, $^2J_{HH}$ = 14.8 Hz, 1H, CH_2), 5.52 (d, $^2J_{HH}$=14.8 Hz, 1H, CH_2), 4.69 (s, 2H, CH_{COD}), 3.96 (s, 3H, CH_3), 3.03 (m, 1H, CH_{COD}), 2.90 (m, 1H, CH_{COD}), 2.27 – 2.12 (m, 2H, C$H_{2,COD}$), 2.12 – 1.99 (m, 1H, C$H_{2,COD}$), 1.82 – 1.68 (m, 2H, C$H_{2,COD}$), 1.62 (s, 1H, C$H_{2,COD}$), 1.60 – 1.51 (m, 1H, C$H_{2,COD}$), 1.43 (m, 1H, C$H_{2,COD}$). ^{13}C NMR (75 MHz, $CDCl_3$) δ 180.9 ($C_{carbene}$-Ir), 136.5 (C_{Ph}), 129.0 (CH_{Ph}), 128.4 (CH_{Ph}), 128.3 (CH_{Ph}), 122.3 ($CH_{imidazole}$), 120.2 ($CH_{imidazole}$), 84.5 (CH_{COD}), 84.2 (CH_{COD}), 54.21 (CH_3), 52.58 (CH_2), 52.4 (CH_3), 37.6 (CH_{COD}), 33.8 (CH_{COD}), 33.2 (CH_{COD}), 31.1 (CH_{COD}), 30.2 (CH_{COD}), 29.7 (CH_{COD}). Anal. Calcd. for $C_{19}H_{25}N_2BrIr\cdot H_2O$ (571.5515): C, 40.00; H, 4.70; N, 5.00. Found: C, 39.51; H, 4.05; N, 4.63. Electrospray MS (Cone 20V) (m/z, fragment): 473.63$[M\text{-}Br]^+$.

Synthesis of 14

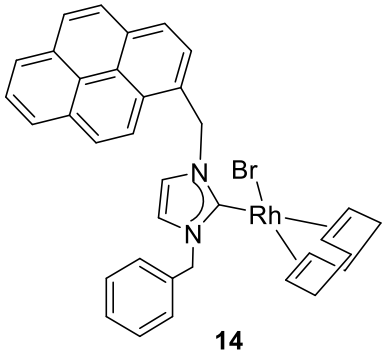

14

A mixture of 1-benzyl-3-(pyren-2-ylmethyl)-1H-imidazol-3-ium bromide (70.0 mg, 0.16 mmol), $[RhCl(COD)]_2$ (39.4 mg, 0.08 mmol), K_2CO_3 (67.0 mg, 0.48 mmol) and KBr (70.0 mg) in THF/DMF (7:2 mL) was stirred at 75 ºC for 8 h. The reaction was carried under N_2. The resulting suspension was cooled to room temperature and the solvent was removed under vacuum. The pure compound **14** was precipitated in a mixture of dichloromethane/hexane to give a yellow solid. Yield: 56% (60.0 mg). ^{1}H NMR (300 MHz, $CDCl_3$) δ 8.53 (d, $^3J_{HH}$ = 9.3 Hz, 1H, CH_{pyrene}), 8.32 – 8.14 (m, 4H, CH_{pyrene}), 8.06 (m, 4H, CH_{pyrene}), 7.37 (m, 5H, CH_{Ph}), 6.69 (d, $^2J_{HH}$ = 14.8 Hz, 1H, CH_2), 6.59 (d, $^2J_{HH}$ = 1.9 Hz, 1H, C$H_{imidazole}$), 6.46 (d, $^2J_{HH}$= 2.0 Hz, 1H, C$H_{imidazole}$), 6.33 (d, $^2J_{HH}$ = 14.8 Hz, 1H, CH_2), 5.87 (dd, $^2J_{HH}$= 2.6 Hz, 2H,CH_2), 5.23 (s, 2H, CH,CH_{COD}), 3.58 (m, 1H, CH_{COD}), 3.48 (m, 1H, CH_{COD}), 2.47 – 2.12 (m, 4H, C$H_{2,COD}$), 1.89 (m, 4H, C$H_{2,COD}$). ^{13}C NMR (75 MHz, $CDCl_3$) δ 183.6 (d, $^1J_{Rh-C}$=50Hz, $C_{carbene}$-Rh),140.5 (Pyr), 135.9 (Pyr), 131.8 (Pyr), 131.4 (Pyr), 131.0 (Pyr), 129.6 (Pyr), 129.0 (Pyr), 129.0 (Pyr), 128.9 (Pyr), 128.1 (Pyr), 127.7 (Pyr), 127.4 (Pyr), 126.4 (Pyr), 125.9 (Pyr), 125.8 (Pyr), 125.1 (C_{Ph}), 125.1 (C_{Ph}), 124.7 (CH$_{Ph}$), 123.3 (CH$_{Ph}$), 121.3 (CH$_{imidazole}$), 120.8 (CH$_{imidazole}$), 98.6 (CH$_{COD}$), 98.5 (CH$_{COD}$), 98.4 (CH$_{COD}$), 69.9 (CH$_{COD}$), 69.7 (CH$_{COD}$), 69.6 (CH$_{COD}$), 69.4 (CH$_{COD}$), 54.7 (CH$_2$), 52.8 (CH$_2$), 32.9 (CH$_{2,COD}$), 32.9 (CH$_{2,COD}$), 29.2 (CH$_{2,COD}$). Anal. Calcd. for $C_{35}H_{32}N_2BrRh{\cdot}CHCl_3$ (782.8291): C, 55.23; H, 4.24; N, 3.57. Found: C, 55.27; H, 4.15; N, 3.29. Electrospray MS (Cone 20V) (m/z, fragment): 583.2 $[M\text{-}Br]^+$.

Preparation of rGO-12

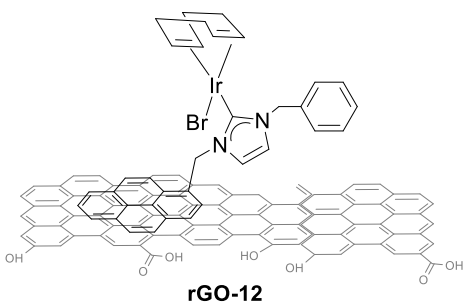

rGO-12

In a round-bottom flask were introduced 150 mg of rGO and 10 mL of CH_2Cl_2. The suspension was sonicated for 30 min. Then, 20.0 mg of compound **12** was added. The suspension was stirred at room temperature for 12 h until the solution become clear. The black solid was filtrated and washed with 2 × 25 mL of CH_2Cl_2, affording the resulting product as a black solid. The filtrates were combined and evaporated to dryness under reduced

pressure. Unsupported compound **12** was analyzed by ^{1}H NMR using anisole as internal standard. Integration of the characteristic signal of anisole (−OMe) versus (CH_2-pyrene) reveals the amount complex that has been deposited on the rGO. The exact amount of complex supported was determined by ICP-MS analysis.

Preparation of rGO-10

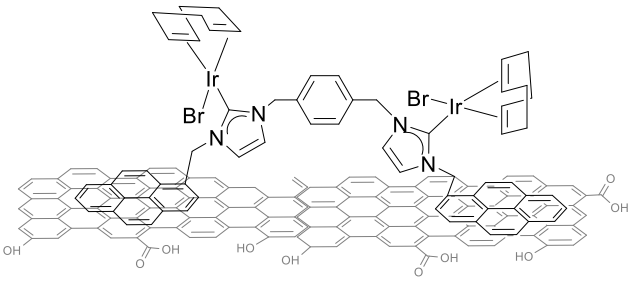

rGO-10

In a round-bottom flask were introduced 240.0 mg of rGO and 10 mL of CH_2Cl_2. The suspension was sonicated for 30 min. Then, 27 mg of compound **10** was added. The suspension was stirred at room temperature for 12 h until the solution become clear. The black solid was filtrated and washed with 2 × 25 mL of CH_2Cl_2, affording the resulting product as a black solid. The filtrates were combined and evaporated to dryness under reduced pressure. Unsupported compound **10** was analyzed by ^{1}H NMR using anisole as internal standard. Integration of the characteristic signal of anisole (−OMe) versus (CH_2-pyrene) reveals the amount complex and Ir that has been deposited on the rGO. The exact amount of Ir supported was determined by ICP-MS analysis.

7.2.3 Synthesis and characterization of compounds of Chapter 5

Ligand **E** (resorcinarene-octaamino-based cavitand) was prepared according to literature procedures.[3]

Ligand **F** (tetra-benzimidazole-based cavitand) was prepared according to literature procedures.[4]

Synthesis of 15

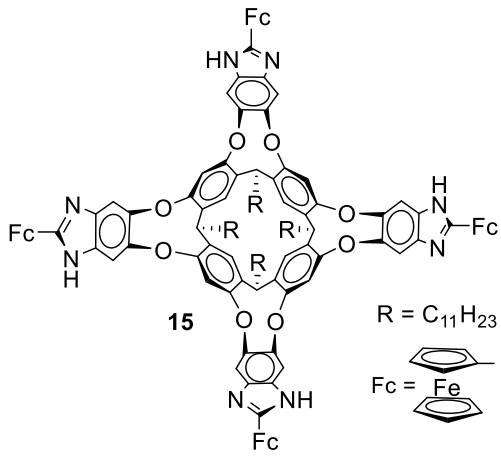

A mixture of **E** (211.7 mg, 0.139 mmol) ferrocene-carboxaldehyde (119.8 mg, 0.56 mmol) in a mixed of CH_2Cl_2:CH_3OH (15:10 mL) was stirred at 65 ºC for 24 h. The final suspension was cooled to room temperature and solvent were removed. Then, acetonitrile (10 mL) was added and stirred at room temperature for 1 h. The resulting brown precipitate was

collected by filtration. The crude product was eluted in a column chromatography of silica gel with dichloromethane: acetone (9:1) to give compound **15** as a red solid. Yield: 65% (208 mg). ^{1}H NMR (500 MHz, benzene-d^6) δ 7.81 (s, 8H, C$H_{benzimidazole}$), 7.70 (s, 4H, C$H_{benzene}$), 7.57 (s, 4H, C$H_{benzene}$), 6.44 (t, $^{3}J_{HH}$ = 8.2 Hz, 4H, CH), 5.09 (s, 4H, CH_{fc}), 4.17 (s, 12H, CH_{fc}), 3.89 (s, 20H, CH_{fc}), 2.55 (s, 8H, CH_2), 1.64 (s, 8, CH_2), 1.56 (d, $^{3}J_{HH}$ = 5.8 Hz, 56H, CH_2), 0.99 (t, $^{3}J_{HH}$ = 6.3 Hz, 12H, CH_3). ^{13}C NMR (75 MHz, benzene-d^6) δ 181.6 (N*C*N), 156.7 (*C*$_{benzimidazole}$), 149.7 (*C*H$_{benzimidazole}$), 135.7 (*C*$_{benzene}$), 117.6 (*C*H$_{benzene}$), 69.7 (*C*$_{fc}$), 67.7 (*C*$_{fc}$), 33.8 (*C*H$_2$), 32.9 (*C*H$_2$), 32.0 (*C*H$_2$), 29.8 (*C*H$_2$), 29.5 (*C*H$_2$), 28.4 (*C*H$_2$), 22.8 (*C*H$_2$), 18.3 (*C*H$_2$), 14.0 (*C*H$_2$), 1.0 (*C*H$_3$). Anal.Calcd. for $C_{140}H_{152}O_8N_8Fe_4$·(4H_2O) (2369.9587): C, 70.94; H, 6.80; N, 4.73. Found: C, 71.21; H, 7.40; N, 4.8. ESI-TOF-MS (positive mode): $[M + 3H]^{3+}$ (m/z 767.0), $[M + 2H]^{2+}$ (m/z 1149.9); $[M + H]^{+}$ (m/z 2298.9).

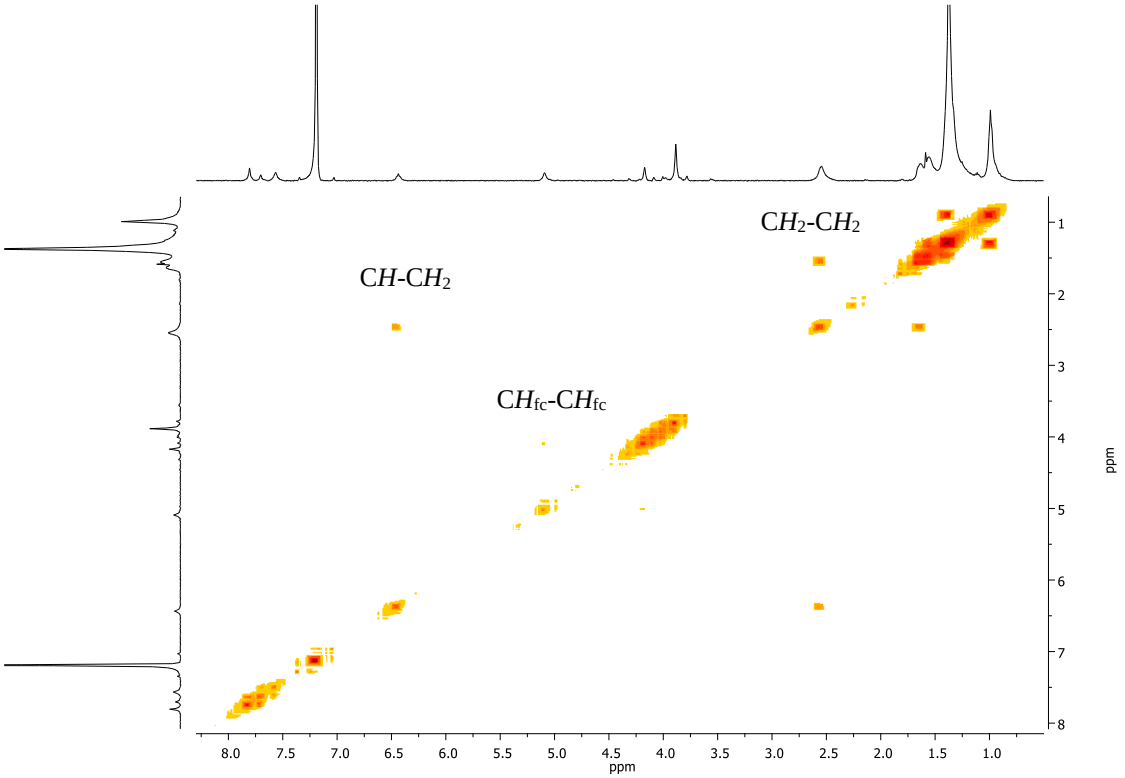

Figure 7.7. ^{1}H-^{1}H COSY spectrum of compound **15** in benzene-d^6

Synthesis of 16I₄

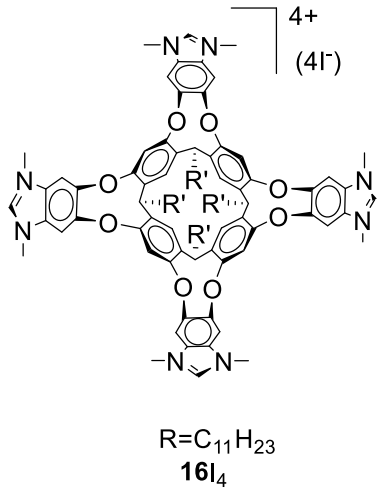

A mixture of tetrabenzimidazole cavitand **F** (480.0 mg, 0.31 mmol) and NaOH (62.5 mg, 1.56 mmol) was stirred in 2 mL of DMSO at room temperature for 2 h. After this time CH_3I (86 μL, 1.24 mmol) was added and the mixture was stirred at 37 ºC for 8 h. Then, CH_3I (860 μL, 12.4 mmol) was added and the mixture was stirred at 100 ºC for 8 h. The final suspension was cooled to room temperature and the crude salt was precipitated in methanol (50 mL). The resulting brown precipitate was collected by filtration, washed with methanol and dissolved in acetone. The solvent was removed under vacuum and the solid was precipitated in methanol and collected by filtration. Compound **16I₄** was obtained as a brown-red solid in a 44% yield (300.1 mg). ^{1}H NMR (500 MHz, DMSO-d^6) δ 9.60 (s, 4H CH_{NHC}), 8.63 (s, 8H, C$H_{\text{benzimidazole}}$), 7.98 (s, 4H, CH_{benzene}), 7.81 (s, 4H, CH_{benzene}), 5.65 (t, 4H,CH), 3.92 (s, 24H, CH_3), 2.43 (m, 8H,CH_2), 1.45 (m, 8H, CH_2), 1.26 (m, 64H, CH_2), 0.87 (t, 12H, CH_3). HRMS ESI-TOF-MS (positive mode): 419.5 $[M-4I]^+$, 601.7 $[M-3I]^{3+}$, 966.0 $[M-2I]^{2+}$.

Synthesis of [16][PF₆]₄

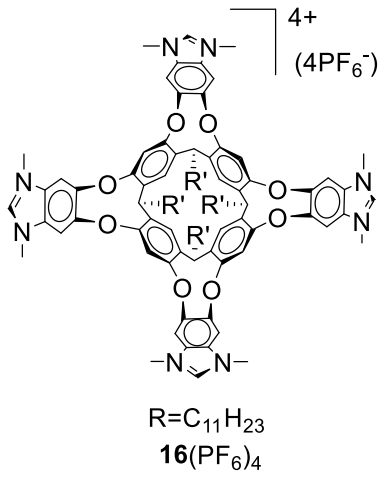

A mixture of compound **16I₄** (90.5 mg, 0.041mmol) was dissolved in acetone (30 mL) and mixed with a solution of NH_4PF_6 (35.2 mg, 0.22 mmol) in CH_3OH (10mL). The reaction was stirred at 40 ºC for 24 h. The final suspension was cooled to room temperature and a white precipitate appears after few minutes. This precipitate was filtered, washed with CH_3OH and dried. This compound **[16][PF₆]₄** was obtained in 86% of yield (80.0 mg). ^{1}H NMR (500 MHz, DMSO-d^6) δ 9.57 (s, 4H CH_{NHC}), 8.63 (s, 8H, CH_{aromatic}), 7.99 (s, 4H, CH_{aromatic}), 7.80 (s, 4H, CH_{aromatic}), 5.66 (t, 4H,CH), 3.91 (s, 24H, CH_3), 2.42 (m, 8H,CH_2), 1.44 (m, 8H,CH_2), 1.25 (m, 64H,CH_2), 0.86 (m, 12H,CH_3). ^{13}C NMR (125 MHz, DMSO-d^6) δ 154.8 (N*C*N), 151.7, 144.8, 136.4, 129.4, 126.0, 115.8, 109.9 (aromatic *C* and *C*H from benzimidazole and benzene groups), 49.1 (*C*H_3), 34.0 (*C*H), 31.8 (*C*H_2), 31.7 (*C*H_2),

29.7 (*C*H_2), 29.6 (*C*H_2), 29.5 (*C*H_2), 29.2 (*C*H_2), 28.2 (*C*H_2), 22.6 (*C*H_2), 14.4 (-CH_2-*C*H_3). Electrospray MS (Cone 20V) (m/z, fragment): 419.7 $[M\text{-}4PF_6]^+$, 607.8 $[M\text{-}3PF_6]^{3+}$.

Synthesis of G

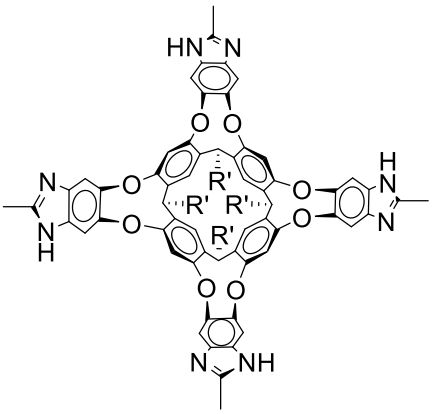

G

A mixture of octaamino-cavitand **E** (418.0 mg, 0.28 mmol) and acetic acid (10 mL) was stirred at 100 ºC for 48 h. After this time the reaction was cooled to room temperature. A saturate solution of K_2CO_3 (aq) was added to the mixture in an ice-water bath until pH=8. A white precipitate appears after few minutes. The precipitate was filtered, washed with water and dried. The crude product was purified by column chromatography. The pure compound was eluted with dichloromethane: methanol (9:1) and precipitated in a mixture of methanol. Compound **G** was obtained in 68% yield (303.8 mg). ^{1}H NMR (500 MHz, CD_2Cl_2-CD_3OD) δ 7.45 (s, 8H, C*H*$_{benzimidazole}$), 7.44 (s, 4H, C*H*$_{benzene}$), 7.19 (s, 4H, C*H*$_{benzene}$), 5.65 (m, 4H, C*H*), 2.37 (s, 12H, C*H*$_3$), 2.19 (m 8H, C*H*$_2$), 1.40 (m, 8H, C*H*$_2$), 1.22 (m, 64H, C*H*$_2$), 0.83 (t, 12H, C*H*$_3$). ^{13}C NMR (75 MHz, DMSO-*d*^{6}) δ 149.1 (N*C*N), 130.8, 127.9, 122.5 (aromatic *C* and *C*H from benzimidazole and benzene groups), 40.0 (*C*H), 39.7 (*C*H_2), 39.4 (*C*H_2), 39.1, 35.5 (*C*H_2), 32.2 (*C*H_2), 31.8 (*C*H_2), 29.6 (*C*H_2), 29.3 (*C*H_2), 26.5 (*C*H_2), 22.6 (CH-*C*H_3), 14.4 (-CH_2-*C*H_3). HRMS ESI-TOF-MS (positive mode): 1619 $[M\text{-}H]^+$.

Synthesis of 17I$_4$

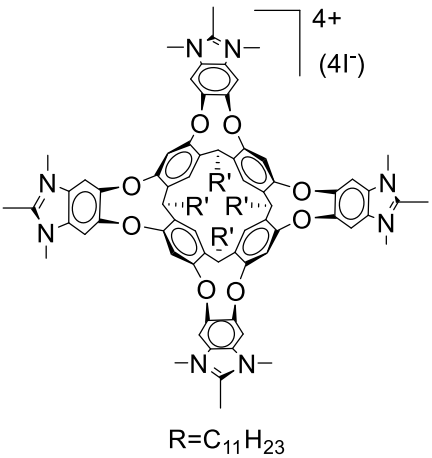

17I$_4$

A mixture of compound **G** (200.0 mg, 0.12 mmol) and NaOH (29.7 mg, 1.56 mmol) was stirred in 2 mL of DMSO at room temperature for 2 h. After this time CH_3I (31 μL, 0.48 mmol) was added and the mixture was stirred at 37 ºC for 8 h. Then, CH_3I (310 μL, 4.8 mmol) was added and the mixture was stirred at 100 ºC for 8 h. The final suspension was cooled to room temperature and the crude salt was brown precipitate was collected by filtration, washed with methanol and dissolved in acetone.

The solvent was removed under vacuum and the solid was precipitated in methanol and collected by filtration. Compound **17I$_4$** was obtained in 70% yield (193.9 mg) as a brown solid. ^{1}H NMR (500 MHz, DMSO-d^6) δ 8.56 (s, 8H, C$H_{benzimidazole}$), 7.96 (s, 4H, C$H_{benzene}$), 7.80 (s, 4H, C$H_{benzene}$), 5.65 (m, 4H, C*H*), 3.87 (s, 24H, CH_3), 2.76 (s, 12H, C$H_{3,NHC}$), 2.42 (m, 8H, CH_2), 1.43 (m, 8H, CH_2), 1.26 (m, 64H, CH_2), 0.85 (t, 12H, CH_3). ^{13}C NMR (126 MHz, DMSO-d^6): δ 154.2 (N*C*N), 153.1, 150.5, 135.6, 128.3, 115.2, 108.6 (aromatic *C* and *C*H from benzimidazole and benzene groups), 33.3 (*C*H), 31.1 (*C*H$_2$), 29.0 (N-*C*H$_3$), 28.9 (*C*H$_2$), 28.8 (*C*H$_2$), 28.5 (*C*H$_2$), 27.6 (*C*H$_2$), 21.9 (CH$_2$-*C*H$_3$), 13.7 (C-*C*H$_3$). HRMS ESI-TOF-MS (positive mode): [M]$^{4+}$ 953.5.

Synthesis of [17][PF$_6$]$_4$

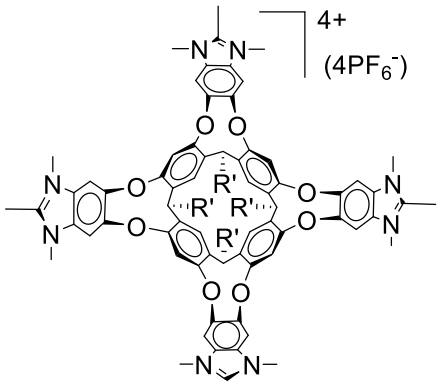

[17][PF$_6$]$_4$

A mixture of compound **[17][I]$_4$** (356.3 mg, 0.161 mmol)was dissolved in acetonitrile (20 mL) and mixed with NH_4PF_6 (138.0 mg, 0.86 mmol). The reaction was stirred at room temperature for 1 h. The final suspension was cooled to room temperature and the solvent was removed. The solid was suspended in CH_3OH, filtered, washed with CH_3OH and dried. This compound **[17][PF$_6$]$_4$** was obtained in 90% yield (300.0 mg). ^{1}H NMR (500 MHz, DMSO-d^6) δ 8.55 (s, 8H, C$H_{benzimidazole}$), 7.95 (s, 4H, C$H_{benzene}$), 7.80 (s, 4H, C$H_{benzene}$), 5.67 (m, 4H, C*H*), 3.84 (s, 24H, CH_3), 2.69 (s, 12H, C$H_{3,NHC}$), 2.43 (m, 8H, CH_2), 1.45 (m, 8H, CH_2), 1.26 (m, 64H, CH_2), 0.85 (t, 12H, CH_3). ^{13}C NMR (125 MHz, DMSO-d^6): δ 154.6, 153.5 (N*C*N), 151.0, 136.0, 128.7, 125.9, 108.9 (aromatic *C* and *C*H from benzimidazole and benzene groups), 33.7 (*C*H$_2$), 31.9 (N-*C*H$_3$), 31.6(*C*H), 29.4 (*C*H$_2$), 29.3 (*C*H$_2$), 29.2 (*C*H$_2$), 29.0 (*C*H$_2$), 28.0 (*C*H$_2$), 22.3 (*C*H$_2$), 14.14 (CH$_2$-*C*H$_3$), 10.69 (C-*C*H$_3$). HRMS ESI-TOF-MS (positive mode): 433.3 [M]$^{4+}$.

Truncated ^{1}H-^{1}H NOESY NMR [17][PF$_6$]$_4$

The NOESY experiments were carried out using a mixture of **[17][PF$_6$]$_4$** ($5\cdot10^{-3}$M) and 2 equivalents of tetrabutylammonium *p*-toluensulfonate (PT-SO_3^-). It shows the close proximity between some proton of the guest and the inner protons of the cavitand cavity.

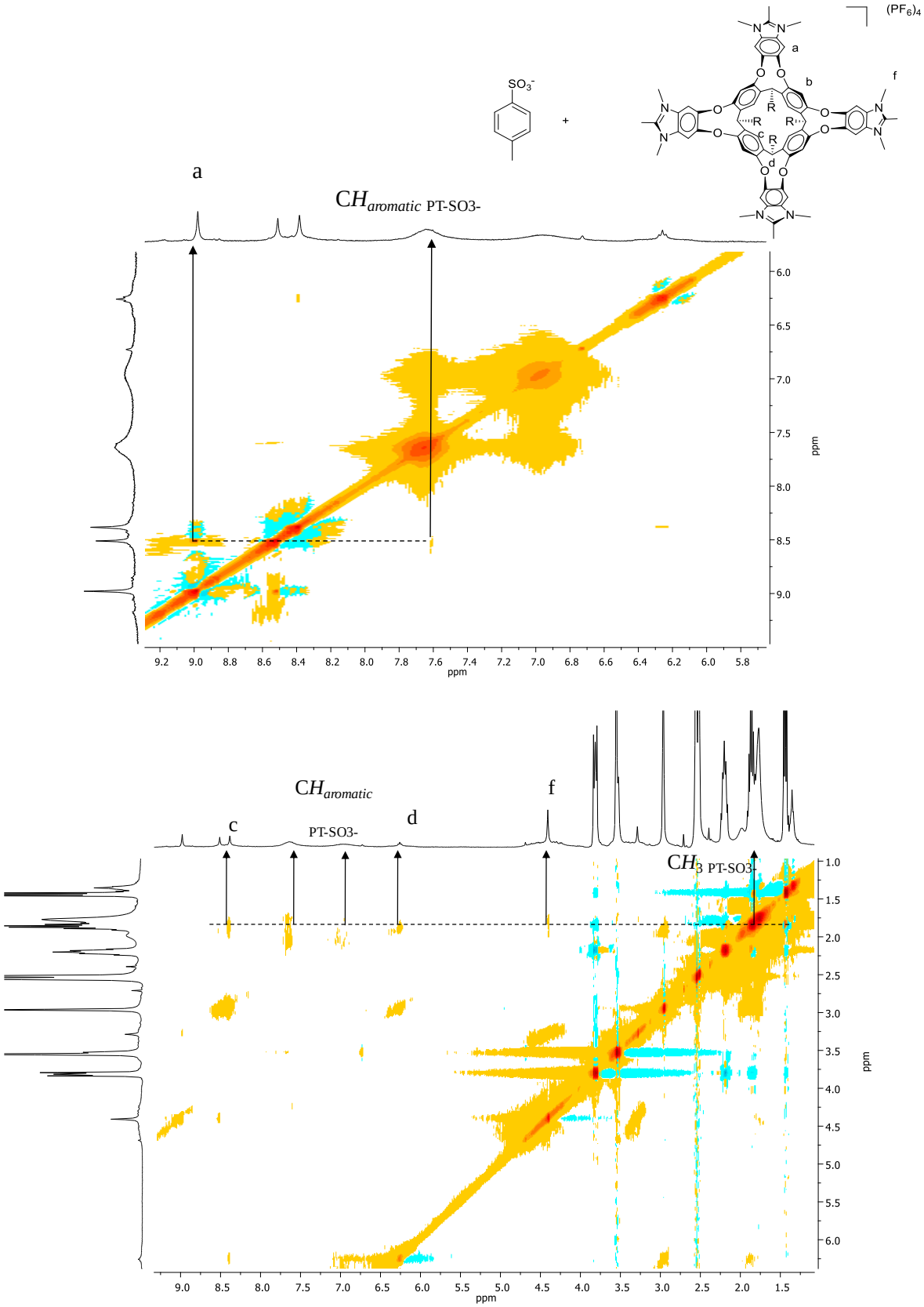

Figure 7.8. Truncated ^{1}H-^{1}H NOESY NMR (400 MHz, DMSO-d^{6}) spectrum of cavitand **[16][PF$_6$]$_4$** 2 mM plus 2 equivalents of PT-SO$_3$

Synthesis of 18

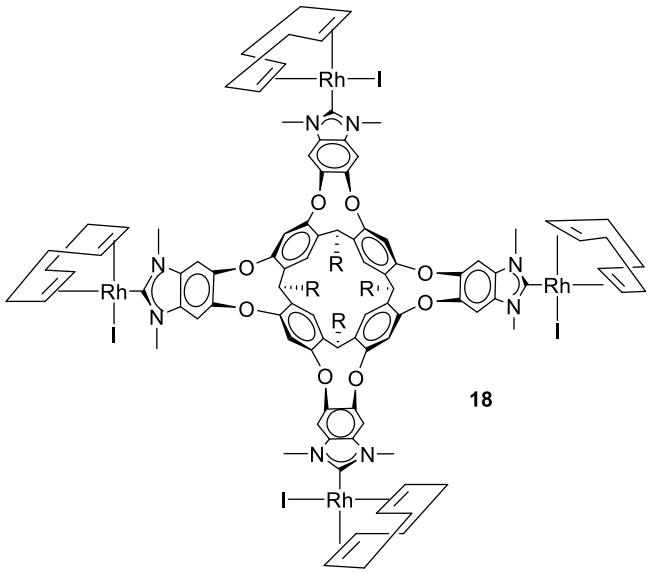

A mixture of compound **16I$_4$** (100.0 mg, 0.05 mmol), [RhCODCl]$_2$ (45.1 mg, 0.09 mmol), KI (30.0 mg, 0.18mmol), K_2CO_3 (75.0 mg, 0.54 mmol) was poured into a Schlenk under vacuum for 2 min. Then, 10 mL of acetone (previously degassed) was added under N_2. Using a reflux system, the mixture was stirred at 60 ºC for 20 h. The final suspension was cooled to room temperature and the solvent was removed under vacuum. The product was redissolved in dichloromethane and filtrated through Celite. The crude product was purified by column chromatography. The pure compound was eluted with dichloromethane: acetone (9:1) and precipitated in a mixture of dichloromethane /hexane. Compound **18** was obtained as an orange solid in a 30% yield (41.0 mg). ^{1}H NMR (500 MHz, CD_2Cl_2): δ 7.5-6.7 (C*H*$_{aromatic}$), 5.96 (C*H*), 5.17 (C*H*$_{COD}$), 4.0 (C*H*$_3$), 3.5-3.35 (C*H*$_2$), 2.41 (C*H*$_{2,COD}$), 2.08 (C*H*$_{2,COD}$), 2.42-1.00 (C*H*$_2$), 0.88 (C*H*$_3$). Anal. Calcd. for $C_{140}H_{184}N_8O_8Rh_4I_4 \cdot 2H_2O$ (3062.2782): C, 54.91; H, 6.18; N, 3.65. Found: C, 54.61; H, 6.22; N, 3.50. HRMS ESI-TOF-MS (positive mode): 2898.8 $[M\text{-}I]^+$ and 1386.0 $[M\text{-}2I]^{2+}$.

7.2.4 Synthesis and characterization of compounds of Chapter 6

The tri-azidimethylbenzene[5] and 4-tert-butylphenyl-iodoacetylene[6] were obtained according to literature procedures.

The proto-imidazole tripod ligand **J** was synthesized according to the literature procedure.[7]

Synthesis of H

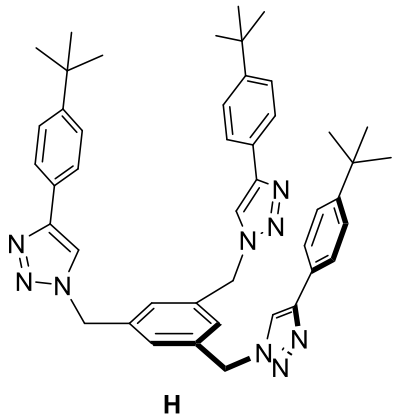

H

A mixture of tri-azidimethylbenzene (68.9 mg, 0.28 mmol), 4-tert-butylphenylacetylene (174.9 mg, 1.10 mmol), $[Cu(CH_3CN)_4](PF_6)$ (50.0 mg, 0.13 mmol), TBTA(23.9 mg, 0.045 mmol) and DIPEA (252 µL, 1.5 mmol) in 3 mL CH_2Cl_2 was stirred during 48 h at room temperature. After this time the resulting suspension was washed with NH_4OH and brine. The product was purified by column chromatography. The pure compound was eluted in a mixture of CH_2Cl_2:AcOEt (7:3) to give a white solid in a 65% yield (130 mg). ^{1}H NMR (400 MHz, $CDCl_3$) δ 7.72 (d, $^3J_{HH}$=8.3 Hz, 6H, CH_{Ph}), 7.68 (s, 3H, C$H_{benzene}$), 7.42 (d, $^3J_{HH}$=8.4 Hz, 6H, CH_{Ph}), 7.19 (s, 3H, C$H_{triazol}$), 5.50 (s, 6H, CH_2), 1.33 (s, 27H, CH_3). ^{13}C NMR (100 MHz, $CDCl_3$) δ 151.7 (C_{Ph}), 148.6 ($C_{triazole}$), 137.3 ($C_{benzene}$), 127.5 (C_{Ph}), 127.4 ($CH_{triazole}$), 125.9 (C_{Ph}), 125.6 ($CH_{benzene}$), 119.6 ($CH_{benzene}$), 53.5 (CH_2), 34.8 ($C_{tertbuyl}$), 31.4 ($CH_{tertbutyl}$). Electrospray accurate mass analysis (positive mode): 718.43296 $[M+H]^+$

Synthesis of I

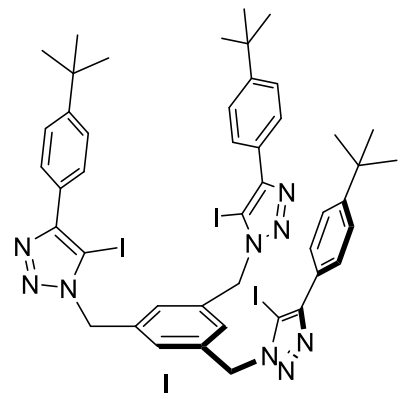

I

A mixture of tri-azidimethylbenzene (54.4 mg, 0.22 mmol), 4-tert-butylphenyl-iodoacetylene (222.9 mg, 0.73 mmol), $[Cu(CH_3CN)_4](PF_6)$ (37.5 mg, 0.1 mmol), TBTA (17.8 mg, 0.04 mmol) in 3 mL CH_2Cl_2 was stirred during 48 h at room temperature. After this time the resulting suspension was washed with NH_4OH and Brine. The product was purified by column chromatography. The pure compound was eluted in a mixture of CH_2Cl_2:AcOEt (7:3) to give a white solid in 70% yield (170.2 mg). ^{1}H NMR (400 MHz, $CDCl_3$) δ 7.87 (d, $^3J_{HH}$ = 8.2 Hz, 6H, CH_{Ph}), 7.48 (d, $^3J_{HH}$=

8.2 Hz, 6H, C*H*$_{Ph}$), 7.23 (s, 3H, C*H*$_{benzene}$), 5.65 (s, 6H, C*H*$_2$), 1.35 (s, 27H, C*H*$_3$). ^{13}C NMR (100 MHz, $CDCl_3$) δ 151.9(*C*$_{Ph}$), 150.4 (*C*$_{triazole}$), 137.5 (*C*$_{benzene}$), 136.1 (*C*H$_{benzene}$), 127.7 (*C*H$_{Ph}$), 127.4 (*C*H$_{Ph}$), 127.2 (*C*$_{Ph}$), 100.7 (*C*-I), 54.0 (*C*H$_2$), 34.9 (*C*$_{tertbutyl}$), 31.1 (*C*H$_{3,tertbutyl}$). Electrospray accurate mass analysis (positive mode): 1096.12354 $[M+H]^+$

Synthesis of K

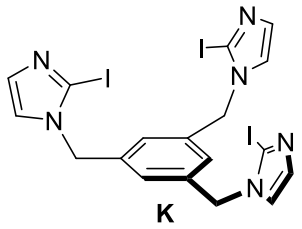

K

Iodoimidazole (200.0 mg, 1.0 mmol) was dissolved in dry CH_3CN and potassium hydroxide (160.0 mg, 2.85 mmol) was added and stirred at room temperature during 2 h. Then, 1,3,5-tris(bromomethyl)benzene (121.3 mg, 0.34 mmol) was added and stir at room temperature during 6 h. After this time the mixture was diluted with acetonitrile and the compound was filtered. The solvent was removed in the high vacuum. The compound was suspended in diethyl ether and sonicated during 30 min. Then, it was filtered and dry under vacuum. The compound was obtained as a white solid in 27% yield (60.1 mg).^{1}H NMR (400 MHz, DMSO-*d*^{6}) δ 7.37 (s, 3H, C*H*$_{imidazole}$), 6.99 (d, 3H, C*H*$_{imidazole}$), 6.90 (d, 3H, C*H*$_{benzene}$), 5.12 (s, 6H, CH_2). ^{13}C NMR (100 MHz, DMSO-*d*^{6}) δ 138.5 (*C*$_{benzene}$), 132.5 (*C*H$_{benzene}$), 125.7 (*C*H), 124.6 (*C*H), 93.4 (*C*-I), 51.9 (*C*H$_2$).

Synthesis of 19(PF$_6$)$_3$

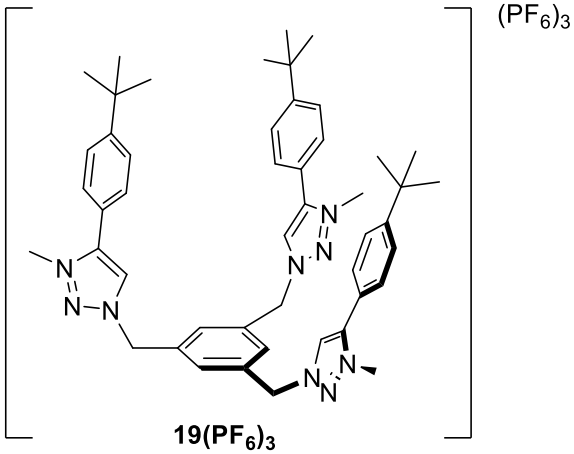

19(PF$_6$)$_3$

Compound **H** (100.0 mg, 0.14 mmol) was dissolved in dry CH_2Cl_2 (5 mL) and trimethyloxonium tetrafluoroborate (67.8 mg, 0.46 mmol) was added. The mixture was stirred at room temperature during 48 h. After that time, diethyl ether was added to the mixture to produce the precipitation of the compound. This salt was filtered and washed with diethyl ether. Then it was dissolved in $CHCl_3$ and it was washed several times with a saturated solution of NH_4PF_6. The organic layers were collected, dried with $MgSO_4$, filtered and solvent was removed. The compound was obtained as a white off solid in a 90% yield (149.0 mg). ^{1}H NMR (400 MHz, $CDCl_3$) δ 8.1 1 (s, 3H, C*H*$_{triazole}$), 7.83 (s, 3H, C*H*$_{benzene}$), 7.48 (broad signal, 12H, C*H*$_{Ph}$), 5.79 (s,

6H, CH_2), 4.28 (s, 9H, CH_3), 1.28(s, 27H, CH_3). ^{13}C NMR (100 MHz, CD_3CN) δ 156.4 (C_{Ph}), 144.6 ($C_{benzene}$), 134.9 ($C_{triazole}$), 131.8 ($CH_{benzene}$), 129.9 (CH_{Ph}), 129.3 ($CH_{triazole}$), 127.5 (CH_{Ph}), 120.2 (C_{Ph}), 57.0 (CH_2), 39.6 (N-CH_3), 35.6 ($C_{tertbutyl}$), 31.1 ($CH_{3,tertbutyl}$). Electrospray accurate mass analysis (positive mode): 1052.42292 $[M\text{-}2PF_6^-]^+$.

Synthesis of 20(PF$_6$)$_3$

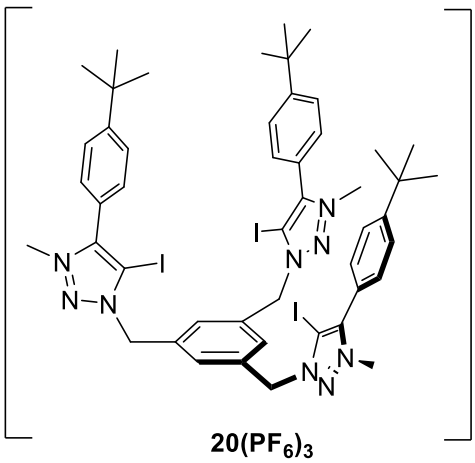

20(PF$_6$)$_3$

Compound **I** (39.1 mg, 0.04mmol) was dissolved in dry CH_2Cl_2 (5 mL) and trimethyloxonium tetrafluoroborate (19.0 mg, 0.13 mmol) was added. The mixture was stirred at room temperature during 48 h. After that time, diethyl ether was added to the mixture to produce the precipitation of the compound. This salt was filtered and washed with diethyl ether. Then it was dissolved in $CHCl_3$ and it was washed several times with a saturated solution of NH_4PF_6. The organic layers were collected, dried with $MgSO_4$, filtered and solvent was removed. The compound was obtained as a white off solid in a 82 % yield (41 mg). ^{1}H NMR (400 MHz, $CDCl_3$) δ 7.79 (s, 3H, C$H_{benzene}$), 7.57 (d, $^3J_{HH}$= 8.2 Hz, 6H, CH_{Ph}), 7.47 (d, $^3J_{HH}$= 8.1 Hz, 6H, CH_{Ph}), 5.81 (s, 6H, CH_2), 4.11 (s, 9H, CH_3), 1.34 (s, 27H, CH_3). ^{13}C NMR (100 MHz, CD_3CN) δ 156.3 (C_{Ph}), 148.0 ($C_{triazole}$), 134.1 ($C_{benzene}$), 130.6 ($CH_{benzene}$), 130.2 (CH_{Ph}), 127.1 (CH_{Ph}), 119.9 (C_{Ph}), 90.0 (*C*-I), 57.4 (CH_2), 39.7 (N-CH_3), 35.3 ($C_{tertbutyl}$), 30.7 ($CH_{3,tertbutyl}$). Electrospray accurate mass analysis (positive mode): 642.57419 $[M\text{-}2PF_6]^{2+}$

Synthesis of 21(PF$_6$)$_3$

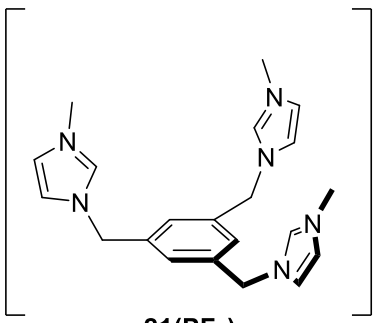

21(PF$_6$)$_3$

Compound **J** (50.0mg, 0.16 mmol) was dissolved in dry CH_2Cl_2 (3 mL) and trimethyloxonium tetrafluoroborate (76.7 mg, 0.52 mmol) was added. The mixture was stirred at room temperature during 24 h. After that time, diethyl ether was added to the mixture to produce the precipitation of the compound. This salt was filtered and washed with diethyl ether and dried under high vacuum. Then it was dissolved in $CHCl_3$ and it was washed several times with a saturated solution of

NH_4PF_6. The organic layers were collected, dried with $MgSO_4$, filtered and solvent was removed. The compound was obtained as a white off solid in a 53% yield (52.0 mg). ^{1}H NMR (400 MHz, DMSO) δ 8.38 (s, 3H, NC*H*N), 6.93 (s, 3H, C*H*$_{imidazole}$) 6.90 (s, 3H, C*H*$_{imidazole}$), 6.63 (s, 3H, C*H*$_{benzene}$), 4.61 (s, 6H, C*H*$_2$), 3.03 (s, 9H, C*H*$_3$).^{13}C NMR (100 MHz, DMSO) δ 137.3 (N*C*N), 136.7 (*C*$_{benzene}$), 128.9 (*C*H$_{benzene}$), 124.6 (*C*H), 122.8 (*C*H), 51.8 (*C*H$_2$), 36.4 (*C*H$_3$). Electrospray accurate mass analysis (positive mode): 653.40780 [M-PF_6^-]$^+$

Synthesis of 22(PF$_6$)$_3$

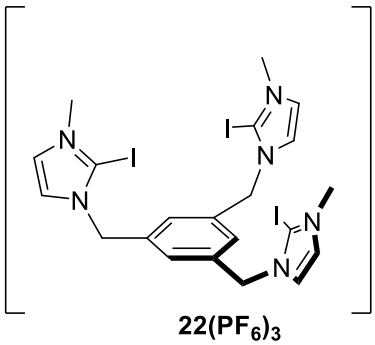

22(PF$_6$)$_3$

Compound **K** (36.5 mg, 0.05 mmol) was dissolved in dry CH_2Cl_2 (5 mL) and trimethyloxonium tetrafluoroborate (25.6 mg, 0.17 mmol) was added. The mixture was stirred at room temperature during 24 h. After that time, diethyl ether was added to the mixture to produce the precipitation of the compound. This salt was filtered and washed with diethyl ether and dried under high vacuum. Then it was dissolved in $CHCl_3$ and it was washed several times with a saturated solution of NH_4PF_6. The organic layers were collected, dried with $MgSO_4$, filtered and solvent was removed. The compound was obtained as a white off solid in a 96% yield (36.6 mg). ^{1}H NMR (400 MHz, DMSO) δ 8.26 (d, 3H, C*H*$_{imidazole}$), 8.20 (d, 3H, C*H*$_{imidazole}$), 7.77 (s, 3H, C*H*$_{benzene}$), 5.91 (s, 6H, C*H*$_2$), 4.42 (s, 9H, C*H*$_3$). ^{13}C NMR (100 MHz, CD_3CN) δ 146.1 (*C*$_{benzene}$), 138.7 (*C*H$_{benzene}$), 137.8 (*C*H), 136.5 (*C*H), 109.4 (*C*-I), 50.2 (CH_2), 40.2 (CH_3). Electrospray accurate mass analysis (positive mode): 246.97277 [M-3PF_6^-]$^+$

7.3 ^{1}H NMR experiments

7.3.1 ^{1}H NMR experiments for the determination of the interaction between complex 8 and pyrene in Chapter 3

We prepared a series of solutions containing both the π-stacking additive (pyrene) and the metal complex **8** in varying proportions while maintaining the total concentration, [**8**]+[π-pirene], constant for each solution (10 mM). A 2:1 $CDCl_3$/CD_3OD (0.6 mL) mixture was used to prepare the samples and record the ^{1}H NMR experiments. The spectra showed that only the resonances due to the protons from the aromatic tag in **8**

were upfield shifted upon addition of increasing amounts of pyrene (Figure 7.9). This result is strongly suggesting that a π–π stacking interaction is taking place between the pyrene tag and the pyrene additive.

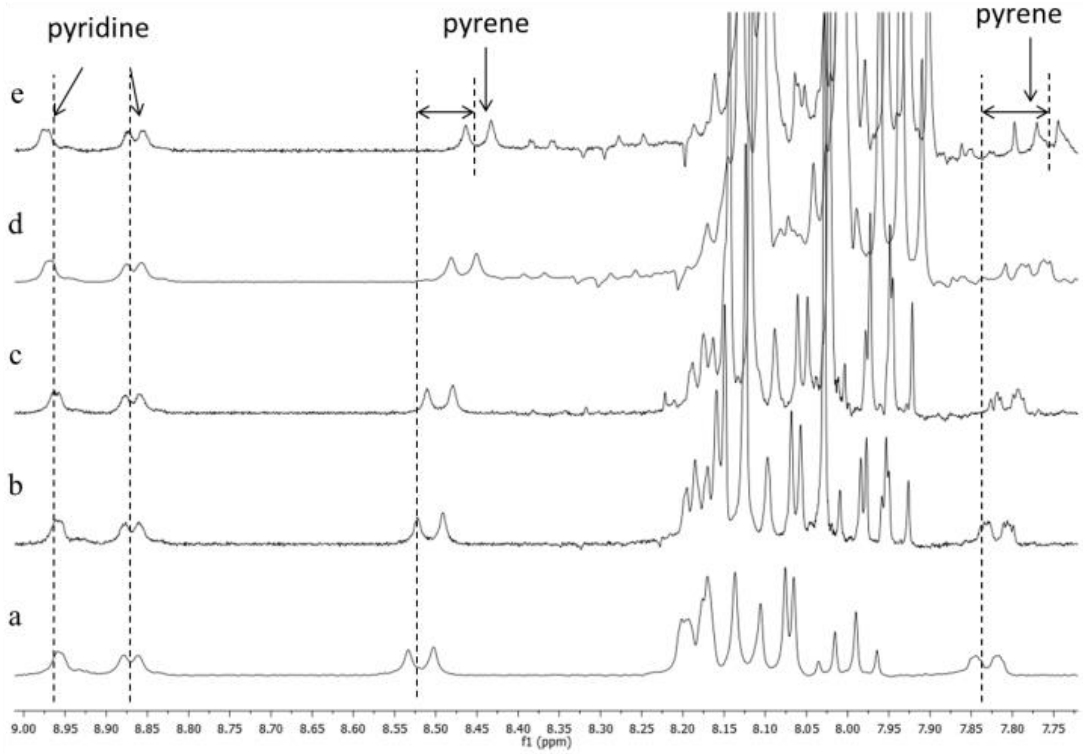

Figure 7.9. ^{1}H NMR spectra (300 MHz, $CDCl_3/CD_3OD$, 298K) of a) complex **8**; b) **8** + 1 equiv. of pyrene; c) **8** + 2 equiv. of pyrene; d) **8** + 5 equiv. of pyrene, e) **8** + 7 equiv. of pyrene

7.3.2 ^{1}H NMR experiments for the determination of the association constants (K_a) of the compounds of Chapter 5

*7.3.2.1 ^{1}H NMR experiments for the determination of the association constants (Ka) of cavitands **15** towards several ammonium salts*

Titration experiments

The guest used for this experiment were Choline chloride, *L*-carnitine, NMe_4Cl, Et_4NCl, $N(C_{16}H_{33})Me_3Cl$ and NBu_4Cl. A solution of compound **15** in benzene-d^6 was prepared and 1 and 2 equiv. of the corresponding guest were added into the NMR tube at room temperature. Then, ^{1}H NMR spectrum was acquired. Integration of the signals from the free host and the complexed host gives the information for the binding constant determination. The same experiment was done in toluene-d^8 using some of the proposed guests.

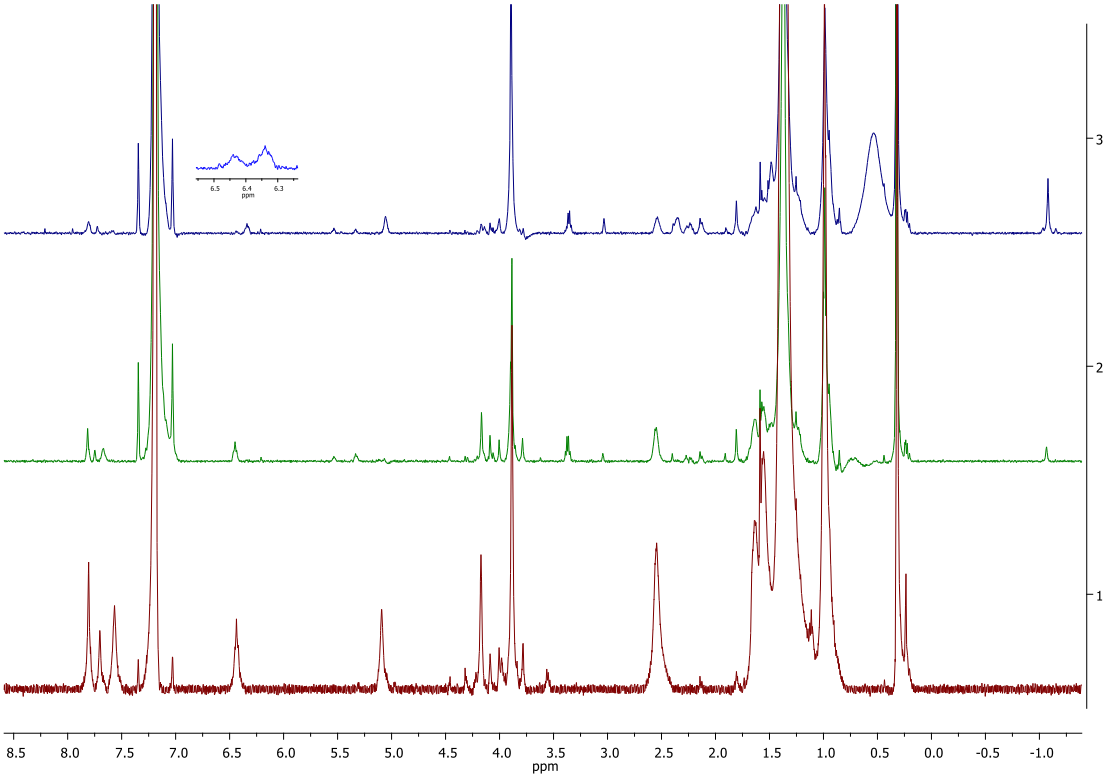

Figure 7.10. ^{1}H NMR (500 MHz) in benzene-d^6 at 30 ºC: (1) Compound **15** (3.5 mM), (2) Compound **15** (3.5 mM) plus 1 equiv. of NMe_4Cl (3) plus 2 equiv of NMe_4Cl

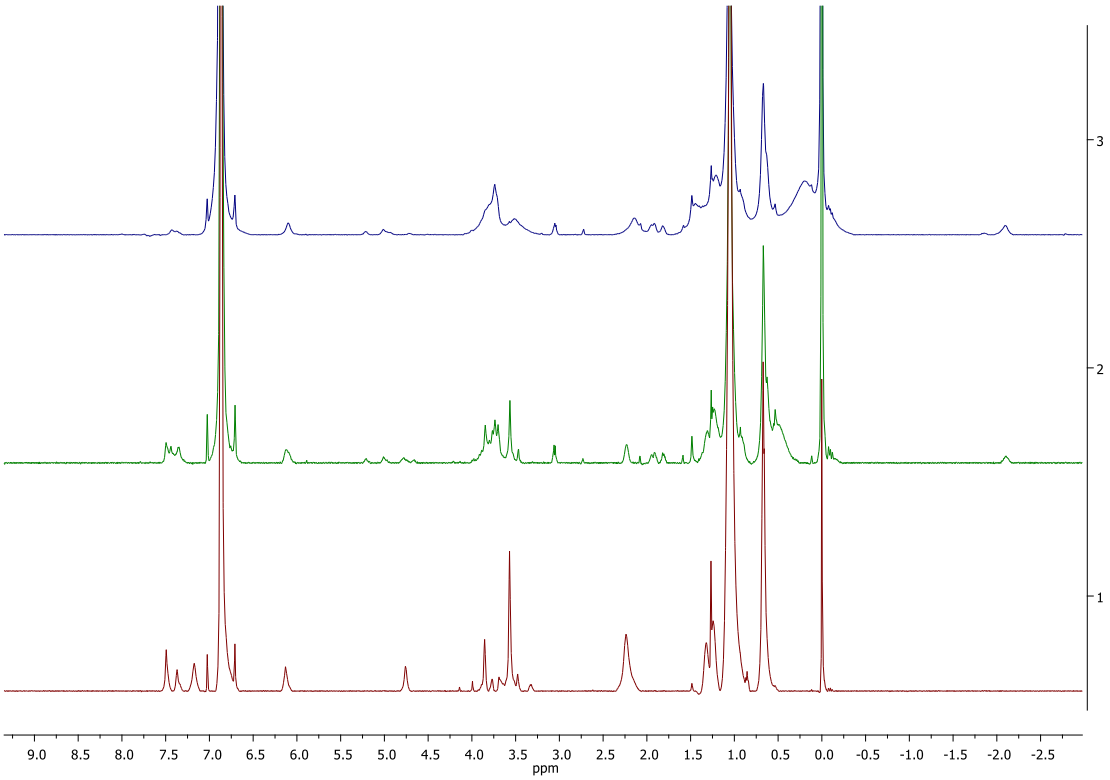

Figure 7.11. ^{1}H NMR (500 MHz) in benzene-d^6 at 30 ºC: (1) Compound **15** (3.5 mM), (2) Compound **15** (3.5 mM) plus 1 equiv. of Et_4NCl (3) plus 2 equiv of Et_4NCl

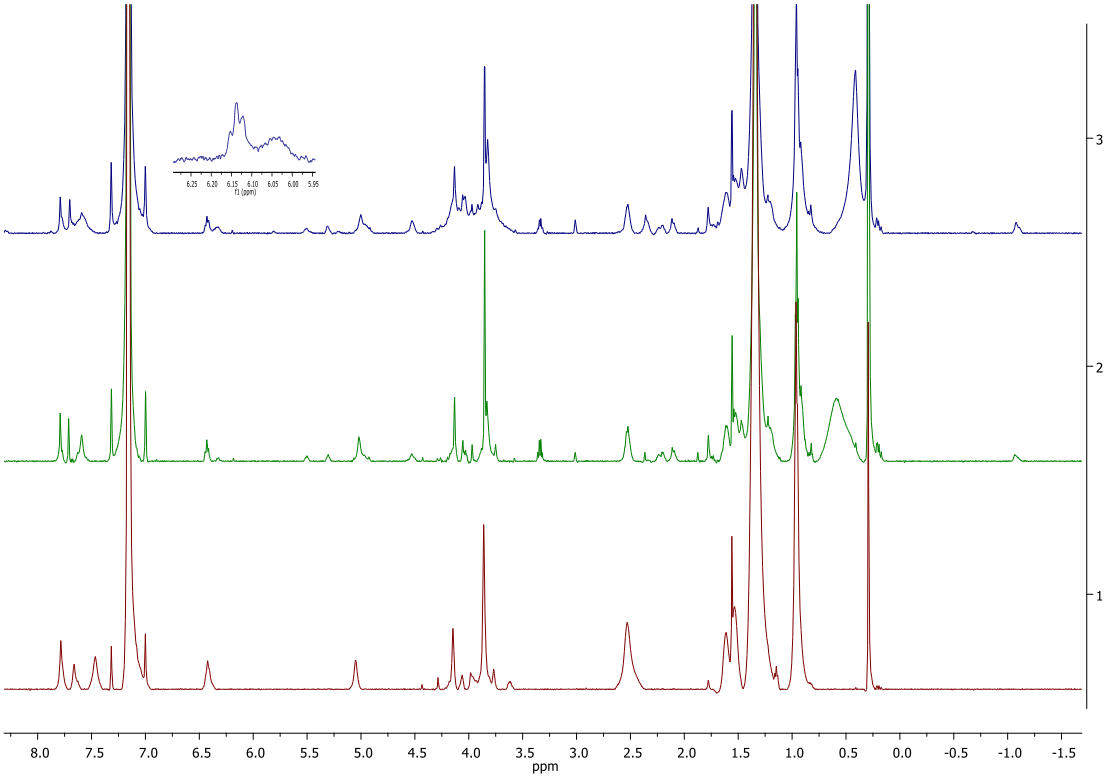

Figure 7.12. ^{1}H NMR (500 MHz) in benzene-d^{6} at 30 ºC: (1) Compound **15** (3.5m M), (2) Compound **15** (3.5 mM) plus 1 equiv. of Choline chloride (3) plus 2 equiv of Choline chloride

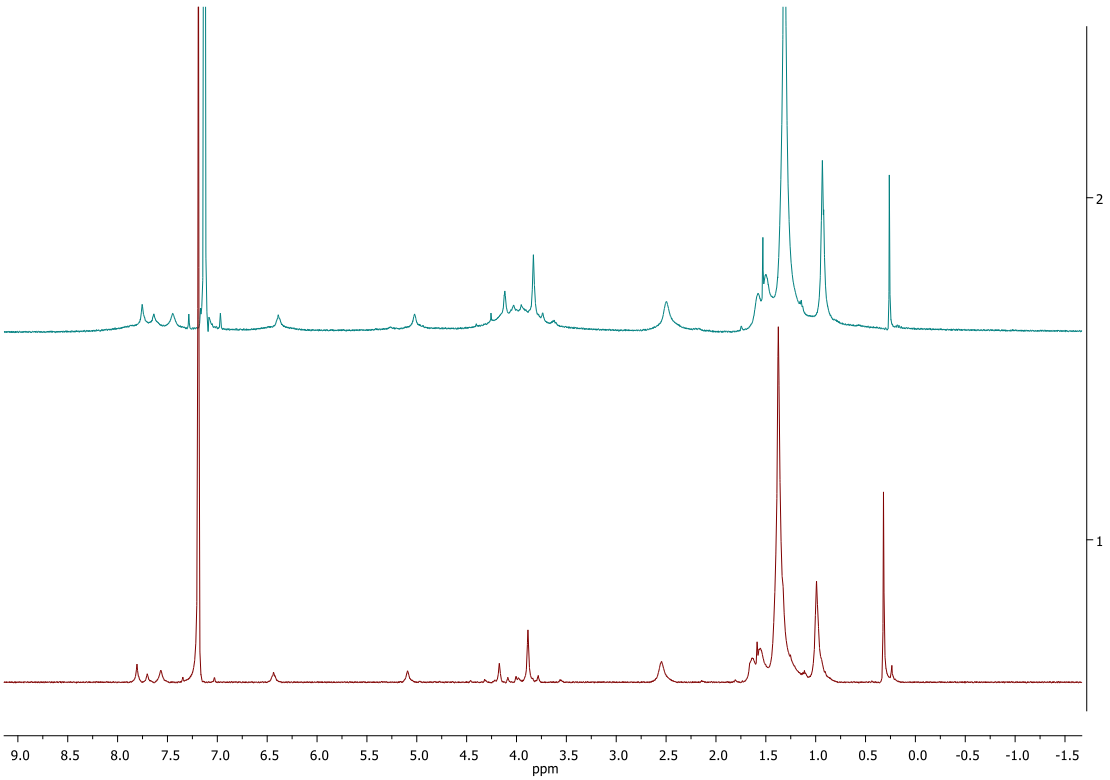

Figure 7.13. ^{1}H NMR (500 MHz) in benzene-d^{6}at 30 ºC: (1) Compound **15** (3.5 mM) (2) Compound **15** (3.5 mM) plus 2 equiv. of *L*-Carnitine

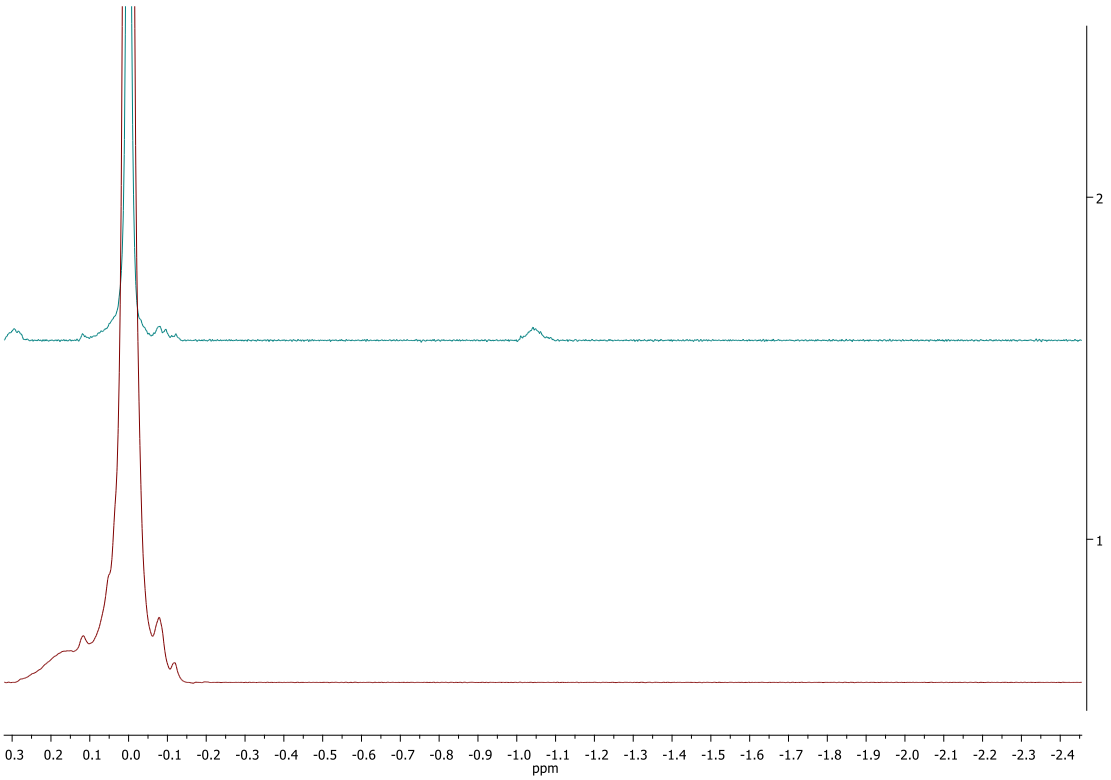

Figure 7.14. ^{1}H NMR (500 MHz) in benzene-d^6 at 30 ºC: (1) Compound **15** (3.5 mM) plus 1 equiv. of *L*-Carnitine (2) Compound **15** (3.5 mM) plus 1 equiv. of *L*-Carnitine and 1 equiv of NBu_4Cl

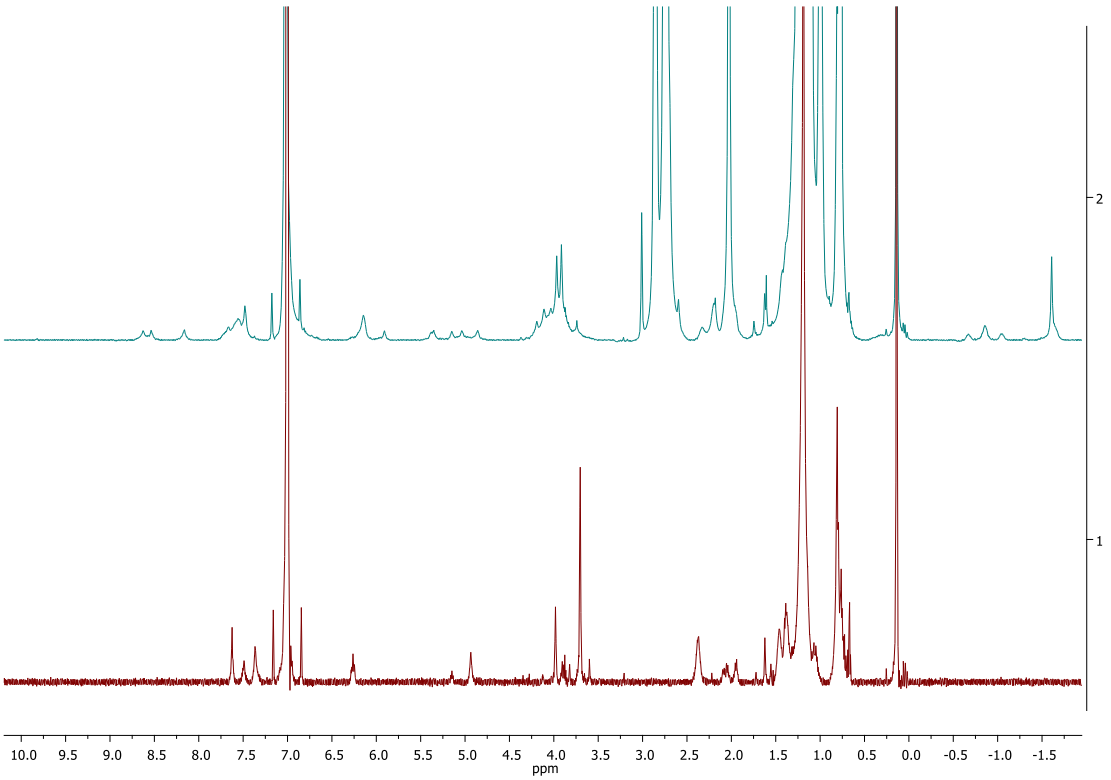

Figure 7.15. ^{1}H NMR (500 MHz) in benzene-d^6 at 30 ºC: (1) Compound **15** (3.5 mM) (2) Compound **15** (3.5 mM) plus 1 equiv. of $N(C_{16}H_{33})Me_3Cl$

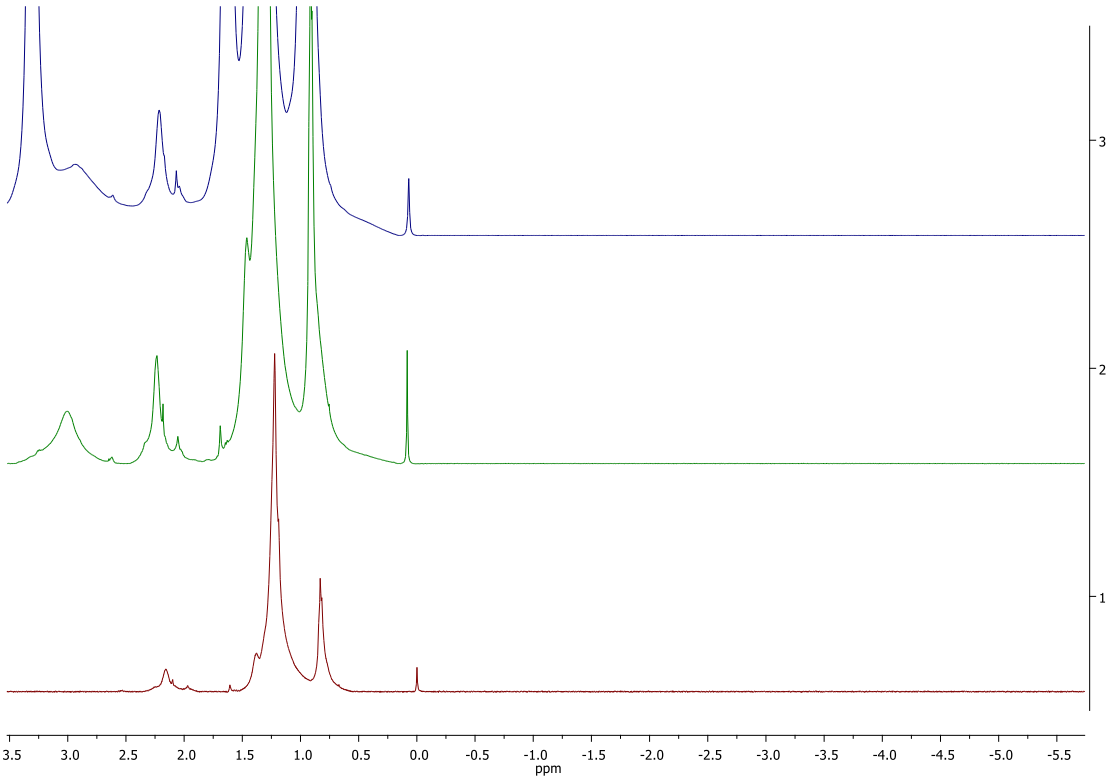

Figure 7.16. ^{1}H NMR (500 MHz) in benzene-d^{6} at 30 ºC: (1) Compound **15** (3.5 mM) (2) Compound **15** (3.5 mM) plus 1 equiv. of NBu_4Cl (3) Compound **15** (3.5 mM) plus 5 equiv. of NBu_4Cl

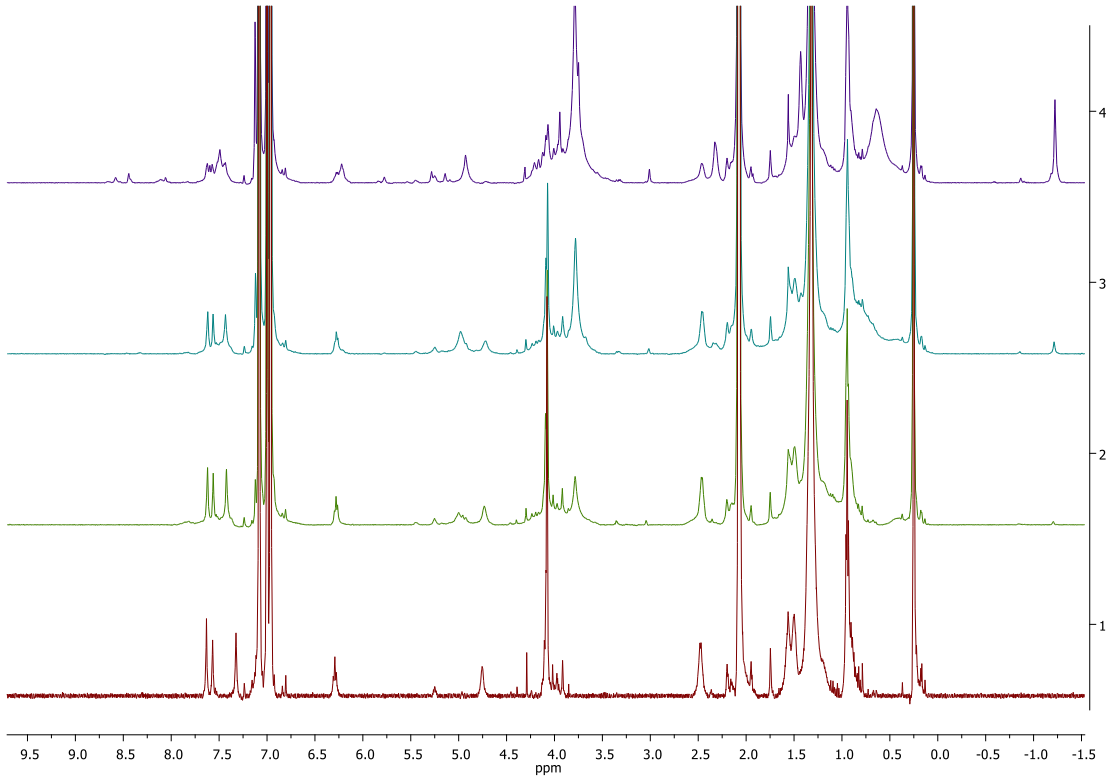

Figure 7.17. ^{1}H NMR (500 MHz) in toluene-d^{8} at 30 ºC: (1) Compound **15** (3.5 mM), (2) Compound **15** (3.5 mM) plus 1 equiv. of NMe_4Cl (3) plus 2 equiv of NMe_4Cl, (3) plus 3 equiv of NMe_4Cl

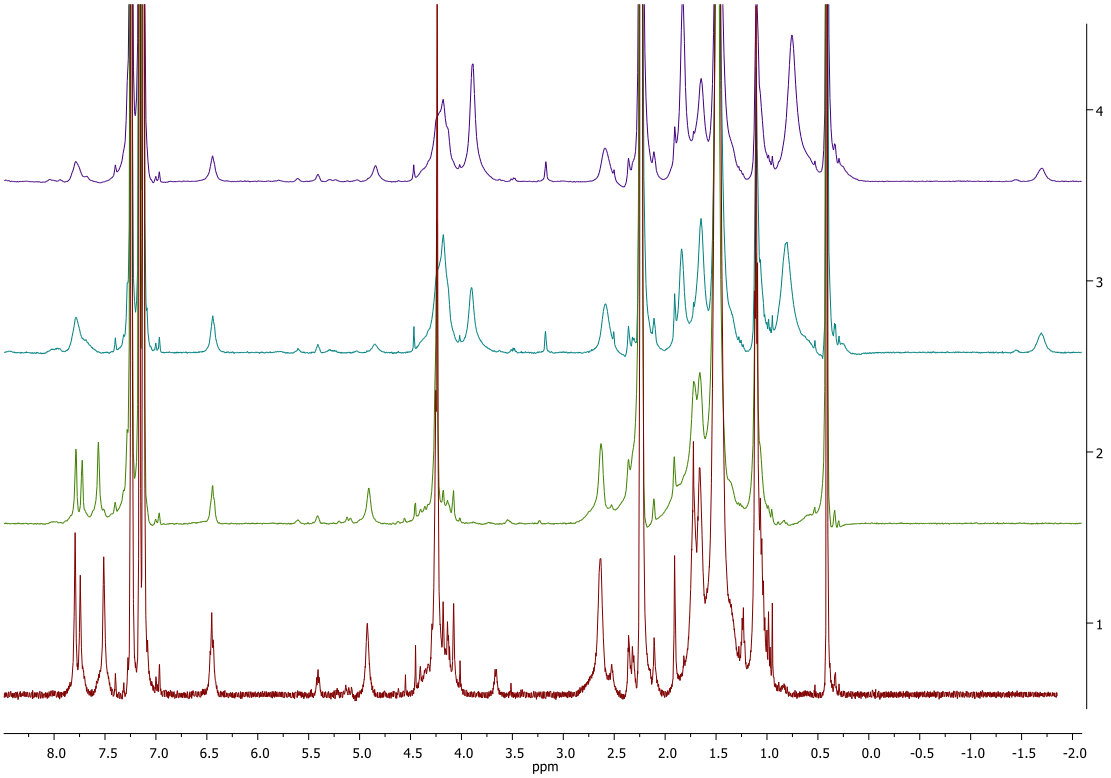

Figure 7.18. ^{1}H NMR (500 MHz) in toluene-d^{8} at 30 ºC: (1) Compound **15** (3.5 mM), (2) Compound **15** (3.5 mM) plus 1 equiv. of Et_4NCl (3) plus 2 equiv of Et_4NCl, (3) plus 3 equiv of Et_4NCl, (4) plus 4 equiv of Et_4NCl

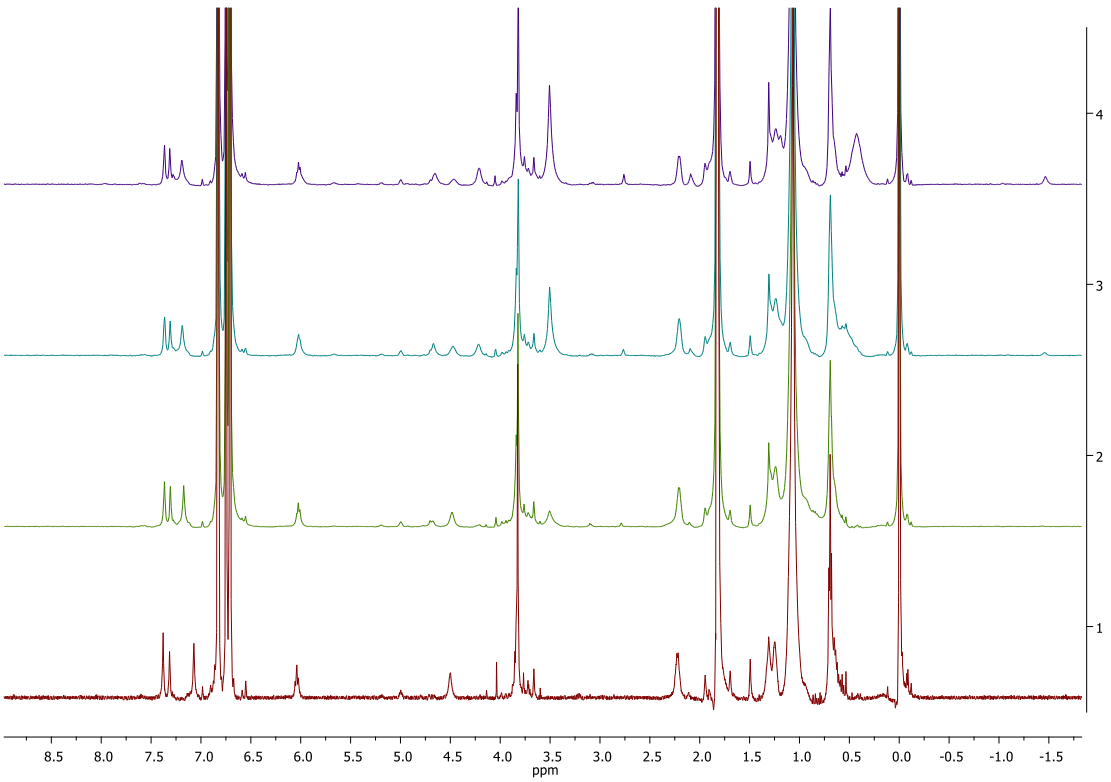

Figure 7.19. ^{1}H NMR (500 MHz) in toluene-d^{8} at 30 ºC: (1) Compound **15** (3.5 mM), (2) Compound **15** (3.5 mM) plus 1 equiv. of Choline chloride (3) plus 2 equiv of Choline chloride, (3) plus 3 equiv of Choline chloride

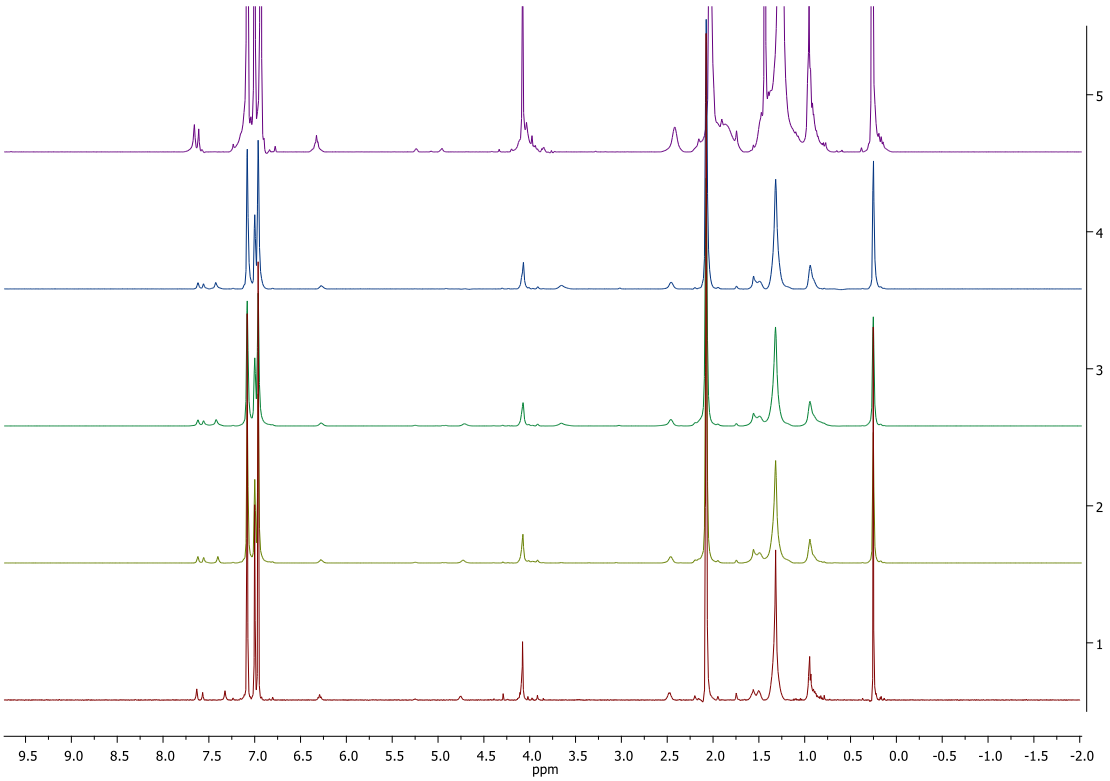

Figure 7.20. ^{1}H NMR (500 MHz) in toluene-d^{8}: (1) Compound **15** (3.5 mM) at 30 ºC, (2) Compound **15** (3.5 mM) plus 1 equiv. of *L*-Carnitine at 30 ºC (3) plus 2 equiv of *L*-Carnitine at 30 ºC, (3) plus 3 equiv of *L*-Carnitine at 30 ºC, (4) plus 3 equiv of *L*-Carnitine at -40 ºC

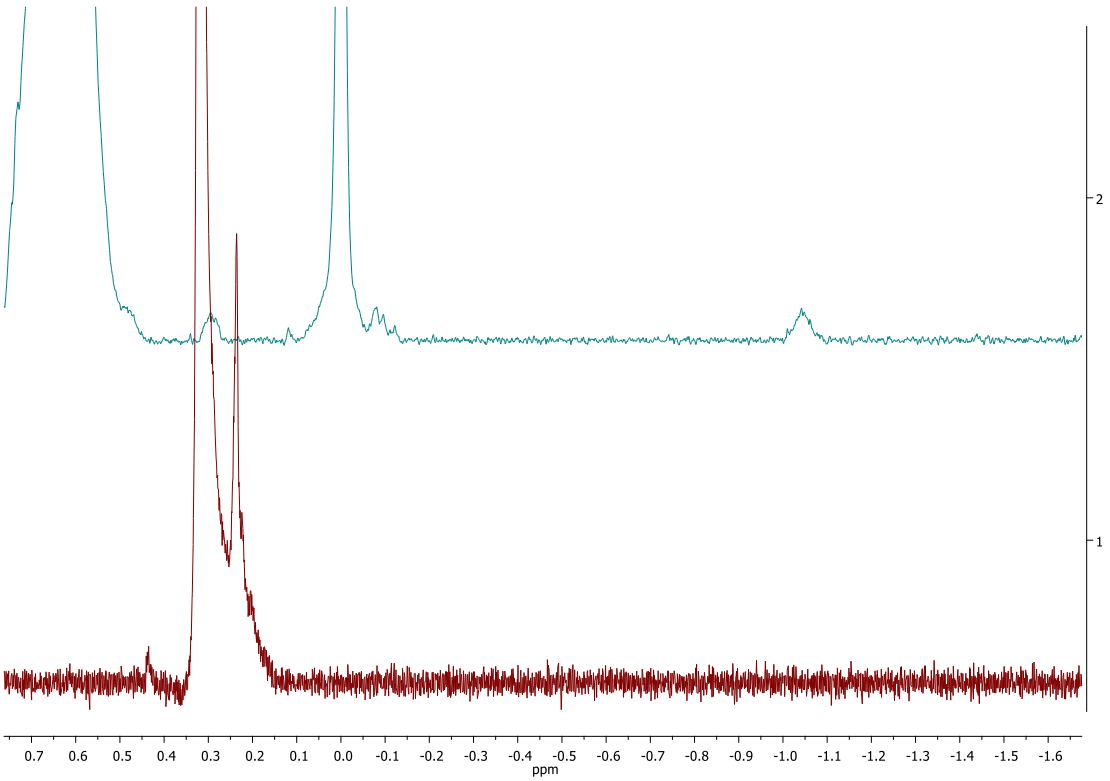

Figure 7.21. ^{1}H NMR (500 MHz) in toluene-d^{8} at 30 ºC: (1) Compound **15** (3.5 mM) plus 2 equiv. of *L*-Carnitine at 30 ºC (2) plus 2 equiv of *L*-Carnitine and 2 equiv of NBu_4Cl

Diffusion ordered NMR Spectroscopy (DOSY)

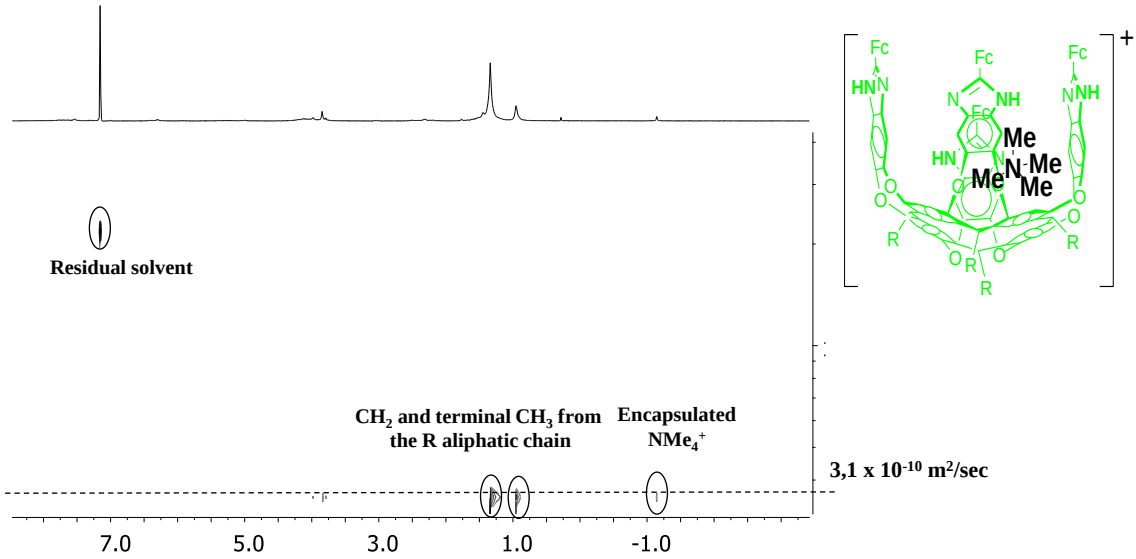

Figure 7.22. Two dimensional diffusion NMR spectrum of the supramolecular complex between the cavitand **15** and NMe_4Cl. Diffusion rates were estimated from the non-overlapped signals from the encapsulated NMe_4^+ and from the CH_2 and CH_3 groups of the aliphatic chain of the cavitand

*7.3.2.2 [1]H NMR experiments for the determination of the association constants (Ka) of cavitands **[16][PF$_6$]$_4$** and **[17][PF$_6$]$_4$** towards several anions*

Titration experiments

The anion recognition capabilities of receptor **[16][PF$_6$]$_4$** towards several anions determined by ^{1}H NMR titration experiments, which were done in DMSO-*d*^{6}. The large downfield shifts of some of the signal protons suggest complexation between **[16][PF$_6$]$_4$** and the anions (Cl^-, Br^-, I^-, ClO_4^-, NO_3^-,$C_6H_5SO_3^-$, $C_7H_8SO_3^-$, CN^-).

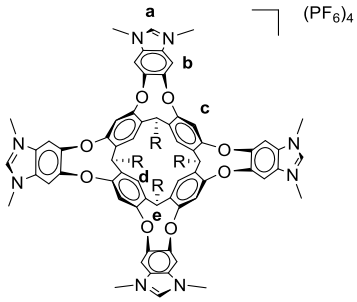

a. Chloride titration

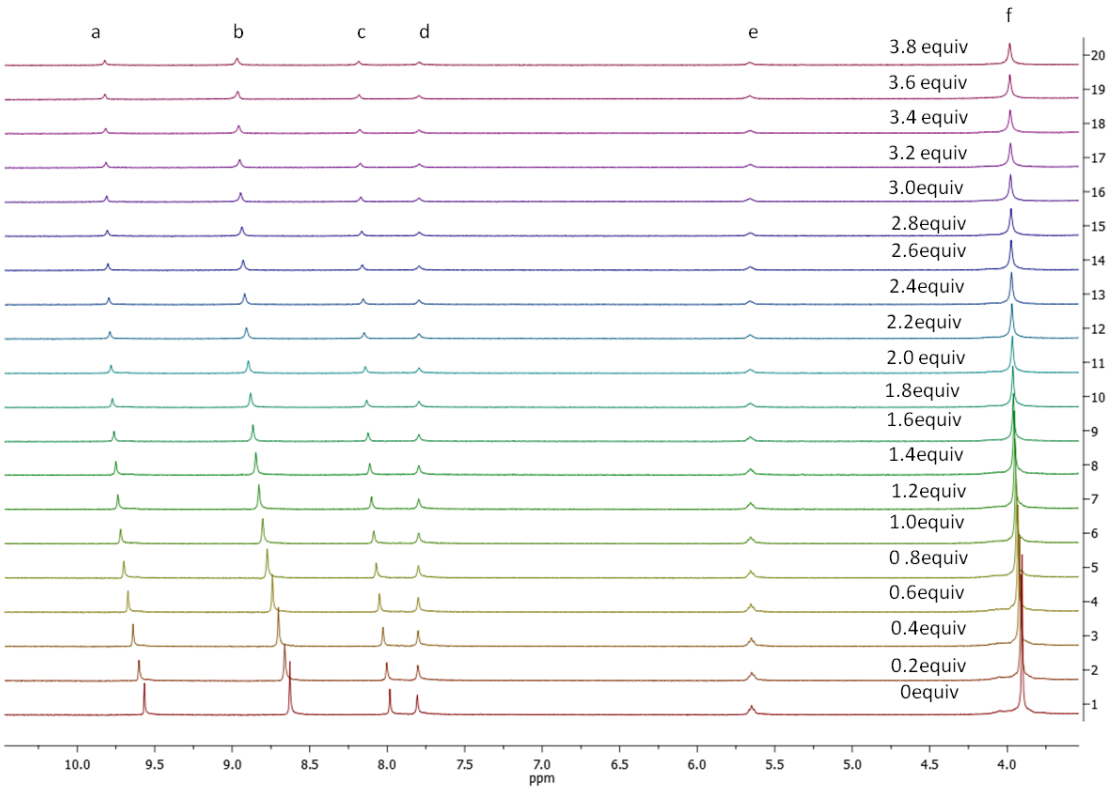

Figure 7.23. Partial ^{1}H NMR (500 Hz) changes observed for the host **[16][PF$_6$]$_4$** in DMSO-*d*^{6} during the addition of Cl^-

Table 6.1: Data values from the titration study of **[16][PF_6]$_4$** with Cl^-

[*[16][PF_6]$_4$*] (M)	**equiv NBu_4Cl**	**δa (ppm)**	**δb (ppm)**	**Δδa (ppm)**	**Δδb (ppm)**	**[NBu_4Cl] (M)**
2,95E-03	0	9,5668	8,6278	0	0	0,00E+00
2,89E-03	0,2	9,6012	8,6617	0,0344	0,0339	5,77E-04
2,89E-03	0,4	9,6397	8,7021	0,0729	0,0743	1,16E-03
2,89E-03	0,6	9,6726	8,741	0,1058	0,1132	1,73E-03
2,89E-03	0,8	9,6993	8,7744	0,1325	0,1466	2,31E-03
2,89E-03	1	9,7197	8,8031	0,1529	0,1753	2,89E-03
2,89E-03	1,2	9,7375	8,8279	0,1707	0,2001	3,47E-03
2,89E-03	1,4	9,7508	8,8472	0,184	0,2194	4,05E-03
2,89E-03	1,6	9,7622	8,866	0,1954	0,2382	4,63E-03
2,90E-03	1,8	9,7727	8,8818	0,2059	0,254	5,21E-03
2,95E-03	2	9,7813	8,8963	0,2145	0,2685	5,90E-03
2,90E-03	2,2	9,789	8,9038	0,2222	0,276	6,38E-03
2,90E-03	2,4	9,7958	8,9189	0,229	0,2911	6,96E-03
2,90E-03	2,6	9,8012	8,9292	0,2344	0,3014	7,54E-03
2,90E-03	2,8	9,805	8,9367	0,2382	0,3089	8,12E-03
2,90E-03	3	9,809	8,945	0,2422	0,3172	8,70E-03
2,90E-03	3,2	9,8138	8,9512	0,247	0,3234	9,29E-03
2,90E-03	3,4	9,8159	8,9578	0,2491	0,33	9,87E-03
2,90E-03	3,6	9,8202	8,9643	0,2534	0,3365	1,05E-02
2,90E-03	3,8	9,8209	8,9665	0,2541	0,3387	1,10E-02

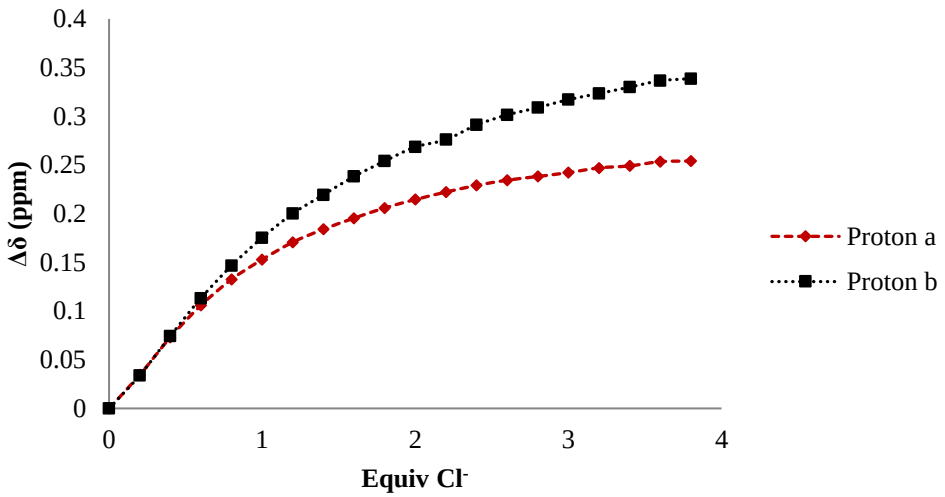

Figure 7.24. Plot of the data values from the titration study of **[16][PF_6]$_4$** with Cl^-

b. Bromide titration

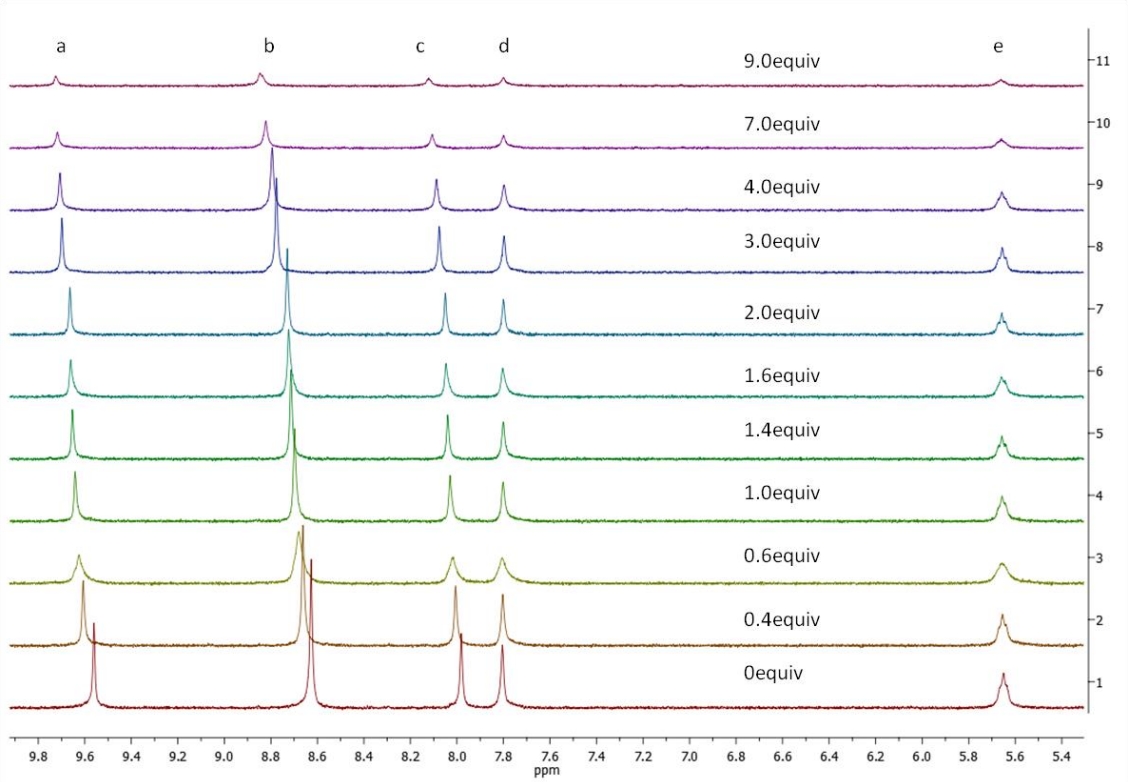

Figure 7.25. Partial ^{1}H NMR (500 Hz) changes observed for the host **[16][PF$_6$]$_4$** in DMSO-*d*^{6} during the addition of Br^-

Table 6.2: Data values from the titration study of **[16][PF$_6$]$_4$** with Br^-

[*[16][PF$_6$]$_4$*] (M)	**equiv NBu$_4$Br**	**δa (ppm)**	**δb (ppm)**	**Δδa (ppm)**	**Δδb (ppm)**	**[NBu$_4$Br] (M)**
3,84E-03	0	9,559	8,63147	0	0	0,00E+00
3,72E-03	0,2	9,587	8,647	0,028	0,01553	7,43E-04
3,72E-03	0,4	9,607	8,66302	0,048	0,03155	1,49E-03
3,72E-03	0,6	9,624	8,6842	0,065	0,05273	2,23E-03
3,73E-03	0,8	9,632	8,6957	0,073	0,06423	2,98E-03
3,73E-03	1	9,642	8,706	0,083	0,07453	3,73E-03
3,73E-03	1,2	9,649	8,716	0,09	0,08453	4,48E-03
3,74E-03	1,4	9,654	8,723	0,095	0,09153	5,23E-03
3,74E-03	1,6	9,66	8,73	0,101	0,09853	5,98E-03
3,74E-03	1,8	9,661	8,74	0,102	0,10853	6,73E-03
3,74E-03	2	9,67	8,75	0,111	0,11853	7,49E-03
3,84E-03	3	9,698	8,78	0,139	0,14853	1,15E-02
3,84E-03	4	9,7131	8,799	0,1541	0,16753	1,54E-02
3,84E-03	6	9,721	8,8299	0,162	0,19843	2,30E-02
3,84E-03	9	9,726	8,841	0,167	0,20953	3,46E-02

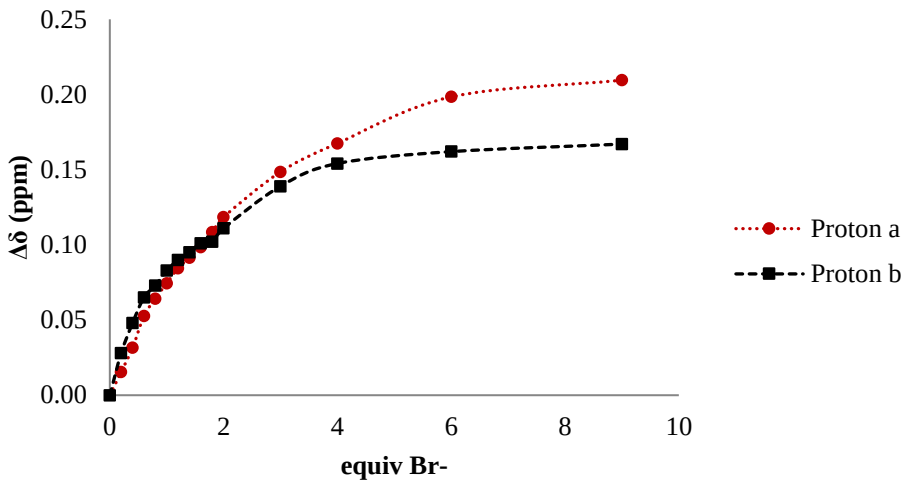

Figure 7.26. Plot of the data values from the titration study of **[16][PF$_6$]$_4$** with Br^-

c. Iodide titration

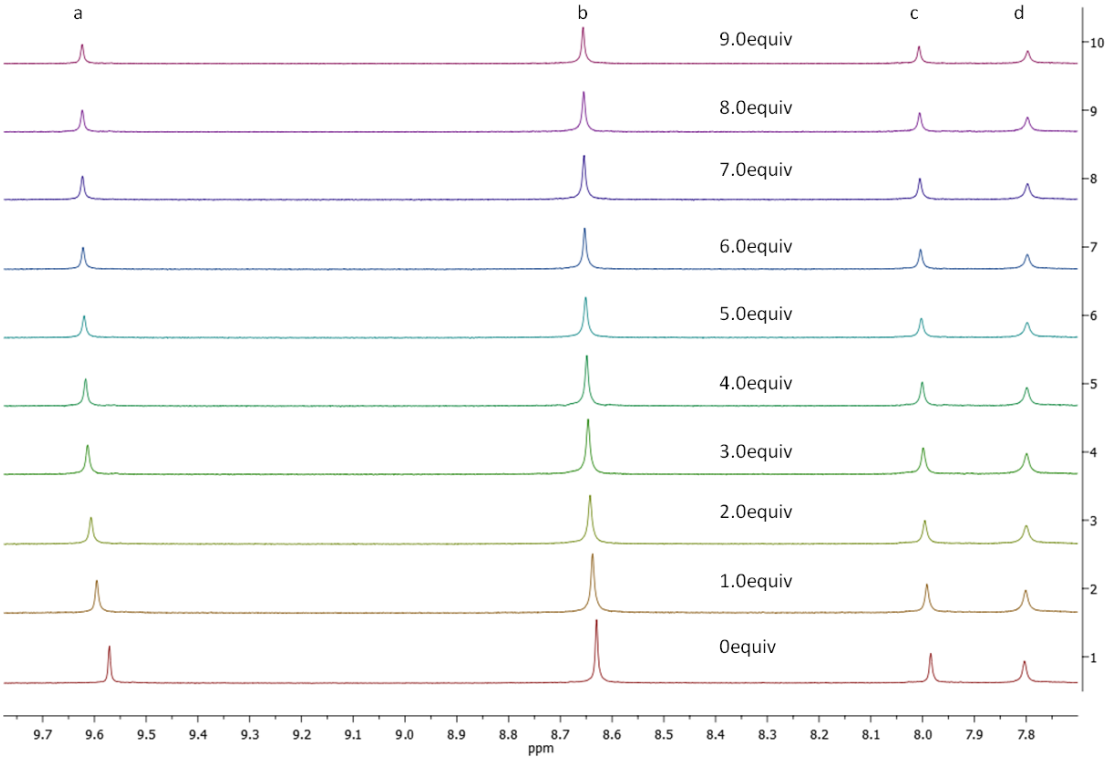

Figure 7.27. Partial ^{1}H NMR (500 Hz) changes observed for the host **[15][PF$_6$]$_4$** in DMSO-*d*^{6} during the addition of I^-

Table 6.3: Data values from the titration study of **[16][PF_6]$_4$** with I^-

[*[16]*[PF_6]$_4$] (M)	**equiv NBu_4I**	**δa (ppm)**	**δb (ppm)**	**Δδa (ppm)**	**Δδb (ppm)**	**[NBu_4I] (M)**
1,55E-02	0	9,572	8,627	0	0	0,00E+00
1,53E-02	1	9,596	8,6377	0,024	0,0107	1,53E-02
1,52E-02	2	9,607	8,6429	0,035	0,0159	3,03E-02
1,50E-02	3	9,613	8,647	0,041	0,02	4,50E-02
1,48E-02	4	9,617	8,649	0,045	0,022	5,93E-02
1,47E-02	5	9,62	8,65	0,048	0,023	7,34E-02
1,45E-02	6	9,622	8,653	0,05	0,026	8,71E-02
1,44E-02	7	9,6225	8,654	0,0505	0,027	1,01E-01
1,42E-02	8	9,6238	8,655	0,0518	0,028	1,14E-01
1,41E-02	9	9,624	8,656	0,052	0,029	1,27E-01

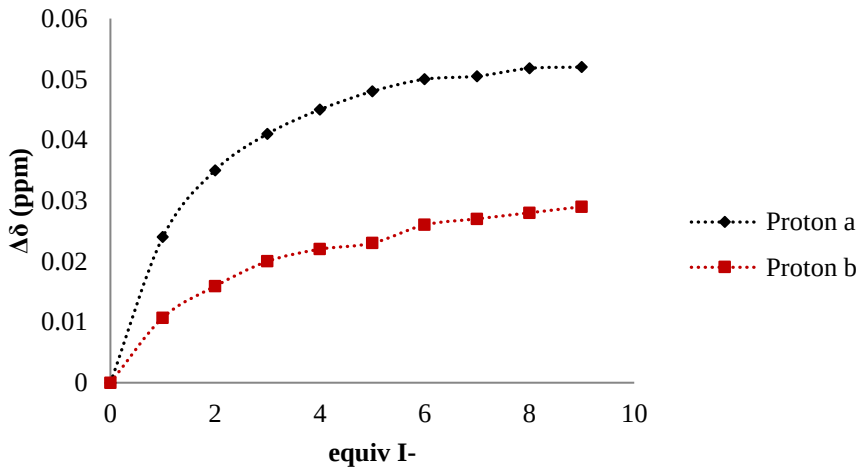

Figure 7.28. Plot of the data values from the titration study of **[16][PF_6]$_4$** with I^-

d. Perchlorate titration.

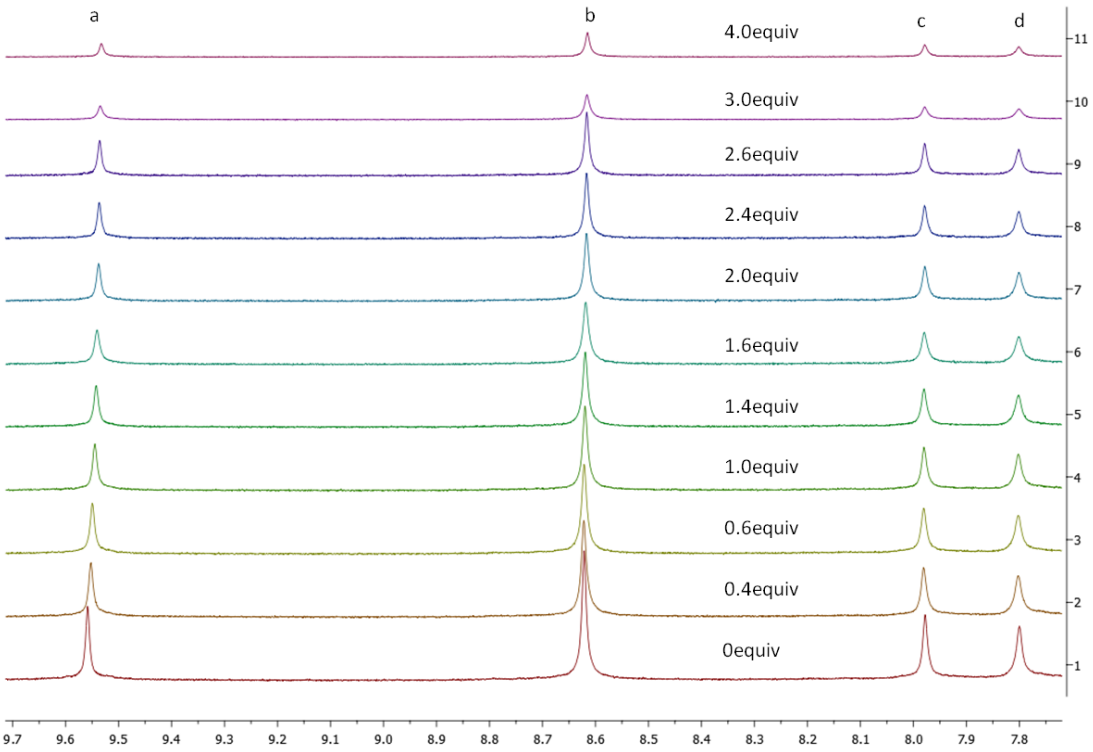

Figure 7.29. Partial ^{1}H NMR (500 Hz) changes observed for the host **[16][PF$_6$]$_4$** in DMSO-*d*^{6} during the addition of ClO_4^-

Table 6.4: Data values from the titration study of **[16][PF$_6$]$_4$** with ClO_4^-

[*[16][PF$_6$]$_4$*] (M)	**equiv NBu$_4$ClO$_4$**	**δ (ppm)**	**Δδ ppm)**	**[NBu$_4$ClO$_4$] (M)**
3,89E-03	0	9,559	0	0,00E+00
3,71E-03	0,2	9,556	0,003	7,42E-04
3,72E-03	0,4	9,551	0,008	1,49E-03
3,73E-03	0,6	9,549	0,01	2,24E-03
3,73E-03	0,8	9,546	0,013	2,99E-03
3,74E-03	1	9,544	0,015	3,74E-03
3,74E-03	1,2	9,542	0,017	4,49E-03
3,75E-03	1,4	9,541	0,018	5,25E-03
3,75E-03	1,6	9,539	0,02	6,01E-03
3,76E-03	1,8	9,538	0,021	6,77E-03
3,76E-03	2	9,537	0,022	7,53E-03
3,77E-03	2,2	9,536	0,023	8,29E-03
3,77E-03	2,4	9,536	0,023	9,05E-03
3,77E-03	2,6	9,535	0,024	9,81E-03
3,78E-03	2,8	9,5345	0,0245	1,06E-02
3,78E-03	3	9,534	0,025	1,13E-02
3,78E-03	3,4	9,532	0,027	1,29E-02
3,79E-03	4	9,531	0,028	1,51E-02
3,55E-03	5	9,53	0,029	1,78E-02

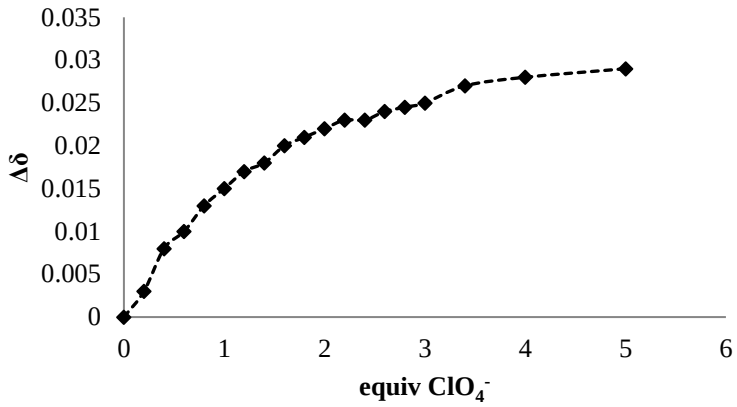

Figure 7.30. Plot of the data values from the titration study of **[16][PF$_6$]$_4$** with ClO_4^-

e. Nitrate titration

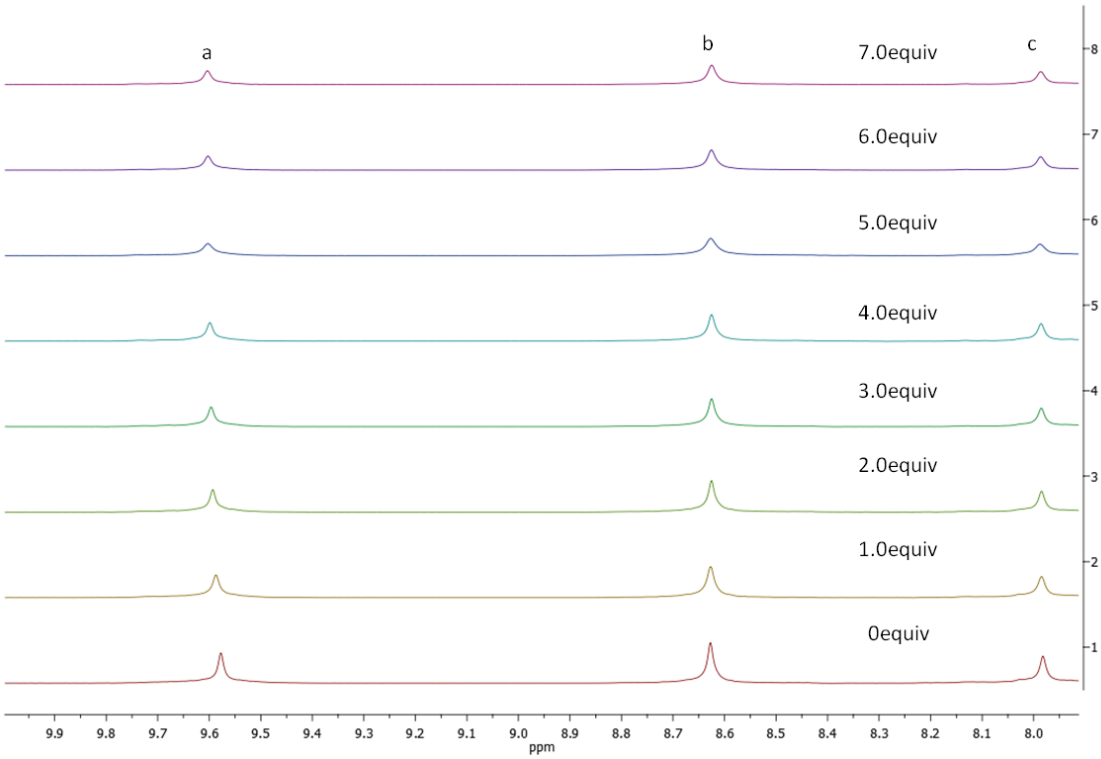

Figure 7.31. Partial ^{1}H NMR (500 Hz) changes observed for the host **[16][PF$_6$]$_4$** in DMSO-*d*^{6} during the addition of NO_3^-

Table 6.5: Data values from the titration study of **[16][PF_6]$_4$** with NO_3^-

[*[16][PF_6]$_4$*] (M)	**equiv NBu_4NO_3**	**δ(ppm)**	**Δδ(ppm)**	**[NBu_4NO_3](M)**
4,65E-03	0	9,56	0	0,00E+00
4,44E-03	1	9,5685	0,0085	4,87E-03
4,45E-03	2	9,5757	0,0157	9,71E-03
4,46E-03	3	9,5789	0,0189	1,45E-02
4,47E-03	4	9,5815	0,0215	1,94E-02
4,47E-03	5	9,5845	0,0245	2,42E-02
4,48E-03	6	9,5855	0,0255	2,90E-02
4,49E-03	7	9,5875	0,0275	3,37E-02
4,49E-03	8	9,5875	0,0275	3,85E-02
4,50E-03	9	9,5875	0,0275	4,33E-02
4,50E-03	10	9,5875	0,0275	4,80E-02

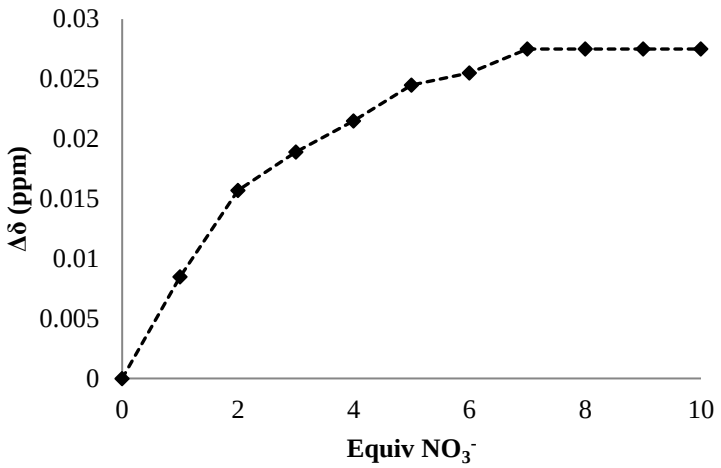

Figure 7.32 Plot of the data values from the titration study of **[16][PF_6]$_4$** with NO_3^-

f. Benzenesulfonate titration

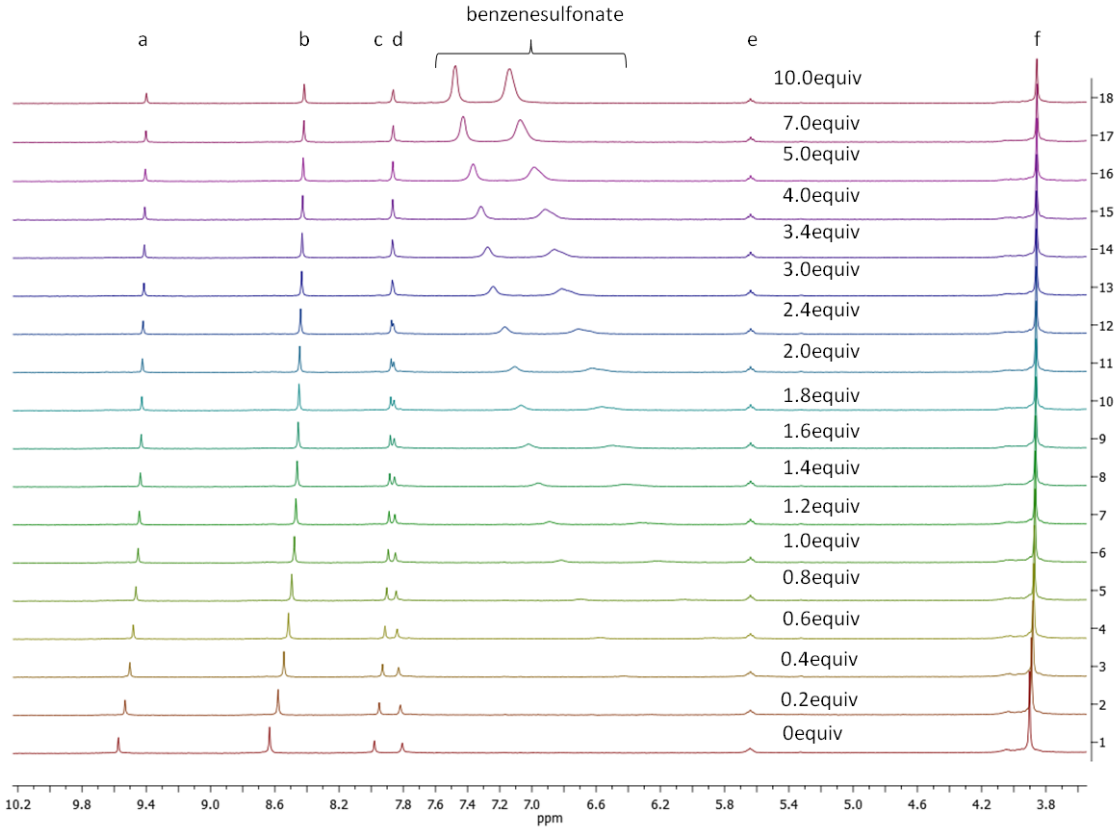

Figure 7.33. Partial ^{1}H NMR (500 Hz) changes observed for the host **[16][PF$_6$]$_4$** in DMSO-*d*^{6} during the addition of $C_6H_5SO_3^-$

Table 6.6: Data values from the titration study of **[16][PF_6]$_4$** with $C_6H_5SO_3^-$

[*[16]*[PF_6]$_4$ (M)	**equiv $NBu_4C_6H_5SO_3$**	**δa (ppm)**	**δb (ppm)**	**δc (ppm)**	**δd (ppm)**	**Δδa (ppm)**	**Δδb(ppm)**	**Δδc (ppm)**	**Δδd (ppm)**	**[$NBu_4C_6H_5SO_3$] (M)**
9,34E-04	0	9,571	8,63	7,978	7,803	0	0	0	0	0,00E+00
9,29E-04	0,2	9,531	8,58	7,95	7,819	-0,04	-0,05	-0,028	0,016	1,86E-04
9,23E-04	0,4	9,503	8,543	7,93	7,83	-0,068	-0,087	-0,048	0,027	3,69E-04
9,18E-04	0,6	9,481	8,516	7,914	7,839	-0,09	-0,114	-0,064	0,036	5,51E-04
9,13E-04	0,8	9,465	8,495	7,903	7,844	-0,106	-0,135	-0,075	0,041	7,30E-04
9,08E-04	1	9,451	8,478	7,894	7,85	-0,12	-0,152	-0,084	0,047	9,08E-04
9,03E-04	1,2	9,443	8,469	7,889	7,853	-0,128	-0,161	-0,089	0,05	1,08E-03
8,98E-04	1,4	9,437	8,461	7,885	7,855	-0,134	-0,169	-0,093	0,052	1,26E-03
8,93E-04	1,6	9,432	8,454	7,881	7,857	-0,139	-0,176	-0,097	0,054	1,43E-03
8,88E-04	1,8	9,428	8,449	7,878	7,858	-0,143	-0,181	-0,1	0,055	1,60E-03
8,83E-04	2	9,425	8,445	7,876	7,859	-0,146	-0,185	-0,102	0,056	1,77E-03
8,74E-04	2,4	9,42	8,439	7,873	7,861	-0,151	-0,191	-0,105	0,058	2,10E-03
8,60E-04	3	9,414	8,433	7,869	7,866	-0,157	-0,197	-0,109	0,063	2,58E-03
8,51E-04	3,4	9,412	8,431	7,867	7,867	-0,159	-0,199	-0,111	0,064	2,89E-03
8,38E-04	4	9,409	8,427	7,866	7,866	-0,162	-0,203	-0,112	0,063	3,35E-03
8,17E-04	5	9,406	8,424	7,865	7,865	-0,165	-0,206	-0,113	0,062	4,08E-03
7,96E-04	6	9,403	8,421	7,864	7,866	-0,168	-0,209	-0,114	0,063	4,78E-03
7,77E-04	7	9,401	8,419	7,863	7,866	-0,17	-0,211	-0,115	0,063	5,44E-03
7,25E-04	10	9,399	8,417	7,862	7,866	-0,172	-0,213	-0,116	0,063	7,25E-03

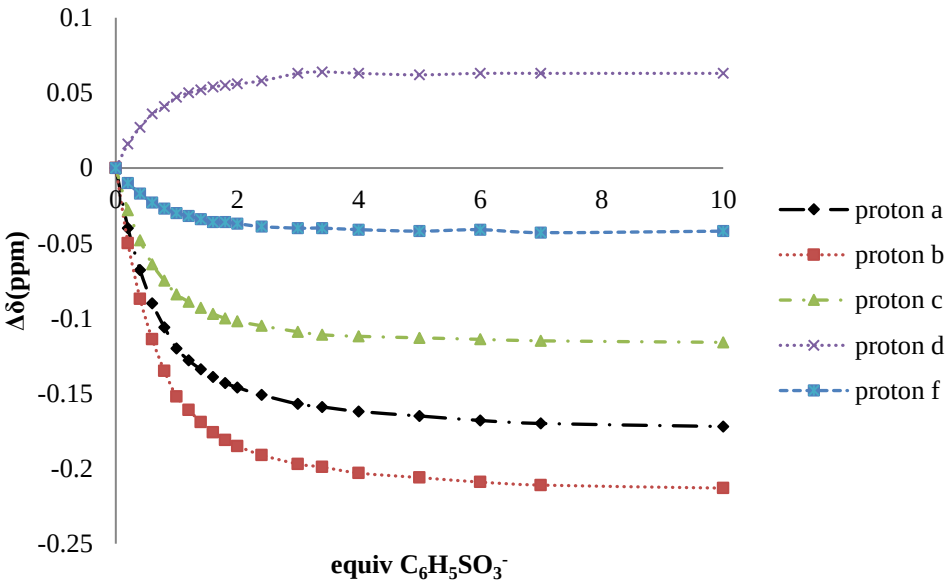

Figure 7.34. Plot of the data values from the titration study of **[16][PF_6]$_4$** with $C_6H_5SO_3^-$

g. *p*-toluensulfonate titration

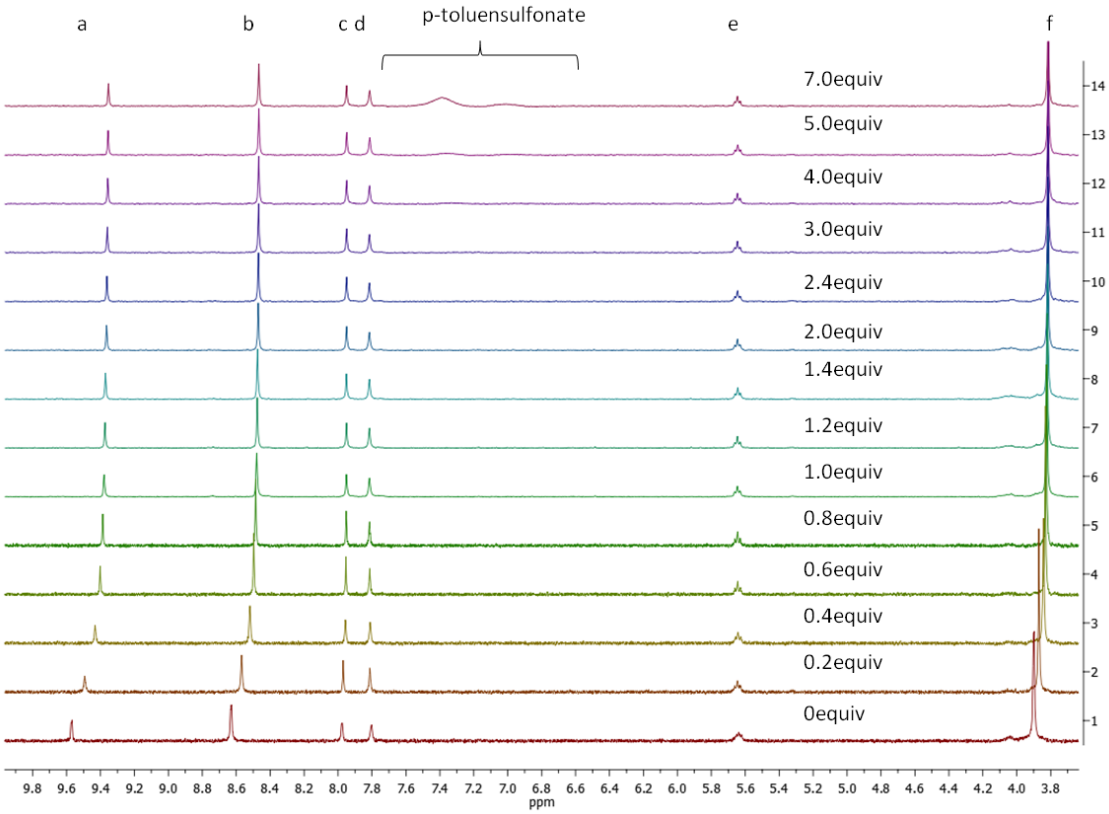

Figure 7.35. Partial ^{1}H NMR (500 Hz) changes observed for the host **[16][PF$_6$]$_4$** in DMSO-*d*^{6} during the addition of $C_7H_8SO_3^-$

Table 6.7: Data values from the titration study of **[16][PF$_6$]$_4$** with $C_7H_8SO_3^-$

[*[16][PF$_6$]$_4$*] (M)	**equiv $NBu_4C_7H_7SO_3$**	**δa (ppm)**	**δb (ppm)**	**δd (ppm)**	**δf (ppm)**	**Δδa (ppm)**	**Δδb (ppm)**	**Δδd (ppm)**	**Δδf (ppm)**	**[$NBu_4C_7H_7SO_3$] (M)**
9,34E-04	0	9,568	8,627	7,798	3,901	0	0	0	0	0,00E+00
9,29E-04	0,2	9,493	8,583	7,812	3,869	-0,075	-0,044	0,014	-0,032	1,86E-04
9,23E-04	0,4	9,431	8,52	7,81	3,842	-0,137	-0,107	0,012	-0,059	3,69E-04
9,18E-04	0,6	9,402	8,497	7,814	3,832	-0,166	-0,13	0,016	-0,069	5,51E-04
9,13E-04	0,8	9,387	8,485	7,815	3,825	-0,181	-0,142	0,017	-0,076	7,30E-04
9,08E-04	1	9,379	8,48	7,815	3,823	-0,189	-0,147	0,017	-0,078	9,08E-04
9,03E-04	1,2	9,374	8,476	7,815	3,821	-0,194	-0,151	0,017	-0,08	1,08E-03
8,98E-04	1,4	9,371	8,475	7,815	3,819	-0,197	-0,152	0,017	-0,082	1,26E-03
8,83E-04	2	9,364	8,471	7,815	3,817	-0,204	-0,156	0,017	-0,084	1,77E-03
8,74E-04	2,4	9,362	8,47	7,815	3,816	-0,206	-0,157	0,017	-0,085	2,10E-03
8,60E-04	3	9,36	8,469	7,815	3,816	-0,208	-0,158	0,017	-0,085	2,58E-03
8,38E-04	4	9,357	8,468	7,814	3,816	-0,211	-0,159	0,016	-0,085	3,35E-03
8,17E-04	5	9,355	8,467	7,813	3,814	-0,213	-0,16	0,015	-0,087	4,08E-03
7,77E-04	7	9,353	8,467	7,814	3,815	-0,215	-0,16	0,016	-0,086	5,44E-03

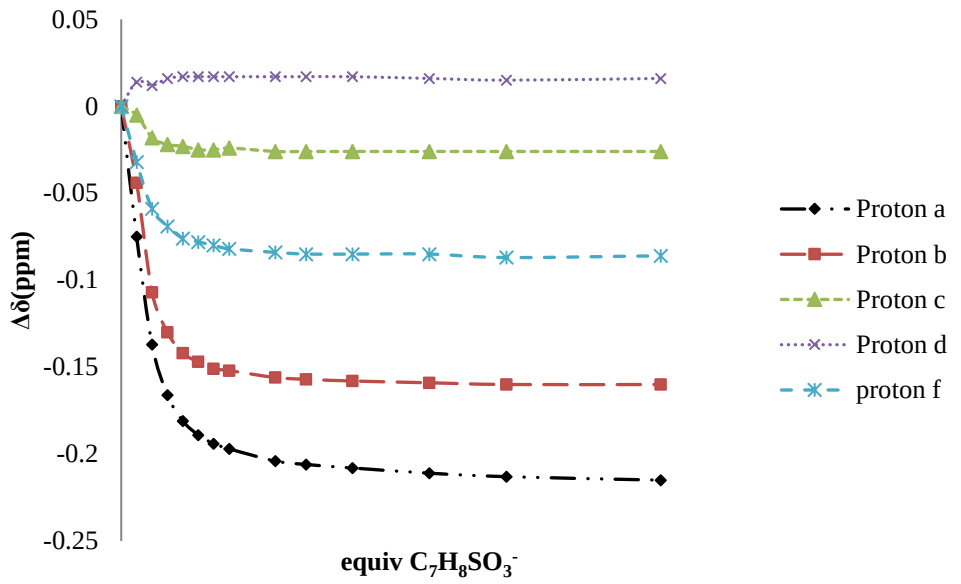

Figure 7.36. Plot of the data values from the titration study of **[16][PF$_6$]$_4$** with $C_7H_8SO_3^-$

h. Cyanide titration

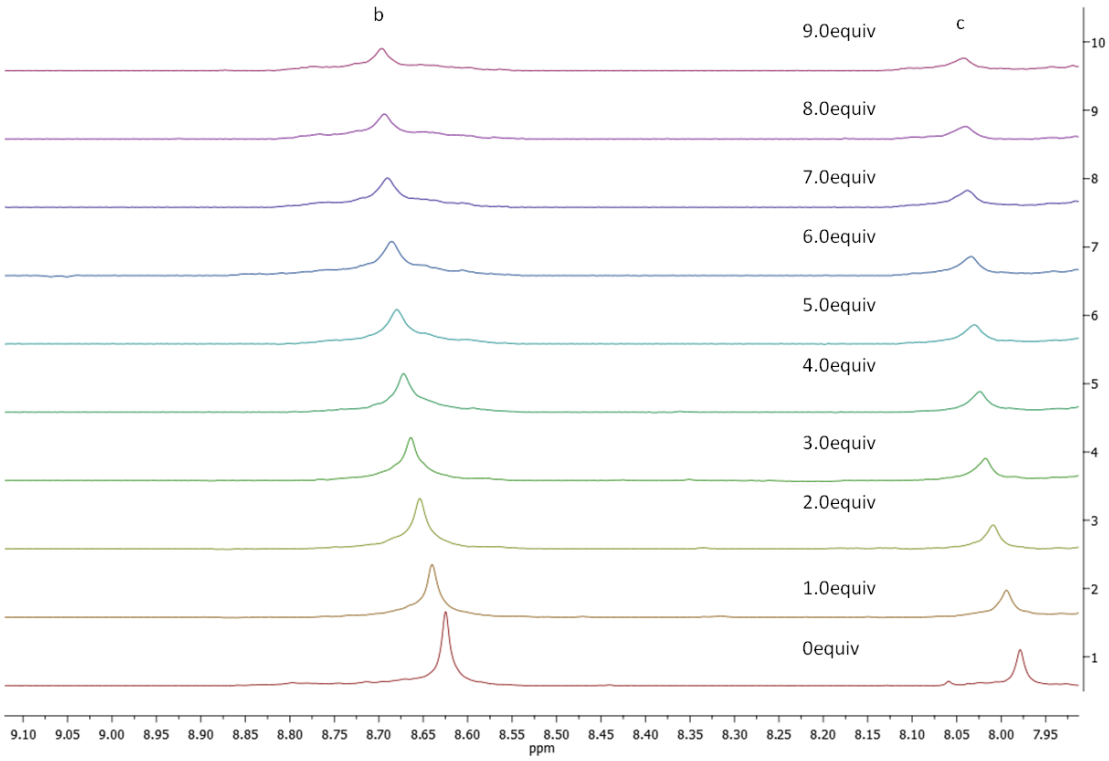

Figure 7.37. Partial ^{1}H NMR (500 Hz) changes observed for the host **[16][PF$_6$]$_4$** in DMSO-*d*^{6} during the addition of CN^-

Table 6.8: Data values from the titration study of **[16][PF_6]$_4$** with CN^-.

[16]*[PF_6]$_4$*] (M)	**equiv NBu_4CN**	**δ(ppm)**	**Δδ(ppm)**	**[NBu_4CN] (M)**
1,89E-03	0	8,6258	0	0,00E+00
1,86E-03	1	8,64	0,0142	1,86E-03
1,84E-03	2	8,6538	0,028	3,68E-03
1,82E-03	3	8,6639	0,0381	5,45E-03
1,80E-03	4	8,672	0,0462	7,18E-03
1,77E-03	5	8,6797	0,0539	8,87E-03
1,75E-03	6	8,6855	0,0597	1,05E-02
1,73E-03	7	8,6903	0,0645	1,21E-02
1,71E-03	8	8,6938	0,068	1,37E-02
1,69E-03	9	8,6967	0,0709	1,52E-02
1,68E-03	10	8,6963	0,0705	1,68E-02

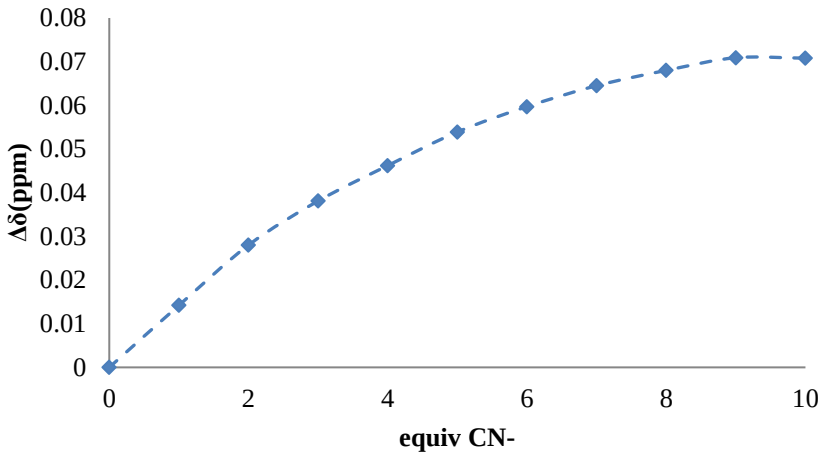

Figure 7.38. Plot of the data values from the titration study of **[16][PF_6]$_4$** with CN^-

i. Hexanoate titration

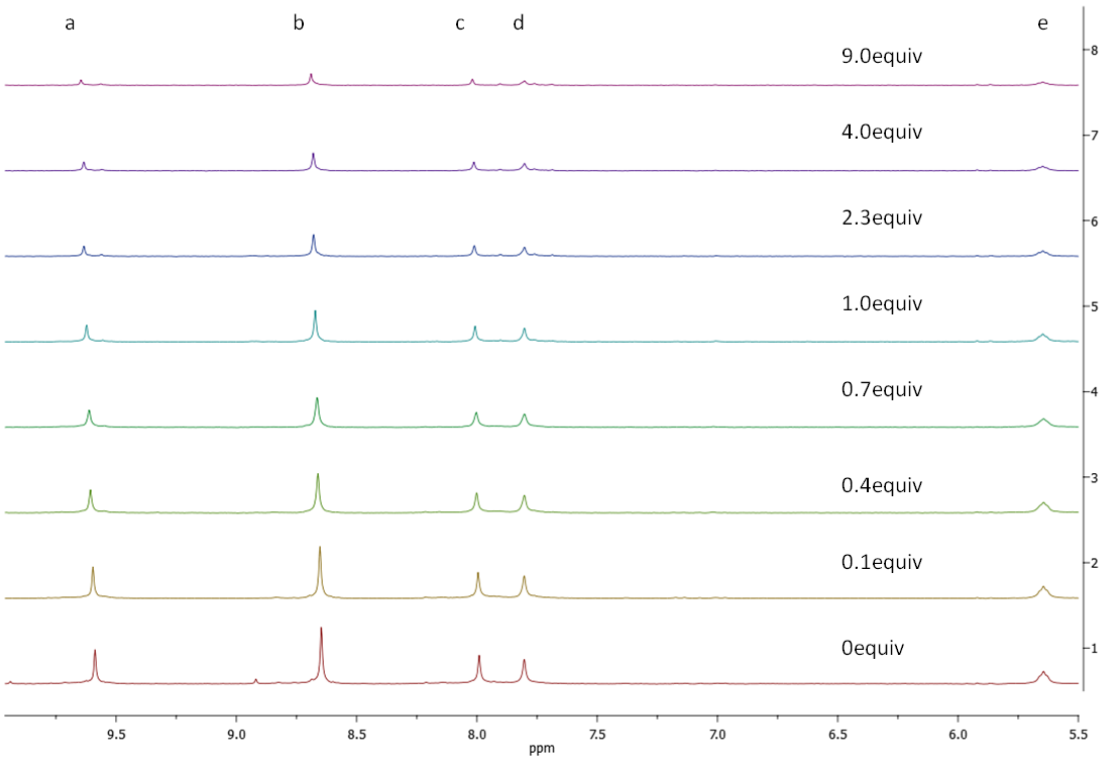

Figure 7.39. Partial ^{1}H NMR (500 Hz) changes observed for the host **[16][PF$_6$]$_4$** in DMSO-*d*^{6} during the addition of $C_6H_8COO^-$

Table 6.9: Data values from the titration study of **[16][PF$_6$]$_4$** with $C_6H_8COO^-$

***[16][PF$_6$]$_4$*](M)**	**equiv $NBu_4C_6H_8COO$**	**δ (ppm)**	**Δδ(ppm)**	**[$NBu_4C_6H_8COO$] (M)**
3,19E-03	0,0	8,6469	0	0,00E+00
2,87E-03	0,1	8,6527	0,0058	3,16E-04
2,55E-03	0,3	8,658	0,0111	6,38E-04
2,23E-03	0,4	8,6644	0,0175	9,38E-04
1,91E-03	0,7	8,6722	0,0253	1,28E-03
1,60E-03	1,0	8,6789	0,032	1,60E-03
1,28E-03	1,5	8,685	0,0381	1,91E-03
9,57E-04	2,3	8,69	0,0431	2,23E-03
6,38E-04	4,0	8,7	0,0531	2,55E-03
3,19E-04	9,0	8,71	0,0631	2,87E-03

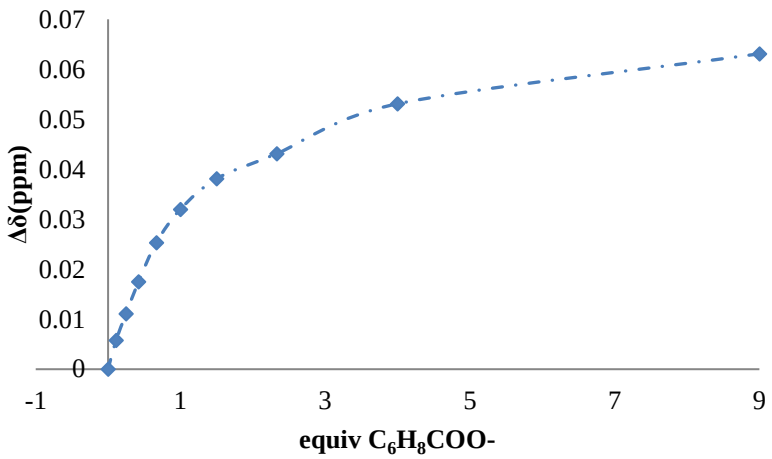

Figure 7.40. Plot of the data values from the titration study of **[16][PF$_6$]$_4$** with $C_6H_8COO^-$.

The anion recognition capabilities of receptor **[17][PF$_6$]$_4$** towards several anions was determined by ^{1}H NMR titration experiments, which were done in DMSO-*d*^{6}. The large downfield shifts of some of the signal protons suggest complexation between **[17][PF$_6$]$_4$** and the anions (Cl^-, Br^-, I^-, ClO_4^-, NO_3^-,$C_6H_5SO_3^-$, $C_7H_8SO_3^-$, CN^-).

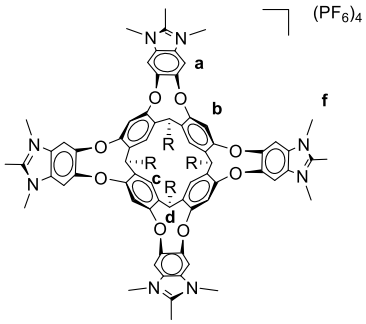

a. Chloride titration

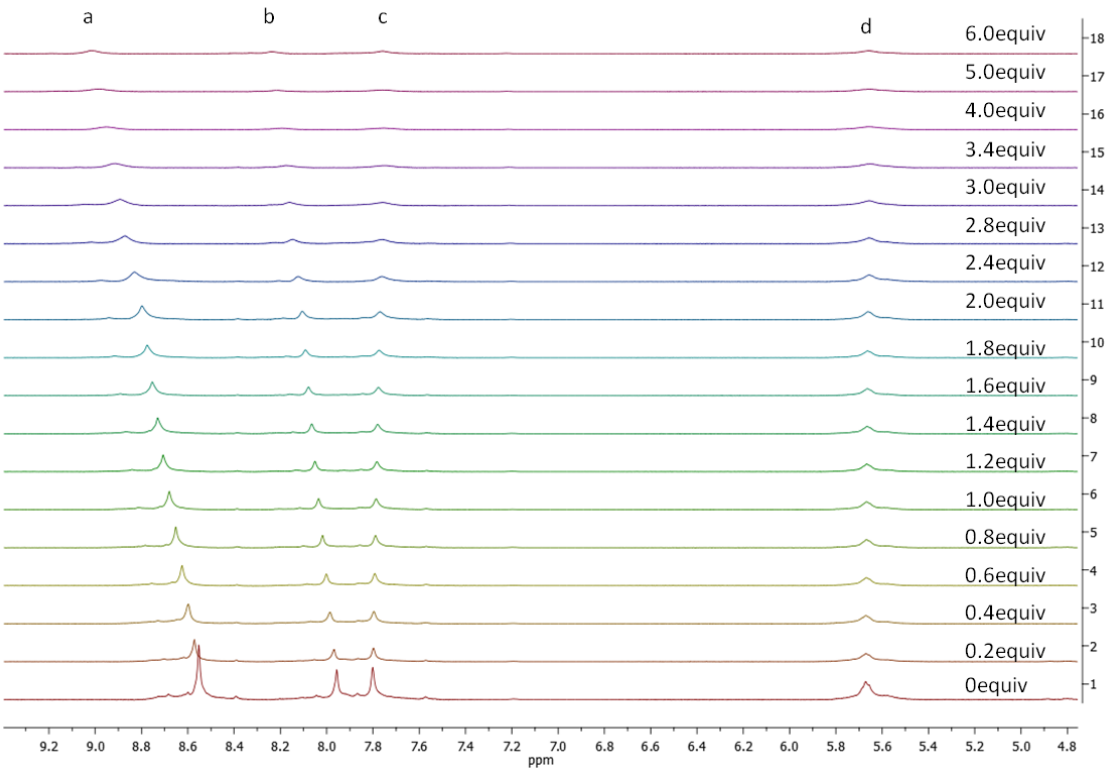

Figure 7.41. Partial ^{1}H NMR (500 Hz) changes observed for the host **[17][PF$_6$]$_4$** in DMSO-*d*^{6} during the addition of Cl^-

Table 6.10: Data values from the titration study of **[17][PF$_6$]$_4$** with Cl^-

[*17*][*PF$_6$*]$_4$] (M)	**equiv NBu$_4$Cl**	**δa (ppm)**	**δb (ppm)**	**Δδa (ppm)**	**Δδb (ppm)**	**[NBu$_4$Cl] (M)**
1,43E-02	0	8,552	7,956	0	0	0,00E+00
1,39E-02	0,2	8,572	7,977	0,02	0,021	2,78E-03
1,35E-02	0,4	8,598	7,985	0,046	0,029	5,42E-03
1,32E-02	0,6	8,625	8,002	0,073	0,046	7,92E-03
1,29E-02	0,8	8,652	8,018	0,1	0,062	1,03E-02
1,26E-02	1	8,68	8,035	0,128	0,079	1,26E-02
1,23E-02	1,2	8,707	8,051	0,155	0,095	1,47E-02
1,20E-02	1,4	8,731	8,064	0,179	0,108	1,68E-02
1,17E-02	1,6	8,753	8,079	0,201	0,123	1,88E-02
1,15E-02	1,8	8,776	8,093	0,224	0,137	2,07E-02
1,12E-02	2	8,79	8,107	0,238	0,151	2,25E-02
1,08E-02	2,4	8,831	8,124	0,279	0,168	2,59E-02
1,04E-02	2,8	8,869	8,148	0,317	0,192	2,90E-02
1,02E-02	3	8,892	8,159	0,34	0,203	3,05E-02
9,78E-03	3,4	8,913	8,178	0,361	0,222	3,32E-02
9,26E-03	4	8,957	8,209	0,405	0,253	3,71E-02
8,52E-03	5	8,984	8,23	0,432	0,274	4,26E-02
7,88E-03	6	9	8,24	0,448	0,284	4,73E-02
7,33E-03	7	9	8,24	0,448	0,284	5,13E-02

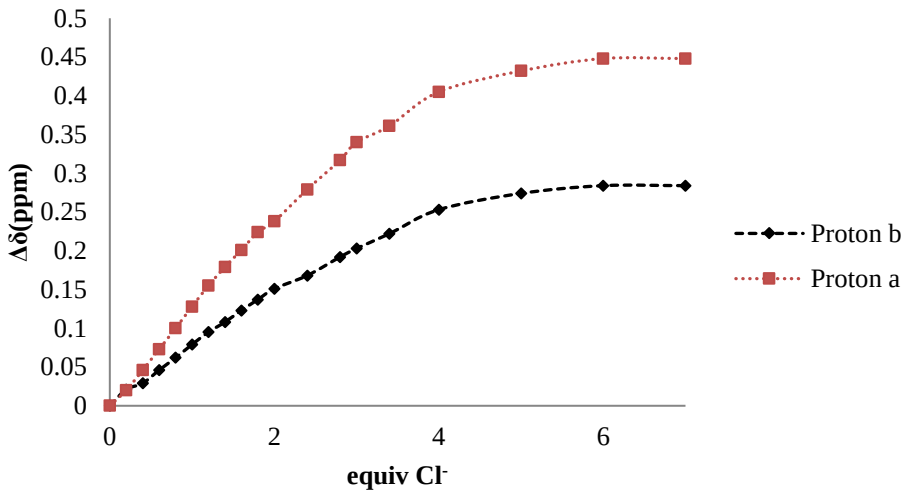

Figure 7.42. Plot of the data values from the titration study of **[17][PF$_6$]$_4$** with Cl^-

b. Bromide titration

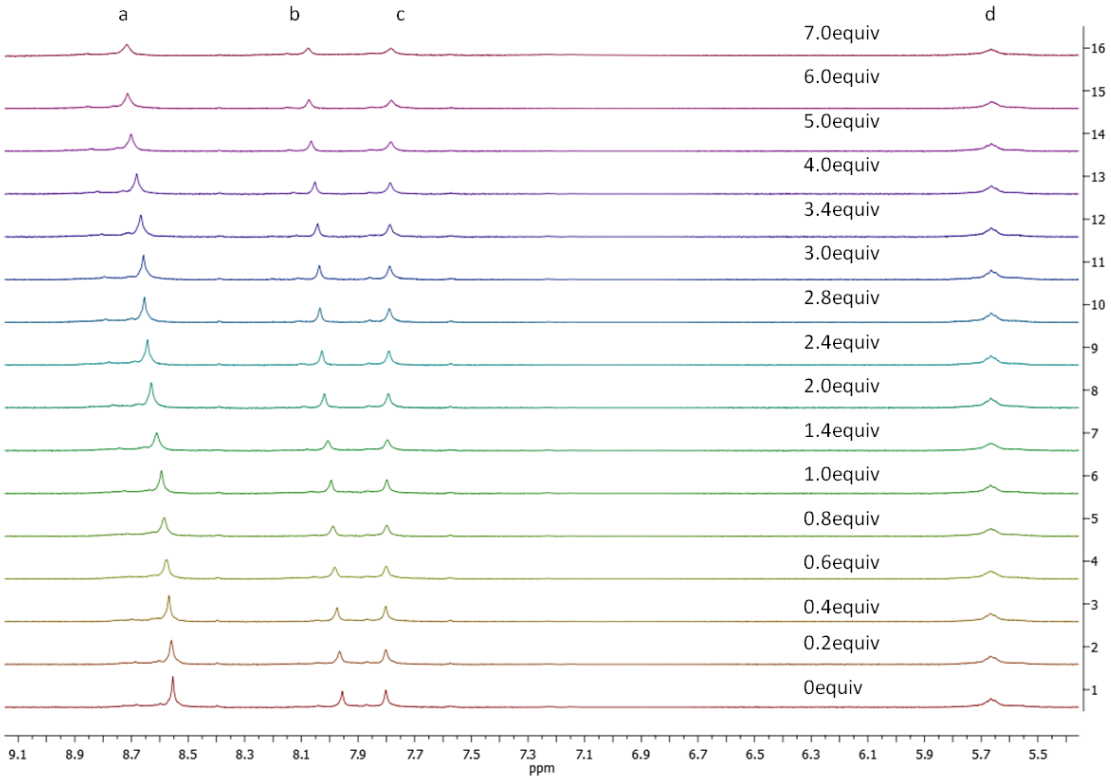

Figure 7.43. Partial ^{1}H NMR (500 Hz) changes observed for the host **[17][PF$_6$]$_4$** in DMSO-*d*^{6} during the addition of Br^-

Table 6.11: Data values from the titration study of **[17][PF$_6$]$_4$** with Br^-

[17][PF$_6$]$_4$] (M)	equiv NBu_4Br	δa (ppm)	δb (ppm)	Δδa (ppm)	Δδb (ppm)	[NBu_4Br] (M)
7,20E-03	0	8,554	7,956	0	0	0,00E+00
7,06E-03	0,2	8,56	7,965	0,006	0,009	1,41E-03
6,93E-03	0,4	8,568	7,973	0,014	0,017	2,77E-03
6,80E-03	0,6	8,577	7,982	0,023	0,026	4,08E-03
6,68E-03	0,8	8,583	7,988	0,029	0,032	5,34E-03
6,56E-03	1	8,594	7,999	0,04	0,043	6,56E-03
6,34E-03	1,4	8,611	8,007	0,057	0,051	8,87E-03
6,03E-03	2	8,63	8,019	0,076	0,063	1,21E-02
5,84E-03	2,4	8,643	8,027	0,089	0,071	1,40E-02
5,66E-03	2,8	8,654	8,035	0,1	0,079	1,58E-02
5,57E-03	3	8,658	8,037	0,104	0,081	1,67E-02
5,41E-03	3,4	8,667	8,043	0,113	0,087	1,84E-02
5,18E-03	4	8,681	8,052	0,127	0,096	2,07E-02
4,84E-03	5	8,701	8,065	0,147	0,109	2,42E-02
4,55E-03	6	8,71	8,073	0,156	0,117	2,73E-02

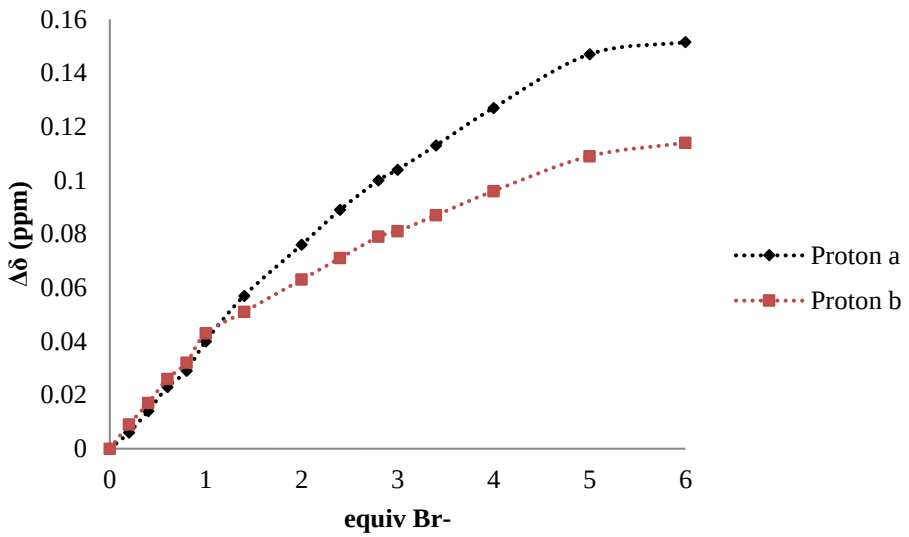

Figure 7.44. Plot of the data values from the titration study of **[17][PF$_6$]$_4$** with Br^-

c. Benzenesulfonate titration

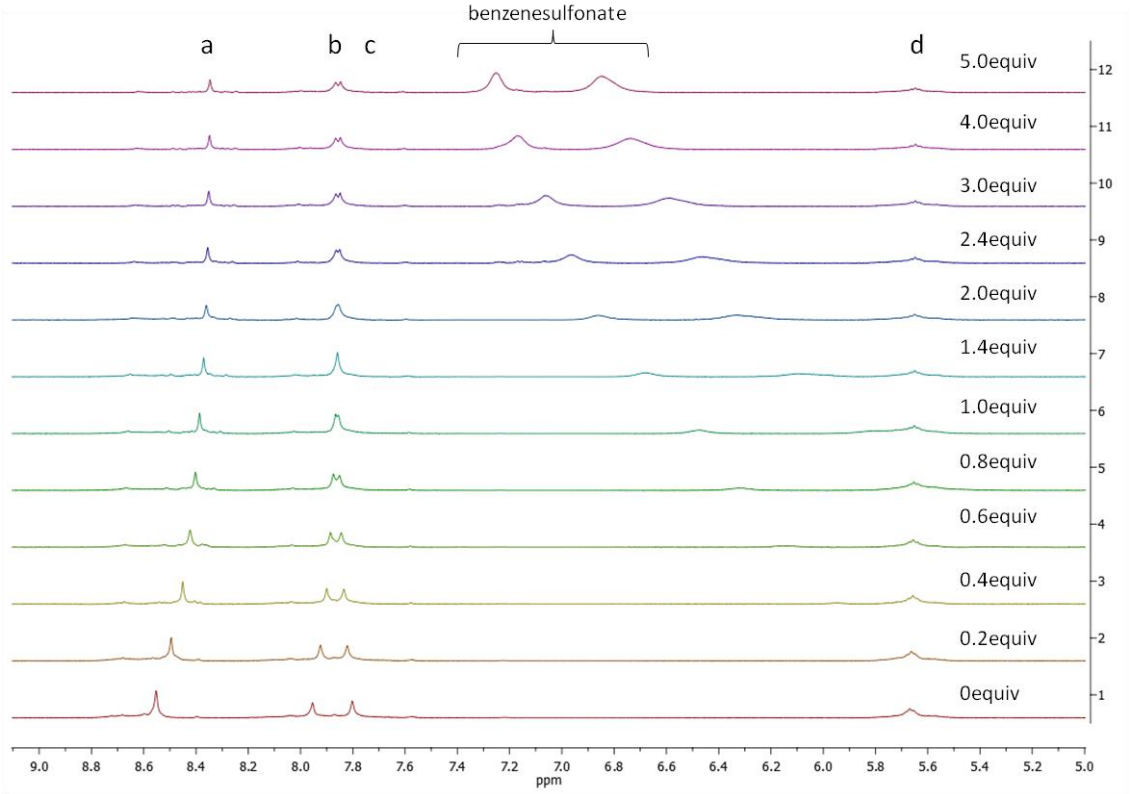

Figure 7.45. Partial ^{1}H NMR (500 Hz) changes observed for the host **[17][PF$_6$]$_4$** in DMSO-*d*^{6} during the addition of $C_6H_5SO_3^-$

Table 6.12: Data values from the titration study of **[17][PF$_6$]$_4$** with $C_6H_5SO_3^-$

[17][PF$_6$]$_4$ (M)	equiv $NBu_4C_6H_5SO_3$	δa (ppm)	δb (ppm)	δc (ppm)	Δδa (ppm)	Δδb (ppm)	Δδc (ppm)	[$NBu_4C_6H_5SO_3$] (M)
0,00876667	0	8,552	7,954	7,802	0	0	0	0
0,00853952	0,2	8,495	7,923	7,823	-0,057	-0,031	0,021	0,001707903
0,00832384	0,4	8,451	7,9	7,834	-0,101	-0,054	0,032	0,003329535
0,00811879	0,6	8,422	7,886	7,844	-0,13	-0,068	0,042	0,004871272
0,0079236	0,8	8,402	7,874	7,85	-0,15	-0,08	0,048	0,006338877
0,00773757	1	8,386	7,865	7,855	-0,166	-0,089	0,053	0,00773757
0,00739055	1,4	8,37	7,859	7,859	-0,182	-0,095	0,057	0,010346766
0,0069247	2	8,36	7,856	7,862	-0,192	-0,098	0,06	0,013849394
0,00664544	2,4	8,355	7,85	7,863	-0,197	-0,104	0,061	0,01594906
0,00626638	3	8,351	7,848	7,865	-0,201	-0,106	0,063	0,018799142
0,00572237	4	8,348	7,847	7,866	-0,204	-0,107	0,064	0,022889469
0,00526527	5	8,346	7,847	7,866	-0,206	-0,107	0,064	0,026326326

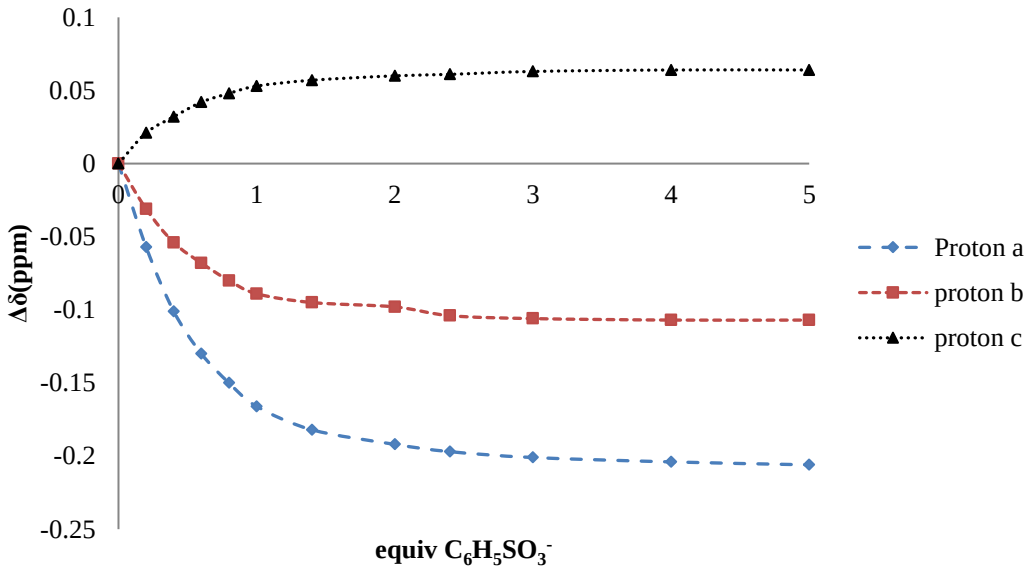

Figure 7.46. Plot of the data values from the titration study of **[17][PF$_6$]$_4$** with $C_6H_5SO_3^-$

d. *p*-toluensulfonate titration

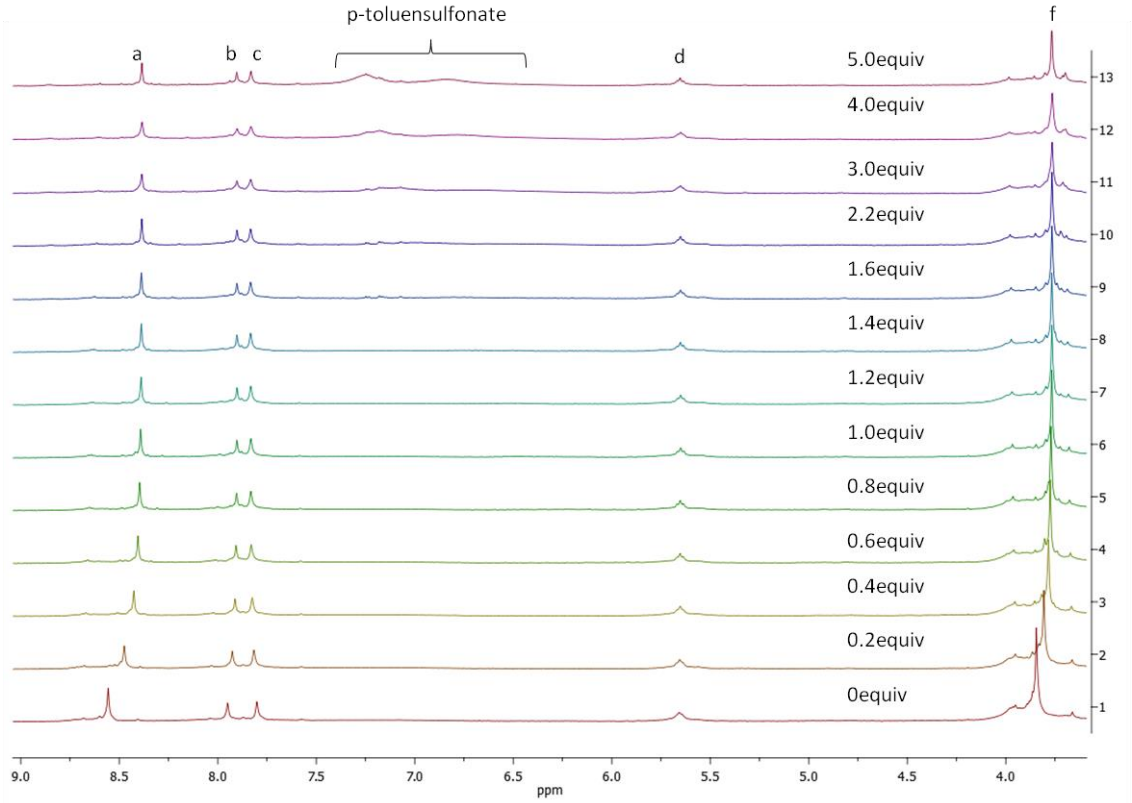

Figure 7.47. Partial ^{1}H NMR (500 Hz) changes observed for the host **[17][PF$_6$]$_4$** in DMSO-*d*^{6} during the addition of $C_7H_8SO_3^-$

Table 6.13: Data values from the titration study of **[17][PF$_6$]$_4$** with $C_7H_8SO_3^-$

[17][PF$_6$]$_4$] (M)	equiv $NBu_4C_7H_7SO_3$	δa (ppm)	δb (ppm)	δc (ppm)	δf (ppm)	Δδa (ppm)	Δδb (ppm)	Δδc (ppm)	Δδf (ppm)	[$NBu_4C_7H_7SO_3$] (M)
2,10E-03	0	8,556	7,95	7,801	3,845	0	0	0	0	0,00E+00
2,10E-03	0,2	8,475	7,927	7,816	3,807	-0,081	-0,023	0,015	-0,038	4,15E-04
2,10E-03	0,4	8,426	7,912	7,826	3,784	-0,13	-0,038	0,025	-0,061	8,18E-04
2,10E-03	0,6	8,405	7,907	7,831	3,775	-0,151	-0,043	0,03	-0,07	1,21E-03
2,10E-03	0,8	8,396	7,905	7,833	3,77	-0,16	-0,045	0,032	-0,075	1,60E-03
2,10E-03	1	8,391	7,903	7,832	3,767	-0,165	-0,047	0,031	-0,078	1,97E-03
2,10E-03	1,2	8,389	7,902	7,833	3,766	-0,167	-0,048	0,032	-0,079	2,33E-03
2,10E-03	1,4	8,388	7,902	7,834	3,766	-0,168	-0,048	0,033	-0,079	2,69E-03
2,10E-03	1,6	8,388	7,902	7,834	3,765	-0,168	-0,048	0,033	-0,08	3,04E-03
2,10E-03	2,2	8,386	7,902	7,834	3,765	-0,17	-0,048	0,033	-0,08	4,03E-03
2,10E-03	3	8,386	7,903	7,833	3,765	-0,17	-0,047	0,032	-0,08	5,26E-03
1,25E-04	4	8,385	7.902	7,832	3,764	-0,171	7894,05	0,031	-0,081	6,64E-03

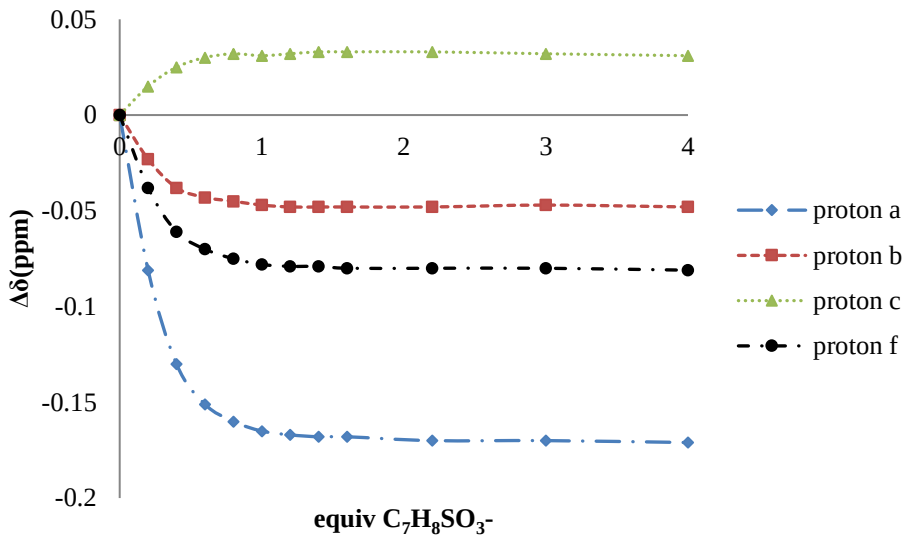

Figure 7.48. Plot of the data values from the titration study of **[17][PF$_6$]$_4$** with $C_7H_8SO_3^-$

Determination of the binding stoichiometry by Job Plot analysis

The stoichiometry of compound **[16][PF$_6$]$_4$** and **[17][PF$_6$]$_4$** with different anions of tetrabutylammonium salts were tested mainly with the study of the binding fitting. Besides, a Job Plot ^{1}H NMR experiment (DMSO-d^6) was also done to support the binding fitting stoichiometry estimation.

a. Tetrabutylammonium chloride and [16][PF$_6$]$_4$

Table 6.14: Data values from the Job plot analysis between **[16][PF$_6$]$_4$** and Cl^-

χ_h	δ(ppm)	Δδ (ppm)	χ_h*Δδ
1	9,562	0	0
0,9	9,571	0,009	0,0081
0,8	9,582	0,02	0,016
0,7	9,599	0,037	0,0259
0,6	9,621	0,059	0,0354
0,5	9,641	0,079	0,0395
0,4	9,655	0,093	0,0372
0,3	9,67	0,108	0,0324
0,2	9,69	0,128	0,0256
0,1	9,747	0,185	0,0185

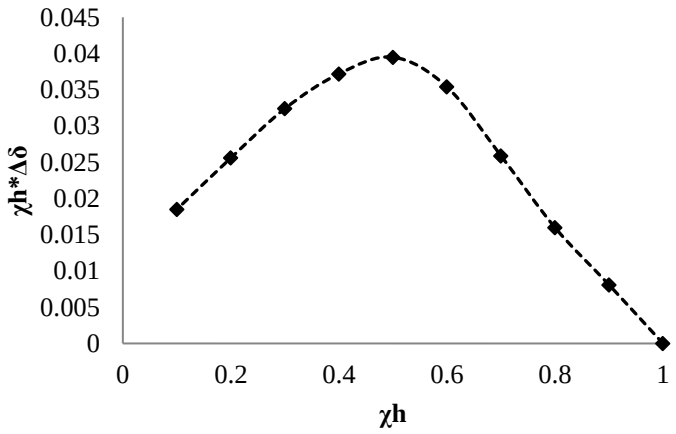

Figure 7.49. Job plot in DMSO-d^6 for the interaction of **[16][PF$_6$]$_4$** and Cl^- showing the 1:1 stoichiometry ([H+G]= $4 \cdot 10^{-3}$ M)

b. Tetrabutylammonium chloride and [17][PF$_6$]$_4$

Table 6.15: Data values from the Job plot analysis between **[17][PF$_6$]$_4$** and Cl^-

χh	ppm	Δppm	χh*Δppm
0,1	8,825	0,265	0,0265
0,2	8,74	0,18	0,036
0,3	8,715	0,155	0,0465
0,4	8,688	0,128	0,0512
0,5	8,665	0,105	0,0525
0,6	8,636	0,076	0,0456
0,7	8,61	0,05	0,035
0,8	8,586	0,026	0,0208
1	8,56	0	0

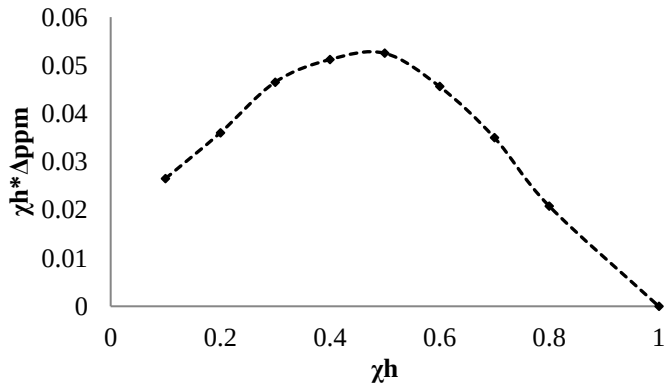

Figure 7.50. Job plot in DMSO-d^6 for the interaction of **[17][PF$_6$]$_4$** and Cl^- showing the 1:1 stoichiometry. ([H+G]= $5 \cdot 10^{-3}$ M)

c. Tetrabutylammonium bromide and [16][PF_6]$_4$

Table 6.16: Data values from the Job plot analysis between **[16][PF_6]$_4$** and Br^-

χ_h	δ(ppm)	Δδ (ppm)	χ_h*Δδ
1	9,564	0	0
0,9	9,573	0,009	0,0081
0,875	9,574	0,01	0,00875
0,75	9,583	0,019	0,01425
0,7	9,588	0,024	0,0168
0,6	9,6	0,036	0,0216
0,5	9,612	0,048	0,024
0,4	9,6225	0,0585	0,0234
0,3	9,635	0,071	0,0213
0,25	9,642	0,078	0,0195
0,125	9,671	0,107	0,013375
0,1	9,676	0,112	0,0112

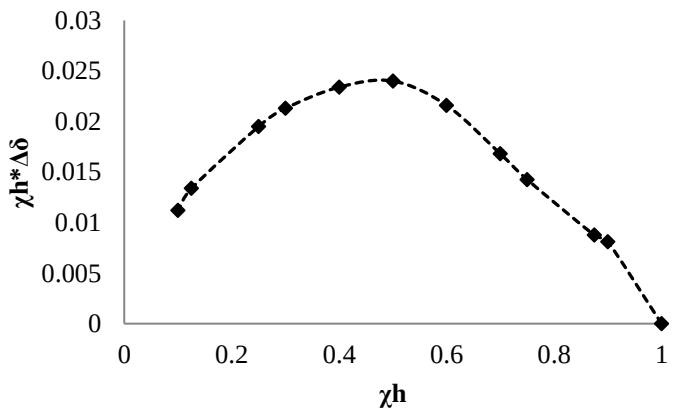

Figure 7.51. Job plot in DMSO-d^6 for the interaction of **[16][PF_6]$_4$** and Br^- showing the 1:1 stoichiometry. ([H+G]= $4 \cdot 10^{-3}$ M)

d. Tetrabutylammonium iodide and [16][PF_6]$_4$

Table 6.17: Data values from the Job plot analysis between **[16][PF_6]$_4$** and I^-

χ_h	δ(ppm)	Δδ (ppm)	χ_h*Δδ
1	9,561	0	0
0,9	9,563	0,002	0,0018
0,8	9,566	0,005	0,004
0,7	9,57	0,009	0,0063
0,6	9,575	0,014	0,0084
0,5	9,58	0,019	0,0095
0,4	9,583	0,022	0,0088
0,3	9,585	0,024	0,0072
0,2	9,587	0,026	0,0052
0,1	9,59	0,029	0,0029

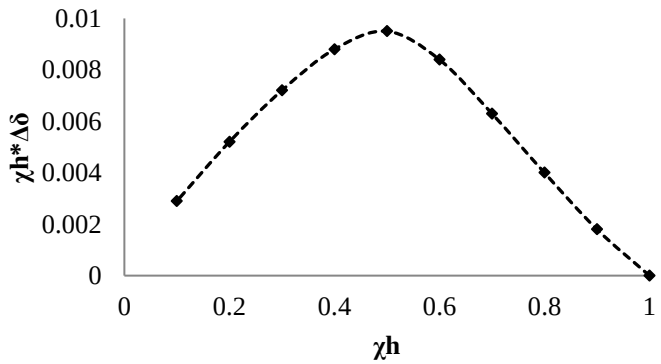

Figure 7.52. Job plot in DMSO-d^6 for the interaction of **[16][PF_6]$_4$** and I^- showing the 1:1 stoichiometry. ([H+G]=4.5·10^{-3} M)

e. Tetrabutylammonium perchlorate and [16][PF_6]$_4$

Table 6.18: Data values from the Job plot analysis between **[16][PF_6]$_4$** and ClO_4^-

χ_h	δ(ppm)	Δδ (ppm)	χ_h*Δδ
1	9,562	0	0
0,9	9,562	0,0004	0,00036
0,8	9,561	0,0012	0,00096
0,7	9,560	0,002	0,0014
0,6	9,559	0,0035	0,0021
0,5	9,557	0,005	0,0025
0,4	9,556	0,006	0,0024
0,3	9,555	0,007	0,0021
0,2	9,554	0,008	0,0016
0,1	9,552	0,01	0,001

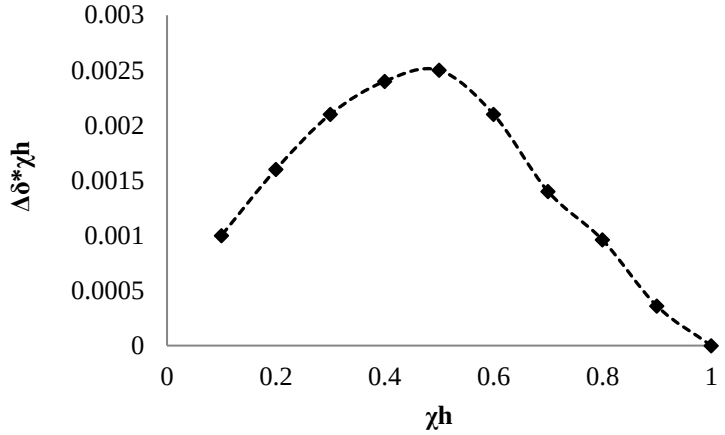

Figure 7.53. Job plot in DMSO-d^6 for the interaction of **[16][PF$_6$]$_4$** and ClO_4^- showing the 1:1 stoichiometry. ([H+G]= $5 \cdot 10^{-3}$ M)

f. Tetrabutylammonium phenylsulfonate and [16][PF$_6$]$_4$

Table 6.19: Data values from the Job plot analysis between **[16][PF$_6$]$_4$** and $C_6H_5SO_3^-$

χ_h	δ(ppm)	Δδ (ppm)	χ_h*Δδ
1	8,627	0	0
0,8	8,58	0,047	0,0376
0,7	8,545	0,082	0,0574
0,6	8,5	0,127	0,0762
0,5	8,44	0,19	0,095
0,4	8,42	0,207	0,0828
0,3	8,402	0,225	0,0675
0,2	8,39	0,237	0,0474

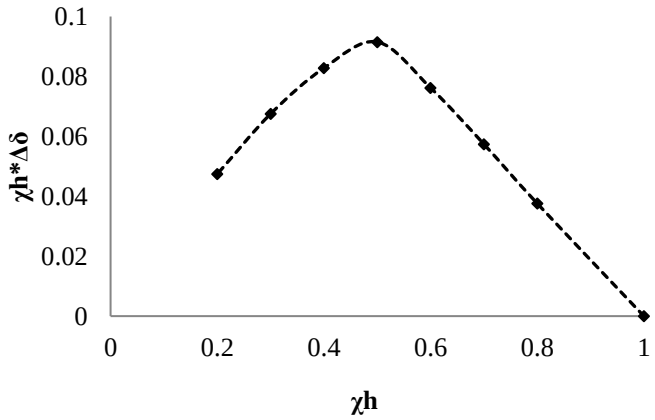

Figure 7.54. Job plot in DMSO-d^6 for the interaction of **[16][PF$_6$]$_4$** and $C_6H_5SO_3^-$ showing the 1:1 stoichiometry. ([H+G]= $4 \cdot 10^{-3}$ M)

g. Tetrabutylammonium hexanoate and $[16][PF_6]_4$

Table 6.20: Data values from the Job plot analysis between $[16][PF_6]_4$ and $C_6H_8COO^-$

χ_h	δ(ppm)	Δδ (ppm)	χ_h*Δδ
1	8,6469	0	0
0,9	8,6527	0,0058	0,00522
0,8	8,658	0,0111	0,00888
0,7	8,6644	0,0175	0,01225
0,6	8,6722	0,0253	0,01518
0,5	8,6789	0,032	0,016
0,4	8,685	0,0381	0,01524
0,3	8,69	0,0431	0,01293
0,2	8,7	0,0531	0,01062
0,1	8,71	0,0631	0,00631

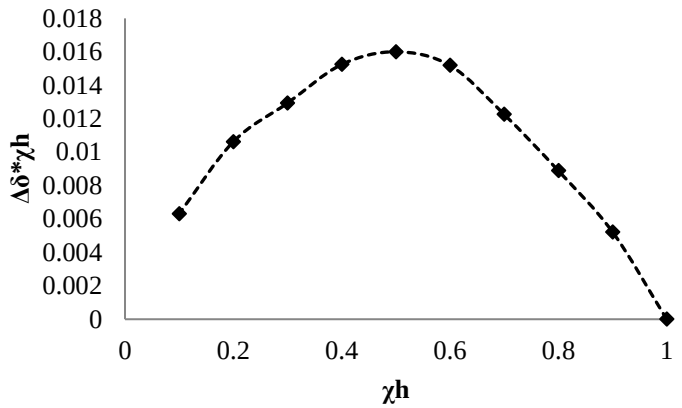

Figure 7.55. Job plot in DMSO-d^6.for the interaction of $[16][PF_6]_4$ and $C_6H_8COO^-$ showing the 1:1 stoichiometry. ([H+G]= $5 \cdot 10^{-3}$ M)

Fitting curves and determination of affinity constants

The 1:1 association constants of receptor $[16][PF_6]_4$ and $[17][PF_6]_4$, K_{11}, were calculated by global nonlinear regression analysis by simultaneously including all protons showing chemical shift variations from the direct use of the bind fitting program available at http://app.supramolecular.org/bindfit.

7.3.3 ^{1}H NMR experiments for the determination of the association constants (Ka) of tripods receptor of chapter 6towards several anions

The anion capabilities recognition of compounds **19(PF$_6$)$_3$**, **20(PF$_6$)$_3$**, **21(PF$_6$)$_3$** and **22(PF$_6$)$_3$** towards several anions was studied by ^{1}H NMR titration experiments carried out in DMSO-*d*^{6}. The large downfield shifts of some of the protons of the imidazolium and triazolium rings suggest complexation between these hosts and anions (Cl^-, Br^-, I^-, $H_2PO_4^-$).

Titrations compound 19(PF$_6$)$_3$

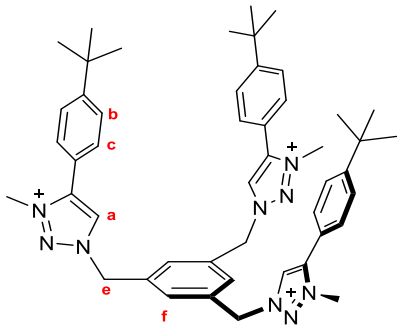

a) Chloride titration

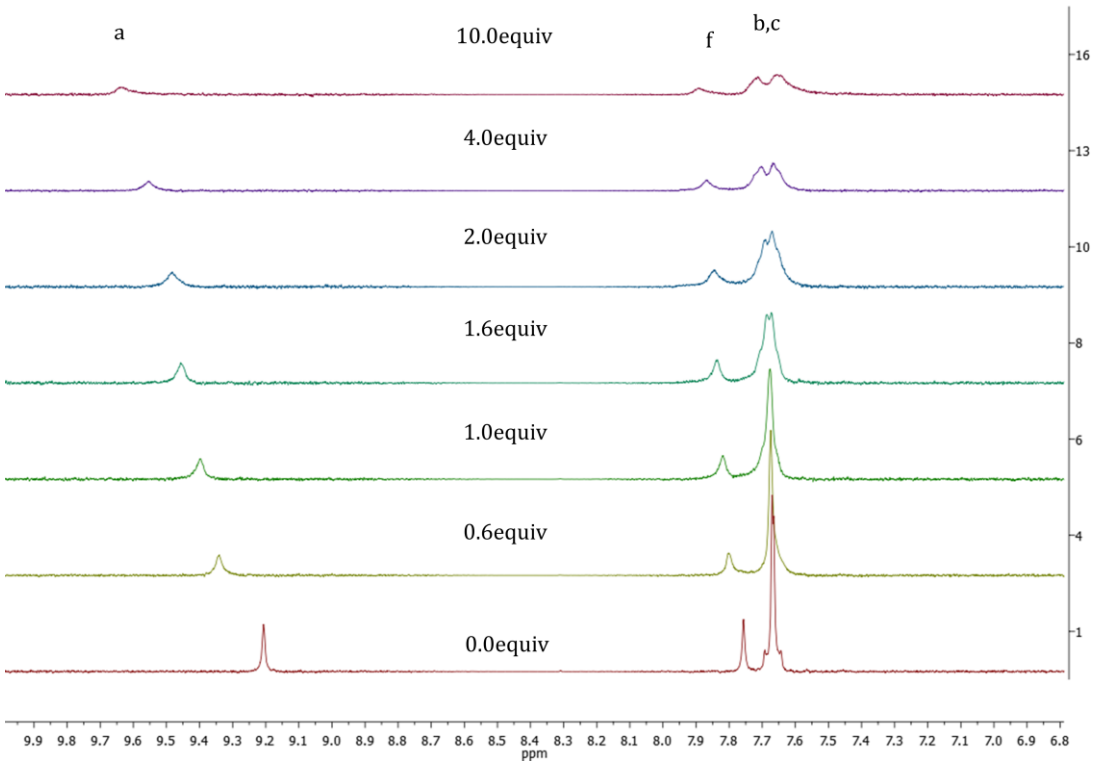

Figure 7.56. Partial ^{1}H NMR (400 Hz) changes observed for the host **19(PF$_6$)$_3$** in DMSO-*d*^{6} during the addition of Cl^-

Table 7.21: Data values from the titration study of **19(PF$_6$)$_3$** with Cl^-

[*19*][*PF$_6$*]$_3$] (M)	Equiv NBu$_4$Cl	δa (ppm)	δf (ppm)	Δδa (ppm)	Δδf (ppm)	[NBu$_4$Cl] (M)
0,002	0,0	9,2064	7,7565	0,0000	0,0000	0
0,001992	0,2	9,2639	7,7753	0,0575	0,0188	0,000398
0,001984	0,4	9,3100	7,7904	0,1036	0,0339	0,000794
0,001976	0,6	9,3417	7,8000	0,1353	0,0435	0,001186
0,001969	0,8	9,3676	7,8084	0,1612	0,0519	0,001575
0,001961	1,0	9,3982	7,8193	0,1918	0,0628	0,001961
0,001953	1,2	9,4233	7,8276	0,2169	0,0711	0,002344
0,001938	1,6	9,4558	7,8376	0,2494	0,0811	0,003101
0,001931	1,8	9,4674	7,8410	0,2610	0,0845	0,003475
0,001923	2,0	9,4821	7,8450	0,2757	0,0885	0,003846
0,001905	2,5	9,5067	7,8536	0,3003	0,0971	0,004762
0,001887	3,0	9,5248	7,8596	0,3184	0,1031	0,00566
0,001869	3,5	9,5540	7,8674	0,3476	0,1109	0,006542
0,001818	5,0	9,5760	7,8748	0,3696	0,1183	0,009091
0,001754	7,0	9,6044	7,8809	0,3980	0,1244	0,012281
0,001667	10,0	9,6300	7,8890	0,4236	0,1325	0,016667

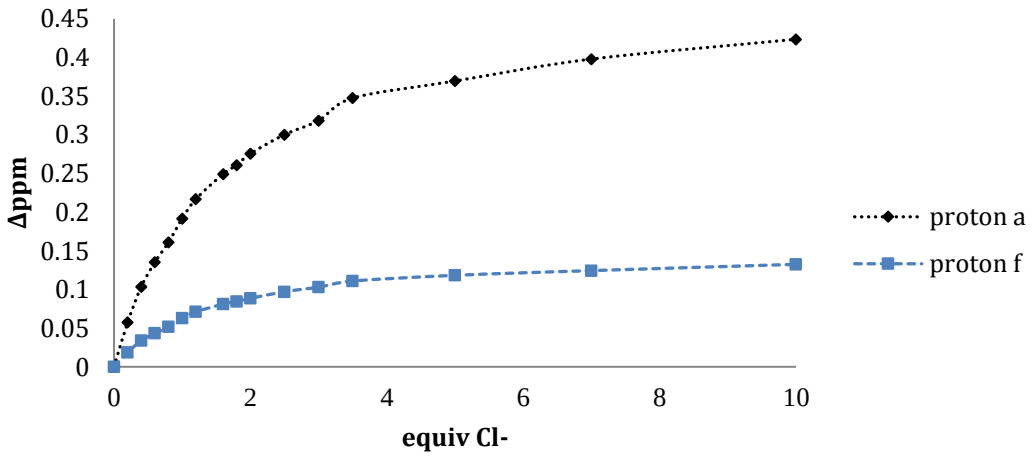

Figure 7.57. Plot of the data values from the titration study of **19(PF$_6$)$_3$** with Cl^-

b) Bromide titration

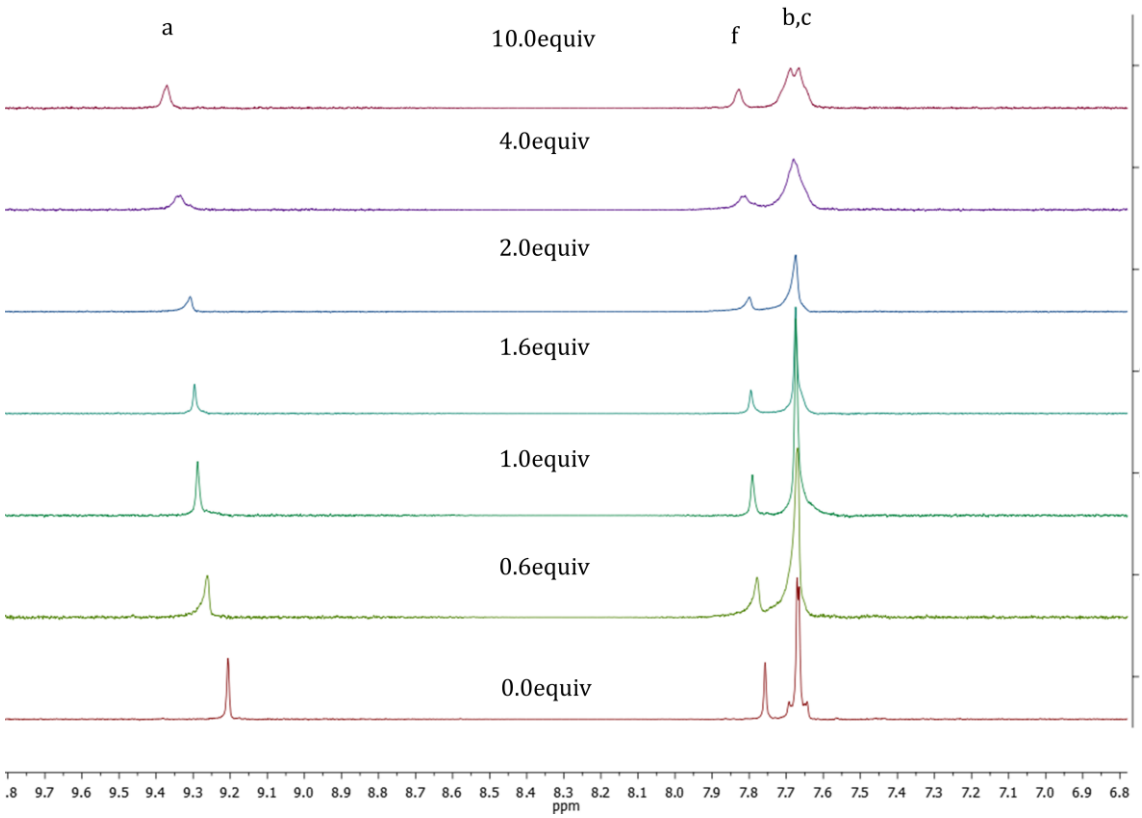

Figure 7.58. Partial ^{1}H NMR (400 Hz) changes observed for the host **19(PF$_6$)$_3$** in DMSO-*d*^{6} during the addition of Br$^-$

Table 7.22: Data values from the titration study of **19(PF$_6$)$_3$** with Br$^-$

[19][PF$_6$]$_3$] (M)	Equiv NBu$_4$Br	δa (ppm)	δf (ppm)	Δδa (ppm)	Δδf (ppm)	[NBu$_4$Br] (M)
0,002	0,0	9,2061	7,7569	0,0000	0	0
0,001992	0,2	9,2100	7,7606	0,0039	0,0037	0,000398
0,001984	0,4	9,2389	7,7703	0,03280	0,0134	0,000794
0,001976	0,6	9,2519	7,7749	0,0458	0,018	0,001186
0,001969	0,8	9,2623	7,7793	0,0562	0,0224	0,001575
0,001961	1,0	9,2719	7,7800	0,0658	0,0231	0,001961
0,001953	1,2	9,2787	7,7809	0,0726	0,02399	0,002344
0,001946	1,4	9,2879	7,7911	0,0818	0,0342	0,002724
0,001938	1,6	9,2962	7,7951	0,0901	0,0382	0,003101
0,001931	1,8	9,2999	7,7961	0,0938	0,0392	0,003475
0,001923	2,0	9,3091	7,8003	0,1030	0,0434	0,003846
0,001905	2,5	9,3158	7,8041	0,1097	0,0472	0,004762
0,001887	3,0	9,3232	7,8074	0,1171	0,0505	0,00566
0,001869	3,5	9,3368	7,8152	0,1307	0,0583	0,006542
0,001818	5,0	9,3455	7,8172	0,1394	0,0603	0,009091
0,001754	7,0	9,3606	7,8241	0,1545	0,0672	0,012281
0,001667	10,0	9,3718	7,8289	0,1657	0,072	0,016667

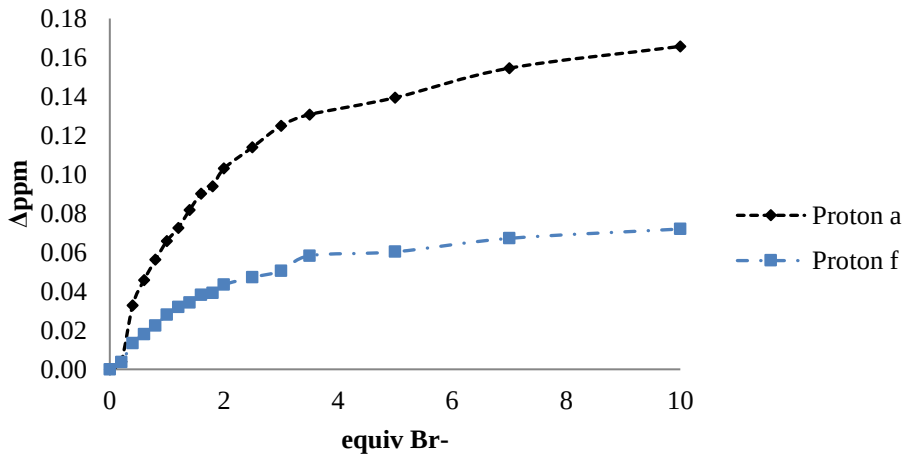

Figure 7.59. Plot of the data values from the titration study of **19(PF$_6$)$_3$** with Br$^-$

c) Iodide titration

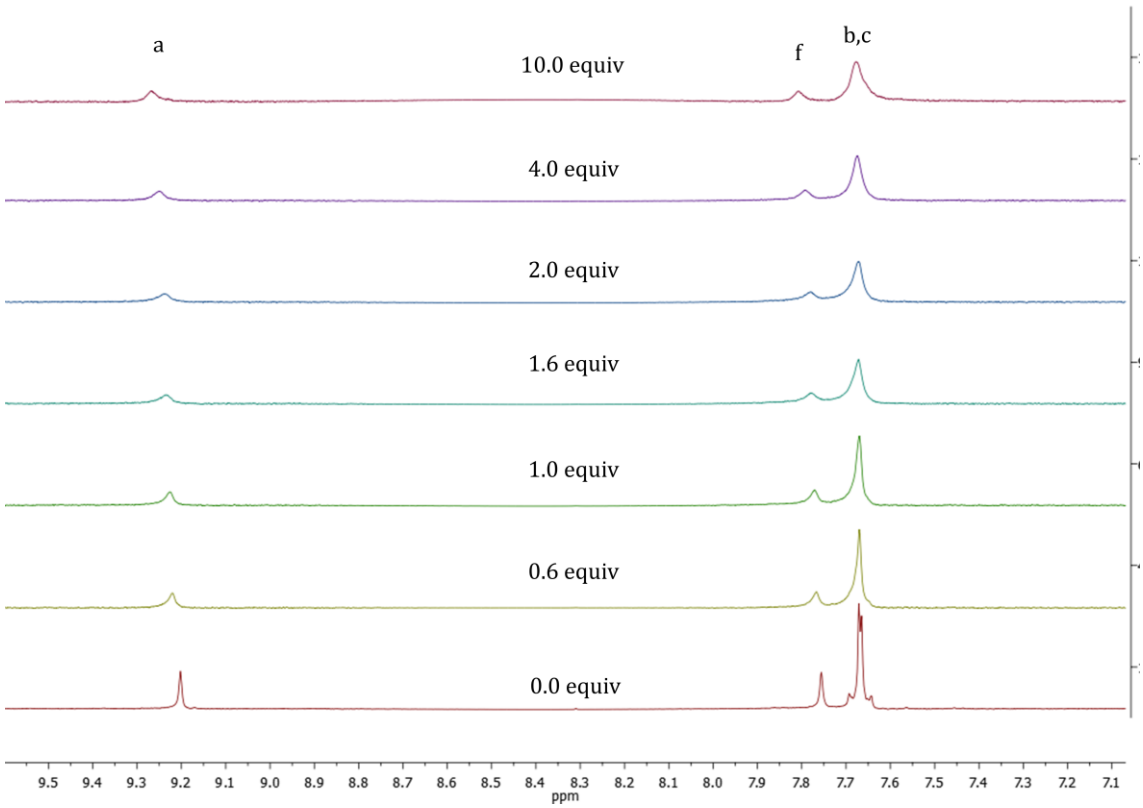

Figure 7.60. Partial ^{1}H NMR (400 Hz) changes observed for the host **19(PF$_6$)$_3$** in DMSO-*d*^{6} during the addition of I$^-$

Table 7.23: Data values from the titration study of **19(PF$_6$)$_3$** with I$^-$

[*19*][*PF$_6$*]$_3$] (M)	equiv NBu$_4$I	δa (ppm)	δf (ppm)	δa(ppm)	Δδf(ppm)	[NBu$_4$I] (M)
0,002	0,0	9,2023	7,755900	0,0000	0,0000	0
0,001992	0,2	9,2090	7,759300	0,0067	0,0034	0,000398
0,001984	0,4	9,2151	7,762700	0,0128	0,0068	0,000794
0,001976	0,6	9,2210	7,767400	0,0187	0,0115	0,001186
0,001969	0,8	9,2225	7,768700	0,0202	0,0128	0,001575
0,001961	1,0	9,2268	7,771700	0,0245	0,0158	0,001961
0,001953	1,2	9,2309	7,775800	0,0286	0,0199	0,002344
0,001946	1,4	9,2336	7,776900	0,0313	0,0210	0,002724
0,001938	1,6	9,2359	7,779000	0,0336	0,0231	0,003101
0,001931	1,8	9,2359	7,780200	0,0336	0,0243	0,003475
0,001923	2,0	9,2408	7,781300	0,0385	0,0254	0,003846
0,001905	2,5	9,2433	7,785400	0,0410	0,0295	0,004762
0,001887	3,0	9,2483	7,788900	0,0460	0,0330	0,00566
0,001869	3,5	9,2506	7,792700	0,0483	0,0368	0,006542
0,001818	5,0	9,2532	7,796000	0,0509	0,0401	0,009091
0,001754	7,0	9,2575	7,802300	0,0552	0,0464	0,012281
0,001667	10,0	9,2600	7,80600	0,0577	0,0501	0,016667

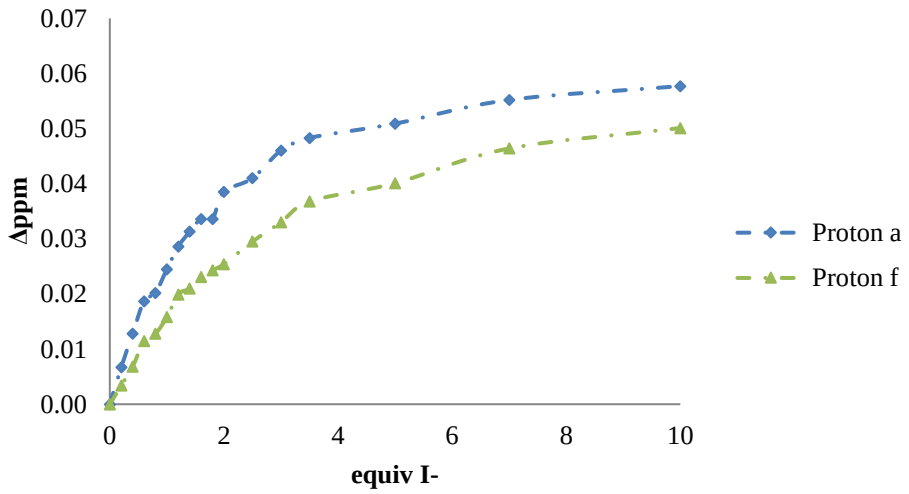

Figure 7.61. Plot of the data values from the titration study of **19(PF$_6$)$_3$** with I$^-$

d) Dihydrogen phosphate titration

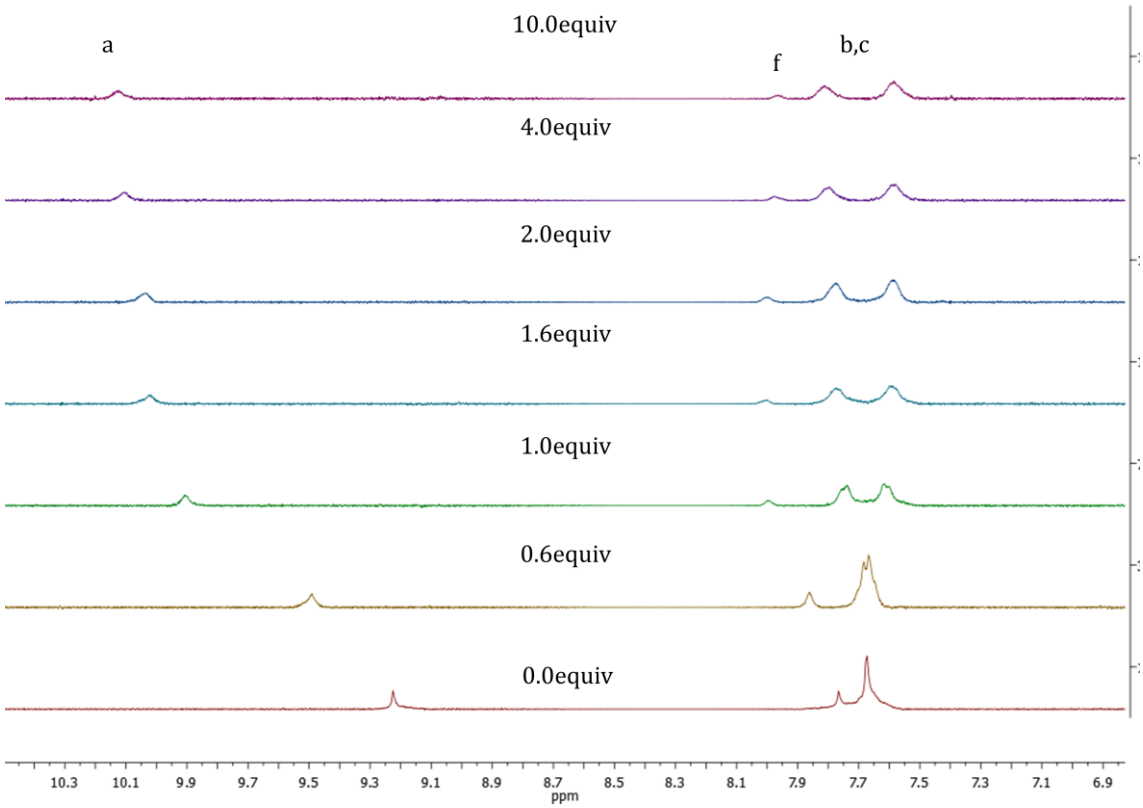

Figure 7.62. Partial ^{1}H NMR (400 Hz) changes observed for the host **19(PF$_6$)$_3$** in DMSO-*d*^{6} during the addition of $H_2PO_4^-$

Table 7.24: Data values from the titration study of **19(PF$_6$)$_3$** with I^-

[*19*][*PF$_6$*]$_3$] (M)	**equiv $NBu_4H_2PO_4$**	**δa (ppm)**	**Δδa (ppm)**	**[$NBu_4H_2PO_4$] (M)**
0,002	0,0	9,2242	0	0
0,001992	0,2	9,3530	0,1288	0,000398
0,001984	0,4	9,4915	0,2673	0,000794
0,001976	0,6	9,6040	0,3798	0,001186
0,001969	0,8	9,7275	0,5033	0,001575
0,001961	1,0	9,8372	0,613	0,001961
0,001953	1,2	9,9052	0,681	0,002344
0,001946	1,4	9,9583	0,7341	0,002724
0,001938	1,6	9,9854	0,7612	0,003101
0,001931	1,8	10,0221	0,7979	0,003475
0,001923	2,0	10,0380	0,8138	0,003846
0,001905	2,5	10,0571	0,8329	0,004762
0,001887	3,0	10,0841	0,8599	0,00566
0,001869	3,5	10,1049	0,8807	0,006542
0,001818	5,0	10,1196	0,8954	0,009091
0,001754	7,0	10,1245	0,9003	0,012281
0,001667	10,0	10,1300	0,9058	0,016667

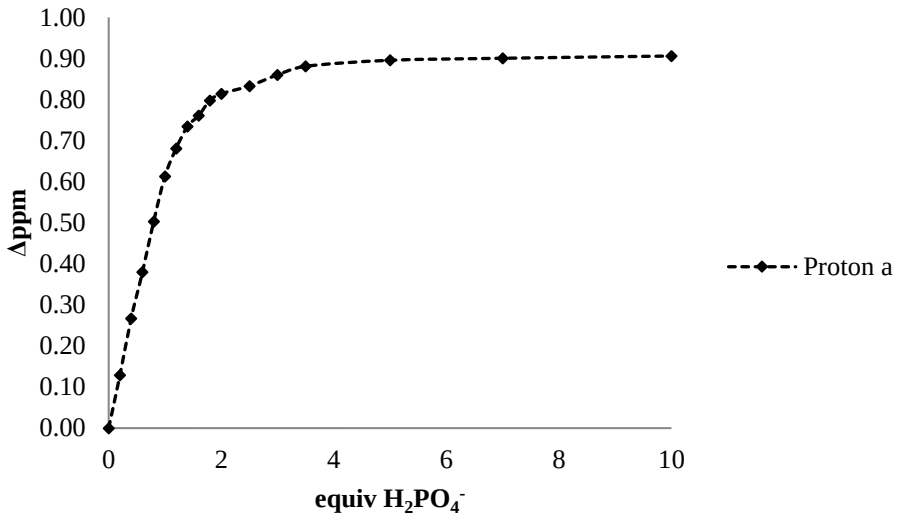

Figure 7.63. Plot of the data values from the titration study of **19(PF$_6$)$_3$** with $H_2PO_4^-$

Titrations compound 20(PF$_6$)$_3$

a) Chloride titration

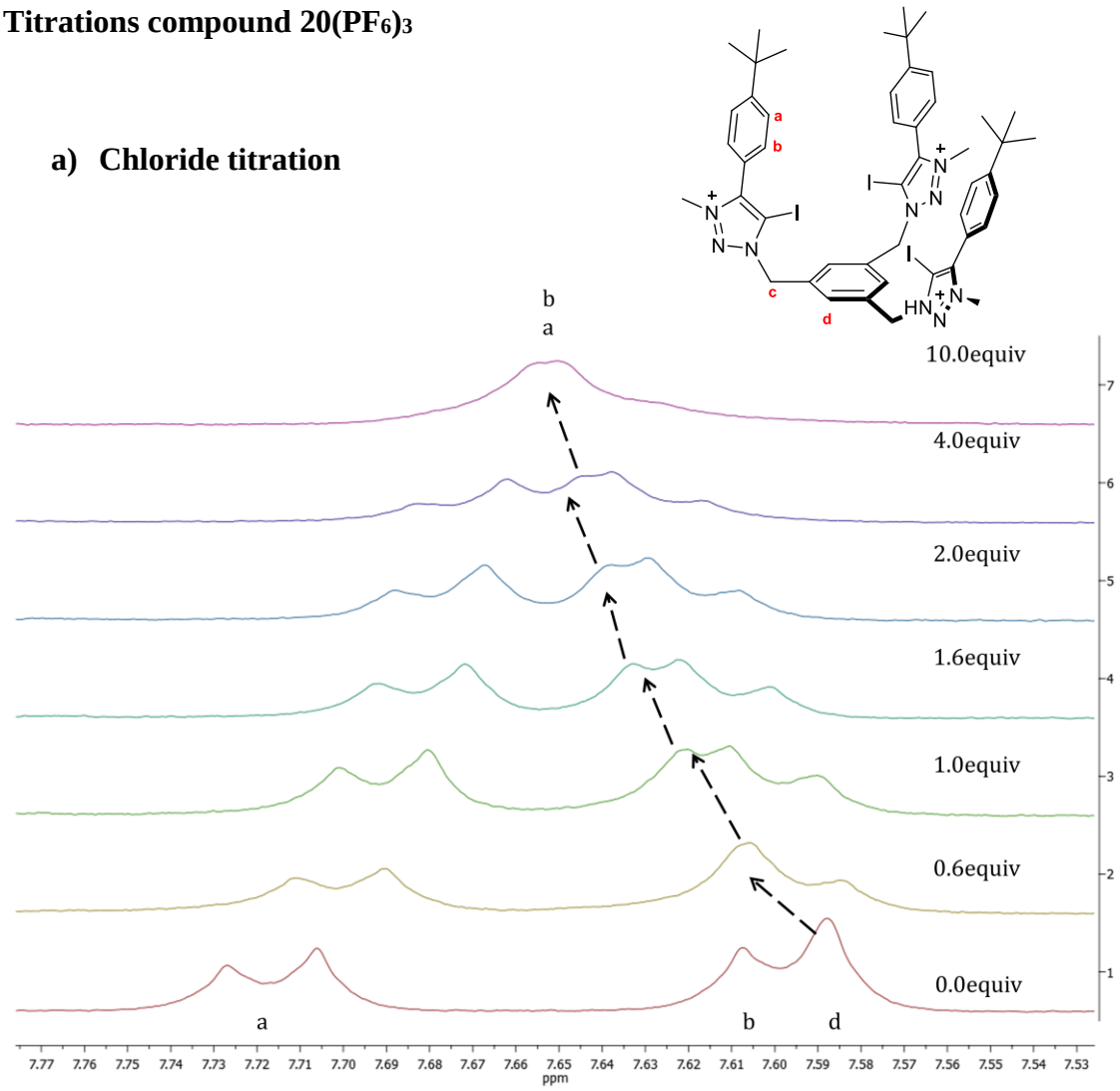

Figure 7.64. Partial ^{1}H NMR (400 Hz) changes observed for the host **20(PF$_6$)$_3$** in DMSO-*d*^{6} during the addition of Cl^-

Table 7.25: Data values from the titration study of **20(PF$_6$)$_3$** with Cl$^-$

[*20*][PF$_6$]$_3$] (M)	equiv NBu$_4$Cl	δa (ppm)	δb (ppm)	δd (ppm)	Δδa (ppm)	Δδb (ppm)	Δδd (ppm)	[NBu$_4$Cl] (M)
0,002	0,0	7,7273	7,7073	7,5887	0	0	0	1,00E-11
0,001992	0,2	7,7214	7,7012	7,5969	-0,0059	-0,0061	0,0082	0,0003984
0,001984	0,4	7,7168	7,6964	7,6045	-0,0105	-0,0109	0,0158	0,0007937
0,001976	0,6	7,7112	7,6909	7,6067	-0,0161	-0,0164	0,018	0,0011858
0,0019685	0,8	7,7096	7,6893	7,612	-0,0177	-0,018	0,0233	0,0015748
0,001960	1,0	7,7039	7,6839	7,6182	-0,0234	-0,0234	0,0295	0,0019608
0,001953	1,2	7,7007	7,6806	7,6216	-0,0266	-0,0267	0,0329	0,0023438
0,001945	1,4	7,6954	7,6758	7,6257	-0,0319	-0,0315	0,037	0,0027237
0,001937	1,6	7,6939	7,6737	7,6299	-0,0334	-0,0336	0,0412	0,0031008
0,001930	1,8	7,692	7,6721	7,6333	-0,0353	-0,0352	0,0446	0,0034749
0,001923	2,0	7,6901	7,6704	7,635	-0,0372	-0,0369	0,0463	0,0038462
0,001904	2,5	7,6878	7,6677	7,638	-0,0395	-0,0396	0,0493	0,0047619
0,001886	3,0	7,6858	7,6653	7,641	-0,0415	-0,042	0,0523	0,0056604
0,001869	3,5	7,6826	7,6629	7,644	-0,0447	-0,0444	0,0553	0,0065421
0,001818	5,0	7,6803	7,6606	7,647	-0,047	-0,0467	0,0583	0,0090909
0,001754	10,0	7,68	7,6606	7,65	-0,0473	-0,0467	0,0613	0,0122807

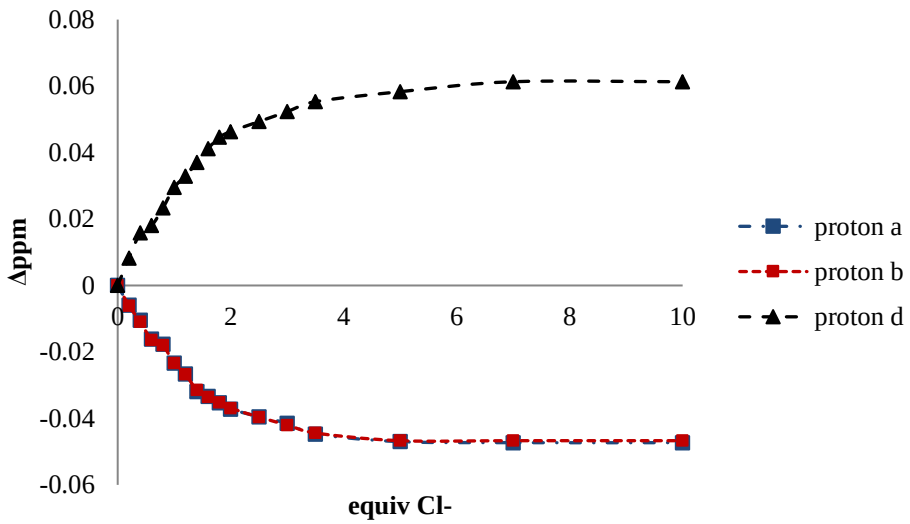

Figure 7.65. Plot of the data values from the titration study of **20(PF$_6$)$_3$** with Cl$^-$

b) Bromide titration

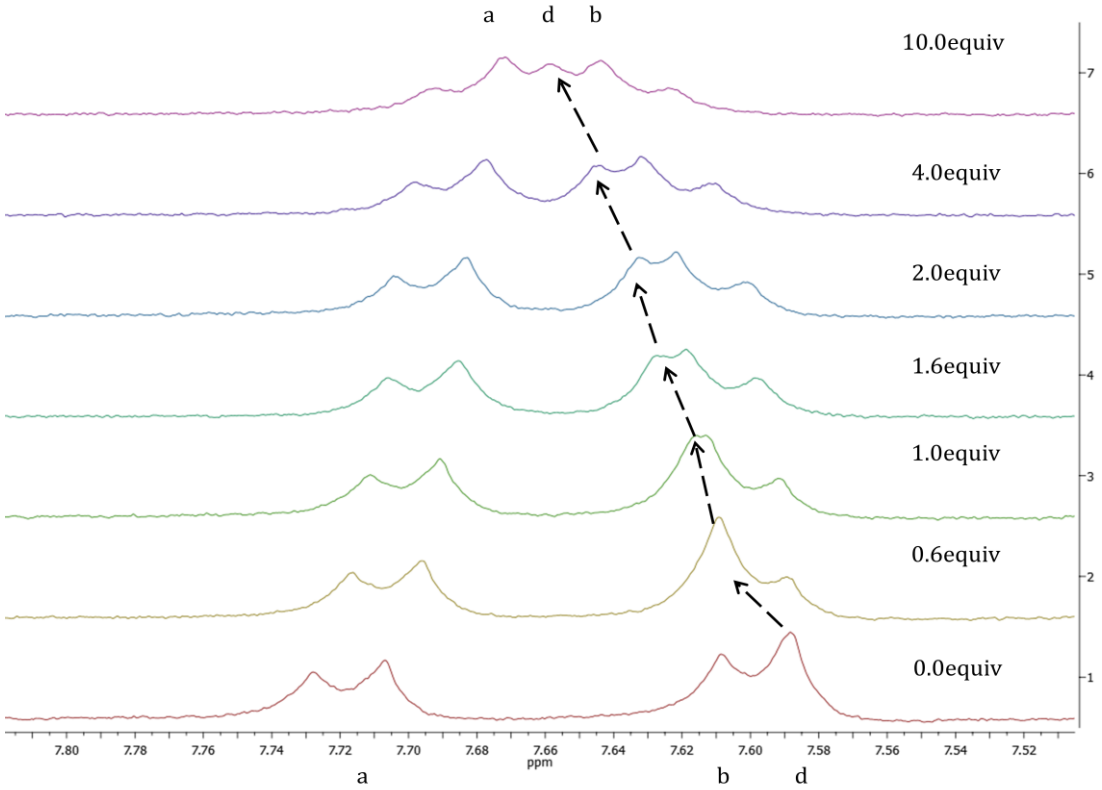

Figure 7.66. Partial ^{1}H NMR (400 Hz) changes observed for the host **20(PF$_6$)$_3$** in DMSO-*d*^{6} during the addition of Br$^-$

Table 7.26: Data values from the titration study of **20(PF$_6$)$_3$** with Br$^-$

[*20*][*PF$_6$*]$_3$] (M)	equiv NBu$_4$Br	δa (ppm)	δb (ppm)	δd (ppm)	Δδa (ppm)	Δδb (ppm)	Δδd (ppm)	[NBu$_4$Br] (M)
0,002000	0,0	7,7272	7,7073	7,5882	0	0	0	0,000000
0,001992	0,2	7,7234	7,7035	7,5936	-0,0038	-0,0038	0,0054	0,000398
0,001984	0,4	7,7197	7,6997	7,6	-0,0075	-0,0076	0,0118	0,000794
0,001976	0,6	7,716	7,6963	7,6087	-0,0112	-0,011	0,0205	0,001186
0,001969	0,8	7,7143	7,6941	7,6119	-0,0129	-0,0132	0,0237	0,001575
0,001961	1,0	7,7119	7,6919	7,6172	-0,0153	-0,0154	0,029	0,001961
0,001953	1,2	7,7099	7,6897	7,622	-0,0173	-0,0176	0,0338	0,002344
0,001946	1,4	7,7069	7,6871	7,625	-0,0203	-0,0202	0,0368	0,002724
0,001938	1,6	7,706	7,6857	7,6279	-0,0212	-0,0216	0,0397	0,003101
0,001931	1,8	7,705	7,6847	7,63	-0,0222	-0,0226	0,0418	0,003475
0,001923	2,0	7,7034	7,6833	7,6321	-0,0238	-0,024	0,0439	0,003846
0,001905	2,5	7,7018	7,6818	7,6367	-0,0254	-0,0255	0,0485	0,004762
0,001887	3,0	7,7004	7,68	7,6397	-0,0268	-0,0273	0,0515	0,005660
0,001869	3,5	7,6979	7,6776	7,6449	-0,0293	-0,0297	0,0567	0,006542
0,001818	5,0	7,6968	7,6763	7,6488	-0,0304	-0,031	0,062	0,009091
0,001754	7,0	7,6935	7,67441	7,6536	-0,0337	-0,03289	0,067	0,012281
0,001667	10	7,6921	7,6722	7,657	-0,0351	-0,0351	0,0688	0,016667

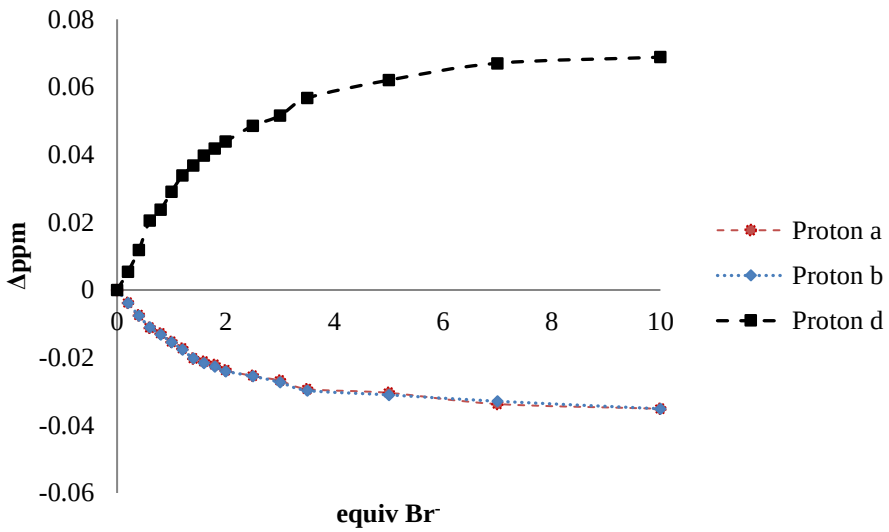

Figure 7.67. Plot of the data values from the titration study of **20(PF$_6$)$_3$** with Br^-

c) Iodide titration

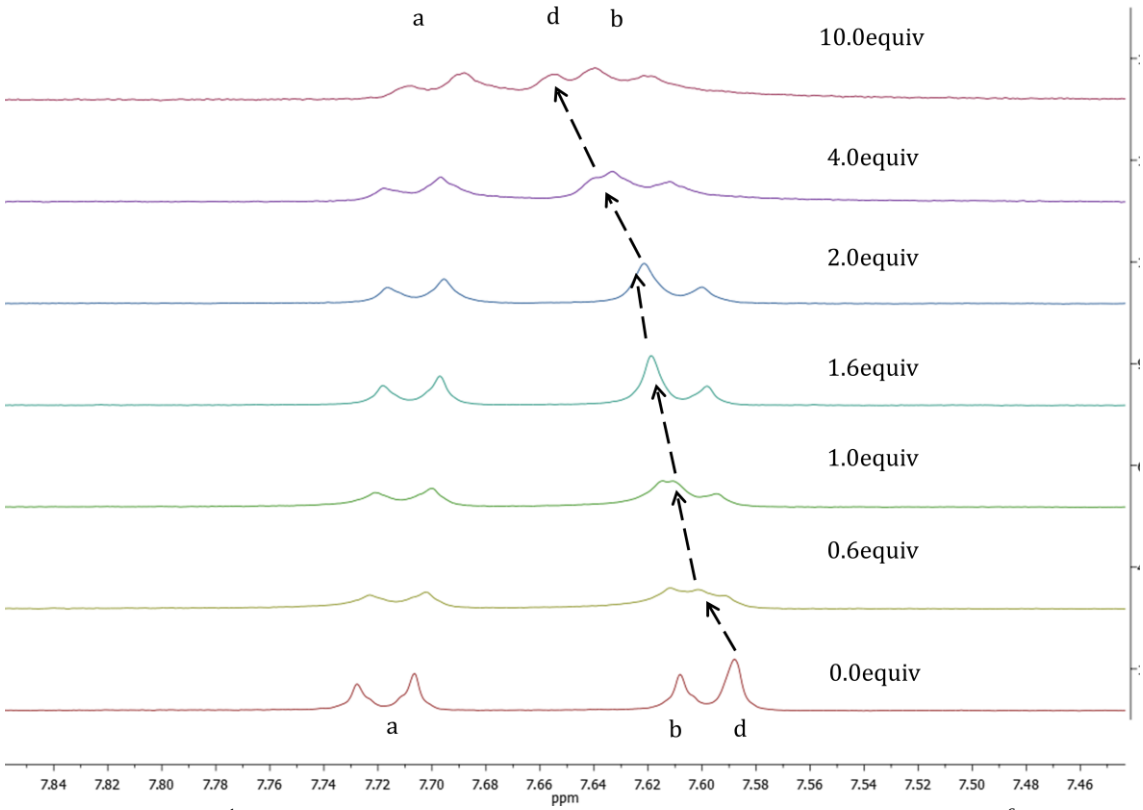

Figure 7.68. Partial ^{1}H NMR (400 Hz) changes observed for the host **20(PF$_6$)$_3$** in DMSO-*d*^{6} during the addition of I^-

Table 7.27: Data values from the titration study of **20(PF$_6$)$_3$** with I^-

[*20*][*PF$_6$*]$_3$] (M)	**equiv NBu$_4$I**	**δa (ppm)**	**Δδa (ppm)**	**[NBu$_4$I] (M)**
0,002	0,0	7,5883	0	0
0,001992	0,2	7,5911	0,0028	0,000398
0,001984	0,4	7,5931	0,0048	0,000794
0,001976	0,6	7,6011	0,0128	0,001186
0,001969	0,8	7,6049	0,0166	0,001575
0,001961	1,0	7,6096	0,0213	0,001961
0,001953	1,2	7,6128	0,0245	0,002344
0,001946	1,4	7,6176	0,0293	0,002724
0,001938	1,6	7,6187	0,0304	0,003101
0,001931	1,8	7,621	0,0327	0,003475
0,001923	2,0	7,6212	0,0329	0,003846
0,001905	2,5	7,6238	0,0355	0,004762
0,001887	3,0	7,6264	0,0381	0,00566
0,001869	3,5	7,6285	0,0402	0,006542
0,001818	5,0	7,6315	0,0432	0,009091
0,001754	7,0	7,6335	0,0452	0,012281
0,001667	10,0	7,638	0,05	0,016667

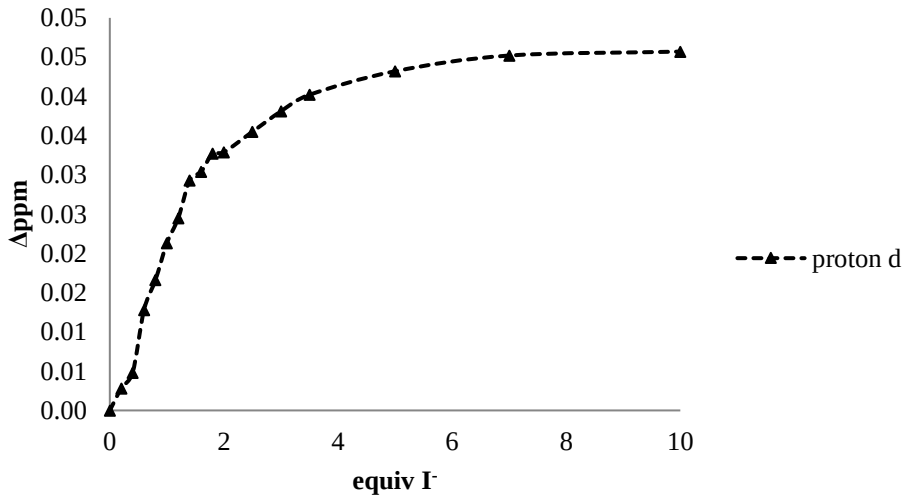

Figure 7.69. Plot of the data values from the titration study of **20(PF$_6$)$_3$** with I^-

d) Dihydrogen phosphate titration

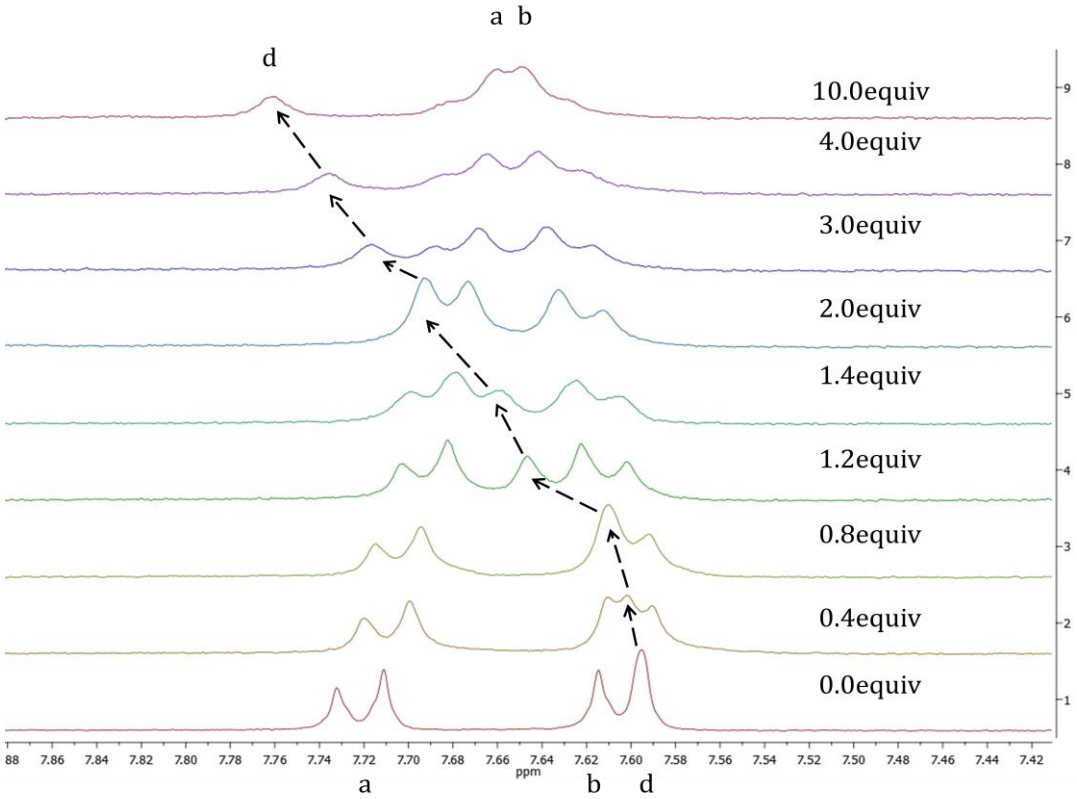

Figure 7.70. Partial ^{1}H NMR (400 Hz) changes observed for the host **20(PF$_6$)$_3$** in DMSO-*d*^{6} during the addition of $H_2PO_4^-$

Table 7.28: Data values from the titration study of **20(PF$_6$)$_3$** with $H_2PO_4^-$

[*20*][*PF$_6$*]$_3$] (M)	**equiv $NBu_4H_2PO_4$**	**δd (ppm)**	**Δδd (ppm)**	**[$NBu_4H_2PO_4$] (M)**
0,002	0,0	7,59	0	0
0,001992	0,2	7,61	0,02	0,000398
0,001984	0,4	7,626	0,036	0,000794
0,001976	0,6	7,639	0,049	0,001186
0,001969	0,8	7,65	0,06	0,001575
0,001961	1,0	7,659	0,069	0,001961
0,001953	1,2	7,67	0,08	0,002344
0,001946	1,4	7,679	0,089	0,002724
0,001938	1,6	7,689	0,099	0,003101
0,001931	1,8	7,696	0,106	0,003475
0,001923	2,0	7,71	0,12	0,003846
0,001905	2,5	7,72	0,13	0,004762
0,001887	3,0	7,73	0,14	0,00566
0,001869	3,5	7,735	0,145	0,006542
0,001818	5,0	7,747	0,157	0,009091
0,001754	7,0	7,752	0,162	0,012281
0,001667	10,0	7,757	0,167	0,016667

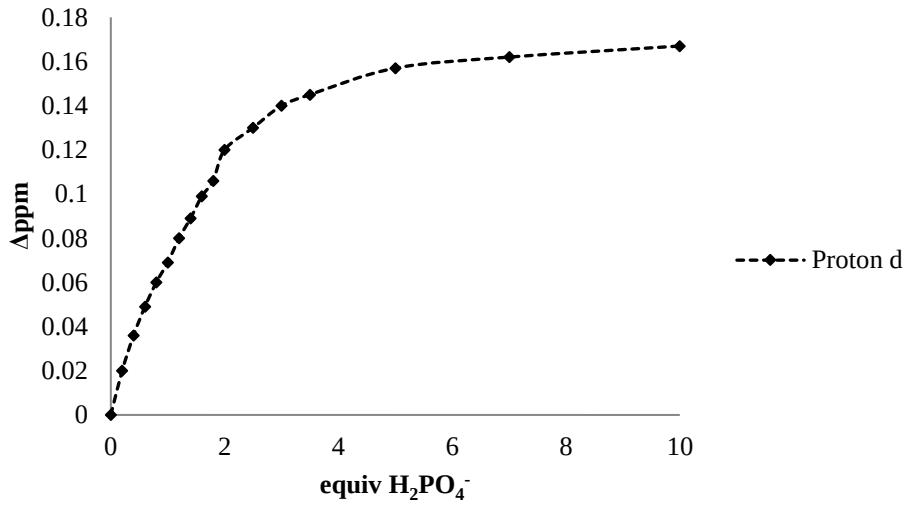

Figure 7.71. Plot of the data values from the titration study of **20(PF$_6$)$_3$** with $H_2PO_4^-$

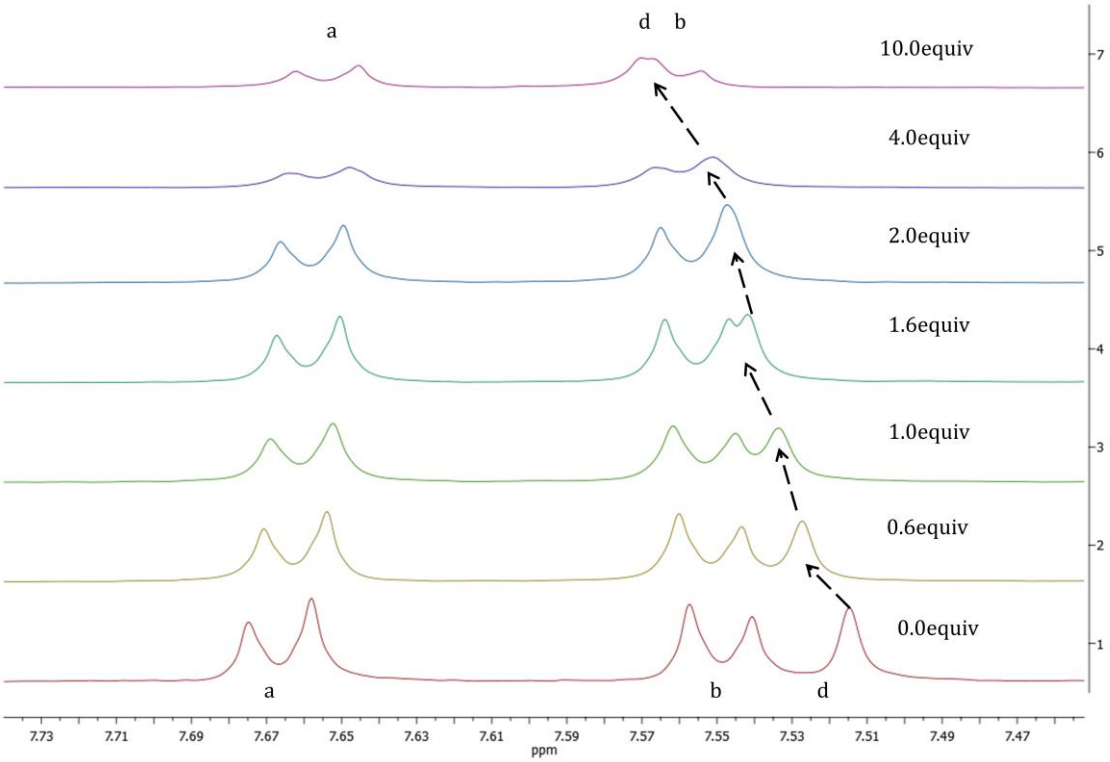

Figure 7.72. Partial ^{1}H NMR (400Hz) changes observed for the host **20(PF$_6$)$_3$** DMSO-*d*^{6}: D_2O (9:1) during the addition of $H_2PO_4^-$

Table 7.29: Data values from the titration study of **20(PF$_6$)$_3$** with $H_2PO_4^-$ (DMSO-d^6: D_2O, 9:1)

[*20*][*PF$_6$*]$_3$] (M)	**equiv $NBu_4H_2PO_4$**	**δd (ppm)**	**Δδd (ppm)**	**[$NBu_4H_2PO_4$] (M)**
0,002	0,0	7,5146	0	0
0,001992	0,2	7,5195	0,0049	0,000398
0,001984	0,4	7,5228	0,0082	0,000794
0,001976	0,6	7,5275	0,0129	0,001186
0,001969	0,8	7,5302	0,0156	0,001575
0,001961	1,0	7,5338	0,0192	0,001961
0,001953	1,2	7,5363	0,0217	0,002344
0,001946	1,4	7,5392	0,0246	0,002724
0,001938	1,6	7,5421	0,0275	0,003101
0,001931	1,8	7,5445	0,0299	0,003475
0,001923	2,0	7,546	0,0314	0,003846
0,001905	2,5	7,549	0,0344	0,004762
0,001887	3,0	7,5512	0,0366	0,00566
0,001869	3,5	7,5535	0,0389	0,006542
0,001818	5,0	7,557	0,0424	0,009091
0,001754	7,0	7,561	0,0464	0,012281
0,001667	10,0	7,566	0,05	0,016667

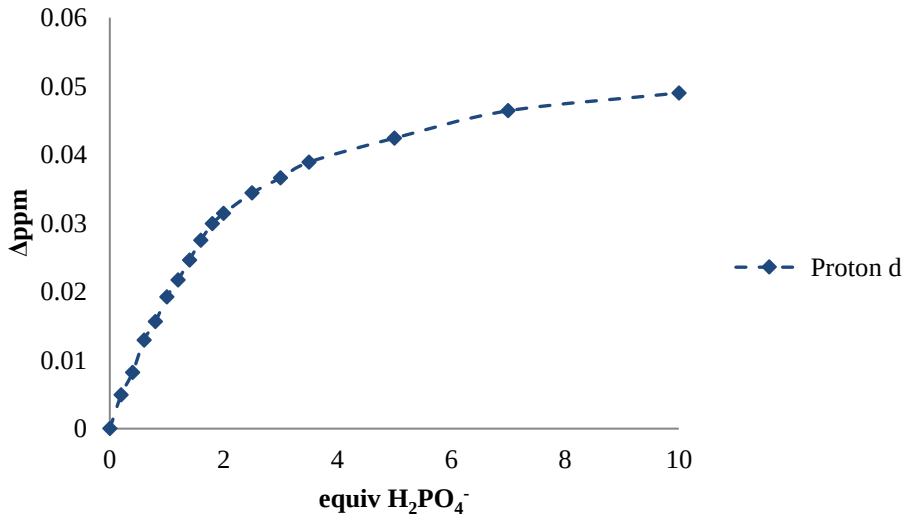

Figure 7.73: Plot of the data values from the titration study of **20(PF$_6$)$_3$** with $H_2PO_4^-$ (DMSO-d^6: D_2O, 9:1)

Titrations compound 21(PF$_6$)$_3$

a) Chloride titration

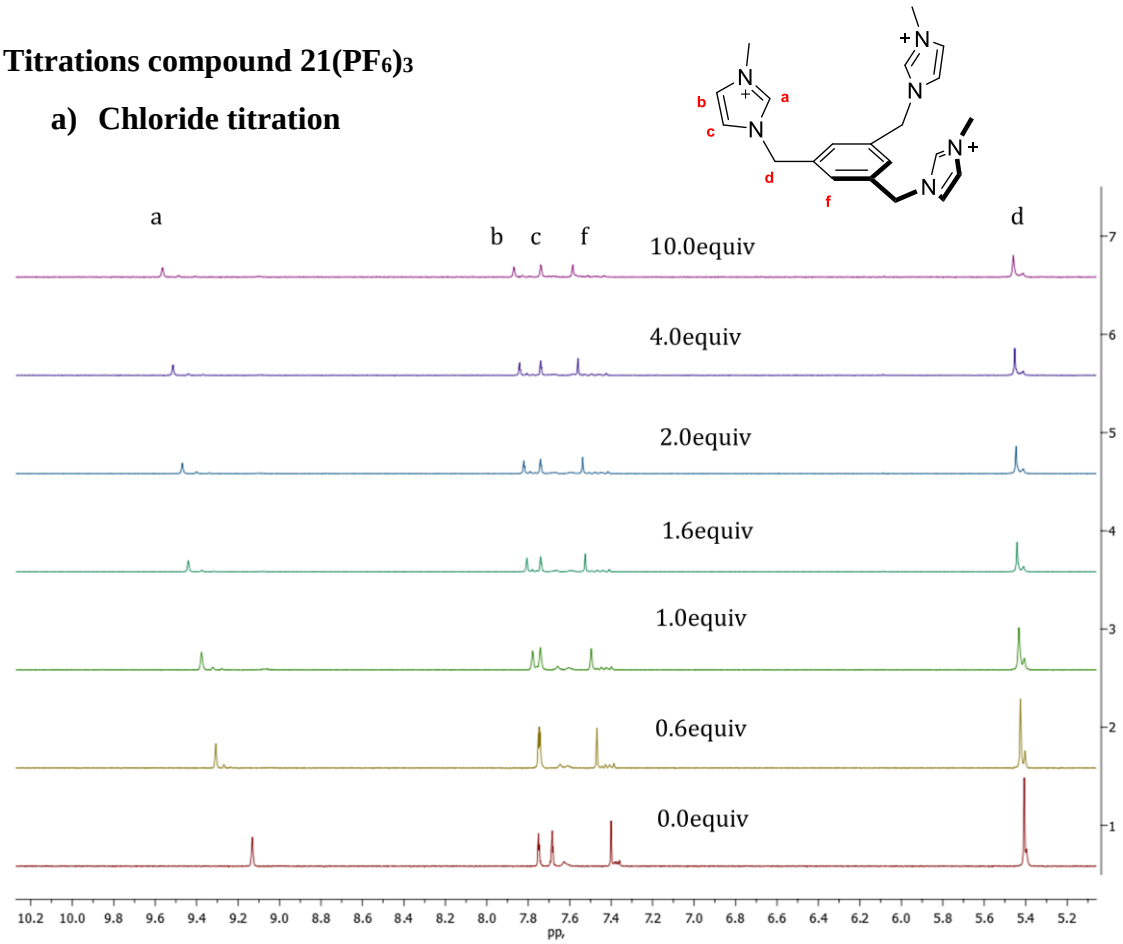

Figure 7.74. Partial ^{1}H NMR (400 Hz) changes observed for the host **21(PF$_6$)$_3$** in DMSO-*d*^{6} during the addition of Cl$^-$

Table 7.30: Data values from the titration study of **21(PF$_6$)$_3$** with Cl$^-$

[*21*][*PF$_6$*]$_3$] (M)	equiv NBu$_4$Cl	δa (ppm)	δf (ppm)	δd (ppm)	Δδa (ppm)	Δδf (ppm)	Δδd (ppm)	[NBu$_4$Cl] (M)
0,002	0,0	9,1310	7,400000	5,407	0	0	0	0
0,001992	0,2	9,2000	7,426000	5,414	0,069	0,026	0,007	0,000398
0,001984	0,4	9,2610	7,451000	5,421	0,13	0,051	0,014	0,000794
0,001976	0,6	9,3080	7,469000	5,426	0,177	0,069	0,019	0,001186
0,001969	0,8	9,3450	7,483000	5,43	0,214	0,083	0,023	0,001575
0,001961	1,0	9,3770	7,497000	5,433	0,246	0,097	0,026	0,001961
0,001953	1,2	9,4020	7,508000	5,436	0,271	0,108	0,029	0,002344
0,001946	1,4	9,4230	7,518000	5,439	0,292	0,118	0,032	0,002724
0,001938	1,6	9,4400	7,525000	5,442	0,309	0,125	0,035	0,003101
0,001931	1,8	9,4560	7,531000	5,444	0,325	0,131	0,037	0,003475
0,001923	2,0	9,4690	7,538000	5,446	0,338	0,138	0,039	0,003846
0,001905	2,5	9,4850	7,546000	5,449	0,354	0,146	0,042	0,004762
0,001887	3,0	9,4980	7,551000	5,45	0,367	0,151	0,043	0,00566
0,001869	3,5	9,5150	7,560000	5,453	0,384	0,16	0,046	0,006542
0,001818	5,0	9,5260	7,566000	5,454	0,395	0,166	0,047	0,009091
0,001754	7,0	9,5460	7,575000	5,457	0,415	0,175	0,05	0,012281
0,001667	10,0	9,5650	7,586000	5,46	0,434	0,186	0,053	0,016667

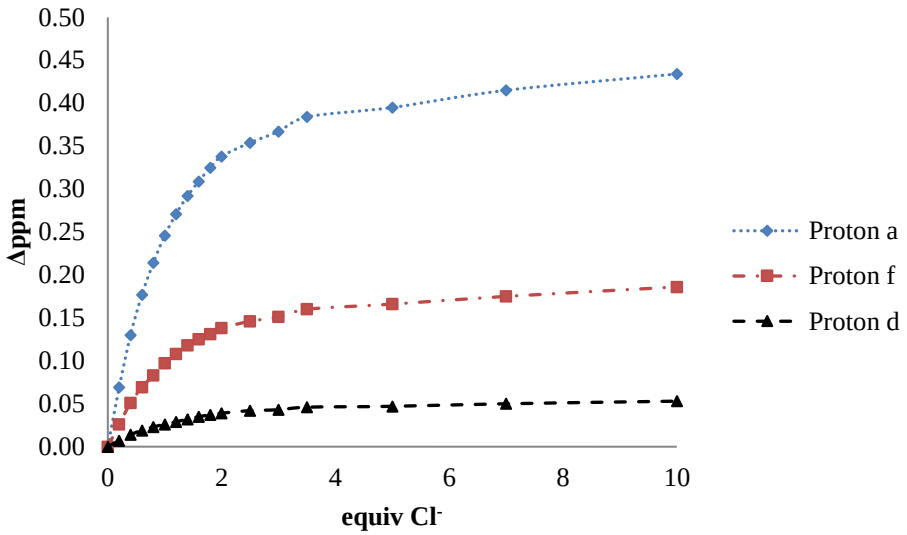

Figure 7.75. Plot of the data values from the titration study of **21(PF$_6$)$_3$** with Cl^-

b) Bromide titration

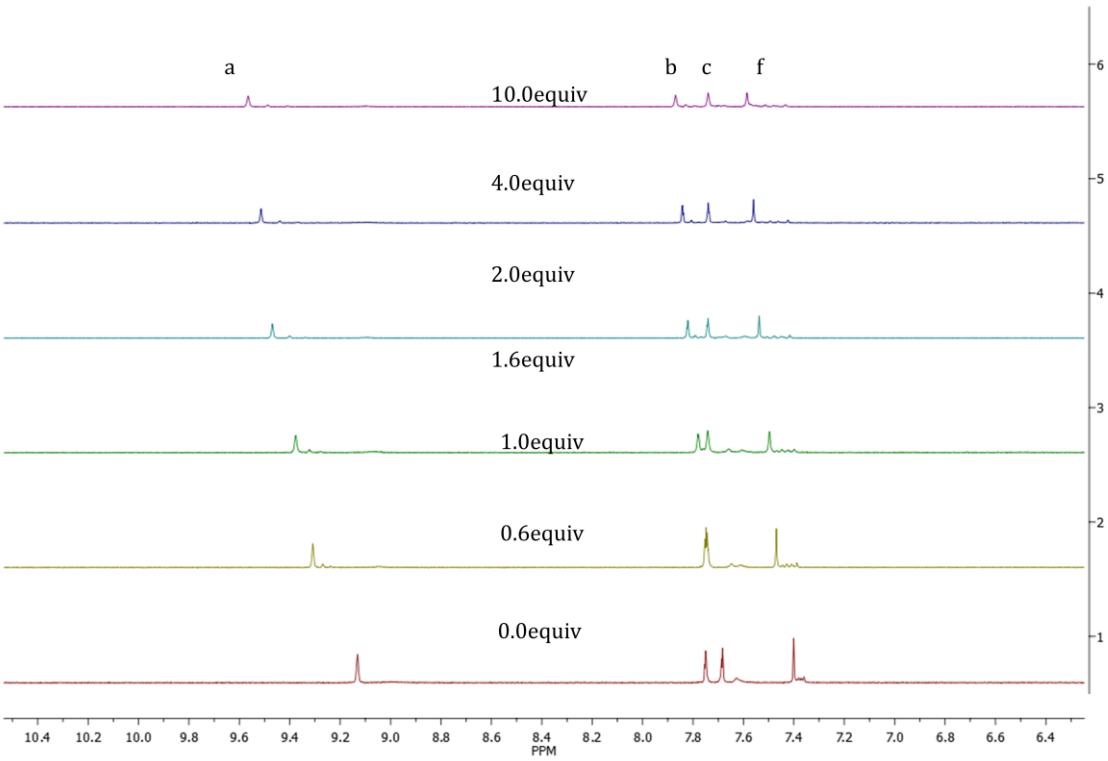

Figure 7.76. Partial ^{1}H NMR (400 Hz) changes observed for the host **21(PF$_6$)$_3$** in DMSO-d^6 during the addition of Br^-

Table 7.31: Data values from the titration study of **21(PF$_6$)$_3$** with Br$^-$

[*21*][*PF$_6$*]$_3$] (M)	equiv NBu$_4$Br	δa (ppm)	δf (ppm)	δd (ppm)	Δδa (ppm)	Δδf (ppm)	Δδd (ppm)	[NBu$_4$Br] (M)
0,002	0,0	9,131	7,399	5,406	0	0	0	0
0,001992	0,2	9,168	7,418	5,414	0,037	0,019	0,008	0,000398
0,001984	0,4	9,193	7,433	5,420	0,062	0,034	0,014	0,000794
0,001976	0,6	9,214	7,443	5,425	0,083	0,044	0,019	0,001186
0,001969	0,8	9,231	7,452	5,429	0,1	0,053	0,023	0,001575
0,001961	1,0	9,245	7,460	5,432	0,114	0,061	0,026	0,001961
0,001953	1,2	9,258	7,468	5,434	0,127	0,069	0,028	0,002344
0,001946	1,4	9,268	7,474	5,437	0,137	0,075	0,031	0,002724
0,001938	1,6	9,2780	7,480	5,440	0,147	0,081	0,034	0,003101
0,001931	1,8	9,287	7,484	5,442	0,156	0,085	0,036	0,003475
0,001923	2,0	9,291	7,485	5,445	0,16	0,086	0,039	0,003846
0,001905	2,5	9,303	7,495	5,447	0,172	0,096	0,041	0,004762
0,001887	3,0	9,311	7,500	5,449	0,18	0,101	0,043	0,00566
0,001869	3,5	9,3210	7,505	5,451	0,19	0,106	0,045	0,006542
0,001818	5,0	9,330	7,511	5,454	0,199	0,112	0,048	0,009091
0,001754	7,0	9,343	7,518	5,456	0,212	0,119	0,05	0,012281
0,001667	10,0	9,358	7,527	5,461	0,227	0,128	0,055	0,016667

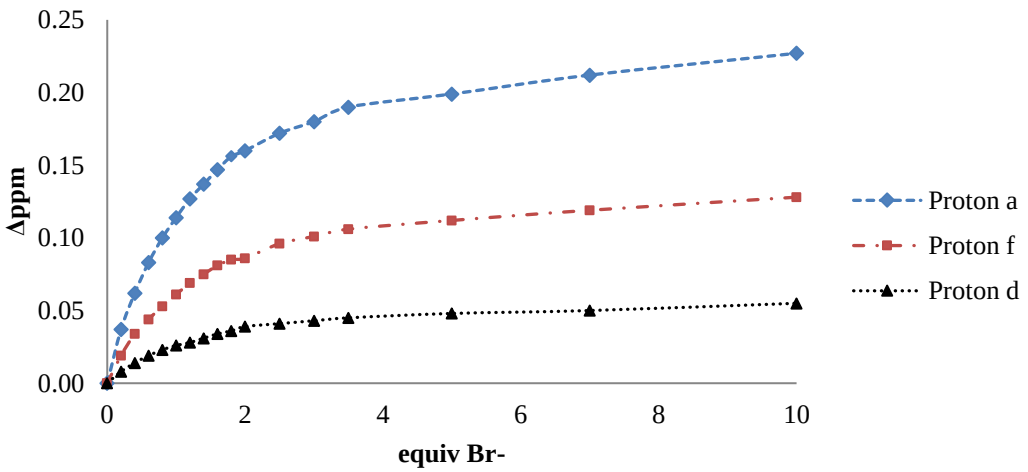

Figure 7.77. Plot of the data values from the titration study of **21(PF$_6$)$_3$** with Br$^-$

c) Iodide titration

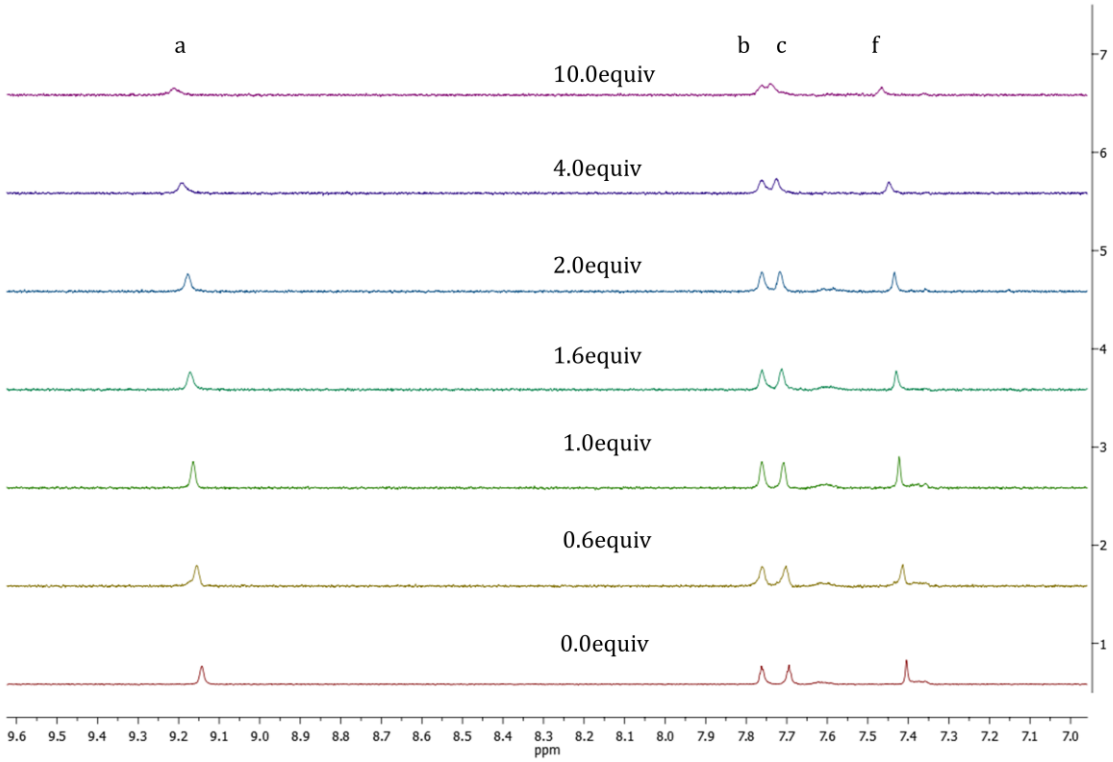

Figure 7.78. Partial ^{1}H NMR (400 Hz) changes observed for the host **21(PF$_6$)$_3$** in DMSO-*d*^{6} during the addition of I^-

Table 7.32: Data values from the titration study of **21(PF$_6$)$_3$** with I^-

[*21*][PF$_6$]$_3$] (M)	**equiv NBu$_4$I**	**δa (ppm)**	**Δδa (ppm)**	**[NBu$_4$I] (M)**
0,002	0,0	9,1308	0,0000	0
0,001992	0,2	9,1385	0,0077	0,000398
0,001984	0,4	9,1457	0,0149	0,000794
0,001976	0,6	9,1495	0,0187	0,001186
0,001969	0,8	9,1531	0,0223	0,001575
0,001961	1,0	9,1573	0,0265	0,001961
0,001953	1,2	9,1585	0,0277	0,002344
0,001946	1,4	9,1605	0,0297	0,002724
0,001938	1,6	9,1617	0,0309	0,003101
0,001931	1,8	9,1650	0,0342	0,003475
0,001923	2,0	9,1680	0,0372	0,003846
0,001905	2,5	9,1719	0,0411	0,004762
0,001887	3,0	9,1770	0,0462	0,00566
0,001869	3,5	9,1800	0,0492	0,006542
0,001818	5,0	9,1872	0,0564	0,009091
0,001754	7,0	9,1932	0,0624	0,012281
0,001667	10,0	9,2000	0,0703	0,016667

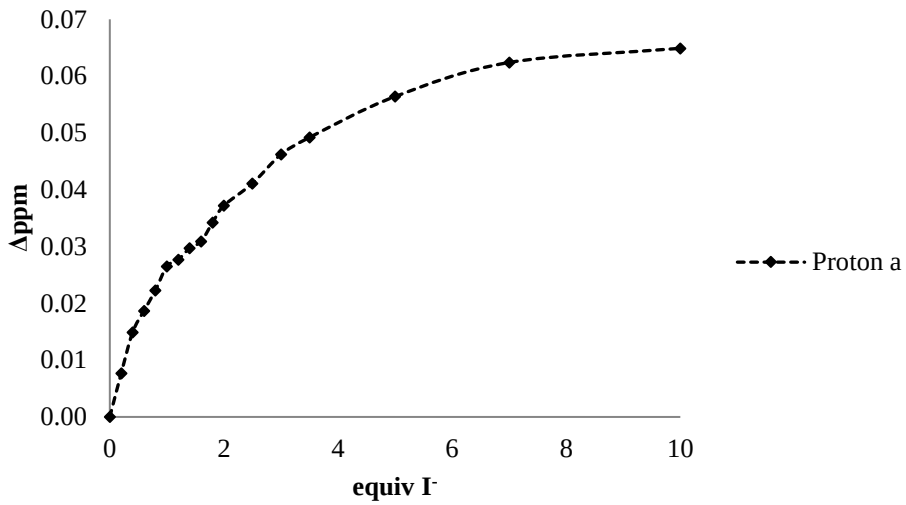

Figure 7.79. Plot of the data values from the titration study of **21(PF$_6$)$_3$** with I^-

Titrations compound 22(PF$_6$)$_3$

a) Chloride titration

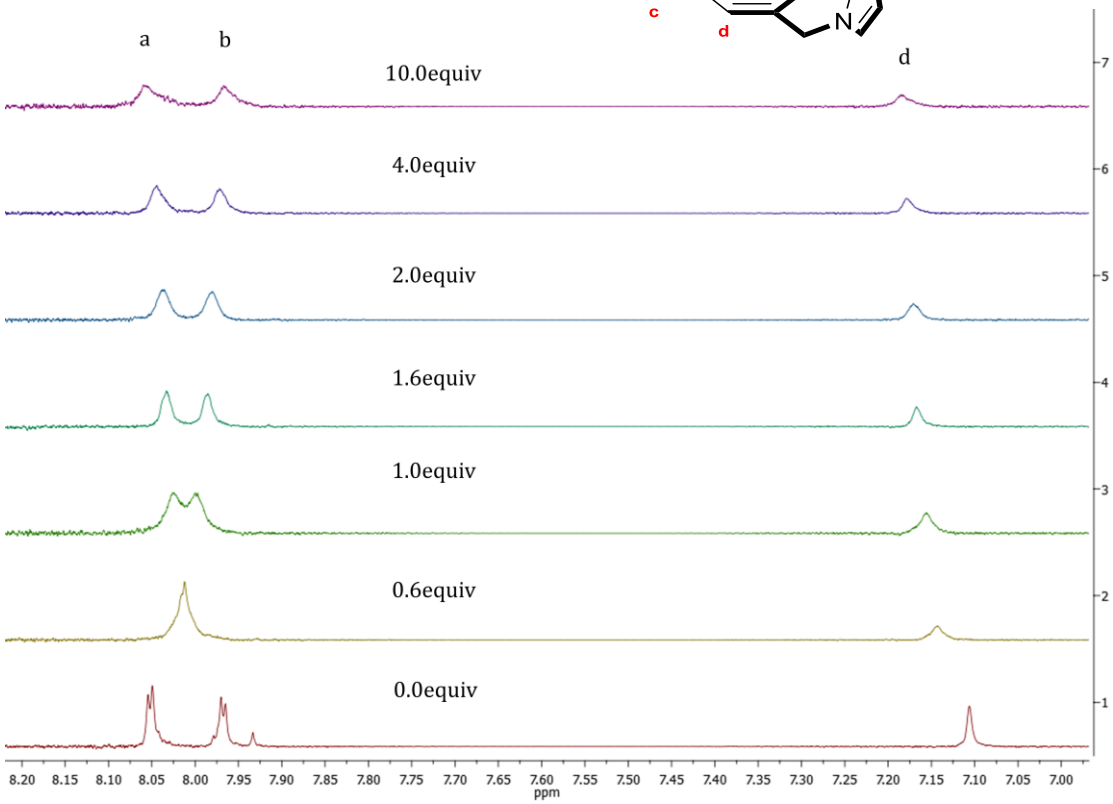

Figure 7.80. Partial ^{1}H NMR (400 Hz) changes observed for the host **22(PF$_6$)$_3$** in DMSO-*d*^{6} during the addition of Cl^-

Table 7.33. Data values from the titration study of **22(PF$_6$)$_3$** with Cl^-

[*22*][*PF$_6$*]$_3$] (M)	equiv NBu_4Cl	δa (ppm)	δf (ppm)	δd (ppm)	Δδa (ppm)	Δδf (ppm)	Δδd (ppm)	[NBu_4Cl] (M)
0,002	0,0	8,0437	7,9593	7,0986	0	0	0	0
0,001992	0,2	8,0320	7,9827	7,1084	-0,0113	0,0234	0,0098	0,000398
0,001984	0,4	8,0153	7,9964	7,1287	-0,0284	0,0371	0,0301	0,000794
0,001976	0,6	8,0030	8,0030	7,1343	-0,0407	0,0437	0,0357	0,001186
0,001969	0,8	8,0007	8,0141	7,1452	-0,043	0,0548	0,0466	0,001575
0,001961	1,0	7,9919	8,0183	7,1500	-0,0518	0,059	0,0514	0,001961
0,001953	1,2	7,9863	8,0217	7,1538	-0,0574	0,0624	0,0552	0,002344
0,001946	1,4	7,9829	8,0249	7,1577	-0,0608	0,0656	0,0591	0,002724
0,001938	1,6	7,9788	8,0259	7,1598	-0,0649	0,0666	0,0612	0,003101
0,001931	1,8	7,9768	8,0290	7,1623	-0,0669	0,0698	0,0637	0,003475
0,001923	2,0	7,9750	8,0311	7,1648	-0,0687	0,0718	0,0662	0,003846
0,001905	2,5	7,9702	8,0310	7,1661	-0,0735	0,0726	0,0675	0,004762
0,001887	3,0	7,9671	8,0330	7,1683	-0,0766	0,0744	0,0697	0,00566
0,001869	3,5	7,9638	8,0366	7,1704	-0,0799	0,0773	0,0718	0,006542
0,001818	5,0	7,9611	8,0414	7,1726	-0,0826	0,0821	0,074	0,009091
0,001754	7,0	7,9584	8,0430	7,1745	-0,0853	0,0837	0,0759	0,012281
0,001667	10,0	7,9559	8,0462	7,1750	-0,0878	0,0869	0,0764	0,016667

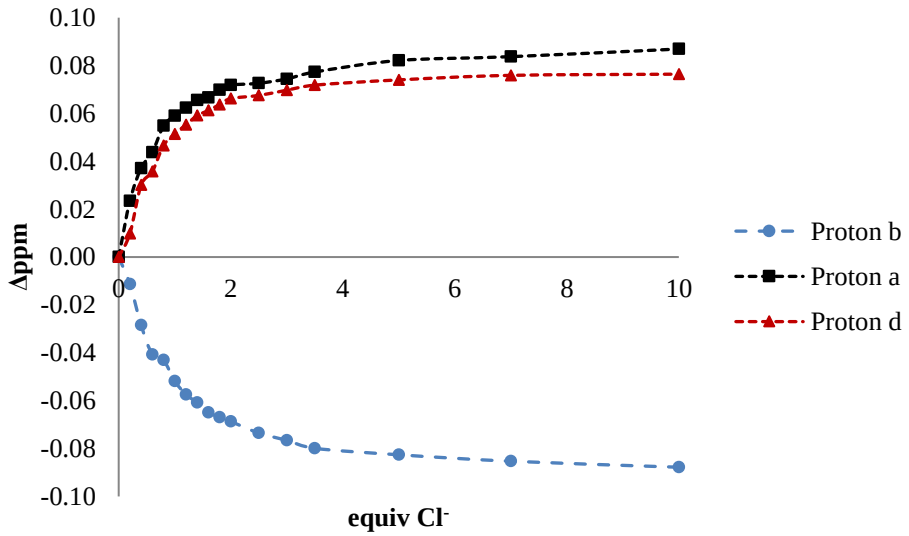

Figure 7.81. Plot of the data values from the titration study of **22(PF$_6$)$_3$** with Cl^-

b) Bromide titration

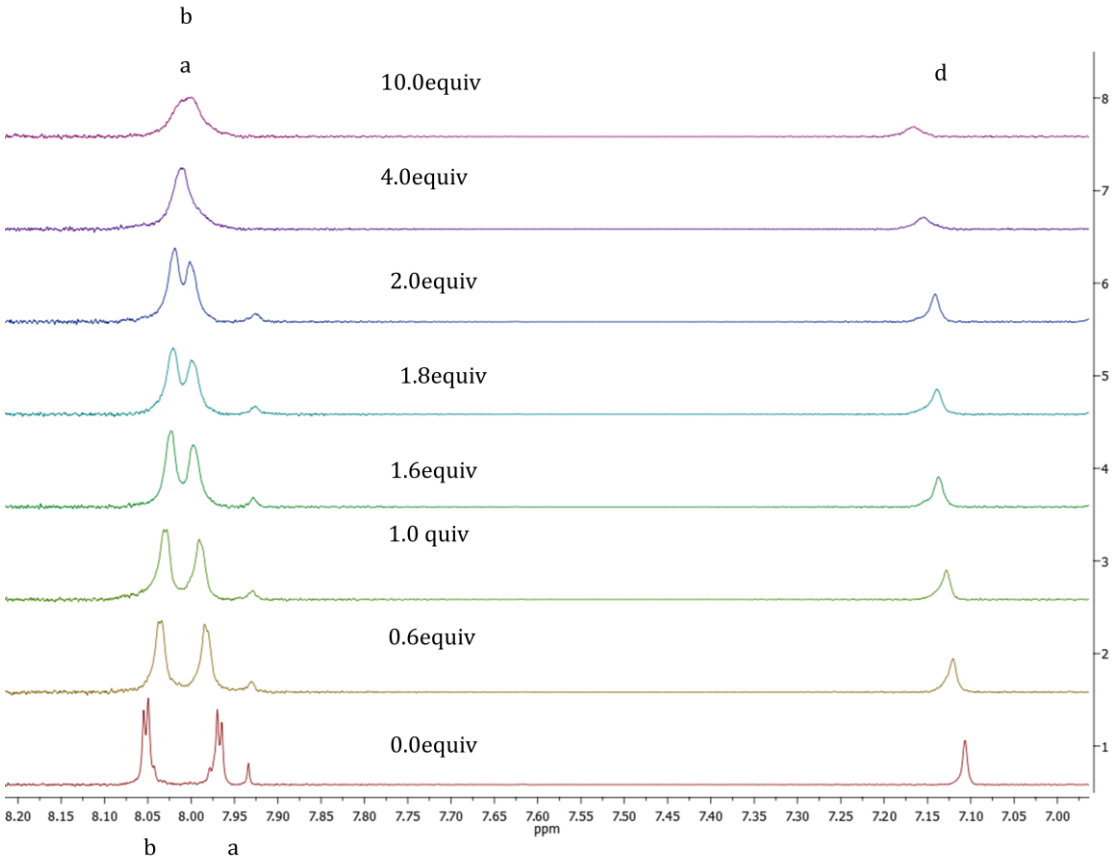

Figure 7.82. Partial ^{1}H NMR (400 Hz) changes observed for the host **22(PF$_6$)$_3$** in DMSO-*d*^{6} during the addition of Br^-.

Table 7.34: Data values from the titration study of **22(PF$_6$)$_3$** with Br$^-$

[*22*][*PF$_6$*]$_3$] (M)	equiv NBu$_4$Br	δa (ppm)	δb (ppm)	δd (ppm)	Δδa (ppm)	Δδb (ppm)	Δδd (ppm)	[NBu$_4$Br] (M)
0,002	0,0	8,0403	7,9553	7,0949	0	0	0	0
0,001992	0,2	8,0369	7,9673	7,1045	-0,0034	0,012	0,0096	0,000398
0,001984	0,4	8,0339	7,9721	7,1110	-0,0064	0,0168	0,0161	0,000794
0,001976	0,6	8,0299	7,9776	7,1145	-0,0104	0,0223	0,0196	0,001186
0,001969	0,8	8,0253	7,9790	7,1174	-0,015	0,0237	0,0225	0,001575
0,001961	1,0	8,0240	7,9834	7,1216	-0,0163	0,0281	0,0267	0,001961
0,001953	1,2	8,0205	7,9858	7,1248	-0,0198	0,0305	0,0299	0,002344
0,001946	1,4	8,0181	7,9879	7,1273	-0,0222	0,0326	0,0324	0,002724
0,001938	1,6	8,0162	7,9890	7,1297	-0,0241	0,0337	0,0348	0,003101
0,001931	1,8	8,0137	7,9903	7,1317	-0,0266	0,035	0,0368	0,003475
0,001923	2,0	8,0119	7,9920	7,1338	-0,0284	0,0371	0,0389	0,003846
0,001905	2,5	8,0086	7,9947	7,1374	-0,0317	0,0394	0,0425	0,004762
0,001887	3,0	8,0020	8,0020	7,1408	-0,0383	0,0467	0,0459	0,00566
0,001869	3,5	8,0020	8,0020	7,1450	-0,0383	0,0467	0,0501	0,006542
0,001818	5,0	8,0020	8,0020	7,1485	-0,0383	0,0467	0,0536	0,009091
0,001754	7,0	8,0020	8,0020	7,1537	-0,0383	0,0467	0,0588	0,012281
0,001667	10,0	8,0020	8,0020	7,1591	-0,0383	0,0467	0,0642	0,016667

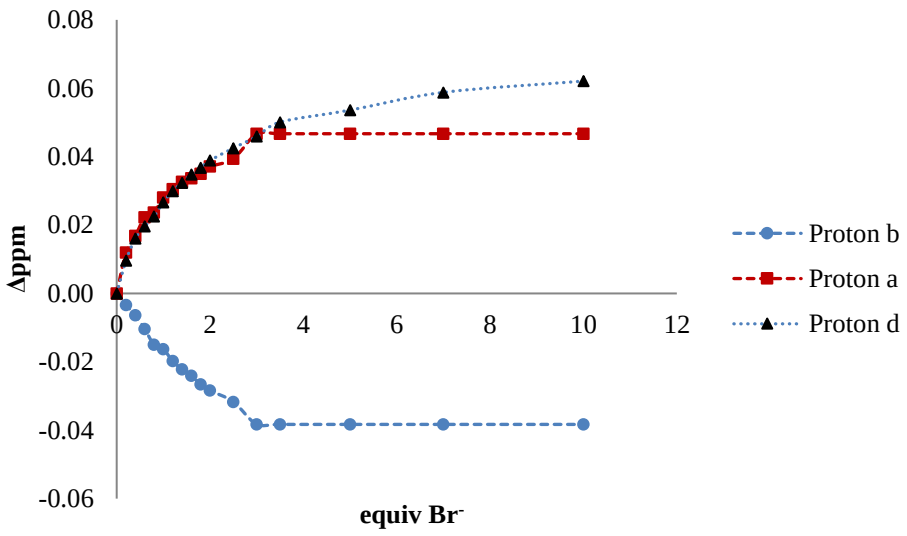

Figure 7.83. Plot of the data values from the titration study of **22(PF$_6$)$_3$** with Br$^-$

c) Iodide titration

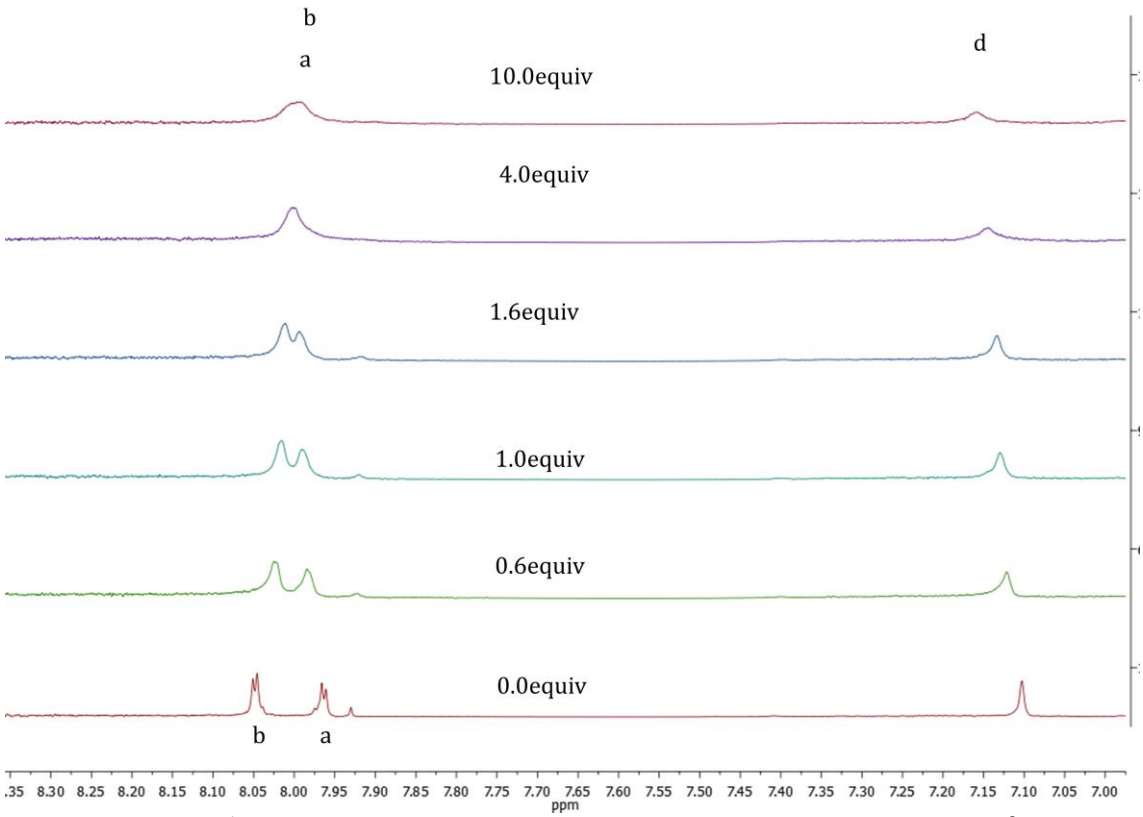

Figure 7.84. Partial ^{1}H NMR (400 Hz) changes observed for the host **22(PF$_6$)$_3$** in DMSO-*d*^{6} during the addition of I^-

Table 7.35: Data values from the titration study of **22(PF$_6$)$_3$** with I^-

[*22*][*PF$_6$*]$_3$] (M)	**equiv NBu$_4$I**	**Δa (ppm)**	**Δδa (ppm)**	**[NBu$_4$I] (M)**
0,002	0,0	7,1029	0,0000	0
0,001992	0,2	7,1040	0,0016	0,000398
0,001984	0,4	7,1110	0,0081	0,000794
0,001976	0,6	7,1145	0,0116	0,001186
0,001969	0,8	7,1174	0,0145	0,001575
0,001961	1,0	7,1216	0,0187	0,001961
0,001953	1,2	7,1248	0,0219	0,002344
0,001946	1,4	7,1273	0,0244	0,002724
0,001938	1,6	7,1297	0,0268	0,003101
0,001931	1,8	7,1317	0,0288	0,003475
0,001923	2,0	7,1338	0,0309	0,003846
0,001905	2,5	7,1374	0,0345	0,004762
0,001887	3,0	7,1408	0,0379	0,00566
0,001869	3,5	7,1460	0,0431	0,006542
0,001818	5,0	7,1485	0,0456	0,009091
0,001754	7,0	7,1530	0,0501	0,012281
0,001667	10,0	7,1545	0,0516	0,016667

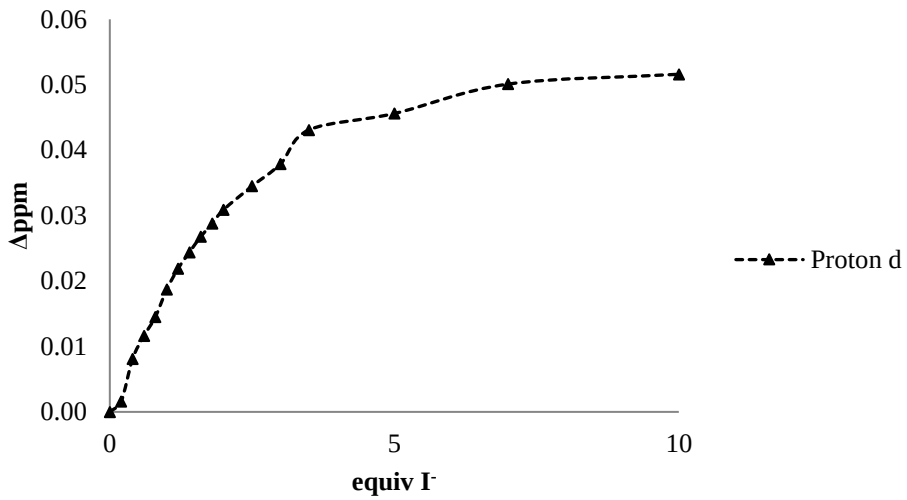

Figure 7.85. Plot of the data values from the titration study of **22(PF$_6$)$_3$** with I^-

d) Dihydrogen phosphate titration

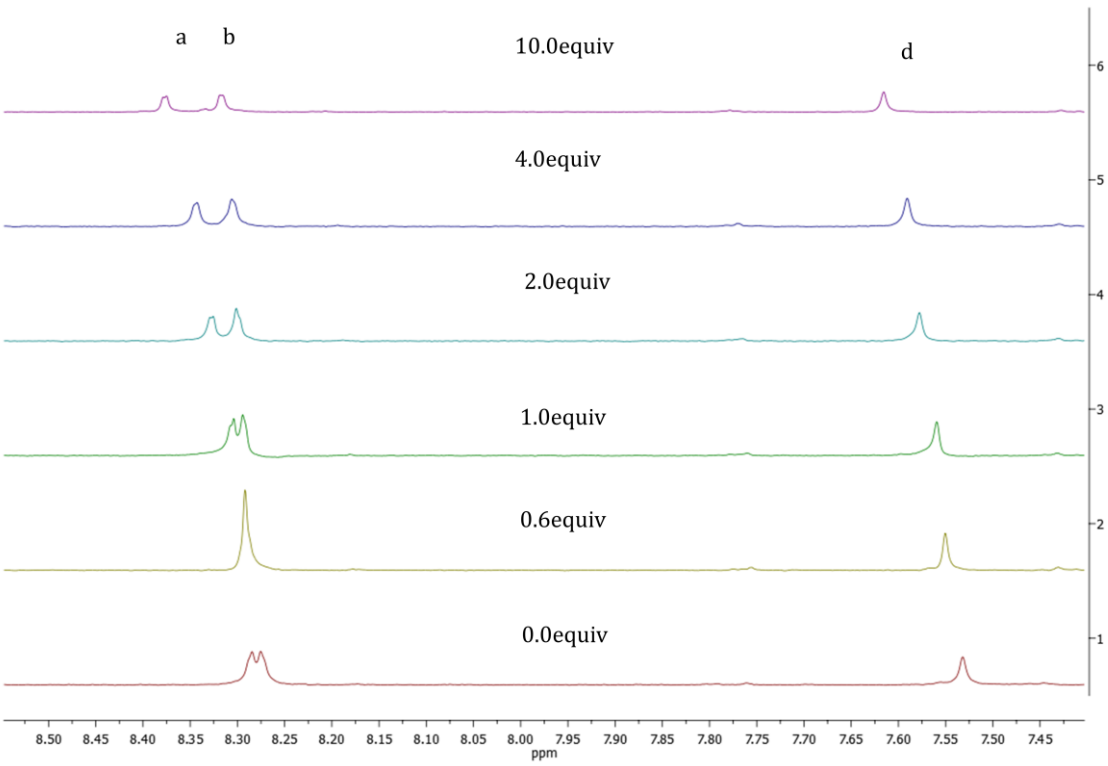

Figure 7.86. Partial ^{1}H NMR (400Hz) changes observed for the host **22(PF$_6$)$_3$** in DMSO-*d*^{6}:D_2O (9:1) during the addition of $H_2PO_4^-$

Table 7.36: Data values from the titration study of **22(PF$_6$)$_3$** with $H_2PO_4^-$

[*22*][*PF$_6$*]$_3$] (M)	equiv $NBu_4H_2PO_4$	δb (ppm)	δd (ppm)	Δδb (ppm)	Δδd (ppm)	[$NBu_4H_2PO_4$] (M)
0,002	0,0	8,2759	7,5323	0	0	0
0,001992	0,2	8,2855	7,5386	0,0096	0,0063	0,000398
0,001984	0,4	8,2890	7,5447	0,0131	0,0124	0,000794
0,001976	0,6	8,2919	7,5504	0,016	0,0181	0,001186
0,001969	0,8	8,2930	7,5549	0,0171	0,0226	0,001575
0,001961	1,0	8,3039	7,5594	0,028	0,0271	0,001961
0,001953	1,2	8,3069	7,5635	0,031	0,0312	0,002344
0,001946	1,4	8,3132	7,5666	0,0373	0,0343	0,002724
0,001938	1,6	8,3167	7,5709	0,0408	0,0386	0,003101
0,001931	1,8	8,3222	7,5741	0,0463	0,0418	0,003475
0,001923	2,0	8,3257	7,5777	0,0498	0,0454	0,003846
0,001905	2,5	8,3291	7,5806	0,0532	0,0483	0,004762
0,001887	3,0	8,3354	7,5850	0,0595	0,0527	0,00566
0,001869	3,5	8,3380	7,5906	0,0621	0,0583	0,006542
0,001818	5,0	8,3449	7,5977	0,069	0,0654	0,009091
0,001754	7,0	8,3540	7,6042	0,0781	0,0719	0,012281
0,001667	10,0	8,3550	7,6042	0,0791	0,07192	0,016667

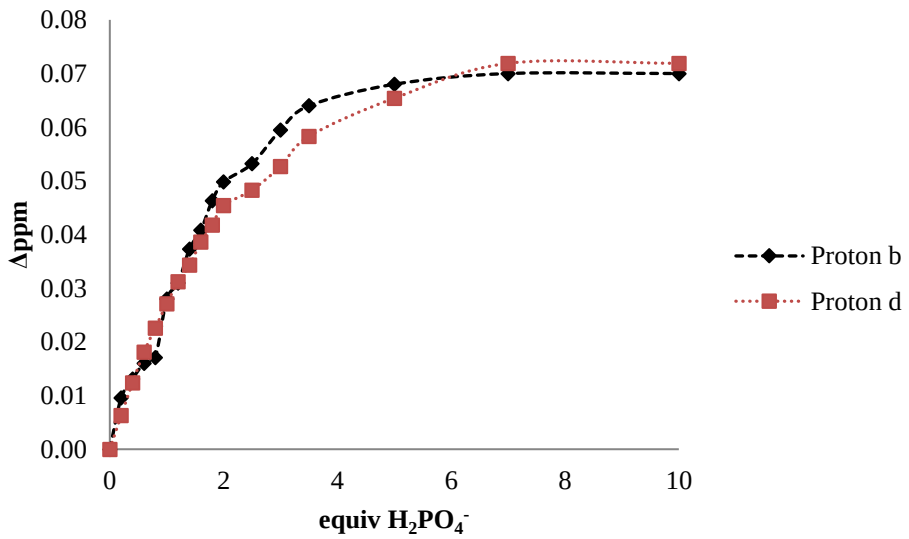

Figure 7.87. Plot of the data values from the titration study of **22(PF$_6$)$_3$** with $H_2PO_4^-$

Fitting curves and determination of affinity constants

The 1:1 association constants of the tripod receptors, K_{11}, were calculated by global nonlinear regression analysis by simultaneously including all protons showing chemical shift variations from the direct use of the bind fitting program available at http://app.supramolecular.org/bindfit.

7.4 HRMS detection of the complexes of chapter 5

A Q-TOF Premier (Waters) mass spectrometer with an electrospray source operating in the V-mode was used.

7.4.1 HRMS detection of the complexes formed between cavitand 15 and different ammonium salts

For the determination of the molecular composition of the supramolecular adducts of **15** with different guests $\mathbf{a}^+$-$\mathbf{e}^+$ and **f**, to a 5 10^{-4} M solution of **15** in $CHCl_3$:CH_3OH (1:1) was added 2 equivalents of the corresponding guest and analyzed by negative and positive ESI-MS.

Apart from that, a competitive experiment was also carried out, where a stock solution of equimolar amount of guests ($\mathbf{a}^+$-$\mathbf{e}^+$ and **f**, $5 \cdot 10^{-4}$ M) were prepared and added to 1 equivalent of **15**. The solutions were also prepared in $CHCl_3$:CH_3OH (1:1).

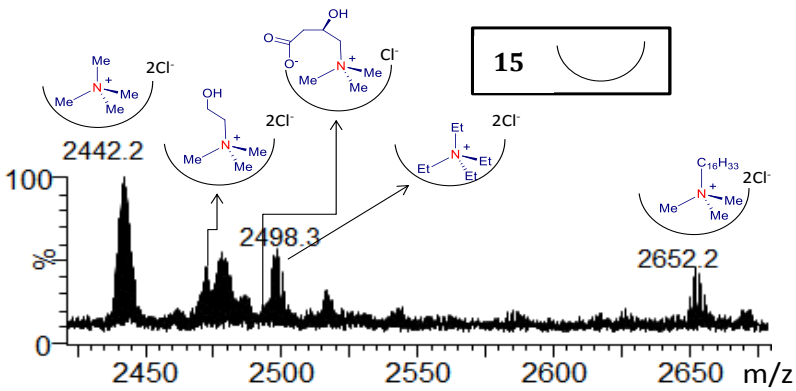

Figure 7.88. Selected region of the ESI-MS spectrum (negative scan mode) of a mixture of **15** and a five-old excess of the halides of $\mathbf{a}^+$-$\mathbf{e}^+$ and **f**. Non-assigned peaks correspond to uncomplexed forms of **15**, such as [**15** + 5H + 4Cl]$^-$ and [**15** + 6H + 5Cl]$^-$.

7.4.2 HRMS detection of the complexes formed between cavitands $[16][PF_6]_4$ and $[17][PF_6]_4$ and different anions

For the determination of the molecular composition of the supramolecular adducts of $\mathbf{[16][PF_6]_4}$ and $\mathbf{[17][PF_6]_4}$ with different guests (Cl^-, Br^-, I^-, ClO_4^-, NO_3^-, $C_6H_5SO_3^-$, $C_7H_8SO_3^-$, CN^-), an equimolar solution of each host and guest ($5 \cdot 10^{-5}$ M), in DMSO:MeOH (1:1), was injected. The positive ESI mass spectra displayed very useful information about the stoichiometry of the supramolecular recognition on the basis of the m/z values and comparison between the observed and the theoretical isotopic pattern of the identifies species. The chemical composition of each peak was assigned by

comparison of the isotope experimental and theoretical patterns, considering natural abundance for all elements, using the MassLynx 4.1 program.

7.5 Catalytic Experiments described in Chapter 3

7.5.1 Catalytic experiments described for Palladium complexes 5-9

General procedure for the acylation of aryl halides with hydrocinnamaldehyde: Molecular Sieves (1g), tetrabutyl-ammonium bromide (16.0 mg, 0.05 mmol), catalyst **5-9**(1–2 mol%), aryl halide (0.5 mmol), hydrocinnamaldehyde (0.6 mmol), pyrrolidine (1.0 mmol), and DMF (2 mL) were added to a 50 mL high-pressure Schlenk tube. The mixture was stirred and heated at 115 ºC for 16 h. The yields of the reaction were calculated by GC and using anisole as internal standard.

General procedure for palladium-catalyzed Suzuki-Miyaura coupling: Under air, a Schlenk tube was charged with catalyst **5-9** (2 mol%), aryl halide (0.5 mmol), the corresponding phenyl boronic acid (0.6 mmol), and Cs_2CO_3 (0.326 g, 1.0 mmol). The Schlenk tube was sealed with a septum and purged with nitrogen three times. Toluene (2 mL) was added. The mixture was stirred and heated at 80 ºC for 2 h. The yields of the reaction were calculated by GC and using anisole as the internal standard.

Kinetics Studies: Time-dependent reaction profiles for the reaction of bromobenzene and 4-tolylboronic acid was carried out for catalyst **6**, catalyst **6** and 10 mol% of pyrene and catalyst **7**. The same reaction conditions describe for the Suzuki-Miyaura coupling were used.

7.5.2 Catalytic experiments described for iridium and rhodium complexes 10-14 and for rGO-10 and rGO-12

General procedure for the transfer hydrogenation: complex **10-14** (0.5 mol % based on the metal) and KOH (0.05 mmol) were placed together in a Schlenk tube with a Teflon cap. The tube was then evacuated and filled with nitrogen three times. 2-Propanol (2 mL) and the corresponding ketone (0.5 mmol) were added, and the mixture was stirred at 100 °C for 1 or 2 h. Yields were determined by GC analyses using anisole (0.5 mmol) as internal standard.

General procedure for the β-alkylation of 1-phenylethanol with primary alcohols: complex **10-13** (0.5 mol % based on the metal) and KOH (1.0 mmol) were placed together in a Schlenk tube with a Teflon cap. The tube was then evacuated and filled

with nitrogen three times. 1-phenylethanol (1.0 mmol), benzyl alcohol (1.0 mmol) and 0.5 mL of dry toluene were added and the mixture was stirred at 100 °C for 8 h. Yields were determined by GC analyses using anisole (1.0 mmol) as internal standard.

Recycling Experiments: In a round-bottom flask, a mixture of 1-phenylethanol (1.0 mmol), benzyl alcohol (1.0 mmol), KOH (1.0 mmol), anisole (1.0 mmol) as internal standard and the **rGO-10** or **rGO-12** (0.5 mol % based on the metal) was refluxed in toluene (1.5 mL) for 8 h. The monitoring of the reaction, yields, and conversions were determined by GC analyses. After completion of each run (8 h), the reaction mixture was allowed to reach room temperature and was filtered. The remaining solid was washed thoroughly with CH_2Cl_2, dried under reduced pressure and reused in the following run.

Kinetics Studies: Time-dependent reaction profiles for the reaction between 1-phenylethanol and benzyl alcohol were obtained for catalysts **10**, **12** and **13** at different concentrations ranging from 0.01-5 mol%. The same reactions conditions describe for the *β*-alkylation were used. Yields determined by GC, using anisole as internal standard. The first plot for each catalyst allows the determination of the reaction order in the substrate, and the apparent rate constant, k_{obs}. The second plot represents log[k_{obs}] *vs* log[cat], and the order in the catalyst concentration is directly determined from the slope of the straight line. The first plots were represented according with the reaction order with respect the substrate.

Catalyst 9

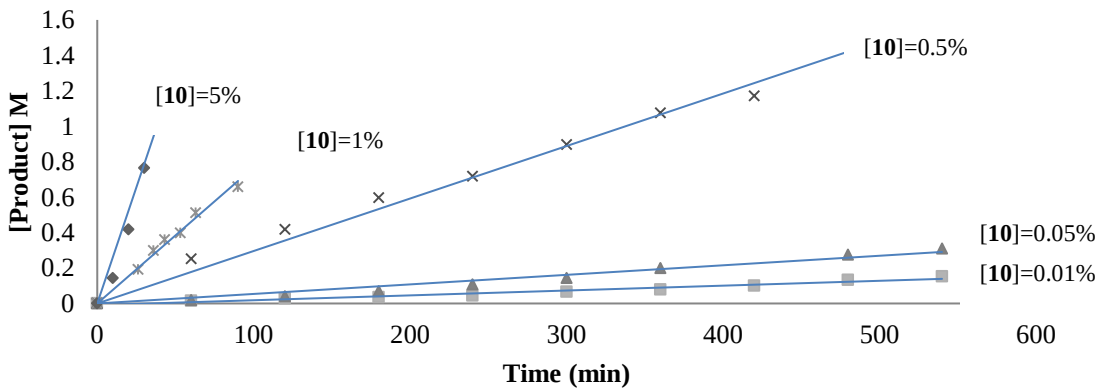

Figure7.89. Time-dependent reaction profile for the reaction between 1-phenylethanol and benzyl alcohol.Reaction conditions: 1-phenylethanol (1.0 mmol), benzyl alcohol (1.0 mmol), KOH (1.0 mmol) in 0.5 mL of toluene at 100 ºC. Yields determined by GC, using anisole as internal standard. Product: 1-phenyl hexanol. Straight lines drawn to guide the eye. Product = 1-phenyl

hexanol *vs* time. The concentration of the catalyst (**10**) rages between 0.01-5 mol%. Straight lines drawn to guide the eye

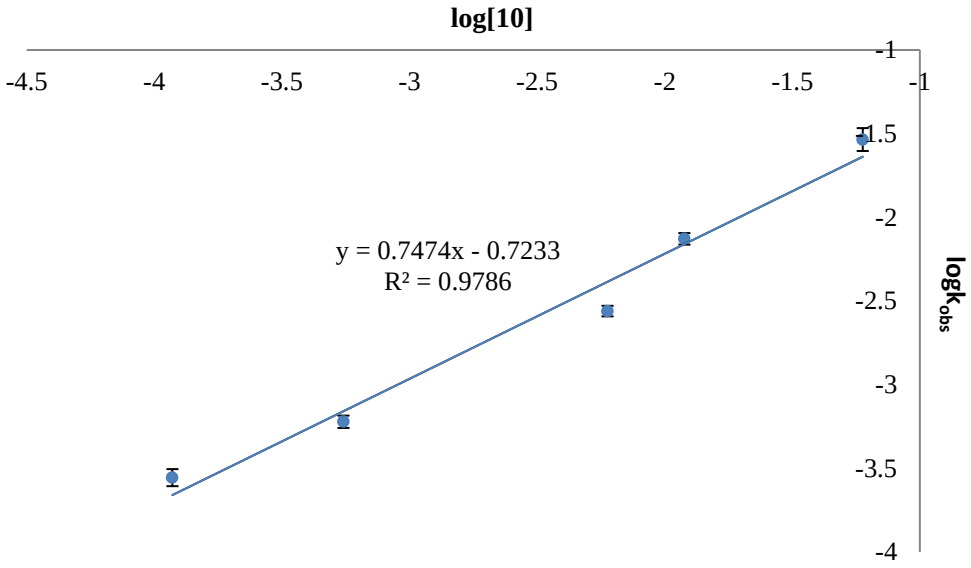

Figure 7.90. Plot of log(k_{obs}) *vs* log[**10**]. The value of the slope with errors is: 0.75±0.06

Catalyst 12

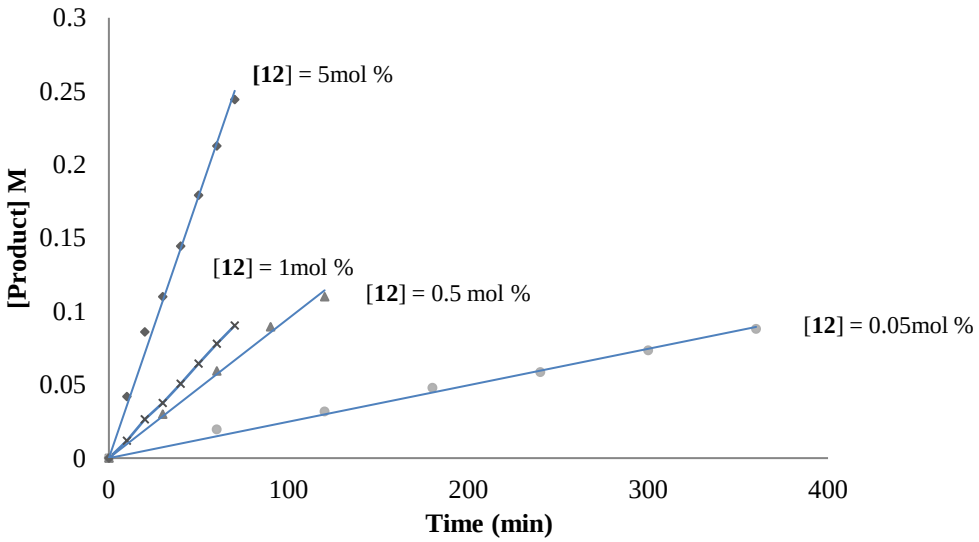

Figure 7.91. Time-dependent reaction profile for the reaction between 1-phenylethanol and benzyl alcohol.Reaction conditions: 1-phenylethanol (1.0 mmol), benzyl alcohol (1.0 mmol), KOH (1.0 mmol) in 0.5 mL of toluene at 100 ºC. Yields determined by GC, using anisole as internal standard. Product: 1-phenyl hexanol. Straight lines drawn to guide the eye. Product = 1-

phenyl hexanol *vs* time. The concentration of the catalyst (**12**) rages between 0.05-5 mol%. Straight lines drawn to guide the eye

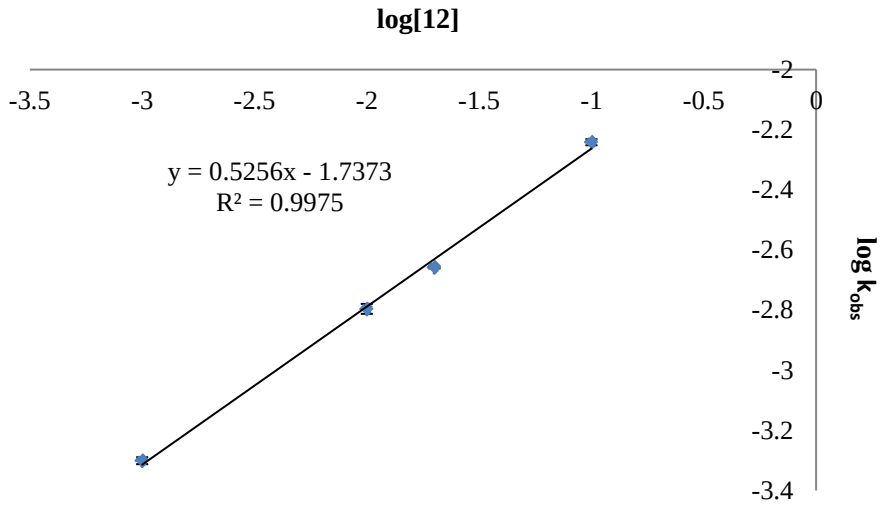

Figure 7.92. Plot of log(k_{obs}) against log[**12**]. The value of the slope with errors is: 0.555±0.008

Catalyst 13

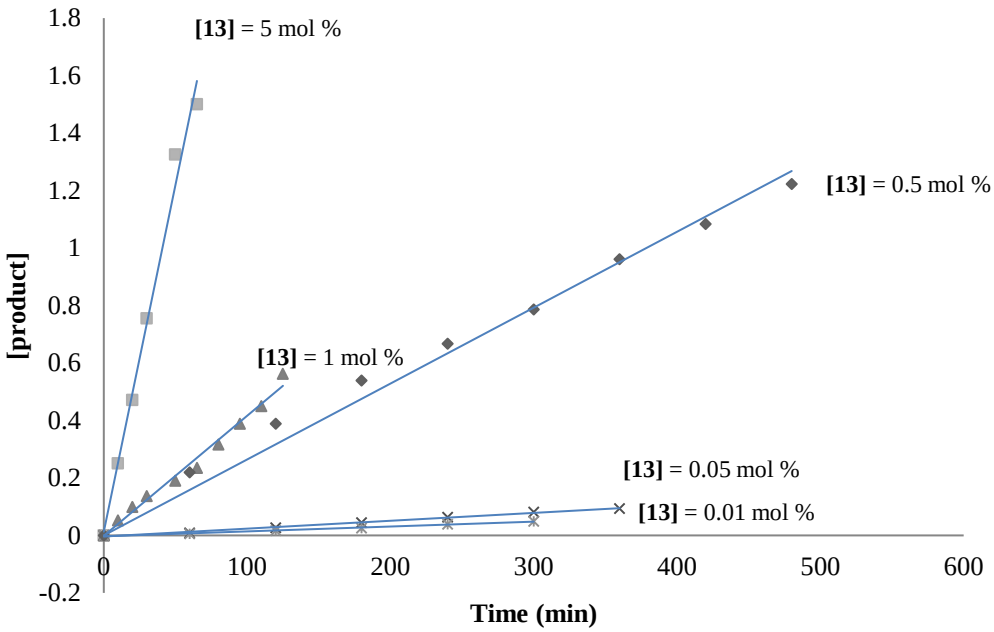

Figure 7.93. Time-dependent reaction profile for the reaction between 1-phenylethanol and benzyl alcohol. Reaction conditions: 1-phenylethanol (1.0 mmol), benzyl alcohol (1.0 mmol), KOH (1.0 mmol) in 0.5 mL of toluene at 100 ºC. Yields determined by GC, using anisole as internal standard. Product: 1-phenyl hexanol. Straight lines drawn to guide the eye.Product = 1-phenyl hexanol*vs* time. The concentration of the catalyst (**13**) rages between 0.01-5 mol%. Straight lines drawn to guide the eye

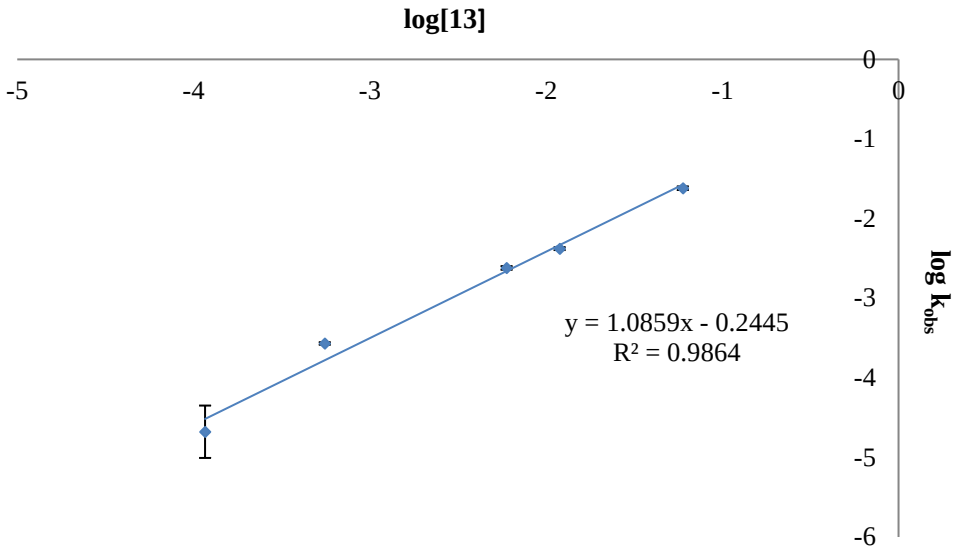

Figure 7.94. Plot of log(k_{obs}) against log[**13**]. The value of the slope with errors is: 1.08±0.07

7.6 Voltammetric Studies of cavitand 15 of Chapter 5

Titration Studies

Differential pulse voltammetry and Cyclic Voltammetry were carried out upon the additions of ammonium salts (Et_4NCl, $N(C_{16}H_{33})Me_3Cl$, NMe_4Cl, Choline chloride, NBu_4Cl).

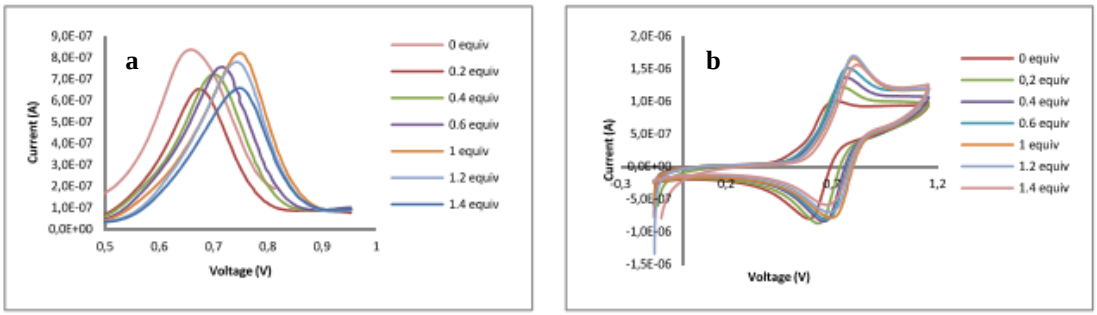

Figure7.95. (a) Differential pulse voltammetry of **15** upon the addition of Et_4NCl, (b) Cyclic Voltammetry of **15** upon the addition of Et_4NCl**.**The data were collected with 0.2 mM of compound **15** in CH_2Cl_2 in presence of 0.1 M NBu_4PF_6. The scan potential was initiated from E_{ocp} to positive direction. Scan rate 0.1 V s^{-1}. Platinum electrode was used

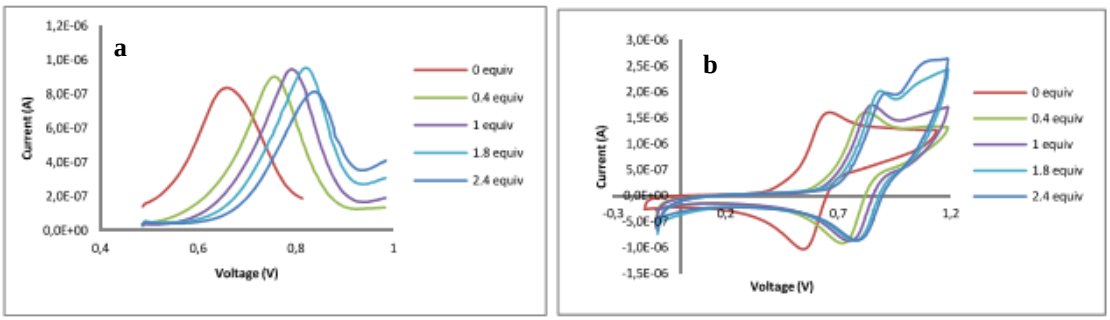

Figure 7.96. (a) Differential pulse voltammetry of **15**upon the addition of $N(C_{16}H_{33})Me_3Cl$, (b) Cyclic Voltammetry of **15** upon the addition of $N(C_{16}H_{33})Me_3Cl$**.** The data were collected with 0.2 mM of compound **15** in CH_2Cl_2 in presence of 0.1 M NBu_4PF_6. The scan potential was initiated from E_{ocp} to positive direction. Scan rate 0.1 V s^{-1}. Platinum electrode was used

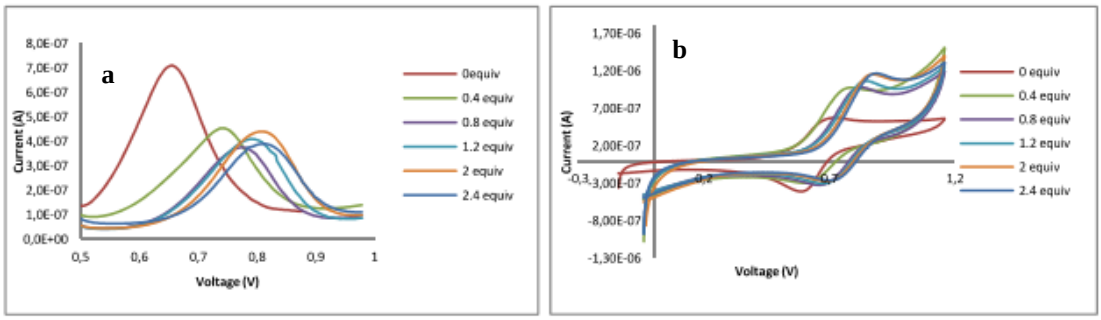

Figure 7.97. (a) Differential pulse voltammetry of **15** upon the addition of NMe_4Cl, (b) Cyclic Voltammetry of **15** upon the addition of NMe_4Cl**.** The data were collected with 0.2 mM of compound **15**

in CH_2Cl_2 in presence of 0.1 M NBu_4PF_6. The scan potential was initiated from E_{ocp} to positive direction. Scan rate

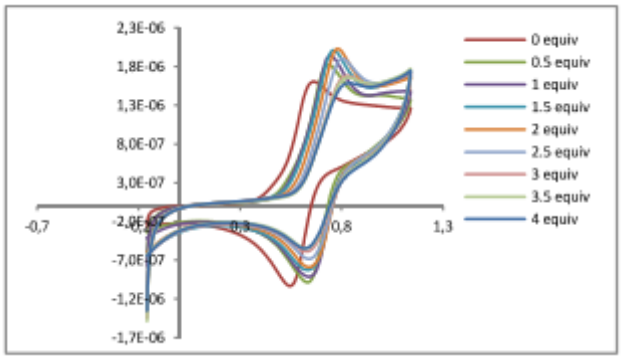

Figure 7.98. Cyclic voltammetry of **15** upon the addition of Choline chloride**.** The data were collected with 0.2 mM of compound **15** in CH_2Cl_2 in presence of 0.1 M NBu_4PF_6. The scan potential was initiated from E_{ocp} to positive direction. Scan rate 0.1 V s^{-1}. Platinum electrode was used

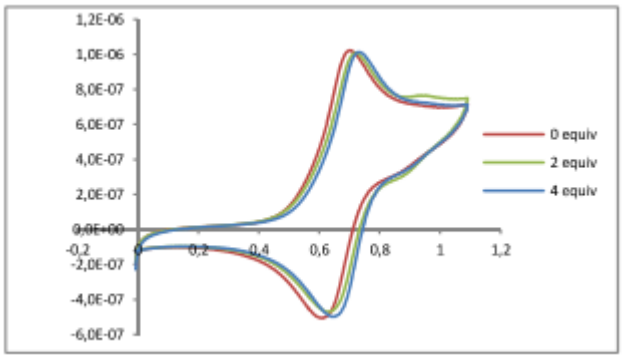

Figure 7.99. Cyclic Voltammetry of **15** upon the addition of NBu_4Cl**.** The data were collected with 0.2 mM of compound **15** in CH_2Cl_2 in presence of 0.1 M NBu_4PF_6. The scan potential was initiated from E_{ocp} to positive direction. Scan rate 0.1 V s^{-1}. Platinum electrode was used

Determination of the binding stoichiometry by Job Plot analysis using CV

The 1:1 binding stoichiometry between cavitand **15** with NMe_4Cl was also confirmed as follows. Two stock solutions were prepared; solution A (1.7 mM of **15** in CH_2Cl_2) and solution B (1.7 mM of NMe_4Cl in CH_2Cl_2). The two solutions were combined to give a series of samples of identical total concentrations but containing different mole fractions of the two components. Cyclic voltammetry data were collected in presence of 0.1 M NBu_4PF_6. The scan potential was initiated from E_{ocp} to positive direction. Scan rate 0.1 V s^{-1}. Platinum electrode was used.

χ_g	E	ΔE	ΔE*χg
0	0,74962	0,00000	0,00000000
0,2	0,91838	0,16876	0,03375244
0,3	0,91071	0,16109	0,04832634
0,5	0,91930	0,16968	0,08483887
0,7	0,82961	0,07999	0,05599146
0,8	0,80011	0,05049	0,04039023
1	0,000000	0,00000	0,0000000

Table 7.37: Experimental data of the cyclic voltammetry where χg is the guest molar fraction and E the oxidation potential observed in each measurement

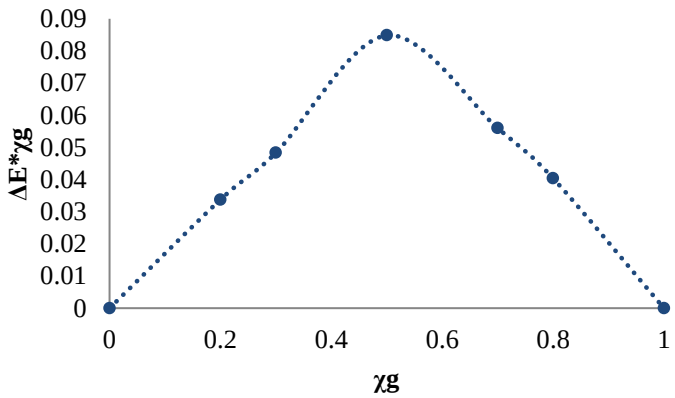

Figure 7.100. Job plots showing the 1:1 stoichiometry of the complexation between **15** and NMe_4Cl in CH_2Cl_2

7.7 UV-Visible experiments of materials rGO 10, rGO12 and catalyst 10 of Chapter 3

The samples were suspended in DMF and sonicated for 5 minutes before the measurements. The molecular complexes were dissolved in DMF (10^{-6}).

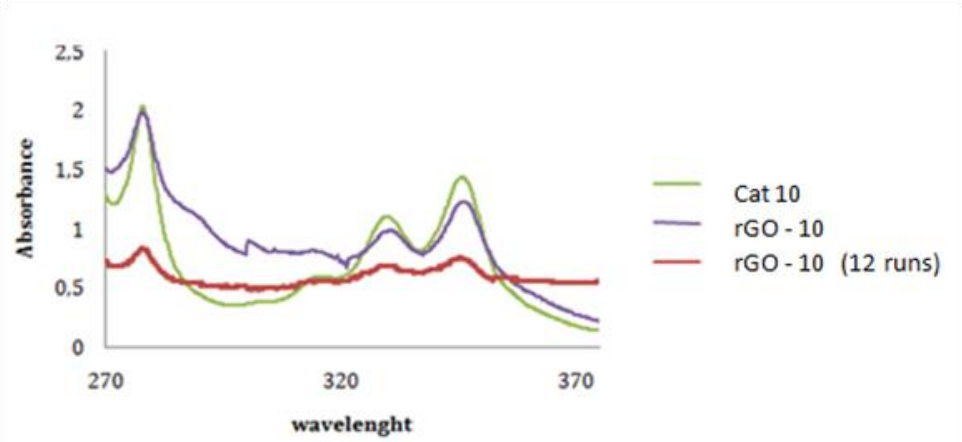

Figure 7.101. UV/Vis spectrum of catalyst **10**, r**GO-10** and r**GO-10** after 12 recycling experiments

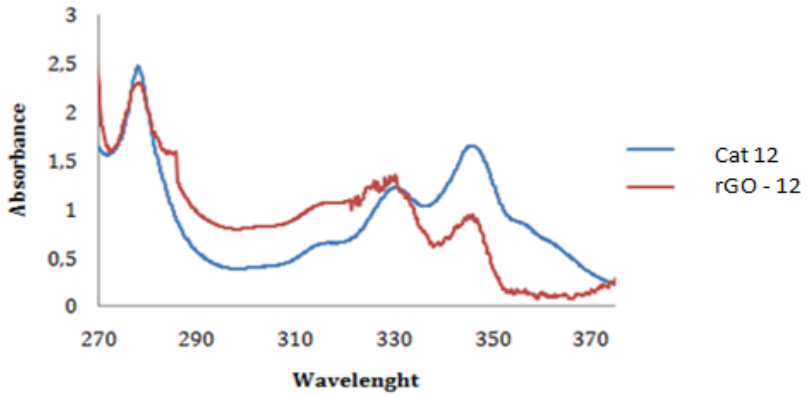

Figure 7.102. UV/Vis spectrum of catalyst **12** and r**GO-12**

7.8 Scanning Electron Microscopy (SEM) images of Chapter 3

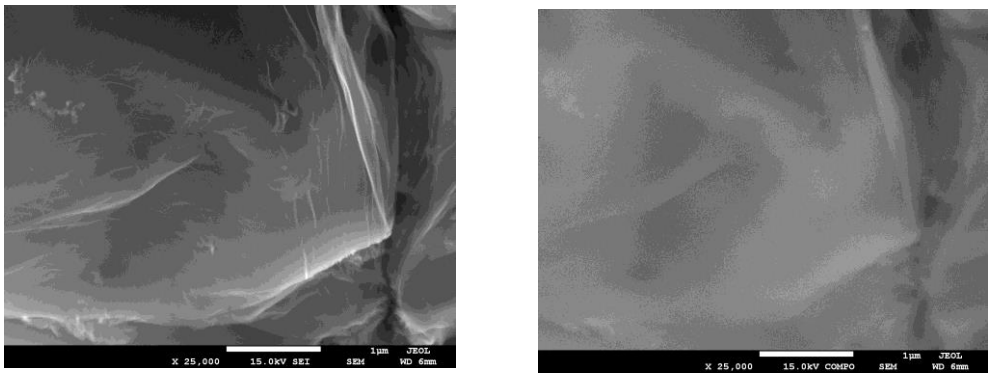

Figure 7.103. SEM images of **rGO-10** hybrid using the secondary electrons (SE) (left) and the back-scattered electrons (BSE) (right) signals of the SEM

Figure 7.104. SEM images of **rGO-12** hybrid using the secondary electrons (SE) (left) and the back-scattered electrons (BSE) (right) signals of the SEM

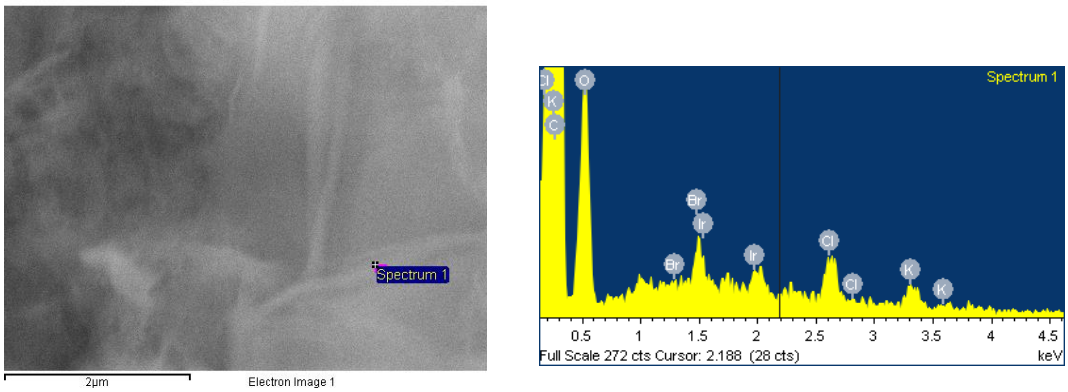

Figure 7.105. SEM images and EDS spectra of **rGO-10**

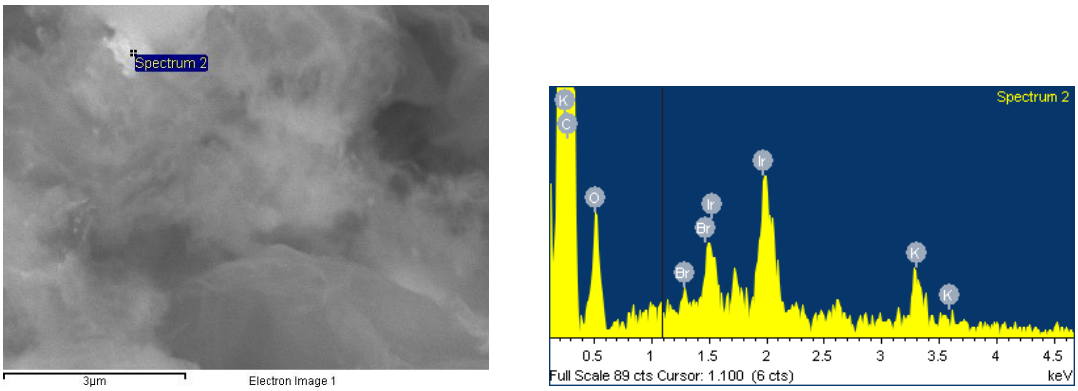

Figure 7.106. SEM images and EDS spectra of **rGO-12**

7.9 High Resolution Transmission Electron Microscopy (HRTEM) images Chapter 3.

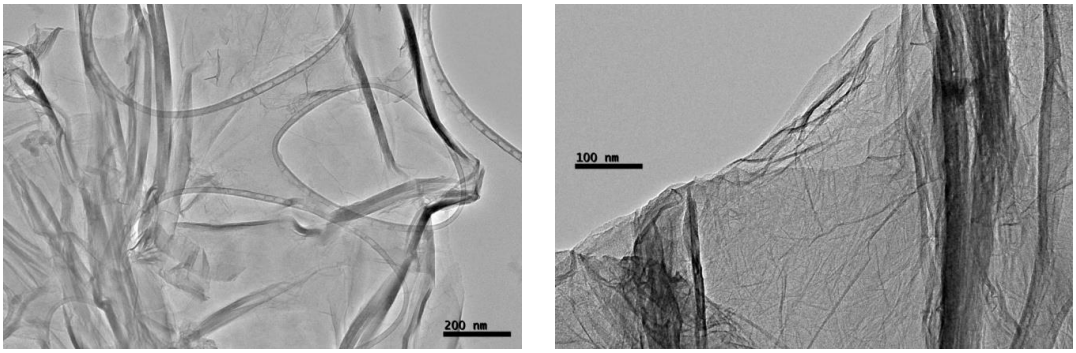

Figure 7.107. HRTEM images of **rGO-10**

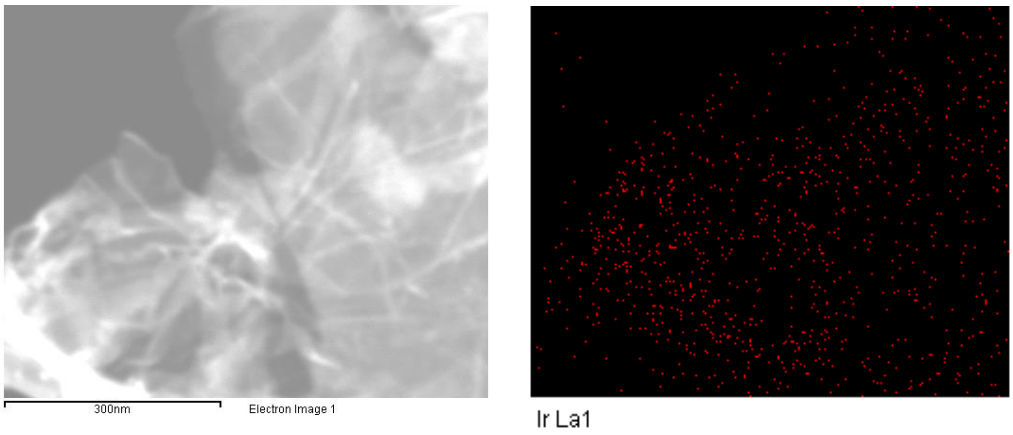

Figure 7.108. STEM image of **rGO-10** (left) and EDS elemental mapping image showing the homogeneous distribution of Iridium (right)

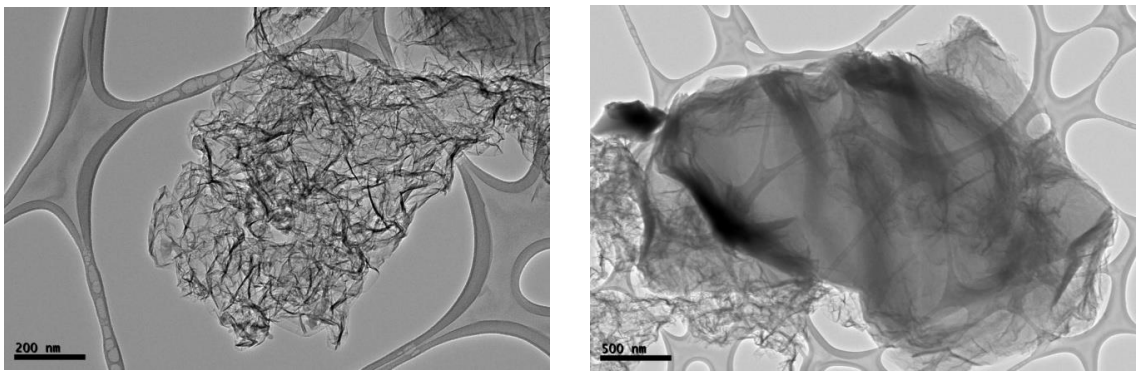

Figure 7.109. HRTEM images of **rGO-12**

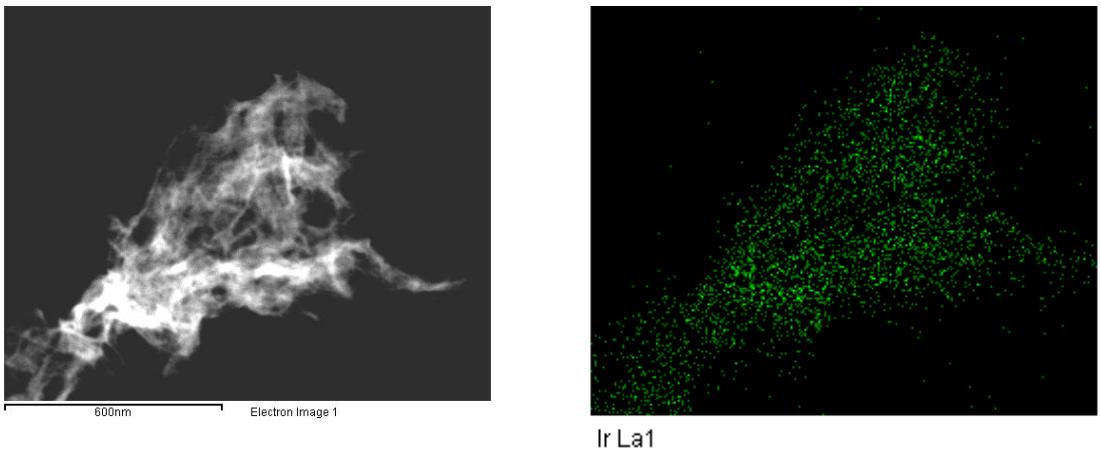

Figure 7.110. STEM image of **rGO-12** (left) and EDS elemental mapping image showing the homogeneous distribution of iridium (right)

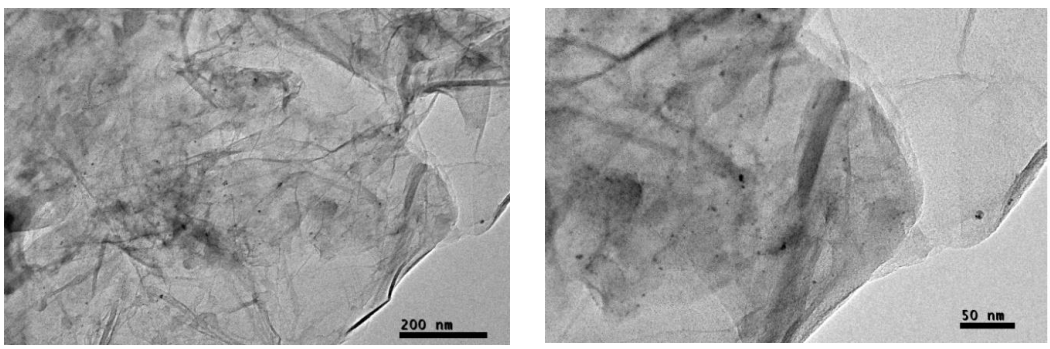

Figure 7.111. HRTEM images of **rGO-10** after 12 catalytic cycles

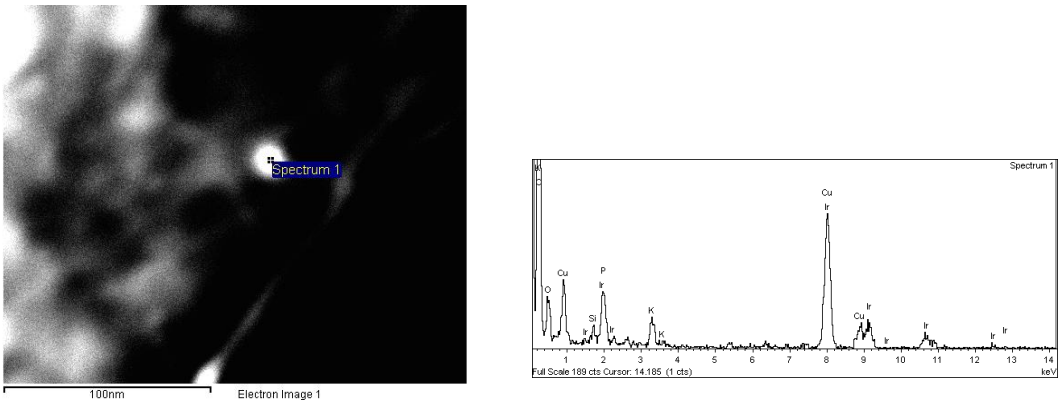

Figure 7.112. STEM images and EDS spectra of **rGO-10**

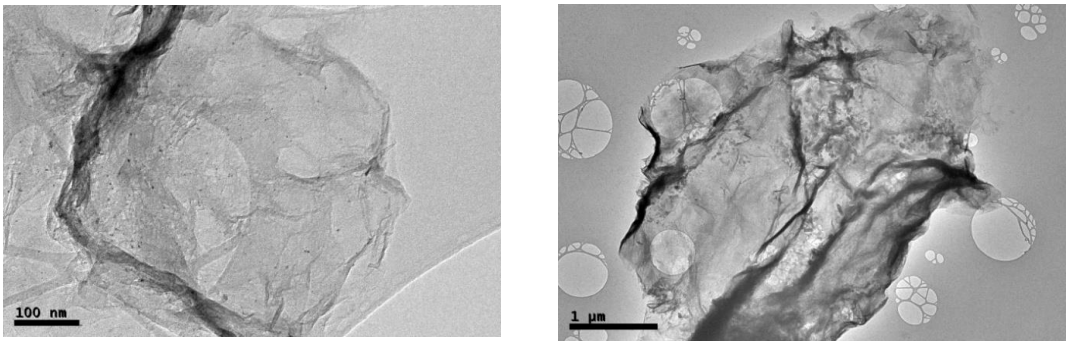

Figure 7.113. HRTEM images of **rGO-12** after 7 catalytic cycles

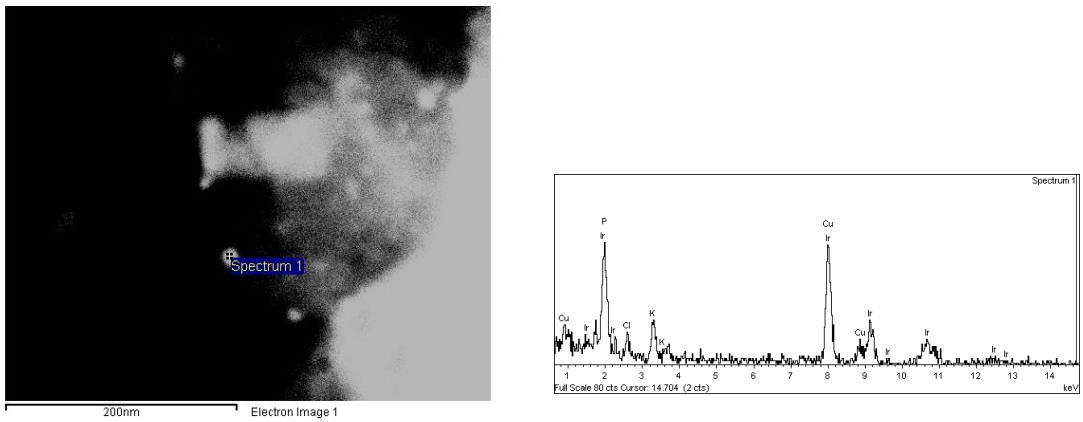

Figure 7.114. STEM images and EDS spectra of **rGO-12**

7.10 X-Ray Crystallography

X-Ray diffraction was performed on single crystals mounted on a MicroMount® polymer tip (MiteGen) in a random orientation. Data collection was performed on a SuperNova, Dual, Cu at zero, Atlas diffractometer. Using Olex2[8], the structures were solved with the ShelXS structure solution program using Direct Methods and refined with the ShelXL[9] refinement package using Least Squares minimisation.

7.10.1 Crystal Structure of compounds of Chapter 2

Crystals for X-ray diffraction of compound **A** were obtained by slow evaporation of a concentrated solution of the compound **A** in methanol. Crystals for X-ray diffraction of compound **1** were obtained by slow diffusion of methanol into a concentrated solution of the compound **1** in dichloromethane. Crystals for X-ray diffraction of compound **2** were obtained by slow diffusion of hexane into a concentrated solution of **2** in dichloromethane. Crystals for X-ray diffraction of compound **3** were obtained by slow diffusion of methanol into a concentrated solution of **3** in dichloromethane.

In the following table the structural parameters, registering conditions and refinement for these structures are described.

Table 7.38: Crystallographic data and structure refinement for compounds **A**, **1**, **2** and **3**

	A	**1**	**2**	**3**
Empirical formula	$C_{30}H_{44}Cl_2N_4O_{10}$	$C_{52}H_{60}Cl_6Ir_2N_4O$	$C_{50}H_{58}Cl_2N_4ORh_2$	$C_{33}H_{27}Cl_3N_4O_3Rh_2$
Formula weight	691.59	1354.14	1007.72	839.76
Temperature/K	200.00(10)	200.05(10)	200.1(3)	293(2)
Crystal system	monoclinic	monoclinic	orthorhombic	triclinic
Space group	I2/c	$P2_1/c$	Pbca	P-1
a/Å	16.6444(3)	21.3681(4)	20.9457(3)	9.3896(2)
b/Å	9.93793(18)	14.0701(3)	19.1797(4)	9.56605(18)
c/Å	21.1486(4)	18.2729(4)	23.0383(5)	19.5108(3)
α/°	90.00	90.00	90.00	87.0246(14)
β/°	93.1009(17)	90.9727(19)	90.00	89.5385(16)
γ/°	90.00	90.00	90.00	61.383(2)
Volume/Å^3	3493.10(11)	5492.97(19)	9255.2(3)	1536.05(5)
Z	4	4	8	2
ρ_{calc}mg/mm^3	1.315	1.637	1.446	1.816
m/mm^{-1}	2.169	5.171	7.141	1.378
F(000)	1464.0	2656.0	4144.0	836.0
Crystal size/mm^3	0.13 × 0.11 × 0.08	0.12 × 0.11 × 0.07	0.13 × 0.11 × 0.1	0.12 × 0.11 × 0.09
2Θ range for data collection	8.38 to 145.3°	5.62 to 55°	7.34 to 122.06°	6.24 to 56.34°
Index ranges	-20 ≤ h ≤ 17, -12 ≤ k ≤ 12, -25 ≤ l ≤ 26	-27 ≤ h ≤ 27, -18 ≤ k ≤ 18, -23 ≤ l ≤ 23	-23 ≤ h ≤ 8, -21 ≤ k ≤ 20, -25 ≤ l ≤ 19	-12 ≤ h ≤ 12, -12 ≤ k ≤ 11, -24 ≤ l ≤ 25
Reflections collected	16163	61595	18009	29137
Independent reflections	3423[R(int) = 0.0412]	12437[R(int) = 0.0343]	6913[R(int) = 0.0394]	6758[R(int) = 0.0348]
Data/restraints/parameters	3423/0/224	12437/6/607	6913/1/533	6758/0/410
Goodness-of-fit on F^2	1.078	1.079	1.224	1.161
Final R indexes [I>=2σ (I)]	R_1 = 0.0521, wR_2 = 0.1539	R_1 = 0.0467, wR_2 = 0.1315	R_1 = 0.0592, wR_2 = 0.1862	R_1 = 0.0353, wR_2 = 0.0783
Final R indexes [all data]	R_1 = 0.0579, wR_2 = 0.1645	R_1 = 0.0589, wR_2 = 0.1414	R_1 = 0.0749, wR_2 = 0.2151	R_1 = 0.0467, wR_2 = 0.0842
Largest diff. peak/hole / e Å^{-3}	0.47/-0.55	2.76/-2.48	1.24/-1.50	1.18/-0.57

7.10.2 Crystal Structure of compound 6 of Chapter 3

Crystals suitable for X-ray study of complex **6** were obtained by slow diffusion of hexane into a concentrated solution of the complex in dichloromethane.

Table 7.39: Crystallographic data and structure refinement for compound **6**

	6
Empirical formula	$C_{70}H_{49}Br_4Cl_{19.5}N_6Pd_2$
Formula weight	2197.86
Temperature/K	220
Crystal system	triclinic
Space group	P-1
a/Å	13.8715(3)
b/Å	13.9886(3)
c/Å	14.2318(3)
α/°	64.449(2)
β/°	61.369(2)
γ/°	62.9117(19)
Volume/Å^3	2076.20(9)
Z	1
ρ_{calc}g/cm^3	1.758
μ/mm^{-1}	3.029
F(000)	1074.0
Crystal size/mm^3	0.475 × 0.286 × 0.135
Radiation	MoKα (λ = 0.71073)
2Θ range for data collection/°	5.686 to 51.978
Index ranges	$-17 \leq h \leq 17$, $-17 \leq k \leq 17$, $-17 \leq l \leq 17$
Reflections collected	41128
Independent reflections	8149 [R_{int} = 0.0403, R_{sigma} = 0.0255]
Data/restraints/parameters	8149/0/469
Goodness-of-fit on F^2	1.042
Final R indexes [I>=2σ (I)]	R_1 = 0.0807, wR_2 = 0.2536
Final R indexes [all data]	R_1 = 0.0999, wR_2 = 0.2849
Largest diff. peak/hole / e Å^{-3}	2.48/-1.93

7.10.3 Crystal Structure of compound $22(BF_4)_3$ of Chapter 6

Crystals suitable for X-ray study of compound **$22(BF_4)_3$** were obtained by slow diffusion of methanolinto a concentrated solution of **$22(BF_4)_3$** (with one equivalent of TBACl) in chloroform.

Table 7.40: Crystallographic data and structure refinement for compound **$22(BF_4)_3$**

	$22(BF_4)_3$
Empirical formula	$C_{22}H_{23}B_2Cl_4F_8I_3N_6$
Formula weight	1067.58
Temperature/K	200.00(14)
Crystal system	orthorhombic
Space group	Pbca
a/Å	13.6312(2)
b/Å	23.5061(4)
c/Å	24.2909(4)
α/°	90
β/°	90
γ/°	90
Volume/Å^3	7783.2(2)
Z	8
ρ_{calc}g/cm^3	1.822
μ/mm^{-1}	2.746
F(000)	4048.0
Crystal size/mm^3	24.2909 × 23.5061 × 13.6312
Radiation	MoKα (λ = 0.71073)
2Θ range for data collection/°	5.674 to 57.832
Index ranges	$-17 \leq h \leq 18$, $-28 \leq k \leq 31$, $-32 \leq l \leq 33$
Reflections collected	77836
Independent reflections	9735 [R_{int} = 0.0357, R_{sigma} = 0.0236]
Data/restraints/parameters	9735/0/431
Goodness-of-fit on F^2	1.053
Final R indexes [I>=2σ (I)]	R_1 = 0.0359, wR_2 = 0.0856
Final R indexes [all data]	R_1 = 0.0537, wR_2 = 0.0978
Largest diff. peak/hole / e Å^{-3}	1.05/-1.01

7.11 Computational details

7.11.1 Computational details of Chapter 5

*7.11.1.1 Computational details of the neutral and oxidized form of cavitand **15***

Density functional theory (DFT) calculations were performed with the CP2K code[10] and based on the PBE exchange-correlation functional,[11] supplemented by a correction for dispersion interactions (D3).[12] The Quickstep[13] algorithm was used to solve the electronic structure problem using a double-zeta plus polarization (DZVP)[14] basis set to represent valence orbitals and plane waves for the electron density (300 Ry cutoff). Valence-core interactions were treated by means of GTH-type pseudopotentials.[15] Wave function optimization was achieved through an orbital transformation method.[16] Models were treated as isolated in a cubic box of 34 Å edge and optimized until gradients were $< 5 \cdot 10^{-4}$ a.u. Restricted calculations were performed for the Fe(II) cavitand (corresponding the the siglet state of the ferrocene moiety), whereas an unrestricted formalism was used for the Fe(III) cavitand (quintet state, assuming a doublet state for each ferrocenium moiety). Spin distribution in the Fe(III) cavitand (optimized open conformation) were consistent with a doublet state for each ferrocenium moiety, with small delocalizations on the aromatic rings. Atomic Mulliken spin moments, summed on a per-residue basis, turned to be the followings: resorcinarene +0.02; linkers 0.23 (each); chlorides (0.11 each); ferrocenium 0.63 each (Fe 0.76 each). Solvent effects (toluene) were included by means of single point calculation with the SMD method[17] as implemented in Gaussian09,[18] calculations were performed at M06 level with 6-31g (d,p) basis set for N, C, O and H,[19] along with the SDD[20] pseudopotential and its associated basis set for Fe, including an f orbital (exp. 2.462).[21]

Both open and closed conformations were considered. Concerning the Fe(II) cavitand, the closed conformation results the most stable in gas phase by 42.1 kcal mol^{-1}. On the contrary, for the Fe(III) cavitand the open conformation is favored by 34.7 kcal mol. Thus, oxidation of the iron center results in a marked change of the equilibrium between open and closed conformations. Optimized geometries are shown in Figure 7.115a,b,c. It may be appreciated that in the closed conformation the ferrocene moieties closely pack, actually closing the cavity. In the oxidized state ferrocenes are oriented outwards and the cavitand walls also open up, resulting in an easily accessible cavity. We rationalize the reversed stability of the two conformers upon oxidation as due to the

increased electrostatic repulsion between ferrocene moieties upon oxidation (Mulliken charges on each ferrocene changes from 0.05e (closed)/0.06e (open) in the Fe(II) cavitand to 0.60e (closed)/0.72e (open) in the Fe(III) cavitand). This behaviour may be exacerbated by the lack of solvent and counterions in the models considered.

Implicit solvent single point calculations were performed in order to account for solvent effects on the energetic difference between open and closed conformations. The magnitude of the energy difference between the two conformers is reduced, however the trend in maintained: the closed state is favored for the Fe(II) cavitand by 25.5 kcal mol^{-1}, whereas the open conformer is the most stable for the oxidized Fe(III) cavitand by 25.7 kcal mol^{-1}.

A model of the Fe(III) cavitand, in which four Cl^- counterions were placed between the ferrocene moieties, was further considered. This arrangement is expected to be the most effective in reducing the electrostatic repulsion between oxidized ferrocenes. In the resulting optimized structure (Figure 7.115d), the Cl^- ions interact with ferrocenes and H-bond to the benzimidazole NH groups. The opening of the rim is reduced compared to structure optimized in the absence of counterions, yet remains open compared to the favored reduced state conformation.

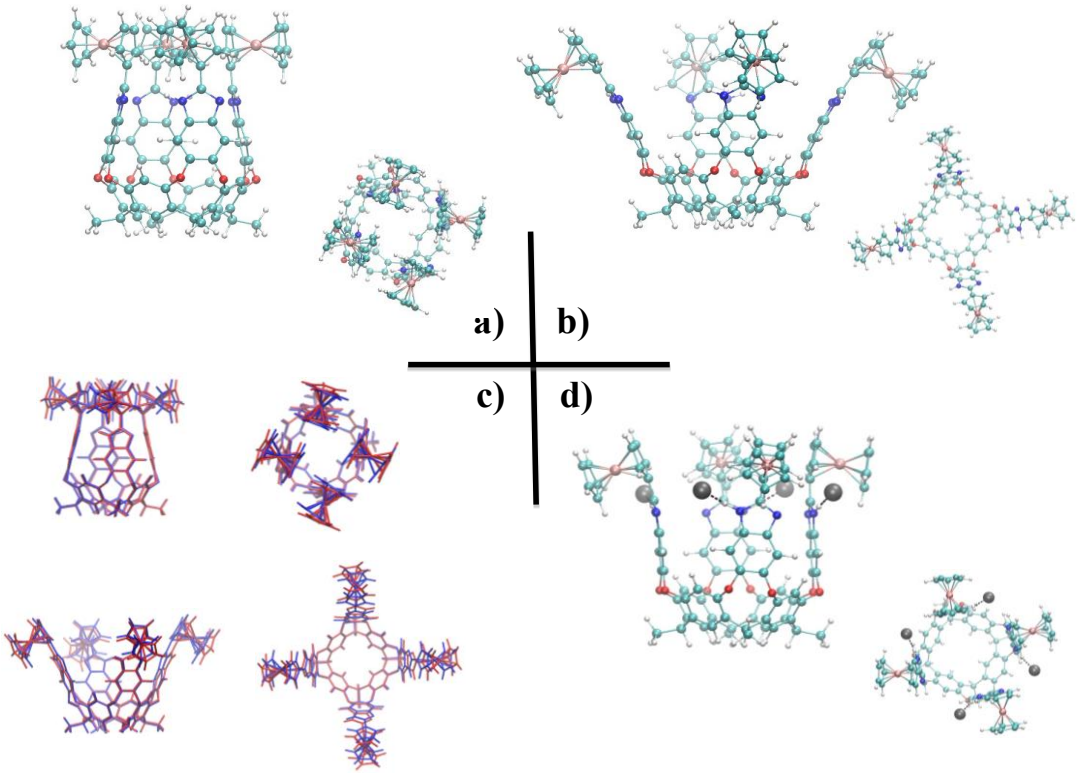

Figure 7.115. DFT(PBE-D3) optimized geometries of the Fe(II) and Fe(III) cavitands. **a)** two views of the favored (closed) conformation of the reduced Fe(II) state; **b)** two views of the favored (open) conformation of the oxidized Fe(III) state; **c)** open and closed conformations of reduced (blue) and oxidized (red) states are shown superimposed; **d)** two views of the Fe(III) cavitand including 4 chloride counterions (shown as grey balls)

*7.11.1.2 Computational details of cavitand **16**$^{4+}$ and **17**$^{4+}$*

Classical MD Simulation. Model System and force field parameters

A simplified model of the cavitand was considered, in which methyl groups were used instead of the full $C_{11}H_{23}$ chains. The cavitand was considered as build from 8 residues, 4 for the scaffold and one for each arm. Atomic point charges were computed for each fragment independently according to the RESP methodology.[22] Amber GAFF parameters were used for bonding and Van der Waals interactions.[23] A model for the solvated cavitand was built with the xleap program from the Amber distribution (www.ambermd.org), including 4 counterions (either Cl^-, I^-, benzenesulfonate) to neutralize the simulation cell and ~1000 DMSO molecules in a cubic cell of ~47 Å edge. Counterions were placed the most favourable interacting sites of the cavitand's electrostatic potential. Force field parameters for DMSO were available from the Amber parameters database (www.ambermd.org).

Molecular dynamics simulations

Classical MD simulations were performed with the NAMD code (http://www.ks.uiuc.edu/Research/namd)[24] at constant temperature (300 K) and pressure (1 atm) under periodic boundary conditions. A 1 fs time step was used to integrate the equations of motion. Short-range non-bonded interactions were computed every 2 MD step, and a full electrostatic evaluation was performed every 4 MD steps using the particle mesh Ewald method[25] on a 64 x 64 x 64 grid. All bonds involving hydrogen atoms were constrained.[26] A cutoff distance of 12 Å was used for non-bonded interactions.

Electrostatic potential maps

The molecular electrostatic potential was computed for the cavitand within a continuum solvent representation using the APBS software (www.poissonboltzmann.org). The same point charges as used in the MD simulations were used. A 97 x 97 x 97 grid with spacing 0.25 Å was used to solve the linearized Poisson equation. The dielectric constant for the cavitand was set to 2, for the solvent to 46.68 (DMSO). The molecular surface was computed using a spheric probe of 1.4 Å radius. Atomic radii were as follows: C 1.70, N 1.55, O 1.50, H 1.30 Å.

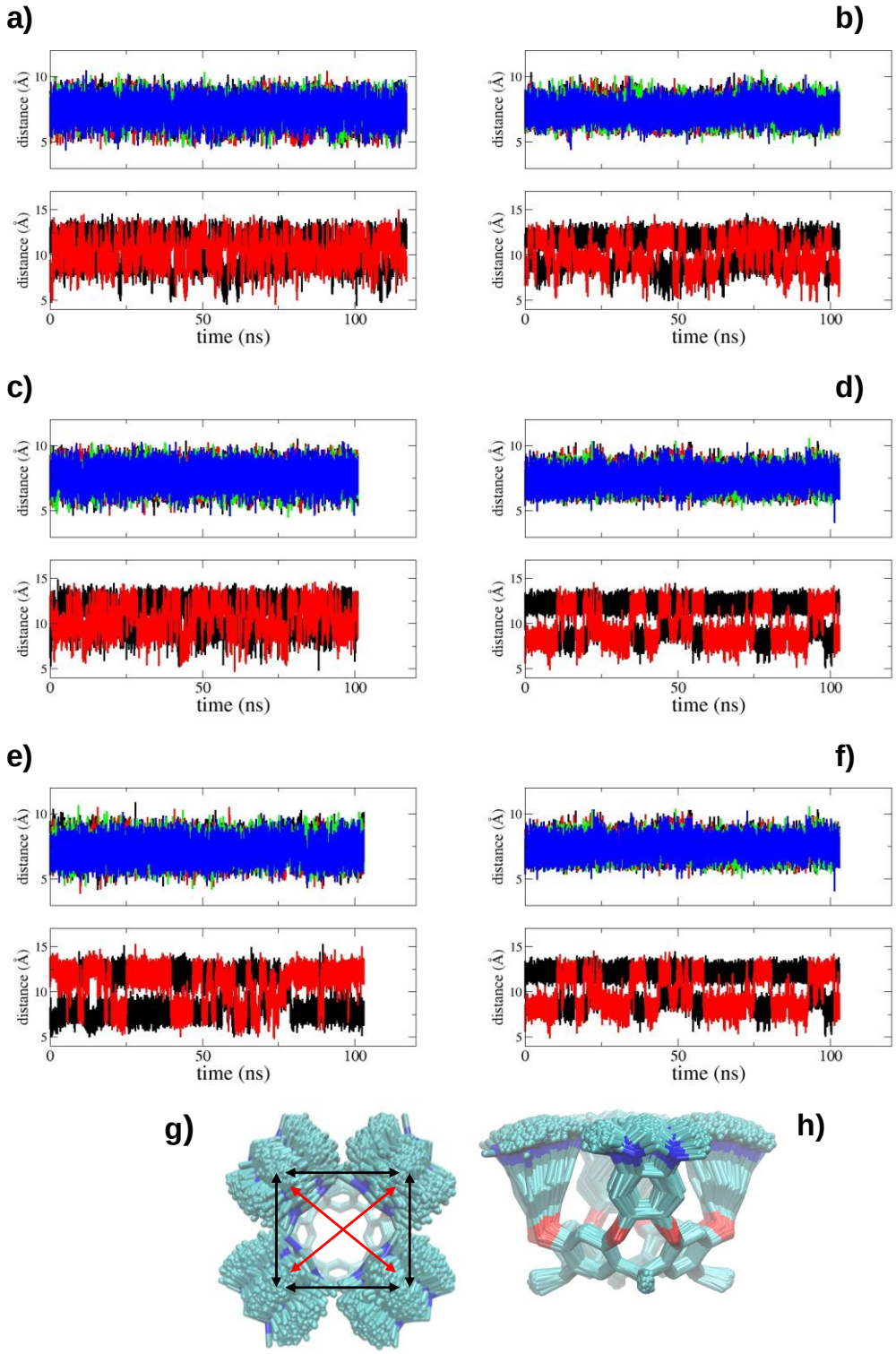

Figure 7.116. MD simulations of **16Cl$_4$(a)** and **17Cl$_4$(b)**, **16I$_4$(c)** and **17I$_4$**(d), **16(BNZ-SO$_3$)$_4$(e)** and **17(BNZ-SO$_3$)$_4$(f)**. The panels show the variation with time of selected distances. In each panel, the top graph shows the distances between adjacent arms (the tip of the arm i.e. the sp^2 C, was used to measure distances, black arrows in panel **g**). The bottom graph shows the distances between opposite arms (red arrows in panel **g**). In **g)** and **h)** a set of 500 equally spaced conformations along the **16I$_4$** simulation were overlapped to show the movements of the arms (**g**, top view; **h**, side view)

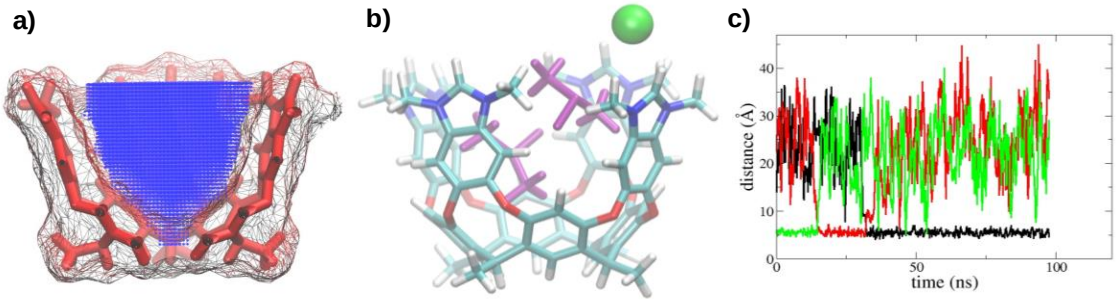

Figure 7.117. a) The cavity of cavitand **16**. A cut close to the axis of the cavitand is shown. The cavitand is shown in red sticks together with its molecular surface, the cavity is shown as blue dots. The cavity was computed with the program epock.[27] **b)** Representative snapshot from the simulation of **16I$_4$**. Two solvent molecules (shown in purple) are located inside the cavitand (one on the bottom and one at the rim) and an iodide (green sphere) is interacting with one arm's tip. **c)** Three DMSO molecules were observed to occupy the bottom of the cavity during the simulation. Reported are the distances between the bottom of the cavity and sulfur atoms of each solvent molecule. Solvent molecules at the cavitand's rim exchange on a faster time scale

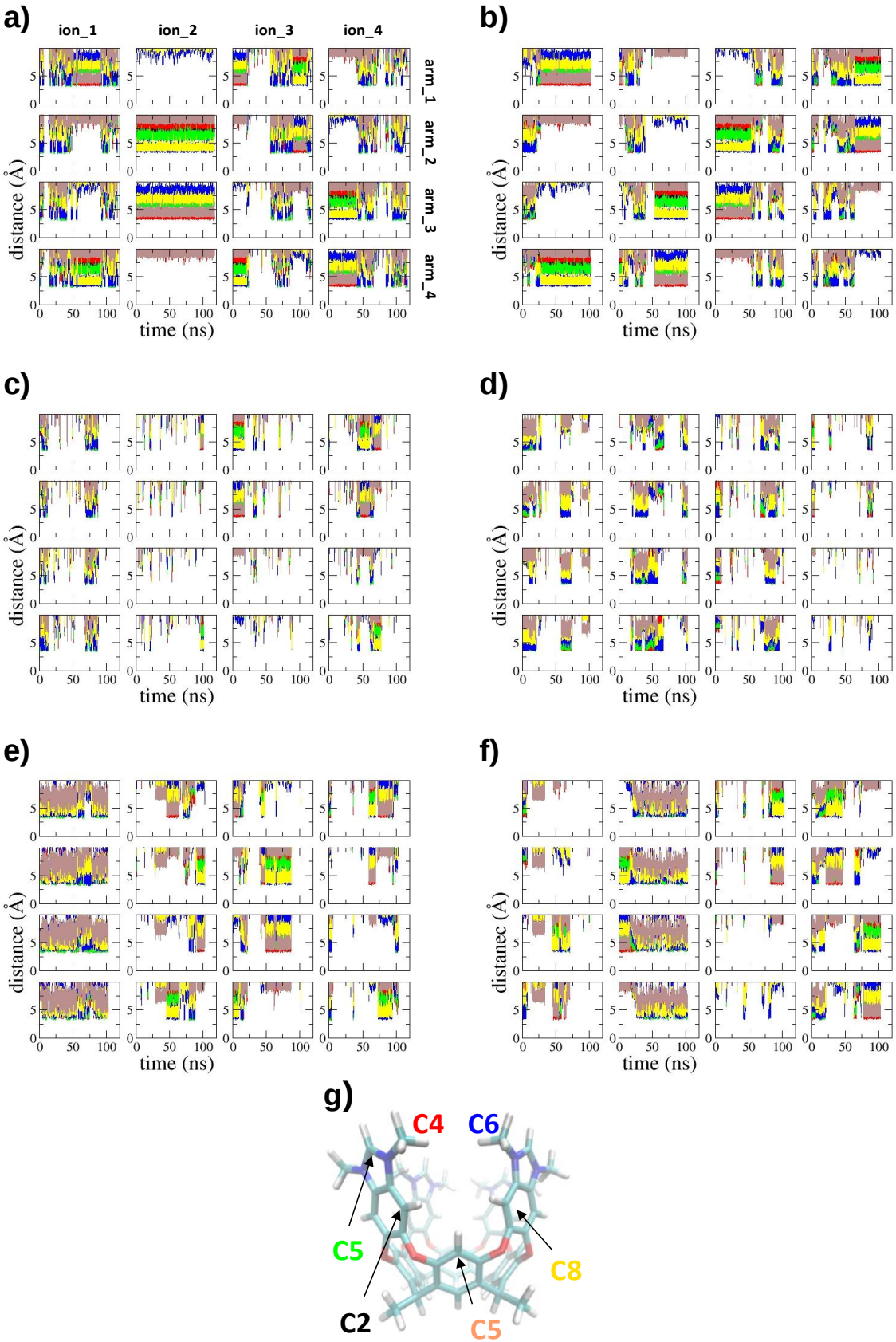

Figure 7.118. MD simulations of **16Cl$_4$(a)** and **17Cl$_4$(b)**, **16I$_4$** (**c**) and **17I$_4$(d)**, **16(BNZ-SO$_3$)$_4$(e)** and **17(BNZ-SO$_3$)$_4$(f)** The panels show the variation with time of distances between the anions and selected

atoms of the cavitand (shown in **g**). In each panel, graphs are organized with anions in columns and arms in rows, as in **a**

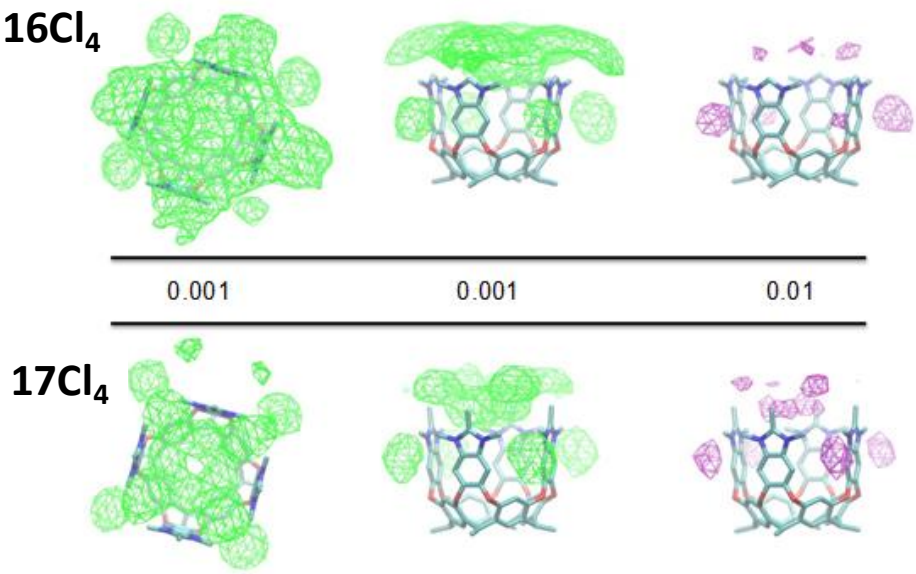

Figure 7.119. MD simulations of **16Cl₄** and **17Cl₄**. The occupancy of anions around the cavitands was computed on a grid over the last 80 ns of each simulation. Isosurfaces at 1‰ and 1% occupancies are shown in green (top and side views) and purple (side view), respectively. The average structure of the cavitand is shown in stick representation

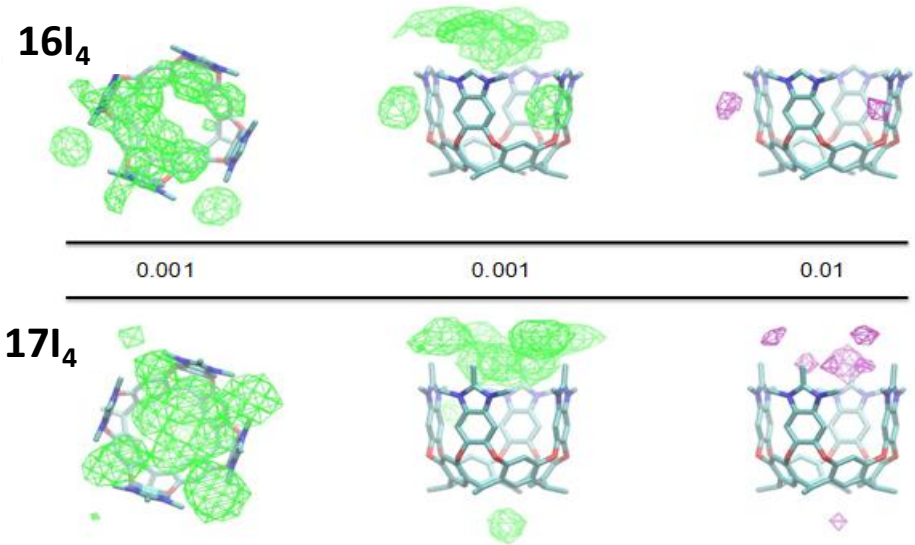

Figure 7.120. MD simulations of **16I₄** and **17I₄**. The occupancy of anions around the cavitands was computed on a grid over the last 80 ns of each simulation. Isosurfaces at 1‰ and 1% occupancies are shown in green (top and side views) and purple (side view), respectively. The average structure of the cavitand is shown in stick representation

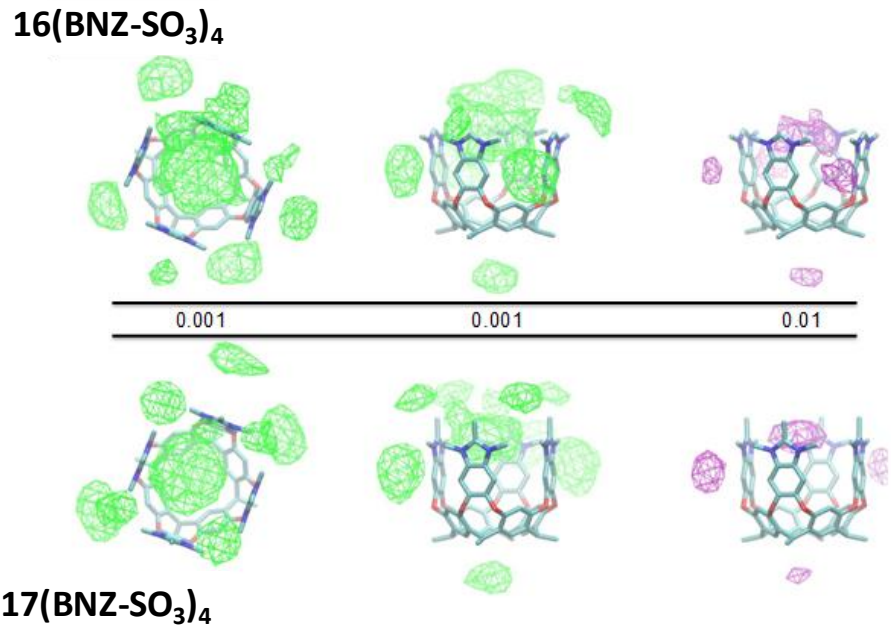

Figure 7.121. MD simulations of **16(BNZ-SO_3)$_4$** and **17(BNZ-SO_3)$_4$**. The occupancy of anions around the cavitands was computed on a grid over the last 80 ns of each simulation. Isosurfaces at 1‰ and 1% occupancies are shown in green (top and side views) and purple (side view), respectively. The average structure of the cavitand is shown in stick representation. The positions of the BNZ-SO_3^- anions were computed using the coordinates of the S atoms

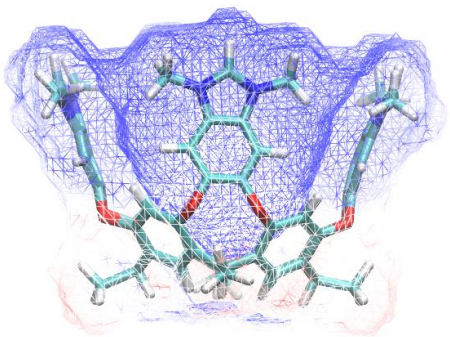

Figure 7.122. Electrostatic potential computed at the Van der Waals surface of the cavitand **16^{4+}**. Blue areas denote regions of positive electrostatic potential (> 10 kT/e)

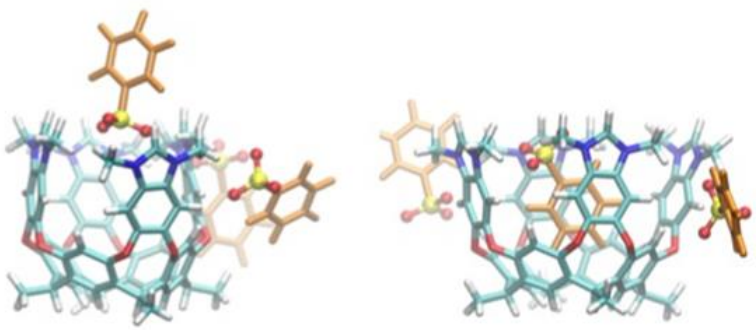

Figure 7.123. Two snapshots from the simulation of **16(BNZ-SO_3)$_4$**. Phenylsulfonate molecules are shown in orange sticks, with oxygen atoms as red balls

Packing coefficient

We addressed the packing of guest molecules in the cavities of cavitands **16^{4+}** and **17^{4+}**.[28] For each cavitand, the cavity was computed with the program epock[27] for 500 snapshots along the MD simulations of **$16I_4$**, **$17I_4$**, **$16(BNZ\text{-}SO_3)_4$** and **$17(BNZ\text{-}SO_3)_4$** and the average estimates were used to compute the packing coefficient. In simulations of **$16I_4$** and **$17I_4$** the cavitands' cavities are occupied on average 2.2 (±0.6) and 2.0 (±0.6) by DMSO molecules (based on the position of the S atom). In simulations **$16(BNZ\text{-}SO_3)_4$** and **$17(BNZ\text{-}SO_3)_4$** the cavitands' cavities are occupied by a benzenesulfonate molecule.

Table 7.25: Packing coefficient.*estimated based on an occupancy of **16^{4+}** DMSO molecules

System	Cavity volume (Å^3)(st. dev.)	Packing coefficient
$16I_4$	294.4 (±24.1)	49%*
$17I_4$	311.3 (±23.7)	46%*
$16(BNZ\text{-}SO_3)_4$	245.1 (±19.0)	49%
$17(BNZ\text{-}SO_3)_4$	291.7 (±20.8)	41%

Table 7.26: Molecular volume (Å^3) occupied by BNZ-SO_3^- and DMSO

Guest molecule	Molecular volume (Å^3)
Benzenesulfonate (BNZ-SO_3)	72.2
Dimethyl sulfoxide (DMSO)	120.5

The epock calculation was based on Bondi Van der Waals radii and a grid spacing of 0.2 Å. The search region was defined as a cylinder aligned to the cavitand's axis and a radius 6 Å. The cavity was capped on the open side based on the position of the outermost H atoms.

7.11.1.3 *Computational details of cavitand* ***17^{4+}***

Quantum Chemical Calculations - Computational Details

Ad initio molecular dynamics (AIMD, see e.gD.Marx and J.Hutter, "Ab initio Molecular Dynamics", Cambridge University Press, 2009) simulations were used to perform a conformational analysis of the cavitand-Rh system. The following procedure was used: initially, 6 ps of gas-phase AIMD at high temperature (800 K) were performed; then, geometries taken every 500 MD steps underwent simulated annealing

until the temperature descended to around 100 K; finally, the resulting geometries were fully optimized.

Calculations were performed with the CP2K code[10] and based on Density Functional Theory.[29] The PBE exchange-correlation functional was used,[11] including a correction for dispersion interactions.[12] The Quickstep algorithm[13] was used to solve the electronic-structure problem, employing a double-zeta plus polarization (DZVP) basis set to represent the valence orbitals and plane waves for the electron density (280 Ry cutoff). Goedecker-Teter-Hutter (GTH)-type pseudopotentials[15a,15c] were used for valence-core interactions. Models were treated as isolated in a cubic box with an edge of 36 Å. A 0.5 fs time step was used to propagate the equations of motion in AIMD simulations. Geometry optimizations were performed until nuclear gradients were smaller than $5x10^{-4}$ a.u.

7.11.2 Computational details of chapter 6

*7.11.2.1 Computational studies of **21**$^{3+}$ and **22**$^{3+}$*

Classical molecular dynamics (MD) simulations.

Explicit solvent classical molecular dynamics (MD) simulations were performed at constant temperature (300 K) and pressure (1 atm) using the NAMD code. Electroneutral models were build including the receptor and three counterions (either Cl^- or PF_6^-). Cubic simulation cells of 47 – 49 Å side including about 900 DMSO molecules were used. A cutoff of 12 Å was used for Van der Waals interactions and the real part of electrostatic interactions. The particle mesh Ewald method was used to treat long range electrostatics on a cubic grid of 64^3 points.[30] All bonds involving H were constraint.[31]

Force field parameters for the DMSO solvent and chloride anions were available from the AMBER distribution[32] Atomic charges for PF_6^- and the receptors were determined according the RESP procedure.[33] For the receptors, an open conformation was used for charge fitting and equivalence of the receptor's arms was imposed. Bonding parameters were available through the GAFF force field.[34] In the case of the iodo-imidazolium based receptor, a parametrization to reproduce halogen bonding at iodine was adapted from Jorgensen and Schyman article.[35] Accordingly, a pseudo-atom (X) of +0.2e charge was placed along the C – I axis at a distance of 1.8 Å from I and harmonic potentials were used to restraint the I – X distance (1.8 Å, force constant 600 kcal $mol^{-1}Å^{-2}$) and C

– I – X angle (linear, force constant 200 kcal $mol^{-1}deg^{-2}$). These sets of parameters reproduce structural features of a reduced model system, slightly overestimating the I – Cl distance.

Quantum chemical calculations.

Quantum chemical calculations were performed using the ORCA software and based on Density Functional Theory (DFT). The B3LYP functional was used to describe electron exchange and correlation.[36] A SVP basis set was used for geometry optimization and TZVP for single point energy evaluation.[37] Relativistic effects were accounted for using the ZORA approximation. Solvent effects were accounted using the COSMO implicit solvent model.[38] The counterpoise correction was used to correct binding energies for the basis set superposition error.[39]

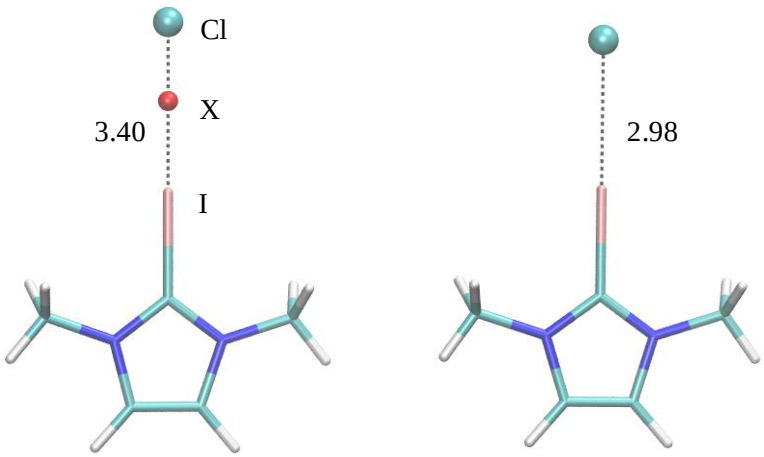

Figure 7.124. Molecular mechanics (left panel) and DFT (right panel) optimized structures of model iodo-imidazolium / chloride complex. The I – Cl distance is shown in Å

Molecular modeling of the 21^{3+} / anion system

Molecular dynamics simulations of the **21^{3+}** receptor were performed in explicit DMSO solvent to characterize the conformational dynamics of the receptor and its interactions with counterions. Independent simulations for PF_6^- and Cl^- counterions were performed. About 100 ns simulations were collected for each system.

a) Conformational analysis.

Each arm of the imidazolium receptor has two routable bonds, potentially giving rise to a high number of conformers. In the present context, the relative distance and orientation of the arms may be used to characterize the receptor conformation. It may be

appreciated from Figure 7.125 that the distribution of distances between the arms of the receptor is markedly dependent on the nature of the counterion (X). For both anions, inter-arm distances display similar distributions, supporting convergence of the simulations and showing that the length of the simulation is appropriate for the present purposes. For X=PF_6^-, broad distributions are observed, whereas for X=Cl^- sharper peaks are displayed at shorter distance (about 7Å). Furthermore, variation of the inter-arm distances appear correlated for X=Cl^-. These data are suggestive of a structuring of the receptor induced by Cl^-, but not by PF_6^-.

b) Binding analysis

The interactions of Cl^- and PF_6^- anions with the receptor are markedly different. In the case of Cl^-, interactions with the N*C*N carbon and the methyl carbon are favored compared to other carbon atoms of the imidazolium rings or of the benzene scaffold. On the contrary, PF_6^- does not display to favor specific interactions with any of the carbon atoms of the receptor. Figure 7.127 shows the distances between the chloride anions and the N*C*N carbon atoms of the imidazolium rings. It may be appreciated that one of the chloride anions (Cl_2) interacts simultaneously with the three arms of the receptor for about 50 ns in the central part of the simulation. Only occasionally one of the interactions is broken. Similarly, Cl_3 interacts with two or three receptor's arms in the initial 30 ns of the simulation. Worth noting that along the simulation two chloride anions may be found close to the receptor at the same time. However, it appears that one is bound more strongly than the other, which displays short lived interactions. Figure 7.126 shows a representative snapshot from the simulation of a tri-coordinated chloride anion, which interacts with the N*C*N carbon and the methyl groups of the three receptor's arms simultaneously. In the case of PF_6^- no such long lasting interactions were observed (Figure 7.128).

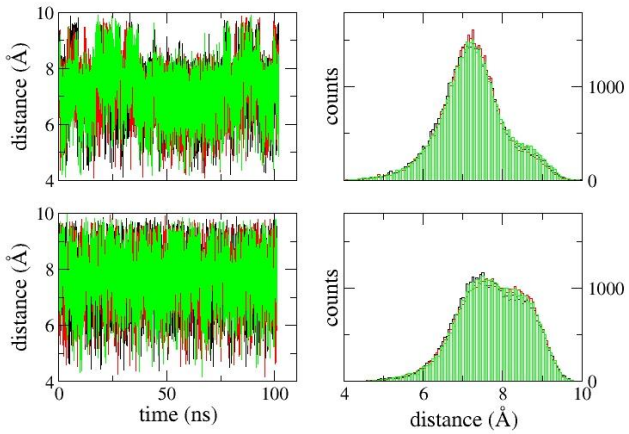

Figure 7.125. MD simulation of **21**$(X)_3$. Distances between the centers of the imidazolium rings of the receptor's arms. Top graphs for **21**$(Cl)_3$, bottom ones for **21**$(PF_6)_3$. Left graphs are the time, right ones the corresponding histograms

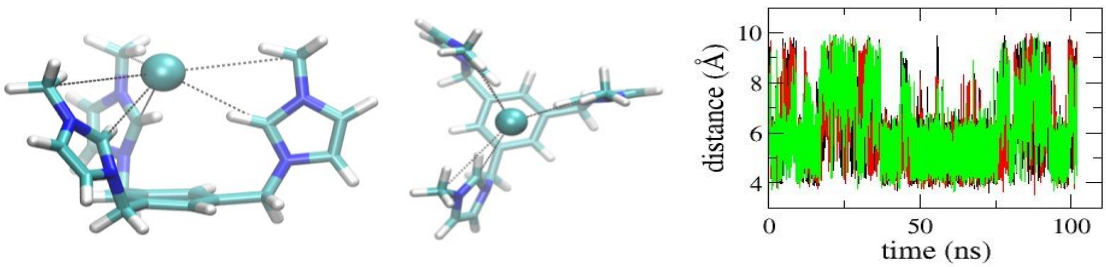

Figure7.126. Side and top views of the receptor – chloride complex at about 50 ns MD simulation of **21**$(Cl)_3$. On the right, the time series of the distances between the N*C*N carbons of the imidazolium rings of the receptors arms are shown

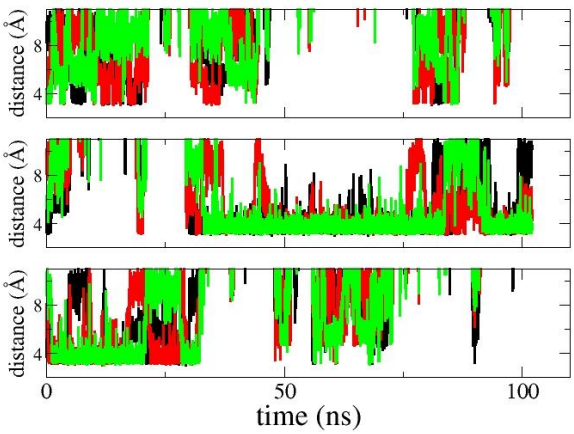

Figure 7.127. MD simulation of **21**$(Cl)_3$. Distances between the chloride anions (one graph per anion) and the N*C*N carbon of the imidazolium rings of the receptor's arms (one curve per arm in each graph)

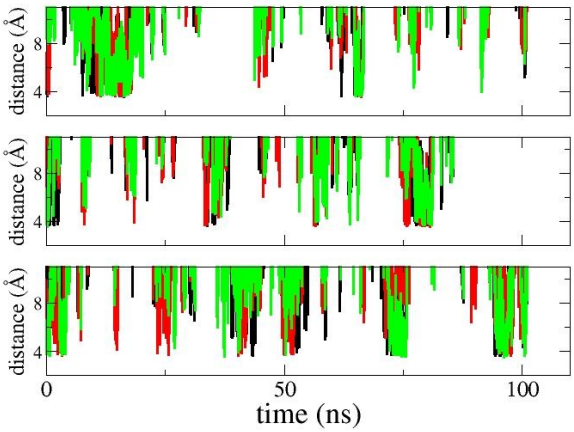

Figure 7.128. MD simulation of **21(PF$_6$)$_3$**. Distances between the phosphorous atom of the hexafluorophosphate anions (one graph per anion) and the NCN carbon of the imidazolium rings of the receptor's arms (one curve per arm in each graph)

Molecular modeling of the **22^{3+}** */ anion system*

Molecular dynamics simulations were performed to for receptor **22^{3+}** in explicit DMSO solvent to characterize the conformational dynamics of the receptor and its interactions with counterions. Simulations were performed starting from different conformations of the receptor and combinations of counterions. About 100 ns simulations were collected for each system.

a) Conformational analysis.

As for the **21^{3+}** receptor, the nature of the counterion has a considerable impact on the conformational properties of the **22^{3+}** receptor. When PF_6^- is the counterion, similar distributions are observed for the inter-arm distances (Figure 7.129). On the contrary, when (at least one) Cl^- is present a marked correlation is observed for the motion of two receptor's arms due to the stable interactions formed between chloride and two C – I moieties. A cluster analysis revealed three populated conformational states (Figure 7.131). The conformation labeled as **c** in Figure 7.130 is responsible for the shoulders in the distributions of inter-arm distances reported in Figure 7.129.

b) Binding analysis.

In the simulation of **22(PF$_6$)$_3$**, PF_6^- displayed unspecific and short lived interactions with the receptor (Figure 7.135), as observed for the **21^{3+}** receptor. On the contrary, highly stable interactions formed between the receptor's arms and Cl anions. Simulations **22(Cl)$_3$_i** (Figure 7.131) and **22(Cl)$_3$_ii** (Figure 7.133) showed two

preferred binding modes of Cl anions, one involving two receptor's arms and another in which only one receptor arm binds Cl. These interactions are maintained throughout the simulations. Simulation **22(Cl)$_3$_ii** was started from a tri-coordinated Cl, but this interaction mode was maintained only for the first 7 ns (Figure 7.133), then one of the arms detached from Cl and bound a second Cl anion (this result is in line with the outcome of quantum chemical calculations, see below). Model **22(Cl)(PF$_6$)$_2$**, was used to investigate the effect of anion composition on the receptor's properties. The simulation was started from a tri-coordinated Cl binding, which however was maintained only during the first few ns, then reverting to a two-coordinated conformation (Figure 7.134). Worth noting in Figures 7.131, 7.133 and 7.134 is the occurrence of short lived interactions with a third receptor's arm. However, these do not involve the C – I unit (see Figure 7.132).

Quantum chemical calculations were performed to compare the energetics of the different binding modes of chloride anions to the **22**$^{3+}$ receptor. Representative structures from the MD simulations were optimized and used to compare the energetics of Cl binding to one, two and three arms of the receptor. Successive binding of the arm's receptor is favourable (Table 7.27). However, passing from two to three arm's coordination the gain in stability is small, due to the cost of bringing together the positively charged arms. Indeed, the energy difference between the open and closed conformations is 9.9 kcal mol^{-1} in favour of the open structure (Figure 7.138, which is about the binding energy of Cl$^-$ to iodo-imidazolium (-10.6 kcal mol^{-1}, Figure 7.139).

We have further compared the energies of the receptor interacting with two Cl$^-$ in different conformations (Figure 7.136). In line with the above results and those from the MD study, binding of one Cl to two arms and one to one arm (Figure 7.136.b,c) is favoured compared to binding of one Cl to three arms and one Cl interacting unspecifically with the receptor (Figure 7.136a).

Quantum chemical calculations were used to compare the strength of anion···HC and anion···IC interactions. The optimized geometries of the model compounds are shown in Figure 7.138 together with the estimated binding energy. Binding based on halogen bonding is favoured by 3.2 kcal mol^{-1}.

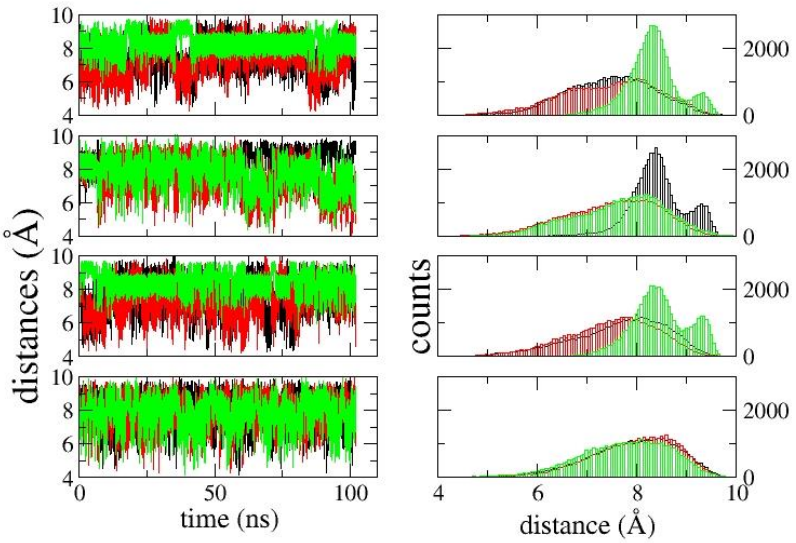

Figure 7.129. MD simulation of **22**$(X)_3$. Distances between the centers of the iodo-imidazolium rings of the receptor's arms. From top to bottom: **22(Cl)$_3$_i**, **22(Cl)$_3$_ii**, **22(Cl)(PF$_6$)$_3$**, **22(PF$_6$)$_3$**. Left graphs are the time series, right ones the corresponding histograms

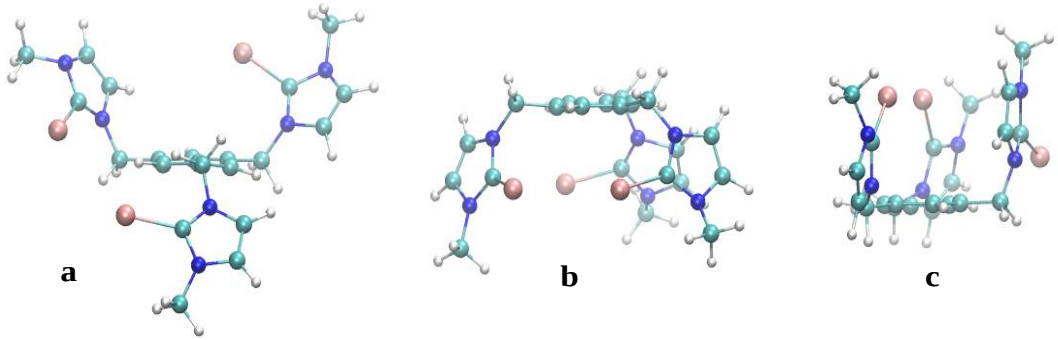

Figure 7.130. Representative snapshots of **22**$^{3+}$ from the MD simulation of model **22(Cl)$_3$**

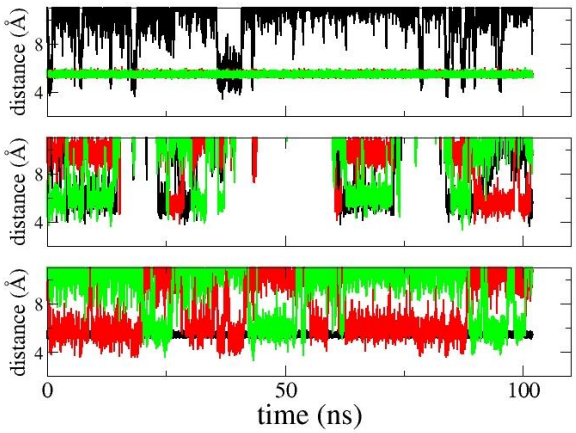

Figure 7.131. MD simulation of **22(Cl)$_3$_i**. Distances between the chloride anions (one graph per anion) and the N*C*N carbon of the iodo-imidazolium rings of the receptor's arms (one curve per arm in each graph)

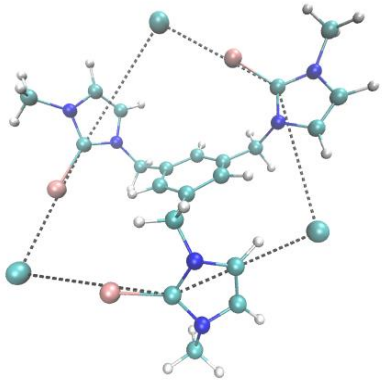

Figure 7.132. Snapshot at 66 ns simulation of the **22(Cl)$_3$** model. Dotted lines highlight selected distance, all of them of similar length (about 5.5 Å)

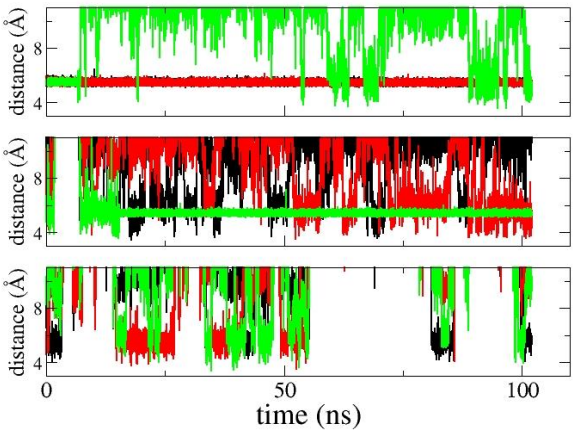

Figure 7.133. MD simulation of **22(Cl)$_3$_ii.** Distances between the chloride anions (one graph per anion) and the N*C*N carbon of the iodo-imidazolium rings of the receptor's arms (one curve per arm in each graph)

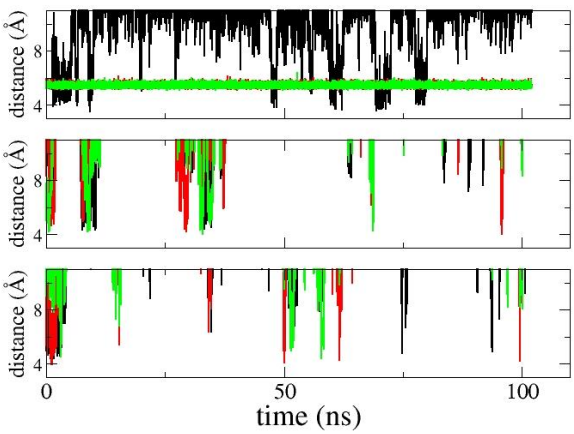

Figure 7.134. MD simulation of **22(Cl)(PF$_6$)$_2$** Distances between the anions (one graph per anion; top: Cl^-, middle and bottom: PF_6^-) and the N*C*N carbon of the iodo-imidazolium rings of the receptor's arms (one curve per arm in each graph)

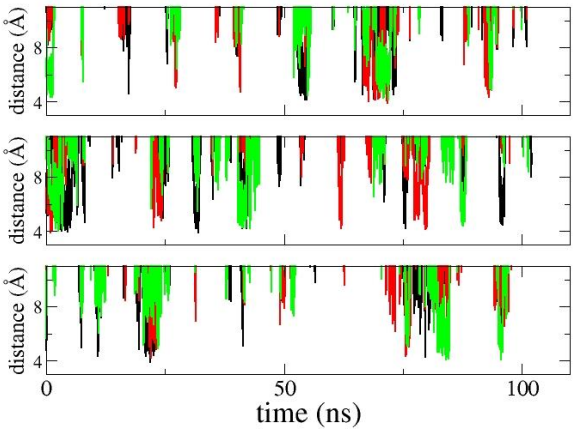

Figure 7.135. MD simulation of **22(PF$_6$)$_3$**. Distances between the phosphorous atom of the hexafluorophosphate anions (one graph per anion) and the NCN carbon of the iodo-imidazolium rings of the receptor's arms (one curve per arm in each graph)

Table 7.27. Conformational energies of the **22^{3+}** receptor interacting with one chloride anion. Energies were estimating based on the conformations shown in Figure 7.136 removing one of the Cl^- anions

number of arms interacting with Cl^-	**Energy (kcal mol^{-1})**
1	6.4
2	1.7
3	0.0

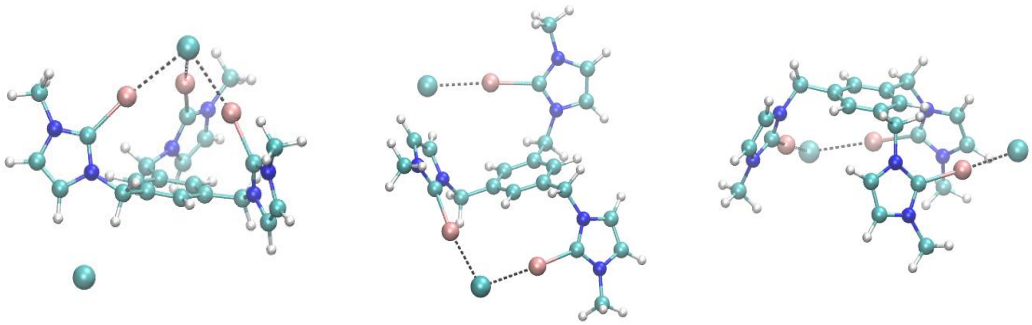

a **b** **c**
0.0 **-5.9** **-5.5**

Figure 7.136. Different binding modes of two Cl anions to the **22^{3+}** receptor. The binding shown in **b** and **c** differ for the orientation of the arms, in **c** being all three on the same side of the benzene plane. Energies are reported in kcal mol^{-1}

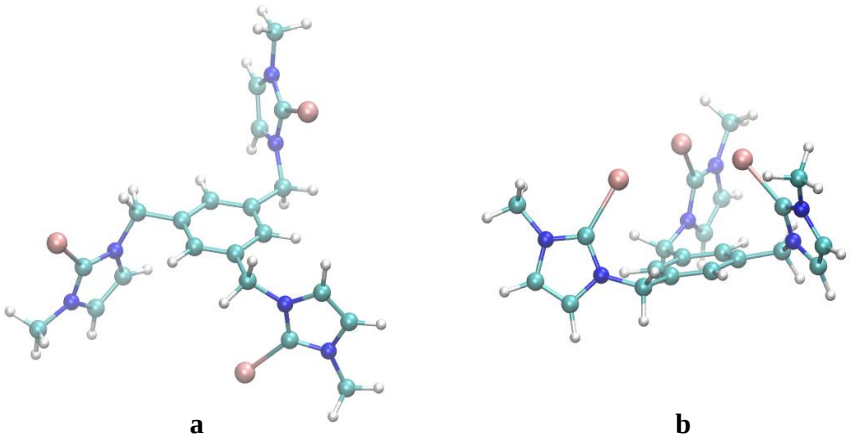

Figure 7.137. Different conformations of receptor $\mathbf{22}^{3+}$. The conformation in **a** is fully optimized without the presence of any counterions. The conformation shown in **b** does not correspond to a stable minimum. Energies are reported in kcal mol^{-1}

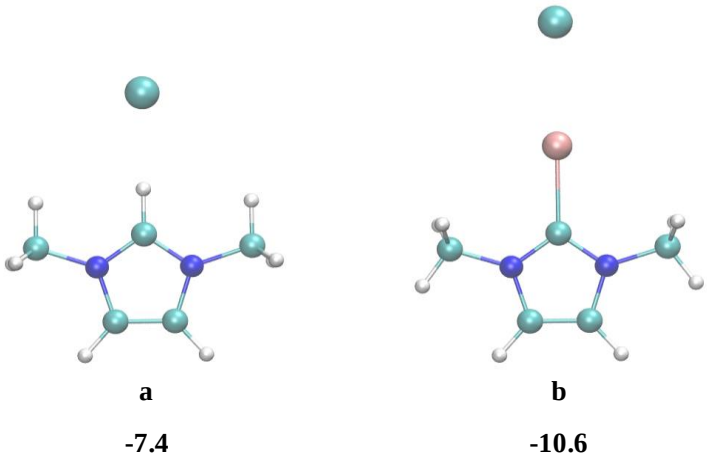

Figure 7.138. Model compounds used to estimate the binding energy of Cl^- to imidazolium (a) and iodo-imidazolium (b). Energies (corrected for the basis set superpositon error) are reported in kcal mol^{-1}

7.12 References

(1) Cabildo, P., Sanz, D., Claramunt, R. M., Bourne, S. A., Alkorta, I., Elguero, J. *Tetrahedron* **1999**, *55*, 2327-2340.

(2) Vlahakis, J. Z., Mitu, S., Roman, G., Rodriguez, E. P., Crandall, I. E., Szarek, W. A. *Bioorg. Med. Chem.* **2011**, *19*, 6525-6542.

(3) a) Zhang, K.-D., Ajami, D., Rebek, J. *J. Am. Chem. Soc.* **2013**, *135*, 18064-18066; b) Hof, F., Trembleau, L., Ullrich, E. C., Rebek, J. *Angew. Chem. Int. Ed.* **2003**, *42*, 3150-3153; c) Purse, B. W., Gissot, A., Rebek, J. *J. Am. Chem. Soc.* **2005**, *127*, 11222-11223.

(4) Far, A. R., Shivanyuk, A., Rebek, J. *J. Am. Chem. Soc.* **2002**, *124*, 2854-2855.

(5) Sander, F., Fluch, U., Hermes, J. P., Mayor, M. *Small* **2014**, *10*, 349-359.

(6) Kilah, N. L., Wise, M. D., Serpell, C. J., Thompson, A. L., White, N. G., Christensen, K. E., Beer, P. D. *J. Am. Chem. Soc.* **2010**, *132*, 11893-11895.

(7) D'Anna, F., Gunaratne, H. Q. N., Lazzara, G., Noto, R., Rizzo, C., Seddon, K. R. *Org. Biomol. Chem.* **2013**, *11*, 5836-5846.

(8) Dolomanov, O. V., Bourhis, L. J., Gildea, R. J., Howard, J. A. K., Puschmann, H. *J. Appl. Crystallogr.* **2009**, *42*, 339-341.

(9) Sheldrick, G. M. *Acta Crystallographica Section A* **2008**, *64*, 112-122.

(10) VandeVondele, J., Krack, M., Mohamed, F., Parrinello, M., Chassaing, T., Hutter, J. *Comput. Phys. Commun.* **2005**, *167*, 103-128.

(11) Perdew, J. P., Burke, K., Ernzerhof, M. *Phys. Rev. Lett.* **1996**, *77*, 3865-3868.

(12) Grimme, S., Antony, J., Ehrlich, S., Krieg, H. *J. Chem. Phys.* **2010**, *132*.

(13) Lippert, G., Hutter, J., Parrinello, M. *Mol. Phys.* **1997**, *92*, 477-487.

(14) VandeVondele, J., Hutter, J. *J. Chem. Phys.* **2007**, *127*.

(15) a) Goedecker, S., Teter, M., Hutter, J. *Phys. Rev. B* **1996**, *54*, 1703-1710; b) Hartwigsen, C., Goedecker, S., Hutter, J. *Phys. Rev. B* **1998**, *58*, 3641-3662; c) Krack, M. *Theor. Chem. Acc.* **2005**, *114*, 145-152.

(16) VandeVondele, J., Hutter, J. *J. Chem. Phys.* **2003**, *118*, 4365-4369.

(17) Marenich, A. V., Cramer, C. J., Truhlar, D. G. *J. Phys. Chem. B* **2009**, *113*, 6378-6396.

(18) Frisch, M. J., Trucks, G. W., Schlegel, H. B., Scuseria, G. E., Robb, M. A., Cheeseman, J. R., Scalmani, G., Barone, V., Mennucci, B., Petersson, G. A., Nakatsuji, H., Caricato, M., Li, X., Hratchian, H. P., Izmaylov, A. F., Bloino, J.,

Zheng, G., Sonnenberg, J. L., Hada, M., Ehara, M., Toyota, K., Fukuda, R., Hasegawa, J., Ishida, M., Nakajima, T., Honda, Y., Kitao, O., Nakai, H., Vreven, T., Montgomery Jr., J. A., Peralta, J. E., Ogliaro, F., Bearpark, M., Heyd, J. J., Brothers, E., Kudin, K. N., Staroverov, V. N., Kobayashi, R., Normand, J., Raghavachari, K., Rendell, A., Burant, J. C., Iyengar, S. S., Tomasi, J., Cossi, M., Rega, N., Millam, J. M., Klene, M., Knox, J. E., Cross, J. B., Bakken, V., Adamo, C., Jaramillo, J., Gomperts, R., Stratmann, R. E., Yazyev, O., Austin, A. J., Cammi, R., Pomelli, C., Ochterski, J. W., Martin, R. L., Morokuma, K., Zakrzewski, V. G., Voth, G. A., Salvador, P., Dannenberg, J. J., Dapprich, S., Daniels, A. D., Farkas, Ö., Foresman, J. B., Ortiz, J. V., Cioslowski, J., Fox, D. J. *Gaussian 09, Revision*; Gaussian, Inc.: Wallinford, CT, **2009**.

(19) Francl, M. M., Pietro, W. J., Hehre, W. J., Binkley, J. S., Gordon, M. S., Defrees, D. J., Pople, J. A. *J. Chem. Phys.* **1982**, *77*, 3654-3665.

(20) Andrae, D., Haussermann, U., Dolg, M., Stoll, H., Preuss, H. *Theor. Chim. Acta* **1990**, *77*, 123-141.

(21) Ehlers, A. W., Bohme, M., Dapprich, S., Gobbi, A., Hollwarth, A., Jonas, V., Kohler, K. F., Stegmann, R., Veldkamp, A., Frenking, G. *Chem. Phys. Lett.* **1993**, *208*, 111-114.

(22) Bayly, C. I., Cieplak, P., Cornell, W. D., Kollman, P. A. *J. Phys. Chem.* **1993**, *97*, 10269-10280.

(23) Wang, J. M., Wolf, R. M., Caldwell, J. W., Kollman, P. A., Case, D. A. *J. Comput. Chem.* **2004**, *25*, 1157-1174.

(24) Phillips, J. C., Braun, R., Wang, W., Gumbart, J., Tajkhorshid, E., Villa, E., Chipot, C., Skeel, R. D., Kale, L., Schulten, K. *J. Comput. Chem.* **2005**, *26*, 1781-1802.

(25) Darden, T., York, D., Pedersen, L. *J. Chem. Phys.* **1993**, *98*, 10089-10092.

(26) Ryckaert, J. P., Ciccotti, G., Berendsen, H. J. C. *J. Comput. Phys.* **1977**, *23*, 327-341.

(27) Laurent, B., Chavent, M., Cragnolini, T., Dahl, A. C. E., Pasquali, S., Derreumaux, P., Sansom, M. S. P., Baaden, M. *Bioinformatics* **2015**, *31*, 1478-1480.

(28) Mecozzi, S., Rebek, J. *Chem. Eur. J.* **1998**, *4*, 1016-1022.

(29) Hohenberg, P., Kohn, W. *Phys. Rev. B* **1964**, *136*, B864-+.

(30) Darden, T., York, D., Pedersen, L. *J. Chem. Phys.* **1993**, *98*, 10089-10092.

(31) Ryckaert, J. P., Ciccotti, G., Berendsen, H. J. C. *J. Comput. Phys.* **1977**, *23*, 327-341.

(32) Fox, T., Kollman, P. A. *J. Phys. Chem. B* **1998**, *102*, 8070-8079.

(33) Bayly, C. I., Cieplak, P., Cornell, W. D., Kollman, P. A. *J. Phys. Chem.* **1993**, *97*, 10269-10280.

(34) Wiberg, K. B., Wang, Y. G. *J. Comput. Chem.* **2004**, *25*, 1127-1132.

(35) Jorgensen, W. L., Schyman, P. *J. Chem. Theory Comput.* **2012**, *8*, 3895-3901.

(36) Becke, A. D. *J. Chem. Phys.* **1993**, *98*, 5648-5652.

(37) Pantazis, D. A., Chen, X. Y., Landis, C. R., Neese, F. *J. Chem. Theory Comput.* **2008**, *4*, 908-919.

(38) Klamt, A., Schuurmann, G. *J. Chem. Soc., Perkin Trans. 2* **1993**, 799-805.

(39) Boys, S. F., Bernardi, F. *Mol. Phys.* **1970**, *19*, 553-556.

Chapter 8.
Diseño de nuevos ligandos para el desarrollo de catalizadores supramoleculares y receptores de iones

En aplicación de la normativa de estudios de doctorado sobre la elaboración de Tesis Doctorales según el programa RD 99/2011 por el que se establece que: *la Tesis Doctoral escrita en una lengua diferente del valenciano o del castellano, en el momento de ser depositada, debe contener un apartado suficientemente amplio en una de estas dos lenguas, y debe formar parte de la encuadernación de la tesis*; el siguiente capítulo contiene un resumen en castellano del trabajo recogido en la presente tesis doctoral.

8.1 Introducción

La presente tesis doctoral está divida en dos partes claramente diferenciadas. La primera parte hace referencia a aspectos relacionados con la química orgánometálica y la catálisis supramolecular. La segunda parte de la tesis se centra en estudios de química supramolecular *host-guest*.

El término "*catálisis supramolecular*" fue introducido en 2008 por el Profesor Van Leuween. El término se refiere a la aplicación de la química supramolecular en el campo de la catálisis homogénea. Este campo está inspirado en la catálisis enzimática, porque utiliza interacciones no-covalentes para acelerar velocidades de reacción y lograr mejores selectividades.[1]

La química supramolecular *host-guest* está basada en el estudio de las interacciones entre un *host* (receptor) y un *guest* (huésped). En general, un *host* es una especie de tamaño mayor que el *guest*, y que presenta una gran cavidad. Ejemplos de *host* son los curcubiturilos, las ciclodextrinas o los calixarenos. El *guest* necesita tener una forma complementaría al *host*, lo que ayuda a mejorar las afinidades y las selectividades entre ellos. Cuando ambas especies interaccionan se genera un sistema denominado complejo *host-guest*.[2]

El diseño y estudio de la influencia de nuevos ligandos orgánicos es de vital importancia para el campo de la química organometálica, la catálisis supramolecular y la química supramolecular *host-guest*. Generalmente, tanto el ligando orgánico que forma parte de un catalizador organometálico, como aquel que es por sí mismo un sensor químico, interacciona con su entorno mediante interacciones del tipo no-covalente. Sin embargo, estas interacciones son difíciles de predecir en la mayoría de los casos, por lo que los efectos producidos entre un catalizador y un sustrato o entre un *host* y un *guest* son generalmente reconocidos "*post-factum*". Esto lleva a que en catálisis supramolecular el objetivo sea lograr determinar la naturaleza, la fortaleza y la

influencia catalítica de todas las interacciones entre el catalizador, el sustrato y el resto de participantes en la catálisis;[1a] mientras que por otro lado, en el campo de la química *host-guest*, el objetivo es estudiar la fortaleza, naturaleza y selectividad de las interacciones no-covalente entre un determinado *host* y un *guest*, para hacer el reconocimiento más efectivo y selectivo.[2-3] Además, en ocasiones también es interesante estudiar la influencia de dichas interacciones en la preparación de los propios catalizadores y/o receptores, puesto que pueden estar involucradas en la generación de determinadas conformaciones y no otras. En definitiva, el objetivo final en ambos campos es generar bien catalizadores y/o receptores mejorados, más eficientes y selectivos estudiando la influencia de las interacciones no-covalentes.

8.2 Resultados y discusión

8.2.1 Aspectos singulares de la coordinación del ligando bis(*p*-xililo) bis(benzoimidazolideno) a fragmentos de iridio y rodio

El término ciclofano históricamente se refiere a compuestos que tienen dos grupos *p*-fenileno uno frente al otro, unidos por puentes de alquilo.[4] Sin embargo, las definiciones más recientes por parte de la IUPAC definen a los ciclofanos (i) como compuestos con un sistema de anillos *mancude* (máximo número de dobles enlaces no acumulativos) o un conjunto de sistemas de anillos *mancude*, y (ii) como átomos y/o cadenas saturadas o insaturadas de componentes alternos de un anillo grande. Los compuestos del tipo ciclofano se caracterizan por su gran fluxionalidad y sus peculiares conformaciones. Atraídos por estas características y convencidos de poder explotarlas al máximo en el campo de la química organometálica, decidimos utilizar la sal de 1,1´,3,3´-bis(α,α´,-*p*-xililo)bis(benzimidazolio) dichloruro (**A**) como precursora de ligando NHC.

El esquema 6.1 muestra la síntesis de la sal 1,1´,3,3´-bis(α,α´,-*p*-xilil)bis(benzimidazolio) dicloruro (**A**), la cual fue previamente descrita por Cabildo y colaboradores.[5]

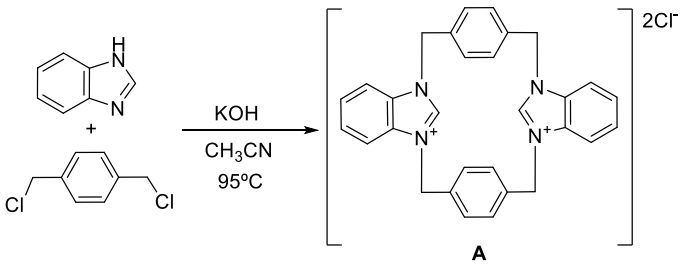

Esquema 8.1. Preparación del compuesto **A**

La estructura molecular obtenida mediante difracción de rayos X de la sal **A**, mostró información muy interesante. Los grupos benzoimidazolio de la estructura se encuentran totalmente encarados, de forma que las distancias entre los dos carbonos (N*C*N) de cada benzoimidazolio es de 5,2 Å, valor que se excede de la distancia típica M-$C_{carbene}$ (3.8-4.3 Å).[6] Este dato nos hizo prever que los complejos preparados a partir de dicha sal siempre serían de naturaleza bimetálica y nunca monometálica tipo quelato. Por otro lado, estos complejos bimetálicos pueden encontrarse en dos conformaciones posibles según la disposición de los fragmentos benzoimidazolideno, la conformación *syn* (mismo sentido*)* y la *anti* (sentidos opuestos).

De esta forma la sal de imidazolio **A** fue utilizada como precursora de carbeno N-heterocíclico, el cual fue coordinado a fragmentos metálicos de Rh e Ir mediante diferentes metodologías de complejación. Los complejos **1** y **3** se obtuvieron por transmetalación a $IrCl_2Cp^*$ y RhClCO del complejo NHC de plata, respectivamente. El complejo **2** se obtuvo mediante generación del carbeno *in situ* con NaOtBu y posterior coordinación a RhClCOD. En el esquema 8.2 se resume la preparación de los complejos **1**, **2** y **3**.

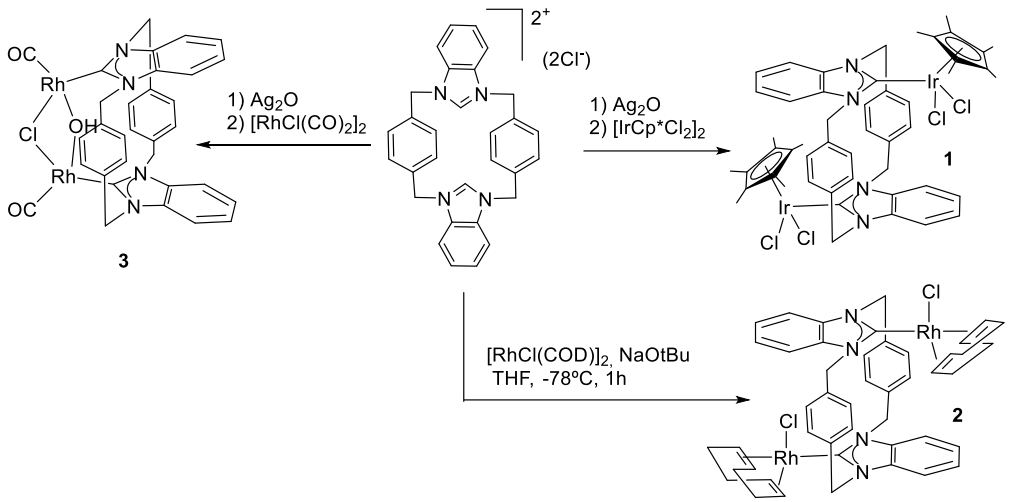

Esquema 8.2. Síntesis de los complejos **1, 2** y **3**

El ligando bis(*p*-xilil)bis(benzoimidazolideno) adoptó una disposición *syn* o *anti,* en función del fragmento metálico al cual se coordinó. La disposición *anti*, permite que los metales estén a mayor distancia unos de otros, favoreciendo un menor impedimento estérico. Esta disposición fue la adoptada cuando se coordinaron fragmentos metálicos más voluminosos (complejos **1** y **2**). Sin embargo, la geometría de los complejos resultantes fue mucho más imprevisible de lo esperado. Como se ha dicho

anteriormente, dos posibles conformaciones *syn* y *anti* pueden generarse al coordinarse los precursores de NHC ciclofano a un metal, en función de la disposición de los benzoimidazolidenos. A su vez, cada una de estas conformaciones puede formar tres posibles atropoisomeros según la disposición de los fragmentos metálicos dentro (*in*) o fuera (*out*) de los planos formados por los benzoimidazolidenos. En el esquema 8.3, se representan los tres atropoisomeros de la conformación *anti* para el complejo **1** (la disposición syn fue descarta por razones de impedimento estérico).

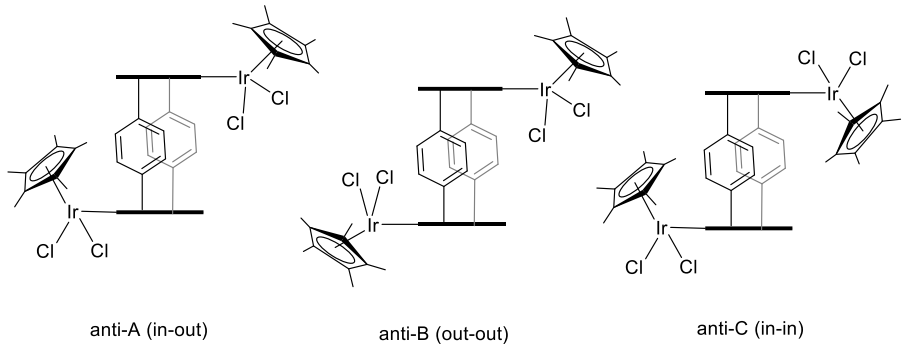

Esquema 8.3. Atropoisomeros de la conformación *anti* para el complejo **1**

En el caso de los complejos **1** y **2**, el atropoisomero formado fue el *in-out*. La geometría fue verificada mediante resonancia magnética nuclear y difracción de rayos X. Además, se llevaron a cabo cálculos de DFT (realizados por el profesor Dimitri Gusev), los cuales corroboraron que efectivamente está es la especie más estable. Las interacciones no covalentes parecen ser las responsables de la estabilización de dicho atropoisomero.

Por otro lado, el resultado obtenido fue muy diferente al utilizar fragmentos metálicos más pequeños y ligandos puente. Este es el caso del complejo **3**, donde la disposición de los metales es *syn*; y además, ambos metales de rodio se encuentran enlazados por un Cl y por un ligando OH.

8.2.2 Estudio de la influencia de grupos funcionales pireno en la actividad catalítica de complejos de paladio e iridio

Uno de los intereses más recientes del grupo de investigación del Prof. Eduardo Peris, es el diseño de nuevos sistemas multimetálicos con ligandos poliaromáticos tipo NHC, para el estudio de sus propiedades en catálisis. El interés generado en torno a este tipo de sistemas se debe a que en trabajos previos se observó una mejora en la actividad catalítica cuando se utilizaron catalizadores con ligandos poliaromáticos.[7] De hecho, este incremento en la actividad catalítica se relaciona con las interacciones tipo π-π

entre sustratos aromáticos y los ligandos poliaromáticos del catalizador. Una de las evidencias que corrobora esta hipótesis es el hecho de que al añadir aditivos de naturaleza aromática, como pireno o hexafluorobenceno, se inhibe la actividad del catalizador con ligandos poliaromáticos. [8]

Con la intención de seguir aportando nuevas evidencias acerca de la importancia de los ligandos del complejo y de la influencia de las interacciones π en catálisis, una familia de complejos de Paladio e Iridio con ligandos NHC de peculiares características fue diseñada y preparada. Se sintetizaron complejos bimetálicos basados en ligandos NHC conectados por grupos xililo o bifenilo, de forma que la distancia metal-metal fuera diferente en cada caso y se pudiera estudiar su posible efecto. Los N-sustituyentes fueron metilo y pireno, con el fin de estudiar cómo afecta en catálisis la presencia de los sustituyentes poliaromáticos del catalizador. Los complejos monometálicos análogos fueron también preparados y sus resultados catalíticos comparados con los bimetálicos, con el objetivo de comparar la influencia al tener dos metales por complejo o un metal por complejo.

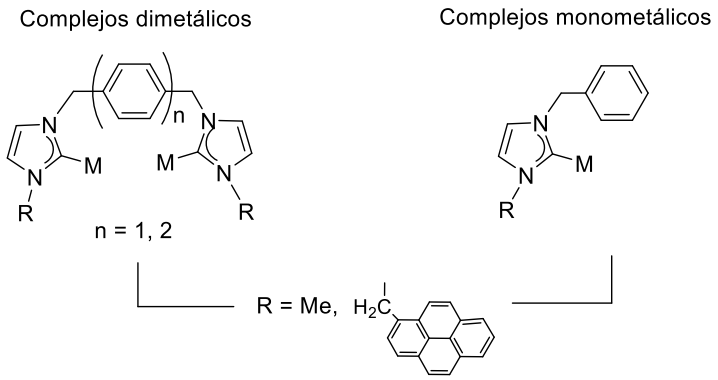

Esquema 8.4. Esquema general de los complejos bimetálicos y monometálicos preparados

8.2.2.1 Descripción de los complejos de Paladio y resultados obtenidos

El esquema 8.5 muestra los complejos de bimetálicos y monometálicos de Paladio preparados. La síntesis de dichos complejos se encuentra descrita en la parte experimental, capítulo 7.

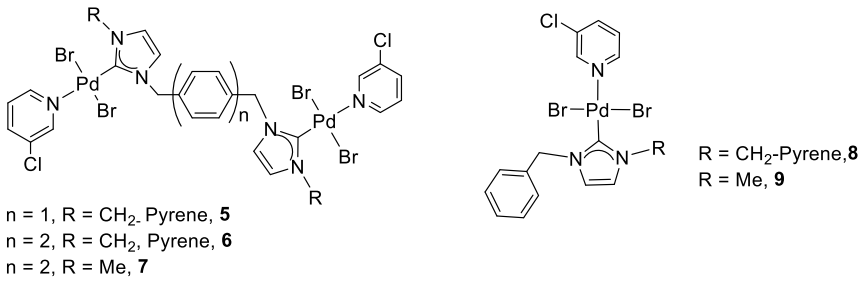

Esquema 8.5. Complejos de paladio utilizados en el estudio

La actividad de los complejos de paladio fue estudiada en la acilación de arilos de haluro con hidrocinamaldehido y en acoplamientos Suzuki-Miyaura entre haluros de arilo y ácidos borónicos. Los resultados obtenidos para ambas catálisis fueron similares:

- El complejo dimetálico de Paladio con distancia metal-metal más larga y sustituyentes pireno (complejo **6**) mostró la mejor eficiencia en catálisis.
- Los complejos bimetálicos fueron más activos que sus análogos monometálicos.
- Los complejos con grupos pireno mostraron mejores eficiencias que sus análogos con metilo.

Estos resultados pueden ser justificados atendiendo a las interacciones de tipo π *intra*-ligando o ligando-sustrato, que puedan sufrir los complejos funcionalizados con sustituyentes poliaromáticos.

Por ejemplo, el hecho de que el catalizador bimétalico con puente xililo (complejo **5**) sea menos activo en catálisis que el complejo con puente bifenilo (complejo **6**), puede ser debido a una interacción *intra*-ligando entre los pirenos del complejo **5**, la cual genera un sistema mucho más impedido estéricamente, sobretodo cerca del entorno del metal. De hecho esta conformación preferente fue verificada mediante cálculos DFT llevados a cabo por el profesor Dimitri Gusev. Este estudio DFT demostró, tal como se muestra en el esquema 8.6, la mayor estabilidad de un sistema "*π-locked*" (con interacción *intra*-ligando) frente a una conformación "*π-unlocked*" (sin interacción *intra*-ligando).

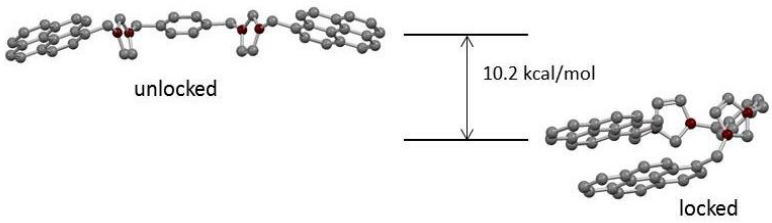

Esquema 8.6. Estructura optimizadas de la sal precursora del complejo **5** (compuesto **C**). Los cálculos se realizaron usando el método M06L-DFT

Por otro lado, la interacción ligando-sustrato aromático también parece ser la responsable del mejor resultado obtenido para los complejos con sustituyentes poliaromáticos. La veracidad de esta hipótesis se confirmó al observar la inhibición de la actividad de los catalizadores con grupos pireno, pero nunca la de los catalizadores con grupos metilo, al añadir cantidades catalíticas de aditivos poliaromáticos como pireno o antraceno.

8.2.2.2 Descripción de los complejos de Iridio y resultados obtenidos

Los complejos de iridio (I) sintetizados se muestran en el Esquema 8.7. La síntesis de dichos complejos se encuentra descrita en la parte experimental, capítulo 7.

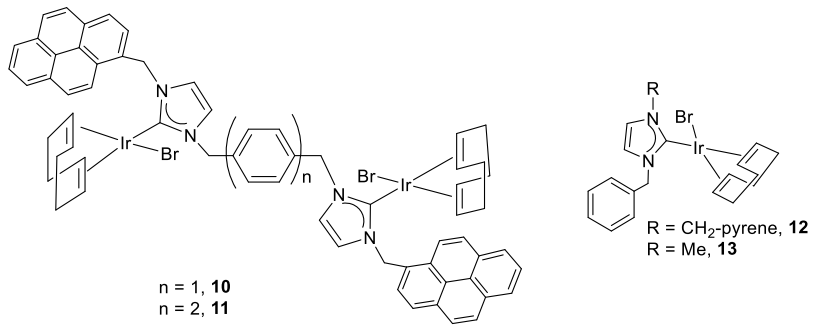

Esquema 8.7. Complejos de iridio utilizados en el estudio

La actividad catalítica de los complejos de Iridio, fue estudiada en reducciones de transferencia de hidrógeno y en la β-alquilación de alcoholes secundarios con alcoholes primarios.

Para el estudio de los catalizadores en procesos de transferencia de hidrógeno, dos reactivos fueron utilizados: acetofenona y ciclohexanona.

Los resultados obtenidos mostraron información muy interesante. En el caso de la reducción de ciclohexanona a ciclohexanol, todos los catalizadores resultaron tener una actividad catalítica similar y se observó que la adición de pireno en cantidades catalíticas no dio lugar a la modificación de la actividad catalítica. Para la reducción de acetofenona para dar 1-feniletanol, el complejo dimetálico **10** resultó ser el más activo. Además, en este caso, al añadir pireno como aditivo (cantidades catalíticas), se observó una inhibición de los catalizadores funcionalizados con sustituyentes pireno (**10**, **11** y **12**), pero no del catalizador con sustituyentes metilo (**13**). Estos resultados claramente demuestran que únicamente cuando el sustrato es aromático y el catalizador tiene sustituyentes aromáticos, hay un efecto supramolecular que influye significativamente en la actividad catalítica.

Por otro lado, en el estudio de la reacción *β*-alquilación de alcoholes secundarios con alcoholes primarios, se comprobó en primer lugar la actividad de los catalizadores en esta reacción. Los reactivos utilizados fueron 1-feniletanol y diferentes alcoholes primarios (benzil alcohol, 3-clorobenzil alcohol, 4-cloro benzil alcohol y butanol). Los resultados mostraron que el complejo **10** fue el catalizador más activo para todas las reacciones probadas.

Para entender mejor el mecanismo de reacción, se estudiaron factores cinéticos, como el orden de reacción con respecto al sustrato y el orden de reacción con respecto al catalizador. Los experimentos ofrecieron resultados fascinantes, los cuales se pueden resumir en dos puntos:

- Cuando se llevó a cabo la reacción con sustratos aromáticos y catalizadores funcionalizados con sustituyentes pireno, el orden de reacción con respecto a la concentración de sustrato fue siempre cero. Cualquier otra combinación dio orden de reacción con respecto al sustrato dos. El orden de reacción cero en estas situaciones es consecuencia de una saturación del catalizador por el sustrato debido a las interacciones del tipo π ligando-sustrato.
- El orden de reacción con respecto a la concentración de catalizador fue <1 para los catalizadores funcionalizados con ligandos pireno. Concretamente fue 0.75 para el complejo **10** y 0.5 para el complejo **12**. Comparativamente, para el complejo **13** (con grupos metilo) el orden de reacción con respecto a la concentración de catalizador fue 1. Este resultado sugiere auto-asociación entre los catalizadores con sustituyentes pireno por interacciones del tipo π ligando-ligando (Esquema 8.8), de forma que las especies no asociadas serían las especias activas. Por tanto, este resultado demuestra como los factores cinéticos en catálisis pueden verse altamente modificados en presencia o no de sustituyentes o ligandos aromáticos.

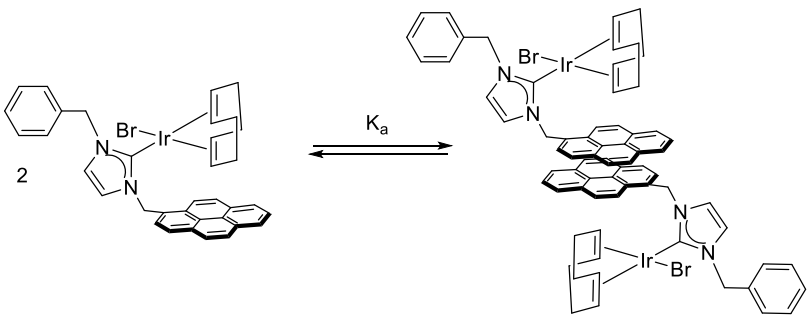

Esquema 8.8. Auto-asociación del complejo **12**

Por último, los complejos de Iridio **10** y **12** fueron soportados sobre una superficie de rGO haciendo nuevamente uso de la interacciones de tipo π entre el ligando aromático de los complejos y el soporte de grafeno. Los materiales obtenidos, **rGO-10** y **rGO-12,** fueron caracterizados por ICP-MS, TEM, EDS, SEM y UV y se estudió su aplicación en catálisis heterogénea. Concretamente, se estudió su actividad y reciclabilidad en la *β*-alquilación de 1-feniletanol con benzilalcohol. Los resultados obtenidos (Figura 8.1) mostraron que mientras el material **rGO-12** (el cual tiene soportado un complejo con un único grupo pireno) solo pudo reciclarse 6 veces, el material **rGO-10** (con dos grupos pireno) pudo reciclarse hasta 12 veces y sin pérdida aparente de actividad.

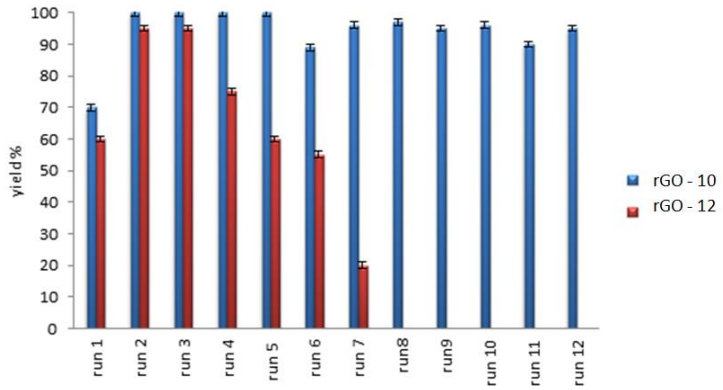

Figure 8.1. Experimentos de reciclado para los materiales rGO-10 y rGO 12 en la reacción de *β*-alquilación de 1-feniletanol con alcohol bencílico. Condiciones de reacción: 1-feniletanol (1 mmol), alcohol bencílico (1 mmol), KOH (1 mmol) and catalizadores **12**-rGO and **10**-rGO en 1.5 mL de tolueno a 100 ºC. Los rendimientos se determinaron por GC, usando anisol como patrón interno

Se determinó el contenido en Ir de los materiales antes y después llevar a cabo todos los ciclos catalíticos mediante ICP-MS, y se observó que el catalizador con únicamente un grupo pireno se desorbe fácilmente, cosa que no pasa en caso del complejo con dos pirenos, el cual está retenido con mayor efectividad al soporte.

8.2.3 Preparación de cavitandos basados en resorcinareno y estudio de sus capacidades en reconomiento molecular

Los cavitandos son moléculas con grandes cavidades capaces de encapsular moléculas de pequeño tamaño o iones.[9] Ejemplos de cavitandos son las ciclodextrinas,[10] calixarenos,[3,11] pillararenos[12] y cucurbiturilos.[13] En esta parte de la tesis, se prestó especial atención al desarrollo de cavitandos basados en calixarenos.

Los calixarenos son macrociclos u oligómeros cíclicos basados en el producto de hidroxialquilación de un fenol y un aldehído.[14] Unos de los calixarenos más ampliamente utilizados son los resorcin[4]arenos.[15] Tal como muestra la Figura 8.9, los resorcin[4]arenos pueden adoptar dos conformaciones diferentes: conformación tipo vaso, la cual es útil para encapsular pequeñas moléculas,[16] y la conformación extendida o tipo cometa, donde la encapsulación se ve desfavorecida. Factores como el pH, el disolvente y/o la temperatura, entre muchos otros, pueden provocar cambios de una conformación a otra.[15]

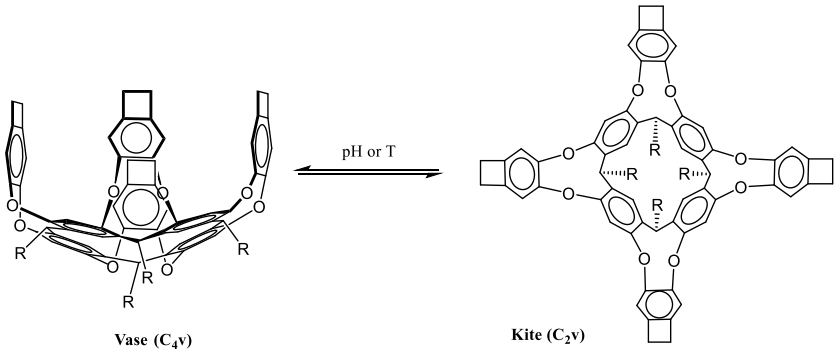

Esquema 8.9. Conformaciones del cavitando resorcinareno

Este capítulo de la tesis se divide en tres subapartdos, los cuales están basados en la funcionalización de la parte superior del cavitando para obtener nuevos compuestos con diferentes propiedades y habilidades.

8.2.3.1 Preparación de un tetra-(imidazolil-ferrocenil)-resorcinareno como receptor (*host*) de cationes tipo redox-reversible

En esta primera parte se describe la preparación y caracterización de un cavitando de tetraferrocenil resorcinareno. La obtención de dicho compuesto se llevó a cabo mediante una reacción de tetraanulación del cavitando octamino resorcinareno[17] y ferroceno carboxialdehido, en una mezcla de diclorometano y metanol (Esquema 8.10).

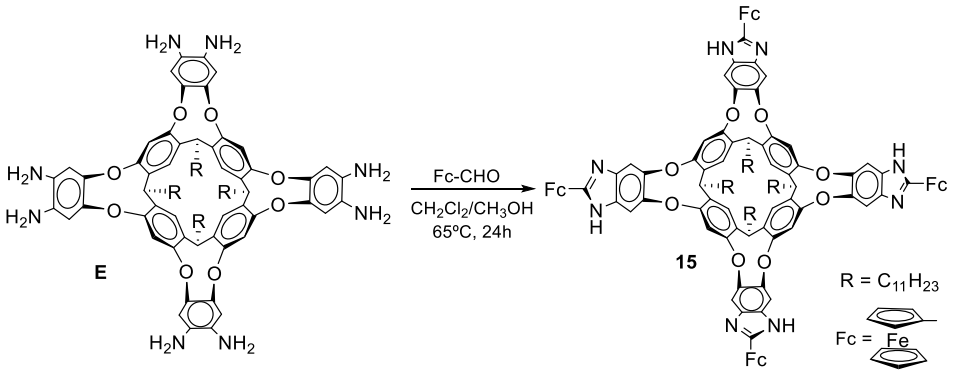

Esquema 8.10. Síntesis del cavitando de tetraferrocenilo resorcinareno

La presencia de los grupos ferrocenilo introduce características interesantes en la molécula de cavitando, por un lado porque sus propiedades de encapsulación pueden ser tipo redox-conmutables, y por otro lado porque ofrecen la posibilidad de utilizar la técnica de la voltametría cíclica para estimar las afinidades *host-guest*.

Los análisis de DFT, realizados por el Profesor Gregori Ujaque y el Dr. Pietro Vidossich, demostraron como de interesante es esta molécula, la cual sufre cambios conformacionales muy importantes de su forma reducida a su forma oxidada. Ambas formas presentan conformación tipo vaso, pero mientras que en la forma neutra los grupos ferrocenilos se encuentran apuntando hacia el interior de cavidad, en la forma oxidada están posicionados hacia el exterior de la misma. Esto corrobora efectivamente que pueda comportarse como un receptor redox-conmutable.

La capacidad de encapsulación del compuesto neutro con una serie de sales de amonio (Figura 8.2) fue analizada inicialmente mediante estudios de resonancia magnética nuclear.

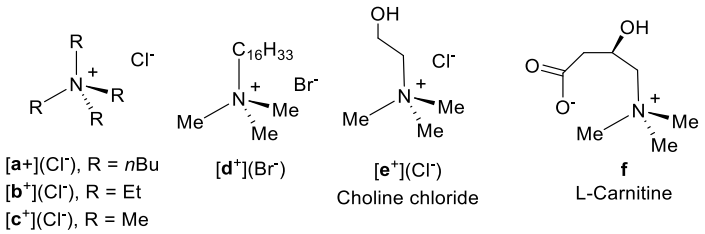

Figura 8.2. Estructuras de las sales de amonio $\mathbf{a}^{+}$-$\mathbf{e}^{+}$ y **f**

La encapsulación de los cationes de las sales de amonio mostradas fue verificada por la presencia de una nueva señal de protón a campo alto, correspondiente a los protones del *guest* encapsulado, los cuales se encuentran mucho mas apantallados debido al entorno químico, y por esa razón aparecen tan desplazados a bajas frecuencias (Figure 8.3).

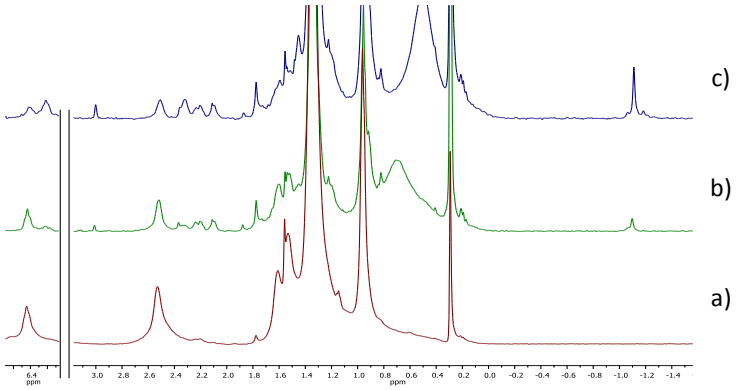

Figura 8.3. Zona representativa del espectro de RMN de protón en benceno-d^6 con una serie de cantidades crecientes de NMe_4Cl. Concentración de **15**: 3.5 mM. Concentración of NMe_4Cl, a) 0 mM, b)

3.5 mM and c) 7 mM. La señal a 6.44 ppm corresponde a la señal de protón del metino del resorcinareno cavitando no complejado. La señal a 6.31 ppm corresponde a la señal del proton del metino del resorcinarene cavitando complejado. La señal a -1.2 ppm es la señal correspondiente a los protones de los grupos metilo del catión NMe_4^+ encapsulado

Todos los cationes de las sales de amonio propuestas fueron encapsulados, a excepción de la del catión tetrabutilamonio. Este último probablemente no se encapsuló debido a su gran tamaño. Sin embargo, el compuesto **f** solo pudo ser encapsulado en presencia de un equivalente de cloruro de tetrabutilammonio, lo cual demostró que la presencia de un anión es elemento indispensable para la encapsulación del compuesto (par-iónico). Los espectros de resonancia magnética nuclear fueron estudiados y los valores de las integrales correspondientes al *host* libre y al complejo generado fueron utilizados para obtener las constantes de asociación *host-guest*.

Posteriormente, se estudió la capacidad de encapsulación del tetraferrocenil resorcinareno haciendo uso de la técnica de voltametría cíclica. Se observó que la adición de cantidades crecientes de *guests* (**b^+-e^+**) produce desplazamientos ΔE positivos, lo cual indica que los desplazamientos de potencial son debidos a la encapsulación de una especie catiónica y no aniónica. Además, esta variación de potencial también es una clara evidencia de la mayor capacidad de encapsulación de la forma neutra con respecto a la oxidada; y por lo tanto, indica la habilidad que posee el cavitando como trampa redox reversible.

Por último, el uso de la técnica de espectrometría de masas ESI reveló dos características importantes sobre la naturaleza de la encapsulación. En primer lugar, ayudó a corroborar que la estequiometria de la asociación entre el *host* y *guest* es 1:1; y en segundo lugar, mostró como de fuerte es la interacción entre ambas especies.

8.2.3.2 Cavitandos tipo tetra-azolium-resorcinareno para el reconocimiento de aniones

Debido al creciente impacto de los aniones en nuestra vida, tanto a nivel biológico como a nivel industrial,[18] el diseño de receptores aniónicos continúa generando un enorme interés en la química supramolecular.[19]

Entre todos los tipos de receptores, los compuestos basados en imidazolio han sido ampliamente investigados por autores como Sato,[20] Alcalde[21] y Kim.[22] Se sabe que el reconocimiento por parte de estas sales de imidazolio está basado en la combinación de

factores electrostáticos y de enlace de hidrógeno. Sin embargo, aunque hay un gran número de receptores basados en sales de imidazol en forma de pinza, dipodal, tripodal y otras formas,[22-23] pocos ejemplos podemos encontrar de receptores basados en sales de imidazolio con macrociclos de geometrías cerradas[16d,21,24] De esta forma nuestro objetivo está basado en la preparación de un nuevo receptor de aniones que combina la carga positiva proporcionada por una sal de imidazolio y una cavidad, lo cual puede favorecer la asociación de este receptor a aniones. Esta idea fue ya utilizada por Yoon y colaboradores previamente, los cuales prepararon un calixareno funcionalizado con cuatro anillos de imidazolio.[16d]

Basándonos en estos precedentes decidimos preparar dos cavitandos de tetra-benzimidazolio (Esquema 8.11, **16(PF$_6$)$_4$** y **17(PF$_6$)$_4$**) y estudiar su habilidad para reconocer aniones. La diferencia entre estos receptores y el resto de compuestos descritos en la bibliografía, es que en este caso los fragmentos de benzimidazolio se encuentran directamente embebidos en el resorcinareno.

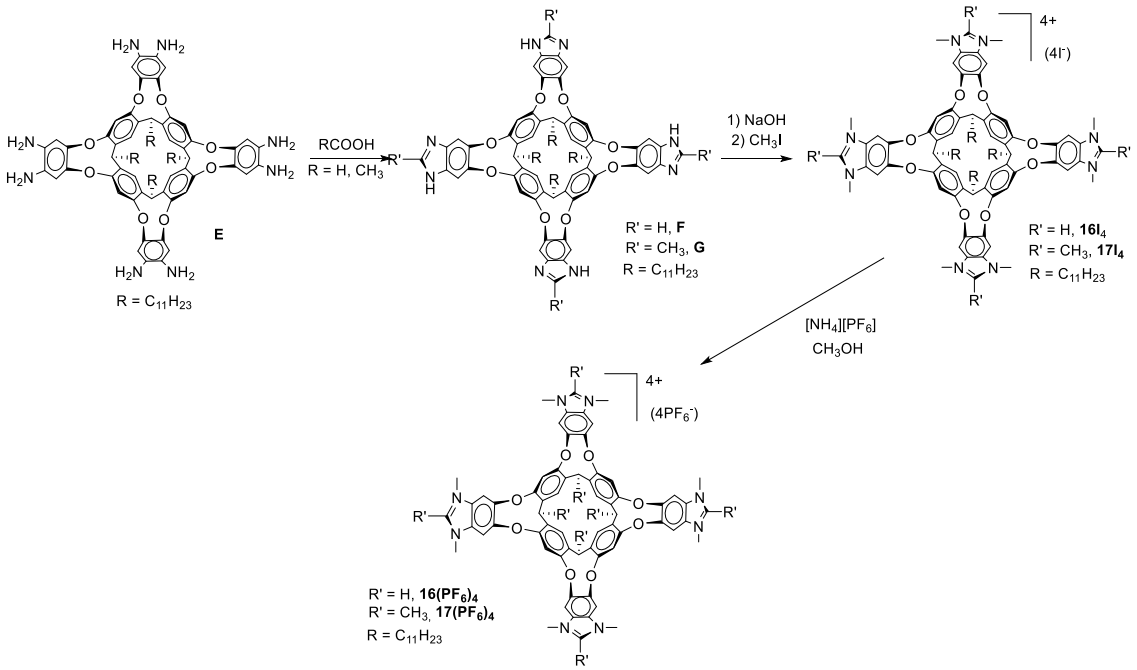

Esquema 8.11. Síntesis de los compuestos **16(PF$_6$)$_4$** y **17(PF$_6$)$_4$**

Como se muestra en el Esquema 8.11, el compuesto se obtuvo nuevamente partiendo del cavitando octamino resorcinareno,[17] el cual fue ciclado con el ácido correspondiente para obtener el compuesto con R'=H o R'=Me. Estos compuestos neutros fueron alquilados con ioduro de metilo y finalmente fueron sometidos a un cambio de contraión. Las sales de tetra-benzoimazolio cavitando con diferente funcionalización en

la parte superior de la cavidad fueron obtenidas para estudiar y comparar la influencia del grupo metilo o hidrógeno en sus capacidades para reconocer iones de diferente naturaleza.

Los compuestos fueron caracterizados por resonancia magnética nuclear y por masas de alta resolución. Se estudió la capacidad de reconocimiento de ambos *hosts* hacia cloruro, bromuro, ioduro, cianuro, nitrato, perclorato, hexanoato, fenilsulfonato y *p*-tolilsulfonato. Para ello se realizaron experimentos de valoración mediante RMN de protón, los cuales mostraron que al añadir cantidades crecientes del anión a reconocer a una muestra del receptor, las señales de protón de dicho receptor afectadas por la interacción con el anión se desplazaban (Figura 8.4).

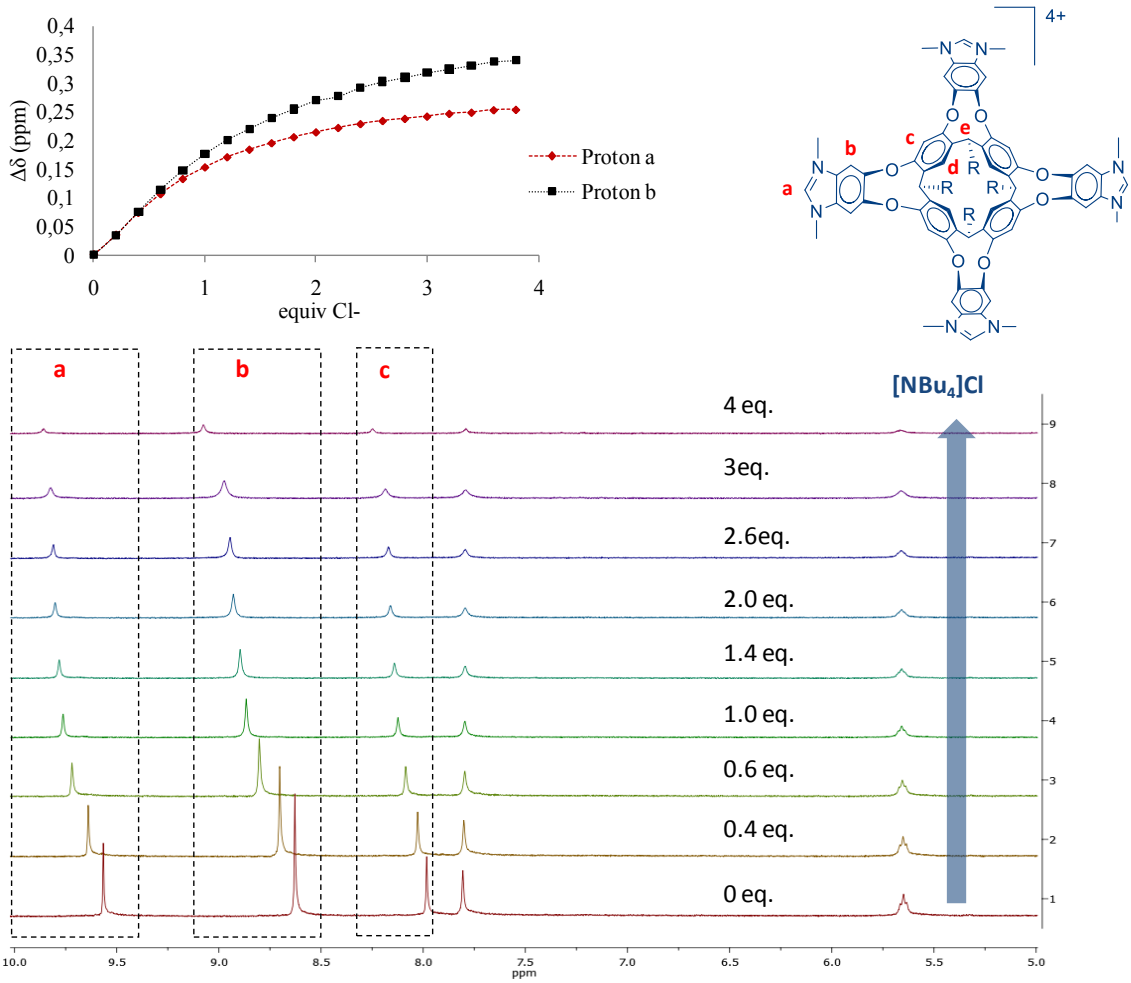

Figure 8.4. Ejemplo de la valoración del receptor $\mathbf{16}^{4+}$ con cloruro en DMSO-d^6

De hecho, los cambios observados en el espectro pudieron ser relacionados con las zonas concretas del *host* donde se producía la interacción con el anión, zonas que a su

vez fueron también verificadas mediantes estudios computacionales (Los cuales fueron llevados a cabo por los Doctores Gregori Ujaque y Pietro Vidossich). De esta forma se demostró que el cavitando **16(PF$_6$)$_4$** (tetra-benzoimidazole resorcinareno), posee en total tres zonas de reconomiento hacía un anión, en función de la naturaleza de este.

Los aniones inorgánicos y el anión hexanoato se reconocen en la parte superior del anillo (borde), aunque los aniones cloro y bromo son capaces de interaccionar también en una segunda zona, la cual se localiza entre los brazos del cavitando. Por último, los aniones con anillos aromáticos (fenilsulfonato y *p*-tolilsulfonato) se reconocen principalmente en el interior de la cavidad debido a la encapsulación de la parte aromática del anión.

Por otro lado, el compuesto **17(PF$_6$)$_4$** (2-methyltetrabenzoimidazole resorcinareno) ha perdido completamente la habilidad de interaccionar por la parte superior (borde) del cavitando con aniones inorgánicos y hexanoato; aunque sigue pudiendo reconocer aniones cloruro y bromuro gracias a la interacción de estos aniones con los brazos del cavitando. Por supuesto, este receptor sigue asociándose fuertemente a los aniones que presentan anillos aromáticos. Es decir, el compuesto **17(PF$_6$)$_4$** presenta dos zonas de reconocimiento.

Además de estudiar las zonas de reconocimiento que ofrece cada receptor, la estequiometria de la reacción y las constantes de asociación fueron obtenidas utilizando los datos extraídos de las valoraciones, los cuales fueron analizados en el programa online *Bindfit*.

8.2.3.3 Síntesis de un nuevo complejo tetrametálico de Rh(I) basado en un ligando tetra-benzoimidazolideno cavitando

En esta última parte centramos nuestra atención en la sal de tetra-benzoimidazolio cavitando **16I$_4$**, la cual puede ser utilizada como precursora de ligando Carbeno N-heterocíclico, el cual puede ser coordinado a diferentes fragmentos metálicos. En nuestro caso, el ligando NHC-cavitando fue coordinado a RhCl(COD).

Para ello se hizo reaccionar la sal **16I$_4$** con dos equivalente de [RhCl(COD)]$_2$ y K_2CO_3 a reflujo de acetona durante 20 h (Esquema 8.12). El nuevo compuesto **18** fue purificado mediante columna cromatografica, obteniéndose en un rendimiento del 30%. Se caracterizó mediante análisis elemental y masas de alta resolución. Sin embargo los espectros de protón mostraron siempre señales muy anchas, independientemente del

disolvente utilizado. Los cálculos computacionales llevados a cabo por el Profesor Gregori Ujaque y el Dr Pietro Vidossich mostraron que este ensanchamiento de la señales estaba ligado a la presencia de muchos mínimos de energía debido a la fluxionalidad de los brazos del resorcinareno. Además de esto, hay que añadir las diferentes conformaciones que pueden también obtenerse derivadas de la presencia del ligando COD.

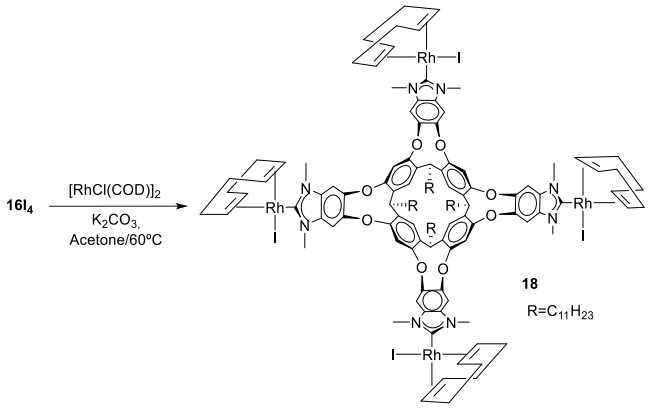

Esquema 8.12. Síntesis del compuesto **18**

8.2.4 Sales de trisazol tripodales para el reconomiento de aniones: enlace de hidrogeno *versus* enlace de halógeno

En este capítulo se describe el trabajo realizado durante la estancia pre-doctoral, la cual fue realizada en el grupo de investigación del Profesor Paul De Beer de la universidad de Oxford, Inglaterra.

Uno de los intereses del grupo de investigación es la síntesis de nuevos receptores de aniones basados en el reconocimiento de estas especies por medio de interacciones de halógeno y mostrando las ventajas que ofrece este tipo de interacción frente al enlace de hidrógeno.[25] El enlace de halógeno se define como una interacción de tipo no-covalente entre el "agujero" σ de un átomo de halógeno polarizado (ácido de Lewis) y una especia rica en electrones (base de Lewis).[26]

Siguiendo este mismo objetivo, el proyecto a desarrollar durante la estancia consistió en el diseño y preparación de cuatro receptores con un esqueleto tripodal de benceno, los cuales se funcionalizaron con tres unidades de imidazolio, triazolio y sus iodo-análogos (Esquema 8.13), con el objetivo de estudiar sus habilidades como receptores de aniones y de comparar las interacciones de halógeno y de hidrógeno. Utilizar un esqueleto tipo tripodal es bastante interesante ya que ofrece la posibilidad de funcionalizar cada brazo

del trípode de forma diferente, así como la posibilidad de que el receptor interaccione con el anión desde tres puntos distintos (efecto quelato). [23j]

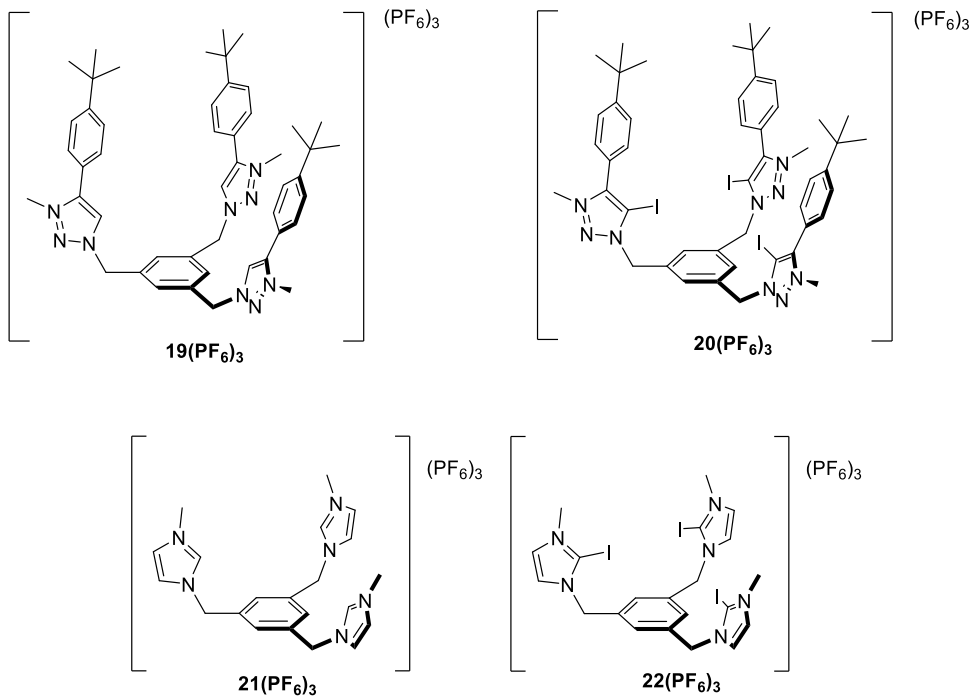

Esquema 8.13. Receptores de imidazol, triazole y los iodo-análogos

Estos receptores fueron caracterizados por resonancia magnética nuclear de protón y de carbono y masas de alta resolución. La capacidad de asociación entre dichos receptores tripodales y diferentes aniones (Cl^-, Br^-, I^- y $H_2PO_4^-$) fue estudiada mediante experimentos de valoración de RMN de protón. Se observaron desplazamientos de las señales de protón que interaccionaban con los aniones. Los datos de las valoraciones se analizaron a través del programa online *Bindfit*, los cuales permitieron conocer tanto la estequiometria del complejo generado, como la constantes de asociación *host-guest*.

Los resultados mostraron que los receptores de halógeno (**20(PF$_6$)$_3$** y **22(PF$_6$)$_3$**) formaban complejos con haluros más fácilmente que los receptores de hidrógeno (**19(PF$_6$)$_3$** y **21(PF$_6$)$_3$**); y a su vez las sales de imidazolio más fácilmente que las de triazolio. Sin embargo, en el caso del anión $H_2PO_4^-$, los receptores de hidrógeno mostraron mayores constantes de asociación que los receptores de halógeno.

Los datos experimentales fueron corroborados mediante estudios teóricos de DFT. Además se mostró que la forma en la que interacciona el complejo *host-guest* del receptor **21(PF$_6$)$_3$** (sal de imidazolio) es completamente diferente a la que presenta el receptor de **22(PF$_6$)$_3$** (sal de iodo-imidazolio). En el caso del receptor de **21(PF$_6$)$_3$** el

anión se sitúa en la posición central entre los tres brazos; sin embargo, en el caso del iodo-imidazole el anión interactúa con dos brazos de la misma molécula de receptor y con otro brazo de otra molécula. De hecho, este último dato fue consistente con los datos experimentales observados mediante difracción de rayos X de dicha molécula (Figure 8.5).

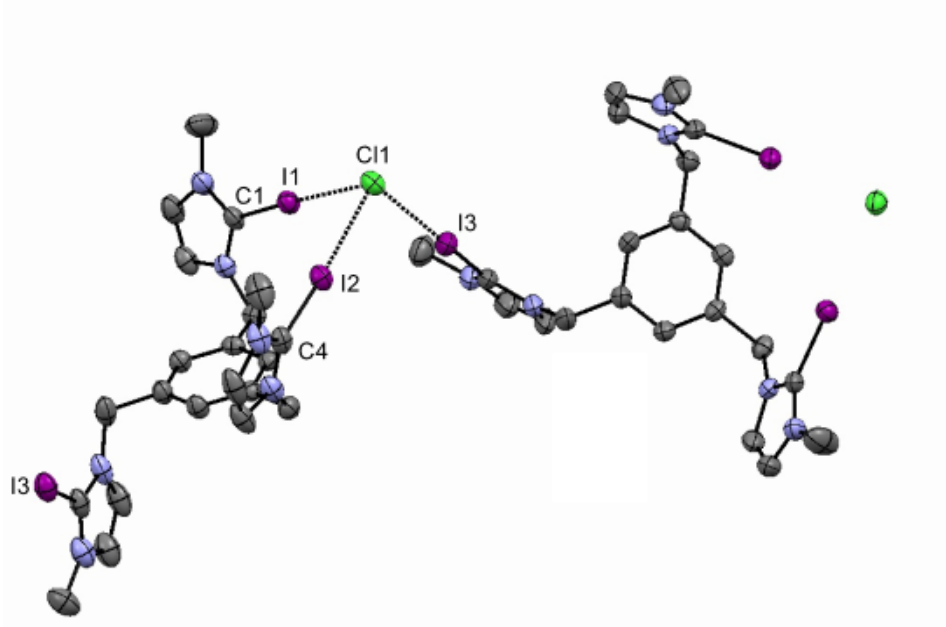

Figura 8.5. Una sección del empaquetamiento cristalino del receptor de iodo-imidazole **22**$^{3+}$. El disolvente y los aniones de BF_4^- han sido omitidos para una mayor claridad.

8.3 Conclusiones

La presente tesis doctoral, aunque está divida en dos partes claramente diferenciadas, tiene el objetivo común de mostrar la gran importancia e influencia que tienen las interacciones no-covalentes en química organométalica y supramolecular, con el fin de preparar catalizadores, receptores y materiales mejorados.

Por una lado, en la primera parte de la tesis se muestra como los catalizadores con ligandos flexibles basados en ciclofano, pueden generar especies organometálicas (de Ir y Rh) con geometrías muy exóticas.

Además y aun más interesante, se investigó y verificó la gran influencia que tiene la naturaleza de los ligandos de un catalizador en catálisis. Para ello fueron preparados complejos de naturaleza bimetálica y monometalica de Pd, Ir y Rh con ligandos NHC funcionalizados con grupos pireno o metilo. Después de haber estudiado y comparado estos complejos en diferentes procesos catalíticos, se demostró la gran influencia de las interacciones tipo π (ligando-ligando, ligando-sustrato y ligando-aditivo), tanto en la actividad catalítica como en los factores cinéticos de los catalizadores (orden respecto al sustrato y al catalizador).

Por otro lado, en la segunda parte de la tesis, el proyecto estuvo principalmente relacionado con en el diseño y preparación de nuevos receptores basados en resorcinarenos. En primer lugar se diseñó un receptor de cationes redox reversible, el cual estaba funcionalizado con cuatro grupos ferroceno. El receptor resultó ser altamente eficiente como trampa redox reversible, ya que se demostró por cálculos DFT, CV y RMN su alta capacidad de encapsulación en su forma neutra y su poca tendencia a la encapsulación en su forma oxidada.

Otra de las aproximaciones estuvo basada en la idea de embeber directamente en la parte superior del resorcinareno grupos benzoimidazolio, los cuales son altamente eficientes en el reconocimiento de aniones. De esta forma se funcionalizó la parte superior del cavitando con cuatros grupos benzoimidazolio para un receptor y con cuatro grupos 2-metil-benzoimidazolio para el otro receptor. Se determinó la capacidad de ambos compuestos como receptores de aniones; y se demostró como pequeños cambios en la preparación de un ligando pueden modificar su capacidad de reconocimiento hacia una u otra especie. La sal de tetrabenzoimidazolio resorcinareno

cavitando también fue utilizada con precursora de ligando NHC, la cual fue coordinada a un fragmento de RhCl(COD).

Por último se mostraron los resultandos obtenidos en la estancia predoctoral, la cual fue realizada en el grupo del Prof. Paul D. Beer de la universidad de Oxford. En esta parte de la tesis se describe la preparación de receptores tripodales basados en sales de imidazolio, triazolio y sus iodo-análogos, los cuales fueron preparados con el objetivo de estudiar sus capacidades en el reconocimiento molecular de aniones y de comparar la fortaleza y selectividad de las interacciones de enlace de halógeno frente a las interacciones de enlace de hidrógeno.

8.4 Referencias

(1) a) Raynal, M., Ballester, P., Vidal-Ferran, A., van Leeuwen, P. *Chem. Soc. Rev.* **2014**, *43*, 1660-1733; b) Raynal, M., Ballester, P., Vidal-Ferran, A., van Leeuwen, P. W. N. M. *Chem. Soc. Rev.* **2014**, *43*, 1734-1787.

(2) Yang, H., Yuan, B., Zhang, X., Scherman, O. A. *Acc. Chem. Res.* **2014**, *47*, 2106-2115.

(3) Rebek, J. *Chem. Commun.* **2000**, 637-643.

(4) a) Cram, D. J., Steinberg, H. *J. Am. Chem. Soc.* **1951**, *73*, 5691-5704; b) Cram, D. J., Cram, J. M. *Acc. Chem. Res.* **1971**, *4*, 204-&.

(5) Cabildo, P., Sanz, D., Claramunt, R. M., Bourne, S. A., Alkorta, I., Elguero, J. *Tetrahedron* **1999**, *55*, 2327-2340.

(6) Herrmann, W. A. *Angew Chem, Int Ed.* **2002**, *41*, 1291-1309.

(7) a) Gonell, S., Poyatos, M., Peris, E. *Angew. Chem. Int. Ed.* **2013**, *52*, 7009-7013; b) Guisado-Barrios, G., Hiller, J., Peris, E. *Chem. Eur. J.* **2013**, *19*, 10405-10411.

(8) a) Valdés, H., Poyatos, M., Peris, E. *Organometallics* **2015**, *34*, 1725-1729; b) Valdés, H., Poyatos, M., Peris, E. *Inorg. Chem.* **2015**, *54*, 3654-3659.

(9) a) D. J. Cram, J. M. C., J. F. Stoddart, *Container Molecules and Their Guests*, The Royal Society of Chemistry, **1994**; b) Palmer, L. C., Rebek, J. *Org. Biomol. Chem.* **2004**, *2*, 3051-3059; c) Trembleau, L., Rebek, J. *Science* **2003**, *301*, 1219-1220; d) Rudkevich, D. M., Rebek, J. *Eur. J. Org. Chem.* **1999**, 1991-2005.

(10) a) Roy, A., Saha, S., Roy, M. N. *Fluid Phase Equilib.* **2016**, *425*, 252-258; b) Saz, J. M., Marina, M. L. *J. Chromatogr., A* **2016**, *1467*, 79-94; c) Sun, W., She, M. Y., Yang, Z., Zhu, Y. L., Ma, S. Y., Shi, Z., Li, J. L. *J. Incl. Phenom. Macrocycl. Chem.* **2016**, *86*, 45-54.

(11) Zhou, Y., Li, H., Yang, Y. W. *Chin. Chem. Lett.* **2015**, *26*, 825-828.

(12) Ogoshi, T., Yamagishi, T. *Eur. J. Org. Chem.* **2013**, 2961-2975.

(13) a) Assaf, K. I., Nau, W. M. *Chem. Soc. Rev.* **2015**, *44*, 394-418; b) Chaban, V. V., Fileti, E. E., Malaspina, T. *Comp. Theor. Chem.* **2016**, *1083*, 7-11; c) Guo, D. S., Uzunova, V. D., Assaf, K. I., Lazar, A. I., Liu, Y., Nau, W. M. *Supramol. Chem.* **2016**, *28*, 384-395; d) Venkataramanan, N. S., Ambigapathy, S. *J. Inclusion Phenom. Macrocyclic Chem.* **2015**, *83*, 387-400; e) Zhang, M. M., Sigwalt, D., Isaacs, L. *Chem. Commun.* **2015**, *51*, 14620-14623.

(14) Moran, J. R., Karbach, S., Cram, D. J. *J. Am. Chem. Soc.* **1982**, *104*, 5826-5828.

(15) Azov, V. A., Beeby, A., Cacciarini, M., Cheetham, A. G., Diederich, F., Frei, M., Gimzewski, J. K., Gramlich, V., Hecht, B., Jaun, B., Latychevskaia, T., Lieb, A., Lill, Y., Marotti, F., Schlegel, A., Schlittler, R. R., Skinner, P. J., Seiler, P., Yamakoshi, Y. *Adv. Funct. Mater.* **2006**, *16*, 147-156.

(16) a) Hof, F., Craig, S. L., Nuckolls, C., Rebek, J. *Angew. Chem. Int. Ed.* **2002**, *41*, 1488-1508; b) Hooley, R. J., Biros, S. M., Rebek, J. *Chem. Commun.* **2006**, 509-510; c) Choi, H. J., Park, Y. S., Song, J., Youn, S. J., Kim, H. S., Kim, S. H., Koh, K., Paek, K. *J. Org. Chem.* **2005**, *70*, 5974-5981; d) Kim, S. K., Kang, B. G., Koh, H. S., Yoon, Y. J., Jung, S. J., Jeong, B., Lee, K. D., Yoon, J. *Org. Lett.* **2004**, *6*, 4655-4658.

(17) a) Zhang, K.-D., Ajami, D., Rebek, J. *J. Am. Chem. Soc.* **2013**, *135*, 18064-18066; b) Hof, F., Trembleau, L., Ullrich, E. C., Rebek, J. *Angew. Chem. Int. Ed.* **2003**, *42*, 3150-3153; c) Purse, B. W., Gissot, A., Rebek, J. *J. Am. Chem. Soc.* **2005**, *127*, 11222-11223.

(18) a) Martinez-Manez, R., Sancenon, F. *Chem. Rev.* **2003**, *103*, 4419-4476; b) Sessler, J. L., Gross, D. E., Cho, W. S., Lynch, V. M., Schmidtchen, F. P., Bates, G. W., Light, M. E., Gale, P. A. *J. Am. Chem. Soc.* **2006**, *128*, 12281-12288; c) Evans, N. H., Beer, P. D. *Angew Chem, Int Ed.* **2014**, *53*, 11716-11754; d) Gale, P. A., Garcia-Garrido, S. E., Garric, J. *Chem. Soc. Rev.* **2008**, *37*, 151-190.

(19) a) Gale, P. A., Busschaert, N., Haynes, C. J. E., Karagiannidis, L. E., Kirby, I. L. *Chem. Soc. Rev.* **2014**, *43*, 205-241; b) Busschaert, N., Caltagirone, C., Van Rossom, W., Gale, P. A. *Chem. Rev.* **2015**, *115*, 8038-8155.

(20) Sato, K., Arai, S., Yamagishi, T. *Tetrahedron Lett.* **1999**, *40*, 5219-5222.

(21) Alcalde, E., Alvarez-Rua, C., Garcia-Granda, S., Garcia-Rodriguez, E., Mesquida, N., Perez-Garcia, L. *Chem. Commun.* **1999**, 295-296.

(22) Ihm, H., Yun, S., Kim, H. G., Kim, J. K., Kim, K. S. *Org. Lett.* **2002**, *4*, 2897-2900.

(23) a) Alhashimy, N., Brougham, D. J., Howarth, J., Farrell, A., Quilty, B., Nolan, K. *Tetrahedron Lett.* **2007**, *48*, 125-128; b) Yun, S., Ihm, H., Kim, H. G., Lee, C. W., Indrajit, B., Oh, K. S., Gong, Y. J., Lee, J. W., Yoon, J., Lee, H. C., Kim, K. S. *J. Org. Chem.* **2003**, *68*, 2467-2470; c) Czirok, J. B., Bojtar, M., Hessz, D., Baranyai, P., Drahos, L., Kubinyi, M., Bitter, I. *Sens. Actuator B-Chem.* **2013**,

182, 280-287; d) Luo, K., Jiang, H. Y., You, J. S., Xiang, Q. X., Guo, S. J., Lan, J. B., Xie, R. G. *Lett. Org. Chem.* **2006**, *3*, 363-367; e) Faggi, E., Porcar, R., Bolte, M., Luis, S. V., Garcia-Verdugo, E., Alfonso, I. *J. Org. Chem.* **2014**, *79*, 9141-9149; f) Gonzalez-Mendoza, L., Altava, B., Burguete, M. I., Escorihuela, J., Hernando, E., Luis, S. V., Quesada, R., Vicent, C. *Rsc Advances* **2015**, *5*, 34415-34423; g) Sabater, P., Zapata, F., Caballero, A., de la Visitacion, N., Alkorta, I., Elguero, J., Molina, P. *J. Org. Chem.* **2016**, *81*, 7448-7458; h) Cai, J. J., Sessler, J. L. *Chem. Soc. Rev.* **2014**, *43*, 6198-6213; i) Bhardwaj, V. K., Sharma, S., Singh, N., Hundal, M. S., Hundal, G. *Supramol. Chem.* **2011**, *23*, 790-800; j) Kuswandi, B., Nuriman, Verboom, W., Reinhoudt, D. N. *Sensors* **2006**, *6*, 978-1017.

(24) a) Chun, Y., Singh, N. J., Hwang, I. C., Lee, J. W., Yu, S. U., Kim, K. S. *Nat. Commun,* **2013**, *4*; b) Dinares, I., de Miguel, C. G., Font-Bardia, M., Solans, X., Alcalde, E. *Organometallics* **2007**, *26*, 5125-5128; c) Dinares, I., de Miguel, C. G., Mesquida, N., Alcalde, E. *J. Org. Chem.* **2009**, *74*, 482-485; d) Wong, W. W. H., Vickers, M. S., Cowley, A. R., Paul, R. L., Beer, P. D. *Org. Biomol. Chem.* **2005**, *3*, 4201-4208.

(25) a) Gilday, L. C., Beer, P. D. *Chem. Eur. J.* **2014**, *20*, 8379-8385; b) Gilday, L. C., Lang, T., Caballero, A., Costa, P. J., Felix, V., Beer, P. D. *Angew Chem, Int Ed.* **2013**, *52*, 4356-4360; c) Kilah, N. L., Wise, M. D., Serpell, C. J., Thompson, A. L., White, N. G., Christensen, K. E., Beer, P. D. *J. Am. Chem. Soc.* **2010**, *132*, 11893-11895; d) Langton, M. J., Robinson, S. W., Marques, I., Felix, V., Beer, P. D. *Nature Chem.* **2014**, *6*, 1039-1043; e) Mullaney, B. R., Thompson, A. L., Beer, P. D. *Angew. Chem. Int. Ed.* **2014**, *53*, 11458-11462; f) Serpell, C. J., Kilah, N. L., Costa, P. J., Felix, V., Beer, P. D. *Angew Chem, Int Ed.* **2010**, *49*, 5322-5326.

(26) Brown, A., Beer, P. D. *Chem. Commun.* **2016**, *52*, 8645-8658.